School of Electrical Engineering, Computing & Mathematical Sciences

Nuclear Dynamics in the Molecular Convergent Close-Coupling Method

Liam Hall Scarlett
0000-0002-9900-9712

This thesis is presented for the Degree of
Doctor of Philosophy
of
Curtin University

November 2021

Declaration

To the best of my knowledge and belief this thesis contains no material previously published by any other person except where due acknowledgement has been made.

This thesis contains no material that has been accepted for the award of any other degree or diploma in any university.

Portions of this thesis contain extracts from my own published work in which the copyright is held by the publisher. In each case the publishers provide the right to use an article or a portion of an article in a thesis or dissertation without requesting permission.

Liam H. Scarlett

November 23, 2021

Summary

This thesis is devoted to the theoretical study of collisions between electrons and the hydrogen molecule (H_2), as well as its five isotopologues (HD, D_2, HT, DT, and T_2). The technique applied is the molecular convergent close-coupling (MCCC) method, which was initially developed during two previous PhD projects [J. S. Savage (2018), M. C. Zammit (2015)]. The particular focus here is on the treatment of nuclear dynamics in the MCCC calculations.

The work presented here was recognised at the 2021 Western Australian Premier's Science Awards, where the candidate was a joint recipient of the Student Scientist of the Year award, for *"an outstanding postgraduate student who has demonstrated a commitment to science at an early stage and shows great promise in reaching the highest levels of excellence"*.

Objectives

The three primary goals of this research project were (a) to produce a large set of vibrationally-resolved collision data for the e^--H_2 system utilising the existing MCCC method along with the adiabatic-nuclei approximation, (b) to facilitate the use of the MCCC cross sections in plasma-modelling applications, and (c) to develop a new variant of the MCCC method which does not rely on the adiabatic-nuclei approximation. Specifically, the main objectives were to:

1. Develop code to perform adiabatic-nuclei calculations with input from the fixed-nuclei MCCC code.

2. Extend previous spherical-coordinate fixed-nuclei calculations [Zammit *et al.*, Phys. Rev. A **95**, 022708 (2017)] of e^--H_2 scattering, by using the spheroidal-coordinate adiabatic-nuclei formalism to produce collision data for scattering on the vibrationally-excited ground electronic state of H_2 and its isotopologues.

3. Perform convergence studies for scattering on excited electronic states to allow similar vibrationally-resolved calculations to be performed.

4. Develop the theoretical methods and code for performing MCCC calculations with the electronic and vibrational levels explicitly coupled, allowing for the investigation of resonances in e^--H_2 scattering.

5. Incorporate rotational transitions into the MCCC method.

Major results

1. Produced the most comprehensive and accurate set of vibrationally-resolved electronic excitation cross sections for e^--H_2 scattering ever produced (approximately 60,000 transitions including the isotopologues). This includes transitions from all bound vibrational levels of the ground electronic state ($X\,^1\Sigma_g^+$) to all bound levels and dissociative excitation of the $b\,^3\Sigma_u^+$, $B\,^1\Sigma_u^+$, $c\,^3\Pi_u$, $a\,^3\Sigma_g^+$, $C\,^1\Pi_u$, $EF\,^1\Sigma_g^+$, $e\,^3\Sigma_u^+$, $B'\,^1\Sigma_u^+$, $d\,^3\Pi_u$, $h\,^3\Sigma_g^+$, $GK\,^1\Sigma_g^+$, $g\,^3\Sigma_g^+$, $i\,^3\Pi_g$, $I\,^1\Pi_g$, $j\,^3\Delta_g$, $J\,^1\Delta_g$, $D\,^1\Pi_u$, and $H\,^1\Sigma_g^+$ states [Scarlett *et al.*, Atom. Data Nucl. Data Tables **137**, 101361 (2021); Atom. Data Nucl. Data Tables **139**, 101403 (2021)] The results obtained were utilised in studies of vibrational excitation of the ground state via radiative decay [Scarlett *et al.*, Plasma Sources Sci. Technol. **28**, 025004 (2019)], dissociation of vibrationally-excited H_2 into neutral fragments [Scarlett *et al.*, Atoms **7**(3), 75 (2019)], and have been incorporated in a collisional-radiative model as part of a collaboration with the Max-Planck Institute of Plasma Physics in Garching, Germany [Wünderlich *et al.*, J. Phys. D: Applied Physics **54**, 115201 (2021)].

2. Demonstrated convergence in electronic excitation, elastic, superelastic, and ionisation cross sections for scattering on the $B\,^1\Sigma_u^+$, $c\,^3\Pi_u$, $a\,^3\Sigma_g^+$, $C\,^1\Pi_u$, and $EF\,^1\Sigma_g^+$ states of H_2, including transitions to all states mentioned in the previous point [Scarlett *et al.*, Phys. Rev. A **103**, 032802 (2021)]. Significant disagreement was found with previous calculations in many cases.

3. Demonstrated errors in the theory which was used in previous calculations of

low-energy e^--H_2 dissociation cross sections that have been used in plasma-modelling applications for the past 20 years [Trevisan *et al.*, Plasma Phys. Contr. Fusion 44 1263 (2002); 44, 2217 (2002)]. Substantial differences were found in the vibrational-level and isotopic dependence of the cross sections when compared to the accurate results produced here [Scarlett *et al.*, Phys. Rev. A **103**, L020801 (2021)].

4. Developed new code to perform vibrational-electronic molecular convergent close-coupling (VE MCCC) calculations. This is the first ever electron-molecule scattering method in which resonant and non-resonant scattering are treated on the same footing and coupled to each other. Calculations were performed in the 10–14 eV energy region, where a number of well-known H_2^- states are located, and cross sections were produced which show rich resonance structures [Scarlett *et al.*, Phys. Rev. Lett. **127**, 223401 (2021)].

5. Performed derivations for incorporating rotational transitions into the MCCC methods. A framework for the future extension of the VE MCCC method to also include coupling to rotational levels was laid out, and an adiabatic-nuclei treatment of rotational motion was used to investigate the polarisation of Fulcher-α fluorescence following electron-impact excitation of the H_2 $d\ ^3\Pi_u$ rotational levels [Scarlett *et al.*, Phys. Rev. A **104**, L040801 (2021)].

Layout of the thesis

Part I - Preliminaries contains introductory material and general theory:

Chapter 1 contains an introduction to the field of collision physics and its applications, a summary of the present state of the field, and the objectives of this project.

Chapter 2 contains a brief overview of quantum scattering theory.

Chapter 3 presents a detailed overview of the electronic and nuclear structure of diatomic molecules, including the various approximations and

forms of the molecular wave functions which will be utilised in later chapters.

Chapter 4 contains an overview of the different molecular scattering processes, as well as various definitions and approximations which are common to most scattering theories.

Chapter 5 contains a review of existing scattering theories, focusing specifically on those which have been applied to electron-molecule scattering.

Part II - Adiabatic-nuclei MCCC describes the adiabatic-nuclei molecular convergent close-coupling method and presents results:

Chapter 6 outlines the development of the fixed-nuclei molecular convergent close-coupling method - the work of a number of current and past members of the Curtin Theoretical Physics Group.

Chapter 7 describes the methodology and implementation of the adiabatic-nuclei molecular close-coupling method.

Chapter 8 presents adiabatic-nuclei results obtained from the fixed-nuclei collision data using a post-processing code developed during this project.

Part III - Vibrational-electronic molecular convergent close-coupling contains the primary new development of the PhD:

Chapter 9 discusses the theoretical details of a new method with the capacity to perform more accurate low-energy molecular scattering calculations, including resonance effects, utilising vibrational-electronic close-coupling.

Chapter 10 presents results for low-energy and resonant scattering on H_2 and its isotopologues, with comparisons to the adiabatic-nuclei approximation.

Part IV - Rotational dynamics discusses rotationally-resolved scattering:

Chapter 11 presents derivations of rotationally-resolved cross sections in the molecular convergent close-coupling formalism.

Chapter 12 presents calculations of the linear polarisation fractions of Fulcher-α emission following electron-impact rotational excitation of the H_2 $d\ ^3\Pi_u$ state.

Finally, *Chapter 13* contains the conclusions and future directions for this research.

A number of appendices contain useful definitions or derivations.

Acknowledgements

The work presented in this thesis was undertaken with financial support from the Australian Government Research Training Program, the Forrest Research Foundation, the Australian Research Council, and the United States Air Force Office of Scientific Research. High-performance computing resources were provided by the Pawsey Supercomputing Centre and National Computational Infrastructure, with funding from the Australian Government and Government of Western Australia, and by the Texas Advanced Computing Center (TACC) at The University of Texas at Austin.

I am grateful to my supervisor Prof. Dmitry Fursa and cosupervisor Prof. Igor Bray for their support and time invested in my education throughout my undergraduate and Honours degrees and my PhD. The difficult task of completing a PhD was made easy having supervisors willing to share with me as much of their time, knowledge, and advice as I needed on a daily basis. I appreciate all of the staff and students of the Theoretical Physics Group at Curtin for providing such a friendly and supportive atmosphere and making it a pleasure to come into the office each day. I'd like to specifically thank Una Rehill for working with me on implementing the rotational excitation code during her Honours project, and for providing feedback on some early versions of my thesis chapters.

This project would not have been possible without the prior work undertaken during the PhDs of Dr. Mark Zammit and Dr. Jeremy Savage. I am particularly thankful to Mark for being a mentor and additional supervisor to me throughout this journey.

During this PhD I have had the pleasure of collaborating with a number of researchers from around the world. I am grateful to Dr. Dirk Wünderlich and Prof. Ursel Fantz for leading our fruitful collaboration on collisional-radiative modelling of hydrogenic plasmas, and Prof. Klaus Bartschat, Dr. Barry Schneider and Dr. Yuri Ralchenko for their assistance and contributions to some of our publications.

It has been a pleasure living in Forrest Hall for the last four years surrounded by other PhD students. I am grateful to Prof. Paul Johnson and Rochelle Gunn for taking care of us, and to the other residents for their friendship and conversations. I must specifically thank my dear friend Gladymar Pérez for her support, encouragement, and companionship throughout our PhDs.

I would not have made it here without my family. I am eternally grateful to my parents for their unending love and support, and for encouraging me to pursue a higher education. I am also grateful to my Auntie Georgie for the many conversations about science and for the encouragement to do a PhD. I am thankful to Priscilla for always being present and filling my life with songs. Most important of all, I thank my beloved partner Katie; your loving company and unconditional support has helped me every step of the way.

Cheers to AJ, DC, JC, and MJK for providing the soundtrack to my PhD.

Acknowledgement of country

We acknowledge Aboriginal and Torres Strait Islander people as the Traditional Custodians of the land and waters of Australia. We also acknowledge the Nyoongar Whadjuk Elders, their people, and their land upon which Curtin University is built.

List of publications

During the candidacy of this PhD project (2018–2021) and the previous Honours year (2017), 20 papers were published in refereed journals. These are listed here in reverse chronological order. Author contribution statements for each publication are provided in Appendix E.

20. **L. H. Scarlett**, I. Bray, and D. V. Fursa, "Electronic and vibrational close-coupling method for resonant electron-molecule scattering", Phys. Rev. Lett. **127**, 223401 (2021) **(Editors' Suggestion)**

19. R. K. Horton, **L. H. Scarlett**, M. C. Zammit, I. Bray, and D. V. Fursa, "Electron energy deposition in molecular hydrogen gas: a Monte-Carlo simulation using convergent close-coupling cross sections", Plasma Sources Sci. Technol. **30**, 115004 (2021)

18. **L. H. Scarlett**, U. S. Rehill, M. C. Zammit, K. Bartschat, I. Bray, and D. V. Fursa, "Linear polarization fractions of Fulcher-α fluorescence in electron collisions with H_2", Phys. Rev. A **104**, L040801 (2021)

17. **L. H. Scarlett**, D. V. Fursa, J. Knol, M. C. Zammit, and I. Bray, "Isotopic and vibrational-level dependence of H_2 dissociation by electron impact", Phys. Rev. A **103**, L020801 (2021)

16. **L. H. Scarlett**, J. S. Savage, D. V. Fursa, I. Bray, M. C. Zammit, and B. I. Schneider, "Convergent close-coupling calculations of electrons scattering on electronically-excited molecular hydrogen", Phys. Rev. A **103**, 032802 (2021)

15. **L. H. Scarlett**, D. V. Fursa, M. C. Zammit, I. Bray, and Yu. Ralchenko, "Complete collision data set for electrons scattering on molecular hydrogen and its isotopologues: II. Fully vibrationally-resolved electronic excitation of the isotopologues of $H_2(X\ ^1\Sigma_g^+)$", At. Data Nucl. Data Tables **139**, 101403 (2021)

14. **L. H. Scarlett**, D. V. Fursa, M. C. Zammit, I. Bray, Yu. Ralchenko, and K. D. Davie, "Complete collision data set for electrons scattering on molecular hydrogen and its isotopologues: I. Fully vibrationally-resolved electronic excitation of $H_2(X\ ^1\Sigma_g^+)$", At. Data Nucl. Data Tables **137**, 101361 (2021)

13. D. Wünderlich, **L. H. Scarlett**, S. Briefi, U. Fantz, M. C. Zammit, D. V. Fursa, and I. Bray, "Application of molecular convergent close-coupling cross sections in a collisional radiative model for the triplet system of molecular hydrogen", J. Phys. D. Appl. Phys. **54**, 115201 (2021)

12. T. Meltzer, J. Tennyson, Z. Masin, M. C. Zammit, **L. H. Scarlett**, D. V. Fursa, and I. Bray, "Benchmark calculations of electron impact electronic excitation of the hydrogen molecule", J. Phys. B **53**, 145204 (2020)

11. **L. H. Scarlett**, J. S. Savage, D. V. Fursa, I. Bray, and M. C. Zammit, "Electron-scattering on molecular hydrogen: convergent close-coupling approach", Eur. Phys. J. D **74**, 36 (2020)

10. N. Mori, R. Utamuratov, **L. H. Scarlett**, D. V. Fursa, A. S. Kadyrov, I. Bray, and M. C. Zammit, "Calculations of positron scattering on the hydrogen molecular ion", J. Phys. B **53**, 015203 (2020)

9. **L. H. Scarlett**, J. S. Savage, D. V. Fursa, M. C. Zammit, and I. Bray, "Electron-impact dissociation of vibrationally-excited molecular hydrogen into neutral fragments", Atoms **7**, 75 (2019)

8. **L. H. Scarlett**, J. K. Tapley, J. S. Savage, D. V. Fursa, M. C. Zammit, and I. Bray, "Vibrational excitation of the H_2 $X\ ^1\Sigma_g^+$ state via electron-impact excitation and radiative cascade", Plasma Sources Sci. Technol. **28**, 025004 (2019)

7. M. Zawadzki, R. Wright, G. Dolmat, M. F. Martin, B. Diaz, L. Hargreaves, D. Coleman, D. V. Fursa, M. C. Zammit, **L. H. Scarlett**, J. K. Tapley, J. S. Savage, I. Bray, and M. A. Khakoo, "Low-energy scattering from molecular hydrogen: excitation of the $X\ ^1\Sigma_g^+ \rightarrow b\ ^3\Sigma_u^+$ transition", Phys. Rev. A **98**, 062704 (2018)

6. J. K. Tapley, **L. H. Scarlett**, J. S. Savage, D. V. Fursa, M. C. Zammit, and I. Bray, "Electron-impact dissociative excitation of singlet states of molecular hydrogen", Phys. Rev. A **98**, 032701 (2018)

5. J. K. Tapley, **L. H. Scarlett**, J. S. Savage, M. C. Zammit, D. V. Fursa, and I. Bray, "Vibrationally resolved electron-impact excitation cross sections for singlet states of molecular hydrogen", J. Phys. B **51**, 144007 (2018)

4. M. Zawadzki, R. Wright, G. Dolmat, M. F. Martin, L. Hargreaves, D. V. Fursa, M. C. Zammit, **L. H. Scarlett**, J. K. Tapley, J. S. Savage, I. Bray, and M. A. Khakoo, "Time-of-flight electron scattering from molecular hydrogen: Benchmark cross sections for excitation of the $X\ ^1\Sigma_g^+ \rightarrow b\ ^3\Sigma_u^+$ transition", Phys. Rev. A **97**, 050702(R) (2018)

The below were written during the Honours year and are not claimed towards this thesis.

3. **L. H. Scarlett**, J. K. Tapley, D. V. Fursa, M. C. Zammit, J. S. Savage, and I. Bray, "Electron-impact dissociation of molecular hydrogen into neutral fragments", Eur. Phys. J. D **72**, 34 (2018)

2. **L. H. Scarlett**, J. K. Tapley, D. V. Fursa, M. C. Zammit, J. S. Savage, and I. Bray, "Low-energy electron-impact dissociative excitation of molecular hydrogen and its isotopologues", Phys. Rev. A **96**, 062708 (2017)

1. **L. H. Scarlett**, M. C. Zammit, D. V. Fursa, and I. Bray, "Kinetic-energy release of fragments from electron-impact dissociation of the molecular hydrogen ion and its isotopologues", Phys. Rev. A **96**, 022706 (2017)

Conference presentations

The work undertaken during this PhD project and the previous Honours year has been presented by the candidate at a number of international conferences. A selection of notable examples is presented below in reverse chronological order.

- **L. H. Scarlett**, D. V. Fursa, and I. Bray, "Electronic and vibrational close-coupling method for resonant electron-molecule scattering", *Contributed talk*, GEC LXXIV, (2021), virtual

- **L. H. Scarlett**, D. V. Fursa, M. C. Zammit, J. S. Savage, and I. Bray, "Rovibrationally-resolved electron scattering on H_2: Molecular convergent close-coupling calculations", *Invited Progress Report*, ICPEAC XXXII, (2021), virtual

- **L. H. Scarlett**, D. V. Fursa, and I. Bray, "Vibronic close-coupling calculations of e^--H_2 scattering", *Contributed talk*, GEC LXXIII, (2020), virtual

- **L. H. Scarlett**, J. S. Savage, D. V. Fursa, M. C. Zammit, and I. Bray, "Electron-impact vibrational excitation of molecular hydrogen", *Invited talk*, POSMOL VIII, (2019), Belgrade, Serbia

- **L. H. Scarlett**, J. K. Tapley, D. V. Fursa, J. S. Savage, M. C. Zammit, and I. Bray, "Vibrationally-resolved electron-impact excitation and dissociation of molecular hydrogen", *Contributed poster*, ICPEAC XXXI, (2019), Deauville, France

- **L. H. Scarlett**, J. K. Tapley, D. V. Fursa, J. S. Savage, I. Bray, and M. C. Zammit, "Vibrationally-resolved electron-impact excitation of molecular hydrogen", *Contributed talk*, GEC LXXI, (2018), Portland, OR, USA

- **L. H. Scarlett**, J. K. Tapley, D. V. Fursa, J. S. Savage, I. Bray, and M. C. Zammit, "Vibrationally-resolved electron-impact excitation of molec-

ular hydrogen", *Contributed talk*, ICAMDATA XI, (2018), Cambridge, MA, USA

- **L. H. Scarlett**, J. K. Tapley, D. V. Fursa, J. S. Savage, M. C. Zammit, and I. Bray, "Vibrationally-resolved electron-impact excitation of molecular hydrogen", *Contributed talk*, GEM XX, (2018), Magnetic Island, Australia

- **L. H. Scarlett**, M. C. Zammit, D. V. Fursa, and I. Bray, "Kinetic energy release of fragments from electron impact dissociation of the molecular hydrogen ion", *Contributed poster*, ICPEAC XXX, (2017), Cairns, Australia

Statement of contribution of others

The convergent close-coupling method was originally developed for electron-atom collisions by Prof. Igor Bray and Prof. Andris Stelbovics. The many subsequent extensions to different scattering systems all utilise the same general techniques and would not have been possible without their original contribution.

The extension to scattering on one- and two-electron diatomic molecular targets was conducted during the PhD projects of Dr. Mark Zammit and Dr. Jeremy Savage, under the supervision of Prof. Dmitry Fursa. The adiabatic-nuclei results for scattering on H_2 presented in Chapter 8 were obtained using a post-processing code developed by the candidate. The fixed-nuclei T-matrix elements required to generate these results were obtained from the molecular scattering code developed by JS, MZ, and DF. The candidate was responsible for determining the appropriate structure and scattering models and performing the fixed-nuclei scattering calculations. The fixed-nuclei calculations were performed in spheroidal coordinates and would not have been possible without JS's development of the spheroidal scattering code. The results pertaining to collisional-radiative modelling presented in Chapter 8 are the product of a collaboration with Dr. Dirk Wünderlich and Prof. Ursel Fantz at the Max Planck Institute for Plasma Physics in Garching, Germany.

The development of the code for the VE MCCC method outlined in Chapter 9 was performed solely by the candidate, under the supervision of Prof. Dmitry Fursa. The electronic V-matrix elements required as input are obtained from code developed by Dr. Savage, and several miscellaneous subroutines were adopted from codes developed by Profs. Fursa and Bray.

The derivations presented in Chapter 11 for the rotational excitation cross sections were conducted by the candidate. These are essentially generalisations of previous derivations which are referenced as appropriate in the text. The im-

plementation of rotational excitations into the adiabatic-nuclei scattering code was conducted primarily by Una Rehill as a part of her undergraduate research project, under the supervision of the candidate. The derivations presented in Chapter 12 for the Fulcher-α linear polarisation fractions were performed by the candidate, with assistance from Prof. Klaus Bartschat. The coding and calculations for the polarisation fractions were performed by the candidate.

All of the results presented in this thesis have been published in various peer-reviewed physics journals as catalogued in the list of publications on page 11. Each of these papers was a collaborative effort, and the personal contributions of the author to each one are detailed in the signed statement of others in Appendix E.

Signature of candidate: 

Signature of supervisor: 

Contents

List of figures

8 Adiabatic-nuclei results for electron scattering on H_2

List of tables

Part I

Preliminaries

Chapter 1

Introduction

1.1 Quantum collisions

The field of quantum collisions is concerned with the study of reactions between fundamental particles, atoms, and molecules. Collisions which take place at this scale are governed by the laws of quantum mechanics, and hence their study is a matter of determining the probability associated with each reaction possible between the two reactants. Scattering probabilities are quantified by the *cross section*, a hypothetical area about the target species which the projectile must hit in order to instigate a specific reaction. The *differential* cross section is illustrated in Fig. 1.1. The projectile is incident on an area $\delta\sigma$ and is scattered into a solid angle $\delta\Omega$ about an angle of deflection θ (note that since the scattering system is cylindrically symmetric we can align the incident direction with the z axis and consider only the zenith scattering angle). The differential cross section is defined as the ratio of $\delta\sigma$ to $\delta\Omega$ in the limit as $\delta\Omega$ approaches zero (remembering that $\delta\sigma$ is a function of $\delta\Omega$):

$$\frac{\mathrm{d}\sigma}{\mathrm{d}\Omega} \equiv \lim_{\delta\Omega\to 0} \frac{\delta\sigma(\delta\Omega)}{\delta\Omega}. \tag{1.1}$$

The differential cross section is a function of the incident projectile energy and scattering angle, and depends also on the type of reaction, e.g. elastic scattering, excitation or ionisation of the target, etc. The *integrated* cross section is defined by

$$\sigma \equiv \iint_{\Omega} \frac{\mathrm{d}\sigma}{\mathrm{d}\Omega}\,\mathrm{d}\Omega \;=\; 2\pi \int_{0}^{\pi} \frac{\mathrm{d}\sigma}{\mathrm{d}\Omega}\sin\theta\,\mathrm{d}\theta. \tag{1.2}$$

This quantity represents the hypothetical area upon which the projectile must be incident for a particular reaction to occur, irrespective of the scattering angle.

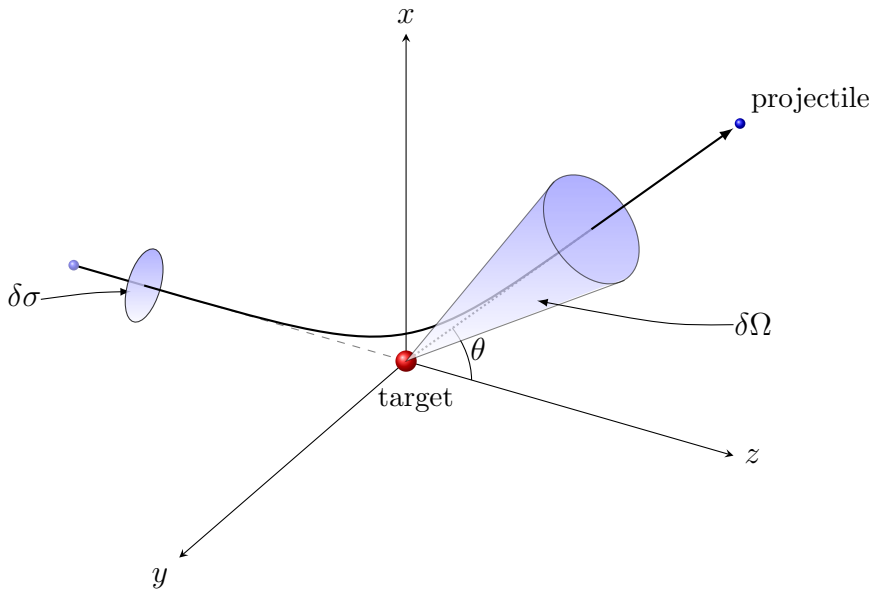

Figure 1.1: Schematic of the scattering process.

Determining the differential and/or integrated cross sections for the various reactions of a particular scattering system are the major aims of a scattering experiment or calculation. This is a challenging task for theorists and experimentalists alike, and it is often the case that both calculations and measurements are performed for a given scattering system in order to provide benchmark data and produce the most accurate set of recommended cross sections.

1.2 Diatomic molecule scattering processes

Diatomic molecules consist of two nuclei, which will be referred to here as nucleus A and nucleus B, along with a number of electrons. A diatom has only one vibrational and one rotational mode, so its state is designated by a vibrational quantum number v, rotational quantum number N, and an index n of the electronic state. Note that n is only an index, and not a principal quantum number, and the use of the symbol N to denote the rotational state assumes a particular angular-momentum coupling case which will be described in Chapter 3. The different types of electron-impact diatomic scattering processes are defined in Table 1.1. Processes which end in a dissociative molecular state (denoted by asterisks) lead

Table 1.1: Definition of electron-impact diatomic scattering processes. Asterisks denote dissociative molecular states. Emission of a photon is denoted by the γ symbol.

$e^- + AB(n,v,N) \rightarrow AB(n,v,N) + e^-$	elastic scattering
$e^- + AB(n,v,N) \rightarrow AB(n',v',N') + e^-$	excitation
$e^- + AB(n,v,N) \rightarrow AB(n',v',N')^* + e^-$ $\rightarrow A + B + e^-$	dissociative excitation
$e^- + AB(n,v,N) \rightarrow AB^+(n',v',N') + 2e^-$	non-dissociative ionisation
$e^- + AB(n,v,N) \rightarrow AB^+(n',v',N')^* + e^-$ $\rightarrow A + B^+ + 2e^-$	dissociative ionisation
$e^- + AB(n,v,N) \rightarrow AB^-(n',v',N')^*$ $\rightarrow A + B^- + e^-$	dissociative attachment
$e^- + AB(n,v,N) \rightarrow AB(n',v',N') + e^-$ $\rightarrow AB(n'',v'',N'') + \gamma + e^-$	excitation radiative decay
$e^- + AB(n,v,N) \rightarrow AB(n',v',N') + e^-$ $\rightarrow AB(n'',v'',N'')^* + \gamma + e^-$ $\rightarrow A + B + \gamma + e^-$	excitation radiative decay dissociation

to break up into atomic fragments. In the case of ionisation, the residual AB^+ ion can be formed in either a dissociative or non-dissociative state, leading to the two different types of ionisation. Dissociation can also proceed via the resonant dissociative attachment processes, where the electron is captured by the target to form the AB^- ion in a dissociative state. Following excitation of non-dissociative states, the excited molecule will spontaneously decay to a lower-energy state via

emission of a photon. The case where the decay ends in a non-dissociative state is referred to as excitation radiative decay (ERD), and when it ends in a dissociative state the process is referred to as excitation radiative-decay dissociation (ERDD).

It is common for measurements or calculations to disregard the nuclear states involved in a transition, assuming the target always begins in its ground state and considering only the final electronic state after the collision. In this case, the term *elastic* scattering is often used to refer to *electronically* elastic scattering, including the sum of all vibrational/rotational transitions within the same electronic state.

1.3 Applications

Atomic and molecular collisions are some of the most fundamental processes in nature. They are the underpinning events in plasma physics and chemical reactions, and by extension, biology and all of life. Electron-atom and electron-molecule collisions play important roles in governing the properties and dynamics of various natural and manufactured plasmas, with important applications in astrophysics, energy, technology, biomedicine, and more [21].

Of interest in the present work are electron collisions with molecular hydrogen (H_2) and its isotopologues (D_2, T_2, HD, HT, and DT). Being the simplest neutral molecule, H_2 is abundant in the universe, and important in a number of applications. A few notable examples are discussed below, with a particular focus on fusion applications which have been the primary motivation of the present research.

1.3.1 Astrophysics

The H_2 molecule is one of the predominant molecular species in atmospheric and interstellar gas clouds and plasmas [22–25]. Electron collisions with H_2 contribute to the heating and cooling of planetary atmospheres and molecular clouds, the latter of which is an important mechanism for stellar formation [26, 27]. The same processes also played important roles during the early formation of the

interstellar medium [28]. The break-up (dissociation) of H_2 in particular has important consequences for astrophysical plasma modelling [24, 25], and is a contributing factor to the plume of energetic atomic hydrogen observed in the atmosphere of Saturn [22].

Measurements of the H_2 emission spectrum can be used to infer the properties of the magnetospherical plasma and details of the atmospheric composition of planets where direct observation is unfeasible. Emissions from atomic and molecular hydrogen are the predominant sources of the auroras in the outer planets [29], and spectroscopic measurements taken from ground-based observatories, satellites, or spacecraft are often used in place of direct measurement [30].

Detailed sets of e^--H_2 cross sections are required for determining astrophysical plasma properties such as molecular vibrational temperature and electron energy distribution functions, and for interpreting spectroscopic data [31, 32]. The isotopologues of H_2, in particular the deuterated molecules HD and D_2, are also important in many astrophysical applications [33–41].

1.3.2 Industry

Plasmas containing atomic and molecular hydrogen are frequently used in the production of various technologies. Amorphous hydrogenated silicon, a non-crystalline form of silicon with hydrogen introduced to it, is deposited in thin films onto plastic or glass in the production of photovoltaic solar cells [42], as well as LCD and LED displays [43]. The most popular method for producing these films is plasma-enhanced chemical vapour deposition. Accurate modelling of e^--H_2 processes in the plasma is vital to control the electrical and optical properties of the film [42], as well as to optimise the rate of deposition [44].

1.3.3 Nuclear fusion

One of the largest scientific projects in the world is the International Thermonuclear Experimental Reactor (ITER) in France. Upon completion, ITER will be the world's largest magnetic-confinement nuclear fusion experiment. The development of fusion reactors will provide a safe and virtually limitless source of energy which produces no long-lived radioactive waste or carbon emissions. The

fusion reaction by nature cannot undergo a runaway chain reaction, making it a much safer alternative to the fission reaction utilised in present-day nuclear power. The primary aims of ITER are to initiate a self-sustaining fusion reaction which produces a ten-fold return on energy, and to test the various regimes of fusion physics. This will pave the way for the next generation of fusion reactors which will be used for power production.

Aside from the financial investment, ITER requires a substantial investment of research. There are many challenges to overcome before fusion energy is realised, such as designing components to survive the conditions inside the reactor, optimising the operation of heating and waste-removal systems, and developing models to aid in plasma diagnostics [45].

Nuclear fusion is the reaction which takes place when two atomic nuclei collide with enough energy to overcome their mutual electrostatic repulsion and become bound by the short-range nuclear force, resulting in a considerable release of energy. The simplest fusion reactions involve the nuclei of various hydrogen isotopes fusing to form helium. These are the processes which take place in the core of the Sun, and which will eventually be harnessed for electricity production in human-engineered fusion devices. The principle complicating factor in creating a fusion reaction is the energy required to overcome the initial repulsion between the nuclei. In the Sun, the pressure in the core due to gravitational forces creates the ideal environment for fusion to take place. To recreate this environment in a fusion reactor, the fuel (isotopes of hydrogen) must be heated to temperatures of the order of millions of degrees. At these temperatures atoms are stripped of their electrons, creating a plasma of high-energy charged particles. ITER will be a toroidal reactor, which uses helical magnetic fields to confine the fusion plasma. Although the high temperatures of the core plasma do not permit the formation of molecules, the cooler plasmas near the walls of the confinement vessel and in the divertor (a device used for the removal of waste from the plasma) do contain molecular species, in fact more than 90% of the neutral hydrogen in the divertor region is molecular. Collisional processes involving H_2 are a major factor in governing the dynamics and properties of the edge and divertor plasmas, which in turn affects the performance of the bulk fusion plasma [46].

Surface-material damage due to plasma-emission radiation and contact with high-energy particles is a major concern for the design and operation of a fusion reactor. There is a particularly strong heat load on the plasma-facing components of the divertor, due to its function of channelling impurities out of the bulk plasma, so the issue of reducing the particle flux on the divertor components has attracted significant attention [47]. The behaviour of the divertor plasma can be categorised into the *attached* and *detached* regimes. The detached regime is characterised by a significant reduction in plasma temperature and particle flux at the divertor targets, and hence operating with a detached divertor plasma has become a key element of the ITER baseline design [48]. Despite its importance, the physics of divertor detachment is still not fully understood, and continued investigation is required in order to exploit the properties of the detached plasma regime in fusion devices [49]. Research involving molecular species is of particular importance, as the presence of molecules can play a crucial role in the ionising-to-recombining plasma transition associated with the detached mode [47].

One of the mechanisms used to heat the bulk plasma in ITER to the temperatures required to initiate fusion will be neutral-beam injection, an external heating process where high-energy neutral atoms are fired into the plasma to deposit their energy during multiple collisions with the plasma constituents. The neutral beam is produced by accelerating ions through an electric field, then neutralising them before injection. In typical plasma-heating applications, neutral-beam injectors (NBIs) utilise a positive-ion source, as positive ions are easier to produce and control during acceleration than negative ions. However, at the power levels and beam-line velocities required for ITER, the neutralisation efficiency of positive-ion sources is degraded, and hence the NBIs at ITER will utilise negative-ion sources. The basic principle of the negative-ion NBI (N-NBI) is that an inductively-coupled plasma is produced by a radio-frequency (RF) driver, and then flows into an expansion chamber where it transitions from an ionising to a recombining plasma. From here, negative ions are extracted in order to form the negative-ion beam [50]. During this process, electrons are also extracted, which is problematic as the number of co-extracted electrons limits the maximum achievable ion-current density due to the energy deposited by these

electrons on beam-line components [51]. Reliable plasma diagnostics for both ionising and recombining plasmas are vital for identifying measures to optimise negative-ion production as well as reduce the number of co-extracted electrons.

Plasma diagnostics and control require detailed knowledge of the plasma properties, such as the electron temperature and density, and the population densities of the ground-state and metastable excited-state plasma species [52]. In plasmas, the collisional excitation, deexcitation and spontaneous-emission processes compete to affect the equilibrium populations of the excited states. These populations in turn determine the photon-emission spectra of the plasma, which has two important consequences. Firstly, the emission-band intensities can inform the choice of surface materials for the plasma-facing components, to minimise radiation-induced damage [53]. Secondly, one of the aims of plasma diagnostics is to measure the emission bands and attempt to reverse-engineer knowledge of parameters such as the electron temperature and density. Both of these endeavours require the use of a population model, a theoretical tool for determining the equilibrium populations using the plasma parameters, and the collision/emission rates as input. Population models can be applied in a forwards or backwards manner to serve both of the aforementioned functions. In the forwards application, a population model is applied to predict the emission spectra, based on known or assumed plasma parameters. In the backwards application, the plasma parameters are unknown, but the emission spectra may be measured using techniques such as optical emission spectroscopy. The population model is then applied, with the input parameters tuned to produce an emission spectra matching the measurement, effectively determining the parameters of the physical plasma. Although there are direct methods for determining the plasma parameters, such as Langmuir-probe measurements, there are a number of circumstances in which a direct approach is difficult. For example, in RF plasmas or magnetically-confined plasmas, electromagnetic fields disturb the current-voltage characteristic of the probe [54], while in reactive plasmas the probe tip can become coated or etched [55]. In these cases a much more reliable determination of the plasma parameters can be achieved using the population-model technique. A second advantage of the indirect process is that it is non-invasive and does not affect the plasma [56].

The behaviour of a plasma can be categorised into three regimes defined by the rate of collisions. For low-collision-rate plasmas, the dominant processes affecting the population of an excited state are electron-impact excitation from the ground state and radiative decay back to the ground state. The excited-state populations in this case are said to be in corona equilibrium [57], and a corona model – a simple population model in which transitions between excited states are neglected – can be applied. For high collision-rate plasmas, the excited states thermalise and their populations follow a simple Boltzmann distribution which is determined by the electron temperature alone. In this case the plasma is said to be in local thermodynamic equilibrium (LTE). For intermediate collision rates neither of these simple cases apply, and a more sophisticated population model must account for the detailed balance between all processes. The class of population models with the broadest range of applicability are the collisional-radiative (CR) models, so called because of their accurate treatment of the competing collision and decay processes. In CR models a large number of collisionally-induced excitation and quenching processes, including transitions between excited states, are balanced with spontaneous decay processes such as radiative emission and predissociation to produce population densities for all states included in the model. This process involves formulating the rate equations for each of the excited-state populations, resulting in a set of coupled differential equations to be solved numerically [52]. When applying CR models to molecular species a large number of rotational, vibrational, and electronic transitions must be included, but approximations may be made by neglecting the rotational and/or vibrational substructures. CR models are applicable from low- to high-collision rate plasmas. In the two limiting cases a CR model should produce the same results as the appropriate corona or LTE model.

1.4 State of the field

1.4.1 Theory

Calculations of electron collisions with the ground electronic state of H_2 have been attempted using a number of different computational methods, with varying levels of approximation. From the 1970's to 2000's a series of approximate calculations were performed using the distorted-wave, Schwinger multichannel, complex Kohn, and R-matrix methods [58–69]. The majority of these calculations were performed using the fixed-nuclei approximation (neglecting nuclear motion to approximate electronic transitions only), and were in most cases inaccurate and restricted to a small set of considered transitions.

Celiberto *et al.* [70] published a large set of electronic excitation cross sections for scattering on vibrationally-excited H_2 and D_2, which were obtained with the semiclassical impact-parameter method. This method is restricted to dipole-allowed transitions, and is accurate only at high incident energies. As a result, the dataset was missing many transitions and was not accurate at low to intermediate impact energies. Celiberto *et al.* [70] additionally provided data for the spin-forbidden low-energy dissociative transition in H_2 and D_2 using another semiclassical (Gryziński) approximation.

Stibbe and Tennyson [71] performed newer R-matrix calculations using the UKRMol suite of computer codes, and provided data for low-energy dissociation of H_2 in the $v = 0$–4 vibrational levels. However, shortly thereafter Trevisan and Tennyson [72–74] claimed that Stibbe and Tennyson [71] had not applied the correct formalism to the study of molecular fragmentation and derived new formulas for the dissociation cross sections. Updated results obtained using the new formulation were found to be similar to the original calculations for $v = 0$, but substantially different for scattering on excited vibrational levels. Furthermore, dissociation cross sections were obtained for scattering on the isotopologues of H_2, and a strong isotope effect was found. The dissociation cross sections of Trevisan and Tennyson [72–74] have been widely adopted in plasma-modelling applications [34, 36, 39, 41, 42, 44, 75–86]. The question of whether or not the

change in formulation was valid is then rather important, and will be revisited later in Chapter 8.

Within the last decade, the widely successful convergent close-coupling (CCC) method has been extended to molecular targets [87]. The molecular CCC (MCCC) method has been applied to electron and positron scattering on H_2^+ and H_2 [88–93], in each case representing the most detailed and accurate calculations performed. In the case of e^--H_2 scattering, the MCCC method was applied in the fixed-nuclei approximation [92], with detailed convergence studies performed to verify the accuracy of a number of excitations, as well as ionisation and elastic scattering. In most cases the MCCC cross sections were found to be substantially different from previous calculations, but in much better agreement with the available measurements. Of particular note is that the MCCC cross section for the first electronic excitation of H_2 was substantially lower above around 15 eV than previous measurements and calculations.

For scattering on excited electronic states of H_2, far fewer calculations have been performed. A handful of transitions for scattering on the first few non-dissociative excited states of H_2 have been investigated using the distorted-wave, Schwinger multichannel, complex scattering potential-ionisation contribution, and impact-parameter approximations [70, 94–97], though there is generally poor agreement between the various calculations. The largest set of excited states considered was in the Gryziński calculations of Wünderlich [98] for ionisation of excited vibrational levels in the first five non-dissociative excited states of H_2 (as well as the ground electronic state). During the current research project, these calculations were updated to correct an error in the treatment of scattering on excited states, as well as extending the results to include the isotopologues of H_2 [99]

A great deal of attention has been directed towards the calculation of resonant scattering cross sections for the e^--H_2 system. The approximations generally applied to non-resonant scattering in molecules are not valid for resonant scattering, and hence entirely different theoretical methods have been required to study resonances. Although there are different variants of resonant scattering theories, each of them is based on the idea of decoupling the resonant and non-resonant

processes and using information such as resonance energies and widths (generally obtained externally from R-matrix calculations) to solve the nuclear dynamics problem separately for each resonant process. Calculations adopting this type of approach have been applied extensively to resonant vibrational excitations and dissociative electron attachment [100–114]. Calculations of resonant scattering involving excited electronic states of D_2 have only recently been performed by Laporta *et al.* [115], although at present these calculations have not been performed for H_2.

During the course of this project, the UKRMol research group have produced a substantial number of new fixed-nuclei cross sections for scattering on the ground state [9] and excited electronic states [116] of H_2. For scattering on the ground electronic state the results were found to be in largely good agreement with the previous MCCC calculations of Zammit *et al.* [93]. Comparison between the results of Ref. [116] and excited-state calculations performed during this project will be made in Chapter 8.

1.4.2 Experiment

The complex structure of molecules poses issues for experiment just as it does for theory. Most importantly, the overlapping rovibrational spectra of each electronic state makes interpretation of electron energy-loss spectra difficult, which in most cases prevents experimentalists from studying specific rovibrational transitions. One exception to this is the low-energy rovibrational excitation of H_2 within the ground electronic state, for which a number of measurements have been taken [117–128]. There were also limited measurements taken for excitation of the $X\,^1\Sigma_g^+(v=0) \rightarrow B\,^1\Sigma_u^+(v=2)$ transition by Srivastava and Jensen [129]. Aside from the above, all other measurements of e^--H_2 scattering have been resolved only in the electronic states involved in the transition [130–137]. During the course of this project, new measurements of the low-energy H_2 dissociative excitation were taken at California State University Fullerton [14, 17], which showed near-perfect agreement with the MCCC calculations which had previously been in substantial disagreement with the older experimental cross sections. This was a remarkable milestone in the field as agreement on this level between theory and

experiment for electron-molecule had not been seen before. These results also served as a strong validation of the accuracy of the MCCC method.

For most of the transitions of interest in the present work, namely scattering on excited vibrational levels and excited electronic states, including transitions resolved in both initial and final vibrational levels, measurements have not been previously attempted. Furthermore, very limited measurements have been performed for electron collisions with the isotopologues of H_2, with only a few total or elastic cross sections available for HD and D_2 [138].

1.5 Objectives

The paucity of both theoretical and experimental data for such a fundamental scattering system is a concern, particularly since e^--H_2 collision data is of great importance in a wide variety of applications. In particular, the accurate collisional-radiative models required for the study of plasmas and the development of plasma diagnostic tools required in fusion research will need data resolved in vibrational, and eventually rotational levels, for a large number of transitions including scattering on both the ground and excited electronic states. This is essentially an impossible feat for experiment, and so it is up to theory to provide the data. At present, many plasma models utilise the compilations of recommended e^--H_2 data from Janev *et al.* [139] and Miles *et al.* [140], which have both been inferred from various experimental and theoretical sources and include data only for non-vibrationally-resolved scattering on H_2 in the ground (electronic and vibrational) state. Hence it is our present goal with the MCCC project to provide a comprehensive set of accurate cross sections which can be applied in future plasma models. The use of the adiabatic-nuclei approximation[1] allows a straightforward application of the existing MCCC codes to the generation of fully vibrationally-resolved data for scattering on the ground and excited states of H_2 and each of its isotopologues.

During the course of this project, we have begun a collaboration with the ITER Technology and Diagnostic Division of the Max-Planck Institute for Plasma

[1] This method will be explained in detail in Chapter 7

Physics in Garching, Germany. The goals of this collaboration are to implement MCCC cross sections in a collisional-radiative model for H_2 (and later its isotopologues), and to benchmark it against real plasma measurements. This collaboration has become one of the driving forces behind the production of H_2 data in this project. The eventual goals for the collaboration are to develop a rigorously tested and accurate collisional-radiative model which can be applied for both attached and detached divertor plasmas, as well as the plasmas in the neutral-beam injectors.

The incorporation of rotational transitions into the MCCC method is another objective for this project. Cross sections resolved in rotational levels will be required for the most accurate collisional-radiative models, and are also important in astrophysical applications. It was the intention during this project to perform the necessary derivations and implement rotational motion into the adiabatic-nuclei code, and to study a few of the most important rotational transitions. The production of large fully rotationally-resolved datasets for H_2 is beyond the scope of this project but is planned for the future.

In addition to the generation of large datasets using the adiabatic-nuclei approximation, it has been a long-standing goal in the MCCC project to investigate the possibility of performing diatomic scattering calculations without the separation of electronic and nuclear motions (as is required in the adiabatic method). This leads to the final objective of developing a new MCCC scattering code based on the concept of applying the close-coupling method to both the electronic and vibrational degrees of freedom. The particular interest along this avenue is developing a method capable of studying resonant scattering without the use of major approximations or requiring the input of resonance data from external calculations. In future work, this method can be applied to the resonant dissociative attachment process.

Chapter 2

Quantum scattering theory

This chapter presents a brief overview of nonrelativistic quantum scattering theory. The following textbooks have been consulted: Bransden [141], Taylor [142], Sakurai and Napolitano [143], and Cohen-Tannoudji *et al.* [144].

2.1 Scattering-system Hamiltonian

The scattering process is governed by the scattering-system Hamiltonian operator

$$\hat{\mathsf{H}} = \hat{\mathsf{K}}_{\mathrm{p}} + \hat{\mathsf{H}}_{\mathrm{t}} + \hat{\mathsf{V}}. \tag{2.1}$$

where $\hat{\mathsf{K}}_{\mathrm{p}}$ is the projectile kinetic-energy operator, $\hat{\mathsf{H}}_{\mathrm{t}}$ is the target Hamiltonian operator, and $\hat{\mathsf{V}}$ is the projectile-target interaction potential operator. The projectile-target interaction potential $\hat{\mathsf{V}}$ can in general be a complex non-local operator. Although physical potentials are real and local, the inclusion of the spin-exchange interaction leads to non-local potentials entering the calculations, and some numerical methods can require the use of complex potentials.

The target Hamiltonian contains all kinetic- and potential-energy operators associated with the internal structure of the target. The eigenstates of $\hat{\mathsf{H}}_{\mathrm{t}}$ are the target states $\{|\phi_n\rangle\}$:

$$\hat{\mathsf{H}}_{\mathrm{t}}|\phi_n\rangle = \epsilon_n|\phi_n\rangle, \tag{2.2}$$

where ϵ_n is the energy of the state $|\phi_n\rangle$. Since they are the eigenstates of a Hermitian operator, the target states form an identity operator:

$$\sum\!\!\!\!\!\!\int_n |\phi_n\rangle\langle\phi_n| = \hat{\mathsf{I}}, \tag{2.3}$$

where the $\sum\!\!\!\!\!\!\int$ symbol indicates a sum over the discrete spectrum and integral over the continuous spectrum of $\hat{\mathsf{H}}_\mathrm{t}$. Together, $\hat{\mathsf{K}}_\mathrm{p}$ and $\hat{\mathsf{H}}_\mathrm{t}$ form the *asymptotic* Hamiltonian $\hat{\mathsf{H}}_0$:

$$\hat{\mathsf{H}}_0 \equiv \hat{\mathsf{K}}_\mathrm{p} + \hat{\mathsf{H}}_\mathrm{t}. \tag{2.4}$$

Since $\hat{\mathsf{K}}_\mathrm{p}$ and $\hat{\mathsf{H}}_\mathrm{t}$ operate on different spaces, the eigenstates of $\hat{\mathsf{H}}_0$ are the asymptotic states $|\phi_n \boldsymbol{q}\rangle$:

$$\hat{\mathsf{H}}_0|\phi_n \boldsymbol{q}\rangle = (\epsilon_n + \epsilon_q)|\phi_n \boldsymbol{q}\rangle, \tag{2.5}$$

where $\epsilon_q = q^2/2$.

2.2 Time dependence

Since the potentials involved in the scattering process are all time-independent, we can seek separable scattering solutions

$$|\Psi(t)\rangle = |\Psi\rangle e^{-iEt} \tag{2.6}$$

where E is the total energy of the scattering state $|\Psi(t)\rangle$. The Schrödinger equation for the scattering state is

$$\hat{\mathsf{H}}|\Psi(t)\rangle = i\frac{\partial}{\partial t}|\Psi(t)\rangle, \tag{2.7}$$

where the spatial component $|\Psi\rangle$ satisfies the time-independent Schrödinger equation:

$$\hat{\mathsf{H}}|\Psi\rangle = E|\Psi\rangle. \tag{2.8}$$

The focus of a time-independent scattering theory is to determine $|\Psi\rangle$, however in formulating the theory, the time-dependent solutions $|\Psi(t)\rangle$ will need to be considered when applying the boundary conditions.

2.3 Scattering states and boundary conditions

The solutions $|\Psi(t)\rangle$ are referred to as scattering states as they describe the entire scattering process at all spatial and temporal coordinates. The decoupled product states $|\phi_n \boldsymbol{q}\rangle$ are referred to as asymptotic states because they describe the system

in a definite configuration with no interaction between the projectile and target. When time dependence is required these states will be denoted

$$|\phi_n \boldsymbol{q}\,(t)\rangle = |\phi_n \boldsymbol{q}\rangle e^{-i(\epsilon_n+\epsilon_q)t}. \tag{2.9}$$

When discussing boundary conditions we refer to the preinteraction asymptote (times long before the collision and projectile coordinates far away from the target) and post-interaction asymptote (times long after the collision and projectile coordinates far away from the target). It is assumed that in a scattering experiment the target has been prepared in a definite initial state $|\phi_i\rangle$ and the projectile has a definite initial energy ϵ_{q_i}, and so we can immediately impose the following boundary condition:

$$\lim_{\substack{r_\mathrm{p}\to\infty \\ t\to-\infty}} |\Psi(t)\rangle = |\phi_i \boldsymbol{q}_i\,(t)\rangle, \tag{2.10}$$

where r_p is the projectile coordinate. The post-interaction boundary condition is not as simple as this; the scattering event is a probabilistic process and hence the post-interaction asymptotic scattering state is a superposition of states, each corresponding to a different final configuration, which collapses into a definite final configuration when a measurement is taken.

Now we turn to obtaining the scattering states $|\Psi(t)\rangle$. The total scattering Hamiltonian $\hat{\mathsf{H}}$ can be expressed was the sum of the asymptotic Hamiltonian and the interaction potential operator:

$$\hat{\mathsf{H}} = \hat{\mathsf{H}}_0 + \hat{\mathsf{V}}. \tag{2.11}$$

Using Eq. (2.11), the scattering-system time-independent Schrödinger equation (2.8) is equivalently given by

$$(E - \hat{\mathsf{H}}_0)|\Psi\rangle = \hat{\mathsf{V}}|\Psi\rangle. \tag{2.12}$$

As this is a linear differential equation, the most general solution is a linear combination of the solution $|\Psi_\mathrm{h}\rangle$ to the homogeneous equation

$$(E - \hat{\mathsf{H}}_0)|\Psi_\mathrm{h}\rangle = 0 \tag{2.13}$$

and the particular solution $|\Psi_\mathrm{p}\rangle$ to Eq. (2.12). The homogeneous solutions are the asymptotic states $|\phi_n \boldsymbol{q}\rangle$, subject to the condition

$$\epsilon_n + \epsilon_q = E, \tag{2.14}$$

and the time-dependent homogeneous solution is given by

$$|\Psi_\mathrm{h}(t)\rangle = |\phi_n \boldsymbol{q}\rangle e^{-iEt}. \tag{2.15}$$

The particular solutions $|\Psi_\mathrm{p}\rangle$ can be obtained using a Green's-operator approach. We define the asymptotic Green's operator by

$$\hat{\mathsf{G}}_0 \equiv \left[E - \hat{\mathsf{H}}_0\right]^{-1}, \tag{2.16}$$

i.e. it is the inverse operator of $(E - \hat{\mathsf{H}}_0)$. Actually, this definition of the Green's operator is not well defined. To demonstrate this, one can attempt to evaluate the coordinate-space matrix elements $\langle \boldsymbol{r}'|\hat{\mathsf{G}}_0|\boldsymbol{r}\rangle$, making use of the projectile- and target-space identity operators defined above:

$$\begin{aligned}\langle \boldsymbol{r}'|\hat{\mathsf{G}}_0|\boldsymbol{r}\rangle &= \sum_n \int_{\mathbb{R}^3} \langle \boldsymbol{r}'|\hat{\mathsf{G}}_0|\phi_n \boldsymbol{q}\rangle\langle \boldsymbol{q}\phi_n|\boldsymbol{r}\rangle \,\mathrm{d}\boldsymbol{q} \\ &= \sum_n \int_{\mathbb{R}^3} \frac{\langle \boldsymbol{r}'|\phi_n \boldsymbol{q}\rangle\langle \boldsymbol{q}\phi_n|\boldsymbol{r}\rangle}{E - \epsilon_n - \epsilon_q} \,\mathrm{d}\boldsymbol{q}. \end{aligned} \tag{2.17}$$

The integrand is singular whenever $\epsilon_q = \epsilon_n - E$ in the momentum-space integral of Eq. (2.17), and hence the matrix elements are undefined. To avoid this issue, the scattering-system energy can be shifted into the complex plane so that the singularities are avoided. There is a choice to shift E into the positive- or negative-imaginary halves of the complex plane, so for now we define the shifted energy as

$$E^\pm \equiv E \pm i\eta. \tag{2.18}$$

A similar definition is made for the Green's operator:

$$\hat{\mathsf{G}}_0^{\pm} \equiv \lim_{\eta \to 0^+} \left[E \pm i\eta - \hat{\mathsf{H}}_0\right]^{-1}. \tag{2.19}$$

Using these definitions, the spatial particular solution can be written as

$$|\Psi_{\mathrm{p}}^{\pm}\rangle = \hat{\mathsf{G}}_0^{\pm}\hat{\mathsf{V}}|\Psi^{\pm}\rangle. \tag{2.20}$$

Having the limit $\eta \to 0^+$ built into the solution ensures that $|\Psi_{\mathrm{p}}^{\pm}\rangle$ is a solution to Eq. (2.12). The time-dependent particular solution is given by

$$|\Psi_{\mathrm{p}}^{\pm}(t)\rangle = \hat{\mathsf{G}}_0^{\pm}\hat{\mathsf{V}}|\Psi^{\pm}\rangle e^{-i(E\pm i\eta)t} = \hat{\mathsf{G}}_0^{\pm}\hat{\mathsf{V}}|\Psi^{\pm}\rangle e^{-iEt}e^{\pm\eta t}, \tag{2.21}$$

and hence the time-dependent general solutions are given by

$$|\Psi_j^{\pm}(t)\rangle = |\phi_j \boldsymbol{q}_j\rangle e^{-iEt} + \hat{\mathsf{G}}_0^{\pm}\hat{\mathsf{V}}|\Psi_j^{\pm}\rangle e^{-iEt}e^{\pm\eta t}. \tag{2.22}$$

The time-independent general solution is defined as

$$|\Psi_j^{\pm}\rangle = |\phi_j \boldsymbol{q}_j\rangle + \hat{\mathsf{G}}_0^{\pm}\hat{\mathsf{V}}|\Psi_j^{\pm}\rangle, \tag{2.23}$$

where the plane waves are given the subscript j to indicate that they are required to satisfy the energy-conservation relation $\epsilon_j + \epsilon_{q_j} = E$.

We are now in a position to consider the boundary conditions of the problem and choose which solution ($|\Psi_j^{+}(t)\rangle$ or $|\Psi_j^{-}(t)\rangle$) to keep. We consider the limiting cases of $t \to \pm\infty$ (times long before and long after the scattering process) and $r \to \infty$ (spatial coordinates far away from the interaction region). First, evaluating the wave function in coordinate space:

$$\langle \boldsymbol{r}_{\mathrm{p}}\boldsymbol{r}_{\mathrm{t}}|\Psi_j^{\pm}(t)\rangle = \langle \boldsymbol{r}_{\mathrm{p}}\boldsymbol{r}_{\mathrm{t}}|\phi_j \boldsymbol{q}_j\rangle e^{-iEt} + \langle \boldsymbol{r}_{\mathrm{p}}\boldsymbol{r}_{\mathrm{t}}|\hat{\mathsf{G}}_0^{\pm}\hat{\mathsf{V}}|\Psi_j^{\pm}\rangle e^{-iEt}e^{\pm\eta t}, \tag{2.24}$$

then inserting a complete set of states:

$$\begin{aligned}\langle \boldsymbol{r}_{\mathrm{p}}\boldsymbol{r}_{\mathrm{t}}|\Psi_j^{\pm}(t)\rangle &= \langle \boldsymbol{r}_{\mathrm{p}}\boldsymbol{r}_{\mathrm{t}}|\phi_j \boldsymbol{q}_j\rangle e^{-iEt} + \sum_n \int \langle \boldsymbol{r}_{\mathrm{p}}\boldsymbol{r}_{\mathrm{t}}|\hat{\mathsf{G}}_0^{\pm}|\phi_n \boldsymbol{q}\rangle\langle \boldsymbol{q}\phi_n|\hat{\mathsf{V}}|\Psi_j^{\pm}\rangle \,\mathrm{d}\boldsymbol{q} e^{-iEt}e^{\pm\eta t} \\ &= \langle \boldsymbol{r}_{\mathrm{p}}\boldsymbol{r}_{\mathrm{t}}|\phi_j \boldsymbol{q}_j\rangle e^{-iEt} + \lim_{\eta\to 0^+}\sum_n \int \frac{\langle \boldsymbol{r}_{\mathrm{p}}\boldsymbol{r}_{\mathrm{t}}|\phi_n \boldsymbol{q}\rangle\langle \boldsymbol{q}\phi_n|\hat{\mathsf{V}}|\Psi_j^{\pm}\rangle}{E - \epsilon_n - \epsilon_{q'} \pm i\eta} \,\mathrm{d}\boldsymbol{q} e^{-iEt}e^{\pm\eta t}. \end{aligned} \tag{2.25}$$

Now applying the asymptotic form of the plane waves

$$\lim_{r\to\infty}\langle \boldsymbol{r}|\boldsymbol{q}\rangle = -\frac{i}{\sqrt{2\pi}qr}\left(e^{iqr}\delta(\hat{\boldsymbol{q}} - \hat{\boldsymbol{r}}) - e^{-iqr}\delta(\hat{\boldsymbol{q}} + \hat{\boldsymbol{r}})\right) \tag{2.26}$$

gives

$$\langle \boldsymbol{r}_\mathrm{p}\boldsymbol{r}_\mathrm{t}|\Psi_j^\pm(t)\rangle \xrightarrow[r\to\infty]{} \langle \boldsymbol{r}_\mathrm{p}\boldsymbol{r}_\mathrm{t}|\phi_j\boldsymbol{q}_j\rangle e^{-iEt} - \lim_{\eta\to 0^+}\sqrt{2\pi}\sum_n \langle \boldsymbol{q}_n\phi_n|\hat{\mathrm{V}}|\Psi_j^\pm\rangle\langle \boldsymbol{r}_\mathrm{t}|\phi_n\rangle \frac{e^{\pm iq_n r_\mathrm{p}}}{r_\mathrm{p}} e^{-iEt}e^{\pm\eta t}. \quad (2.27)$$

The presence of the $e^{\pm\eta t}$ factor in the second term yields the following temporal limits:

$$\lim_{t\to-\infty}\langle \boldsymbol{r}_\mathrm{p}\boldsymbol{r}_\mathrm{t}|\Psi_j^+(t)\rangle = \langle \boldsymbol{r}_\mathrm{p}\boldsymbol{r}_\mathrm{t}|\phi_j\boldsymbol{q}_j\rangle e^{-iEt} \quad (2.28)$$

$$\lim_{t\to+\infty}\langle \boldsymbol{r}_\mathrm{p}\boldsymbol{r}_\mathrm{t}|\Psi_j^-(t)\rangle = \langle \boldsymbol{r}_\mathrm{p}\boldsymbol{r}_\mathrm{t}|\phi_j\boldsymbol{q}_j\rangle e^{-iEt}. \quad (2.29)$$

The above results have the following interpretation. The solution $|\Psi_j^+(t)\rangle$ has incoming plane-wave boundary conditions, since as $t\to-\infty$ it converges to the asymptotic state $|\phi_j\boldsymbol{q}_j(t)\rangle$. In other words, $|\Psi_j^+(t)\rangle$ is the scattering state which evolved from the initial state $|\phi_j\boldsymbol{q}_j(t)\rangle$. The second term in Eq. (2.27) for the $|\Psi_j^+(t)\rangle$ state represents a superposition of outgoing spherical waves, each one corresponding to a different scattering transition $j\to n$. The coefficients of $\langle \boldsymbol{r}_\mathrm{t}|\phi_n\rangle \exp(iq_n r_\mathrm{p})/r_\mathrm{p}$ in the summation over n are the probability amplitudes, or *scattering* amplitudes, for the transitions. The scattering amplitude for the transition $j\to n$ is hence defined by

$$F_{nj}(\boldsymbol{q}_n) \equiv -4\pi^2\langle \boldsymbol{q}_n\phi_n|\hat{\mathrm{V}}|\Psi_j^+\rangle, \quad (2.30)$$

where the $4\pi^2$ factor comes from enforcing the same normalisation of the incoming and outgoing waves. The outgoing momentum $\boldsymbol{q}_n$ is given the subscript n to indicate that it is dependent on the final target state in order to satisfy conservation of energy. The direction of $\boldsymbol{q}_n$ indicates the direction in which the scattering amplitude is evaluated. To summarise, we say that the state $|\Psi_j^+(t)\rangle$ satisfies incoming plane-wave and outgoing spherical-wave boundary conditions. The second solution $|\Psi_j^-(t)\rangle$ corresponds to the time-reversed process and satisfies incoming spherical-wave and outgoing plane-wave boundary conditions. The solution $|\Psi_j^-(t)\rangle$ does not represent a physical state but will serve a mathematical purpose later on.

2.4 Transition probabilities

The physical state $|\Psi_i^+(t)\rangle$ is the state which evolved from the initial state $|\phi_i \boldsymbol{q}(t)\rangle$. At some time long after the scattering event ($t \to \infty$), a measurement is performed. We define the transition probability as the probability that when the system is measured it will be found to be in a state which asymptotically converges to the state $|\phi_f \boldsymbol{q}_f(t)\rangle$. The scattering state $|\Psi_f^-(t)\rangle$ satisfies this boundary condition, and we note that

$$\langle \Psi_f^-(t)| = \langle \boldsymbol{q}_f \phi_f | e^{iE't} + e^{iE't} e^{-\eta t} \langle \Psi_f^-| \hat{\mathsf{V}} \hat{\mathsf{G}}_0^- \tag{2.31}$$

$$\lim_{t\to\infty} \langle \Psi_f^-(t)| = \langle \boldsymbol{q}_f \phi_f | e^{iE't}. \tag{2.32}$$

Here, to be general, we allow the total energy $E' = \epsilon_f + \epsilon_{q_f}$ of the state $|\Psi_f^-(t)\rangle$ to differ from the total energy E of the true scattering state $|\Psi^+(t)\rangle$. The transition probability amplitude is given by

$$A_{f\leftarrow i}(\boldsymbol{q}_f, \boldsymbol{q}_, t) = \langle \Psi_f^-(t) | \Psi_i^+(t) \rangle, \tag{2.33}$$

but since we are only interested in times long after the collision, we define

$$A_{f\leftarrow i}(\boldsymbol{q}_f, \boldsymbol{q}_i) = \lim_{t\to\infty} \langle \Psi_f^-(t) | \Psi_i^+(t) \rangle \tag{2.34}$$

$$= \langle \boldsymbol{q}_f \phi_f | \phi_i \boldsymbol{q}_i \rangle e^{i(E-E')t} + \langle \boldsymbol{q}_f \phi_f | \hat{\mathsf{G}}_0^+ \hat{\mathsf{V}} | \Psi_i^+ \rangle \lim_{t\to\infty} e^{-i(E-E')t} e^{\eta t}. \tag{2.35}$$

In the above, a number of the terms in $\langle \Psi_f^-(t) | \Psi_i^+(t) \rangle$ have been dropped since they trivially go to zero as $t \to \infty$. Noting that $|\phi_f \boldsymbol{q}_f\rangle$ is an eigenstate of $\hat{\mathsf{H}}_0$ with energy E':

$$\langle \boldsymbol{q}_f \phi_f | \hat{\mathsf{G}}_0^+ = \lim_{\eta\to 0^+} \langle \boldsymbol{q}_f \phi_f | \frac{1}{E - E' + i\eta}, \tag{2.36}$$

we have that

$$A_{f\leftarrow i}(\boldsymbol{q}_f, \boldsymbol{q}_i) = \langle \boldsymbol{q}_f \phi_f | \phi_i \boldsymbol{q}_i \rangle e^{i(E-E')t} + \langle \boldsymbol{q}_f \phi_f | \hat{\mathsf{V}} | \Psi_i^+ \rangle \lim_{t\to\infty} \lim_{\eta\to 0^+} \frac{e^{-i(E-E'+i\eta)t}}{E - E' + i\eta} \tag{2.37}$$

$$= \langle \boldsymbol{q}_f \phi_f | \phi_i \boldsymbol{q}_i \rangle e^{i(E-E')t} - 2\pi i \langle \boldsymbol{q}_f \phi_f | \hat{\mathsf{V}} | \Psi_i^+ \rangle \delta(E - E'), \tag{2.38}$$

where we have utilised the limit

$$\lim_{t\to\infty}\lim_{\eta\to 0^+}\frac{e^{-i(y+i\eta)t}}{y+i\eta} = -2\pi i\delta(y). \tag{2.39}$$

Now using the fact that the asymptotic states $|\phi\boldsymbol{q}\rangle$ form a complete set, the final expression for the asymptotic transition probability amplitude is given by

$$A_{f\leftarrow i}(\boldsymbol{q}_f,\boldsymbol{q}_i) = \delta_{fi}\delta(\boldsymbol{q}_f-\boldsymbol{q}_i) - 2\pi i\langle\boldsymbol{q}_f\phi_f|\hat{\mathrm{V}}|\Psi_i^+\rangle\delta(E-E'). \tag{2.40}$$

Note that the $e^{i(E-E')}$ factor in the first term has been dropped since the Dirac-δ functions imply $E=E'$.

The evolution of a pre-interaction asymptotic state $|\phi_i\boldsymbol{q}_i(t)\rangle$ into a scattering state $|\Psi_i^+(t)\rangle$ with incoming boundary conditions coinciding with $|\phi_i\boldsymbol{q}_i(t)\rangle$ can be represented by the mapping

$$\hat{\Omega}_+ \colon |\phi_i\boldsymbol{q}_i(t)\rangle \mapsto |\Psi_i^+(t)\rangle. \tag{2.41}$$

Similarly, we represent the time-reversed evolution of the post-interaction asymptotic state $|\phi_f\boldsymbol{q}_f(t)\rangle$ into the non-physical scattering state $|\Psi_f^-(t)\rangle$ with outgoing plane-wave boundary conditions coinciding with $|\phi_f\boldsymbol{q}_f(t)\rangle$ by the mapping

$$\hat{\Omega}_- \colon |\phi_f\boldsymbol{q}_f(t)\rangle \mapsto |\Psi_f^-(t)\rangle. \tag{2.42}$$

The operators $\hat{\Omega}_\pm$ are the Møller wave operators, and according to their definitions above we have

$$\hat{\Omega}_+|\phi_i\boldsymbol{q}_i(t)\rangle = |\Psi_i^+(t)\rangle \tag{2.43}$$

$$\hat{\Omega}_-|\phi_f\boldsymbol{q}_f(t)\rangle = |\Psi_f^-(t)\rangle. \tag{2.44}$$

The $i\to f$ transition probability amplitude can now be written in terms of the asymptotic states as

$$A_{f\leftarrow i}(\boldsymbol{q}_f,\boldsymbol{q}_i) = \lim_{t\to\infty}\langle\Psi_f^-(t)|\Psi_i^+(t)\rangle = \lim_{t\to\infty}\langle\boldsymbol{q}_f\phi_f(t)|\hat{\Omega}_-^\dagger\hat{\Omega}_+|\phi_i\boldsymbol{q}_i(t)\rangle. \tag{2.45}$$

2.5 The scattering and transition operators

As seen in Eq. (2.40), the transition probabilities are independent of time (for times sufficiently long after the scattering event), so from here onwards we drop the time dependence and speak only in terms of mappings between stationary states. Accordingly, we allow a slight misuse of notation, and denote the transition probability amplitude as

$$A_{f\leftarrow i}(\boldsymbol{q}_f, \boldsymbol{q}_i) = \langle \phi_f \boldsymbol{q}_f | \hat{\Omega}_-^\dagger \hat{\Omega}_+ | \phi_i \boldsymbol{q}_i \rangle, \tag{2.46}$$

where, although the Møller operators were defined in terms of mediating the evolution of one state into another (an inherently time-dependent process), we also allow them to map stationary states onto one another. We now define another operator $\hat{\mathsf{S}}$, the *scattering* operator:

$$\hat{\mathsf{S}} \equiv \hat{\Omega}_-^\dagger \hat{\Omega}_+. \tag{2.47}$$

The effect of $\hat{\mathsf{S}}$ is to map a pre-interaction ($t \to -\infty$) asymptotic state $|\phi_i \boldsymbol{q}_i\rangle$ directly onto a post-interaction asymptotic state. Hence the transition probability amplitudes can be written directly as elements of the S matrix:

$$A_{f\leftarrow i}(\boldsymbol{q}_f, \boldsymbol{q}_i) = S_{fi}(\boldsymbol{q}_f, \boldsymbol{q}_i) = \langle \boldsymbol{q}_f \phi_f | \hat{\mathsf{S}} | \phi_i \boldsymbol{q}_i \rangle. \tag{2.48}$$

Using Eq. (2.40) we write for the S matrix

$$S_{fi}(\boldsymbol{q}_f, \boldsymbol{q}_i) = \delta_{fi}\delta(\boldsymbol{q}_f - \boldsymbol{q}_i) - 2\pi i \langle \boldsymbol{q}_f \phi_f | \hat{\mathsf{V}} | \Psi_i^+ \rangle \delta(E - E'). \tag{2.49}$$

At this point, it is useful to introduce yet another operator, the *transition* operator $\hat{\mathsf{T}}$. The transition operator is defined by

$$\hat{\mathsf{T}} | \phi_i \boldsymbol{q}_i \rangle = \hat{\mathsf{V}} | \Psi_i^+ \rangle. \tag{2.50}$$

Using this definition, we can rewrite Eq. (2.49) as

$$S_{fi}(\boldsymbol{q}_f, \boldsymbol{q}_i) = \delta_{fi}\delta(\boldsymbol{q}_f - \boldsymbol{q}_i) - 2\pi i \langle \boldsymbol{q}_f \phi_f | \hat{\mathsf{T}} | \phi_i \boldsymbol{q}_i \rangle \delta(E - E'), \tag{2.51}$$

which gives a simple expression for $\hat{\mathsf{S}}$ in terms of $\hat{\mathsf{T}}$:

$$\hat{\mathsf{S}} = \hat{\mathsf{I}} - 2\pi i \hat{\mathsf{T}}, \tag{2.52}$$

and for S in terms of the T matrix (the matrix of $\hat{\mathsf{T}}$):

$$S_{fi}(\boldsymbol{q}_f, \boldsymbol{q}_i) = \delta_{fi}\delta(\boldsymbol{q}_f - \boldsymbol{q}_i) - 2\pi i T_{fi}(\boldsymbol{q}_f, \boldsymbol{q}_i). \tag{2.53}$$

The significance of the S matrix is that since measurements will generally have information only about the asymptotic pre- and post-interaction states, all of the information available to experiment is contained within the S matrix (or $\hat{\mathsf{S}}$ operator).

2.6 Transition rate and cross sections

We are now in a position to evaluate the scattering quantities of experimental interest: the cross sections. The rate $w_{f\leftarrow i}$ at which the transition $i \to f$ occurs is given by the time derivative of the probability:

$$w_{f\leftarrow i}(t) = \frac{\partial}{\partial t}\left|A_{f\leftarrow i}(\boldsymbol{q}_f, \boldsymbol{q}_i, t)\right|^2. \tag{2.54}$$

Again, we are interested in times long after the collision, so we wish to evaluate

$$w_{f\leftarrow i} = \lim_{t\to\infty} \frac{\partial}{\partial t}\left|A_{f\leftarrow i}(\boldsymbol{q}_f, \boldsymbol{q}_i, t)\right|^2. \tag{2.55}$$

We make a necessary assumption that the experiment does not attempt to measure elastically-scattered electrons in the forward ($\hat{\boldsymbol{q}}_f = \hat{\boldsymbol{q}}_i$) direction as it is impossible to distinguish between electrons which are scattered in the forwards direction and electrons which are simply unscattered. This allows us to neglect the $\langle \boldsymbol{q}_f \phi_f | \phi_i \boldsymbol{q}_i \rangle$ term, and following similar steps taken to get to Eq. (2.37), we

have

$$w_{f\leftarrow i} = \left|\langle \boldsymbol{q}_f\phi_f|\hat{\mathsf{T}}|\phi_i\boldsymbol{q}_i\rangle\right|^2 \lim_{t\to\infty}\lim_{\eta\to 0^+}\frac{\partial}{\partial t}\frac{e^{2\eta t}}{(E-E')^2+\eta^2} \tag{2.56}$$

$$= \left|\langle \boldsymbol{q}_f\phi_f|\hat{\mathsf{T}}|\phi_i\boldsymbol{q}_i\rangle\right|^2 \lim_{t\to\infty}\lim_{\eta\to 0^+}\frac{2\eta e^{2\eta t}}{(E-E')^2+\eta^2} \tag{2.57}$$

$$= 2\pi\left|\langle \boldsymbol{q}_f\phi_f|\hat{\mathsf{T}}|\phi_i\boldsymbol{q}_i\rangle\right|^2 \delta(E-E'), \tag{2.58}$$

where we have used the limit

$$\lim_{\eta\to 0^+}\frac{\eta}{(E-E')^2+\eta^2} = \pi\delta(E-E'). \tag{2.59}$$

The transition rate is evidently independent of time for large t.

In the case of transitions into a continuum of states, the transition rate must be defined in terms of an integration:

$$w_{f\leftarrow i} = \int_{[\boldsymbol{\alpha}]} 2\pi\left|\langle \boldsymbol{q}_f\phi_f|\hat{\mathsf{T}}|\phi_i\boldsymbol{q}_i\rangle\right|^2 \delta(E-E')\rho(\boldsymbol{\alpha})\,\mathrm{d}\boldsymbol{\alpha}, \tag{2.60}$$

where $\boldsymbol{\alpha}$ stands for the set of parameters which characterise the continuum, $[\boldsymbol{\alpha}]$ is the parameter space of $\boldsymbol{\alpha}$, $\rho(\boldsymbol{\alpha})$ is the density of states, and $\mathrm{d}\boldsymbol{\alpha}$ stands for the collective differentials of each parameter. The density of states is dependent on the choice of normalisation for the wavefunction, and is determined by

$$\int_{[\boldsymbol{\alpha}]} |\boldsymbol{\alpha}\rangle\langle\boldsymbol{\alpha}|\rho(\boldsymbol{\alpha})\,\mathrm{d}\boldsymbol{\alpha} = \hat{\mathsf{I}}_{\boldsymbol{\alpha}}, \tag{2.61}$$

where $\hat{\mathsf{I}}_{\boldsymbol{\alpha}}$ stands for the product of identity operators for each parameter in $\boldsymbol{\alpha}$.

For now we shall assume that only the scattered projectile is represented by a continuum, (of $\boldsymbol{q}_f$). Cases such as ionisation or dissociation where the final states of the target form a continuum will be treated specifically in later sections. Throughout this thesis we will assume the following standard normalisation of

the plane waves:

$$\langle \boldsymbol{r}|\boldsymbol{q}\rangle = \frac{1}{(2\pi)^{3/2}} e^{i\boldsymbol{q}\cdot\boldsymbol{r}} \tag{2.62}$$

$$\int_{\mathbb{R}^3} \langle \boldsymbol{q}'|\boldsymbol{r}\rangle\langle \boldsymbol{r}|\boldsymbol{q}\rangle \,\mathrm{d}\boldsymbol{r} = \delta(\boldsymbol{q}-\boldsymbol{q}'), \tag{2.63}$$

which implies the following unity resolution:

$$\int_{\mathbb{R}^3} \langle \boldsymbol{r}'|\boldsymbol{q}\rangle\langle \boldsymbol{q}|\boldsymbol{r}\rangle \,\mathrm{d}\boldsymbol{q} = \delta(\boldsymbol{r}-\boldsymbol{r}'). \tag{2.64}$$

The outgoing projectile can be characterised by its energy E_f and direction Ω, so Eq. (2.61) becomes

$$\iint_{\Omega}\int_{0}^{\infty} \langle \boldsymbol{r}'|\boldsymbol{q}\rangle\langle \boldsymbol{q}|\boldsymbol{r}\rangle \rho(E_f,\Omega)\,\mathrm{d}E_f\,\mathrm{d}\Omega = \delta(\boldsymbol{r}'-\boldsymbol{r}). \tag{2.65}$$

Substituting $\mathrm{d}\boldsymbol{q} = q\,\mathrm{d}E\,\mathrm{d}\Omega$ into Eq. (2.64) and comparing with Eq. (2.65) gives

$$\rho(E_f,\Omega) = q_f, \tag{2.66}$$

and hence the transition rate becomes

$$w_{f\leftarrow i} = 2\pi q_f \iint_{\Omega}\int_{0}^{\infty} \left|\langle \boldsymbol{q}_f\phi_f|\hat{\mathsf{T}}|\phi_i\boldsymbol{q}_i\rangle\right|^2 \delta(E-E')\,\mathrm{d}E_f\,\mathrm{d}\Omega, \tag{2.67}$$

$$= 2\pi q_f \iint_{\Omega} \left|\langle \boldsymbol{q}_f\phi_f|\hat{\mathsf{T}}|\phi_i\boldsymbol{q}_i\rangle\right|^2 \mathrm{d}\Omega, \tag{2.68}$$

where the integration over E_f is removed by the $\delta(E-E')$ term which enforces energy conservation on the scattered energy E_f. It is natural now to define the transition rate for scattering into the differential solid angle $\mathrm{d}\Omega$ as

$$\mathrm{d}w_{f\leftarrow i} = 2\pi q_f \left|\langle \boldsymbol{q}_f\phi_f|\hat{\mathsf{T}}|\phi_i\boldsymbol{q}_i\rangle\right|^2 \mathrm{d}\Omega. \tag{2.69}$$

The cross section $\mathrm{d}\sigma$ associated with transitions into $\mathrm{d}\Omega$ is defined by the ratio of the transition rate to the incident current density j_i, which for the choice of

normalisation in Eq. (2.62) is

$$j_i = \frac{q_i}{(2\pi)^3}, \tag{2.70}$$

giving

$$\mathrm{d}\sigma_{f\leftarrow i} = (2\pi)^4 \frac{q_f}{q_i} \left| \langle \boldsymbol{q}_f \phi_f | \hat{\mathsf{T}} | \phi_i \boldsymbol{q}_i \rangle \right|^2 \mathrm{d}\Omega, \tag{2.71}$$

and finally the differential cross section

$$\frac{\mathrm{d}\sigma_{f\leftarrow i}}{\mathrm{d}\Omega} = (2\pi)^4 \frac{q_f}{q_i} \left| \langle \boldsymbol{q}_f \phi_f | \hat{\mathsf{T}} | \phi_i \boldsymbol{q}_i \rangle \right|^2. \tag{2.72}$$

In terms of the scattering amplitude, the differential cross section is

$$\frac{\mathrm{d}\sigma_{f\leftarrow i}}{\mathrm{d}\Omega} = \frac{q_f}{q_i} \left| F_{f,i}(\boldsymbol{q}_f, \boldsymbol{q}_i) \right|^2, \tag{2.73}$$

and the integral cross section is defined by

$$\sigma_{f\leftarrow i} = \iint_{\Omega} \frac{\mathrm{d}\sigma_{f\leftarrow i}}{\mathrm{d}\Omega} \mathrm{d}\Omega. \tag{2.74}$$

2.7 Partial-wave analysis

The T-matrix element $\langle \boldsymbol{q}_f \phi_f | \hat{\mathsf{T}} | \phi_i \boldsymbol{q}_i \rangle$ is dependent on the three-dimensional vectors $\boldsymbol{q}_f$ and $\boldsymbol{q}_i$, requiring methods of solution to consider six dimensions for the projectile alone. A standard approach to simplifying the scattering equations is the method of partial waves, where the projectile plane waves are expanded in terms of definite orbital angular momenta:

$$\langle \boldsymbol{r} | \boldsymbol{q} \rangle = \frac{1}{(2\pi)^{3/2}} e^{i\boldsymbol{q}\cdot\boldsymbol{r}} = \sqrt{\frac{2}{\pi}} \frac{1}{qr} \sum_{\ell=0}^{\infty} \sum_{m=-\ell}^{+\ell} i^\ell u_\ell(kr) Y_\ell^m(\hat{\boldsymbol{r}}) Y_\ell^{m*}(\hat{\boldsymbol{q}}), \tag{2.75}$$

and $u_\ell(qr)$ are the solutions to the radial free-particle Schrödinger equation:

$$\left[-\frac{1}{2} \frac{\mathrm{d}^2}{\mathrm{d}r^2} + \frac{\ell(\ell+1)}{2r^2} - \frac{q^2}{2} \right] u_\ell(qr) = 0. \tag{2.76}$$

In the cases of scattering on charged targets or the use of numerical methods such as distorting potentials then the asymptotic projectile states are not plane waves and the expansion in Eq. (2.75) contains additional phase shifts, while Eq. (2.76) contains an additional potential term. However, neither or these will

be of relevance in the present work.

Using Eq. (2.75), the partial-wave expansion of the T-matrix element is

$$\langle \boldsymbol{q}_f \phi_f | \hat{\mathsf{T}} | \phi_i \boldsymbol{q}_i \rangle = \frac{1}{q_f q_i} \sum_{\substack{\ell_f m_f \\ \ell_i m_i}} i^{\ell_i - \ell_f} \langle q_f \ell_f m_f \phi_f | \hat{\mathsf{T}} | \phi_i q_i \ell_i m_i \rangle Y_{\ell_f}^{m_f}(\hat{\boldsymbol{q}}_f) Y_{\ell_i}^{m_i *}(\hat{\boldsymbol{q}}_i), \quad (2.77)$$

where $|q\ell m\rangle$ are defined by

$$\langle \boldsymbol{r} | q\ell m \rangle = \sqrt{\frac{2}{\pi}} \frac{1}{r} u_\ell(qr) Y_\ell^m(\hat{\boldsymbol{r}}). \quad (2.78)$$

Substitution of Eq. (2.77) into whichever scattering equations have been formulated for the full T-matrix element then allows the simplification of the equations into a form which can be solved for the partial-wave T-matrix elements. Rather than reconstructing the full T-matrix afterwards, the cross sections can be obtained directly from the partial-wave matrix elements. Recalling the definition of the scattering amplitude given in Eq. (2.30), it can be expressed in terms of the partial-wave expansion of T as follows:

$$F_{f,i}(\boldsymbol{q}_f, \boldsymbol{q}_i) = -\frac{4\pi^2}{q_f q_i} \sum_{\substack{\ell_f m_f \\ \ell_i m_i}} i^{\ell_i - \ell_f} \langle q_f \ell_f m_f \phi_f | \hat{\mathsf{T}} | \phi_i q_i \ell_i m_i \rangle Y_{\ell_f}^{m_f}(\hat{\boldsymbol{q}}_f) Y_{\ell_i}^{m_i *}(\hat{\boldsymbol{q}}_i). \quad (2.79)$$

Defining the partial-wave scattering amplitudes

$$F_{f\ell_f m_f, i\ell_i m_i}(q_f, q_i) = -\frac{4\pi^2}{q_f q_i} \langle q_f \ell_f m_f \phi_f | \hat{\mathsf{T}} | \phi_i q_i \ell_i m_i \rangle, \quad (2.80)$$

Eq. (2.79) can be written more compactly as

$$F_{f,i}(\boldsymbol{q}_f, \boldsymbol{q}_i) = \sum_{\substack{\ell_f m_f \\ \ell_i m_i}} i^{\ell_i - \ell_f} F_{f\ell_f m_f, i\ell_i m_i}(q_f, q_i) Y_{\ell_f}^{m_f}(\hat{\boldsymbol{q}}_f) Y_{\ell_i}^{m_i *}(\hat{\boldsymbol{q}}_i). \quad (2.81)$$

The differential cross section (2.73) can then be expressed as

$$\frac{\mathrm{d}\sigma_{f \leftarrow i}}{\mathrm{d}\Omega} = \frac{q_f}{q_i} \sum_{\substack{\ell'_f m'_f \\ \ell'_i m'_i}} \sum_{\substack{\ell_f m_f \\ \ell_i m_i}} i^{\ell'_f - \ell'_i + \ell_i - \ell_f} F_{f\ell'_f m'_f, i\ell'_i m'_i}(q_f, q_i) F_{f\ell_f m_f, i\ell_i m_i}(q_f, q_i) \times Y_{\ell'_f}^{m'_f *}(\hat{\boldsymbol{q}}_f) Y_{\ell'_i}^{m'_i}(\hat{\boldsymbol{q}}_i) Y_{\ell_f}^{m_f}(\hat{\boldsymbol{q}}_f) Y_{\ell_i}^{m_i *}(\hat{\boldsymbol{q}}_i). \quad (2.82)$$

An expression for the integrated cross section can be obtained by integrating over

the scattered direction $\hat{\boldsymbol{q}}_f$. From the orthogonality of the spherical harmonics, we have

$$\iint_{\Omega} Y_{\ell'_f}^{m'_f *}(\hat{\boldsymbol{q}}_f) Y_{\ell_f}^{m_f}(\hat{\boldsymbol{q}}_f)\, \mathrm{d}\hat{\boldsymbol{q}}_f = \delta_{\ell'_f \ell_f} \delta_{m'_f m_f}, \tag{2.83}$$

and assuming the usual convention that the z axis is aligned with the incident beam we have

$$Y_{\ell_i}^{m_i}(\hat{\boldsymbol{z}}) Y_{\ell_i}^{m_i}(\hat{\boldsymbol{z}}) = \frac{2\ell_i + 1}{4\pi} \delta_{m_i,0}. \tag{2.84}$$

The integrated cross section is then given by

$$\sigma_{f \leftarrow i} = \frac{1}{4\pi} \frac{q_f}{q_i} \sum_{\substack{\ell_f m_f \\ \ell_i m_i}} (2\ell_i + 1) \left| F_{f\ell_f m_f, i\ell_i m_i}(q_f, q_i) \right|^2 . \tag{2.85}$$

In practice, the partial-wave expansion tends to be defined somewhat differently to what is presented above in order to exploit additional symmetries of the scattering system, and in the case of molecular scattering the common analytical treatments of rotational motion also lead to different cross-section formulas. Nevertheless, the above is sufficient to convey the principles of partial-wave analysis, and the specific application to molecular scattering in the MCCC method will be given in Chapter 6.

2.8 Chapter 2 summary

The details of quantum scattering theory provided here, while brief, ought to provide sufficient background for a reader with an undergraduate-level understanding of quantum mechanics to follow the remaining chapters presented in this thesis, and appreciate the details of the MCCC theory. This chapter is included in the hope that future students joining the MCCC project can use this as a starting point for learning the tools of the trade.

It is made evident in this chapter that all of the physics in a scattering experiment is contained within the T matrix. Although it is possible to solve for the coordinate-space scattering wave function explicitly, and indeed there are methods which do this, all collision data of interest can be obtain by solving directly for the T matrix. One of the unique aspects of the CCC and MCCC methods

is the approach of formulating the scattering equations in momentum space explicitly for the T-matrix elements, and is one of the reasons for its computational efficiency.

Chapter 3

Structure of diatomic molecules

This chapter presents an overview of the theory of diatomic molecule structure. The following textbooks have been consulted: Brown and Carrington [145] and Lefebvre-Brion and Field [146]. Specific details of the structure calculations performed in the present work are provided in Chapter 6.

3.1 The total molecular Hamiltonian

The total Hamiltonian for a diatomic molecular with nuclear masses M_1 and M_2 and N_e electrons, with respect to an arbitrary origin in spherical coordinates is

$$\hat{\mathsf{H}} = -\frac{1}{2}\sum_{i=1}^{N_\mathrm{e}}\nabla_i^2 - \sum_{\alpha=1}^{2}\frac{1}{M_\alpha}\nabla_\alpha^2 + \sum_{j>i=1}^{N_\mathrm{e}}\frac{1}{|\boldsymbol{r}_i-\boldsymbol{r}_j|} - \sum_{\alpha=1}^{2}\sum_{i=1}^{N_\mathrm{e}}\frac{Z_\alpha}{|\boldsymbol{R}_\alpha-\boldsymbol{r}_i|} + \frac{Z_1Z_2}{|\boldsymbol{R}_1-\boldsymbol{R}_2|}, \tag{3.1}$$

where $\boldsymbol{R}$ and $\boldsymbol{r}$ are the nuclear and electronic coordinates, respectively. It is more convenient to work in a coordinate frame with the origin placed at the geometric centre of the nuclei. The transformation of the Hamiltonian into this coordinate system is given in tedious detail in Ref. [145], and here we just state the final result:

$$\begin{aligned}\hat{\mathsf{H}} = -\frac{1}{2}\sum_{i=1}^{N_\mathrm{e}}\nabla_i^2 - \frac{1}{2(M_1+M_2)}\sum_{i,j=1}^{N_\mathrm{e}}\nabla_i\cdot\nabla_j - \frac{1}{2\mu}\nabla_{\boldsymbol{R}}^2 + \sum_{j>i=1}^{N_\mathrm{e}}\frac{1}{|\boldsymbol{r}_i-\boldsymbol{r}_j|} \\ - \sum_{i=1}^{N_\mathrm{e}}\left[\frac{Z_1}{\left|\frac{\boldsymbol{R}}{2}-\boldsymbol{r}_i\right|} + \frac{Z_2}{\left|\frac{\boldsymbol{R}}{2}+\boldsymbol{r}_i\right|}\right] + \frac{Z_1Z_2}{R}.\end{aligned} \tag{3.2}$$

The individual terms of this Hamiltonian are:

- $-\frac{1}{2}\sum_{i=1}^{N_\mathrm{e}}\nabla_i^2$ kinetic energy operators of the N_e electrons, where ∇_i^2 is the

Laplacian operator in terms of the electronic coordinates $\boldsymbol{r}_i$ relative to the origin at the geometric centre of the nuclei.

- $-\frac{1}{2(M_1+M_2)}\sum_{i,j=1}^{N_\mathrm{e}}\nabla_i\cdot\nabla_j$ mass-polarisation term, which describes the response of the centre of mass to the movement of the electrons.
- $-\frac{1}{2\mu}\nabla^2_{\boldsymbol{R}}$ nuclear kinetic-energy operator, where μ is the nuclear reduced mass and $\nabla^2_{\boldsymbol{R}}$ is the Laplacian operator in terms of the internuclear vector $\boldsymbol{R}$.
- $\sum_{j>i=1}^{N_\mathrm{e}}\frac{1}{|\boldsymbol{r}_i-\boldsymbol{r}_j|}$ electron-electron potential.
- $\sum_{i=1}^{N_\mathrm{e}}\left[\frac{Z_1}{\left|\frac{\boldsymbol{R}}{2}-\boldsymbol{r}_i\right|}+\frac{Z_2}{\left|\frac{\boldsymbol{R}}{2}+\boldsymbol{r}_i\right|}\right]$ electron-nuclear potential.
- $\frac{Z_1Z_2}{R}$ nuclear potential, where Z_1 and Z_2 are the nuclear charges.

To simplify, we define

$$V_{ij}\equiv\frac{1}{|\boldsymbol{r}_i-\boldsymbol{r}_j|} \tag{3.3}$$

$$V_i\equiv\frac{Z_1}{\left|\frac{\boldsymbol{R}}{2}-\boldsymbol{r}_i\right|}+\frac{Z_2}{\left|\frac{\boldsymbol{R}}{2}+\boldsymbol{r}_i\right|}, \tag{3.4}$$

so that the Hamiltonian can be written as

$$\hat{\mathsf{H}}=-\frac{1}{2}\sum_{i=1}^{N_\mathrm{e}}\nabla_i^2-\frac{1}{2(M_1+M_2)}\sum_{i,j=1}^{N_\mathrm{e}}\nabla_i\cdot\nabla_j-\frac{1}{2\mu}\nabla^2_{\boldsymbol{R}}+\sum_{j>i=1}^{N_\mathrm{e}}V_{ij}-\sum_{i=1}^{N_\mathrm{e}}V_i+\frac{Z_1Z_2}{R}. \tag{3.5}$$

3.2 The Born-Oppenheimer approximation

The Born-Oppenheimer approximation neglects the mass-polarisation term, and assumes that the total molecular wave function can be expressed as a product of an electronic wave function (which depends on $\boldsymbol{R}$ only parametrically), and a nuclear wave function:

$$\Phi(\boldsymbol{r}_1,\boldsymbol{r}_2,\ldots,\boldsymbol{R})=\Phi_\mathrm{el}(\boldsymbol{r}_1,\boldsymbol{r}_2,\ldots;\boldsymbol{R})\Phi_\mathrm{nucl}(\boldsymbol{R}), \tag{3.6}$$

where Φ_{el} is an eigenstate of the electronic Hamiltonian:

$$\hat{\mathsf{H}}_{\text{el}}|\Phi_{\text{el}}\rangle = \epsilon_{\text{el}}|\Phi_{\text{el}}\rangle \tag{3.7}$$

$$\hat{\mathsf{H}}_{\text{el}} = -\frac{1}{2}\sum_{i=1}^{N_{\text{e}}}\nabla_i^2 + \sum_{j>i=1}^{N_{\text{e}}} V_{ij} - \sum_{\alpha=1}^{2}\sum_{i=1}^{N_{\text{e}}} V_i. \tag{3.8}$$

Here, ϵ_{el} is the energy of the electronic state. We also define the nuclear Hamiltonian

$$\hat{\mathsf{H}}_{\text{nucl}} = -\frac{1}{2\mu}\nabla_{\boldsymbol{R}}^2 + \frac{Z_1 Z_2}{R}, \tag{3.9}$$

so that the Born-Oppenheimer total molecular Hamiltonian can be written as

$$\hat{\mathsf{H}}_{\text{BO}} = \hat{\mathsf{H}}_{\text{el}} + \hat{\mathsf{H}}_{\text{nucl}}. \tag{3.10}$$

The Schrödinger equation for the Born-Oppenheimer states is

$$(\hat{\mathsf{H}}_{\text{el}} + \hat{\mathsf{H}}_{\text{nucl}})\Phi_{\text{el}}\Phi_{\text{nucl}} = \varepsilon_{\text{el}-\text{nucl}}\Phi_{\text{el}}\Phi_{\text{nucl}}, \tag{3.11}$$

where $\varepsilon_{\text{el-nucl}}$ is the total (electronic plus nuclear motion) state energy. Since Φ_{el} is an eigenstate of $\hat{\mathsf{H}}_{\text{el}}$ with energy ϵ_{el}, this can be rearranged to give the Schrödinger equation for the nuclear wave functions:

$$\hat{\mathsf{H}}_{\text{nucl}}\Phi_{\text{nucl}} + \epsilon_{\text{el}}(R)\Phi_{\text{nucl}} = \varepsilon_{\text{el}-\text{nucl}}\Phi_{\text{nucl}}. \tag{3.12}$$

As will be shown later, the best choices of approximate molecular wave function are actually linear combinations of the Born-Oppenheimer products (3.6) which are adapted to satisfy certain symmetry requirements.

3.3 Transformation to molecule-fixed frame

The structure calculation can be simplified by a transformation to a molecule-fixed (also called body-frame) axis which rotates with $\hat{\boldsymbol{R}}$. We choose the new coordinate system so that the body-frame z axis points along the internuclear vector $\boldsymbol{R}$, and relate the body-frame and lab-frame coordinate systems by a passive rotation with Euler angles (α, β, γ). Note that γ describes the orientation of the body-frame axes about the body-frame z axis and is therefore redundant

as there are no off-axis nuclei in diatomic molecules. The nuclear kinetic-energy operator in terms of the new coordinates is given by

$$-\frac{1}{2\mu}\nabla^2_{\boldsymbol{R}} = -\frac{1}{2\mu R^2}\frac{\partial}{\partial R}\left(R^2\frac{\partial}{\partial R}\right) \tag{3.13}$$

$$-\frac{1}{2\mu R^2}\left[\frac{1}{\sin\alpha}\frac{\partial}{\partial\alpha}\left(\sin\alpha\frac{\partial}{\partial\alpha}\right)+\frac{1}{\sin^2\alpha}\left(\frac{\partial^2}{\partial\beta^2}+\frac{\partial^2}{\partial\gamma^2}-2\cos\alpha\frac{\partial^2}{\partial\beta\partial\gamma}\right)\right]$$

$$= -\frac{1}{2\mu R^2}\frac{\partial}{\partial R}\left(R^2\frac{\partial}{\partial R}\right)+\frac{1}{2\mu R^2}\hat{\mathbf{J}}^2_{\mathrm{r}}, \tag{3.14}$$

where $\hat{\mathbf{J}}^2_{\mathrm{r}}$ is the squared rotational angular-momentum operator. Since the electronic Hamiltonian does not contain any explicit dependence on the nuclear orientation (only dependence on the relative position of the electrons and nuclei), the transformation of the electronic Hamiltonian to the body frame is trivial. Each operator is simply redefined to act on the body-frame electronic coordinates, and conversion between the lab-frame and body-frame wave functions is given by

$$\Phi^{(\mathrm{lab})}_{\mathrm{el}}(\boldsymbol{r}_1,\boldsymbol{r}_2;\boldsymbol{R}) = \Phi^{(\mathrm{b})}_{\mathrm{el}}(\boldsymbol{r}^{(\mathrm{b})}_1,\boldsymbol{r}^{(\mathrm{b})}_2,R), \tag{3.15}$$

where the body-frame wave functions $\Phi^{(\mathrm{b})}_{\mathrm{el}}$ are the eigenstates of the electronic Hamiltonian with the operators defined to act on the body-frame coordinates. The spin states in the lab frame can be represented in terms of states quantised with respect to the $\hat{\boldsymbol{R}}$ axis:

$$|sm_s\rangle = \sum_{\Sigma_s} D^{s*}_{m_s\Sigma_s}(\hat{\boldsymbol{R}})|s\Sigma_s\rangle, \tag{3.16}$$

where m_s and Σ_s are the lab-frame and body-frame spin projections, and $D^{s*}_{m_s\Sigma_s}$ is a Wigner-D function.

3.4 Electronic structure

3.4.1 Symmetries of the electronic Hamiltonian

Operators which commute with the Hamiltonian correspond to good quantum numbers. Here we check whether some of the standard quantum mechanical operators commute with the diatomic electronic Hamiltonian. Each are well-known

to commute with the single-particle kinetic-energy operator, and it follows that they commute with the two-electron kinetic-energy operator, so it only remains to test their commutativity with the diatomic electronic potential. Each operator here is defined in the body frame. Note that the operator corresponding to the orbital angular-momentum projection on the internuclear axis will be denoted $\hat{\Lambda}$ rather than $\hat{\mathsf{L}}_z$, so that the "z" subscript can be reserved for projections onto the laboratory-frame z axis. More detailed derivations of the results presented here can be found in Appendix D.

- Orbital angular-momentum (squared) operator $\hat{\mathsf{L}}^2$

  The $\hat{\mathsf{L}}^2$ operator can be written as

$$\hat{\mathsf{L}}^2 = \sum_{i=1}^{N_\mathrm{e}} \left[\frac{1}{\sin^2\theta_i} \frac{\partial^2}{\partial \phi_i^2} + \frac{1}{\sin\theta_i} \frac{\partial}{\partial \theta_i} \sin\theta_i \frac{\partial}{\partial \theta_i} \right], \tag{3.17}$$

  and hence the commutator $[\hat{\mathsf{L}}^2, \hat{\mathsf{V}}]$ is

$$[\hat{\mathsf{L}}^2, \hat{\mathsf{V}}] = \sum_{i=1}^{N_\mathrm{e}} \left[\sin\theta_i \left(2 \frac{\partial V}{\partial \theta_i} \frac{\partial}{\partial \theta_i} + \frac{\partial^2 V}{\partial \theta_i^2} \right) + \cos\theta_i \frac{\partial V}{\partial \theta_i} + \frac{1}{\sin^2\theta_i} \left(2 \frac{\partial V}{\partial \phi_i} \frac{\partial}{\partial \phi_i} + \frac{\partial^2 V}{\partial \phi_i^2} \right) \right]. \tag{3.18}$$

  As a result, the orbital angular momentum is not a good quantum number for diatomic molecules since the θ dependence of the nuclear potential leads to

$$\frac{\partial V}{\partial \theta_i} \neq 0. \tag{3.19}$$

- Orbital angular-momentum projection operator $\hat{\Lambda}$

  The orbital angular-momentum projection operator can be written as

$$\hat{\Lambda} = -i \sum_{i=1}^{N_\mathrm{e}} \frac{\partial}{\partial \phi_i}, \tag{3.20}$$

  and it can be shown that the commutator $[\hat{\Lambda}, \hat{\mathsf{V}}]$ is

$$[\hat{\Lambda}, \hat{\mathsf{V}}] = i \sum_{i=1}^{N_\mathrm{e}} \frac{\partial V_i}{\partial \phi_i} - i \sum_{i=1}^{N_\mathrm{e}} \sum_{j>1}^{N_\mathrm{e}} \left[\frac{\partial V_{ij}}{\partial \phi_i} + \frac{\partial V_{ij}}{\partial \phi_j} \right] = 0. \tag{3.21}$$

The commutator is zero by virtue of the facts that the electron-nuclear potential V_i is independent of ϕ_i, and the electron-electron potentials satisfy

$$\frac{\partial V_{ij}}{\partial \phi_i} = -\frac{\partial V_{ij}}{\partial \phi_j}. \tag{3.22}$$

As a result, the orbital angular-momentum projection onto the internuclear axis *is* a good quantum number for diatomic molecules.

- Body-frame space inversion operator $\hat{\mathsf{t}}$

  The effect of the body-frame space inversion operator on the electron-electron and electron-nuclear potentials is

$$\hat{\mathsf{t}} V_{ij} = \frac{1}{|-\boldsymbol{r}_i + \boldsymbol{r}_j|} = V_{ij} \tag{3.23}$$

$$\hat{\mathsf{t}} V_i = \frac{Z_2}{\left|\frac{\boldsymbol{R}}{2} - \boldsymbol{r}_i\right|} + \frac{Z_1}{\left|\frac{\boldsymbol{R}}{2} + \boldsymbol{r}_i\right|}, \tag{3.24}$$

  and hence the commutator $[\hat{\mathsf{t}}, \hat{\mathsf{V}}]$ is

$$[\hat{\mathsf{t}}, \hat{\mathsf{V}}] = \sum_{i=1}^{N_\mathrm{e}} \left[\frac{Z_2 - Z_1}{\left|\frac{\boldsymbol{R}}{2} - \boldsymbol{r}_i\right|} + \frac{Z_1 - Z_2}{\left|\frac{\boldsymbol{R}}{2} + \boldsymbol{r}_i\right|} \right] \hat{\mathsf{t}}. \tag{3.25}$$

  As a result, the electronic parity is a good quantum number for homonuclear diatomics ($Z_1 = Z_2$).

So far, we have shown that the electronic parity and electronic orbital angular-momentum projection on the internuclear axis are both conserved quantities for homonuclear diatomics. It is also assumed in non-relativistic quantum mechanics that the total spin is conserved. Furthermore, the diatomic potential has reflection symmetry through any plane containing the internuclear axis. Since the system is cylindrically symmetric we can, without loss of generality, consider only the reflection through the xz plane. This operation can be denoted by $\hat{\mathsf{M}}_y$ (M for mirror):

$$\hat{\mathsf{M}}_y : y \to -y. \tag{3.26}$$

It can be shown that $\hat{\mathsf{M}}_y$ is anticommutative with $\hat{\Lambda}$, i.e.

$$\hat{\mathsf{M}}_y \hat{\Lambda} = -\hat{\Lambda} \hat{\mathsf{M}}_y. \tag{3.27}$$

If we denote by $|\Lambda\rangle$ an electronic state with angular-momentum projection Λ, then the state $\hat{\mathsf{M}}_y|\Lambda\rangle$ satisfies

$$\hat{\Lambda}\hat{\mathsf{M}}_y|\Lambda\rangle = -\Lambda\hat{\mathsf{M}}_y|\Lambda\rangle. \tag{3.28}$$

In other words, the $\hat{\mathsf{M}}_y$ operator acts on a state $|\Lambda\rangle$ to produce another state with equal but opposite angular-momentum projection. This is true of course only when $|\Lambda| > 0$. In the special case that $\Lambda = 0$ we have $\hat{\Lambda}|\Lambda\rangle = -\hat{\Lambda}|\Lambda\rangle$, and hence when acting on a $\Lambda = 0$ state the $\hat{\mathsf{M}}_y$ and $\hat{\Lambda}$ operators commute. As a result, the eigenstates of $\hat{\Lambda}$ with $\Lambda = 0$ are simultaneously eigenstates of $\hat{\mathsf{M}}_y$, and since reflecting through the xz plane twice should return the original state:

$$\hat{\mathsf{M}}_y\hat{\mathsf{M}}_y|\Lambda = 0\rangle = |\Lambda = 0\rangle, \tag{3.29}$$

the eigenvalues of the $|\Lambda = 0\rangle$ states under the $\hat{\mathsf{M}}_y$ operation are necessarily ± 1. The two consequences of the above are:

1. $|\Lambda| > 0$ states occur in degenerate pairs with angular-momentum projections $\pm\,|\Lambda|$.

2. The states with $\Lambda = 0$ are each either symmetric or antisymmetric under reflection through a plane containing the internuclear axis.

3.4.2 Molecular term symbols

The symmetries of an electronic state are specified in its *term symbol*:

$$^{2s+1}\Lambda^{\pm}_{g/u}. \tag{3.30}$$

Here, s is the total electronic spin, and $2s+1$ is the spin multiplicity. For example, two-electron molecules can have spin $s = 0$ (singlet, $2s + 1 = 1$) or spin $s = 1$ (triplet, $2s + 1 = 3$). The symbol Λ is again the angular-momentum projection on the internuclear axis, with the following conventions used:

$$\Sigma : \Lambda = 0, \qquad \Pi : \Lambda = \pm 1, \qquad \Delta : \Lambda = \pm 2, \qquad \Phi : \Lambda = \pm 3, \tag{3.31}$$

and so on, following the Greek-letter analogue of the $S, P, D, F, \ldots$ convention of atomic term symbols. The subscripts g or u refer to even (*gerade*) or odd (*ungerade*) parity. The superscript $\pm$ is applied to the Σ states (those with $\Lambda = 0$) to specify whether they are symmetric $(+)$ or antisymmetric $(-)$ under reflection through a plane containing the internuclear axis. As an example, a state with spin $s = 1$, angular-momentum projection $\Lambda = 0$, even parity, and which is symmetric under the aforementioned reflection has the term symbol $^3\Sigma_g^+$. For the $\Lambda \neq 0$ states the $\pm$ superscript does not form part of the electronic term symbol, although to make matters confusing a $\pm$ superscript is used on $\Lambda \neq 0$ term symbols for a separate reason when introducing rotational levels. This will be discussed in detail later.

In order to distinguish between the multiple electronic state of a given symmetry, a Latin character is prepended to the term symbol according to the following conventions:

1. The ground electronic state is assigned the letter X
2. Electronic states with the same spin as the ground state are given capital letters, while those with different spin are given lower-case letters
3. In principle, the excited states should be assigned letters in alphabetical order, although there are many cases where this convention is not upheld for historical reasons.

For example, the ground state of H_2 (singlet, even parity) has the label $X\ ^1\Sigma_g^+$, while the ground state of O_2 (triplet, even parity) is $X\ ^3\Sigma_g^-$.

3.4.3 Electronic states and potential-energy curves of H_2

A range of accurate electronic structure calculations have been previously performed for H_2 [147–152]. In this section, the potential-energy curves from these calculations will be used to introduce the low-lying H_2 electronic states. Details of the electronic structure underlying the scattering calculations performed in the present work will be given in Chapter 6.

Fig. 3.1 shows the potential-energy curves of the first 27 electronic states of H_2 (27 including Λ degeneracy). The first three electronic states are explicitly

labelled, and the potential-energy curve of the H_2^+ ion is also shown. At internuclear separations larger than around 1 a_0, the electronic structure becomes more complex, as states which share the same atomic limit become non-degenerate and split into multiple potential-energy curves. At even larger separations, the states converge to a limit corresponding to molecular dissociation into two atomic fragments. The states shown here all dissociate into one H($1s$) atom and one H atom in either the ground or an excited state, as indicated on the figure.

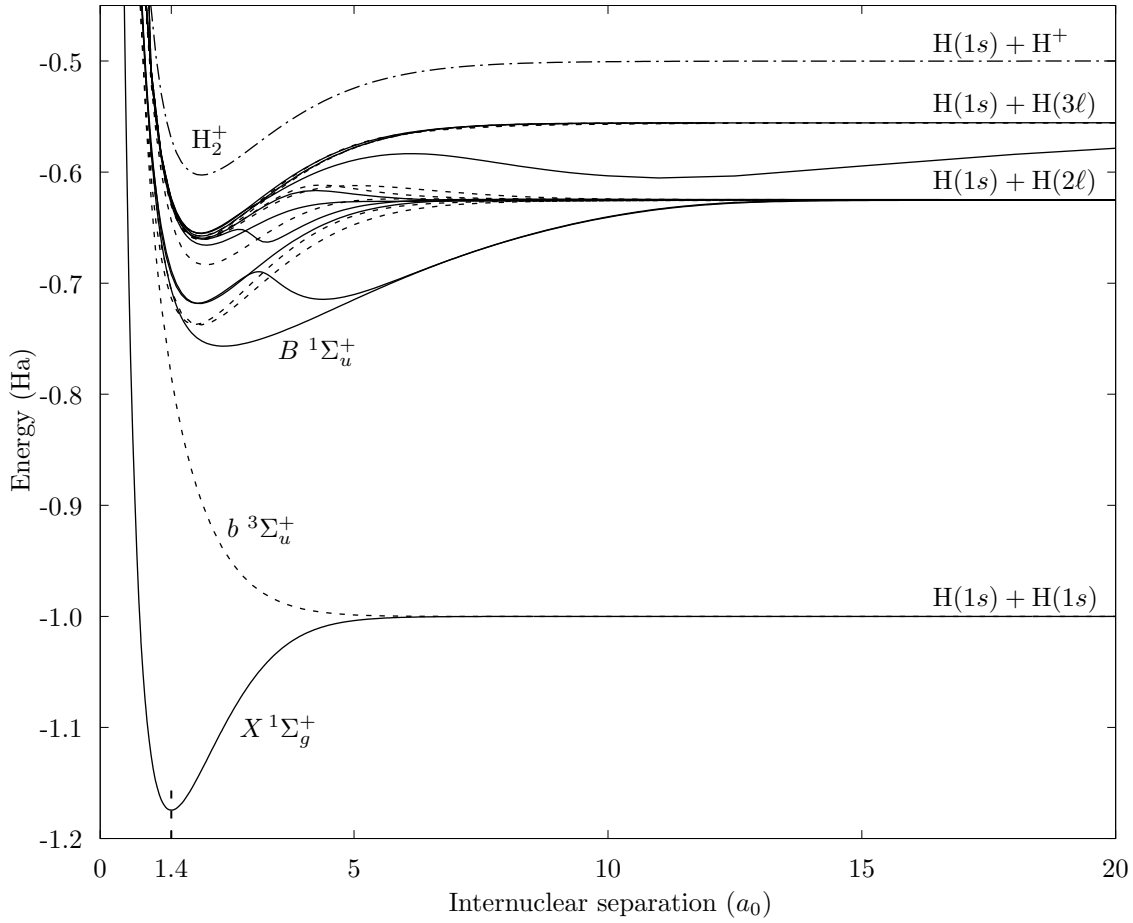

Figure 3.1: Potential-energy curves (including the nuclear repulsion term) of the $n = 1$–3 electronic states of H_2. Solid lines indicate singlet states, while dashed lines indicate triplet states. The vertical dashed line at 1.4 a_0 indicates the equilibrium point of the ground state. The potential-energy curves have been taken from various literature sources [147–152].

When the internuclear separation is set to zero, the H_2 electronic energies (with the nuclear-repulsion term removed) are equivalent to the helium atom energies. It can be convenient to group diatomic electronic states together according

to which atomic states they correspond to in the united-atoms limit. Fig. 3.2 lists each of the electronic states of H_2 up to $n = 4$ in the atomic limit, indicating which atomic helium state each one corresponds to. Those states labelled with $[n\ell]$ rather than a Latin character have not yet been formally identified.

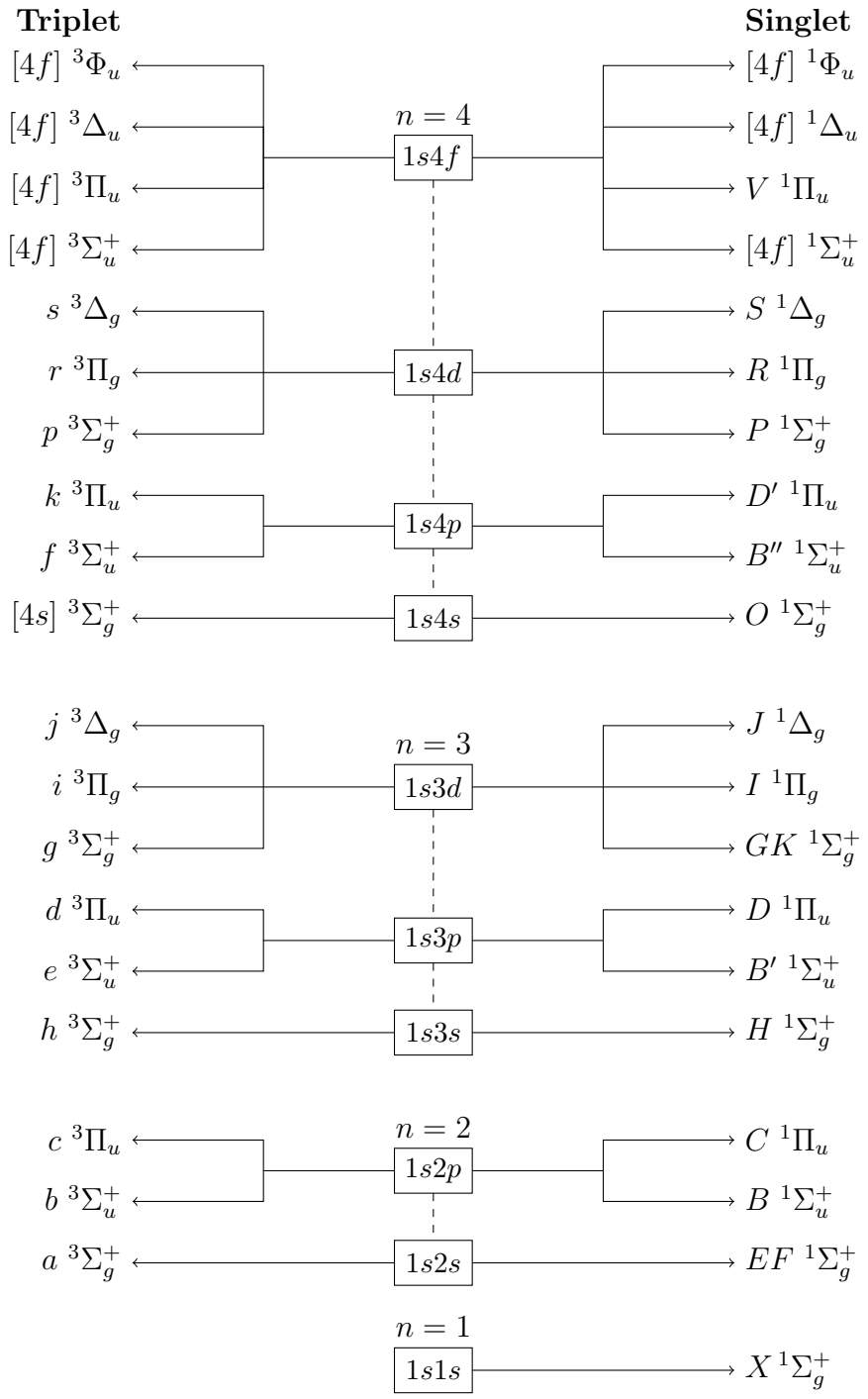

Figure 3.2: Diagram of the electronic states of H_2 and the atomic helium states they converge to in the united-atoms limit. Note that the helium states are labelled according to their dominant electronic configuration.

3.5 Nuclear motion

The vibrational and rotational components of the nuclear wave functions can be considered analogues to the radial and angular components of the wave functions for a central potential. We seek separable nuclear wave functions of the form

$$\Phi_{\text{nucl}}(\boldsymbol{R}) = \frac{1}{R}\nu(R)\phi_{\text{rot}}(\hat{\boldsymbol{R}}), \tag{3.32}$$

where R is the internuclear distance, $\nu(R)$ is the vibrational wave function, $\hat{\boldsymbol{R}}$ is the orientation of the internuclear axis, and $\phi_{\text{rot}}(\hat{\boldsymbol{R}})$ is the rotational wave function. Assuming the nuclear repulsion potential Z_1Z_2/R has been absorbed into the electronic energy $\epsilon_n(R)$, the nuclear wave functions must satisfy

$$-\frac{1}{2\mu}\frac{\partial^2}{\partial R^2}\nu(R)\phi_{\text{rot}}(\hat{\boldsymbol{R}}) + \left[\frac{1}{2\mu R^2}\hat{\mathsf{J}}_{\text{r}}^2 + \epsilon_n(R) - \varepsilon_{\text{el}-\text{nucl}}\right]\nu(R)\phi_{\text{rot}}(\hat{\boldsymbol{R}}) = 0, \tag{3.33}$$

which can be rearranged to give

$$-\frac{R^2}{\nu(R)}\frac{\mathrm{d}^2}{\mathrm{d}R^2}\nu(R) + 2\mu R^2\left[\epsilon_n(R) - \varepsilon_{\text{el}-\text{nucl}}\right] = -\frac{1}{\phi_{\text{rot}}(\hat{\boldsymbol{R}})}\hat{\mathsf{J}}_{\text{r}}^2\phi_{\text{rot}}(\hat{\boldsymbol{R}}). \tag{3.34}$$

Here, $\varepsilon_{\text{el-nucl}}$ is the total (electronic plus nuclear) state energy. Since the electronic energy $\epsilon_n(R)$ appears in this equation in a similar manner that the potential energy usually appears in the Schrödinger equation, it is commonly referred to as the *potential-energy curve*. In this sense, it represents the effective potential in which the nuclei move. It is worth noting, however, that it is really the *total* electronic energy and does not represent a physical potential.

Since the left-hand side of Eq. (3.34) depends only on R, and the right-hand side depends only on $\hat{\boldsymbol{R}}$, the standard separation-of-variables approach can be applied by setting both sides equal to a constant λ, giving the separated vibrational and rotational wave equations:

$$-\frac{1}{2\mu}\frac{\mathrm{d}^2}{\mathrm{d}R^2}\nu(R) + \frac{\lambda}{2\mu R^2}\nu(R) + \epsilon_n(R)\nu(R) = \varepsilon_{\text{el}-\text{nucl}}\nu(R) \tag{3.35}$$

$$\hat{\mathsf{J}}_{\text{r}}^2\phi_{\text{rot}}(\hat{\boldsymbol{R}}) = \lambda\phi_{\text{rot}}(\hat{\boldsymbol{R}}). \tag{3.36}$$

The value of λ will be determined in Section 3.5.2 when the rotational wave

functions are identified.

3.5.1 Hund's angular-momentum coupling cases

The total angular momentum $\boldsymbol{J}$ of a diatomic molecule has contributions from a number of different types of angular momenta, and unfortunately there are just as many different notations for them. Here we mostly follow the notation of Brown and Carrington [145], which is summarised in Table 3.1. Note that

Table 3.1: Angular momenta and quantum numbers of diatomic molecules.

Kind of angular momentum	Operator	Quantum numbers		
		Total	Projection onto	
			$\hat{\boldsymbol{z}}$	$\hat{\boldsymbol{R}}$
Electronic orbital angular momentum	$\hat{\mathbf{L}}$	ℓ		Λ
Electronic spin	$\hat{\mathbf{s}}$	s	m_s	Σ_s
Total electronic angular momentum	$\hat{\mathbf{J}}_{\mathrm{e}} = \hat{\mathbf{L}} + \hat{\mathbf{s}}$	J_{e}		$\Omega = \Lambda + \Sigma_s$
Rotational angular momentum	$\hat{\mathbf{J}}_{\mathrm{r}}$	J_{r}		0
Total without spin	$\hat{\mathbf{N}} = \hat{\mathbf{J}}_{\mathrm{r}} + \hat{\mathbf{L}}$	N	m_N	Λ
Total without nuclear spin	$\hat{\mathbf{J}} = \hat{\mathbf{L}} + \hat{\mathbf{s}} + \hat{\mathbf{J}}_{\mathrm{r}}$	J	m_J	Ω
Nuclear spin	$\hat{\mathbf{I}}$	I	m_I	Σ_I

we are using $\boldsymbol{J}$ for the total angular momentum *without nuclear spin*. From the start we assume that the nuclear spin is completely decoupled from the electronic and rotational momenta, so from now on we simply refer to the "total" angular momentum $\boldsymbol{J}$ and neglect the nuclear spin until it is necessary to consider it later on.

The way in which we actually represent $\boldsymbol{J}$ and the set of good quantum numbers we work with depends on how we choose to couple the various angular momenta. For example, in Hund's case (a) we assume strong spin-orbit coupling and well-defined projections of $\boldsymbol{\ell}$ and $\boldsymbol{s}$ onto the internuclear axis $\hat{\boldsymbol{R}}$. In this case we define the total electronic angular momentum $\boldsymbol{J}_\mathrm{e}$, which has a well defined component Ω along the internuclear axis. The $\boldsymbol{\ell}$ and $\boldsymbol{s}$ vectors rapidly precess about the internuclear axis and so we couple the rotational angular momentum $\boldsymbol{J}_\mathrm{r}$ to $\boldsymbol{\Omega}$ to form the total angular momentum $\boldsymbol{J}$. In Hund's case (b) we assume weak spin-orbit coupling, which means the spin vector $\boldsymbol{s}$ is not strongly affected by the rotation of the internuclear axis, and hence Σ_s and Ω are not well defined. In this case we couple $\boldsymbol{\Lambda}$ (defined as $\Lambda\hat{\boldsymbol{R}}$) with the rotational angular momentum $\boldsymbol{J}_\mathrm{r}$ to form $\boldsymbol{N}$, which is then coupled with $\boldsymbol{s}$ to form $\boldsymbol{J}$. These two cases are summarised in Table 3.2 and illustrated in Fig. (3.3). In the present work we

Table 3.2: Angular-momentum coupling in Hund's cases (a) and (b).

Angular momentum	Hund's case (a)	Hund's case (b)
Total electronic	$\boldsymbol{J}_\mathrm{e} = \boldsymbol{\Omega}$	–
Total without spin	–	$\boldsymbol{N} = \boldsymbol{J}_\mathrm{r} + \boldsymbol{\Lambda}$
Total	$\boldsymbol{J} = \boldsymbol{J}_\mathrm{r} + \boldsymbol{\Omega}$	$\boldsymbol{J} = \boldsymbol{N} + \boldsymbol{s}$

operate entirely within the Hund's case (b) coupling scheme. In case (b) the rotational angular momentum is given by $\boldsymbol{J}_\mathrm{r} = \boldsymbol{N} - \boldsymbol{\Lambda}$, and since $\boldsymbol{J}_\mathrm{r}$ and $\boldsymbol{\Lambda}$ are orthogonal, the $\hat{\mathsf{J}}_\mathrm{r}^2$ operator can be expressed as

$$\hat{\mathsf{J}}_\mathrm{r}^2 = \hat{\mathsf{N}}^2 - \hat{\Lambda}^2. \tag{3.37}$$

3.5.2 Rotational wave functions

According to Eq. (3.36), the rotational wave functions $\phi_\mathrm{rot}(\hat{\boldsymbol{R}})$ are the eigenstates of the squared rotational angular-momentum operator $\hat{\mathsf{J}}_\mathrm{r}^2 = \hat{\mathsf{N}}^2 - \hat{\Lambda}^2$.

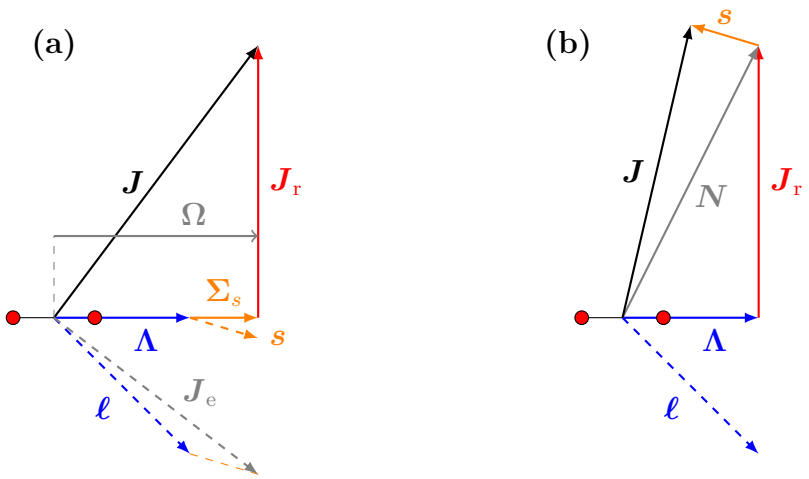

Figure 3.3: Angular-momentum coupling diagram for Hund's cases (a) and (b). Dashed arrows indicate quantities which are not well defined.

Using the fact that

$$[\hat{\mathsf{N}}^2, \hat{\mathsf{N}}_z] = 0 \tag{3.38}$$

$$[\hat{\mathsf{N}}^2, \hat{\Lambda}] = 0 \tag{3.39}$$

$$[\hat{\mathsf{N}}_z, \hat{\Lambda}] = 0, \tag{3.40}$$

we have a set of commuting operators $\{\hat{\mathsf{N}}^2, \hat{\mathsf{N}}_z, \hat{\Lambda}\}$ which in turn each commute with the Hund's case (b) rotational Hamiltonian ($\hat{\mathsf{N}}_z$ is the operator corresponding to the m_N observable). Hence the rotational wave functions can be identified as the simultaneous eigenstates of $\hat{\mathsf{N}}^2$, $\hat{\mathsf{N}}_z$, and $\hat{\Lambda}$:

$$\phi_{\text{rot}}(\hat{\boldsymbol{R}}) = \langle \hat{\boldsymbol{R}} | N m_N \Lambda \rangle \tag{3.41}$$

$$\langle \hat{\boldsymbol{R}} | N m_N \Lambda \rangle = \sqrt{\frac{2N+1}{8\pi^2}} D^{N*}_{m_N,\Lambda}(\hat{\boldsymbol{R}}) \tag{3.42}$$

$$\hat{\mathsf{N}}^2 | N m_N \Lambda \rangle = N(N+1) | N m_N \Lambda \rangle \tag{3.43}$$

$$\hat{\mathsf{N}}_z | N m_N \Lambda \rangle = m_N | N m_N \Lambda \rangle \tag{3.44}$$

$$\hat{\Lambda} | N m_N \Lambda \rangle = \Lambda | N m_N \Lambda \rangle, \tag{3.45}$$

where $D^{N*}_{m_N,\Lambda}$ is a Wigner D function. The separation constant in Eqs. (3.35–3.36) is then given by

$$\lambda = N(N+1) - \Lambda^2. \tag{3.46}$$

3.5.3 Vibrational wave functions

With the separation constant λ now identified, the vibrational wave equation (3.35) is

$$\left[-\frac{1}{2\mu}\frac{\mathrm{d}^2}{\mathrm{d}R^2} + \frac{N(N+1)-\Lambda^2}{2\mu R^2} + \epsilon_n(R) - \varepsilon_{nvN}\right]\nu_{nvN}(R) = 0, \tag{3.47}$$

where now we are being specific about denoting the electronic state n and labelling the vibrational wave function ν_{nvN} by the electronic, vibrational, and rotational quantum numbers it depends on. If we had formulated our rovibrational states in Hund's case (a) then the numerator in the centrifugal term would have been $J(J+1)-\Omega^2$.

Once the electronic state n and rotational state N are specified, the set of vibrational wave functions are found by solving Eq. (3.47) using standard methods for solving the one-dimensional Schrödinger equations. Since μ is large, the centrifugal term is generally negligible except for sufficiently high rotational levels. In calculations where the rotational structure is neglected it is common for the centrifugal term to be excluded.

3.5.4 Electronic spin functions

In Hund's case (b) the electronic spin is not coupled to the internuclear axis so instead we couple it to the lab-frame z axis and denote the spin states as $|sm_s\rangle$. For a two-electron molecule such as H_2, in terms of the individual electron spins the two-electron spin function is

$$|sm_s\rangle = \sum_{m_{s_1}m_{s_2}} C^{sm_s}_{s_1m_{s_1},s_2m_{s_2}}|s_1m_{s_1}\rangle|s_2m_{s_2}\rangle. \tag{3.48}$$

3.6 The total molecular wave function

We have now specified the individual solutions to the separated electronic, vibrational, and rotational Schrödinger equations. However, since the separation of electronic and nuclear motions is not rigorous, the simple product of electronic, vibrational, and rotational wave functions is not necessarily the best representation of the true total molecular state. In this section, we take such product wave

functions and adapt them to satisfy certain symmetry requirements of the total molecular system.

For simplicity, the electronic states will be denoted $|\Phi_n^{\pm\Lambda}\rangle$, where n specifies the electronic state up to the value of $|\Lambda|$. The nuclear spin states will be denoted $|Im_I\rangle$. Hence, the basis functions are

$$|\Phi_n^{\pm\Lambda}\rangle|sm_s\rangle|\nu_{nvN}\rangle|Nm_N \pm\Lambda\rangle|Im_I\rangle, \tag{3.49}$$

where $|\nu_{nvN}\rangle$ is the vibrational state (showing its dependence on the rotational level N), and $|Nm_N \pm\Lambda\rangle$ is the rotational state (showing its dependence on Λ).

A true eigenstate of the total molecular Hamiltonian is guaranteed to be a simultaneous eigenstate of whichever operators commute with the Hamiltonian, such as:

$\hat{\mathsf{J}}^2, \hat{\mathsf{J}}_z,$	defined above
$\hat{\mathsf{E}}^*,$	space fixed inversion operator
$\hat{\mathsf{t}},$	body-frame inversion operator
$\hat{\mathsf{P}}_{12},$	electronic permutation operator
$\hat{\mathsf{P}}_{AB},$	nuclear permutation operator.

The way the basis functions (3.49) have been constructed ensures they are already eigenstates of $\hat{\mathsf{J}}^2$, $\hat{\mathsf{J}}_z$, and $\hat{\mathsf{t}}$ (the $\hat{\mathsf{t}}$ operator inverts the electronic wave function in the body frame and determines the parity — u or g — of the electronic state).

3.6.1 Parity-adapted spatial states

Since in Hund's case (b) the electronic and nuclear spins are not coupled to the internuclear axis, the space-fixed inversion operator $\hat{\mathsf{E}}^*$ acts only on the spatial components of the wave function. As shown in Appendix D, the spatial states of well-defined parity π (eigenvalues of ±1 under the $\hat{\mathsf{E}}^*$ operation) are

$$\begin{aligned}&|\Phi_n\,\nu_{nvN}\,Nm_N\,\pi\rangle \\ &= \frac{1}{\sqrt{2(1+\delta_{\Lambda,0})}}\left[|\Phi_n^{+\Lambda}\rangle|\nu_{nvN}\rangle|Nm_N +\Lambda\rangle + \pi(-1)^{N+\sigma}|\Phi_n^{-\Lambda}\rangle|\nu_{nvN}\rangle|Nm_N -\Lambda\rangle\right],\end{aligned} \tag{3.50}$$

where the $\delta_{\Lambda,0}$ in the normalisation constant ensures that the state is still properly normalised in the $\Lambda = 0$ case. The variable σ is introduced to account for the

behaviour of the Σ^- states under the $\hat{\mathsf{E}}^*$ operation, and is defined to be odd for Σ^- states and even otherwise.

3.6.2 Permutation symmetry

We assume that the electronic states $|\Phi_n^{\pm\Lambda}\rangle$ have already been explicitly antisymmetrised with respect to the electronic permutation operator $\hat{\mathsf{P}}_{12}$, so now we just consider the nuclear permutation operator. Brown and Carrington [145] give the effect of $\hat{\mathsf{P}}_{AB}$ on the already parity-adapted states:

$$\hat{\mathsf{P}}_{AB}|\Phi_n\,\nu_{nvN}\,Nm_N\,\pi\rangle = \pi(-1)^t|\Phi_n\,\nu_{nvN}\,Nm_N\,\pi\rangle, \tag{3.51}$$

hence for a Λ_g state the $(+)$ parity states are symmetric and the $(-)$ parity states are antisymmetric with respect to $\hat{\mathsf{P}}_{AB}$. The opposite holds for the Λ_u states.

For homonuclear molecules the nuclear spin states $|Im_I\rangle$ come in two forms: the *para* wave function has nuclear spin $I = 0$, and is antisymmetric under nuclear permutation, while the *ortho* wave function has $I = 1$ and is symmetric under nuclear permutation.

3.6.3 Forming the total molecular states

We are now in a position to build the total molecular wave functions, including spin states:

$$|\Phi_n\,sm_s\,\nu_{nvN}\,Nm_N\,Im_I\,\pi\rangle = |\Phi_n\,\nu_{nvN}\,Nm_N\,\pi\rangle|sm_s\rangle|Im_I\rangle. \tag{3.52}$$

In order to have a total molecular wave function which is antisymmetric under nuclear permutation we must make appropriate combinations of states with given electronic parity, total parity, and nuclear spin. For example a *para* spin state (antisymmetric under $\hat{\mathsf{P}}_{AB}$) can be paired with a parity-adapted state of $(+)$ total parity and $(+)$ electronic parity (symmetric under $\hat{\mathsf{P}}_{AB}$) to give a state which is all-together antisymmetric under nuclear permutation. All of the antisymmetric combinations are outlined in Table (3.3).

Table 3.3: Antisymmetric combinations of the parity-adapted states (3.50) and nuclear spin states.

Parity-adapted state		nuclear state
electronic parity	total parity	
+	+	para
−	−	para
+	−	ortho
−	+	ortho

3.6.3.1 Simple case: $\Sigma^{\pm}$ states

For the Σ^+ states ($\Lambda = 0$, $\sigma =$ even) the parity-adapted molecular state

$$|nvNM_N\pi\rangle = \frac{1}{2}\left[|\Phi_n\Lambda\rangle|vN\rangle|Nm_N\Lambda\rangle + \pi(-1)^N|\Phi_n\Lambda\rangle|vN\rangle|Nm_N\Lambda\rangle\right] \quad (3.53)$$

is undefined whenever $\pi(-1)^N = -1$. Hence for $\pi = +1$ parity states we require that N is even and vice versa for $\pi = -1$ parity states. For a Σ^- state the opposite is true since there is an additional factor of (-1) in between the two functions. A given electronic parity and nuclear spin then places a constraint on the parity of N, which can be inferred from Table 3.3. These constraints are summarised in Table 3.4.

Table 3.4: Constraints on the rotational quantum number N for $\Sigma^{\pm}$ states.

elect. state	nuclear state	$(-1)^N$	elec. state	nuclear state	$(-1)^N$
Σ_g^+	ortho	−	Σ_g^-	ortho	+
Σ_g^+	para	+	Σ_g^-	para	−
Σ_u^+	ortho	+	Σ_u^-	ortho	−
Σ_u^+	para	−	Σ_u^-	para	+

3.6.3.2 General diatomic states

For the $|\Lambda| > 0$ states, both parity states $(+)$ and $(-)$ are valid, subject to the antisymmetry constraints laid out in Table 3.3. This means that all states come in parity doublets

$$\frac{1}{\sqrt{2}}\left[|\Phi_n^{+\Lambda}\rangle|Nm_N\ +\Lambda\rangle + |\Phi_n^{-\Lambda}\rangle|Nm_N\ -\Lambda\rangle\right]|\nu_{nvN}\rangle|sm_s\rangle|Im_I\rangle, \qquad \pi = (-1)^N$$

and (3.54)

$$\frac{1}{\sqrt{2}}\left[|\Phi_n^{+\Lambda}\rangle|Nm_N\ +\Lambda\rangle - |\Phi_n^{-\Lambda}\rangle|Nm_N\ -\Lambda\rangle\right]|\nu_{nvN}\rangle|sm_s\rangle|Im_I\rangle, \qquad \pi = (-1)^{N+1}. \tag{3.55}$$

In this case it is not convenient to refer to states by their total parity as the ordering of the two states alternates with successive values of N, e.g. when N is even the $(+)$ parity state is the upper state in the parity doublet but when N is odd the $(-)$ parity state is the upper state. An alternate convention is to separate the electronic state into the e and f bands, where e refers to states with parity $(-1)^N$ and f refers to states with parity $(-1)^{N+1}$. The common spectroscopic notation is to use a "+" superscript on the electronic state label to refer to the e band and a "−" superscript to refer to the f band. Although the $\pm$ superscripts on the $\Lambda > 0$ states refer to a different physical property than similar superscripts on $\Lambda = 0$ states ($\Sigma^{\pm}$ states), the constraints they place on the relationships between electronic parity, total parity, N, and the nuclear spin are the same. For example, the $d\ ^3\Pi_u^-$ label refers to molecular states consisting of the $d\ ^3\Pi_u$ electronic state and nuclear states with total parity $\pi = (-1)^{N+1}$, so for a para nuclear spin state we require $(-)$ overall parity (referring back to Table 3.3) which restricts N to being even. By the same reasoning a $d\ ^3\Pi_u^+$ para state requires odd N. Before going further it is important to note that the total molecular wave function is only required to be antisymmetric under nuclear permutation when the nuclei are identical fermions (e.g. protons or tritons). When the nuclei are identical bosons (e.g. the spin-1 deuterons of the D_2 molecule) the wave function should be symmetric under nuclear permutation. When the nuclei are not identical (as is the case for the heteronuclear isotopologues) there are no (anti)symmetry requirements with respect to nuclear permutation. For the

general homonuclear case, the constraints on N are summarised in Table 3.5.

Table 3.5: Constraints on the quantum number N and total molecular parity π for homonuclear diatomics given the electronic symmetry $\Lambda_t^{\pm}$ and either fermionic or bosonic nuclei in the ortho or para spin configurations. Note that t refers to the electronic parity.

	$\Lambda_t^{\pm}$	fermions		bosons	
		$(-1)^N$	π	$(-1)^N$	π
ortho ($I = 1$):	Λ_g^+	$-$	$-$	$+$	$+$
	Λ_g^-	$+$	$-$	$-$	$+$
	Λ_u^+	$+$	$+$	$-$	$-$
	Λ_u^-	$-$	$+$	$+$	$-$
para ($I = 0$):	Λ_g^+	$+$	$+$	$-$	$-$
	Λ_g^-	$-$	$+$	$+$	$-$
	Λ_u^+	$-$	$-$	$+$	$+$
	Λ_u^-	$+$	$-$	$-$	$+$

From the perspective of performing scattering calculations we assume the ortho or para characteristic does not change during the collision so we can use Table 3.5 to determine which of the states in the parity doublet to use, given a nuclear spin state and the parity of N. For example with a Λ_g state of para H_2 (nuclei are fermions and $I = 0$), having even N requires that we use the lower state in the parity doublet.

3.6.4 Allowed rotational levels

In Hund's case (b) we refer to different rotational levels by the N quantum number, but since N also contains a contribution from Λ it is not always indexed from 0. For example Π states have N ranging from 1 upwards. In general:

$$N = \Lambda, \Lambda + 1, \ldots \tag{3.56}$$

3.7 Chapter 3 summary

This chapter has presented an overview of the theory of diatomic molecular structure in the Born-Oppenheimer approximation. The separation of electronic and nuclear motion has been discussed, and various important properties of the electronic target states have been described. The approach to calculating the electronic and vibrational molecular states in the present work will be discussed in Chapters 6–7. The rotational component of the Born-Oppenheimer molecular states can be expressed analytically, and their form in Hund's case (b) has been given here. The process of adapting the Born-Oppenheimer basis states to satisfy the symmetries of the diatomic Hamiltonian has been described, and the form of the symmetry-adapted rovibronic molecular wave function has been given. This will become important in Chapter 11 when the rotationally-resolved cross section formulas are derived.

Chapter 4

Scattering on diatomic molecules

This chapter covers various definitions and theoretical approaches commonly applied to scattering on diatomic molecules within the *adiabatic-nuclei* and non-relativistic approximations. The different types of scattering processes for diatomics were defined previously in Table 1.1 of Chapter 1. A summary of specific methods utilised to solve the scattering equations is provided in the following chapter.

The standard scattering-theory definition of the differential cross section (DCS) for a target transition $n_i v_i N_i m_{N_i} \rightarrow n_f v_f N_f m_{N_f}$ is

$$\frac{\mathrm{d}\sigma^{\mathcal{S}}_{n_f v_f N_f m_{N_f}, n_i v_i N_i m_{N_i}}}{\mathrm{d}\Omega} = \frac{q_f}{q_i} \left| F^{\mathcal{S}}_{n_f v_f N_f m_{N_f}, n_i v_i N_i m_{N_i}}(\boldsymbol{q}_f, \boldsymbol{q}_i) \right|^2, \tag{4.1}$$

where n_f and n_i refer to the final and initial electronic states, q_f and q_i are the final and initial projectile linear momenta, $\mathcal{S}$ is the total scattering-system spin, and $F^{\mathcal{S}}_{f,i}$ is the *scattering amplitude*. The scattering amplitude is related to the total scattering wave function (for the projectile + target system) by

$$F^{\mathcal{S}}_{n_f v_f N_f m_{N_f}, n_i v_i N_i m_{N_i}}(\boldsymbol{q}_f, \boldsymbol{q}_i) = -4\pi^2 \langle \boldsymbol{q}_f \Phi_{n_f v_f N_f m_{N_f}} | \hat{\mathsf{V}}^{\mathcal{S}} | \Psi^{\mathcal{S}(+)}_{n_i v_i N_i m_{N_i}} \rangle, \tag{4.2}$$

where $\Phi_{n_f v_f N_f m_{N_f}}$ is the final target state, $\hat{\mathsf{V}}$ is the projectile-target interaction potential operator, and $\Psi^{\mathcal{S}(+)}_{n_i v_i N_i m_{N_i}}$ is the total scattering wave function. The Schrödinger equation for $\Psi^{\mathcal{S}(+)}_{n_i v_i N_i m_{N_i}}$ is

$$(\hat{\mathsf{K}}_0 + \hat{\mathsf{H}}_\mathrm{t} + \hat{\mathsf{V}}^{\mathcal{S}} - E) | \Psi^{\mathcal{S}(+)}_{n_i v_i N_i m_{N_i}} \rangle = 0, \tag{4.3}$$

where $\hat{\mathsf{K}}_0$ is the projectile kinetic-energy operator, $\hat{\mathsf{H}}_\mathrm{t}$ is the target Hamiltonian, and E is the total scattering-system energy. The dependence of the scattering

wave function on the initial target state is specified by the subscripts $n_i v_i N_i m_{N_i}$, and the superscript $(+)$ indicates outgoing spherical-wave boundary conditions. These details, and the derivations of Eqs (4.1–4.2), were discussed in Chapter 2. It is common to define the T-matrix element

$$\langle \boldsymbol{q}_f \Phi_{n_f v_f N_f m_{N_f}} | \hat{\mathsf{T}}^{\mathcal{S}} | \Phi_{n_i v_i N_i m_{N_i}} \boldsymbol{q}_i \rangle = \langle \boldsymbol{q}_f \Phi_{n_f v_f N_f m_{N_f}} | \hat{\mathsf{V}}^{\mathcal{S}} | \Psi^{\mathcal{S}(+)}_{n_i v_i N_i m_{N_i}} \rangle, \tag{4.4}$$

so that the scattering amplitude is given by

$$F^{\mathcal{S}}_{n_f v_f N_f m_{N_f}, n_i v_i N_i m_{N_i}}(\boldsymbol{q}_f, \boldsymbol{q}_i) = -4\pi^2 \langle \boldsymbol{q}_f \Phi_{n_f v_f N_f m_{N_f}} | \hat{\mathsf{T}}^{\mathcal{S}} | \Phi_{n_i v_i N_i m_{N_i}} \boldsymbol{q}_i \rangle. \tag{4.5}$$

4.1 The adiabatic-nuclei approximation

The adiabatic-nuclei approximation is a commonly-applied method in molecular scattering in which the Born-Oppenheimer approximation is applied to the total scattering wave function. This is justified by noting that the factor of $1/\mu$ in the nuclear kinetic-energy operator allows it to be treated as a small perturbation in the total scattering Hamiltonian for sufficiently large electronic energies, satisfying the criteria of the general adiabatic theorem in quantum mechanics [153]. The approximation amounts to the decoupling of the electronic and nuclear motions, allowing the electronic dynamics to be treated separately for each fixed nuclear geometry.

We denote by $\Phi_n^{\pm\Lambda}$ the target wave function for the electronic state n with orbital angular-momentum projection $\pm\Lambda$ on the internuclear axis, and assume that the spin component $|sm_s\rangle$ has been absorbed into this definition, so that the molecular wave function is given by

$$\Phi_{nvNm_N}(\tilde{\boldsymbol{r}}, \boldsymbol{R}) = \frac{1}{\sqrt{2(1+\delta_{\Lambda,0})}} \Big[\Phi_n^{+\Lambda}(\tilde{\boldsymbol{r}}^{(\mathrm{b})}; \boldsymbol{R}) \nu_{nvN}(R) \phi_{Nm_N+\Lambda}(\hat{\boldsymbol{R}}) + \pi(-1)^{N+\sigma} \Phi_n^{-\Lambda}(\tilde{\boldsymbol{r}}^{(\mathrm{b})}; \boldsymbol{R}) \nu_{nvN}(R) \phi_{Nm_N-\Lambda}(\hat{\boldsymbol{R}}) \Big], \tag{4.6}$$

where $\tilde{\boldsymbol{r}}$ stands for all target electron coordinates, $\boldsymbol{R}$ is the nuclear separation/orientation vector, ν_{nv} is the vibrational wave function, and $\phi_{Nm_N\pm\Lambda}(\hat{\boldsymbol{R}})$ is the rotational wave function. Note that $\Phi_n^{\pm\Lambda}$ are electronic wave functions which only

parametrically depend on the internuclear vector. The analogous approximation for the total scattering wave function is

$$\Psi^{\mathcal{S}(+)}_{n_i v_i N_i m_{n_i}}(\boldsymbol{r}_0, \tilde{\boldsymbol{r}}, \boldsymbol{R}) \tag{4.7}$$
$$= \frac{1}{\sqrt{2(1+\delta_{\Lambda_i,0})}}\Big[\Psi^{+\Lambda_i \mathcal{S}(+)}_{n_i}(\boldsymbol{r}_0, \tilde{\boldsymbol{r}}; \boldsymbol{R})\nu_{n_i v_i N_i}(R)\phi_{N_i m_{N_i}+\Lambda_i}(\hat{\boldsymbol{R}})$$
$$+ \pi_i(-1)^{N_i+\sigma}\Psi^{-\Lambda_i \mathcal{S}(+)}_{n_i}(\boldsymbol{r}_0, \tilde{\boldsymbol{r}}; \boldsymbol{R})\nu_{n_i v_i N_i}(R)\phi_{N_i m_{n_i}-\Lambda_i}(\hat{\boldsymbol{R}})\Big],$$

where $\boldsymbol{r}_0$ is the lab-frame projectile coordinate, and $\Psi^{\pm\Lambda_i \mathcal{S}(+)}_{n_i}$ are electronic scattering wave functions obtained with $\boldsymbol{R}$ treated parametrically.

For the most part, the present work will be concerned with the calculation of cross sections which are not resolved in the target rotational levels, i.e. with the final rotational levels summed over and initial rotational sublevels averaged over:

$$\sigma_{n_f v_f, n_i v_i N_i} = \frac{1}{2N_i+1}\sum_{N_f m_{N_f}}\sum_{m_{N_i}} \sigma_{n_f v_f N_f m_{N_f}, n_i v_i N_i m_{N_i}}. \tag{4.8}$$

Rather than explicitly summing the rotationally-resolved cross sections, it is common to derive cross-section formulas in which the sums have been performed analytically. To simplify these derivations, the adiabatic-nuclei scattering wave function is generally written as

$$\Psi^{\mathcal{S}(+)}_{n_i v_i N_i m_{n_i}}(\boldsymbol{r}_0, \tilde{\boldsymbol{r}}, \boldsymbol{R}) = \Psi^{\mathcal{S}(+)}_{n_i}(\boldsymbol{r}_0, \tilde{\boldsymbol{r}}; \boldsymbol{R})\nu_{n_i v_i N_i}(R)\phi_{N_i m_{N_i}}(\hat{\boldsymbol{R}}), \tag{4.9}$$

where $\phi_{N m_N}$ (with Λ removed) are the rigid-rotor rotational wave functions:

$$\phi_{N m_N}(\hat{\boldsymbol{R}}) = Y^{m_N}_N(\hat{\boldsymbol{R}}). \tag{4.10}$$

In this treatment, the Λ-degenerate electronic states are now treated as separate states, so the electronic index n should be understood to range over all electronic states with both positive and negative Λ. As shown in Ref. [87], the cross section $\sigma_{n_f v_f, n_i v_i N_i}$ summed over N_f is independent of N_i within the adiabatic-nuclei approximation, so the dependence on N_i will be dropped hereafter.

For a fixed internuclear vector $\boldsymbol{R}$, the electronic scattering wave functions

are the solutions to

$$(\hat{\mathsf{K}}_0 + \hat{\mathsf{H}}_{\mathrm{t,el}} + \hat{\mathsf{V}}^{\mathcal{S}} - E_{\mathrm{el}})|\Psi^{\mathcal{S}(+)}_{n_i}\rangle = 0, \tag{4.11}$$

where $\hat{\mathsf{H}}_{\mathrm{t,el}}$ is the electronic target Hamiltonian defined in Eq. (3.8), and E_{el} is the total *electronic* energy.

By applying the adiabatic-nuclei approximation, the scattering problem has been simplified substantially to require only the solution of Eq. (4.11) at a number of fixed internuclear vectors $\boldsymbol{R}$, after which the full scattering wave function can be recovered. As discussed in the following sections, the problem can actually be reduced further to explicitly consider only one internuclear orientation.

It is important to note that this method relies on the assumption that the scattering wave function responds adiabatically to the nuclear motion. At low projectile energies this assumption is not valid and the approximation becomes inaccurate. For resonant processes, where the projectile is temporarily captured by the target, the adiabatic-nuclei approximation completely breaks down. Studies of resonant electron-molecule collisions apply entirely separate techniques, which will be discussed in the review of scattering theories in Chapter 5.

4.2 Partial-wave expansion of the scattering amplitude

The partial-wave expansion is a method commonly utilised in scattering theory to simplify calculations by allowing certain angular components to be treated analytically. In the present case this has the additional benefit of allowing the rotational motion to be treated analytically, so that Eq. (4.11) needs to be solved at only a single nuclear orientation $\hat{\boldsymbol{R}}$.

The computation of cross sections in the adiabatic-nuclei approximation requires the electronic scattering amplitudes

$$F^{\mathcal{S}}_{n_f,n_i}(\boldsymbol{q}_f, \boldsymbol{q}_i; \boldsymbol{R}) = -4\pi^2 \langle \boldsymbol{q}_f \Phi_{n_f} | \hat{\mathsf{T}}^{\mathcal{S}} | \Phi_{n_i} \boldsymbol{q}_i \rangle \tag{4.12}$$

to be obtained (with $\boldsymbol{R}$ treated as a parameter). The method of partial waves

proceeds by expanding the projectile wave functions in a basis of spherical harmonics. In general, the form of the expansion depends on whether or not the target is charged, or if numerical methods such as distorting potentials have been utilised. Since neither of these are relevant in the present work we consider only the simple plane-wave expansion:

$$\langle \boldsymbol{r}|\boldsymbol{q}\rangle = \sqrt{\frac{2}{\pi}}\frac{1}{qr}\sum_{L=0}^{\infty}\sum_{m_L=-L}^{+L} i^L u_L(qr) Y_L^{m_L}(\hat{\boldsymbol{r}}) Y_L^{m_L *}(\hat{\boldsymbol{q}}), \tag{4.13}$$

and hence the scattering amplitude can be written as

$$\begin{aligned} &F^{\mathcal{S}}_{n_f,n_i}(\boldsymbol{q}_f,\boldsymbol{q}_i;\boldsymbol{R}) \\ &\quad = -4\pi^2\frac{1}{q_f q_i}\sum_{\substack{L_f m_{L_f}\\ L_i m_{L_i}}} i^{L_i-L_f}\langle q_f L_f m_{L_f}\Phi_{n_f}|\hat{\mathsf{T}}^{\mathcal{S}}|\Phi_{n_i} q_i L_i m_{L_i}\rangle Y_{L_f}^{m_{L_f}}(\hat{\boldsymbol{q}}_f) Y_{L_i}^{m_{L_i}*}(\hat{\boldsymbol{q}}_i), \end{aligned} \tag{4.14}$$

where $|qLm_L\rangle$ are defined by

$$\langle \boldsymbol{r}|qLm_L\rangle = \sqrt{\frac{2}{\pi}}\frac{1}{r}u_L(qr)Y_L^{m_L}(\hat{\boldsymbol{r}}), \tag{4.15}$$

and $u_L(qr)$ are the solutions to the one-dimensional free-particle Schrödinger equation:

$$\left[-\frac{1}{2}\frac{\mathrm{d}^2}{\mathrm{d}r^2} + \frac{L(L+1)}{2r^2} - \frac{q^2}{2}\right] u_L(qr) = 0. \tag{4.16}$$

For non-distorted plane-wave projectile wave functions, u_L are the Riccati-Bessel functions.

Defining the partial-wave scattering amplitudes

$$F^{\mathcal{S}}_{n_f L_f m_{L_f}, n_i L_i m_{L_i}}(q_f,q_i) = -\frac{4\pi^2}{q_f q_i} i^{L_i-L_f}\langle q_f L_f m_{L_f}\Phi_{n_f}|\hat{\mathsf{T}}^{\mathcal{S}}|\Phi_{n_i} q_i L_i m_{L_i}\rangle, \tag{4.17}$$

Eq. (4.14) can be written as

$$F^{\mathcal{S}}_{n_f,n_i}(\boldsymbol{q}_f,\boldsymbol{q}_i;\boldsymbol{R}) = \sum_{\substack{L_f m_{L_f}\\ L_i m_{L_i}}} F^{\mathcal{S}}_{n_f L_f m_{L_f}, n_i L_i m_{L_i}}(q_f,q_i) Y_{L_f}^{m_{L_f}}(\hat{\boldsymbol{q}}_f) Y_{L_i}^{m_{L_i}*}(\hat{\boldsymbol{q}}_i). \tag{4.18}$$

It is standard to align the lab-frame z axis with the incident projectile direction

$\hat{\boldsymbol{q}}_i$, which reduces Eq. (4.18) to

$$F^{\mathcal{S}}_{n_f,n_i}(\boldsymbol{q}_f,\boldsymbol{q}_i;\boldsymbol{R}) = \sum_{L_f m_{L_f}} \sum_{L_i} \frac{\hat{L}_i}{\sqrt{4\pi}} F^{\mathcal{S}}_{n_f L_f m_{L_f}, n_i L_i 0}(q_f,q_i) Y^{m_{L_f}}_{L_f}(\hat{\boldsymbol{q}}_f), \tag{4.19}$$

where we have defined

$$\hat{L} = \sqrt{2L+1}. \tag{4.20}$$

4.3 Rotation into body frame

Calculations can be simplified by performing a coordinate transformation into a frame which rotates with the internuclear vector $\boldsymbol{R}$. The origin of the body frame is chosen to coincide with the geometric centre of the nuclei, and the body-frame z axis is aligned with $\hat{\boldsymbol{R}}$. In this frame, the incident projectile direction $\hat{\boldsymbol{q}}_i$ is not aligned with the z axis, so the dependence on $\hat{\boldsymbol{q}}_i$ is kept explicit. The body-frame scattering amplitude is defined as

$$F^{\mathcal{S}}_{n_f,n_i}(\boldsymbol{q}^{(\mathrm{b})}_f,\boldsymbol{q}^{(\mathrm{b})}_i;R) = -4\pi^2 \langle \boldsymbol{q}^{(\mathrm{b})}_f \Phi_{n_f} | \hat{\mathsf{T}}^{\mathcal{S}} | \Phi_{n_i} \boldsymbol{q}^{(\mathrm{b})}_i \rangle, \tag{4.21}$$

where $|\boldsymbol{q}^{(\mathrm{b})}\rangle$ are projectile states defined in the body frame. The partial-wave expansions of the body-frame scattering amplitude and T-matrix element in terms of spherical harmonics with angular-momentum projections Λ_L on the $\hat{\boldsymbol{R}}$ axis are:

$$\begin{aligned} &\langle \boldsymbol{q}^{(\mathrm{b})}_f \Phi_{n_f} | \hat{\mathsf{T}}^{\mathcal{S}} | \Phi_{n_i} \boldsymbol{q}^{(\mathrm{b})}_i \rangle \\ &\qquad = \frac{1}{q_f q_i} \sum_{\substack{L_f \Lambda_{L_f} \\ L_i \Lambda_{L_i}}} i^{L_i - L_f} \langle q_f L_f \Lambda_{L_f} \Phi_{n_f} | \hat{\mathsf{T}}^{\mathcal{S}} | \Phi_{n_i} q_i L_i \Lambda_{L_i} \rangle Y^{\Lambda_{L_f}}_{L_f}(\hat{\boldsymbol{q}}^{(\mathrm{b})}_f) Y^{\Lambda_{L_i}*}_{L_i}(\hat{\boldsymbol{q}}^{(\mathrm{b})}_i) \end{aligned} \tag{4.22}$$

$$F^{\mathcal{S}}_{n_f,n_i}(\boldsymbol{q}^{(\mathrm{b})}_f,\boldsymbol{q}^{(\mathrm{b})}_i;R) = \sum_{\substack{L_f \Lambda_{L_f} \\ L_i \Lambda_{L_i}}} F^{\mathcal{S}(\mathrm{b})}_{n_f L_f \Lambda_{L_f}, n_i L_i \Lambda_{L_i}}(q_f,q_i) Y^{\Lambda_{L_f}}_{L_f}(\hat{\boldsymbol{q}}^{(\mathrm{b})}_f) Y^{\Lambda_{L_i}*}_{L_i}(\hat{\boldsymbol{q}}^{(\mathrm{b})}_i), \tag{4.23}$$

where the body-frame partial-wave amplitudes are defined as

$$F^{\mathcal{S}(\mathrm{b})}_{n_f L_f \Lambda_{L_f}, n_i L_i \Lambda_{L_i}}(q_f,q_i) = -\frac{4\pi^2}{q_f q_i} i^{L_i - L_f} \langle q_f L_f \Lambda_{L_f} \Phi_{n_f} | \hat{\mathsf{T}}^{\mathcal{S}} | \Phi_{n_i} q_i L_i \Lambda_{L_i} \rangle. \tag{4.24}$$

The body- and lab-frame partial-wave scattering amplitudes can be related

via rotation of the partial-wave functions:

$$\langle \boldsymbol{r}|qLm_L\rangle = \sum_{\Lambda_L} D^{L*}_{m_L\Lambda_L}(\hat{\boldsymbol{R}})\langle \boldsymbol{r}^{(\mathrm{b})}|qL\Lambda_L\rangle, \tag{4.25}$$

where $D^L_{m_L\Lambda_L}$ is a Wigner-D function, Λ_L is the projection of L on $\hat{\boldsymbol{R}}$, and $\boldsymbol{r}^{(\mathrm{b})}$ is the body-frame coordinate corresponding to $\boldsymbol{r}$. The lab-frame partial-wave amplitudes (4.17) can then be expressed as

$$F^{\mathcal{S}}_{n_fL_fm_{L_f},n_iL_im_{L_i}}(q_f,q_i) = \sum_{\Lambda_{L_f}\Lambda_{L_i}} D^{L_f}_{m_{L_f}\Lambda_{L_f}}(\hat{\boldsymbol{R}})D^{L_i}_{0\Lambda_{L_i}}(\hat{\boldsymbol{R}})F^{\mathcal{S}(\mathrm{b})}_{n_fL_f\Lambda_{L_f},n_iL_i\Lambda_{L_i}}(q_f,q_i). \tag{4.26}$$

Hence, the lab-frame scattering amplitude (4.19) is

$$\begin{aligned} &F^{\mathcal{S}}_{n_f,n_i}(\boldsymbol{q}_f,\boldsymbol{q}_i;\boldsymbol{R}) \\ &\quad= \sum_{\substack{L_fL_i\\ \Lambda_{L_f}\Lambda_{L_i}}} \frac{\hat{L}_i}{\sqrt{4\pi}} D^{L_f}_{m_{L_f}\Lambda_{L_f}}(\hat{\boldsymbol{R}})F^{\mathcal{S}(\mathrm{b})}_{n_fL_f\Lambda_{L_f},n_iL_i\Lambda_{L_i}}(q_f,q_i)\sum_{m_{L_f}} D^{L_i*}_{0\Lambda_{L_i}}(\hat{\boldsymbol{R}})Y^{m_{L_f}}_{L_f}(\hat{\boldsymbol{q}}_f). \end{aligned} \tag{4.27}$$

Note that the rotation of the projectile and target spin states has not been considered, as it turns out the scattering amplitudes depend only on the total spin $\mathcal{S}$ and not the spin projections.

4.4 Vibrationally-resolved cross-section formulas

Expressions for the integral and differential cross sections following the above definition (4.27) of the lab-frame scattering amplitude have been given by Zammit *et al.* [87] and are stated here without derivation.

In order to perform analytic sums over the rotational quantum numbers, it is necessary to neglect the dependence of the vibrational wave functions on the rotational level. Hence, we replace $\nu_{nvN}(R)$ with $\nu_{nv}(R)$, which are the solutions to the vibrational Schrödinger equation (3.47) with the centrifugal term neglected. Since the vibrational wave functions only weakly depend on the rotational level for small N, this is a reasonable approximation. The adiabatic-nuclei scattering

amplitude for the transition $n_i v_i N_i m_{N_i} \to n_f v_f N_f m_{N_f}$ is then given by

$$F^{\mathcal{S}}_{n_f v_f N_f m_{N_f}, n_i v_i N_i m_{N_i}}(\boldsymbol{q}_f, \boldsymbol{q}_i) = \langle \phi_{N_f m_{N_f}} \nu_{n_f v_f} | F^{\mathcal{S}}_{n_f v_f, n_i v_i}(\boldsymbol{q}_f, \boldsymbol{q}_i; \boldsymbol{R}) | \nu_{n_i v_i} \phi_{N_i m_{N_i}} \rangle. \tag{4.28}$$

The DCS summed over final rotational levels and averaged over initial rotational sublevels,

$$\frac{\mathrm{d}\sigma^{\mathcal{S}}_{n_f v_f, n_i v_i}}{\mathrm{d}\Omega} = \frac{1}{2N_i + 1} \sum_{N_f m_{N_f}} \sum_{m_{N_i}} \frac{\mathrm{d}\sigma^{\mathcal{S}}_{n_f v_f N_f m_{N_i}, n_i v_i N_i m_{N_i}}}{\mathrm{d}\Omega}, \tag{4.29}$$

is given by

$$\begin{aligned} \frac{\mathrm{d}\sigma^{\mathcal{S}}_{n_f v_f, n_i v_i}}{\mathrm{d}\Omega} = \frac{q_f}{q_i} \frac{1}{4\pi^2} \sum_{\substack{L_f L_i \\ \Lambda_{L_f} \Lambda_{L_i}}} \sum_{\substack{L'_f L'_i \\ \Lambda'_{L_f} \Lambda'_{L_i}}} (-1)^{\Lambda'_{L_i} + \Lambda'_{L_f}} \hat{L}_i \hat{L}'_i \hat{L}_f \hat{L}'_f \ \delta_{\Lambda_{L_i} - \Lambda'_{L_i}, \Lambda_{L_f} - \Lambda'_{L_f}} \\ \times \langle \nu_{n_f v_f} | F^{\mathcal{S}(\mathrm{b})}_{n_f L_f \Lambda_{L_f}, n_i L_i \Lambda_{L_i}} | \nu_{n_i v_i} \rangle \langle \nu_{n_f v_f} | F^{\mathcal{S}(\mathrm{b})}_{n_f L'_f \Lambda'_{L_f}, n_i L'_i \Lambda'_{L_i}} | \nu_{n_i v_i} \rangle \\ \times \sum_L \frac{1}{\hat{L}^2} C^{L0}_{L_i 0, L'_i 0} C^{L0}_{L_f 0, L'_f 0} C^{L(\Lambda'_{L_i} - \Lambda_{L_i})}_{L_i(-\Lambda_{L_i})} C^{L(\Lambda_{L_f} - \Lambda'_{L_f})}_{L_f \Lambda_{L_f}, L'_f(-\Lambda'_{L_f})} P_L(\cos\theta), \end{aligned} \tag{4.30}$$

where $C^{\ell m}_{\ell_1 m_1, \ell_2 m_2}$ are the standard Clebsch-Gordan coefficients, P_L is the Legendre polynomial of order L, and θ is the lab-frame scattering angle. Eq. (4.30) can be analytically integrated over solid angle to give the vibrationally-resolved integral cross section:

$$\sigma^{\mathcal{S}}_{n_f v_f, n_i v_i} = \frac{q_f}{q_i} \frac{1}{4\pi} \sum_{\substack{L_f L_i \\ \Lambda_{L_f} \Lambda_{L_i}}} \left| \langle \nu_{n_f v_f} | F^{\mathcal{S}(\mathrm{b})}_{n_f L_f \Lambda_{L_f}, n_i L_i \Lambda_{L_i}} | \nu_{n_i v_i} \rangle \right|^2. \tag{4.31}$$

Spin-averaged cross sections (generally what is compared with experiment) are obtained with the following:

$$\frac{\mathrm{d}\sigma_{n_f v_f, n_i v_i}}{\mathrm{d}\Omega} = \sum_{\mathcal{S}} \frac{2\mathcal{S} + 1}{2(2s_i + 1)} \frac{\mathrm{d}\sigma^{\mathcal{S}}_{n_f v_f, n_i v_i}}{\mathrm{d}\Omega}, \tag{4.32}$$

$$\sigma_{n_f v_f, n_i v_i} = \sum_{\mathcal{S}} \frac{2\mathcal{S} + 1}{2(2s_i + 1)} \sigma^{\mathcal{S}}_{n_f v_f, n_i v_i}, \tag{4.33}$$

where s_i is the initial spin of the target, and the sum is over all valid total scattering system spins $\mathcal{S}$. Throughout the rest of this section the dependence on $\mathcal{S}$ will be retained, with the understanding that Eqs. (4.32–4.33) are applied

to all cross sections to produce final spin-averaged quantities.

4.5 Choice of outgoing momentum

The outgoing projectile momentum q_f as it appears in Eqs (4.30) and (4.31) is defined by

$$q_f = \sqrt{2\left[E_{\rm in} - \varepsilon_{n_f v_f, n_i v_i}\right]}, \tag{4.34}$$

where $E_{\rm in}$ is the incident energy, and $\varepsilon_{n_f v_f, n_i v_i}$ is the vibrationally-resolved excitation energy. An alternative choice which is often made is to replace q_f with the R-dependent momentum obtained using the vertical (electronic) excitation energy $\epsilon_{n_f,n_i}(R)$:

$$q_f(R) = \sqrt{2\left[E_{\rm in} - \epsilon_{n_f,n_i}(R)\right]}, \tag{4.35}$$

in which case Eq. (4.31) becomes

$$\sigma^{\mathcal{S}}_{n_f v_f, n_i v_i} = \frac{1}{q_i}\frac{1}{4\pi} \sum_{\substack{L_f L_i \\ \Lambda_{L_f}\Lambda_{L_i}}} \left| \langle \nu_{n_f v_f} | \sqrt{q_f(R)} F^{\mathcal{S}({\rm b})}_{n_f L_f \Lambda_{L_f}, n_i L_i \Lambda_{L_i}} | \nu_{n_i v_i} \rangle \right|^2, \tag{4.36}$$

and a similar expression holds for the DCS. With this choice of q_f, Eq. (4.36) no longer reproduces the correct threshold, i.e. the cross section does not go to zero at the physical threshold. As shown later, however, this definition can be useful when summing over vibrational levels.

4.6 Cross sections for dissociative excitation

Molecular dissociation occurs following excitation of an unbound vibrational level. Each electronic potential-energy curve supports a continuum of dissociative vibrational wave functions, each one representing the production of atomic fragments of a particular kinetic energy. The standard approach to treating dissociative excitation is to define the energy-differential cross section

$$\frac{{\rm d}\sigma^{\mathcal{S}({\rm diss})}_{n_f, n_i v_i}}{{\rm d}E_{\rm k}} = \frac{q_f}{q_i}\frac{1}{4\pi} \sum_{\substack{L_f L_i \\ \Lambda_{L_f}\Lambda_{L_i}}} \left| \langle \nu_{n_f E_{\rm k}} | F^{\mathcal{S}({\rm b})}_{n_f L_f \Lambda_{L_f}, n_i L_i \Lambda_{L_i}} | \nu_{n_i v_i} \rangle \right|^2, \tag{4.37}$$

where $\nu_{n_f E_\mathrm{k}}(R)$ is the dissociative vibrational wave function with kinetic energy E_k. These functions are obtained simply by solving the vibrational Schrödinger equation (3.47) with the energy set to

$$\varepsilon_{nv} = E_\mathrm{k} + D_n, \tag{4.38}$$

where D_n is the asymptotic limit of the potential-energy curve. The total dissociative excitation cross section for the electronic state n_f is then given by

$$\sigma^{\mathcal{S}(\mathrm{diss})}_{n_f,n_i v_i} = \int_0^\infty \frac{\mathrm{d}\sigma^{\mathcal{S}(\mathrm{diss})}_{n_f,n_i v_i}}{\mathrm{d}E_\mathrm{k}}\,\mathrm{d}E_\mathrm{k}. \tag{4.39}$$

Here, the upper integration bound can be truncated to the maximum allowed kinetic-energy release E_k, based on energy-conservation requirements.

The normalisation of the dissociative wave functions must be chosen appropriately. The use of Eq. (4.37) assumes the following normalisation to a Dirac-δ function in energy:

$$\int_0^\infty \nu_{nE_\mathrm{k}}(R)\nu_{nE'_\mathrm{k}}(R)\,\mathrm{d}R = \delta(E_\mathrm{k} - E'_\mathrm{k}). \tag{4.40}$$

This choice of normalisation also implies the following resolution of unity for the total (bound + continuum) vibrational spectrum:

$$\sum_v \nu_{nv}(R)\nu_{nv}(R') + \int_0^\infty \nu_{nE_\mathrm{k}}(R)\nu_{nE_\mathrm{k}}(R')\,\mathrm{d}E_\mathrm{k} = \delta(R - R'). \tag{4.41}$$

The use of Eq. (4.37), and the manner in which the ν_{nE_k} should be normalised was called into question by Trevisan and Tennyson [72], who derived alternative equations which produce substantially different results. These issues will be discussed in detail in Chapter 8, where it will be shown that the approach summarised in this section is indeed correct.

4.7 Summing over vibrational levels

To obtain an overall excitation cross section for an electronic state n_f, Eq. (4.31) must be summed over the final vibrational levels v_f. The dependence of q_f on each specific vibrational transition precludes this sum from being performed analytically, so it is therefore necessary to explicitly compute each vibrationally-resolved cross section and sum them:

$$\sigma^{\mathcal{S}}_{n_f,n_iv_i} = \sum_{v_f} \sigma^{\mathcal{S}}_{n_fv_f,n_iv_i} + \int_0^\infty \frac{\mathrm{d}\sigma^{\mathcal{S}(\mathrm{diss})}_{n_f,n_iv_i}}{\mathrm{d}E_\mathrm{k}}\,\mathrm{d}E_\mathrm{k}, \tag{4.42}$$

where the sum is over all bound vibrational levels. However, if Eq. (4.36) is applied to remove the dependence of q_f on the final vibrational level, and a similar approach is taken for the dissociative transitions, the unity resolution (4.41) can be utilised to analytically sum over the bound levels and integrate over the continuum, giving

$$\sigma^{\mathcal{S}}_{n_f,n_iv_i} = \langle \nu_{n_iv_i} | \sigma^{\mathcal{S}}_{n_f,n_i} | \nu_{n_iv_i} \rangle, \tag{4.43}$$

where $\sigma^{\mathcal{S}}_{n_f,n_i}$ is the R-dependent electronic excitation cross section, defined by

$$\sigma^{\mathcal{S}}_{n_f,n_i}(R) = \frac{q_f}{q_i}\frac{1}{4\pi} \sum_{\substack{L_fL_i \\ \Lambda_{L_f}\Lambda_{L_i}}} \left| F^{\mathcal{S}(\mathrm{b})}_{n_fL_f\Lambda_{L_f},n_iL_i\Lambda_{L_i}} \right|^2. \tag{4.44}$$

Similarly, this approach can be applied to the DCS, giving

$$\frac{\mathrm{d}\sigma^{\mathcal{S}}_{n_f,n_iv_i}}{\mathrm{d}\Omega} = \langle \nu_{n_iv_i} | \frac{\mathrm{d}\sigma^{\mathcal{S}}_{n_f,n_i}}{\mathrm{d}\Omega} | \nu_{n_iv_i} \rangle, \tag{4.45}$$

where $\mathrm{d}\sigma^{\mathcal{S}}_{n_f,n_i}/\mathrm{d}\Omega$ is the R-dependent DCS obtained by replacing the adiabatic-nuclei partial-wave amplitudes in Eq. (4.30) with the R-dependent amplitudes.

4.8 The fixed-nuclei approximation

The fixed-nuclei approximation is a further approximation of Eqs (4.43–4.45) which requires the evaluation of the R-dependent cross sections at only a single value of R. Performing a Taylor-series expansion of $\sigma^{\mathcal{S}}_{n_f,n_i}(R)$ about some point

R_0 gives

$$\sigma^{\mathcal{S}}_{n_f,n_i}(R) = \sigma^{\mathcal{S}}_{n_f,n_i}(R_0) + \left(\frac{\mathrm{d}}{\mathrm{d}R}\sigma^{\mathcal{S}}_{n_f,n_i}(R)\right)_{R=R_0}(R-R_0) + \cdots, \tag{4.46}$$

and hence Eq. (4.43) is, up to first-order variation in R:

$$\sigma^{\mathcal{S}}_{n_f,n_iv_i} \approx \sigma^{\mathcal{S}}_{n_f,n_i}(R_0) + \left(\frac{\mathrm{d}}{\mathrm{d}R}\sigma^{\mathcal{S}}_{n_f,n_i}(R)\right)_{R=R_0}(R_\mathrm{m}-R_0), \tag{4.47}$$

where R_m is the mean internuclear separation of the state n_iv_i:

$$R_\mathrm{m} = \langle \nu_{n_iv_i}|R|\nu_{n_iv_i}\rangle. \tag{4.48}$$

Evidently, the best choice of R_0 is R_m, since it gives first-order accuracy without requiring knowledge of the R derivatives of the cross sections. The fixed-nuclei approximation is then stated as

$$\sigma^{\mathcal{S}}_{n_f,n_iv_i} \approx \sigma^{\mathcal{S}}_{n_f,n_i}(R_\mathrm{m}). \tag{4.49}$$

An analogous expression also holds for the fixed-nuclei DCS.

This approximation holds only for scattering on the ground vibrational level ($v_i = 0$), since this vibrational wave function is approximately Gaussian in shape, and hence R values in the vicinity of R_m make the dominant contribution to the integration over R in Eq. (4.43). Since Eqs (4.43–4.45) are expressions for the cross sections summed over final vibrational levels, the fixed-nuclei approximation yields results only for total excitation of a given electronic state (summed/integrated over final bound/dissociative vibrational levels).

4.9 The Franck-Condon approximation

The Franck-Condon approximation is a simple method for reintroducing the vibrational motion without needing the electronic scattering problem to be solved at multiple internuclear separations (as required in the adiabatic-nuclei calculations). This approach assumes that the electronic scattering amplitudes are independent of the internuclear separation, allowing them to be factored out of the vibrational integrations. The cross section for the transition $n_iv_i \to n_fv_f$ is

then given by

$$\sigma_{n_f v_f, n_i v_i} = \sigma^{\mathrm{FN}}_{n_f v_f, n_i v_i} \left| \langle \nu_{f v_f} | \nu_{i v_i} \rangle \right|^2 , \tag{4.50}$$

where $\sigma^{\mathrm{FN}}_{n_f v_f, n_i v_i}$ is the fixed-nuclei electronic scattering cross section. The quantity $\left| \langle \nu_{f v_f} | \nu_{i v_i} \rangle \right|^2$ is referred to as the Franck-Condon factor.

4.10 The “square-root” approximation

The evaluation of Eq. (4.31) requires an integration over R for each partial wave. Although this is not a costly exercise on modern-day computers, numerical instabilities can arise when interpolating each partial-wave amplitude in order to perform the integration. The “square-root” approximation is an approximation for the spin-averaged vibrationally-resolved cross section:

$$\sigma_{n_f v_f, n_i v_i} \approx \left| \langle \nu_{n_f v_f} | \sqrt{\sigma_{n_f, n_i}(R)} | \nu_{n_i v_i} \rangle \right|^2 , \tag{4.51}$$

where $\sigma_{n_f, n_i}(R)$ is the spin-averaged R-dependent electronic-excitation cross section. This method allows the partial-wave amplitudes to be summed first to produce $\sigma_{n_f, n_i}(R)$, after which only $\sigma_{n_f, n_i}(R)$ must be interpolated.

It is difficult to justify the use of this approximation, although it is possible to show that it is accurate if each partial-wave amplitude has a similar R-dependence, i.e.

$$F^{\mathcal{S}(\mathrm{b})}_{n_f L_f \Lambda_{L_f}, n_i L_i \Lambda_{L_i}}(q_f, q_i, R) \approx C^{\mathcal{S}}_{n_f L_f \Lambda_{L_f}, n_i L_i \Lambda_{L_i}} \, f(R) \tag{4.52}$$

for some function $f(R)$ and constants $C^{\mathcal{S}}_{n_f L_f \Lambda_{L_f}, n_i L_i \Lambda_{L_i}}$. This method also produces the correct sum over final vibrational levels, i.e

$$\sum_{v_f} \left| \langle \nu_{n_f v_f} | \sqrt{\sigma_{n_f, n_i}(R)} | \nu_{n_i v_i} \rangle \right|^2 = \langle \nu_{n_i v_i} | \sigma_{n_f, n_i}(R) | \nu_{n_i v_i} \rangle, \tag{4.53}$$

which places a limit on the magnitude of the error in the approximation. In practice, though, it is not possible to assess the accuracy of the approximation without making comparison to the true adiabatic-nuclei cross sections. If it can be verified in this way that the approximation is valid, then in cases where calculated cross sections are affected by numerical instabilities, it can be useful to work

within this framework since it is much simpler to ensure that $\sigma_{n_f,n_i}(R)$ is a smooth function of R than it is for each individual partial-wave amplitude.

In order to ensure the correct excitation thresholds, Eq. (4.51) can be modified as follows:

$$\sigma_{n_f v_f, n_i v_i} \approx q_f \left| \langle \nu_{n_f v_f} | \sqrt{\sigma_{n_f,n_i}(R)/q_f(R)} | \nu_{n_i v_i} \rangle \right|^2 . \tag{4.54}$$

In this way, Eq. (4.54) is an approximation to the initial definition of the adiabatic-nuclei cross section (4.31), while Eq. (4.51) is an approximation to the alternative definition given in Eq. (4.36).

4.11 The energy-balancing method

In a theoretical study of electron-impact dissociative excitation of the H_2 $b\ ^3\Sigma_u^+$ state, Stibbe and Tennyson [71] suggested an alternative formulation of the adiabatic-nuclei method, in order to correct issues at low energies resulting from violation of energy conservation. The R-dependent scattering amplitudes which appear in the adiabatic-nuclei cross-section formula (4.31) are the result of fixed-nuclei scattering calculations where the outgoing projectile momentum q_f is determined by the vertical excitation energy (difference between the two potential-energy curves at a given R), via

$$q_f(R) = \sqrt{2\left[E_{\text{in}} - \epsilon_{n_f,n_i}(R)\right]}. \tag{4.55}$$

Hence, the R-dependent amplitudes are undefined whenever the incident energy is at or below the fixed-nuclei excitation energy. At near-threshold energies this can lead to situations where the R-dependent amplitudes are undefined over part or all of the integration domain in Eq. (4.31). This issue was discussed in detail by Shugard and Hazi [154], who suggested a solution involving the computation of R-dependent amplitudes which are "off-shell" (within the fixed-nuclei model) so that they can be chosen with the physically correct q_f per vibrational transition. For many scattering theories the calculation of off-shell scattering amplitudes is not possible, so Stibbe and Tennyson [71] suggested a simpler approach where the fixed-nuclei outgoing momentum is set equal to the physical q_f, and the

incident momentum is allowed to vary with R so that the R-dependent scattering amplitudes remain on shell. Writing the dependence of the amplitudes on the incident energy and internuclear separation explicitly, the adiabatic-nuclei cross section in this case is given by

$$\sigma^{\mathcal{S}}_{n_f v_f, n_i v_i} = \frac{q_f}{q_i}\frac{1}{4\pi} \sum_{\substack{L_f L_i \\ \Lambda_{L_f}\Lambda_{L_i}}} \left| \langle \nu_{n_f v_f} | F^{\mathcal{S}(\mathrm{b})}_{n_f L_f \Lambda_{L_f}, n_i L_i \Lambda_{L_i}}(R, E_{n_f v_f, n_i v_i}(R, E_{\mathrm{in}})) | \nu_{n_i v_i} \rangle \right|^2 , \tag{4.56}$$

where the modified incident energy $E_{n_f v_f, n_i v_i}$ is given in terms of the true incident energy E_{in}, vibrationally-resolved excitation energy $\varepsilon_{n_f v_f, n_i v_i}$, and vertical excitation energy ϵ_{n_f, n_i}:

$$E_{n_f v_f, n_i v_i}(R) = E_{\mathrm{in}} - \varepsilon_{n_f v_f, n_i v_i} + \epsilon_{n_f, n_i}(R). \tag{4.57}$$

The fixed-nuclei outgoing momentum $q_f(R)$ corresponding to this modified incident energy is independent of R by construction, and equal to the physical outgoing momentum for each vibrational transition. Although this approach comes with the tradeoff that the R-dependent amplitudes are now evaluated with the incorrect incident energy, it does ensure they are well-defined at all values of R for the integration in Eq. (4.56).

Although Stibbe and Tennyson [71] initially developed this approach for studies of dissociative excitation, it can be readily applied to both bound and dissociative transitions. When working within the square-root approximation (4.51), the energy-balancing method can be applied by simply evaluating the R-dependent cross section $\sigma_{n_f, n_i}(R)$ at the modified incident energy:

$$\sigma_{n_f v_f, n_i v_i} = \left| \langle \nu_{n_f v_f} | \sqrt{\sigma_{n_f, n_i}(R, E_{n_f v_f, n_i v_i}(R, E_{\mathrm{in}}))} | \nu_{n_i v_i} \rangle \right|^2 . \tag{4.58}$$

It should be noted that the energy-balancing method enforces the correct excitation thresholds, so here there is no need to modify Eq. (4.58) along the lines of Eq. (4.54).

4.12 Chapter 4 summary

This chapter has discussed the definitions of the adiabatic- and fixed-nuclei approximations, and provided a number of important equations for evaluating electron-molecule cross sections once the fixed-nuclei scattering problem has been solved. Some of the methods for solving the fixed-nuclei problem will be discussed in Chapter 5. The formulas presented here are for cross sections which are summed/averaged over the final/initial rotational levels of the target. Rotationally-resolved cross-section formulas will be derived in Chapter 11.

Chapter 5

Review of scattering theories

This chapter provides a brief outline of some of the various theoretical methods which have been applied to e^--H_2 collisions. The focus here is on the different treatments of the electronic dynamics; the various approximations applied to the nuclear dynamics in molecular scattering calculations were discussed in Chapter 4. Only those methods which are referred to later in the thesis are discussed in this chapter.

5.1 Classical and semiclassical methods

While atomic and molecular collisions are inherently quantum-mechanical processes, some theoretical methods treat the whole or part of the problem using classical approaches. While this must come at the expense of accuracy, and generally limits the types of processes which can be studied, the benefit of such an approach is the simplicity of the implementation and the reduced computational expense compared to fully quantum-mechanical methods. Classical or semiclassical methods are generally most accurate for large incident energies.

5.1.1 Gryziński method

This method was originally derived by Gryziński [155], and developed further by Bauer and Bartky [156]. The Gryziński method applies the binary-encounter approximation, which assumes that each pair of particles in the scattering system interact separately. In particular, it is assumed that the processes of electron-impact excitation and ionisation can be modelled as a classical collision between two free electrons. In order to apply the Gryziński method, all that is required is

knowledge of the excitation energies for the various transitions of interest, after which the cross section is given by simple formulas depending only on the energies involved. The method can be considered semiclassical in the sense that the target excitation energies must be obtained from quantum-mechanical calculations, but in terms of treating the collision dynamics this is an entirely classical approximation.

The Gryziński method has been applied by Wünderlich [98, 99] to the study of electron-impact ionisation of H_2 and its isotopologues. Despite the classical approach, the results for ionisation of the H_2 ground state were in good agreement with experiment. The simplicity of the approach allowed a large set of cross sections to be obtained for ionisation of vibrationally- and electronically-excited states. The nuclear dynamics in these calculations were accounted for using the Franck-Condon approximation (see Sec. 4.9). The same method was applied by Celiberto *et al.* [157] to the dissociative ionisation of vibrationally-excited D_2. The Gryziński method, along with the Franck-Condon approximation, was also applied by Celiberto *et al.* [158] to studies of dissociative electronic excitation of H_2 in excited vibrational levels.

5.1.2 Impact-parameter method

Impact-parameter (IP) methods in general are semiclassical approaches to a scattering problem in which the target is treated quantum-mechanically, but the projectile is treated classically. Classically, the projectile is asymptotically characterised by its velocity and the so-called impact parameter, the perpendicular distance between the projectile's initial straight-line trajectory and the target centre. IP methods require the scattering amplitudes to be evaluated as a function of the impact parameter before it is integrated over.

The IP method was first applied to electron scattering on molecules by Hazi [159], who studied electron collisions with H_2, F_2, and N_2 within the fixed-nuclei approximation. It was later implemented again by Celiberto and Rescigno [160] in studies of electronic excitation of vibrationally-excited H_2 and D_2, with the nuclear motion accounted for with the adiabatic-nuclei approximation to allow studies of scattering on vibrationally-excited targets. Since then the IP method

has been applied by Celiberto and co-authors to studies of electron collisions with numerous molecules, including calculations of many optically-allowed transitions in H_2 and its isotopologues [70, 160–164]. For large incident energies, the IP calculations reproduce the Born-approximation results, ensuring the correct cross-section behaviour in the high-energy limit. At low to intermediate energies the IP results are well-known to be too large, but they are still a considerable improvement over the Born approximation. The IP method is also only applicable to optically-allowed transitions, and hence studies of dipole- or spin-forbidden transitions must be performed with alternative approaches.

5.2 Quantum-mechanical methods

5.2.1 Schwinger multichannel method

The Schwinger multichannel (SMC) method has its roots in the Schwinger variational principle (SVP) of quantum scattering [165]. The SVP was fist applied to electron-molecule scattering by McKoy and co-authors [166–171]. The SMC method was a natural extension of this which includes multichannel coupling, exchange, and polarisation effects, and can be applied to arbitrary molecules possessing long-range dipole potentials [172]. It has been utilised in studies of electron and positron scattering on a variety of both small and large molecules [173–176]. In the case of H_2, the SMC method has been applied to electron scattering on the $X\,^1\Sigma_g^+$, $c\,^3\Pi_u$, and $a\,^3\Sigma_g^+$ states within the fixed-nuclei approximation [94, 95, 177]. There have been no SMC studies of e^--H_2 scattering with nuclear dynamics incorporated.

5.2.2 The distorted-wave approximation

The distorted-wave (DW) approximation is a perturbation method in which the projectile is treated using distorted waves calculated in the field of the target. The total scattering wave function is represented as the product of the initial unperturbed target state and the projectile distorted wave [178]. The inclusion of an approximate exchange potential in addition to the static target potential

in the calculation of the distorted waves allows spin-exchange transitions to be studied. The DW approximation is most accurate at larger incident energies, and in the high-energy limit it reproduces the results of the Born approximation. At lower energies, the DW approximation is an improvement over the Born approximation, but is less accurate than non-perturbative methods. The DW method has been applied to e^--H_2 scattering in a number of papers, using the fixed-nuclei approximation for studies of low-lying electronic excitations [67, 68], and the adiabatic-nuclei approximation for studies of dissociative excitation [69]. The DW method ignores interchannel coupling, and is applicable only at intermediate to high energies.

5.2.3 The *R*-matrix method

The R-matrix method was first introduced in studies of nuclear scattering [179], and extended to electron-atom scattering by Burke *et al.* [180]. The fundamental concept of the method is the separation of configuration space into the *internal* and *external* regions. In the internal region, exchange and correlation effects between the projectile and target electrons are treated rigorously by diagonalising the scattering Hamiltonian to obtain $(N+1)$-electron wave functions and energies (where N is the number of target electrons). In the outer region, the projectile-target interaction is assumed to be mediated only by long-range potentials, with exchange and correlation effects neglected [181]. The boundary between the two regions is known as the R-matrix sphere.

The R-matrix method is an *ab initio* technique, however the accuracy of the calculated cross sections depends strongly on the number of target states included in the coupled-state expansion of the $(N+1)$-electron wave function, the number of terms included in the partial-wave expansion of the projectile wave function, and the size of the R-matrix sphere. The choice of radius for the R-matrix sphere is influenced by the requirement for the $(N+1)$-electron wave functions to be contained within the sphere, and the increasing computational expense associated with larger radii. The former places restrictions on the types of calculations which may be performed, since more diffuse $(N+1)$-electron states may leak outside the R-matrix sphere. As a result, R-matrix calculations become difficult when

large internuclear separations or large projectile angular momenta are required.

Early R-matrix calculations for the fundamental $X\,{}^1\Sigma_g^+ \rightarrow b\,{}^3\Sigma_u^+$ transition were performed in the fixed-nuclei approximation by Baluja *et al.* [182] and Branchett and Tennyson [65], with both utilising only small target-state expansions. Later calculations were performed by Stibbe and Tennyson [71] using the UK Molecular R-matrix (UKRMol) suite of computer programs, with 9 target states included in the calculations (counting degenerate states twice). During the course of this project, improved calculations for scattering on the $X\,{}^1\Sigma_g^+$ state of H_2 in the fixed-nuclei approximation were performed by Meltzer *et al.* [9] using the UKRMol+ suite, which allows the use of a much larger R-matrix radius, and hence the use of larger basis sets. Similar calculations were also performed for scattering on excited electronic states [116]. Comparison of these results with the results obtained during the current project will be made in Chapter 8. It is worth noting that the UKRMol and UKRMol+ codes do not utilise pseudostates to model ionisation channels, restricting the range of validity in the calculations to low incident energies (below the ionisation threshold).

5.2.4 Complex scattering potential–ionisation contribution

The "complex scattering potential–ionisation contribution" (CSP-ic) method is a semi-empirical method developed by Joshipura *et al.* [183], wherein the collision dynamics are modelled using a complex local potential readily obtained once the target wave functions are known. The potential includes the real static and exchange potentials, as well as a complex absorption potential to model inelastic processes. The ionisation cross section is extracted from calculations of the inelastic cross section by defining an approximate energy-dependent "break-up ratio", which is determined by semi-empirical means. This approach has been applied to a number of molecules [183–187], including ionisation of the metastable $c\,{}^3\Pi_u$ state of H_2 [97]. A comparison of this result with the present calculations will be made in Chapter 8.

5.2.5 Convergent close-coupling method

Born out of earlier coupled-channel optical calculations [188], the convergent close-coupling (CCC) method was developed by Bray and Stelbovics [189] and initially applied to studies of electron scattering on atomic hydrogen. The CCC method is an implementation of the close-coupling theory, where the total scattering wave function is expanded in the set of target states, resulting in a set of coupled equations for the scattering quantities of interest. The close-coupling method is, in principle, an *ab initio* technique, however the accuracy of the calculated cross sections strongly depends on the completeness of the set of included target states. In particular, coupling to target states in the continuum must be accounted for, but before the advent of CCC there were no theoretical methods which attempted this in a systematic way. One of the defining qualities of the CCC method is the representation of the target in a basis of square-integrable ("L^2") functions built from Laguerre polynomials. As the size of the basis is increased the low-lying states generated converge to true target eigenstates, while the remaining pseudostates (so-called because they diagonalise the target Hamiltonian but are not eigenstates) provide a quadrature rule for summing over the discrete target spectrum and integrating over the target continuum. Hence, by including the pseudostates in the close-coupling expansion one obtains a tractable method for treating the infinite target spectrum with a finite-sized expansion.

Since the original application of CCC to e^--H scattering, the method has been extended to quasi one-electron atomic targets (those which can be modelled by a single electron above a frozen Hartree-Fock core) [190], and quasi two-electron targets [191, 192]. In order to study positron collisions with atomic targets, a "two-centre" implementation of CCC was developed [193, 194], in which the rearrangement channels of positronium formation are included explicitly via a second expansion in terms of positronium states. The CCC method has also been extended further with a separate implementation for ion-atom scattering [195–200].

During the past decade, the molecular CCC (MCCC) method has been developed during the PhD projects of Zammit [201] and Savage [202]. The MCCC code was implemented using the fixed-nuclei approximation, and applied to elec-

tron and positron scattering on H_2 and H_2^+ [88–93, 203]. For electron scattering on H_2^+ and positron scattering on H_2, calculations were performed in the adiabatic-nuclei approximation [90, 92]. The MCCC calculations for e^--H_2 scattering rigorously demonstrated convergence with respect to the projectile and target expansions in cross sections for elastic scattering, excitation, and ionisation, within the fixed-nuclei approximation. The converged MCCC results were in many cases substantially different from previous calculations. In particular, the MCCC cross section for the important $X\ ^1\Sigma_g^+ \rightarrow b\ ^3\Sigma_u^+$ transition was up to a factor of two lower than previous theory *and* measurements above 12 eV. This situation was resolved later when updated measurements were taken with a new apparatus at California State University Fullerton, and were found to be in near-perfect agreement with the MCCC predictions [14, 17]. Agreement between theory and experiment on this level was unprecedented in electron-molecule collisions, and reinforced the accuracy of the MCCC calculations. A more detailed discussion of the MCCC theory is given in Chapter 6.

5.3 Chapter 5 summary

Although the basic physics of non-relativistic collisions is well understood and is described simply by the Schrödinger equation, actually solving the scattering equations is a difficult computational feat. Hence, a number of approximations have been developed to simplify the calculations, although this comes at the expense of the accuracy and generality of the method. A number of approximate electronic-scattering calculations have been applied to the e^--H_2 collision complex, and those which are referred to in later chapters have been discussed here. The driving principle of the convergent close-coupling method, which is applied in the present work, is to solve the scattering equations essentially without approximation in order to produce data for all transitions of interest over broad energy ranges.

Part II

Adiabatic-nuclei MCCC

Chapter 6

Fixed-nuclei molecular convergent close-coupling method

This chapter provides a brief summary of the fixed-nuclei (FN) MCCC method formulated in both spherical and prolate spheroidal coordinates. Both implementations, including expressions for the V-matrix elements, have been described in detail previously by Zammit *et al.* [87] and Savage [202]. The MCCC method is formulated in the non-relativistic approximation, where the total scattering-system electron spin $\mathcal{S}$ is treated as a good quantum number.

The spherical MCCC implementation is formulated in the standard spherical coordinate system (r, θ, ϕ). The spheroidal MCCC implementation is formulated in the modified prolate spheroidal coordinates (ρ, η, ϕ), defined as

$$\rho = \frac{r_1 + r_2}{2} - \frac{R}{2} \in [0, \infty) \tag{6.1}$$

$$\eta = \frac{r_1 - r_2}{R} \in [-1, 1), \tag{6.2}$$

along with the standard azimuthal angle ϕ, in terms of distances r_1 and r_2 from the two foci positioned at the nuclei. With this definition of the coordinate system, the spheroidal radial coordinate ρ is analogous to the spherical radial coordinate r, since

$$\lim_{R \to 0} \rho = r. \tag{6.3}$$

6.1 Target states

6.1.1 One-electron states

The one-electron target states (states of H_2^+) are characterised by their orbital angular-momentum projection Λ, parity π, spin s, and spin projection Σ (Λ and Σ are both defined as projections onto the internuclear axis). The one-electron states are denoted by $|\phi_n^{\Lambda\pi s\Sigma}\rangle$, where n is an index variable (not a quantum number), and are obtained via a configuration-interaction (CI) calculation in a basis of Laguerre-type states:

$$|\phi_n^{\Lambda\pi s\Sigma}\rangle = \sum_{j=1}^{N_j} C_j^{(n)} |k_j \ell_j \Lambda_j s_j \Sigma_j\rangle. \tag{6.4}$$

In the spherical-coordinate implementation, the basis states are given by

$$\langle \boldsymbol{r}|k_j \ell_j \Lambda_j s_j \Sigma_j\rangle = \frac{1}{r}\varphi_{k_j \ell_j}(r) Y_{\ell_j}^{\Lambda_j}(\hat{\boldsymbol{r}})|s_j \Sigma_j\rangle, \tag{6.5}$$

where Y_ℓ^Λ are the spherical harmonics, $|s\Sigma\rangle$ are one-electron spin states, and $\varphi_{k\ell}$ are the radial Laguerre functions:

$$\varphi_{k\ell}(r) = \sqrt{\frac{\alpha_\ell (k-\ell)!}{(k+\ell)(k+2\ell)!}} (2\alpha_\ell r)^{\ell+1} e^{-\alpha_\ell r} L_{k-1}^{2\ell+1}(2\alpha_\ell r). \tag{6.6}$$

Here, $L_{k-1}^{2\ell+1}$ is the associated Laguerre polynomial of order $2\ell+1$. The CI coefficients $C_j^{(n)}$ in Eq. (6.4) are found by diagonalising the one-electron target Hamiltonian $\hat{\mathsf{H}}_\mathrm{t}$ using standard numerical methods. Since the basis must be truncated to allow numerical solution, the resulting states in Eq. (6.4) are *pseudostates*. They satisfy

$$\langle \phi_{n'}^{\Lambda\pi s\Sigma}|\hat{\mathsf{H}}_\mathrm{t}|\phi_n^{\Lambda\pi s\Sigma}\rangle = \epsilon_n \delta_{n'n} \tag{6.7}$$

for all n, where ϵ_n is the pseudostate energy. For sufficiently large basis sizes, the low-lying discrete states are good representations of true spectroscopic states, which satisfy

$$\hat{\mathsf{H}}_\mathrm{t}|\phi_n^{\Lambda\pi s\Sigma}\rangle = \epsilon_n |\phi_n^{\Lambda\pi s\Sigma}\rangle. \tag{6.8}$$

The procedure for generating one-electron states in spheroidal coordinates

closely follows what was outlined above for the spherical implementation. The primary distinction is that the spheroidal Laguerre radial basis functions are defined by

$$\varphi_{k\Lambda}(\rho) = \sqrt{\alpha_\Lambda \frac{(k-1)!}{(k+\Lambda-1)!}} (\alpha_\Lambda \rho)^{\Lambda/2} e^{-\alpha_\Lambda \rho/2} L_{k-1}^{\Lambda}(\alpha_\Lambda \rho). \tag{6.9}$$

Note that the radial functions and exponential falloffs are specified by the value of Λ rather than ℓ. The three-dimensional basis functions are still expressed in terms of spherical harmonics:

$$\langle \boldsymbol{\rho} | k\ell\Lambda s\Sigma \rangle = \varphi_{k\Lambda}(\rho) Y_\ell^\Lambda(\hat{\boldsymbol{\rho}}) | s\Sigma \rangle, \tag{6.10}$$

so that the basis functions can be assigned a well-defined value of ℓ. However, note the distinction that the spheroidal basis functions do not contain an equivalent of the $1/r$ factor in the spherical basis functions (6.5). This is because the spheroidal differential volume element

$$\mathrm{d}V = \left[\left(\rho + \frac{R}{2} \right)^2 - \left(\frac{R}{2} \eta \right)^2 \right] \mathrm{d}\rho \, \mathrm{d}\eta \, \mathrm{d}\phi \tag{6.11}$$

is non-separable and does not contain easily-cancelled factors as in the spherical case ($\mathrm{d}V = r^2 \sin\theta \, \mathrm{d}r \, \mathrm{d}\theta \, \mathrm{d}\phi$).

6.1.2 Two-electron states

The spherical-coordinate two-electron target states are represented in a basis of two-electron configurations formed from the one-electron Laguerre basis in Eq. (6.5). For the purposes of calculating spatial wave functions, spin-dependence can be neglected except in determining the allowed configurations (to satisfy the exclusion principle). To improve the accuracy of the two-electron structure calculation, one or more one-electron molecular states can be used to replace the corresponding Laguerre basis functions. For example, the $X\ {}^2\Sigma_g$ H_2^+ state can replace the Laguerre function with $k = 1$ and $\ell = \Lambda = 0$, and so on.

The spherical-coordinate two-electron wave functions are represented in the

following form:

$$\Phi_n^{\Lambda\pi s\Sigma_s}(\boldsymbol{r}_1,\boldsymbol{r}_2) = \frac{1}{r_1 r_2}\sum_{\alpha\beta} C_{\alpha,\beta}^{(n)}\phi_\alpha(\boldsymbol{r}_1)\phi_\beta(\boldsymbol{r}_2) \tag{6.12}$$

$$\phi_\alpha(\boldsymbol{r}) = \varphi_\alpha(r)Y_{\ell_\alpha}^{\Lambda_\alpha}(\hat{\boldsymbol{r}}), \tag{6.13}$$

with the antisymmetry requirement built in to the CI coefficients which satisfy $C_{\alpha,\beta}^{(n)} = (-1)^s C_{\alpha\beta}^{(n)}$. Since the one-electron basis in which configurations are constructed contains both Laguerre basis functions with a well-defined ℓ, and one-electron molecular states with a mixture of contributions from all ℓ, the representation given in Eq. (6.12) in which each α and β corresponds to a specific ℓ is only possible after a procedure to sum together the contributions from multiple radial functions for each given ℓ, to give φ_α. In the spheroidal case, the target wave functions are represented as

$$\Phi_n^{\Lambda\pi s\Sigma_s}(\boldsymbol{\rho}_1,\boldsymbol{\rho}_2) = \sum_{\alpha\beta} C_{\alpha,\beta}^{(n)}\phi_\alpha(\boldsymbol{\rho}_1)\phi_\beta(\boldsymbol{\rho}_2). \tag{6.14}$$

As before, the two-electron states are pseudostates which satisfy

$$\langle\Phi_{n'}^{\Lambda\pi s\Sigma}|\hat{\mathsf{H}}_{\mathrm{t}}|\Phi_n^{\Lambda\pi s\Sigma}\rangle = \epsilon_n\delta_{n'n}, \tag{6.15}$$

and the discrete states which adequately represent true spectroscopic states satisfy

$$\hat{\mathsf{H}}_{\mathrm{t}}|\Phi_n^{\Lambda\pi s\Sigma}\rangle = \epsilon_n|\Phi_n^{\Lambda\pi s\Sigma}\rangle. \tag{6.16}$$

A useful property of the underlying Laguerre basis is that the pseudostates resulting from diagonalising the target Hamiltonian form a quadrature rule for the sum and integral over the true discrete and continuum target eigenstates [204–207], in the sense that

$$\lim_{N\to\infty}\sum_{n=1}^{N}|\Phi_n\rangle\langle\Phi_n| = \sum_{j=1}^{\infty}|\bar{\Phi}_j\rangle\langle\bar{\Phi}_j| + \int_0^\infty |\bar{\Phi}_c\rangle\langle\bar{\Phi}_c|\,\mathrm{d}c, \tag{6.17}$$

where $|\bar{\Phi}_j\rangle$ are the true discrete eigenstates, $|\bar{\Phi}_c\rangle$ are true continuum eigenstates with energy c relative to the ionisation threshold, and N is the number of pseudostates. Since the Hamiltonian is a Hermitian operator, the right-hand side of

Eq. (6.17) is the identity operator acting in the electronic target space. Therefore, defining the projection operator

$$\hat{\mathsf{I}}^N = \sum_{n=1}^{N} |\Phi_n\rangle\langle\Phi_n| \tag{6.18}$$

we have

$$\lim_{N\to\infty} \hat{\mathsf{I}}^N = \hat{\mathsf{I}}. \tag{6.19}$$

6.2 Momentum-space Lippmann-Schwinger equation

The electronic scattering states are the solutions to

$$(E - \hat{\mathsf{H}})|\Psi_{n_i}^{\mathcal{S}}\rangle = 0, \tag{6.20}$$

where $\hat{\mathsf{H}}$ is the total scattering-system Hamiltonian:

$$\hat{\mathsf{H}} = \hat{\mathsf{K}}_0 + \hat{\mathsf{H}}_\mathrm{t} + \hat{\mathsf{V}}_\mathrm{dir}. \tag{6.21}$$

Here, $\hat{\mathsf{K}}_0$ is the projectile kinetic-energy operator, $\hat{\mathsf{H}}_\mathrm{t}$ is the target electronic Hamiltonian, and $\hat{\mathsf{V}}_\mathrm{dir}$ is the projectile-target direct interaction potential. The reason for denoting it as "direct" will become clear further down. In this chapter all operators and states are defined in the molecular body frame. In the case of electron scattering, $|\Psi_{n_i}^{\mathcal{S}}\rangle$ must be antisymmetric with respect to exchange of the projectile electron with any of the target electrons. Therefore, it is convenient to express it in an explicitly antisymmtrised form:

$$|\Psi_{n_i}^{\mathcal{S}}\rangle = \mathcal{A}|\psi_{n_i}^{\mathcal{S}}\rangle, \tag{6.22}$$

where

$$\mathcal{A} = 1 - \sum_{j=1}^{N_\mathrm{e}} \hat{\mathsf{P}}_{0j} \tag{6.23}$$

is the antisymmetrisation operator, and $|\psi_{n_i}^{\mathcal{S}}\rangle$ is a state of arbitrary symmetry which will be solved for. In Eq. (6.23), $\hat{\mathsf{P}}_{0j}$ is the electron exchange operator, and N_e is the number of target electrons.

Defining the asymptotic Hamiltonian

$$\hat{\mathsf{H}}_0 = \hat{\mathsf{K}}_0 + \hat{\mathsf{H}}_\mathrm{t}, \tag{6.24}$$

Eq. (6.20) becomes

$$(E - \hat{\mathsf{H}})|\psi_{n_i}^{\mathcal{S}}\rangle = (E - \hat{\mathsf{H}}) \sum_{j=1}^{N_\mathrm{e}} \hat{\mathsf{P}}_{0j}|\psi_{n_i}^{\mathcal{S}}\rangle \tag{6.25}$$

$$(E - \hat{\mathsf{H}}_0)|\psi_{n_i}^{\mathcal{S}}\rangle = \hat{\mathsf{V}}_\mathrm{dir}|\psi_{n_i}^{\mathcal{S}}\rangle + (E - \hat{\mathsf{H}}) \sum_{j=1}^{N_\mathrm{e}} \hat{\mathsf{P}}_{0j}|\psi_{n_i}^{\mathcal{S}}\rangle \tag{6.26}$$

$$(E - \hat{\mathsf{H}}_0)|\psi_{n_i}^{\mathcal{S}}\rangle = \hat{\mathsf{V}}|\psi_{n_i}^{\mathcal{S}}\rangle, \tag{6.27}$$

where we have defined

$$\hat{\mathsf{V}} = \hat{\mathsf{V}}_\mathrm{dir} + \hat{\mathsf{V}}_\mathrm{exch} \tag{6.28}$$

$$\hat{\mathsf{V}}_\mathrm{exch} = (E - \hat{\mathsf{H}}) \sum_{j=1}^{N_\mathrm{e}} \hat{\mathsf{P}}_{0j}. \tag{6.29}$$

Here, $\hat{\mathsf{V}}_\mathrm{exch}$ is the exchange potential operator. While it does not correspond to a physical potential, it plays the role of a potential in the Schrödinger equation (6.27) for $|\psi_{n_i}^{\mathcal{S}}\rangle$. In reality, this term is merely a consequence of the requirement that the total scattering wave function is antisymmetric with respect to electron exchange.

The central idea of the close-coupling method is the multichannel expansion of the total scattering state:

$$|\psi_{n_i}^{\mathcal{S}}\rangle = \sum\!\!\!\!\!\!\int_j |\bar{\Phi}_j\rangle\langle\bar{\Phi}_j|\psi_{n_i}^{\mathcal{S}}\rangle, \tag{6.30}$$

where the sum/integral sign indicates a summation over the discrete and integral over the continuum target eigenstates $|\bar{\Phi}_j\rangle$. To date, no close-coupling method has been developed which is capable of treating the target continuum in Eq. (6.30) using true continuum states. The approach taken in the CCC and MCCC methods is to write the multichannel expansion using the pseudostate

projection operator (6.18):

$$|\psi_{n_i}^{\mathcal{S}}\rangle = \hat{\mathsf{I}}^N|\psi_{n_i}^{\mathcal{S}}\rangle \tag{6.31}$$

By virtue of Eq. (6.19), the two forms of the multichannel expansion in Eqs. (6.30) and (6.31) are formally equivalent in the limit as $N \to \infty$. The $\hat{\mathsf{I}}^N$-projected transition operator, defined by

$$\hat{\mathsf{T}}^N|\Phi_{n_i}\boldsymbol{q}_i : \mathcal{S}\rangle = \hat{\mathsf{I}}^N\hat{\mathsf{V}}\,\hat{\mathsf{I}}^N|\psi_{n_i}^{\mathcal{S}}\rangle, \tag{6.32}$$

therefore satisfies

$$\lim_{N\to\infty}\hat{\mathsf{T}}^N|\Phi_{n_i}\boldsymbol{q}_i : \mathcal{S}\rangle = \hat{\mathsf{T}}|\Phi_{n_i}\boldsymbol{q}_i : \mathcal{S}\rangle. \tag{6.33}$$

Inserting the multichannel expansion from Eq. (6.31) into Eq. (6.27), and projecting on the left by $\hat{\mathsf{I}}^N$ gives

$$\hat{\mathsf{I}}^N(E-\hat{\mathsf{H}}_0)\hat{\mathsf{I}}^N|\psi_{n_i}^{\mathcal{S}}\rangle = \hat{\mathsf{I}}^N\hat{\mathsf{V}}\,\hat{\mathsf{I}}^N|\psi_{n_i}^{\mathcal{S}}\rangle. \tag{6.34}$$

Now defining the $\hat{\mathsf{I}}^N$-projected asymptotic Green's operator with outgoing spherical-wave boundary conditions:

$$\hat{\mathsf{G}}_0^{N(+)} = \lim_{\epsilon\to 0^+}\hat{\mathsf{G}}_0^N(\epsilon) \tag{6.35}$$

$$\hat{\mathsf{G}}_0^N(\epsilon)\left[\hat{\mathsf{I}}^N(E-\hat{\mathsf{H}}_0+i\epsilon)\hat{\mathsf{I}}^N\right] = \hat{\mathsf{I}}^N, \tag{6.36}$$

the $\hat{\mathsf{I}}^N$-projected Schrödinger equation in Eq. (6.34) can be transformed into the Lippmann-Schwinger equation:

$$\hat{\mathsf{I}}^N|\psi_{n_i}^{\mathcal{S}(+)}\rangle = \hat{\mathsf{I}}^N|\Phi_{n_i}\boldsymbol{q}_i : \mathcal{S}\rangle + \hat{\mathsf{G}}_0^{N(+)}\hat{\mathsf{I}}^N\hat{\mathsf{V}}\,\hat{\mathsf{I}}^N|\psi_{n_i}^{\mathcal{S}(+)}\rangle, \tag{6.37}$$

where $|\Phi_{n_i}\boldsymbol{q}_i : \mathcal{S}\rangle$ are the eigenstates (with total electron spin $\mathcal{S}$) of the asymptotic Hamiltonian, which play the role of the homogeneous term of the general solution in Eq. (6.37). Note that the scattering state $|\psi_{n_i}^{\mathcal{S}(+)}\rangle$ has now been given the superscript $(+)$ to indicate the boundary conditions enforced by the Green's operator defined in Eq. (6.35).

The Lippmann-Schwinger equation for the $\hat{\mathsf{I}}^N$-projected T-matrix element, Eq. (6.32), is obtained by multiplying Eq. (6.37) on the left by $\langle\mathcal{S} : \boldsymbol{q}_f\Phi_{n_f}|\hat{\mathsf{I}}^N\hat{\mathsf{V}}\,\hat{\mathsf{I}}^N$,

giving

$$\langle \mathcal{S} : \boldsymbol{q}_f \Phi_{n_f} | \hat{\mathsf{T}}^N | \phi_{n_i} \boldsymbol{q}_i : \mathcal{S} \rangle \tag{6.38}$$
$$= \langle \mathcal{S} : \boldsymbol{q}_f \Phi_{n_f} | \hat{\mathsf{V}} | \Phi_{n_i} \boldsymbol{q}_i : \mathcal{S} \rangle + \langle \mathcal{S} : \boldsymbol{q}_f \Phi_{n_f} | \hat{\mathsf{V}} \, \hat{\mathsf{I}}^N \hat{\mathsf{G}}_0^{N(+)} \, \hat{\mathsf{I}}^N \hat{\mathsf{T}}^N | \Phi_{n_i} \boldsymbol{q}_i : \mathcal{S} \rangle.$$

For simplicity, the dependence of the T- and V-matrix elements on $\mathcal{S}$ will be dropped from here on, and restored only when necessary. Note also that the $\hat{\mathsf{I}}^N$ operator has been dropped whenever acting on a target state, as it is assumed that all target states appearing in Eq. (6.38) come from the same set of pseudostates defining $\hat{\mathsf{I}}^N$.

Since the pseudostates diagonalise the target Hamiltonian, we have that

$$\langle \boldsymbol{q}' \Phi_{n'} | \hat{\mathsf{G}}_0^{N(+)} | \Phi_n \boldsymbol{q} \rangle = G_n^{(+)}(q) \delta_{n',n} \delta(\boldsymbol{q}' - \boldsymbol{q}), \tag{6.39}$$

where

$$G_0^{(+)}(q) = \lim_{\epsilon \to 0^+} \frac{1}{E - \epsilon_n - \epsilon_q + i\epsilon} \tag{6.40}$$

is the Green's function. Therefore, by inserting a complete set of projectile states on either side of $\hat{\mathsf{G}}_0^{N(+)}$ in Eq. (6.38) we obtain

$$\langle \boldsymbol{q}_f \Phi_{n_f} | \hat{\mathsf{T}}^N | \Phi_{n_i} \boldsymbol{q}_i \rangle \tag{6.41}$$
$$= \langle \boldsymbol{q}_f \Phi_{n_f} | \hat{\mathsf{V}} | \Phi_{n_i} \boldsymbol{q}_i \rangle + \sum_{n=1}^{N} \iiint_{\mathbb{R}^3} \langle \boldsymbol{q}_f \Phi_{n_f} | \hat{\mathsf{V}} | \Phi_n \boldsymbol{q} \rangle G_n^{(+)}(q) \langle \boldsymbol{q} \Phi_n | \hat{\mathsf{T}}^N | \Phi_{n_i} \boldsymbol{q}_i \rangle \, \mathrm{d}\boldsymbol{q}.$$

As a result of Eq. (6.32), the T-matrix elements obtained by solving Eq. (6.41) converge to the correct values as the size of the pseudostate expansion is increased:

$$\lim_{N \to \infty} \langle \boldsymbol{q}_f \Phi_{n_f} | \hat{\mathsf{T}}^N | \Phi_{n_i} \boldsymbol{q}_i \rangle = \langle \boldsymbol{q}_f \Phi_{n_f} | \hat{\mathsf{T}} | \Phi_{n_i} \boldsymbol{q}_i \rangle. \tag{6.42}$$

Therefore, to obtain arbitrarily accurate results it is sufficient to vary convergence with respect to N to within the desired precision.

In order to remove the three-dimensional integration over momentum space in Eq. (6.41), the body-frame partial-wave expansion in Eq. (4.22) is applied to the T- and V-matrix elements, giving (after some simplification) the partial-wave

Lippmann-Schwinger equation:

$$\langle q_f L_f \Lambda_{L_f}\, \Phi_{n_f} | \hat{\mathsf{T}} | \Phi_{n_i}\, q_i L_i \Lambda_{L_i} \rangle = \langle q_f L_f \Lambda_{L_f}\, \Phi_{n_f} | \hat{\mathsf{V}} | \Phi_{n_i}\, q_i L_i \Lambda_{L_i} \rangle \tag{6.43}$$
$$+ \sum_{n=1}^{N} \sum_{L=0}^{L_{\max}} \sum_{\Lambda_L=-L}^{L} \int_0^\infty \langle q_f L_f \Lambda_{L_f}\, \Phi_{n_f} | \hat{\mathsf{V}} | \Phi_n\, q L \Lambda_L \rangle G_n^{(+)}(q) \langle q L \Lambda_L\, \Phi_n | \hat{\mathsf{T}} | \Phi_{n_i}\, q_i L_i \Lambda_{L_i} \rangle \, \mathrm{d}q.$$

Here, projectile partial waves are included up to some $L_{\max}$, with the accuracy of the partial-wave T-matrix elements verified by checking for convergence with respect to increasing $L_{\max}$.

Since the total scattering system orbital angular-momentum projection Λ_{tot} and parity Π_{tot} are good quantum numbers, Eq. (6.43) is solved separately for each combination of Λ_{tot}, Π_{tot}, and $\mathcal{S}$. The method of solution, by discretisation of the momentum-space domain and conversion into a system of linear equations, is described in Ref. [87], and will be discussed in the context of vibrational-electronic MCCC calculations in Chapter. 9. Once the partial-wave T-matrix elements are calculated, cross sections are obtained as outlined in Chapter 4 Sec. 4.4.

The partial-wave Lippmann-Schwinger equation in the spheroidal implementation has the same form as Eq. (6.43), with the replacement of the spherical L with the spheroidal pseudo-angular-momentum λ:

$$\langle q_f L_f \Lambda_{\lambda_f}\, \Phi_{n_f} | \hat{\mathsf{T}} | \Phi_{n_i}\, q_i \lambda_i \Lambda_{\lambda_i} \rangle = \langle q_f \lambda_f \Lambda_{\lambda_f}\, \Phi_{n_f} | \hat{\mathsf{V}} | \Phi_{n_i}\, q_i \lambda_i \Lambda_{\lambda_i} \rangle \tag{6.44}$$
$$+ \sum_{n=1}^{N} \sum_{\lambda=0}^{\lambda_{\max}} \sum_{\Lambda_\lambda=-\lambda}^{\lambda} \int_0^\infty \langle q_f \lambda_f \Lambda_{\lambda_f}\, \Phi_{n_f} | \hat{\mathsf{V}} | \Phi_n\, q \lambda \Lambda_\lambda \rangle G_n^{(+)}(q) \langle q \lambda \Lambda_\lambda\, \Phi_n | \hat{\mathsf{T}} | \Phi_{n_i}\, q_i \lambda_i \Lambda_{\lambda_i} \rangle \, \mathrm{d}q.$$

This arises from the different projectile partial-wave expansion in the spheroidal implementation, in terms of the spheroidal harmonics $\Upsilon_\lambda^{\Lambda_\lambda}$ rather than spherical harmonics:

$$\langle \boldsymbol{\rho} | \boldsymbol{q} \rangle = \sqrt{\frac{2}{\pi}} \frac{1}{q} \sum_{\lambda=0}^{\infty} \sum_{\Lambda_\lambda=-\lambda}^{\lambda} i^\lambda \Xi_\lambda^{\Lambda_\lambda}(\rho; c) \Upsilon_\lambda^{\Lambda_\lambda}(\hat{\boldsymbol{\rho}}; c) \Upsilon_\lambda^{\Lambda_\lambda *}(\hat{\boldsymbol{q}}; c). \tag{6.45}$$

Here, $c = qR/2$ is the spheroidal pseudomomentum. The projection Λ_λ of λ on the internuclear axis is equivalent to the spherical-coordinate orbital angular-momentum projection since both coordinate systems possess the same cylindrical symmetry about the internuclear axis. The method for obtaining the radial func-

tions $\Xi_{\lambda}^{\Lambda_\lambda}$ is described in Ref. [202]. The partial-wave expansions of the T- and V-matrix elements are of the same form in spheroidal coordinates as in spherical coordinates, with the replacement of the spherical partial-wave matrix elements with the spheroidal analogue. The spheroidal partial-wave matrix elements can be converted into the equivalent spherical matrix elements using the following relation:

$$\begin{aligned}&\langle q_f L_f \Lambda_{L_f}\, \Phi_{n_f} | \hat{\mathsf{T}} | \Phi_{n_i}\, q_i L_i \Lambda_{L_i} \rangle \qquad (6.46)\\ &= \sum_{\lambda_f \lambda_i} i^{\lambda_i - L_i + L_f - \lambda_f} \langle Y_{L_f}^{\Lambda_{L_f}} | \Upsilon_{\lambda_f}^{\Lambda_{\lambda_f}}(c_f) \rangle \langle Y_{L_i}^{\Lambda_{L_i}} | \Upsilon_{\lambda_i}^{\Lambda_{\lambda_i}}(c_i) \rangle \langle q_f \lambda_f \Lambda_{\lambda_f}\, \Phi_{n_f} | \hat{\mathsf{T}} | \Phi_{n_i}\, q_i \lambda_i \Lambda_{\lambda_i} \rangle,\end{aligned}$$

with $\Lambda_{L_f} = \Lambda_{\lambda_f}$ and $\Lambda_{L_i} = \Lambda_{\lambda_i}$. The same relation holds also for the V-matrix elements. The method for obtaining the overlaps of the spherical and spheroidal harmonics is described in Ref. [202].

Once the spheroidal partial-wave T-matrix elements are obtained, the formulas given in Chapter 4 for the *fixed-nuclei* cross sections still hold, with L replaced with λ as appropriate. However, since the spheroidal coordinate system is inherently dependent on the internuclear separation, the adiabatic-nuclei scattering amplitudes can only be obtained by converting the spheroidal T-matrix elements into spherical matrix elements before performing the integration over R.

6.3 H_2 scattering V-matrix elements (spherical)

The spherical V-matrix elements for electron-H_2 scattering are given in Ref. [87], and are included here for completeness.

The direct potential function $V_{\rm dir}(\boldsymbol{r}_0, \boldsymbol{r}_1, \boldsymbol{r}_2; \boldsymbol{R})$ can be expressed as

$$V_{\rm dir}(\boldsymbol{r}_0, \boldsymbol{r}_1, \boldsymbol{r}_2) = V_0(\boldsymbol{r}_0; \boldsymbol{R}) + V_{01}(\boldsymbol{r}_0, \boldsymbol{r}_1) + V_{02}(\boldsymbol{r}_0, \boldsymbol{r}_2), \qquad (6.47)$$

where V_0 is the projectile-nuclear potential:

$$V_0(\boldsymbol{r}_0;\boldsymbol{R}) = \frac{z_0}{\left|\boldsymbol{r}_0+\frac{\boldsymbol{R}}{2}\right|} + \frac{z_0}{\left|\boldsymbol{r}_0-\frac{\boldsymbol{R}}{2}\right|} \tag{6.48}$$

$$= z_0\sum_{\ell=0}^{\infty}(1+(-1)^\ell)\sqrt{\frac{4\pi}{2\ell+1}}v_\ell(r_0;R/2)Y_\ell^0(\hat{\boldsymbol{r}}_0), \tag{6.49}$$

and $V_{i,j}$ is the electron-electron potential:

$$V_{i,j}(\boldsymbol{r}_i,\boldsymbol{r}_j) = z_i z_j\sum_{\ell=0}^{\infty}\sum_{m=-\ell}^{\ell}\frac{4\pi}{2\ell+1}v_\ell(r_i,r_j)Y_\ell^{-m}(\hat{\boldsymbol{r}}_i)Y_\ell^m(\hat{\boldsymbol{r}}_j). \tag{6.50}$$

In Eqs. (6.49) and (6.50), v_ℓ is defined by

$$v_\ell(r,r') = \frac{[\min(r,r')]^\ell}{[\max(r,r')]^{\ell+1}}. \tag{6.51}$$

Due to symmetry, the direct matrix elements for V_{01} and V_{02} are identical, so the direct potential is simplified to

$$V_{\rm dir} = V_0 + 2V_{01}. \tag{6.52}$$

Using the representation of the target wave functions given in Eq. (6.12) and the definition of the spherical partial-wave functions given in Eq. (4.15) , the direct V-matrix elements are given by

$$\begin{aligned}\langle q'L'\Lambda_{L'}\,\Phi_{n'}|\hat{\rm V}_{\rm dir}|\Phi_n\,qL\Lambda_L\rangle &= \frac{2z_0}{\pi}\delta_{\Lambda'_{\rm tot},\Lambda_{\rm tot}}\delta_{\Pi'_{\rm tot},\Pi_{\rm tot}}\delta_{\mathcal{S}',\mathcal{S}}\delta_{s',s} \\ &\times\sum_{\alpha'\beta'}\sum_{\alpha\beta}C^{(n')}_{\alpha',\beta'}C^{(n)}_{\alpha,\beta}\langle\phi_{\beta'}|\phi_\beta\rangle\sum_{\ell m}(-1)^{\ell+m}C^{L0}_{L'0,\ell0}C^{L'\Lambda'}_{L\Lambda,\ell(-m)} \\ &\times\Big[\delta_{m,0}\langle\phi_{\alpha'}|\phi_\alpha\rangle(1+(-1)^\ell)\int_0^\infty u_{L'}(q'r_0)v_\ell(r_0,R/2)\,{\rm d}r_0 u_L(qr_0) \\ &\quad -2(-1)^\ell C^{\ell_\alpha m_\alpha}_{\ell_\alpha 0,\ell 0}\int_0^\infty\int_0^\infty u_{L'}(qr_0)\varphi_{\alpha'}(r_1)v_\ell(r_0,r_1)u_L(qr_0)\varphi_\alpha(r_1)\,{\rm d}r_0\,{\rm d}r_1\Big].\end{aligned} \tag{6.53}$$

The Kronecker-δ symbols in Eq. (6.53) mean that the direct V-matrix element is non-zero only when the scattering system orbital angular-momentum projection $\Lambda_{\rm tot}$, parity $\Pi_{\rm tot}$, and spin $\mathcal{S}$ is conserved, as well as the target spin s.

The exchange V-matrix element is somewhat more complicated, and is given

by

$$\langle q'L'\Lambda_{L'}\,\phi_{n'}|\hat{\mathsf{V}}_{\rm exch}|\phi_n\,qL\Lambda_L\rangle = \delta_{\Lambda'_{\rm tot},\Lambda_{\rm tot}}\delta_{\Pi'_{\rm tot},\Pi_{\rm tot}}\delta_{\mathcal{S}',\mathcal{S}} \tag{6.54}$$

$$\times \sum_{\alpha'\beta'}\sum_{\alpha\beta} C^{(n')}_{\alpha',\beta'}C^{(n)}_{\alpha,\beta}\left\{\sqrt{(2s'+1)(2s+1)}(-1)^{s'+s+1}\begin{Bmatrix} 1/2 & 1/2 & s' \\ 1/2 & \mathcal{S} & s\end{Bmatrix}\right.$$

$$\times \Big[(E-\epsilon_{q'}-\epsilon_q-1/R)\langle q'L'\Lambda'|\phi_\alpha\rangle\langle\phi_{\alpha'}|qL\Lambda\rangle\langle\phi_{\beta'}|\phi_\beta\rangle$$

$$-\langle q'L'\Lambda'|V_0|\phi_\alpha\rangle\langle\phi_{\alpha'}|qL\Lambda\rangle\langle\phi_{\beta'}|\phi_\beta\rangle - \langle q'L'\Lambda'|\phi_\alpha\rangle\langle\phi_{\alpha'}|V_1|qL\Lambda\rangle\langle\phi_{\beta'}|\phi_\beta\rangle$$

$$-\langle q'L'\Lambda|\phi_\alpha\rangle\langle\phi_{\alpha'}|qL\Lambda\rangle\langle\phi_{\beta'}|\hat{\mathsf{H}}_2|\phi_\beta\rangle - \langle q'L'\Lambda'\,\phi_{\alpha'}|V_{01}|\phi_\alpha\,qL\Lambda\rangle\langle\phi_{\beta'}|\phi_\beta\rangle$$

$$\left.-\langle q'L'\Lambda'\,\phi_{\beta'}|V_{02}|\phi_\alpha\,\phi_\beta\rangle\langle\phi_{\alpha'}|qL\Lambda\rangle - \langle\phi_{\alpha'}\,\phi_{\beta'}|V_{12}|qL\Lambda\,\phi_\beta\rangle\langle q'L'\Lambda'|\phi_\alpha\rangle\Big]\right\},$$

where $\hat{\mathsf{H}}_2$ is the one-electron Hamiltonian acting in coordinate $\boldsymbol{r}_2$. Note that Eqs. (6.53) and (6.54) have not included any terms arising from the use of a distorting potential or the resolution of non-uniqueness, as neither have been utilised in the present work.

6.4 H_2 scattering V-matrix elements (spheroidal)

In spheroidal coordinates, the projectile-nuclear potential is given by

$$V_0(\boldsymbol{\rho}_0) = \frac{z_0(2\rho_0+R)}{\left(\rho_0+\frac{R}{2}\right)^2-\left(\frac{R}{2}\eta_0\right)^2}, \tag{6.55}$$

and the electron-electron potential is expanded as

$$V_{01}(\boldsymbol{\rho}_0,\boldsymbol{\rho}_1) = 4\pi\sum_{L=0}^{\infty}\sum_{m_L=-L}^{L}\tilde{P}_L^{|m_L|}(\rho_<)\tilde{Q}_L^{|m_L|}(\rho_>)Y_L^{-m_L}(\eta_0,\phi_0)Y_L^{m_L}(\eta_1,\phi_1), \tag{6.56}$$

where

$$\rho_< = \min(\rho_0,\rho_1) \tag{6.57}$$

$$\rho_> = \max(\rho_0,\rho_1), \tag{6.58}$$

and $\tilde{P}$ and $\tilde{Q}$ are defined in terms of the Ferrers functions as detailed in Ref. [202]. The denominator of the projectile-nuclear potential cancels with the spheroidal volume integration weight, so the matrix element is given simply by

$$\langle q'\lambda'\Lambda_{\lambda'}\,\Phi_{n'}|V_0|\Phi_n\,q\lambda\Lambda_\lambda\rangle = \delta_{n'n}\delta_{\Lambda_{\lambda'}\Lambda_\lambda}\int_0^\infty \Xi_{\lambda'}^{\Lambda_\lambda}(\rho_0,c')V_{\lambda'\lambda}^{\Lambda_\lambda}(\rho_0,c',c)\Xi_\lambda^{\Lambda_\lambda}(\rho_0,c)\,\mathrm{d}\rho_0, \tag{6.59}$$

where

$$V_{\lambda'\lambda}^{\Lambda_\lambda}(\rho_0,c',c) = z_0(2\rho_0+R)\sum_\ell \langle\Upsilon_{\lambda'}^{\Lambda_\lambda}(c')|Y_\ell^{\Lambda_\lambda}\rangle\langle Y_\ell^{\Lambda_\lambda}|\Upsilon_\lambda^{\Lambda_\lambda}(c)\rangle. \tag{6.60}$$

The electron-electron matrix elements are given by

$$\begin{aligned}\langle q'\lambda'\Lambda_{\lambda'}\,\Phi_{n'}|V_{12}|\Phi_n\,q\lambda\Lambda_\lambda\rangle &= \delta_{\Pi'_{\mathrm{tot}},\Pi_{\mathrm{tot}}}\delta_{\Lambda'_{\mathrm{tot}},\Lambda_{\mathrm{tot}}}\delta_{\mathcal{S}',\mathcal{S}}\delta_{s',s}\sum_{\alpha'\beta'}\sum_{\alpha\beta}C_{\alpha',\beta'}^{(n')}C_{\alpha,\beta}^{(n)}\langle\phi_{\beta'}|\phi_\beta\rangle \\ &\times\sum_{Lm_L}(2L+1)\int_0^\infty \Xi_{\lambda'}^{\Lambda_\lambda}(\rho_0,c')J_{L,-m_L}^{(q',q)}(\rho_0)f_{Lm_L}^{(\alpha',\alpha)}(\rho_0)\Xi_\lambda^{\Lambda_\lambda}(\rho_0,c)\,\mathrm{d}\rho_0,\end{aligned} \tag{6.61}$$

where $J_{L,-m_L}^{(q',q)}(\rho_0)$ is a spheroidal angular quadratic, and $f_{Lm_L}^{(\alpha',\alpha)}(\rho_0)$ is a function obtained by integrating the summand of Eq. (6.56) along with the one-electron orbitals $\phi_{\alpha'}(\boldsymbol{\rho}_1)$ and $\phi_\alpha(\boldsymbol{\rho}_1)$ over $\boldsymbol{\rho}_1$. Both are defined in Ref. [202].

The spheroidal exchange matrix elements have the same form as Eq. (6.54), but with the individual terms within the square brackets evaluated differently following the definitions of V_0 and V_{12} in spheroidal coordinates. The reader is referred to Ref. [202] for further details.

6.5 Analytical Born completion

Analytical Born completion (ABC) is a method for accelerating the rate of convergence with respect to the size of the projectile partial-wave expansion. The ABC method is an application of Kummer's transformation, an established method for accelerating the convergence of an infinite series by replacing it with the sum of a highly convergent series and a series which can be evaluated in closed form [208]. In effect, the ABC method completes the partial-wave expansion up to infinity using the partial-wave Born ICS for all $L > L_{\max}$ (or $\lambda > \lambda_{\max}$ in the spheroidal

implementation), which relies on the validity of the Born approximation for high partial waves.

The Born approximation replaces the T-matrix element with the V-matrix element in the definition of the scattering amplitude. The "analytical" Born cross section $\sigma^{(\mathrm{AB})}_{n_f,n_i}$ is obtained by performing an expansion of the 3D direct V-matrix element in spherical harmonics:

$$\langle \boldsymbol{q}_f \Phi_{n_f} | \hat{\mathrm{V}}_{\mathrm{dir}} | \Phi_{n_i} \boldsymbol{q}_i \rangle = \sum_{\ell m} i^\ell \underset{\ell m}{V^{(\mathrm{AB})}_{n_f,n_i}}(Q) Y^{m*}_\ell(\hat{\boldsymbol{Q}}), \tag{6.62}$$

where $\boldsymbol{Q}$ is the momentum transfer vector, and $\underset{\ell m}{V^{(\mathrm{AB})}_{n_f,n_i}}(Q)$ are the Born matrix elements. Details on the calculation of the Born matrix elements in the spherical MCCC method can be found in Ref. [87], and details specific to the spheroidal implementation in Ref. [202]. The analytical Born integrated cross section (summed over final rotational levels) is then given by

$$\sigma^{(\mathrm{AB})}_{n_f,n_i} = 4\pi^3 \frac{q_f}{q_i} \iint_{\mathbb{R}^2} \sum_{\ell m} \underset{\ell m}{V^{(\mathrm{AB})}_{n_f,n_i}}(Q)\, \mathrm{d}\Omega, \tag{6.63}$$

where the scattering angle θ is related to the angle $\theta_{\boldsymbol{Q}}$ between $\boldsymbol{Q}$ and $\boldsymbol{q}_i$ by

$$\theta_{\boldsymbol{Q}} = \arccos\left(\left[q_i - q_f \cos\theta \right] / Q \right). \tag{6.64}$$

Since the evaluation of the Born matrix elements is fast there are no issues with convergence with respect to the spherical Harmonic expansion.

The Born approximation can also be applied to the partial-wave scattering amplitudes, giving the partial-wave Born cross section $\sigma^{(\mathrm{PWB})}_{n_f,n_i}$. The expression for this cross section is identical to Eq. (4.44), but with the scattering amplitude evaluated using the V-matrix elements in place of T-matrix elements. Since $\sigma^{(\mathrm{PWB})}_{n_f,n_i}$ uses the same projectile partial-wave expansion as the cross section $\sigma^{(\mathrm{CC})}_{n_f,n_i}$ obtained from the close-coupling calculations, it can be subtracted from $\sigma^{(\mathrm{AB})}_{n_f,n_i}$ to give the Born contribution from the higher partial waves up to infinity. The cross section including ABC is hence given by

$$\sigma_{n_f,n_i} = \sigma^{(\mathrm{CC})}_{n_f,n_i} + \sigma^{(\mathrm{AB})}_{n_f,n_i} - \sigma^{(\mathrm{PWB})}_{n_f,n_i}. \tag{6.65}$$

The convergence of this cross section must still be verified with respect to the number of partial waves included in the close-coupling calculation, but with ABC applied it is much faster than the convergence of the purely close-coupling cross section alone. Cross sections for dipole-forbidden transitions (including spin-exchange transitions) have much faster partial-wave convergence than for dipole-allowed transitions, and in these cases the ABC procedure is typically not necessary.

6.6 Calculation parameters

This section describes some of the more important input parameters to the MCCC calculations required to understand the models described in the following chapter.

6.6.1 Two-electron Laguerre basis

The Laguerre basis used to form the two-electron configurations is specified by the maximum orbital angular momentum $\ell_{\max}$, number of Laguerre functions N_ℓ ($0 \leq \ell \leq \ell_{\max}$), and the exponential falloffs. For simplicity, the number of Laguerre functions is generally chosen to be

$$N_\ell = N_0 - \ell, \tag{6.66}$$

where N_0 is the number of $\ell = 0$ functions. The exponential falloffs can also be chosen independently for each ℓ in the spherical implementation, and for each Λ in the spheroidal implementation. To simplify the calculations, the configurations are constructed with one electron allowed to occupy any orbital in the Laguerre basis, and the other restricted to a smaller selection of orbitals, which can be increased to test for convergence in the target-state energies.

6.6.2 Target states in scattering calculation

Once the targets states are generated for each target symmetry and arranged by energy, a certain number are chosen to be utilised in the scattering equations. Although in atomic CCC calculations and previous fixed-nuclei MCCC calculations

it is common to include all generated states in order to implement the solution to non-uniqueness issues in electron scattering, it has so far been found impractical to do this in the adiabatic-nuclei calculations which require a much larger basis to ensure accurate target states at larger internuclear separations. Hence, convergence will generally be tested within a fixed structure model by choosing progressively larger numbers of states in the close-coupling expansion.

6.6.3 Partial-wave expansion

The size of the projectile partial-wave expansion is determined by the parameter $L_{\max}$ (in the spherical implementation), or $\lambda_{\max}$ (in the spheroidal implementation). The projection of L (or λ) is allowed to range over all valid values. The calculations are performed separately for each value of the total scattering-system orbital angular-momentum projection $\Lambda_{\rm tot}$, parity $\Pi_{\rm tot}$, and spin $\mathcal{S}$, with $\Lambda_{\rm tot}$ ranging from 0 to $L_{\max}$ (or $\lambda_{\max}$), $\Pi_{\rm tot}$ equal to 1 and -1 (for homonuclear molecules), and both spin channels (when applicable).

6.7 Code profiling and performance improvements

At the onset of this PhD project, the fixed-nuclei spherical and spheroidal implementations of the MCCC method had been implemented for electrons and positrons scattering on H_2^+ and H_2. In order to perform the adiabatic-nuclei calculations which formed the first part of the present PhD project, it was necessary to reduce the computational expense of the fixed-nuclei calculations. One of the tasks undertaken by the candidate was to profile the code and optimise it for efficiency. The Fortran code was run through the MAP profiler from the ARM Forge debug and profile suite. The most computationally-expensive portion of the calculations was identified to be the evaluation of the exchange V-matrix elements. Rewrites to this subroutine and other parts of the code resulted in a considerable improvement in the calculation speed. Fig. 6.1 compares the runtime as a function of the number of channels included in the scattering calculations for the original and improved MCCC codes. There is an overall speed-up close to a

factor of 4. Improvements such as this can have a substantial impact on scientific output, since for molecular targets the calculations tend to push the limits of the available computational resources.

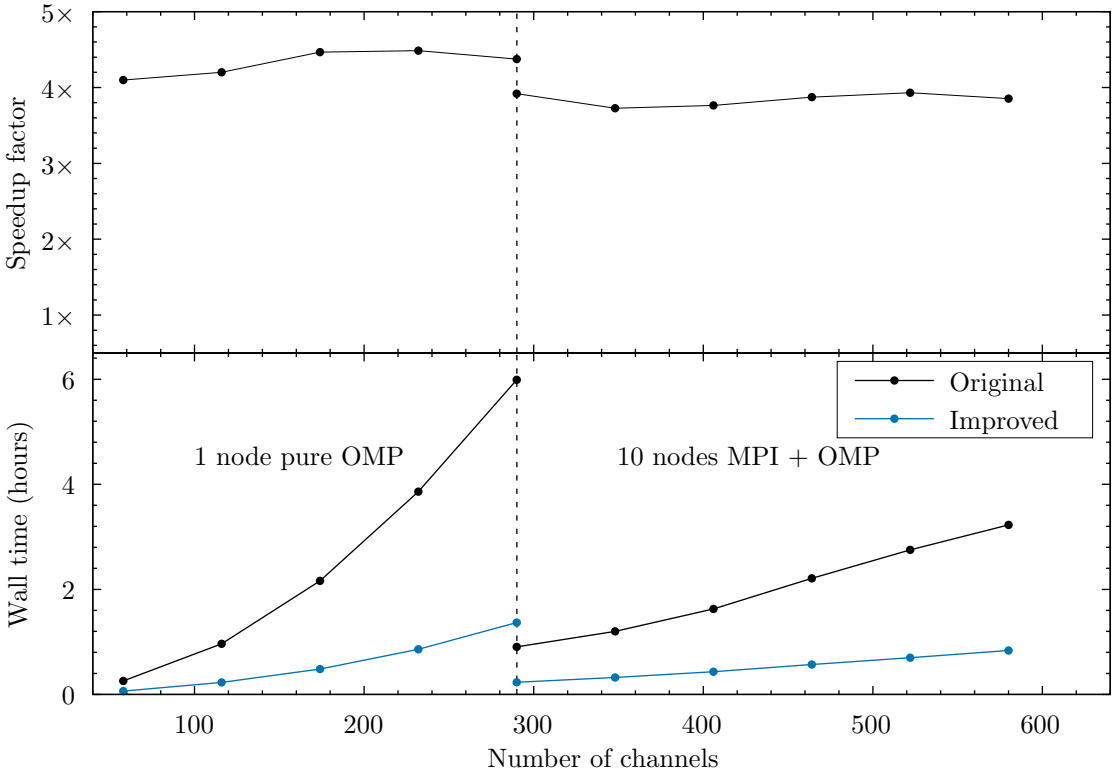

Figure 6.1: Performance improvement in the MCCC calculations after code profiling and rewrites to optimise efficiency. The wall time is presented as a function of number of channels included in the calculations for the original and improved codes. To the left of the dashed vertical line, the calculations were run on a single supercomputer node with only OpenMP (OMP) parallelisation. To the right of the line, calculations were run using 10 nodes with a hybrid MPI/OpenMP parallelism scheme. The top panel shows the speedup factor between the original and improved codes.

6.8 Chapter 6 summary

This chapter has provided an overview of the structure and scattering calculations in the fixed-nuclei MCCC method. The MCCC method has been implemented in both spherical-coordinate [201] and spheroidal-coordinate [202] implementations, and it is the latter which is utilised in the present work for a better representation

of the target structure at larger internuclear separations. The MCCC calculations depend on a number of input parameters, some of which have been described here and will be referred to in Chapter 7 when the various e^--H_2 scattering models are discussed.

Chapter 7

Adiabatic-nuclei calculations

This chapter presents details of the adiabatic-nuclei calculations which were performed for electrons scattering on H_2 and its isotopologues, including the electronic structure and scattering models utilised, generation of vibrational wave functions, and calculation of adiabatic-nuclei cross sections. Sec. 7.6 provides an in-depth discussion of the issues surrounding conflicting treatments of dissociative excitation in the literature. Limited results are shown in this chapter, only for the purpose of illustrating the discussions in the text, with a detailed presentation of results given in the following chapter.

Some sections contain text or figures adapted from published works by the candidate [4–7]. The publishers (Elsevier and the American Physical Society) provide the right to use an article or a portion of an article in a thesis or dissertation without requesting permission.

7.1 Vibrational wave functions

With rotational motion neglected, the vibrational wave functions $\nu_{nv}(R)$ are the solutions to

$$\hat{\mathsf{H}}_n^{\mathrm{vib}}|\nu_{nv}\rangle = \varepsilon_{nv}|\nu_{nv}\rangle, \tag{7.1}$$

where $\hat{\mathsf{H}}_n^{\mathrm{vib}}$ is the Born-Oppenheimer vibrational Hamiltonian for the electronic state n:

$$\hat{\mathsf{H}}_n^{\mathrm{vib}} = -\frac{1}{2\mu}\frac{\mathrm{d}^2}{\mathrm{d}R^2} + \epsilon_n(R), \tag{7.2}$$

and ε_{nv} is the vibronic state energy. In Eq. (7.2), $\epsilon_n(R)$ is the potential-energy curve of the electronic state n, and μ is the nuclear reduced mass. The values of μ for each isotopologue of H_2 are given in Table 7.1.

Table 7.1: Nuclear reduced masses μ of each of the isotopologues of H_2.

Molecule	μ (atomic units)
H_2	918.1
HD	1223.9
HT	1376.4
D_2	1835.2
DT	2200.9
T_2	2748.5

The vibrational wave functions are represented by an expansion in a basis of Laguerre-type functions:

$$\nu_{nv}(R) = \sum_{j=0}^{N-1} C_j^{(nv)} \varphi_j(R) \tag{7.3}$$

$$\varphi_j(R) = \frac{\sqrt{\alpha}}{j+1}(2\alpha R) e^{-\alpha R} L_j^1(2\alpha R), \tag{7.4}$$

where L_j^1 are the associated Laguerre polynomials of order 1, α is a tunable exponential falloff parameter, and N is the number of basis functions (not to be confused with the rotational quantum number N). In the present calculations, $\alpha = 10$ was found to be most appropriate for all electronic states. The CI coefficients $C_j^{(nv)}$ are obtained by solving the generalised eigenvalue problem

$$\sum_{j=0}^{N-1} \langle \varphi_i | \hat{\mathsf{H}}_n^{\mathrm{vib}} | \varphi_j \rangle C_j^{(ni)} = \varepsilon_{ni} \sum_{j=0}^{N-1} \langle \varphi_i | \varphi_j \rangle C_j^{(ni)}, \tag{7.5}$$

and the number N of basis functions can be increased until convergence is reached in the calculated energies and wave functions. The bound vibrational energies for most electronic states converge by $N = 50$–100, but for the purposes of ensuring a fine discretisation of the dissociative continua $N = 300$ was used for all states. With the present choice of basis in Eq. (7.4), the kinetic-energy and overlap

matrix elements have simple analytical forms:

$$\langle\varphi_i|\hat{\mathsf{K}}_{\mathrm{v}}|\varphi_j\rangle = -\frac{\alpha^2}{2\mu}\delta_{ij} + \frac{\alpha^2}{\mu}\langle\varphi_i|\varphi_j\rangle \tag{7.6}$$

$$\langle\varphi_i|\varphi_j\rangle = \begin{cases} 0, & j > i+1 \\ -\frac{1}{2}, & j = i \pm 1. \end{cases} \tag{7.7}$$

These expressions are derived in the more general case of including rotational motion in Appendix C.

The vibrational structure calculations are performed utilising accurate potential-energy curves from the literature [147–152]. The vibrational wave functions for each of the non-dissociative $n = 1$–3 electronic states of H_2 are presented in Fig. 7.1. There are four states with two minima: $EF\ ^1\Sigma_g^+$, $H\ ^1\Sigma_g^+$, $GK\ ^1\Sigma_g^+$, and $I\ ^1\Pi_g$. The vibrational wave functions for these states are initially split into two series, one per potential well, before joining above the barrier separating the wells. The $H\ ^1\Sigma_g^+$ state is the most diffuse of the $n = 1$–3 electronic states, supporting 72 bound vibrational levels. The outer-well levels are not clearly seen in Fig. 7.1, since they extend far beyond 10 a_0. The cross sections for excitation of these levels from the $X\ ^1\Sigma_g^+$ are insignificant due to the small overlap they have with any of the bound $X\ ^1\Sigma_g^+$ vibrational levels. The outer well of the $I\ ^1\Pi_g$ state is very shallow, supporting only 5 bound vibrational levels which are predominantly located beyond 6 a_0. For this state the barrier between the two wells is higher than the dissociative limit of the potential-energy curve, so there are no bound levels above the barrier. For the states with potential barriers above the dissociative limit ($I\ ^1\Pi_g$ as well as $h\ ^3\Sigma_g^+$ and $i\ ^3\Pi_g$), there is the possibility of forming quasi-bound states which can either lead to tunnelling through the barrier, or radiative decay to lower electronic states. In the present work, quasi-bound levels are not studied.

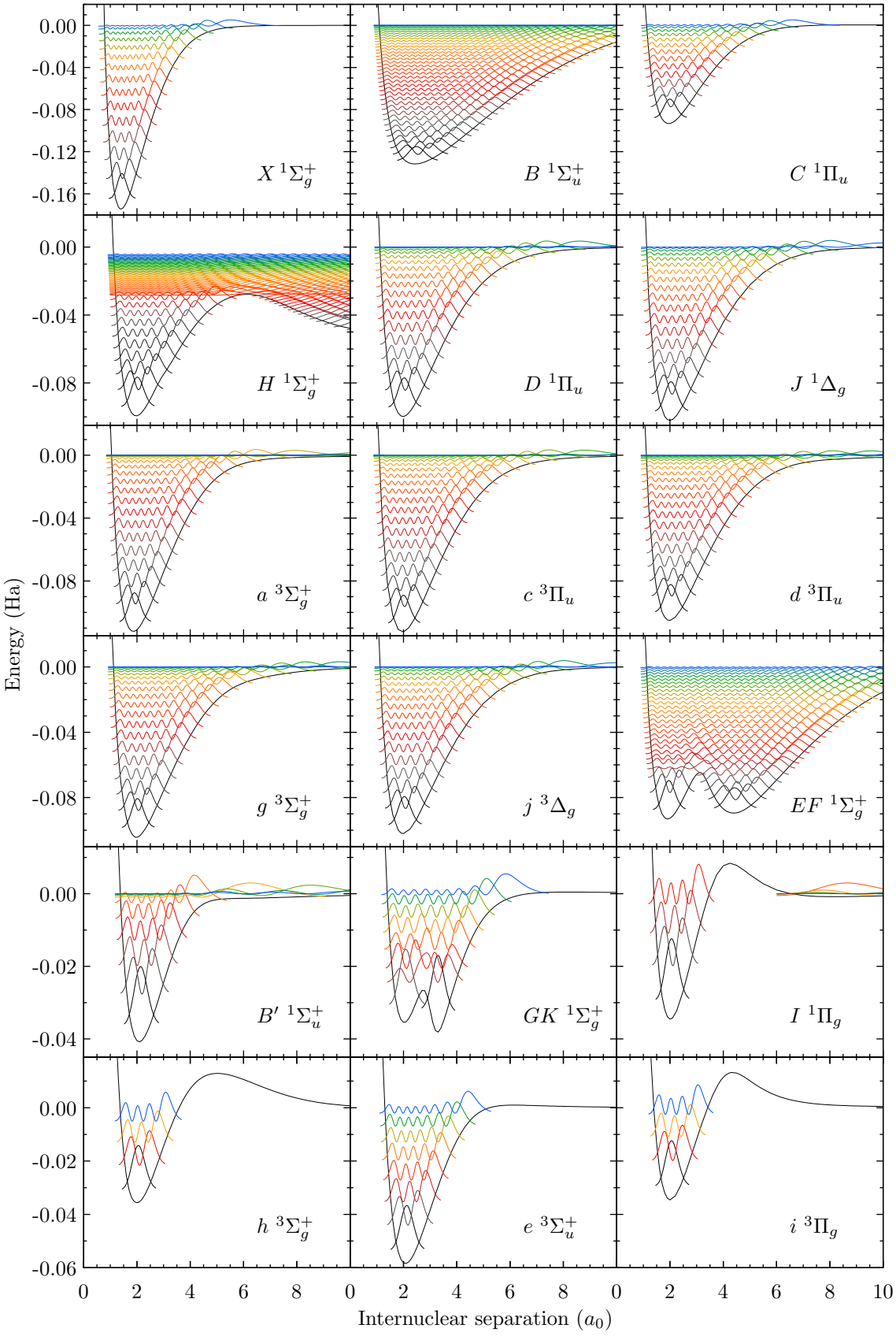

Figure 7.1: Vibrational wave functions for each of the non-dissociative $n = 1$–3 electronic states of H_2. The electronic-state potential-energy curves have been shifted so that the dissociative limit is at 0 Ha.

The vibrational-state energies for the $n = 1$–3 states of H_2 are compared with accurate calculations from Fantz and Wünderlich [209] in Table 7.2. To save space, a maximum of 15 levels is presented for each electronic state, but the level of agreement between the present energies and those of Ref. [209] for $v > 14$ is similar to what is seen for $v \leq 14$. There are a few differences between the present vibrational levels and those of Fantz and Wünderlich [209]; for the $I\ ^1\Pi_g$ state Fantz and Wünderlich [209] do not consider the outer-well levels, for some states (e.g. $B'\ ^1\Sigma_u^+$) there are one or more additional levels close to the dissociation threshold identified in this work, and for the $H\ ^1\Sigma_g^+$ state the inner/outer-well sequence differs slightly between these calculations and Ref. [209] (here $v = 8$ and 13 are located in the inner well while in Ref. [209] they are in the outer well). However, the present assignment of the $v = 8$ and 13 levels to the inner well is in agreement with the calculations of Ross *et al.* [210].

Table 7.2: Vibrational-state energies for H_2, compared with the calculations of Fantz and Wünderlich [209] ("Ref."). A maximum of 15 levels is shown for each electronic state. Asterisks denote vibrational wave functions located in the outer well of a double-minima curve.

	$X\ ^1\Sigma_g^+$		$B\ ^1\Sigma_u^+$		$C\ ^1\Pi_u$		$EF\ ^1\Sigma_g^+$	
v	E_v	Ref.	E_v	Ref.	E_v	Ref.	E_v	Ref.
0	-1.1645	-1.1644	-0.7536	-0.7536	-0.7128	-0.7128	-0.7125	-0.7125
1	-1.1456	-1.1454	-0.7476	-0.7475	-0.7023	-0.7023	-0.7117*	-0.7117*
2	-1.1277	-1.1275	-0.7417	-0.7417	-0.6924	-0.6924	-0.7063*	-0.7063*
3	-1.1108	-1.1107	-0.7360	-0.7360	-0.6831	-0.6831	-0.7019	-0.7019
4	-1.0950	-1.0948	-0.7305	-0.7305	-0.6744	-0.6744	-0.7011*	-0.7011*
5	-1.0802	-1.0801	-0.7251	-0.7251	-0.6663	-0.6662	-0.6962*	-0.6962*
6	-1.0665	-1.0664	-0.7198	-0.7198	-0.6587	-0.6587	-0.6927	-0.6927
7	-1.0538	-1.0537	-0.7147	-0.7147	-0.6518	-0.6518	-0.6913*	-0.6913*
8	-1.0423	-1.0421	-0.7098	-0.7098	-0.6455	-0.6455	-0.6874	-0.6874
9	-1.0318	-1.0317	-0.7050	-0.7050	-0.6398	-0.6398	-0.6843	-0.6843
10	-1.0226	-1.0225	-0.7003	-0.7003	-0.6349	-0.6349	-0.6815	-0.6815
11	-1.0147	-1.0146	-0.6958	-0.6958	-0.6307	-0.6307	-0.6781	-0.6781
12	-1.0082	-1.0082	-0.6914	-0.6914	-0.6274	-0.6274	-0.6748	-0.6749
13	-1.0035	-1.0035	-0.6872	-0.6872	-0.6252	-0.6252	-0.6717	-0.6717
14	-1.0006	-1.0007	-0.6830	-0.6830			-0.6685	-0.6685

Table 7.2: (continued)

	$B'\ ^1\Sigma_u^+$		$GK\ ^1\Sigma_g^+$		$I\ ^1\Pi_g$		$J\ ^1\Delta_g$	
v	E_v	Ref.	E_v	Ref.	E_v	Ref.	E_v	Ref.
0	-0.6612	-0.6612	-0.6578*	-0.6577*	-0.6544	-0.6544	-0.6523	-0.6523
1	-0.6526	-0.6526	-0.6557	-0.6557	-0.6448	-0.6448	-0.6422	-0.6422
2	-0.6448	-0.6448	-0.6494	-0.6494	-0.6359	-0.6359	-0.6326	-0.6327
3	-0.6378	-0.6378	-0.6456	-0.6456	-0.6278	-0.6278	-0.6238	-0.6237
4	-0.6318	-0.6318	-0.6404	-0.6404	-0.6256*	–	-0.6154	-0.6153
5	-0.6274	-0.6274	-0.6357	-0.6357	-0.6252*	–	-0.6075	-0.6075
6	-0.6260	-0.6260	-0.6314	-0.6314	-0.6251*	–	-0.6001	-0.6001
7	-0.6255	-0.6255	-0.6278	-0.6278	-0.6250*	–	-0.5933	-0.5933
8	-0.6252	-0.6252	-0.6253	-0.6253	-0.6250*	–	-0.5870	-0.5870
9	-0.6250	–					-0.5812	-0.5811
10							-0.5759	-0.5759
11							-0.5711	-0.5711
12							-0.5669	-0.5669
13							-0.5633	-0.5633
14							-0.5603	-0.5603

	$D'\ ^1\Pi_u$		$H\ ^1\Sigma_g^+$		$a\ ^3\Sigma_g^+$		$c\ ^3\Pi_u$	
v	E_v	Ref.	E_v	Ref.	E_v	Ref.	E_v	Ref.
0	-0.6500	-0.6500	-0.6496	-0.6496	-0.7311	-0.7311	-0.7320	-0.7319
1	-0.6399	-0.6398	-0.6395	-0.6395	-0.7196	-0.7196	-0.7213	-0.7213
2	-0.6303	-0.6303	-0.6304	-0.6303	-0.7087	-0.7087	-0.7112	-0.7112
3	-0.6213	-0.6213	-0.6224	-0.6224	-0.6985	-0.6984	-0.7016	-0.7016
4	-0.6129	-0.6129	-0.6150	-0.6150	-0.6888	-0.6887	-0.6926	-0.6926
5	-0.6050	-0.6050	-0.6081	-0.6081	-0.6796	-0.6796	-0.6841	-0.6840
6	-0.5977	-0.5977	-0.6046*	-0.6045*	-0.6711	-0.6711	-0.6761	-0.6760
7	-0.5909	-0.5909	-0.6029*	-0.6029*	-0.6632	-0.6631	-0.6686	-0.6685
8	-0.5847	-0.5847	-0.6017	-0.6017*	-0.6558	-0.6558	-0.6616	-0.6616
9	-0.5790	-0.5790	-0.6013*	-0.6013*	-0.6491	-0.6491	-0.6551	-0.6551
10	-0.5738	-0.5738	-0.5997*	-0.5998*	-0.6430	-0.6430	-0.6492	-0.6492
11	-0.5693	-0.5693	-0.5983*	-0.5984*	-0.6377	-0.6377	-0.6439	-0.6439
12	-0.5653	-0.5653	-0.5968*	-0.5969*	-0.6331	-0.6332	-0.6391	-0.6391
13	-0.5620	-0.5620	-0.5960	-0.5959*	-0.6296	-0.6296	-0.6350	-0.6350
14	-0.5593	-0.5593	-0.5955*	-0.5955*	-0.6272	-0.6272	-0.6315	-0.6316

Table 7.2: (continued)

	$d\ ^3\Pi_u$		$g\ ^3\Sigma_g^+$		$j\ ^3\Delta_g$		$g\ ^3\Sigma_g^+$	
v	E_v	Ref.	E_v	Ref.	E_v	Ref.	E_v	Ref.
0	-0.6554	-0.6553	-0.6542	-0.6541	-0.6523	-0.6523	-0.6785	-0.6785
1	-0.6451	-0.6451	-0.6435	-0.6435	-0.6422	-0.6422	-0.6691	-0.6690
2	-0.6355	-0.6355	-0.6336	-0.6336	-0.6327	-0.6327	-0.6603	-0.6603
3	-0.6264	-0.6264	-0.6243	-0.6243	-0.6238	-0.6238	-0.6521	-0.6521
4	-0.6178	-0.6178	-0.6156	-0.6155	-0.6154	-0.6154	-0.6446	-0.6446
5	-0.6098	-0.6098	-0.6074	-0.6073	-0.6075	-0.6075	-0.6378	-0.6378
6	-0.6023	-0.6023	-0.5997	-0.5997	-0.6002	-0.6002	-0.6319	-0.6319
7	-0.5953	-0.5953	-0.5927	-0.5926	-0.5934	-0.5934	-0.6270	-0.6270
8	-0.5888	-0.5888	-0.5861	-0.5861	-0.5870	-0.5870		
9	-0.5828	-0.5828	-0.5801	-0.5801	-0.5812	-0.5812		
10	-0.5773	-0.5774	-0.5747	-0.5747	-0.5759	-0.5759		
11	-0.5724	-0.5724	-0.5700	-0.5700	-0.5712	-0.5712		
12	-0.5681	-0.5681	-0.5660	-0.5660	-0.5670	-0.5670		
13	-0.5643	-0.5643	-0.5628	-0.5629	-0.5633	-0.5634		
14	-0.5612	-0.5612	-0.5604	-0.5604	-0.5603	-0.5604		

	$h\ ^3\Sigma_g^+$		$i\ ^3\Pi_g$	
v	E_v	Ref.	E_v	Ref.
0	-0.6558	-0.6558	-0.6545	-0.6544
1	-0.6466	-0.6466	-0.6448	-0.6448
2	-0.6380	-0.6379	-0.6358	-0.6358
3	-0.6300	-0.6300	-0.6275	-0.6275

The different reduced mass μ for each isotopologue leads to distinct vibrational spectra. In Fig. 7.2, the $v = 0$ vibrational wave function in the $X\,^1\Sigma_g^+$ state is compared for each isotopologue. As the reduced mass increases, the $v = 0$ level is shifted to lower energies and its wave function becomes narrower, with the peak shifted slightly towards smaller internuclear separations. The number of bound vibrational levels in each state is summarised in Table 7.3. For the isotopologues, the present inner/outer-well sequence of vibrational levels for the $H\ ^1\Sigma_g^+$ state also differs from the results of Fantz and Wünderlich [209].

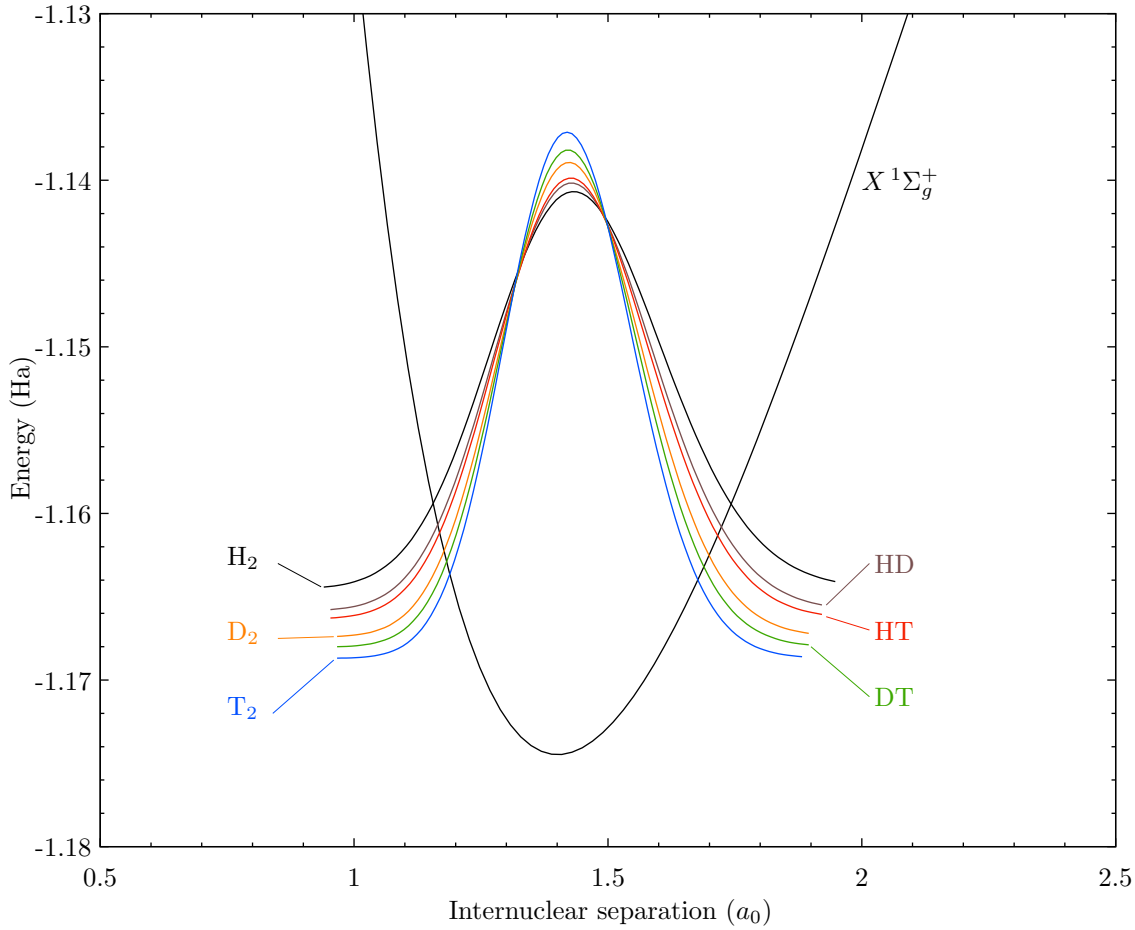

Figure 7.2: Vibrational wave functions for $v = 0$ in the ground state of H_2, D_2, T_2, HD, HT, and DT. Each wave is shifted vertically by its energy.

Table 7.3: The number of bound vibrational levels in each of the electronic states of the isotopologues of H_2 under consideration in the present work.

State	H_2	HD	HT	D_2	DT	T_2	State	H_2	HD	HT	D_2	DT	T_2
$X\ ^1\Sigma_g^+$	15	18	19	22	24	26	$a\ ^3\Sigma_g^+$	22	25	27	31	34	38
$B\ ^1\Sigma_u^+$	40	46	49	57	62	69	$c\ ^3\Pi_u$	22	26	27	31	34	38
$EF\ ^1\Sigma_g^+$	33	39	41	47	52	58	$e\ ^3\Sigma_u^+$	8	9	10	12	13	15
$C\ ^1\Pi_u$	14	16	17	19	21	24	$h\ ^3\Sigma_g^+$	4	5	5	6	7	7
$B'\ ^1\Sigma_u^+$	10	11	12	14	15	17	$d\ ^3\Pi_u$	21	24	26	30	33	37
$GK\ ^1\Sigma_g^+$	9	10	11	12	13	15	$g\ ^3\Sigma_g^+$	20	23	25	29	32	35
$I\ ^1\Pi_g$	9	10	11	12	14	16	$i\ ^3\Pi_g$	4	4	5	5	6	7
$J\ ^1\Delta_g$	18	22	23	27	29	33	$j\ ^3\Delta_g$	19	22	23	27	29	33
$H\ ^1\Sigma_g^+$	72	84	89	102	112	125							
$D\ ^1\Pi_u$	19	22	23	27	29	33							

Another notable effect of the changing vibrational spectrum for different values of μ is that the highest vibrational levels for some isotopologues can extend much further in R than for H_2. Fig. 7.3 compares the wave functions (squared) of the highest bound level in each isotopologue. The highest bound level in T_2

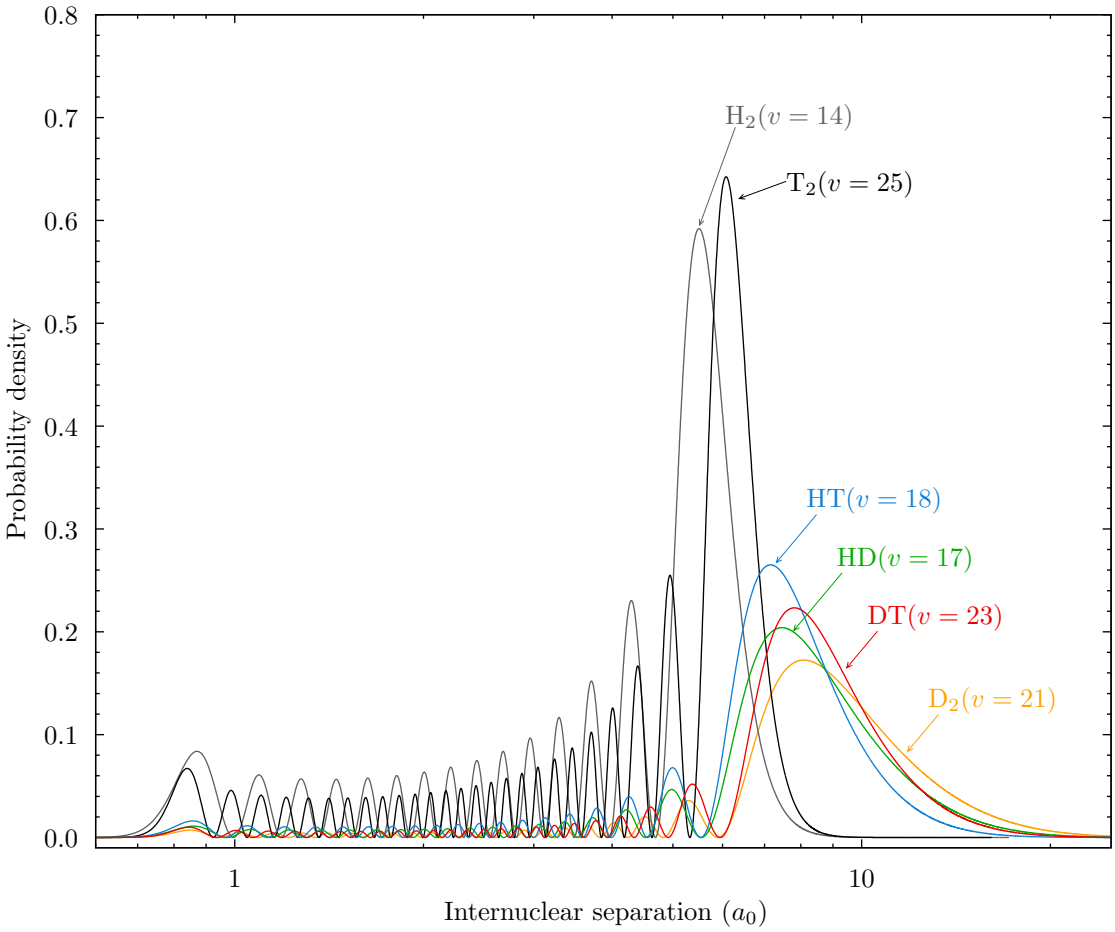

Figure 7.3: The highest bound vibrational wave function (squared) in the $X\,^1\Sigma_g^+$ state of H_2, HD, HT, D_2, DT, and T_2.

($v = 25$) does not extend much further in R than the $v = 14$ level of H_2, while for the remaining isotopologues the highest bound levels extend up to approximately 20 a_0.

7.2 Electronic structure

For the purposes of performing the adiabatic-nuclei calculations, which require an accurate target representation at larger internuclear separations than those considered in the fixed-nuclei approximation, the electronic structure and scattering

calculations have been performed using the spheroidal-coordinate implementation of the MCCC method [202]. The structure model outlined in this section resulted from detailed testing performed during this PhD project to yield sufficiently accurate energies and oscillator strengths for the $n = 1$–3 states. Since larger Laguerre basis sizes result in a denser discretisation of the ionisation continuum, it was necessary to find a balance between the competing requirements of accurate target structure and a continuum discretisation for which the calculations would be tractable.

The electronic structure calculations are optimised with the use of a hybrid-basis approach. The majority of the basis orbitals are the Laguerre functions given by Eq. (6.10), with $k \leq 12 - \ell$, $\ell \leq 3$, $|m| \leq \ell$, and $\alpha_m = 0.8$. However, the $1s$ orbital is replaced with an accurate H_2^+ $X\ ^2\Sigma_g$ state calculated from a preliminary one-electron diagonalisation in a large basis ($N_\ell = 60 - \ell, \ell \leq 8$). The $2s$, $2p$, $3d$, and $4f$ orbitals are then replaced with shorter-ranged Laguerre functions using the following R-dependent exponential falloff parameters

$$\alpha_{m=0}(R) = \begin{cases} 0.03R^2 - 0.32R + 2.8 & 0.0 \leq R \leq 4.0 \\ 2.0 & 4.0 < R \end{cases} \tag{7.8}$$

for $m = 0$ functions and

$$\alpha_{m>0}(R) = \begin{cases} 0.052R^2 - 0.52R + 3.8 & 0.0 \leq R \leq 5.0 \\ 2.6 & 5.0 < R \end{cases} \tag{7.9}$$

for $m > 0$ functions (taken from Savage [202]). These orbitals are important in representing the "inner" molecular electron, and optimising their exponential falloff parameters with R ensures the accuracy of the calculated target states over the range of internuclear separations of interest. The set of configurations utilised for the two-electron structure calculation contains all "frozen-core" configurations $(1s, n\ell)$, and correlation configurations $(n\ell, n'\ell')$ with both electrons allowed to occupy the $1s$, $2s$, $3s$, $2p$, $3p$, $3d$, $4d$, $5d$, and $4f$ orbitals.

In Table 7.4, the energies of the $n = 1$–3 H_2 electronic states at the internuclear separations $R = 1.4$ a_0 and 2.0 a_0 from the present spheroidal structure calculation are compared with accurate values from the literature [147–152]. The

value $R = 1.4\ a_0$ is the equilibrium separation of the $X\,^1\Sigma_g^+$, close to the mean separation $R_\mathrm{m} = 1.448\ a_0$ of the H_2 $v = 0$ vibrational wave function, and $R = 2.0\ a_0$ is close to the mean separations of the $v = 0$ levels in the $n = 2$ electronic states. The mean internuclear separations of the $v = 0$ levels are also given in Table 7.4 for the n = 1–2 states. In Fig. 7.4, the present potential-energy curves over $R \in [0, 9]\ a_0$ are compared with the accurate curves from the same literature sources. The calculated energies are in good agreement with accurate values for the internuclear separations spanned by the v = 0–10 vibrational levels of the H_2 $X\,^1\Sigma_g^+$ state ($R \leq 5.0\ a_0$), with errors generally less than 5% for the larger R values spanned by the 11–14 levels ($R \leq 8.0\ a_0$). The effect of the less accurate electronic structure at larger values of R for each isotopologue will be investigated later in Sec. 7.5.

7.3 *R*-dependent cross sections and convergence analysis

Adiabatic-nuclei calculations require the input of R-dependent electronic collision data for each transition. Performing convergence studies at the level of adiabatic-nuclei cross sections would be too resource-intensive due to the large number of calculations required for every scattering model. Instead, the approach taken in this work is to verify convergence within the fixed-nuclei approximation, and then apply the converged scattering model to all internuclear separations required. This section describes the convergence studies performed for electrons scattering on the ground and excited electronic states of H_2, as well as the generation of the sets of R-dependent cross sections utilised later in the adiabatic-nuclei calculations.

Table 7.4: Two-electron energies (in Ha) of electronic states of H_2 at the internuclear distances $R = 1.4$ and 2.0 a_0. Comparisons are made with accurate structure calculations from the literature [147–152]. The states are grouped according to their atomic-limit principal quantum number. For the $n = 1$–2 states the mean internuclear separation R_m of the $v = 0$ vibrational level is also presented.

State	R_m	Energy ($R = 1.4\ a_0$)		Energy ($R = 2.0\ a_0$)	
		Present	Ref.	Present	Ref.
		$n = 1$			
$X\ ^1\Sigma_g^+$	1.448	-0.7835	-0.7842[a]	-1.1360	-1.1381[a]
		$n = 2$			
$b\ ^3\Sigma_u^+$	–	-0.7835	-0.7842[b]	-0.8967	-0.8971[b]
$B\ ^1\Sigma_u^+$	2.518	-0.7047	-0.7058[c]	-0.7503	-0.7521[c]
$c\ ^3\Pi_u$	2.022	-0.7060	-0.7066[b]	-0.7369	-0.7375[b]
$a\ ^3\Sigma_g^+$	1.928	-0.7133	-0.7136[b]	-0.7357	-0.7361[b]
$C\ ^1\Pi_u$	2.016	-0.6881	-0.6887[d]	-0.7177	-0.7182[d]
$EF\ ^1\Sigma_g^+$	1.978	-0.6914	-0.6920[e]	-0.7172	-0.7177[e]
		$n = 3$			
$e\ ^3\Sigma_u^+$		-0.6435	-0.6435[b]	-0.6831	-0.6832[b]
$B'\ ^1\Sigma_u^+$		-0.6283	-0.6287[c]	-0.6650	-0.6655[c]
$d\ ^3\Pi_u$		-0.6286	-0.6288[b]	-0.6606	-0.6607[b]
$h\ ^3\Sigma_g^+$		-0.6301	-0.6303[b]	-0.6602	-0.6606[b]
$GK\ ^1\Sigma_g^+$		-0.6263	-0.6265[e]	-0.6599	-0.6604[e]
$g\ ^3\Sigma_g^+$		-0.6263	-0.6266[b]	-0.6595	-0.6598[b]
$i\ ^3\Pi_g$		-0.6260	-0.6262[b]	-0.6592	-0.6596[b]
$I\ ^1\Pi_g$		-0.6260	-0.6262[f]	-0.6591	-0.6595[f]
$j\ ^3\Delta_g$		-0.6252	-0.6253[b]	-0.6574	-0.6576[f]
$J\ ^1\Delta_g$		-0.6251	-0.6253[f]	-0.6573	-0.6576[f]
$D\ ^1\Pi_u$		-0.6234	-0.6236[d]	-0.6551	-0.6553[d]
$H\ ^1\Sigma_g^+$		-0.6241	-0.6244[e]	-0.6547	-0.6549[e]

[a]Kolos *et al.* [147]
[b]Staszewska and Wolniewicz [152]
[c]Staszewska and Wolniewicz [148]
[d]Wolniewicz and Staszewska [150]
[e]Wolniewicz and Dressler [149]
[f]Wolniewicz [151]

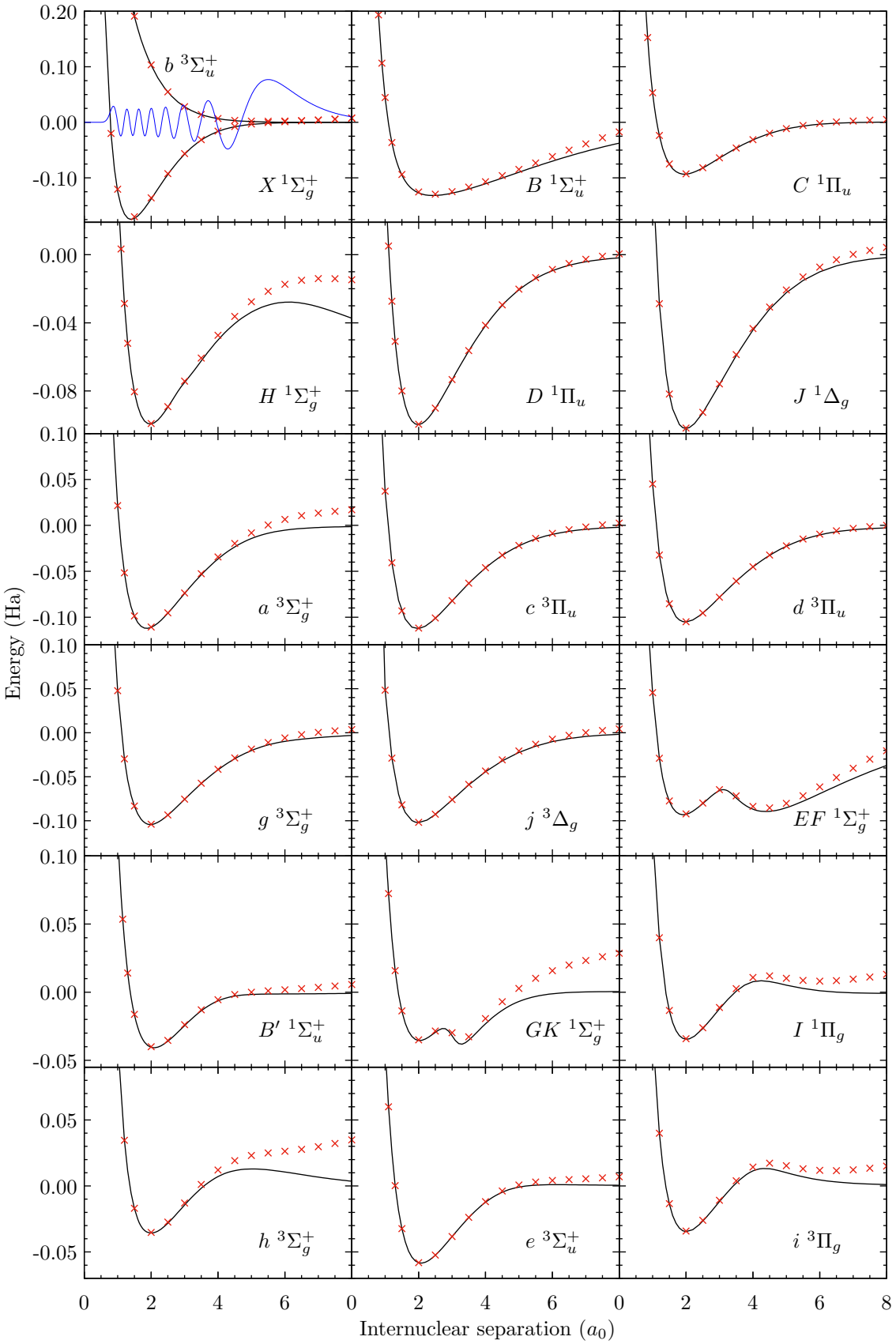

Figure 7.4: Potential-energy curves from the present spheroidal structure calculation (symbols), compared with accurate energies from the literature (lines). References for the literature values are as stated in Table 7.4. Also presented is the $v = 14$ vibrational wave functions in the $X\ ^1\Sigma_g^+$ state.

7.3.1 Scattering on the $X\,^1\Sigma_g^+$ state

For scattering on the $X\,^1\Sigma_g^+$ state, detailed fixed-nuclei convergence studies have previously been performed with the spherical-coordinate MCCC method by Zammit *et al.* [93]. The largest model, which guaranteed convergence in elastic scattering, excitation, and ionisation cross sections, included 491 target states in the close-coupling expansion, and utilised a projectile partial-wave expansion with $L_{\max} = 8$. The limitations of the previous fixed-nuclei calculations are that they are not accurate at near-threshold energies, and are not resolved in the vibrational levels of the target.

One of the aims of this PhD project was to perform adiabatic-nuclei calculations for scattering on the ground electronic states which are similar in accuracy to the previous fixed-nuclei results [93] (in terms of convergence), but accurate to lower energies and with the inclusion of vibrational resolution and isotopic effects. The spheroidal-coordinate structure model detailed in Sec. 7.2 was utilised to provide sufficient accuracy at larger internuclear separations. However, the number of electronic target states generated with this model was in excess of 1000, and it was simply unfeasible to include them all in the scattering calculations. Therefore, it was necessary to identify a smaller subset of target states to include which would still yield sufficient convergence in the transitions of interest, while allowing for tractable calculations. An unfortunate result of this necessity is that the issue of non-uniqueness in electron scattering cannot be resolved in the present calculations, as the solution normally applied in CCC methods requires that all target states be included in the close-coupling calculations [190]. Although on-shell T-matrix elements and cross sections are formally unique, the issue of non-uniqueness can result in numerical instabilities. In the present case these instabilities must be fixed manually.

For the purposes of this project, it was necessary to achieve convergence in the low-lying excitations only, with elastic scattering and ionisation deferred for later work. Two scattering models were adopted for the spheroidal-coordinate calculations using the structure model described in the previous section. The MCC(27) model includes each of the $n = 1$–3 states listed in Table 7.4 (a total of 27 states with degeneracies counted), and the MCCC(210) model includes all

bound states generated in the structure calculation and additional continuum pseudostates up to an excitation energy of 35 eV (from the ground state at $R = 1.448\ a_0$). Both models used a projectile partial-wave expansion with $L_{\max} = 6$ for incident energies below 20 eV, and $L_{\max} = 10$ elsewhere[1]. The number of states of each target symmetry included in both models is summarised in Table 7.5. The number of bound and continuum pseudostates is also given for $R = 1.448\ a_0$ (these numbers vary slightly with R).

Table 7.5: Total number of target states in the MCC(27) and MCCC(210) models for each target symmetry (Λ, π, s). The number of bound states and continuum pseudostates are also shown for $R = 1.448\ a_0$.

Symmetry	MCC(27)	MCCC(210)	MCCC(491)
$^1\Sigma_g$	4	17	35
$^1\Sigma_u$	2	15	31
$^3\Sigma_g$	3	15	32
$^3\Sigma_u$	2	15	31
$^1\Pi_g$	2	16	16
$^1\Pi_u$	4	28	31
$^3\Pi_g$	2	16	16
$^3\Pi_u$	4	30	31
$^1\Delta_g$	2	16	16
$^1\Delta_u$	0	14	14
$^3\Delta_g$	2	14	15
$^3\Delta_u$	0	14	14
$^1\Phi_g$	0	0	0
$^1\Phi_u$	0	0	14
$^3\Phi_g$	0	0	0
$^3\Phi_u$	0	0	14
bound	27	56	92
continuum	0	154	399

[1]Note that the calculations are performed in spheroidal coordinates with $\lambda_{\max} = L_{\max}$ before the T-matrix elements are converted to spherical coordinates via Eq. (6.46).

In Table 7.6, the parallel, perpendicular, and total static dipole polarisabilities of the $X\,^1\Sigma_g^+$ state in the MCC(27), MCCC(210), and MCCC(491) models is compared with the accurate calculations of Kołos and Wolniewicz [211]. As expected, the MCC(27) model does not have the correct polarisability, as it lacks an account of coupling to ionisation channels. The MCCC(210) polarisability is in good agreement with Kołos and Wolniewicz [211] – slightly better than the MCCC(491) model due to the more accurate structure model.

Table 7.6: Static dipole polarisability of the $X\,^1\Sigma_g^+$ state at $R = 1.4\ a_0$ in the MCC(27), MCCC(210), and MCCC(491) models described in the text. Comparison is made with the calculations of Kołos and Wolniewicz [211].

	$\alpha_\parallel$	$\alpha_\perp$	α
MCC(27)	4.68	2.71	3.37
MCCC(210)	6.42	4.57	5.18
MCCC(491)	6.43	4.64	5.23
Ref. [211]	6.38	4.58	5.18

In Fig. 7.5, the fixed-nuclei MCC(27) and MCCC(210) cross sections are compared with those obtained by Zammit *et al.* [93] using the MCCC(491) model. The MCCC(210) model adequately reproduced the MCCC(491) calculations for almost all transitions. The most notable exception is the $EF\ ^1\Sigma_g^+$ excitation, where the MCCC(210) results are systematically higher than MCCC(491) by around 20%. However, by comparing the calculated optical oscillator strengths in the spherical and spheroidal structure models with accurate calculations, it can be argued that any differences between the two sets of excitation cross sections are predominately due to the more accurate target structure in the MCCC(210) model. A detailed comparison of the spherical and spheroidal structure accuracies is given in Ref. [10]. The MCCC(210) ionisation cross section is in good agreement with MCCC(491) below 100 eV. However, above 100 eV the MCCC(210) model is not converged due to the smaller number of continuum pseudostates. The MCC(27) results for excitation all show the same behaviour of overestimating the

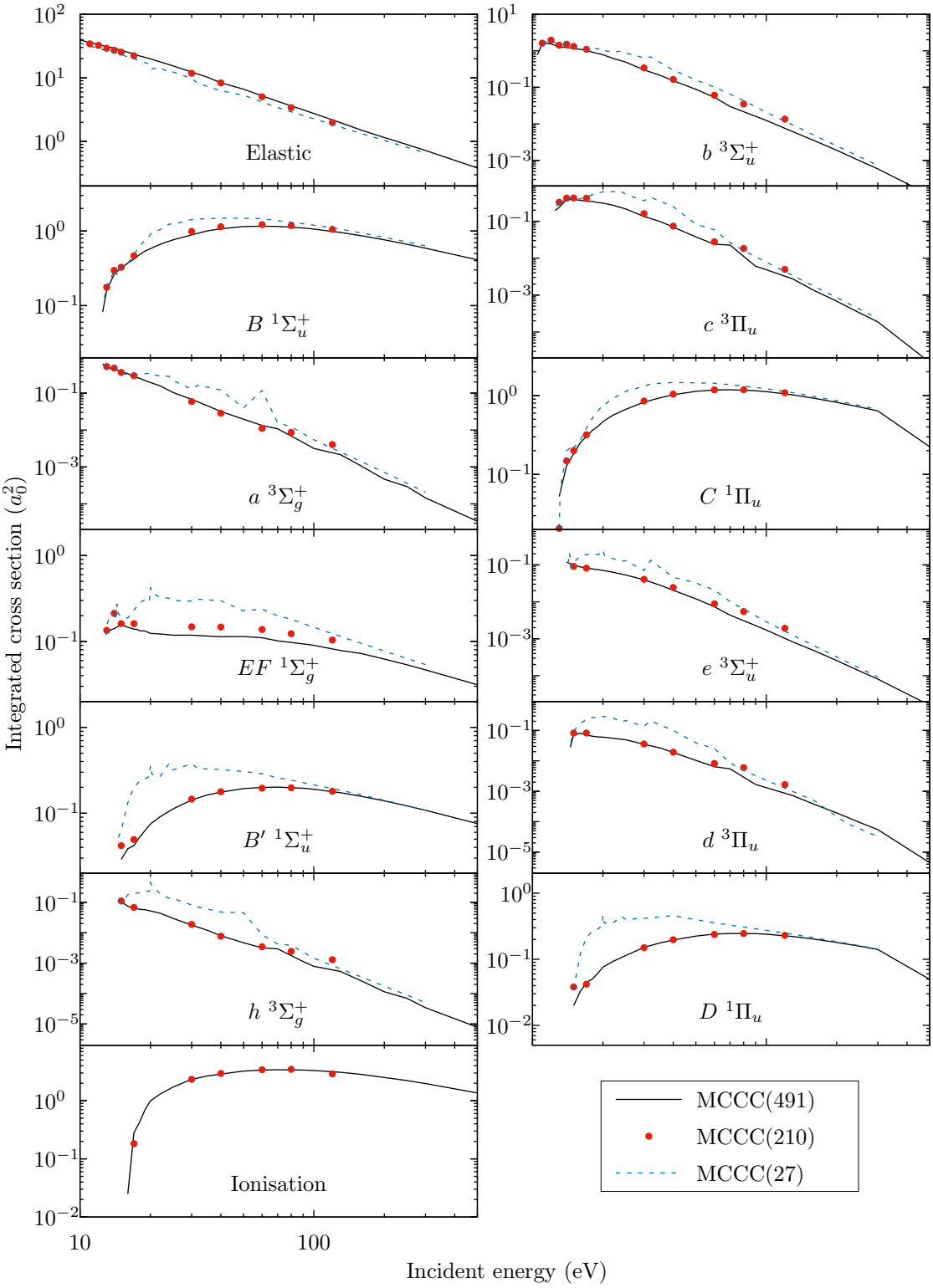

Figure 7.5: Comparison of the present 27- and 210-state spheroidal calculations [MCC(27), MCCC(210)] with the previously published spherical 491-state results [MCCC(491)] of Zammit *et al.* [93] for elastic scattering and ionisation cross sections, and cross sections for excitation of a selection of $n = 2$–3 states. All calculations are performed in the fixed-nuclei approximation with $R = 1.448\ a_0$.

cross section at low to intermediate energies, but converging to the MCCC(210) results at higher energies where interchannel coupling is less important.

Calculations using the MCCC(210) model have been performed with 20 R points between 0.8 and 8.0 a_0 for 10 incident energies between 10 and 40 eV. At 60, 80, and 120 eV fewer R points have been used (8 between 0.8 and 8.0 a_0) as there is less variation in the R-dependent cross sections at higher energies. The computationally-cheaper MCC(27) model has been run on finer energy and R grids: 25 energies between 1 and 40 eV, and an additional 25 energies up to 500 eV, each with 25 R points between 0.8 and 8.0 a_0. Since the MCC(27) model is sufficiently converged above 120 eV, these results are used to extend the MCCC(210) cross sections up to 500 eV. Energies down to 1 eV are required for the $X\ ^1\Sigma_g^+ \rightarrow b\ ^3\Sigma_u^+$ transition, which at these energies is also converged in the MCC(27) model. In order to increase the density of energy and R points in the MCCC(210) calculations between 10 and 120 eV, a procedure was adopted in which cross sections from the MCC(27) model are scaled as a function of energy and R to fit the MCCC(210) results. The reliability of this approach was demonstrated in Ref. [16].

When evaluating adiabatic-nuclei cross sections summed over final vibrational levels, any numerical instabilities resulting from non-uniqueness issues or pseudoresonances in the underlying fixed-nuclei cross sections largely disappear [10], however specific vibrational transitions can be much more sensitive to variations in the R-dependent collision data. In order to obtain reliable adiabatic-nuclei cross sections, it was necessary to ensure that the fixed-nuclei cross sections at every value of R are a smooth function of energy. To produce a set of smooth R-dependent cross sections, analytic functions were fitted to the cross sections for each value of R, before recompiling them as a set of R-dependent cross sections at each incident energy.

7.3.2 Scattering on the $n = 2$ states

Scattering on excited electronic states has not been previously studied with the MCCC method. Hence, it is necessary to perform more detailed convergence analysis in the present work. Convergence studies for scattering on the $n = 2$

states were carried out at $R = 2.0\ a_0$, which is close to the $v = 0$ mean internuclear separation of these states (between 1.928 and 2.518 a_0). Calculations have been performed using a projectile partial-wave expansion with maximum spheroidal pseudo-angular-momentum $L_{\max} = 10$ for the following models: MCC(27), MCC(56), MCCC(96), MCCC(158), and MCCC(210). The number of states per target symmetry in each model is summarised in Table 7.7. The MCC(56) model includes all bound electronic states (at $R = 2.0\ a_0$), and the larger models include all bound states with increasing numbers of continuum pseudostates, to test the effect of coupling to ionisation channels. Calculations have also been performed using the first Born approximation for comparison with the close-coupling results.

Table 7.7: Total number of target states in the MCC(27), MCC(56), MCCC(96), MCCC(158), and MCCC(210) models for each target symmetry (Λ, π, s). The number of bound states and continuum pseudostates are also shown for $R = 2.0\ a_0$.

Symmetry	MCC(27)	MCC(56)	MCCC(96)	MCCC(158)	MCCC(210)
$^1\Sigma_g$	4	6	8	13	35
$^1\Sigma_u$	2	4	7	11	31
$^3\Sigma_g$	3	5	8	12	32
$^3\Sigma_u$	2	5	7	12	31
$^1\Pi_g$	2	2	3	6	16
$^1\Pi_u$	4	4	6	10	31
$^3\Pi_g$	2	2	3	6	16
$^3\Pi_u$	4	4	7	11	31
$^1\Delta_g$	2	2	4	6	16
$^1\Delta_u$	0	1	3	5	14
$^3\Delta_g$	2	2	4	6	15
$^3\Delta_u$	0	1	3	5	14
bound	27	56	56	56	56
continuum	0	0	40	102	154

Table 7.8 presents the static dipole polarisability of the ground electronic state and first five non-dissociative excited states, averaged over the $v = 0$ vibrational wave function in each state, for each of the scattering models described above. The contributions to the MCCC(210) polarisability from the bound and continuum spectra are given in Table 7.9. These quantities can be helpful in making qualitative predictions of the importance of coupling to ionisation channels and dependence of cross sections on the initial state. For example, the polarisabilities of the excited states converge faster than for the ground state, and the contributions from the continuum are much smaller. Therefore, we should

Table 7.8: Static dipole polarisabilities for the $X\ ^1\Sigma_g^+$, $B\ ^1\Sigma_u^+$, $c\ ^3\Pi_u$, $a\ ^3\Sigma_g^+$, $C\ ^1\Pi_u$, and $EF\ ^1\Sigma_g^+$ states, averaged over the $v = 0$ wave functions. Comparisons are made between each of the scattering models described in the text.

Model	$X\ ^1\Sigma_g^+$	$B\ ^1\Sigma_u^+$	$c\ ^3\Pi_u$	$a\ ^3\Sigma_g^+$	$C\ ^1\Pi_u$	$EF\ ^1\Sigma_g^+$
MCCC(210)	5.42	131	302	2793	1327	2137
MCCC(158)	5.11	130	302	2793	1327	2137
MCCC(96)	4.41	118	301	2793	1327	2136
MCC(56)	3.89	113	300	2792	1326	2136
MCC(27)	3.59	105	299	2791	1324	2133

Table 7.9: Contributions from the bound and continuum spectra to the MCCC(210) static dipole polarisabilities in Table 7.8.

Source	$X\ ^1\Sigma_g^+$	$B\ ^1\Sigma_u^+$	$c\ ^3\Pi_u$	$a\ ^3\Sigma_g^+$	$C\ ^1\Pi_u$	$EF\ ^1\Sigma_g^+$
Bound	71%	86%	97%	97%	99%	98%
Cont.	29%	14%	3%	3%	1%	2%

expect to see faster convergence in the cross sections for scattering on excited states, and a smaller effect of coupling to ionisation channels. The much larger polarisabilities for the excited states indicate that the total cross sections should be substantially larger compared to scattering on the ground state.

Fig. 7.6 presents convergence studies for a selection of transitions, chosen to represent the cases of slowest convergence. Even for the slowest-converging transitions, the rate of convergence is much faster than it is for scattering on the ground electronic state [93]. For many transitions, coupling to ionisation channels has negligible effect, while for scattering on the ground state it was found to be very important at energies above the ionisation threshold [93]. In all cases, the excitation cross sections presented in Fig. 7.6 are well converged using the MCCC(210) model, and we have confirmed that the situation is the same for all transitions presented in this work. For elastic scattering and ionisation the MCCC(210) model is also sufficient, although the slightly jagged behaviour at the peak of the ionisation cross sections suggests that a slightly larger model is required for convergence. Since this is only a minor issue over a small energy region the final results can simple be smoothed at the peak.

The principle concern regarding convergence is that transitions with smaller excitation energies typically require larger projectile partial-wave expansions. For the MCCC(210) model, fixed-nuclei calculations have been performed at $R = 2.0\ a_0$ with $L_{\max} = 6$, 10, 15, 20, and 25 in order to conduct partial-wave convergence studies. A selection of convergence studies are presented in Fig. 7.7, again chosen to represent the cases with slowest convergence. The results are presented both with and without the use of the analytic Born completion method (ABC, described in Chapter 6) to demonstrate the improved rate of convergence when it is used. As expected, the partial-wave convergence for scattering on these excited states is much slower than it was for scattering on the ground state [93], with $L_{\max} = 20$ required to reach convergence in a number of transitions. Even with this large partial-wave expansion the ABC method still plays an important role. It has been confirmed that the MCCC(210) model with $L_{\max} = 20$ and the ABC method yields converged cross sections for all transitions considered in this work. For the spin-exchange transitions and many dipole-forbidden transitions,

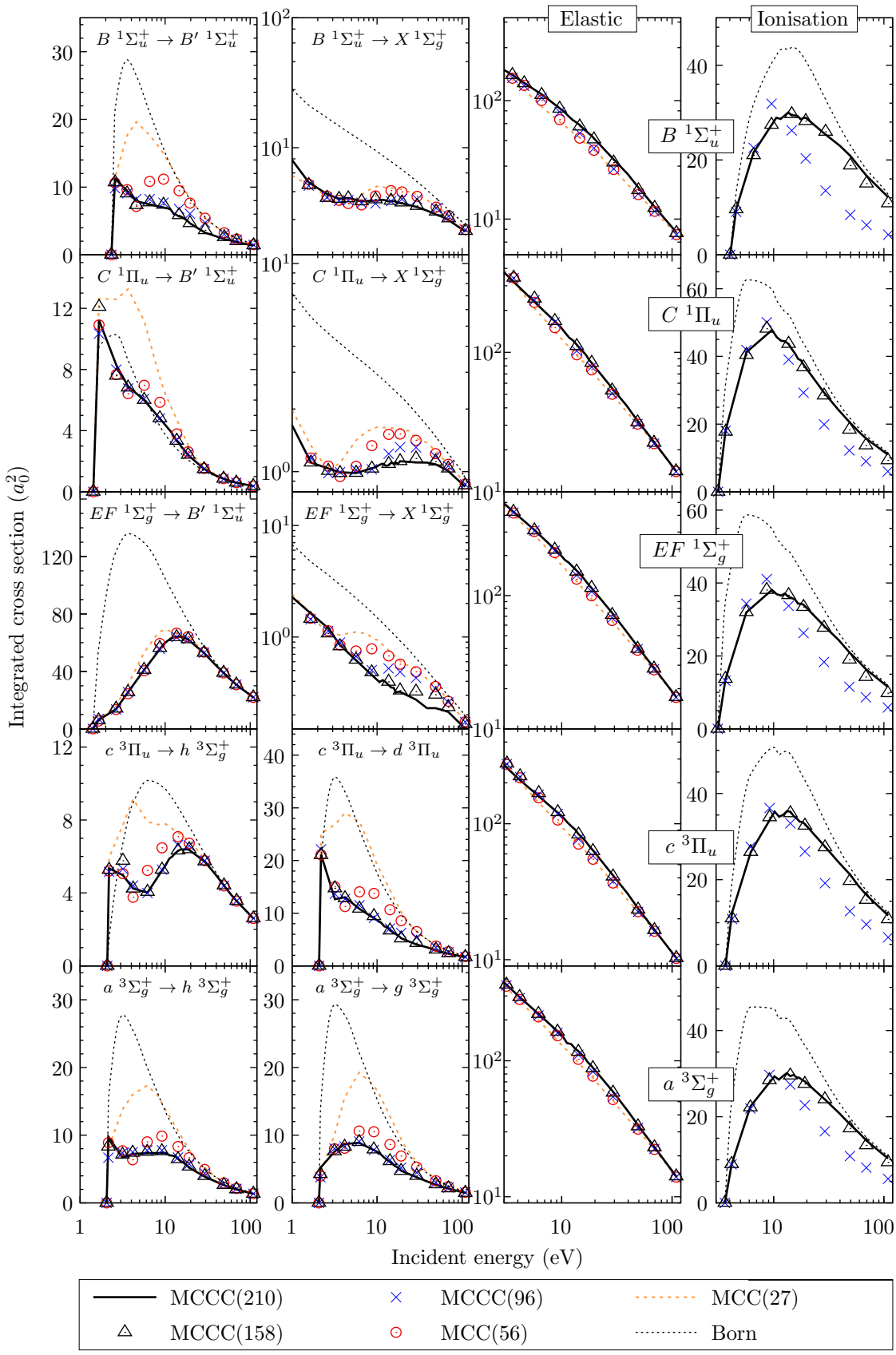

Figure 7.6: Fixed-nuclei ($R = 2.0\ a_0$) convergence studies for a selection of transitions from excited states of H_2. Convergence is tested with respect to the number of target states included in the close-coupling expansion.

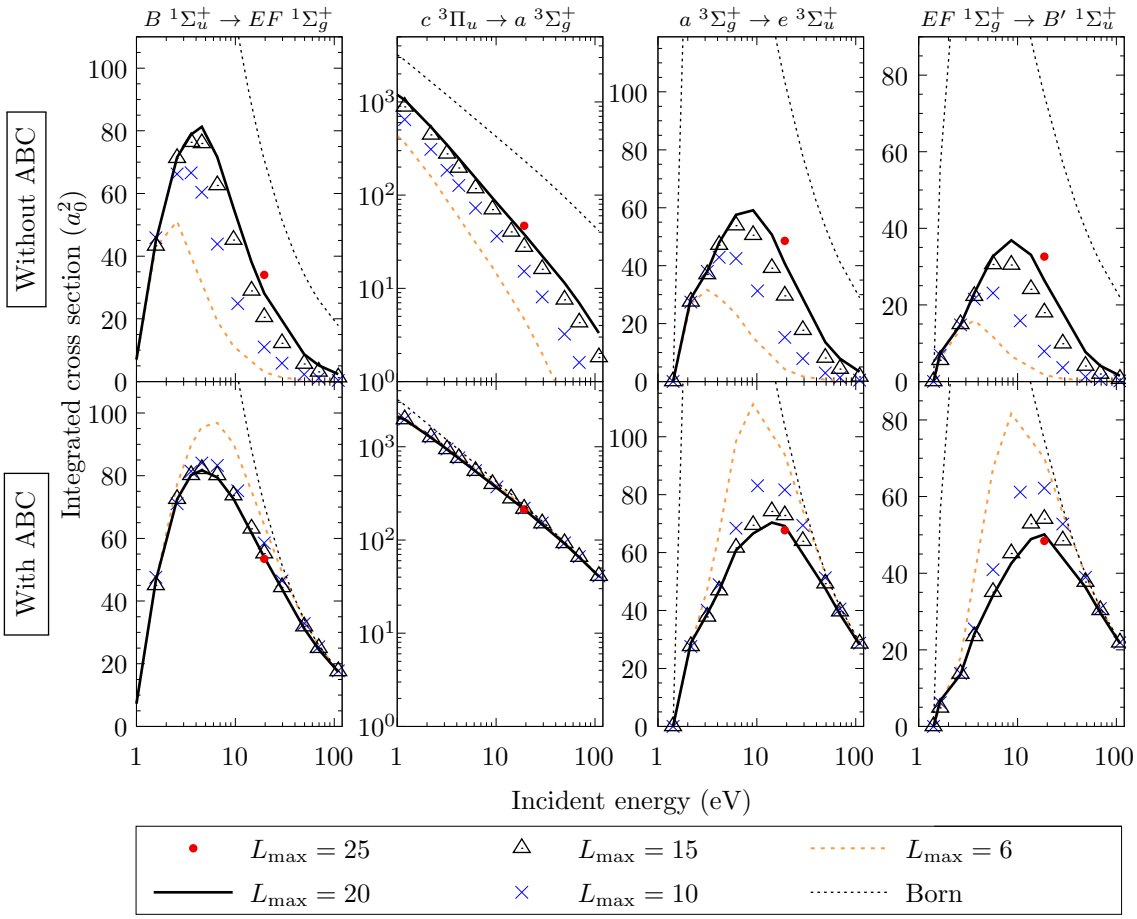

Figure 7.7: Partial-wave convergence studies, performed in the fixed-nuclei approximation with $R = 2.0\ a_0$, for a selection of transitions from excited states of H_2. On the left, MCCC(210) cross sections are shown without the use of the analytic Born completion (ABC) method, and on the right are the same results with the ABC method utilised.

a partial-wave expansion with $L_{\max} = 6$ is sufficient, but for the dipole-allowed transitions the partial-wave convergence is very slow, and it is computationally unfeasible to obtain accurate cross sections without the ABC method. The behaviour of the $c\ ^3\Pi_u \rightarrow a\ ^3\Sigma_g^+$ transition is particularly interesting. Due to the small energy difference between these states the partial-wave convergence is slow, but the Born approximation becomes valid at relatively low incident energies. As a result, without the ABC method even the $L_{\max} = 20$ cross section is up to an order of magnitude smaller than the converged cross section.

For the purposes of performing adiabatic-nuclei calculations for scattering on the $v = 0$ level of the $n = 2$ electronic states, fixed-nuclei calculations have been performed at 10 evenly spaced points between $R = 1.25$ and $3.5\ a_0$, which covers

the $v = 0$ vibrational wave function of each state, and is sufficient to accurately interpolate the cross sections over R. The MCC(27) $L_{\max} = 10$ model is used up to 1 eV, and then the MCCC(210) $L_{\max} = 20$ is used up to 200 eV. Beyond 200 eV the Born approximation is sufficient, and this has been used to extend the cross sections for spin-allowed transitions up to 1000 eV.

7.4 Adiabatic-nuclei calculations

The fixed-nuclei calculations performed with the MCCC(210) model suffer from some numerical instabilities, particularly for transitions with smaller cross sections. The most likely reason for this is the fact that it was not feasible to resolve non-uniqueness in these calculations. As discussed in Sec. 7.3.1, it was possible to reliably smooth the fixed-nuclei cross sections as a function of energy, however it would not be practical to attempt a similar fix to the partial-wave T-matrix elements. Therefore, the adiabatic-nuclei calculations are performed using the "square-root" approximation discussed in Sec. 4.10, which only require input of the R-dependent cross sections.

To confirm that the square-root approximation is reasonably accurate, test calculations have been performed to confirm that it reproduces the true adiabatic-nuclei cross section in those cases where the R-dependent T-matrix elements are stable enough to reliably interpolate. Before this can be done, there is an issue which must be resolved concerning the sign of the electronic T-matrix elements. When the fixed-nuclei structure calculation is performed, the overall sign of the electronic states is arbitrary. This can be most clearly seen by noting that the sign of the CI coefficient for a specific electronic configuration can change at random as the internuclear separation is varied. Although the calculation of fixed-nuclei cross sections is not affected by the sign of the T-matrix elements, spurious sign changes in the R-dependent T-matrix elements make it impossible to integrate them over R. The fix to this problem is illustrated in Fig. 7.8, where the CI coefficients for a few of the dominant configurations in the $EF\ ^1\Sigma_g^+$, $H\ ^1\Sigma_g^+$, $I\ ^1\Pi_g$, and $B\ ^1\Sigma_u^+$ states are presented as a function of R. The panels on the left-hand side display the CI coefficients without correction, showing multiple

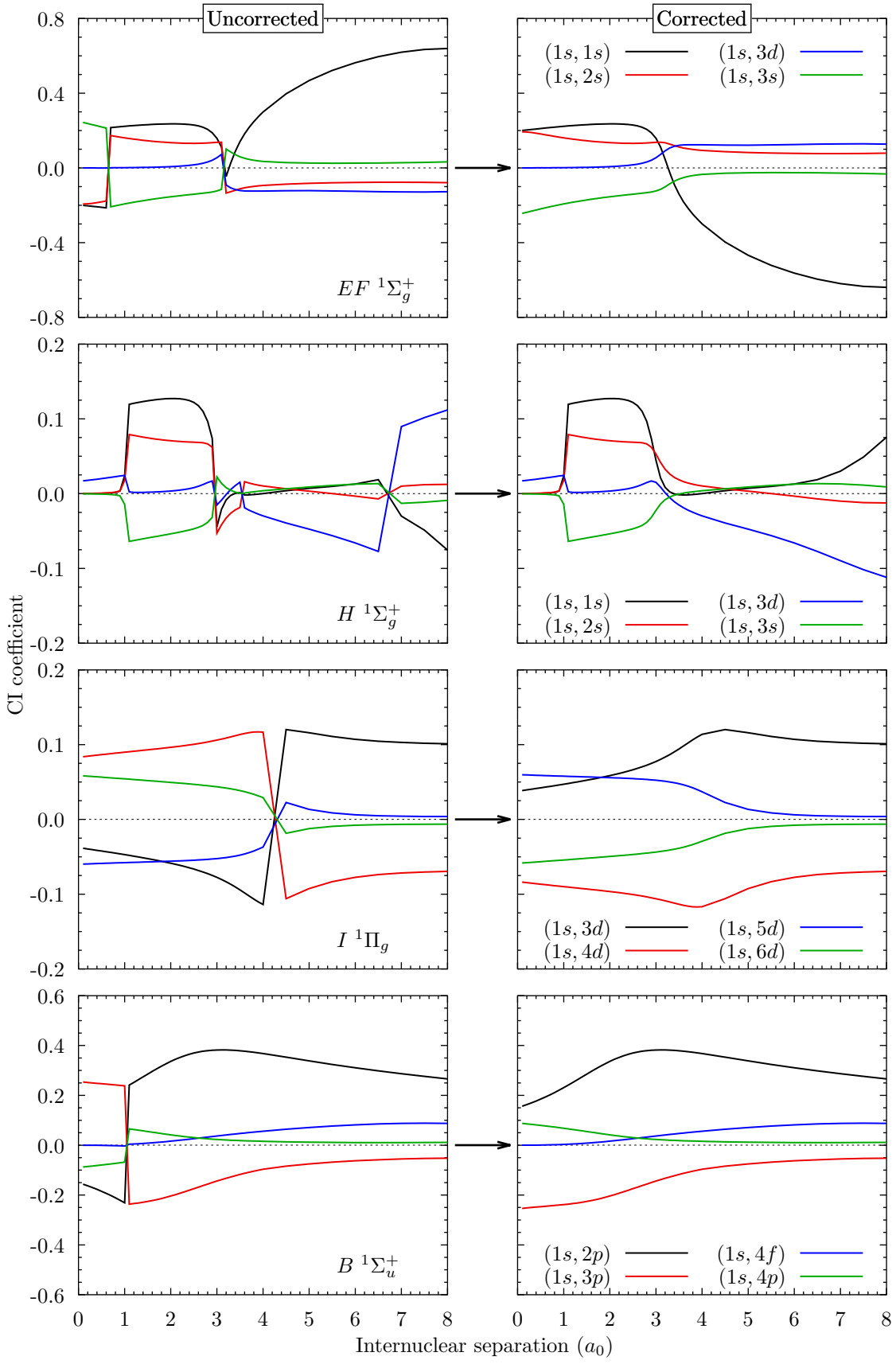

Figure 7.8: CI coefficients for four of the dominant configurations in the $EF\ ^1\Sigma_g^+$, $H\ ^1\Sigma_g^+$, $I\ ^1\Pi_g$, and $B\ ^1\Sigma_u^+$ states, illustrating the correction required to ensure there are no spurious sign changes in the R-dependent T-matrix elements.

values of R where there has been an obvious change in the target-state sign. The most reliable way that we have found to fix this problem is to inspect the CI coefficients of each state and provide an input file to the calculations specifying the sign of a particular CI coefficient. Then the entire CI vector for the state can be multiplied by -1 when necessary to ensure the given coefficient has the desired sign. The right-hand panels in Fig. 7.8 show the corrected CI coefficients. It is obvious that some coefficients naturally do change sign at various R points, so in many cases it is necessary to specify the sign of one or more coefficients in multiple R intervals. For the purposes of testing the square-root approximation, comparisons were made using T-matrix elements and fixed-nuclei cross sections from the MCC(27) model, since it was run with a larger number of R points and

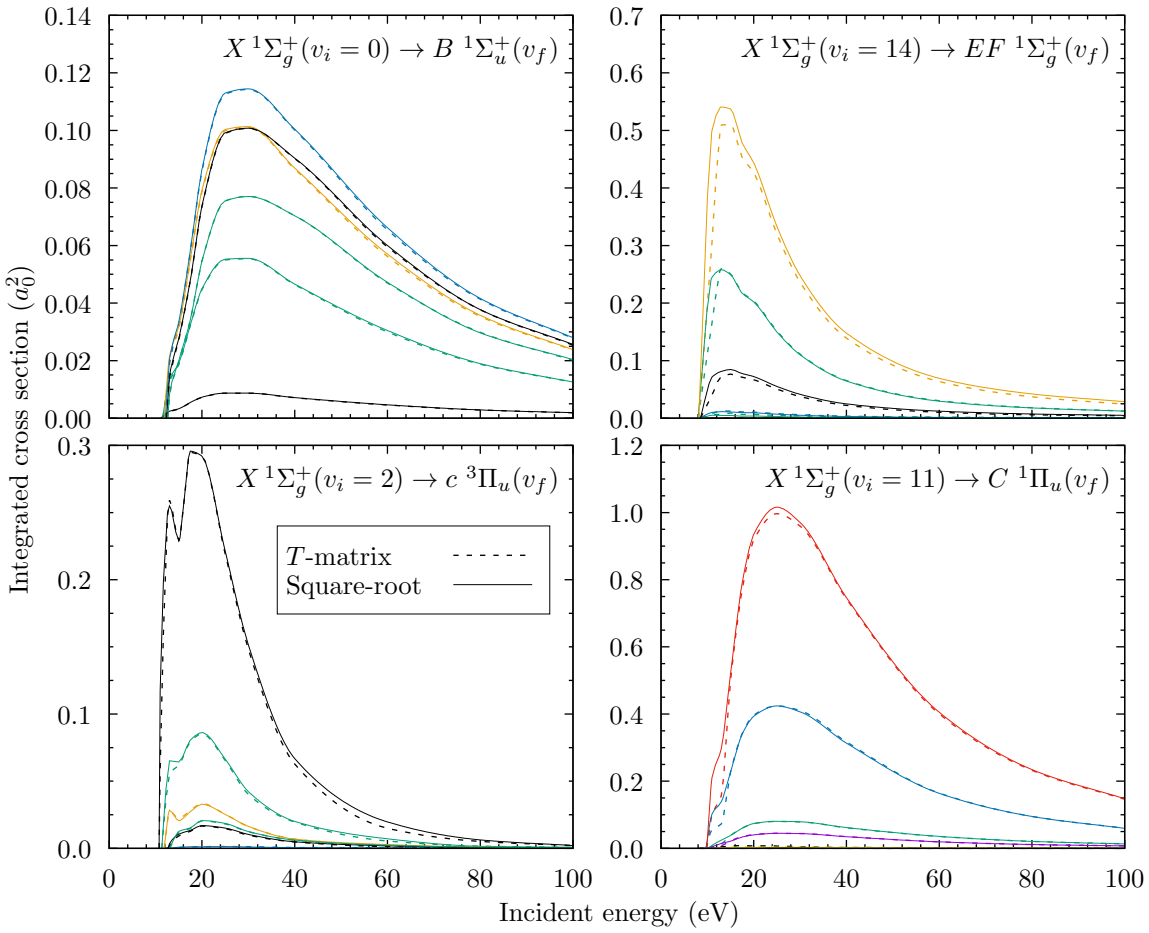

Figure 7.9: A selection of cross sections calculated with the MCC(27) model using R-dependent T-matrix elements in the adiabatic approximation (dashed lines), compared with the "square-root" approximation (solid lines). Each line corresponds to a different final vibrational level v_f.

hence the integration over the R-dependent T-matrix elements can be performed most reliably. Fig. 7.9 presents the comparison for a selection of transitions, demonstrating that the square-root approximation is sufficiently accurate (either perfect or accurate to within a few percent). A similar level of accuracy has been confirmed for all transitions considered in this work.

7.4.1 Bound excitations

At near threshold energies, the shifting threshold in the R-dependent cross section can lead to spurious oscillations in the adiabatic-nuclei cross section. To remedy this, we apply Stibbe and Tennyson's energy-balancing correction [71] (see Eq. (4.58) and surrounding discussion). To illustrate the effect of the correction, Fig. 7.10 compares the cross sections for the $X\,{}^1\Sigma_g^+(v_i = 4) \rightarrow a\,{}^3\Sigma_g^+(v_f = 1)$

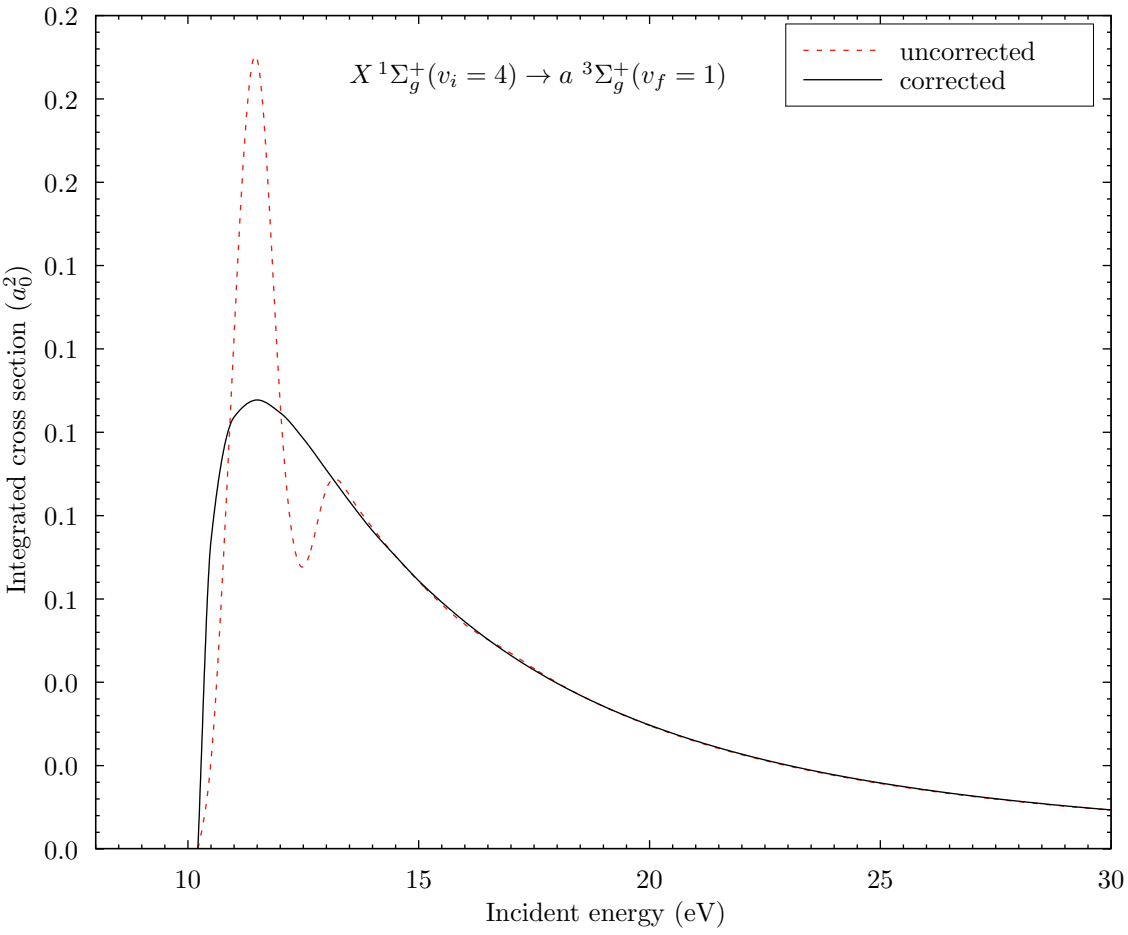

Figure 7.10: Comparison of cross sections for the $X\ {}^1\Sigma_g^+(v_i = 4) \rightarrow a\ {}^3\Sigma_g^+(v_f = 1)$ transition with and without the energy-balancing correction discussed in the text.

transition calculated with and without it. At lower energies there are oscillations in the uncorrected cross section which are not present in the corrected cross section. At higher energies, the two approaches yield identical results. For superelastic transitions, which do not have a threshold energy, the analytical sum over final vibrational levels given in Eq. (4.43) is applied directly, without the energy-balancing modification.

7.4.2 Dissociative excitation

Rather than explicitly integrating the energy-differential dissociation cross section as outlined in Sec. 4.6, it is simpler to adopt a pseudostate treatment of dissociation analogous to the treatment of ionisation in the atomic and molecular CCC methods. In this case, the analogues to the electronic pseudostates in the ionisation continuum are the vibrational pseudostates in the dissociative continuum obtained from diagonalising Eq. (7.2). The completeness of the vibrational pseudostates:

$$\lim_{N\to\infty} \sum_{v=0}^{N} |\nu_{nv}\rangle\langle\nu_{nv}| = \hat{1} \tag{7.10}$$

guarantees that summing the cross sections for excitation of the dissociative pseudostates is equivalent to integrating the energy-differential dissociation cross section, in the limit as the number of pseudostates tends to infinity. Hence, the accuracy of the dissociation cross section can be verified by testing for convergence with respect to the number of pseudostates. Fig. 7.11 presents some example dissociative pseudostates in the $b\ ^3\Sigma_u^+$ state of H_2. Similar pseudostates are generated in the continua of all other electronic states in order to obtain dissociative excitation cross sections.

7.4.3 Total ionisation (for scattering on $n = 2$ states)

For ionisation, there is no single outgoing energy associated with the R-dependent cross section, since it is already summed over ionising pseudostates at each R, so for the purposes of applying the energy-balancing method it is assumed that the

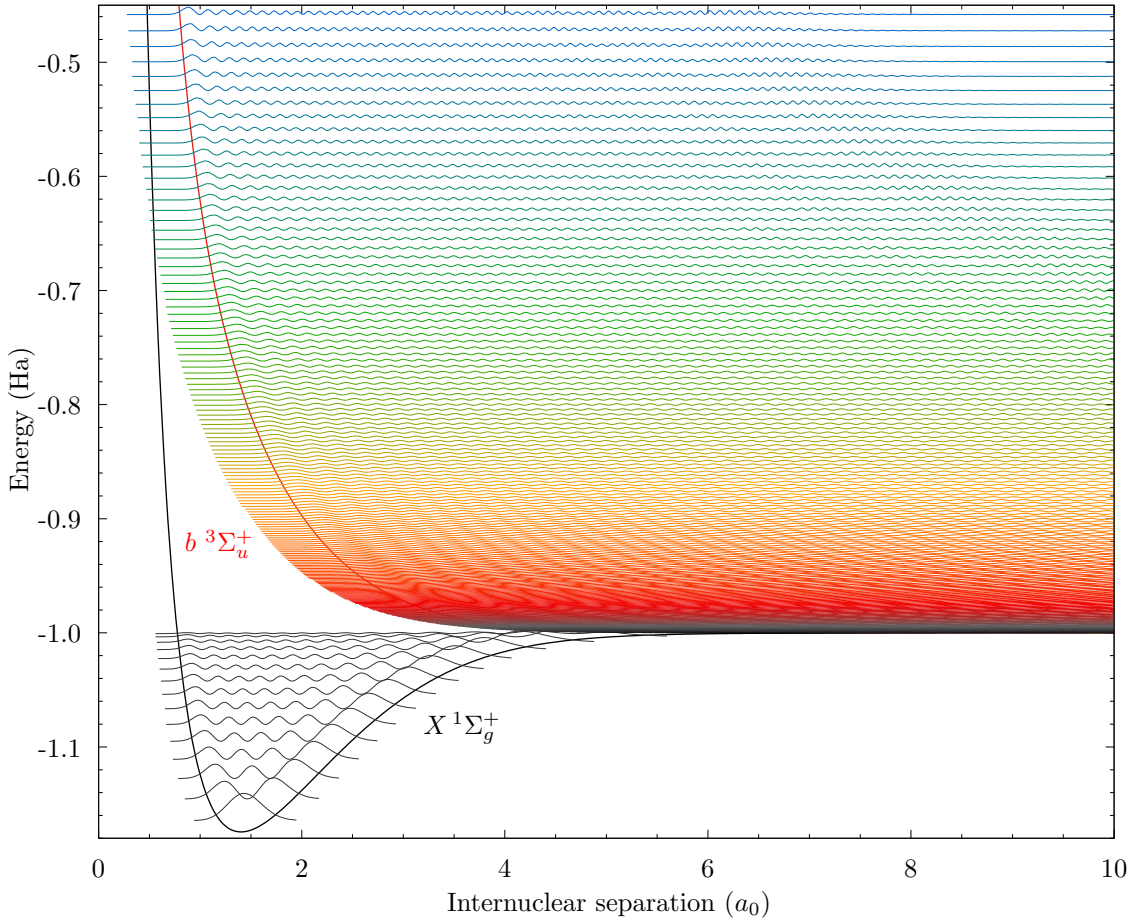

Figure 7.11: Dissociative vibrational pseudostates in the $b\ ^3\Sigma_u^+$ state of H_2. Also shown are the bound vibrational wave functions in the $X\ ^1\Sigma_g^+$ state.

fixed-nuclei outgoing energy is equal to

$$E_f(R) = E_i - \epsilon_i^{\text{ion}}(R), \tag{7.11}$$

where E_i is the incident energy and ϵ_i^{ion} is the ionisation potential for the initial electronic state i. In the evaluation of Eq. (4.58), the final vibrational levels are calculated in the potential-energy curve of the residual H_2^+ ion in its ground electronic state. Although this is not formally correct, since the fixed-nuclei ionisation cross section includes contributions from ionisation with excitation (leading to the production of H_2^+ in excited electronic states), at the energies where this is possible (more than 10 eV above the ionisation threshold) the approach adopted here is equivalent to analytically summing over final levels with Eq. (4.43).

7.4.4 Grand-total cross sections (for scattering on $n = 2$ states)

To obtain grand-total cross sections (GTCS – sum of elastic, excitation, and ionisation cross sections), Eq. (4.43) is applied using the R-dependent GTCS, which includes contributions from more discrete excitations than explicitly considered in the evaluation of adiabatic-nuclei excitation cross sections (i.e. electronic states with $n > 3$). At low energies, the GTCS is dominated by the $v = 0 \rightarrow 0$ elastic cross section, which is unaffected by energy balancing, and the superelastic cross sections, which do not utilise energy balancing, and hence Eq. (4.43) is valid.

7.5 Uncertainty estimates

The three major sources of uncertainty in the present results are the target-structure accuracy, the level of convergence in the R-dependent scattering calculations, and the use of the adiabatic-nuclei approximation. Zammit *et al.* [93] estimated that the uncertainty in the spherical MCCC(491) calculations due to convergence was less than 5% across all electronic transitions. Since the MCCC(210) model adopted here adequately reproduces the MCCC(491) results for excitation, with exceptions explained by the more accurate target structure, an uncertainty of 5% due to convergence is assumed for the present calculations.

The excitation energy $\epsilon_{f,i} = \epsilon_f - \epsilon_i$ is a good indicator of the structure accuracy and its effects on the accuracy of the scattering cross sections. In order to give an overall estimate of the uncertainty in the transitions from an initial vibrational level v_i in the $X\,^1\Sigma_g^+$ state to an excited electronic state f, the relative error in the excitation energy is averaged over the v_i vibrational wave function, giving:

$$u_{f,iv_i}^{\text{struc.}} = \langle \nu_{iv_i} | \left| \frac{\epsilon_{f,i} - \epsilon_{f,i}^{\text{exact}}}{\epsilon_{f,i}^{\text{exact}}} \right| | \nu_{iv_i} \rangle, \tag{7.12}$$

where $\epsilon_{f,i}$ is the excitation energy from the present structure calculations, and $\epsilon_{f,i}^{\text{exact}}$ is the "exact" excitation energy obtained using the accurate potential-energy curves from Refs. [147–152]. For scattering on the $X\,^1\Sigma_g^+$ state, the uncertainties obtained from Eq. (7.12) are less than 1% for all initial vibrational levels, so

for simplicity an overall uncertainty of 6% is assumed (including the 5% from convergence).

Since this is only an approximate error analysis, to avoid giving the impression that the 6% figure is a precise statement of the uncertainty it is rounded up to provide a final uncertainty of 10% in the MCCC(210) H_2 cross sections. This should cover any additional sources of error such as choices of integration grids, general numerical instabilities, and the use of the adiabatic-nuclei approximation.

The various steps discussed in this chapter to improve the adiabatic-nuclei cross sections, aside from removing unwanted oscillations and instabilities in the cross sections, do not have any substantial effect compared to the sources of error mentioned above.

7.6 Errors in the treatment of dissociation in the literature

The cross sections for dissociation of vibrationally-excited H_2, HD, and D_2 through the $b\ ^3\Sigma_u^+$ state recommended in the well-known reviews of Yoon *et al.* [138, 212] come from the R-matrix calculations of Trevisan and Tennyson [73] and Trevisan and Tennyson [74] (hereafter referred to collectively as TT02). The results of TT02, which also include HT, DT, and T_2, have long been considered the most accurate dissociation cross sections for H_2 and its isotopologues, and are widely used in applications. During the course of this project, it became apparent that there are major discrepancies between the MCCC and R-matrix calculations of the $b\ ^3\Sigma_u^+$ dissociation cross sections. Interestingly, the two methods are similar in their treatment of both the electronic and nuclear dynamics, but differ in their fundamental definitions of the dissociation cross section, leading to conflicting isotopic and vibrational-level dependencies in the calculations. The formalism applied by TT02 was previously developed by Trevisan and Tennyson [72] (TT01). In this section, the standard treatment of dissociation adopted in the MCCC calculations is compared with the alternative formulation suggested by TT01, and the origin of the disagreement between the two approaches is determined. The discussion here, which was published in Ref. [4], is limited to the

$b\ ^3\Sigma_u^+$ dissociative excitation, but can be applied more generally to dissociative excitation through any electronic state.

The standard treatment of dissociative excitation was described in Sec. 4.6. In the current section, the method is restated using the definitions, notation, and units used by Trevisan and Tennyson [72] to allow straightforward comparison. Trevisan and Tennyson [72] present their derivations in SI units, and adopt the same definition as Lane [213] of the partial-wave T matrix elements. Using Trevisan and Tennyson's notation [72], the expression for the energy-differential cross section for dissociation of the vibrational level v into atomic fragments of asymptotic kinetic energy E_k in the standard formulation is

$$\frac{\mathrm{d}\sigma}{\mathrm{d}E_\mathrm{out}} = \frac{\pi}{k_\mathrm{in}^2} \sum_{\substack{\ell' m' \\ \ell m}} \left| \langle \nu_{E_\mathrm{k}} | T_{\ell' m', \ell m}(R; E_\mathrm{in}) | \nu_v \rangle \right|^2 , \tag{7.13}$$

where E_in and k_in are the incident projectile energy and wavenumber, and ν are the vibrational wave functions. The energies of the scattered electron and dissociating fragments are related by

$$E_\mathrm{k} = E_\mathrm{in} - D_v - E_\mathrm{out}, \tag{7.14}$$

where D_v is the threshold dissociation energy of the vibrational level v [71], and E_out is the outgoing projectile energy. This relationship makes it possible to treat the energy-differential cross section as a function of either E_out or E_k. When this method has been applied in previous work [15, 19, 20, 58, 61, 63, 64, 68, 70, 71, 90, 96, 177, 214–216], Eq. (7.13) is not derived explicitly for the case of dissociation since the derivation follows exactly the same steps summarised by Lane [213] for the non-dissociative vibrational-excitation cross section. The only difference is the replacement of the final bound vibrational wave function with an appropriately-normalised continuum wave function $\nu_{E_\mathrm{k}}(R)$. In principle the continuum normalisation is arbitrary so long as the density of final states is properly accounted for. According to standard definitions [144], the density of states ρ for the vibrational continuum satisfies the following relation:

$$\int_0^\infty \nu_{E_\mathrm{k}}(R) \nu_{E_\mathrm{k}}(R') \rho(E_\mathrm{k})\, \mathrm{d}E_\mathrm{k} = \delta(R - R'), \tag{7.15}$$

giving a clear relationship between the continuum-wave normalisation and density. Since the formulas presented by Lane [213] for non-dissociative excitations are written in terms of bound vibrational wave functions, with a density of states equal to unity (by definition), the most straightforward adaption to dissociation simply replaces them with continuum wave functions normalised to have unit density as well. Indeed, many of the previous works [20, 58, 71, 96, 158, 162] which have applied the adiabatic-nuclei, rather than fixed-nuclei, method to dissociation explicitly state that the continuum wave functions are energy normalised, which implies unit density and the following resolution of unity:

$$\int_0^\infty \nu^*_{E_\mathrm{k}}(R)\nu_{E_\mathrm{k}}(R')\,\mathrm{d}E_\mathrm{k} = \delta(R-R'). \tag{7.16}$$

The works which have applied the fixed-nuclei method also implicitly assume energy normalisation, since the fixed-nuclei approximation utilises Eq. (7.16) to integrate over the dissociative states analytically. Note that Eq. (7.16) implies the functions ν_{E_k} have dimensions of $1/\sqrt{\text{energy}\cdot\text{length}}$. The bound vibrational wave functions are normalised according to

$$\int_0^\infty \nu^*_v(R)\nu_{v'}(R)\,\mathrm{d}R = \delta_{v'v}, \tag{7.17}$$

and hence they have dimensions of $1/\sqrt{\text{length}}$. The electronic T-matrix elements defined by Lane [213] are dimensionless, and the integration over R implied by the bra-kets in Eq. (7.13) cancels the combined dimension of 1/length from the vibrational wave functions, so it is evident that the right-hand side of Eq. (7.13) has dimensions of area/energy as required (note that $1/k^2_\mathrm{in}$ has dimensions of area).

The standard approach to calculating dissociation cross sections has been applied extensively in the literature [15, 19, 20, 58, 61, 63, 64, 68, 70–72, 90, 96, 177, 214–216]. It is also consistent with well-established methods for computing bound-continuum radiative lifetimes or photodissociation cross sections, which replace discrete final states with dissociative vibrational wave functions. The latter are either energy normalised [217], or normalised to unit asymptotic

amplitude with the energy-normalisation factor included explicitly in the dipole matrix-element formulas [218, 219].

TT01 criticised the standard technique, claiming that a proper theoretical formulation for dissociation did not exist, and suggested that a more rigorous derivation for the specific case where there are three fragments in the exit channels is required. They arrived at an expression which is markedly different from the standard approach:

$$\frac{\mathrm{d}\sigma}{\mathrm{d}E_{\mathrm{out}}} = \frac{m_{\mathrm{H}}}{4\pi^3 m_{\mathrm{e}}} \frac{E_{\mathrm{k}}}{E_{\mathrm{in}}} \sum_{\substack{\ell' m' \\ \ell m}} \left| \langle \nu_{E_{\mathrm{k}}} | T_{\ell' m', \ell m}(R; E_{\mathrm{in}}) | \nu_v \rangle \right|^2 . \tag{7.18}$$

Here m_{H} is the hydrogen nuclear mass, which is replaced with the deuteron or triton mass in their later investigation into dissociation of D_2 and T_2 [73]. Comparing Eqs. (7.13) and (7.18), TT01's formula is different by a factor of $m_{\mathrm{H}} E_{\mathrm{k}} / 2\pi^4 \hbar^2$ (the T-matrix elements here are the same as those in Eq. (7.13)). The distinguishing feature of TT01's approach and the reason for the mass-dependence in their formula was said to be the explicit consideration of the density of dissociating states. There are two major issues here: firstly, the energy-normalised wave functions used in Eqs. (7.13) and (7.18) have unit density so it is unusual that taking this into account should have any effect, and secondly, TT01's expression for the energy-differential cross section has dimensions of

$$\dim \left[\frac{\mathrm{d}\sigma}{\mathrm{d}E_{\mathrm{out}}} \right] = \frac{1}{\text{energy}}, \tag{7.19}$$

which suggests an error in the derivation. As a result, the integral cross sections for scattering on $H_2(v = 0)$ presented in TT01 and for vibrationally-excited H_2, HD, D_2, HT, DT, and T_2 presented in TT02 using the same method appear to be incorrect.

TT01's derivation uses a density of states corresponding to (three-dimensional) momentum normalisation. However, rather than calculating momentum-normalised vibrational wave functions, TT01 use energy-normalised functions and apply a correction factor

$$\xi^2 = 2\hbar \left(\frac{E_{\mathrm{k}}}{m_{\mathrm{H}}} \right)^{1/2} = \frac{\hbar p_{\mathrm{k}}}{\mu} \tag{7.20}$$

to the cross section to account for a conversion from energy to momentum nor-

malisation. Since the vibrational wave functions are one-dimensional, it is not obvious how to normalise them to three-dimensional momentum. Although TT01 do not state explicitly how they choose to define the momentum normalisation, Eq. (7.20) corresponds to a conversion from energy normalisation to (one-dimensional) wavenumber normalisation [220]. The density of states for this choice of normalisation is

$$\rho(E_\mathrm{k}) = \frac{\mu}{\hbar p_\mathrm{k}}, \tag{7.21}$$

which cancels exactly with the correction factor in Eq. (7.20). This is to be expected since Eq. (7.15) shows clearly that any factors applied to the continuum wave functions to change the normalisation must lead to the inverse factor (squared) being applied to the density of states. It is the mismatch between continuum normalisation and density of states which leads to some of the additional factors, such as the nuclear mass, in TT01's final cross section formula. Using a consistent normalisation and density of states, it is possible to follow the remaining steps taken by TT01 in their derivation and arrive at an expression identical to the standard formula given in Eq. (7.13). This is shown explicitly further down in Sec. 7.6.1.

The novelty of TT01's reformulated approach to dissociation has been acknowledged numerous times and the results have been widely adopted. Perhaps in part due to being recommended by Yoon *et al.* [138, 221] and included in the Quantemol database [222], the cross sections and rate coefficients given by TT02 have been applied in a number of different plasma models, most notably in the astrophysics community [34, 36, 39, 41, 42, 44, 75–86]. The formalism of TT01 was also used by Gorfinkiel *et al.* [223] to study the electron-impact dissociation of H_2O, and it has been reiterated a number of times that this method is necessary to accurately treat dissociation in the adiabatic-nuclei approximation [224–226]. Gorfinkiel *et al.* [223] found in particular that for some dissociative transitions in H_2O the formalism of TT01 gives results up to a factor of two different to the fixed-nuclei method even 10 eV above threshold. If correct, this result would invalidate the use of the fixed-nuclei method in dissociation calculations, for example in the R-matrix calculations of Refs. [227–229].

Fig. 7.12 compares the MCCC and TT01/02 results for dissociation of H_2 in

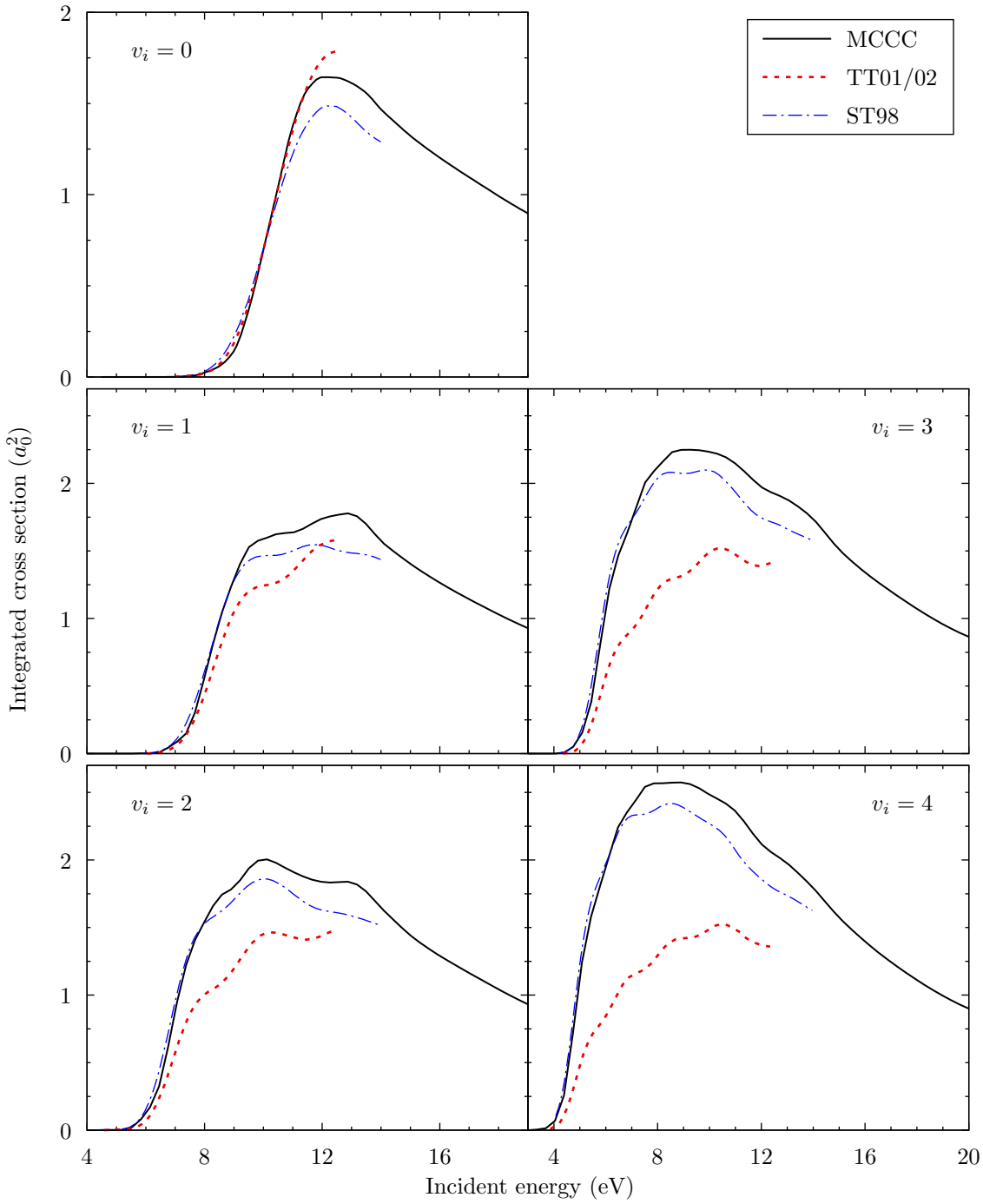

Figure 7.12: Comparison of the $X\ ^1\Sigma_g^+(v) \rightarrow b\ ^3\Sigma_u^+$ dissociation cross sections calculated by Stibbe and Tennyson [71] and Trevisan and Tennyson [72] and Trevisan and Tennyson [73] (ST98 and TT01/02, respectively), with the molecular convergent close-coupling (MCCC) calculations for scattering on the $v = 0$–4 levels of H_2.

the initial vibrational states $v = 0$–4. Also shown are the earlier R-matrix results of Stibbe and Tennyson [71] (ST98), which were performed using the standard formulation given in Eq. (7.13). Both sets of R-matrix calculations used the same

underlying T-matrix elements, calculated previously in an investigation into H_2^- resonances [230], so the differences between them is only due to TT01's alternative cross-section formula. The ST98 and MCCC cross sections are in good agreement, with small differences near the cross section maximum likely due to the use of different electronic scattering models. TT01's cross section for the $v = 0$ level of H_2 is only about 10% different from ST98's results at the maximum, and up to around 10 eV the two are essentially the same. It is perhaps puzzling that the additional factor of $m_H E_k / 2\pi^4\hbar^2$ in Eq. (7.18) has only a small effect, but it turns out that the average value of this factor is fortuitously close to 1 (in Hartree atomic units) in the 0–6 eV range of E_k corresponding to incident energies up to 10 eV (see TT01's Fig. 8). This coincidence disappears for scattering on excited vibrational levels, where the formulation of TT01 predicts significantly different results. The cross sections for dissociation of excited vibrational levels presented in TT02 are up to a factor of 2 smaller than the MCCC and ST98 results. To explain this, Fig. 7.13 presents the MCCC energy-differential cross section as a

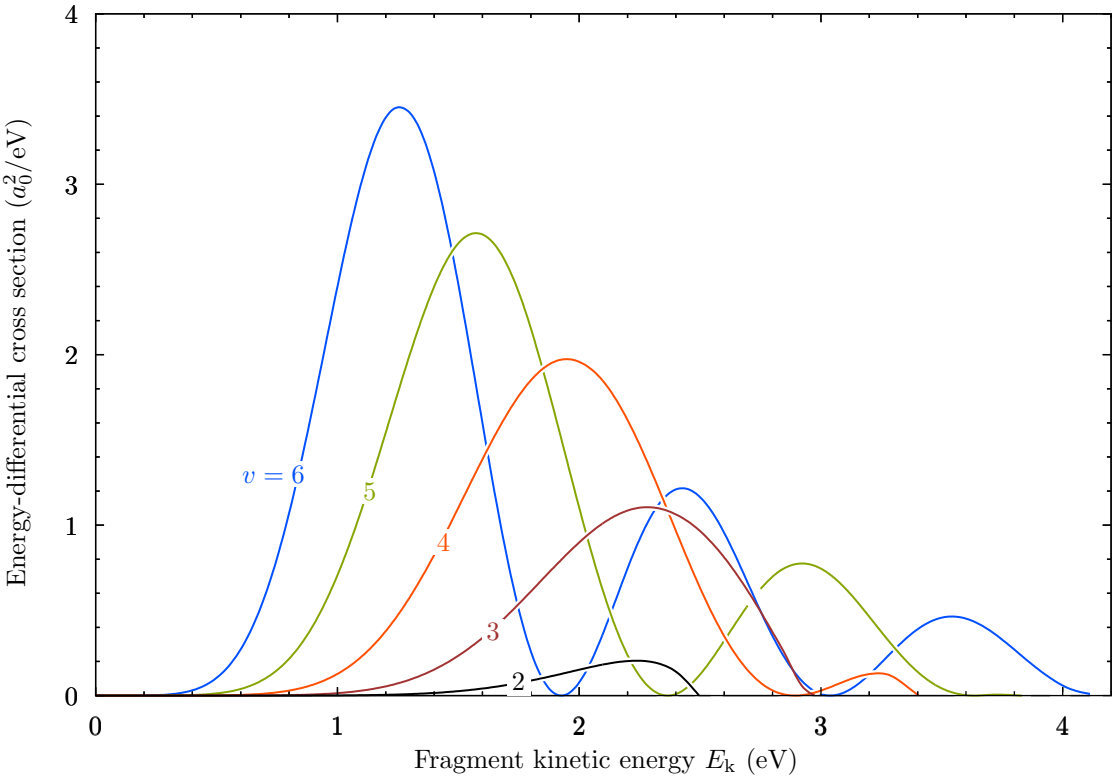

Figure 7.13: Energy-differential dissociation cross section as a function of the fragment kinetic energy E_k for 6.0-eV electrons scattering on the $v = 2$–6 vibrational levels of H_2.

function of E_k for 6-eV electrons scattering on the $v = 2$–6 levels of H_2, showing that the cross section peaks at progressively smaller values of E_k as the initial vibrational level is increased. In TT01's formalism, the suppression in this region caused by the smaller value of their additional factor in Eq. (7.18) for small E_k leads to a substantial reduction in the integrated cross section for scattering on higher vibrational levels.

Further to the different vibrational dependence, the mass factor in Eq. (7.18) leads to an unusually large isotopic dependence in the dissociation cross sections. Fig. 7.14 compares the MCCC and TT02 cross sections for dissociation of H_2, D_2, and T_2 in the $v = 0$ level. TT02's results for D_2 are two times larger than for H_2, and for T_2 they are three times larger. The MCCC calculations show only a small

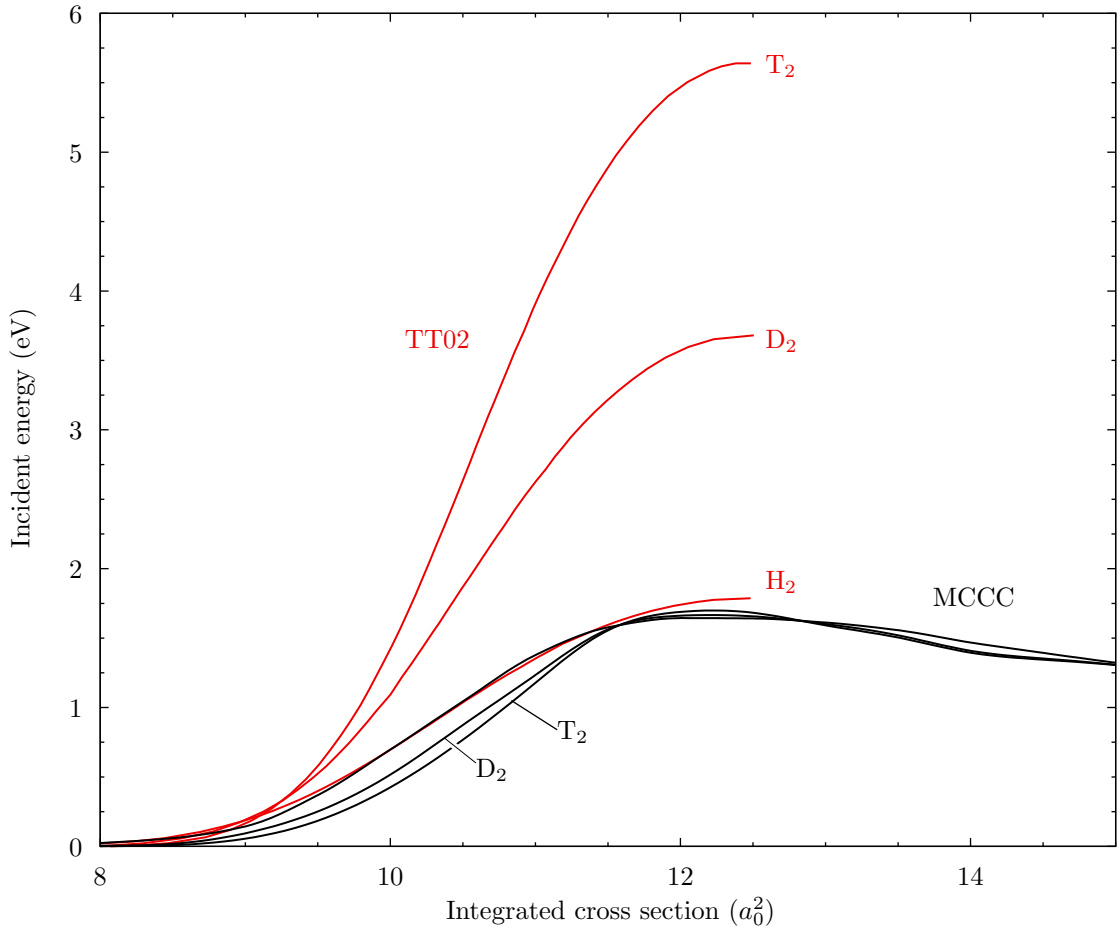

Figure 7.14: Comparison of the $X\ ^1\Sigma_g^+(v = 0) \rightarrow b\ ^3\Sigma_u^+$ dissociation cross sections calculated by Trevisan and Tennyson [73] (TT02), with the molecular convergent close-coupling (MCCC) calculations for scattering on H_2, D_2, and T_2.

isotope effect at low energies due to the slightly higher dissociation thresholds of the heavier targets. TT02 stated that their predicted scaling of cross sections with isotopic mass should be expected for all dissociative processes, however this is purely an artefact of the incorrect formalism that they have applied.

In this section, it has been shown that the standard dissociation formalism is valid, and the cross-section formula derived by TT01/02 [72–74] is incorrect. Although the cross section for dissociation of the H_2 $X\,^1\Sigma_g^+(v=0)$ level is (fortuitously) not severely affected by the errors in the formalism applied, the R-matrix results for dissociation of vibrationally-excited or isotopically-substituted H_2 are in serious error. For this reason, the MCCC cross sections, which apply the standard formalism, should be used in place of the R-matrix results of TT01/02 [72–74] in all applications.

7.6.1 Corrected derivation

Here a corrected derivation of the adiabatic-nuclei dissociation cross section is given, following the same ideas laid out by Trevisan and Tennyson [72] (TT01). Rather than treating rotational motion explicitly, TT01's derivation assumes a fixed nuclear orientation during the collision and then applies a classical orientation-averaging technique. This approach is valid and formally equivalent to summing over final rotational levels using the closure of the rotational wave functions [87]. With the orientation fixed, the parameter $\hat{\boldsymbol{R}}$ is removed from the set of dynamical variables and the nuclear motion is treated as a purely one-dimensional problem.

Standard quantum mechanics texts, such as Sakurai and Napolitano [143], derive expressions for the scattering transition rate. For the present case it can be written as

$$w_{i\to f} = \frac{2\pi}{\hbar} |T_{f,i}|^2 \, \rho_\mathrm{e}(E_\mathrm{out}, \Omega) \rho_\mathrm{v}(E_\mathrm{k}) \, \mathrm{d}E_\mathrm{out} \, \mathrm{d}\Omega, \tag{7.22}$$

where E_out and Ω are the scattered electron energy and direction, E_k is the asymptotic kinetic energy of the dissociating fragments, and ρ_v and ρ_e are the density of states for the target vibrational continuum and scattered electron continuum, respectively. Here,

$$T_{f,i} = \langle \boldsymbol{p}_f \nu_{E_\mathrm{k}} \Phi_f | \hat{\mathsf{T}} | \Phi_i \nu_v \boldsymbol{p}_i \rangle \tag{7.23}$$

is the T-matrix element linking the final and initial scattering states, where $\boldsymbol{p}_f$ and $\boldsymbol{p}_i$ are the final and initial projectile plane waves, ν_{E_k} is the continuum vibrational wave function for the dissociating fragments, ν_v is the bound vibrational wave function for initial level v, and Φ_f and Φ_i are the final and initial electronic states. Note that Eq. (7.22) assumes the $\hat{\mathsf{T}}$ operator is defined in terms of the scattering operator $\hat{\mathsf{S}}$ by $\hat{\mathsf{S}} = \hat{\mathsf{I}} - 2\pi i \hat{\mathsf{T}}$ [143]. This derivation assumes the standard momentum-normalised plane waves for the incident and scattered electrons:

$$\langle \boldsymbol{r} | \boldsymbol{p} \rangle = \frac{1}{(2\pi\hbar)^{3/2}} e^{i\boldsymbol{p}\cdot\boldsymbol{r}/\hbar} \tag{7.24}$$

$$\int_{\mathbb{R}^3} \langle \boldsymbol{p}' | \boldsymbol{r} \rangle \langle \boldsymbol{r} | \boldsymbol{p} \rangle \, \mathrm{d}\boldsymbol{r} = \delta(\boldsymbol{p}' - \boldsymbol{p}), \tag{7.25}$$

which implies the following unity resolution:

$$\int_{\mathbb{R}^3} \langle \boldsymbol{r}' | \boldsymbol{p} \rangle \langle \boldsymbol{p} | \boldsymbol{r} \rangle \, \mathrm{d}\boldsymbol{p} = \delta(\boldsymbol{r}' - \boldsymbol{r}), \tag{7.26}$$

and incident current density

$$j_i = \frac{p_i}{m_\mathrm{e}(2\pi\hbar)^3} = \frac{\hbar k_i}{m_\mathrm{e}(2\pi\hbar)^3}, \tag{7.27}$$

with $k_i = p_i/\hbar$. According to standard definitions [143], the cross section $\mathrm{d}\sigma$ associated with the transition rate in Eq. (7.22) is

$$\begin{aligned} \mathrm{d}\sigma &= \frac{w}{j_i} \\ &= \frac{\hbar m_\mathrm{e}(2\pi)^4}{k_i} |T_{f,i}|^2 \, \rho_\mathrm{e}(E_\mathrm{out}, \Omega) \rho_\mathrm{v}(E_\mathrm{k}) \, \mathrm{d}E_\mathrm{out} \, \mathrm{d}\Omega, \end{aligned} \tag{7.28}$$

and hence the double differential cross section (DDCS) is

$$\frac{\mathrm{d}^2\sigma}{\mathrm{d}E_\mathrm{out} \, \mathrm{d}\Omega} = \frac{\hbar m_\mathrm{e}(2\pi)^4}{k_i} |T_{f,i}|^2 \, \rho_\mathrm{e}(E_\mathrm{out}, \Omega) \rho_\mathrm{v}(E_\mathrm{k}). \tag{7.29}$$

Note that Eq. (7.29) differs slightly from the formulas given by Ohlsen [231], Fuchs [232], and Tostevin *et al.* [233] (used by TT01) since Refs. [231–233] use

the alternative momentum normalisation

$$\int_{\mathbb{R}^3} \langle \boldsymbol{p}'|\boldsymbol{r}\rangle\langle \boldsymbol{r}|\boldsymbol{p}\rangle \,\mathrm{d}\boldsymbol{r} = (2\pi\hbar)^3\delta(\boldsymbol{p}'-\boldsymbol{p}) \tag{7.30}$$

and hence TT01's Eq. (10) differs from Eq. (7.29) by a factor of $1/(2\pi\hbar)^3$.

Now ρ_e and ρ_v are evaluated. The relationship between continuum-state normalisation and density of states can be found in quantum mechanics texts such as Cohen-Tannoudji *et al.* [144]:

$$\int_{[\boldsymbol{\beta}]} \int_0^\infty |\epsilon,\boldsymbol{\beta}\rangle\langle\boldsymbol{\beta},\epsilon|\rho(\epsilon,\boldsymbol{\beta})\,\mathrm{d}\epsilon\,\mathrm{d}\boldsymbol{\beta} = \hat{\mathsf{I}}, \tag{7.31}$$

where $\hat{\mathsf{I}}$ is the identity operator, ϵ is the continuum-state energy, $\boldsymbol{\beta}$ stands for the set of remaining parameters which characterise the state, and $[\boldsymbol{\beta}]$ is the parameter space of $\boldsymbol{\beta}$. The scattered electron can be characterised by its energy E_out and direction Ω, and Eq. (7.31) becomes

$$\int_\Omega \int_0^\infty \langle \boldsymbol{r}'|\boldsymbol{p}\rangle\langle\boldsymbol{p}|\boldsymbol{r}\rangle\rho_\mathrm{e}(E_\mathrm{out},\Omega)\,\mathrm{d}E_\mathrm{out}\,\mathrm{d}\Omega = \delta(\boldsymbol{r}'-\boldsymbol{r}). \tag{7.32}$$

Substituting $\mathrm{d}\boldsymbol{p} = m_\mathrm{e}p\,\mathrm{d}E\,\mathrm{d}\Omega$ into Eq. (7.26) and comparing with Eq. (7.32) gives

$$\rho_\mathrm{e}(E_\mathrm{out},\Omega) = \hbar m_\mathrm{e} k_\mathrm{out}. \tag{7.33}$$

For the vibrational continuum Eq. (7.31) becomes

$$\int_0^\infty \nu_{E_\mathrm{k}}(R')\nu_{E_\mathrm{k}}(R)\rho_\mathrm{v}(E_\mathrm{k})\,\mathrm{d}E_\mathrm{k} = \delta(R'-R). \tag{7.34}$$

If energy-normalised vibrational wave functions are used (as done by TT01), then from the unity resolution

$$\int_0^\infty \nu_{E_\mathrm{k}}(R')\nu_{E_\mathrm{k}}(R)\,\mathrm{d}E_\mathrm{k} = \delta(R'-R), \tag{7.35}$$

it follows that the density of vibrational states is simply

$$\rho_\mathrm{v}(E_\mathrm{k}) = 1. \tag{7.36}$$

Note that Eq. (7.36) implies the following asymptotic form of the vibrational wave functions:

$$\lim_{R\to\infty} \nu_{E_\mathrm{k}}(R) = \frac{1}{\hbar}\sqrt{\frac{2\mu}{k\pi}}\sin(kR+\delta), \tag{7.37}$$

where

$$k = \frac{1}{\hbar}\sqrt{2\mu E_\mathrm{k}}. \tag{7.38}$$

Substituting Eqs. (7.33) and (7.36) into Eq. (7.29) gives the following expression for the DDCS:

$$\frac{\mathrm{d}^2\sigma}{\mathrm{d}E_\mathrm{out}\,\mathrm{d}\Omega} = \hbar^2 m_\mathrm{e}^2 (2\pi)^4 \frac{k_\mathrm{out}}{k_\mathrm{in}} \left|T_{f,i}\right|^2 . \tag{7.39}$$

The relationship between the T matrix and scattering amplitude for various normalisations of the projectile plane waves and relationships between $\hat{\mathsf{S}}$ and $\hat{\mathsf{T}}$ can be found in the appendix of Morrison and Sun [220]:

$$T_{fi} = \frac{|c|^2}{d}\frac{\hbar^2}{4\pi m_\mathrm{e}} F_{fi}, \tag{7.40}$$

where the constants c and d are found from

$$\langle \boldsymbol{r}|\boldsymbol{p}\rangle = c(2\pi)^{-3/2} e^{i\boldsymbol{p}\cdot\boldsymbol{r}/\hbar} \tag{7.41}$$

$$\hat{\mathsf{S}} = \hat{\mathsf{I}} + 2id\hat{\mathsf{T}}. \tag{7.42}$$

For the momentum-normalised plane waves (7.24) and the definition $\hat{\mathsf{S}} = \hat{\mathsf{I}} - 2\pi i\hat{\mathsf{T}}$ assumed in Eq. (7.22) [143] it is clear that

$$c = \frac{1}{\hbar^{3/2}}, \qquad d = \pi, \tag{7.43}$$

giving:

$$T_{fi} = \frac{1}{(2\pi)^2 i\hbar m_\mathrm{e}} F_{fi}, \tag{7.44}$$

and hence

$$\frac{\mathrm{d}^2\sigma}{\mathrm{d}E_\mathrm{out}\,\mathrm{d}\Omega} = \frac{k_\mathrm{out}}{k_\mathrm{in}} \left|F_{fi}\right|^2 . \tag{7.45}$$

At this point it is evident that we have arrived at the expected result that the DDCS is simply given by the standard differential cross section formula.

To express the DDCS in terms of the same partial-wave T-matrix elements

in TT01's formulas, Eqs. (6) and (7) of Malegat [234] are now applied to give

$$\frac{\mathrm{d}^2\sigma}{\mathrm{d}E_{\mathrm{out}}\,\mathrm{d}\Omega} = \frac{k_{\mathrm{out}}}{k_{\mathrm{in}}}\,|F_{fi}|^2 \tag{7.46}$$

$$= \sum_t A^t_{fi} P_t(\cos\theta), \tag{7.47}$$

where the coefficients A^t_{fi} are given in Malegat's Eq. (8). Note that, according to Malegat's definitions, Eq. (7.47) is the orientation-averaged DDCS. After integration over the scattered-electron solid angle, the energy-differential cross section is given by

$$\frac{\mathrm{d}\sigma}{\mathrm{d}E_{\mathrm{out}}} = 4\pi A^0_{fi}$$

$$= \frac{\pi}{k_i^2} \sum_{\substack{\ell' m' \\ \ell m}} \left|\langle \nu_{E_{\mathrm{k}}} | T_{\ell' m', \ell m}(R; E_{\mathrm{in}}) | \nu_v \rangle\right|^2 , \tag{7.48}$$

where $T_{\ell' m', \ell m}$ are the same partial-wave T-matrix elements defined by TT01. The explicit form of $A^0_{f,i}$ can be inferred from TT01 by inspection of their Eq. (29).

7.7 Chapter 7 summary

This chapter has given an overview of the MCCC structure and scattering calculations performed in the present work. Convergence studies have been performed, and the generation of R-dependent electronic scattering cross sections for use in the adiabatic-nuclei calculations has been discussed. The specific procedures for performing the MCCC adiabatic-nuclei calculations have been summarised, and uncertainty estimates have been given. Issues surrounding the proper treatment of dissociative excitation have been investigated, prompted by claims in the literature [72–74] that the standard approach, which is applied in the present work, is invalid. It has been shown here that this is not the case, and that the standard dissociation formalism is in fact correct. These findings were published in Ref. [4].

Chapter 8

Adiabatic-nuclei results for electron scattering on H_2

This chapter presents vibrationally-resolved results for electron scattering on H_2 and its isotopologues, obtained from the adiabatic-nuclei calculations described in Chapter 7. Rotationally-resolved scattering will be discussed later in Chapters 11 and 12. Some sections contain text or figures adapted from published works by the candidate [5–7, 12]. The publishers (Elsevier, the American Physical Society, and MDPI) provide the right to use an article or a portion of an article in a thesis or dissertation without requesting permission.

The calculations presented in this section were motivated by the importance of comprehensive sets of data for the e^--H_2 collision system, and the lack of accurate data available in the literature. H_2 and its isotopologues are present in the ground state as well as excited vibrational and electronic states in fusion, atmospheric, and interstellar plasmas [22–25, 235, 236]. Cross sections resolved in both final and initial vibrational levels, for scattering on a range of electronic states, are required for determining plasma properties and the interpretation of spectroscopic data [31, 32].

The majority of previous theoretical and experimental studies have been directed towards producing estimates of cross sections for electron-impact excitation from the ground electronic and vibrational state [221]. Most of the available theoretical data for scattering on excited vibrational levels have been obtained using the semiclassical impact-parameter (IP) method [159, 160], and are not resolved in the final vibrational levels [70, 96, 159, 160, 162, 237, 238]. These results are larger by a factor of two than the available measurements between 20 and

60 eV for scattering on the $X\,^1\Sigma_g^+(v=0)$ state, and are likely to be inaccurate for $v_i > 0$ as well [160].

For scattering on excited states, a handful of calculations have been done for specific transitions using approximate methods, but until recently no single method has been applied to the generation of a large set of cross sections. During the course of this PhD project, a new set of R-matrix calculations was published for scattering on excited electronic states of H_2 in the fixed-nuclei approximation [116]. These will be discussed further in Sec. 8.3, and compared with the present MCCC calculations. To date, no measurements have been performed for scattering on excited electronic or vibrational states of H_2 or its isotopologues.

The results presented in this chapter are the product of the adiabatic-nuclei calculations described in Chapter 7, and are organised as follows:

Section 8.1: fully vibrationally-resolved results for scattering on all vibrational levels of the $X\,^1\Sigma_g^+$ state of H_2 and its five isotopologues [6, 7].

Section 8.2 cross sections for dissociation of H_2 into all neutral fragments [12].

Section 8.3: results for scattering on the $v = 0$ vibrational level of the $n = 2$ electronic states of H_2 [5].

Section 8.4: an example of the utilisation of the present cross sections in a collisional-radiative model for H_2 [8].

Section 8.5: discussion of the online database developed during this project to host the MCCC results.

8.1 Vibrationally-resolved electronic excitation from the $X\,^1\Sigma_g^+$ state

Fully vibrationally-resolved cross sections have been calculated for scattering on all bound levels of the $X\,^1\Sigma_g^+$ state of each isotopologue (H_2, HD, HT, D_2, DT, T_2), considering excitation of all bound levels and dissociative excitation of each $n = 2$–3 electronic state (see Table 7.3 of Chapter 7 for the number of levels in each state). The total number of cross sections generated from these calculations

is in excess of 60,000. In this section, a selection of results for scattering on H_2 are presented, and isotopic effects are discussed. The results presented here have been published in Refs. [6, 7].

Fig. 8.1 compares a selection of MCCC results for total electronic excitation (summed over final bound and dissociative vibrational levels) of the $B\ ^1\Sigma_u^+$, $C\ ^1\Pi_u$, $B'\ ^1\Sigma_u^+$, and $D\ ^1\Pi_u$ states of H_2 with the impact-parameter calculations of Celiberto *et al.* [70]. Each result demonstrates the same trend, with the

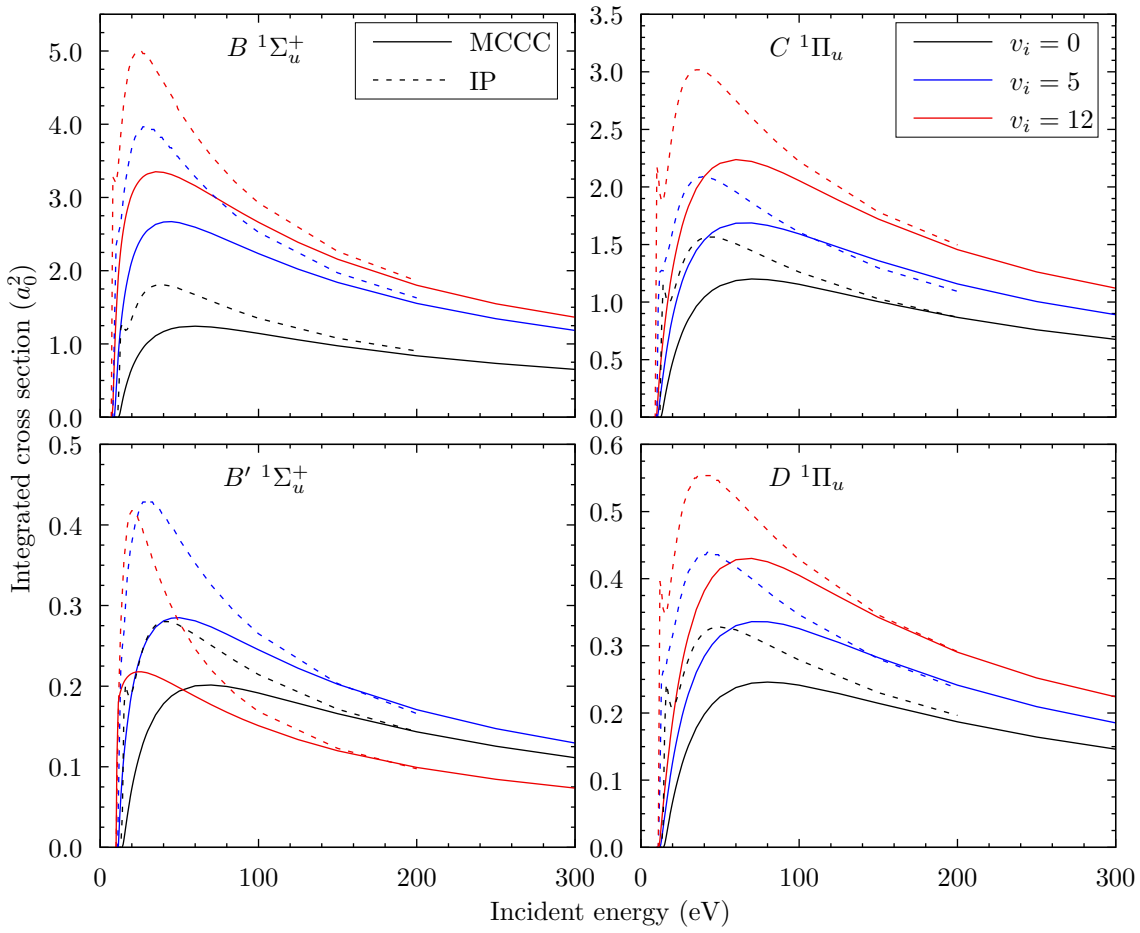

Figure 8.1: Electron-impact cross sections summed over all final vibrational levels in the $B\ ^1\Sigma_u^+$, $C\ ^1\Pi_u$, $B'\ ^1\Sigma_u^+$, and $D\ ^1\Pi_u$, states of H_2. The present MCCC results (solid lines) are compared with the impact-parameter (IP) calculations of Celiberto *et al.* [70] (dashed lines).

semiclassical impact-parameter results overestimating the cross section by up to a factor of two at low to intermediate energies. By 200 eV incident energies, the two calculations are in good agreement, since the impact-parameter approximation becomes valid in the high-energy limit. The large differences between

the MCCC and impact-parameter results seen in Fig. 8.1 are seen in all electronic transitions, for scattering on all vibrational levels of the $X\,^1\Sigma_g^+$ state. The comparison is the same for scattering on D_2 as well (scattering on the other isotopologues was not considered by Celiberto *et al.* [70]). Even without considering resolution in the final vibrational levels, the MCCC calculations for electronic excitation already prove to be a substantial improvement over what was previously available. Furthermore, the impact-parameter method can only be applied to dipole-allowed transitions, so the calculation of dipole- and spin-forbidden transitions in the present calculations for scattering on excited vibrational levels in many cases represents the first ever available data.

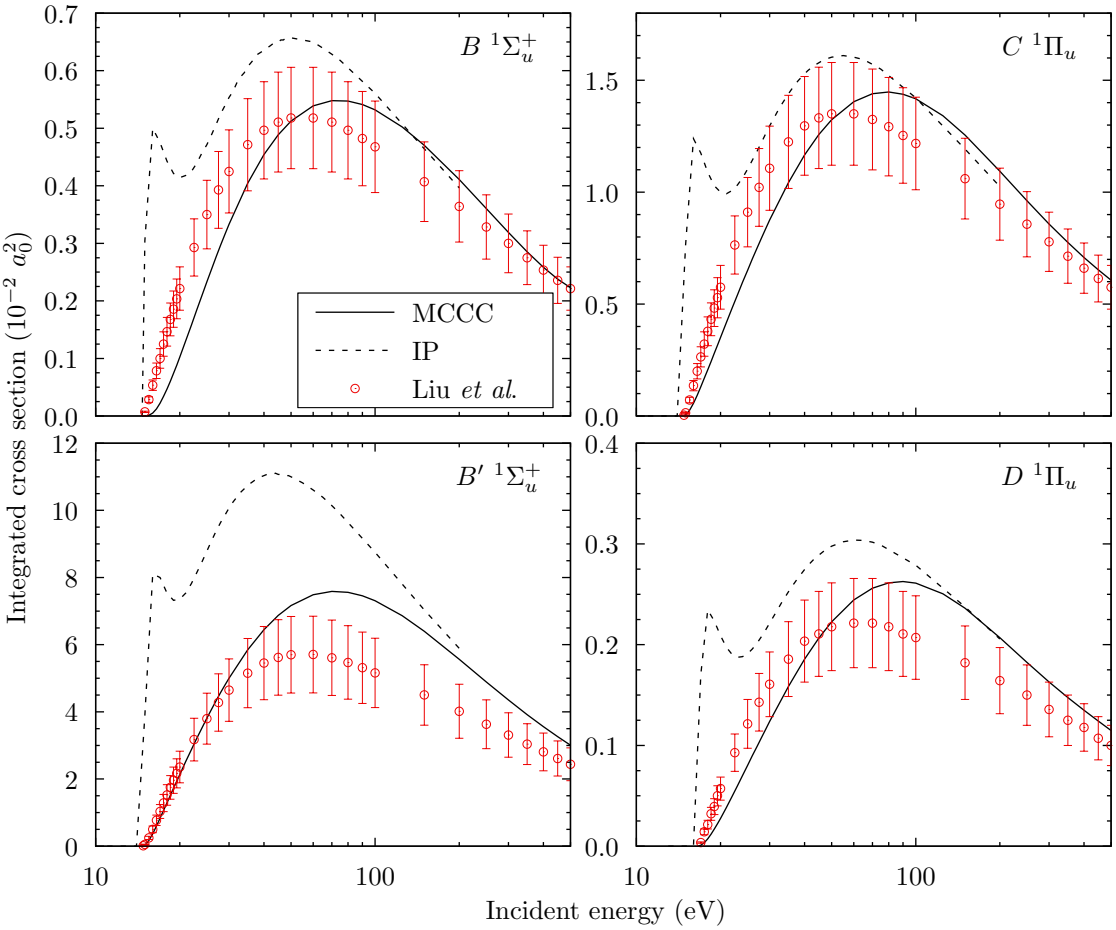

Figure 8.2: Electron-impact cross sections for dissociative excitation of the $B\,^1\Sigma_u^+$, $C\,^1\Pi_u$, $B'\,^1\Sigma_u^+$, and $D\,^1\Pi_u$, states of H_2 from the $X\,^1\Sigma_g^+(v_i = 0)$ state. The MCCC results are compared with the impact-parameter (IP) calculations [70], and the semi-empirical calculations of Liu *et al.* [239].

Fig. 8.2 presents dissociative excitation cross sections of the $B\,^1\Sigma_u^+$, $C\,^1\Pi_u$,

$B'\ ^1\Sigma_u^+$, and $D\ ^1\Pi_u$ states for scattering on the $X\ ^1\Sigma_g^+(v_i = 0)$ state of H_2. The MCCC results are compared with the impact-parameter calculations [70], and the semi-empirical calculations of Liu *et al.* [239]. The latter were obtained by scaling experimentally-determined excitation functions to fit the Born dissociative-excitation cross section at high incident energies. The comparison with the impact-parameter results is the same as it was for total electronic excitation in Fig. 8.1. All three sets of cross sections appear to converge towards the same values in the high-energy limit, and at intermediate energies the MCCC results are in much better agreement with Liu *et al.* [239] than with the impact-parameter calculations. Liu *et al.* [239] assumed that the excitation function is nearly identical for all *ungerade* states, while in the MCCC calculations there are some differences between these four ungerade states, as evidenced by the varying degrees of agreement with the results of Liu *et al.* [239]. Furthermore, the energy position of the cross-section maximum is somewhat larger in the MCCC calculations than that of Ref. [239].

Fig. 8.3 presents cross sections for dissociative excitation of the $B\ ^1\Sigma_u^+$, $C\ ^1\Pi_u$, $B'\ ^1\Sigma_u^+$, $b\ ^3\Sigma_u^+$, $e\ ^3\Sigma_u^+$, and $c\ ^3\Pi_u$ electronic states of H_2. Each transition shows a substantial dependence on the initial vibrational level. Aside from the repulsive $b\ ^3\Sigma_u^+$ state, which is the most important pathway to direct dissociation, the cross sections for dissociative excitation are generally small. For many electronic states, the dissociative excitation cross section for scattering on the $v = 0$ level of the $X\ ^1\Sigma_g^+$ state is an order of magnitude smaller than for scattering on some of the excited vibrational levels. For the singlet states, previous calculations of these cross sections were also performed by Celiberto *et al.* [70] using the impact-parameter method, with the comparison being essentially the same as seen in Fig. 8.1 for the total excitation cross sections.

Aside from the R-matrix calculations of Trevisan and Tennyson [72–74] discussed in the previous chapter, the only previous calculations of low-energy dissociation of vibrationally-excited H_2 and D_2 through the $b\ ^3\Sigma_u^+$ state are the semiclassical calculations of Celiberto *et al.* [70], which utilised the Gryziński method to treat the electronic dynamics, and the standard dissociation formalism with the Franck-Condon (FC) approximation to treat the nuclear dynamics. The

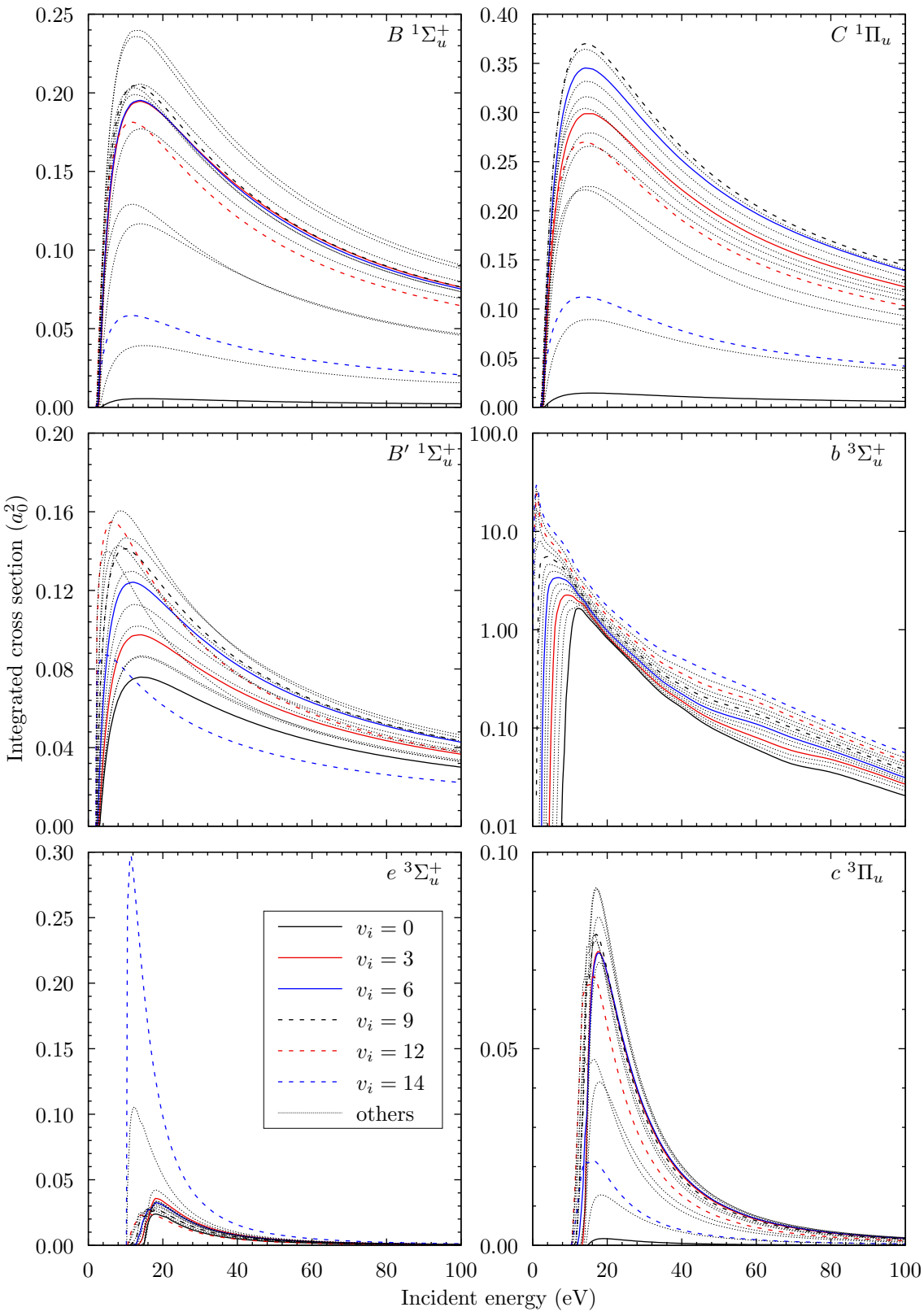

Figure 8.3: Electron-impact cross sections for dissociative excitation of the $B\,^1\Sigma_u^+$, $C\,^1\Pi_u$, $B'\,^1\Sigma_u^+$, $b\,^3\Sigma_u^+$, $e\,^3\Sigma_u^+$, and $c\,^3\Pi_u$ electronic states of H_2. Each line represents a different initial vibrational level in the $X\,^1\Sigma_g^+$ ground electronic state.

FC approximation assumes the electronic excitation cross section is independent of R, making it more inaccurate for the higher vibrational levels with more diffuse wave functions. Fig. 8.4 compares the MCCC $b\ ^3\Sigma_u^+$ cross sections for scattering on all bound vibrational levels of H_2 with the results of Celiberto *et al.* [70]. The approximate methods utilised by Celiberto *et al.* [70] do not correctly model the significant dependence on vibrational level.

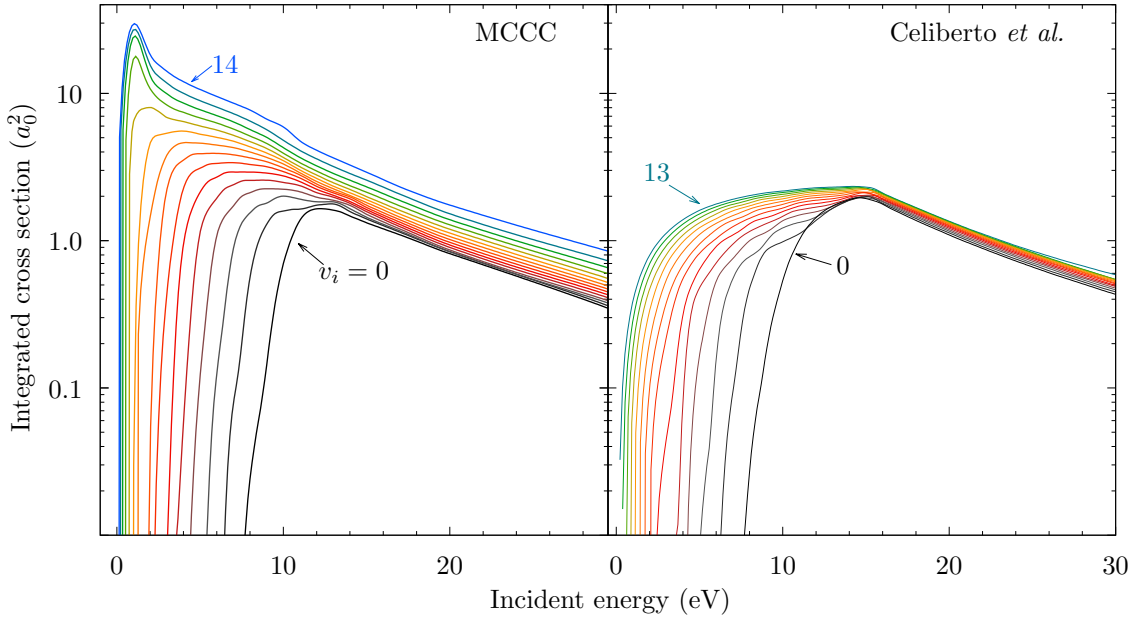

Figure 8.4: Comparison of the $X\ ^1\Sigma_g^+(v) \rightarrow b\ ^3\Sigma_u^+$ dissociation cross sections calculated by Celiberto *et al.* [70] with the molecular convergent close-coupling (MCCC) calculations [7]. The cross section increases with initial vibrational level from $v = 0$ to 14 (Celiberto et al. include only up to $v = 13$).

8.2 Dissociation into neutral fragments

Fig. 8.5 presents the total cross section for dissociation of vibrationally-excited H_2 into neutral fragments. These were obtained using the MCCC vibrationally-resolved cross sections, considering direct dissociative excitation, predissociation, and dissociation following radiative decay, and were published in Ref. [12]. At low energies, the dissociation cross section is entirely comprised of the $b\ ^3\Sigma_u^+$ excitation. The unusual shapes present in some curves are the result of higher electronic-state excitations becoming open as the incident energy increases. Over

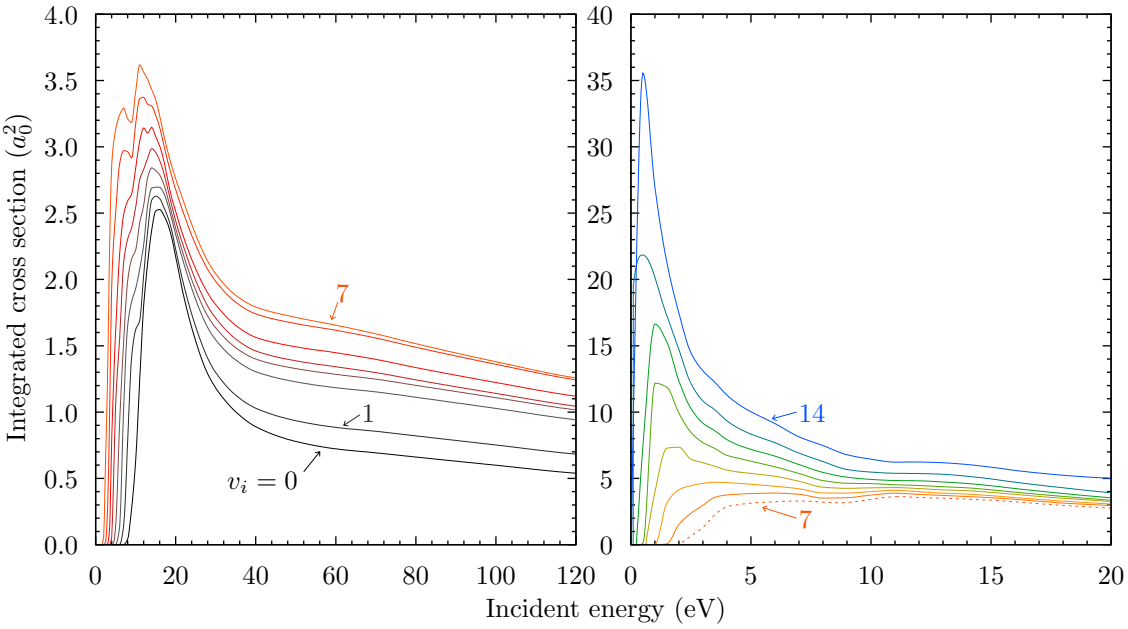

Figure 8.5: Electron-impact dissociation cross section for scattering on all bound vibrational levels of the H_2 ground electronic state. The cross sections rise monotonically with increasing vibrational level v_i.

the entire energy range, the dissociation cross sections are significantly enhanced for scattering on excited vibrational levels, illustrating the importance of vibrationally-resolved collision data for modelling environments where molecules are present in vibrationally-excited states, such as fusion plasmas. No previous calculations of the total neutral dissociation cross section have been performed over the entire range of incident energies, and only one (fairly old) experiment has been performed [240]. The measurements of Ref. [240] were used by Yoon *et al.* [221] to produce a recommended cross section for this process. Fig. 8.6 compares the present $v_i = 0$ neutral dissociation cross section with the recommended data of Yoon *et al.* [221]. At low energies there is good agreement between the two, while between 20 and 60 eV the MCCC calculations are somewhat lower than the measurements. Given the size of the experimental error bars the discrepancy is not cause for particular concern, and considering the age of the measurements (close to 60 years old at time of writing) the level of agreement is impressive. Nonetheless, it would be desirable to have updated measurements taken in order to resolve the discrepancies, however slight, and determine the most accurate cross section for neutral dissociation. Fig. 8.6 also shows the contributions from the triplet and singlet excitations to the $v_i = 0$ dissociation cross section. The triplet excitations

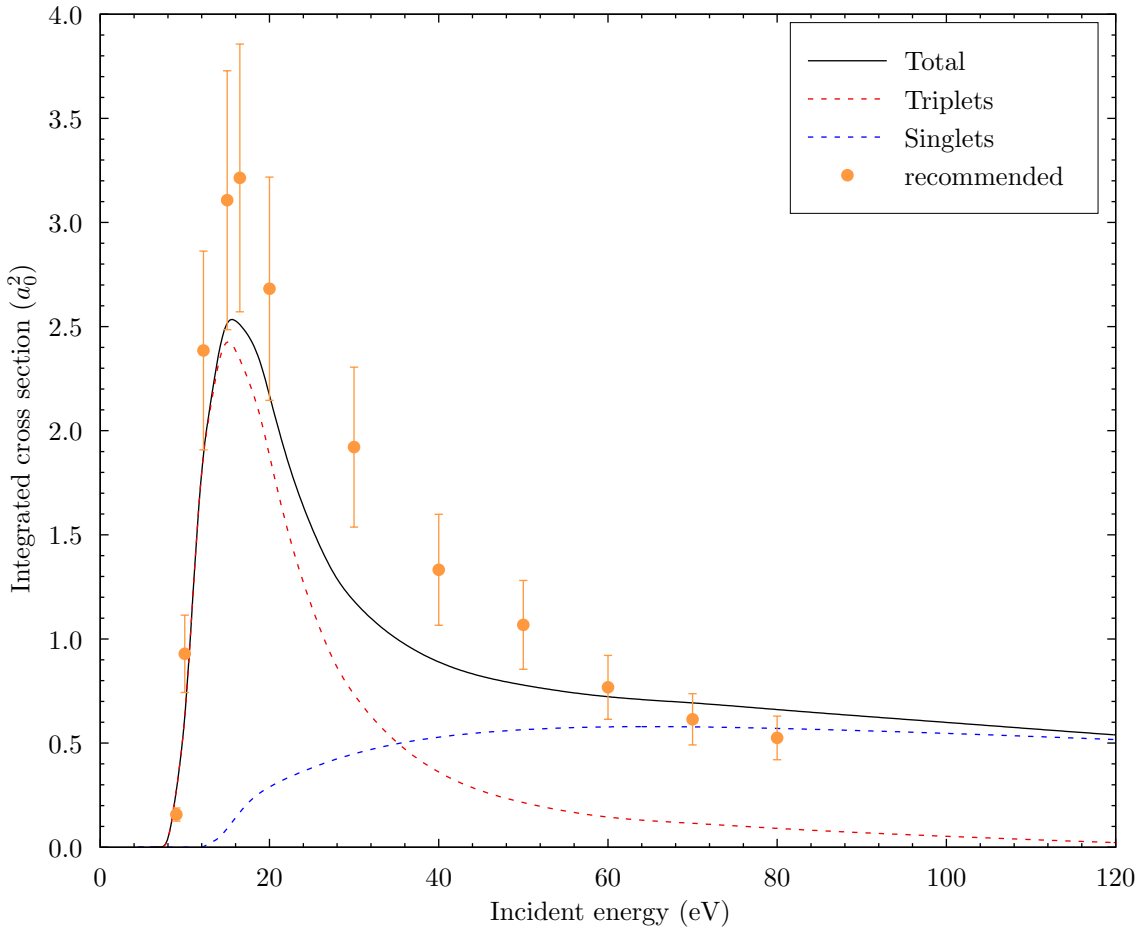

Figure 8.6: Electron-impact dissociation cross section for scattering on the ground vibrational level of the $X\,^1\Sigma_g^+$ state of H_2. Comparison is made with the recommended data of Yoon *et al.* [221]. The contributions from the triplet and singlet excitations is also shown.

are most important at lower incident energies, while above approximately 40 eV the singlet excitations are more important.

Figs. 8.7–8.11 present cross sections for excitation of bound vibrational levels in the $B\,^1\Sigma_u^+$, $C\,^1\Pi_u$, $c\,^3\Pi_u$, $a\,^3\Sigma_g^+$, and $EF\,^1\Sigma_g^+$ states of H_2. For all states, not only the magnitude of the total cross section, but also the distribution of excited final levels is heavily dependent on the initial vibrational levels. For H_2 excitation processes resolved in the final vibrational level, these are the first data to be published [7], and will allow for the first ever collisional-radiative models to be constructed for H_2 with full vibrational resolution. Similar cross sections have been produced for excitation of each of the $n = 2$–3 electronic states (refer to Table 7.4), and are available online at `mccc-db.org`.

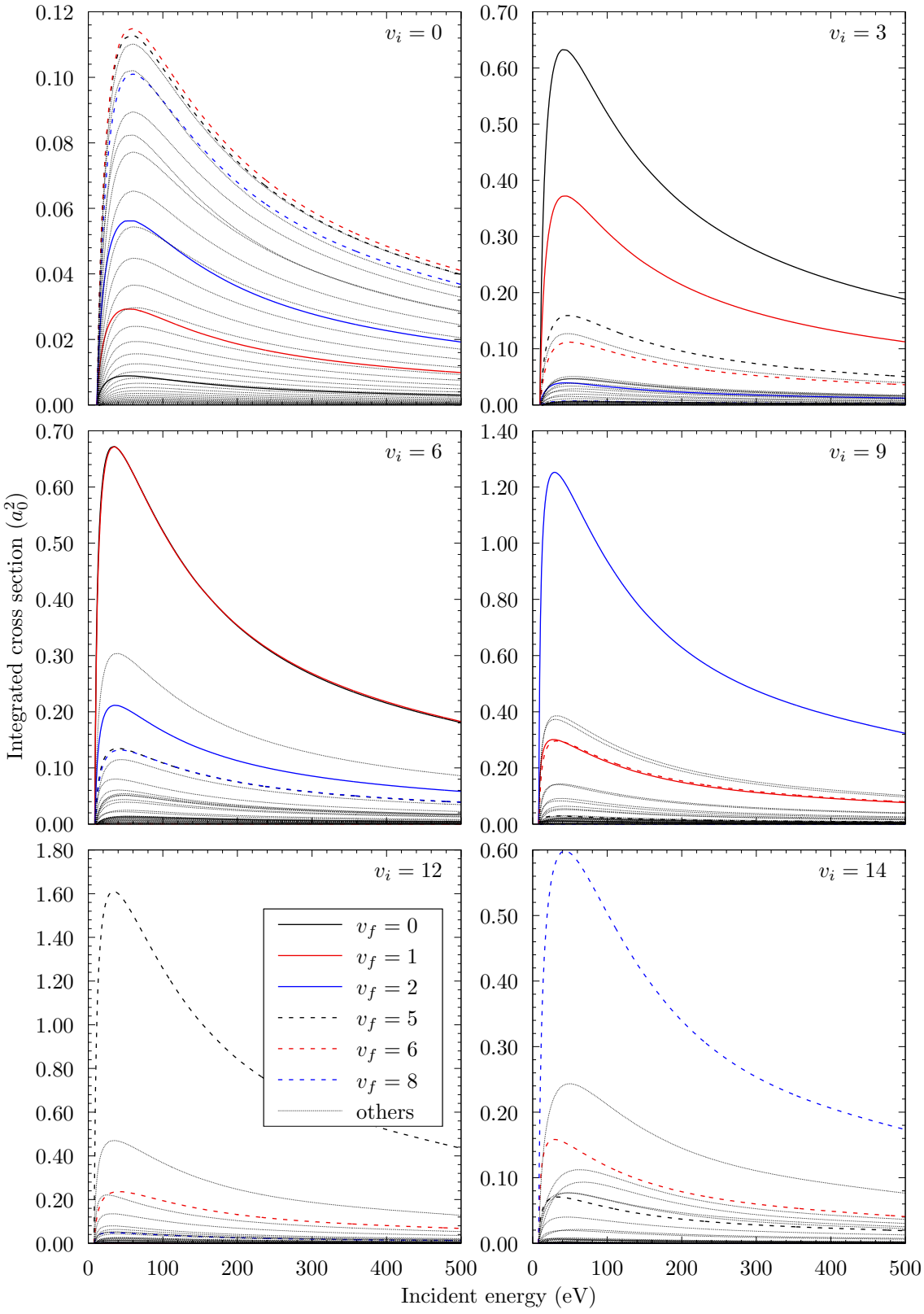

Figure 8.7: Electron-impact cross sections for excitation of bound vibrational levels in the $B\ ^1\Sigma_u^+$ state of H_2. Each panel represents a different initial vibrational level in the $X\ ^1\Sigma_g^+$ ground electronic state, and each line a different final vibrational level in the $B\ ^1\Sigma_u^+$ state.

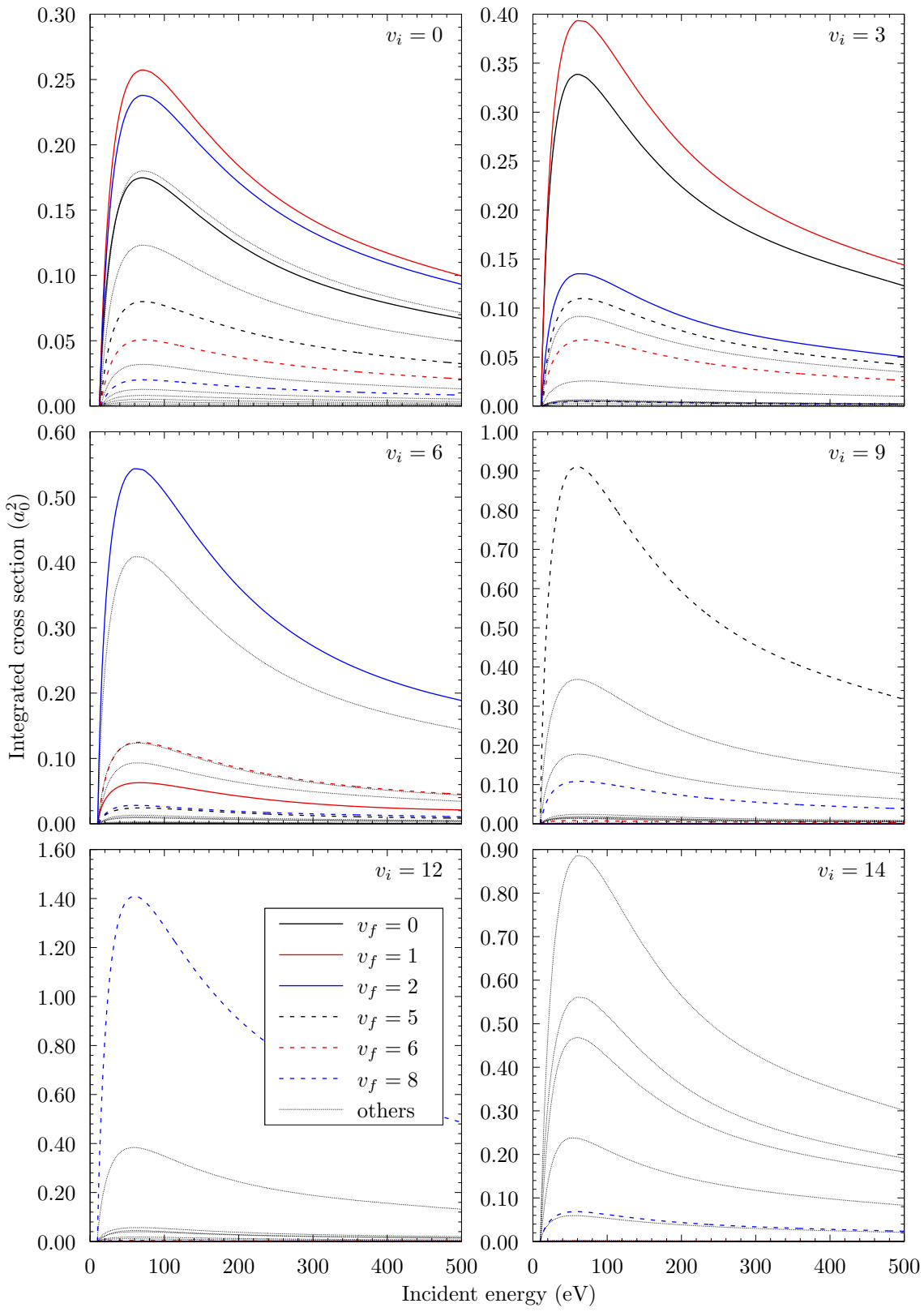

Figure 8.8: Electron-impact cross sections for excitation of bound vibrational levels in the $C\ ^1\Pi_u$ state of H_2. Each panel represents a different initial vibrational level in the $X\ ^1\Sigma_g^+$ ground electronic state, and each line a different final vibrational level in the $C\ ^1\Pi_u$ state.

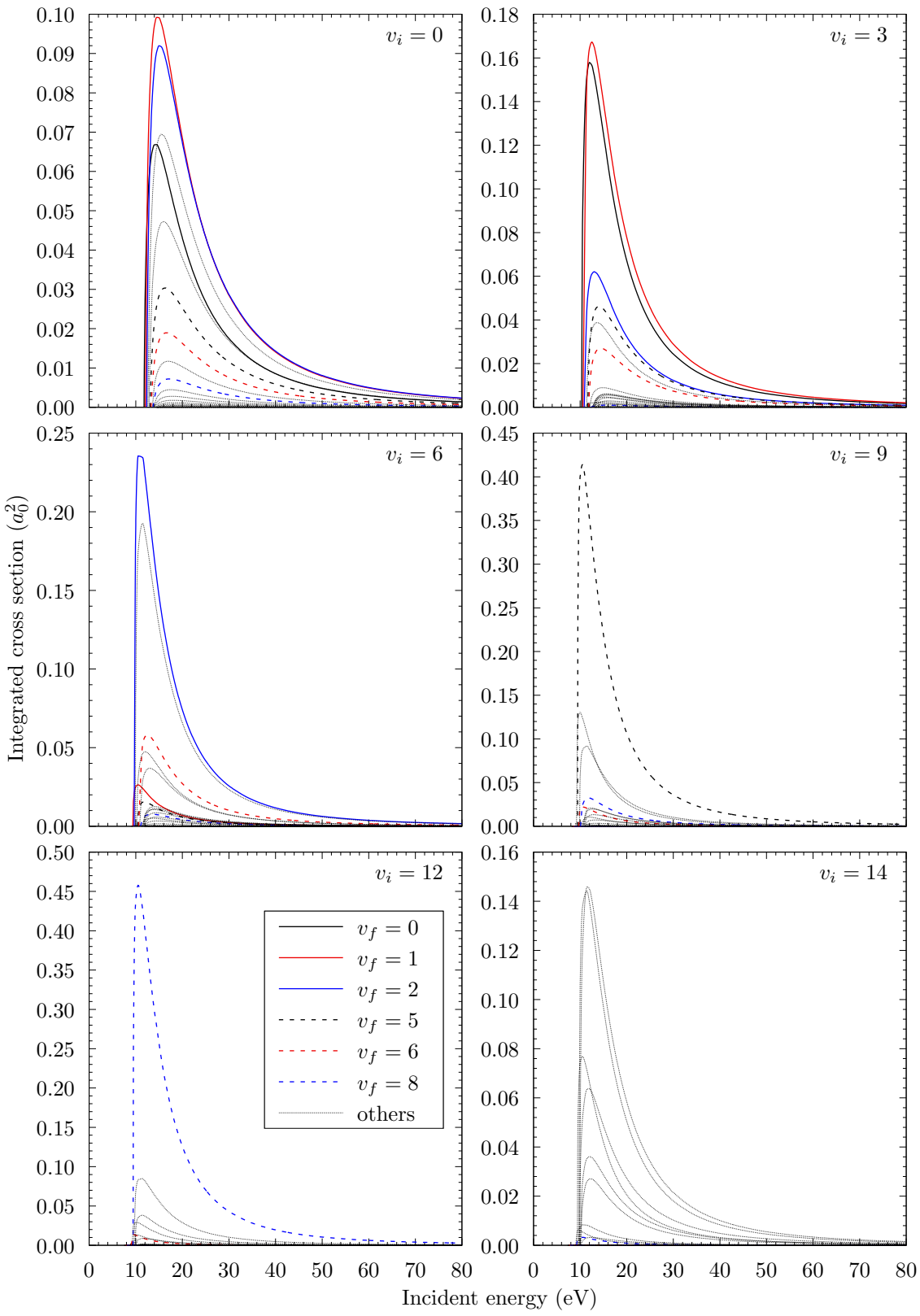

Figure 8.9: Electron-impact cross sections for excitation of bound vibrational levels in the $c\ ^3\Pi_u$ state of H_2. Each panel represents a different initial vibrational level in the $X\ ^1\Sigma_g^+$ ground electronic state, and each line a different final vibrational level in the $c\ ^3\Pi_u$ state.

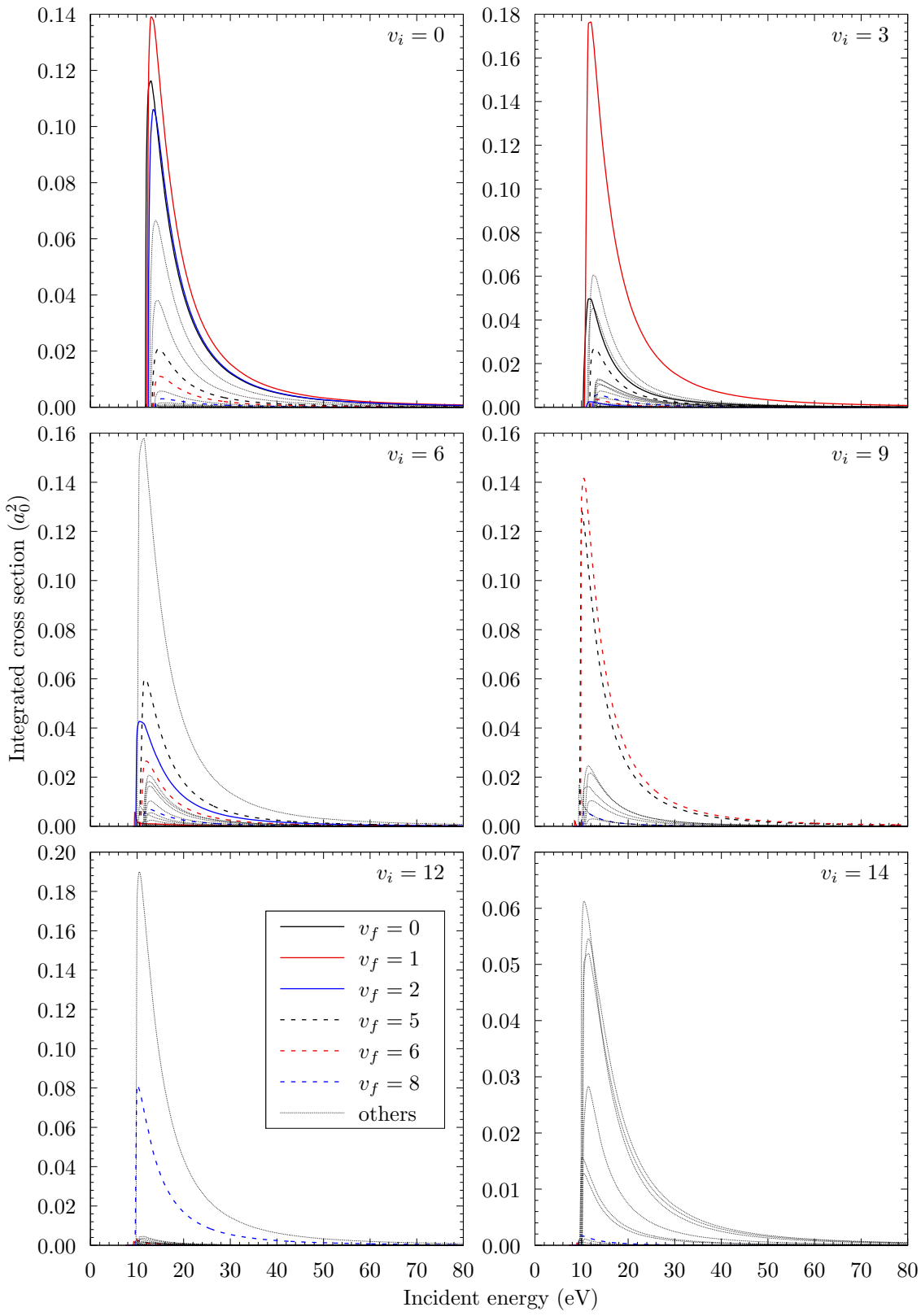

Figure 8.10: Electron-impact cross sections for excitation of bound vibrational levels in the $a\ ^3\Sigma_g^+$ state of H_2. Each panel represents a different initial vibrational level in the $X\ ^1\Sigma_g^+$ ground electronic state, and each line a different final vibrational level in the $a\ ^3\Sigma_g^+$ state.

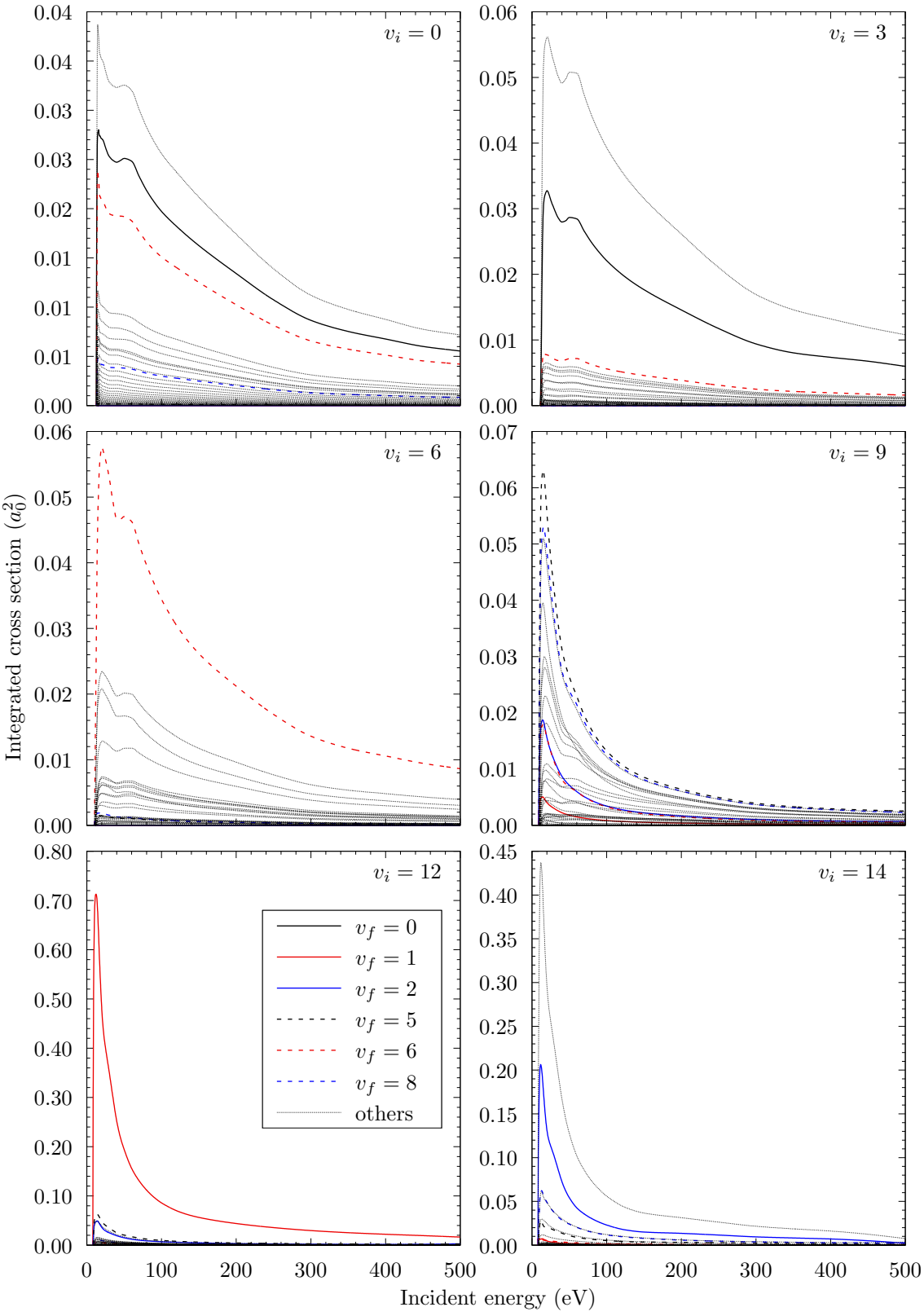

Figure 8.11: Electron-impact cross sections for excitation of bound vibrational levels in the $EF\ ^1\Sigma_g^+$ state of H_2. Each panel represents a different initial vibrational level in the $X\ ^1\Sigma_g^+$ ground electronic state, and each line a different final vibrational level in the $EF\ ^1\Sigma_g^+$ state.

8.2.1 Isotopic effects

This section investigates the similarities and differences between cross sections for H_2 and its isotopologues. These results have been published in Ref. [6]. Fig. 8.12 presents cross sections for dissociative excitation and total electronic excitation (summed over v_f, including dissociative excitation) of the $B\ ^1\Sigma_u^+$, $B'\ ^1\Sigma_u^+$, $c\ ^3\Pi_u$, $h\ ^3\Sigma_g^+$ states from the $v_i = 0$ level of the $X\ ^1\Sigma_g^+$ state in each isotopologue. The

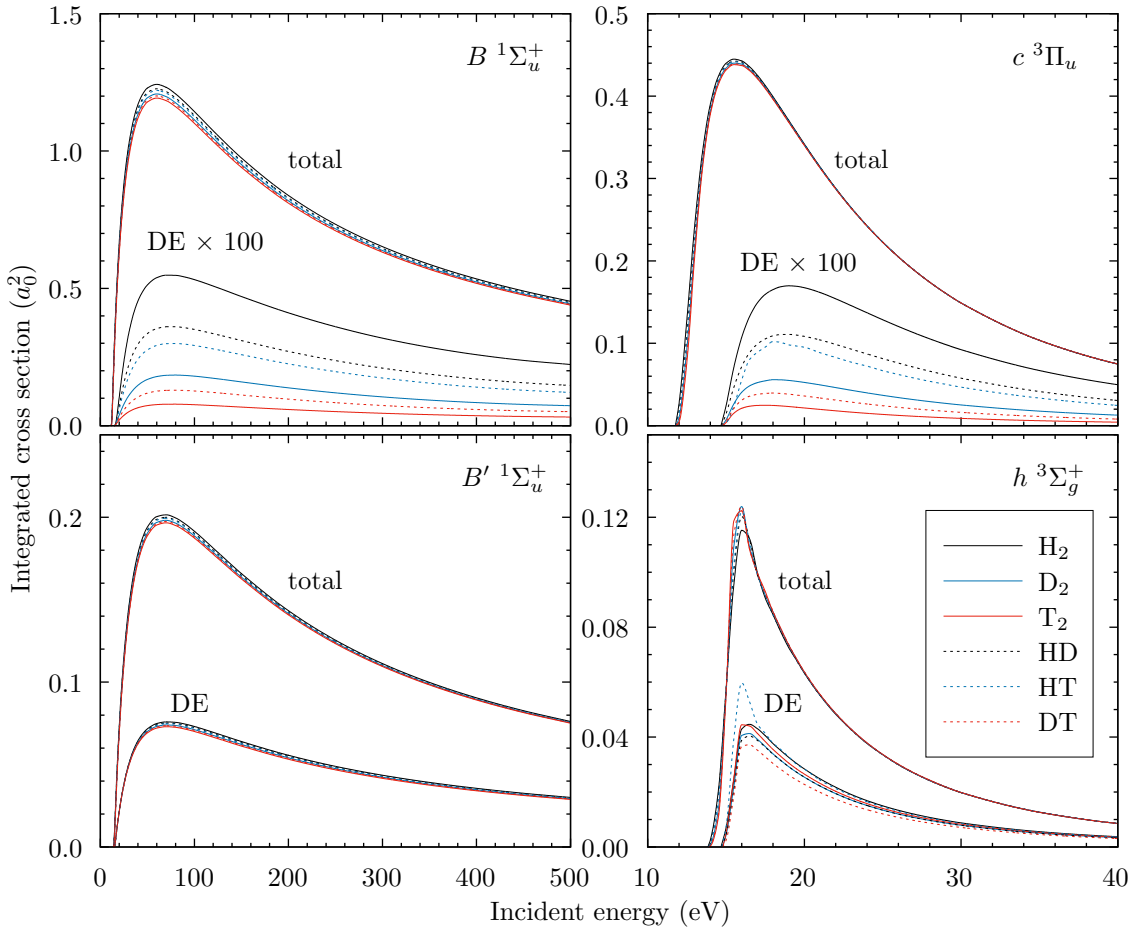

Figure 8.12: Electron-impact cross sections for total electronic excitation (summed over final vibrational levels) and dissociative excitation (DE) of the $B\ ^1\Sigma_u^+$, $B'\ ^1\Sigma_u^+$, $c\ ^3\Pi_u$, and $h\ ^3\Sigma_g^+$ states of H_2, D_2, T_2, HD, HT, and DT from the $X\ ^1\Sigma_g^+(v = 0)$ state. For the $B\ ^1\Sigma_u^+$ and $c\ ^3\Pi_u$ states, the DE cross sections have been multiplied by a factor of 100 for clarity.

total electronic excitation cross sections show little dependence on the molecular mass, with any small differences (e.g. only up to 5% difference between H_2 and T_2 for the $B\ ^1\Sigma_u^+$ excitation) being a result of the variation in mean internuclear separation of the $v_i = 0$ vibrational wave function as the reduced mass is increased.

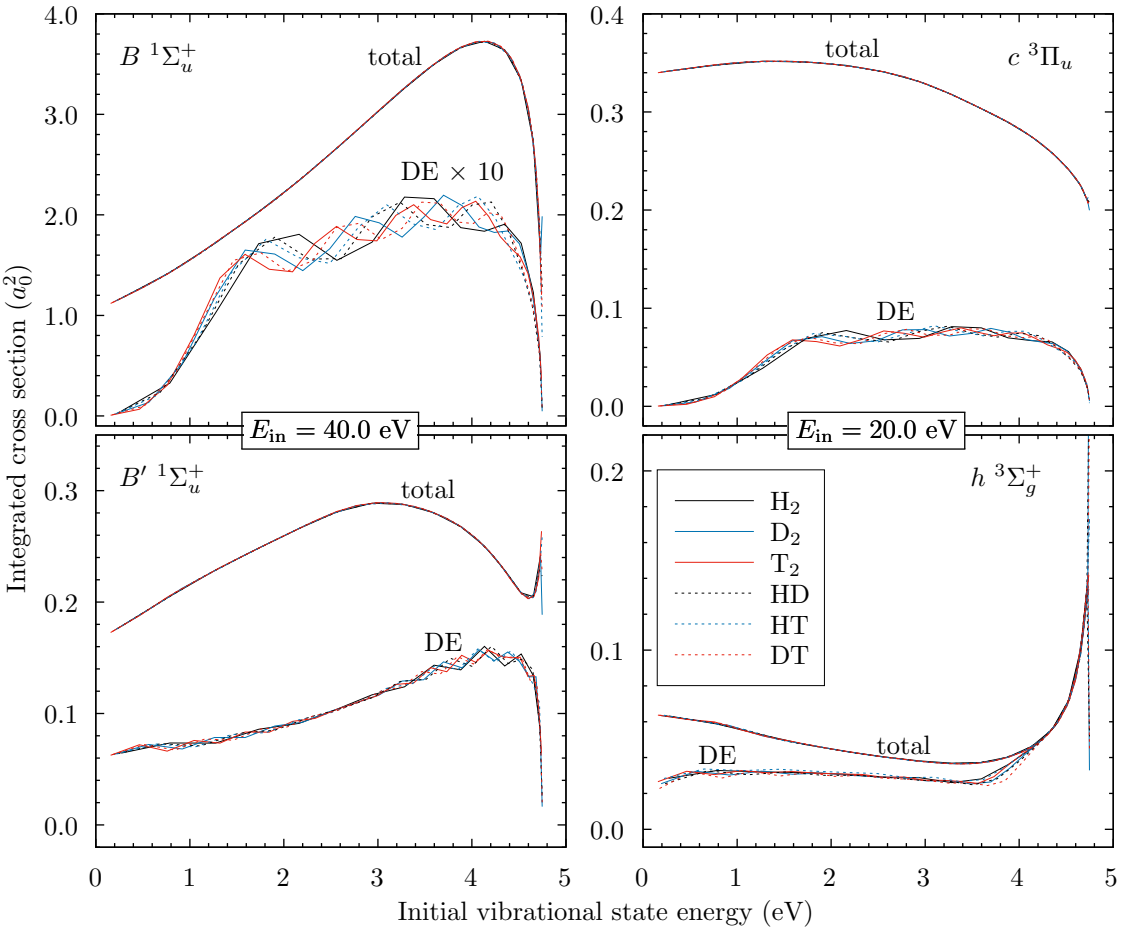

Figure 8.13: Electron-impact cross sections for total electronic excitation and dissociative excitation (DE) of the $B\ ^1\Sigma_u^+$, $B'\ ^1\Sigma_u^+$, $c\ ^3\Pi_u$, and $h\ ^3\Sigma_g^+$ states of H_2, D_2, T_2, HD, HT, and DT from excited vibrational levels in the $X\ ^1\Sigma_g^+$ state. The cross sections are presented as a function of the initial vibrational level energy (relative to the $X\ ^1\Sigma_g^+$ equilibrium energy) at a fixed incident energy (40 and 20 eV). For the $B\ ^1\Sigma_u^+$ state, the DE cross sections have been multiplied by a factor of 10 for clarity.

The lack of substantial isotopic effects in the $v_i = 0$ total electronic excitation cross sections presented in Fig. 8.12 is common to all electronic states considered in this work. The dissociative excitation cross sections for the $B\ ^1\Sigma_u^+$ and $c\ ^3\Pi_u$ states show significant variations depending on the isotopologue. For all states considered in this work, those which support a larger number of bound vibrational levels (and therefore have a smaller dissociative excitation cross section due to the larger sum of Franck-Condon overlaps) generally have larger isotopic effects in the dissociative excitation cross section.

Fig. 8.13 presents the same cross sections as Fig. 8.12 for scattering on all

initial vibrational levels at a fixed incident energy (40 eV for the $B\ ^1\Sigma_u^+$ and $B'\ ^1\Sigma_u^+$ states and 20 eV for the $c\ ^3\Pi_u$ and $h\ ^3\Sigma_g^+$ states). The results are shown as a function of the energy of the initial vibrational state (relative to the equilibrium electronic energy of the $X\ ^1\Sigma_g^+$ state) to allow comparison between the isotopologues which each have a different number of bound vibrational levels. When compared in this way it can be seen that there are essentially no isotopic effects in the total electronic excitation cross sections, and only relatively minor variations in the dissociative excitation cross sections. However, there will likely be important isotopic effects in applications which require the use of fully vibrationally-resolved collision data (such as CR modelling) due to the distinct vibrational spectra of each molecule.

In low-temperature plasmas, one of the most important electronically-inelastic processes is the excitation of the repulsive $b\ ^3\Sigma_u^+$ state. Below around 12 eV, this process is the only mechanism for dissociation of H_2 into neutral fragments [18]. Fig. 8.14 illustrates the vibrational-level dependence of this cross section for scattering on D_2, and the isotopic dependence for scattering on the $v = 0$ level of each isotopologue. There is a strong dependence on the initial vibrational level, which

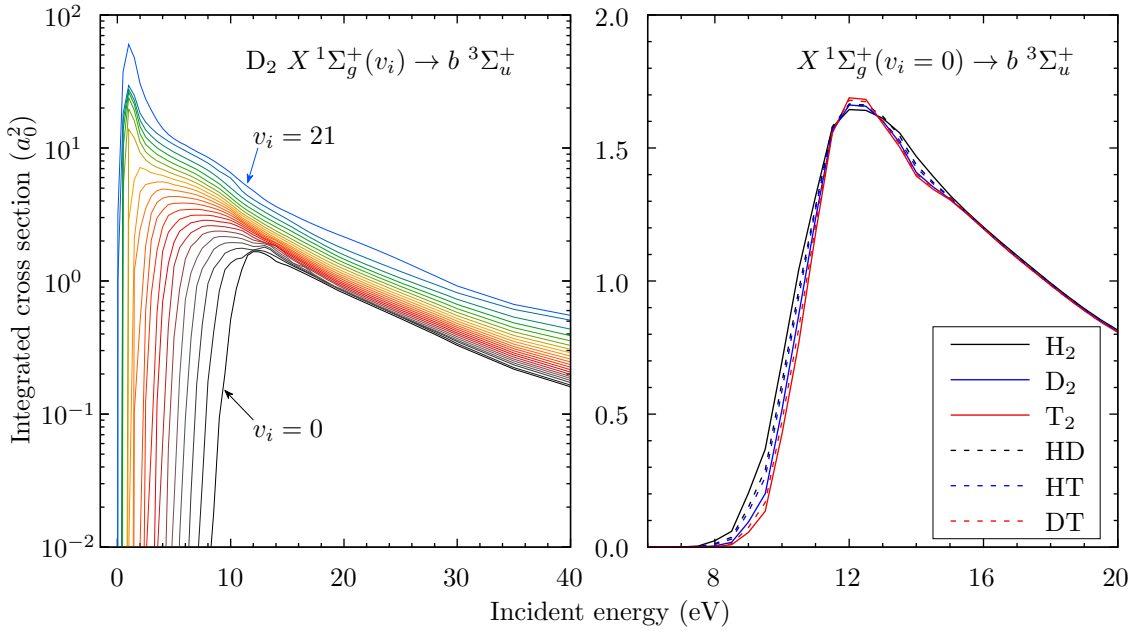

Figure 8.14: Cross sections for dissociation via excitation of the repulsive $b\ ^3\Sigma_u^+$ state. Left: dependence of the cross section on the initial vibrational level v for D_2. Right: isotopic effect in the $v = 0$ cross section.

is similar for scattering on all isotopologues. As seen for the transitions discussed

in previous paragraphs, there is only a small isotopic effect (note that for the repulsive state the dissociative and total excitation cross sections are equivalent), and in this case it manifests only at energies below 16 eV.

8.3 Scattering on the $n = 2$–3 excited electronic states

This section presents results for scattering on the $n = 2$–3 states of H_2. At present, calculations have been performed only for scattering on the $v = 0$ level of each state, with results summed over final vibrational levels. The calculation details and convergence studies were described in Chapter 7. The results and analysis presented here were published in Ref. [5].

8.3.1 Previous calculations

Until recently, the available data for scattering on excited electronic states of H_2 was limited to a handful of calculations using a variety of methods, none of which considered the entire range of transitions considered here. Sartori *et al.* [94, 95] used the Schwinger multichannel (SMC) method to obtain cross sections for elastic and superelastic scattering on the $c\ ^3\Pi_u(v = 0)$ and $a\ ^3\Sigma_g^+(v = 0)$ states, as well as the $c\ ^3\Pi_u(v = 0) \rightarrow a\ ^3\Sigma_g^+$ excitation. Rescigno & Orel (as cited in Ref. [241]) applied the first Born approximation (FBA) to study the $c\ ^3\Pi_u(v = 0) \rightarrow a\ ^3\Sigma_g^+$ transition. Joshipura *et al.* [97] used the approximate complex scattering potential-ionisation contribution (CSP-ic) method to estimate the elastic, ionisation, and grand-total cross sections for scattering on the $c\ ^3\Pi_u(v = 0)$ state. Wünderlich [99] used the classical Gryziński approximation to obtain ionisation cross sections for scattering on the ground state and all $n = 2$ states of H_2, including ionisation of excited vibrational levels. Laricchiuta *et al.* [96] used the semiclassical impact-parameter (IP) method to calculate fully vibrationally-resolved cross sections for a few dipole-allowed transitions from the $c\ ^3\Pi_u$ and $a\ ^3\Sigma_g^+$ states, while Celiberto *et al.* [70] provided cross sections calculated with the same method for the $B\ ^1\Sigma_u^+ \rightarrow I\ ^1\Pi_g$ transition. Recently, Meltzer and Tennyson [116] applied the UKRMol+ method in the FN approximation

(with $R = 2.0\ a_0$) to produce a set of cross sections for scattering on the first 12 excited states of H_2. The UKRMol+ calculations utilise a close-coupling expansion with 85 target states and a projectile partial-wave expansion with $L_{\max} = 6$, but do not apply the analytical Born completion (ABC) method to account for higher partial-wave contributions. As discussed in Sec. 7.3.2, the MCCC calculations for the dipole-allowed transitions with $L_{\max} = 6$ are in substantial error due to insufficiently large $L_{\max}$, so the UKRMol+ results should be similarly inaccurate for these transitions. The present MCCC calculations are the only attempt so far to produce a set of cross sections for superelastic, elastic, excitation, and ionisation processes using the same theoretical method. The calculations described in this section are summarised in Table 8.1. No measurements for scattering on excited states of H_2 have been reported.

Table 8.1: A summary of the various theoretical approaches which have been applied to electrons scattering on excited electronic states of H_2. Abbreviations for the scattering methods are as defined in the text.

Reference	Method	Results available
Sartori *et al.* [94, 95]	SMC	Superelastic, elastic, $c\ ^3\Pi_u \rightarrow a\ ^3\Sigma_g^+$
Joshipura *et al.* [97]	CSP-ic	Ionisation, grand-total (scattering on $c\ ^3\Pi_u$ only)
Wünderlich [99]	Gryziński	Ionisation of $n = 1$–2 states
Laricchiuta *et al.* [96]	IP	$c\ ^3\Pi_u \rightarrow \left\{h\ ^3\Sigma_g^+, g\ ^3\Sigma_g^+\right\}$, $a\ ^3\Sigma_g^+ \rightarrow d\ ^3\Pi_u$
Celiberto *et al.* [70]	IP	$B\ ^1\Sigma_u^+ \rightarrow I\ ^1\Pi_g$
Rescigno and Orel [241]	FBA	$c\ ^3\Pi_u \rightarrow a\ ^3\Sigma_g^+$
Meltzer and Tennyson [116]	UKRMol+	Superelastic, elastic, excitation of all $n = 2$ states and half of the $n = 3$ states (scattering on $n = 2$ and half of the $n = 3$ states)
This work [5]	MCCC	Superelastic, elastic, ionisation, grand-total, excitation of all $n = 1$–3 states (scattering on $n = 2$ states)

8.3.2 Elastic, ionisation, and grand-total cross sections

Figs. 8.15, 8.16, and 8.17 present elastic, ionisation, and grand-total cross sections for scattering on the $n = 2$ states, and compare with the available SMC [94, 95], CSP-ic [97], Gryziński [99], and UKRMol+ [116] calculations. The MCCC and

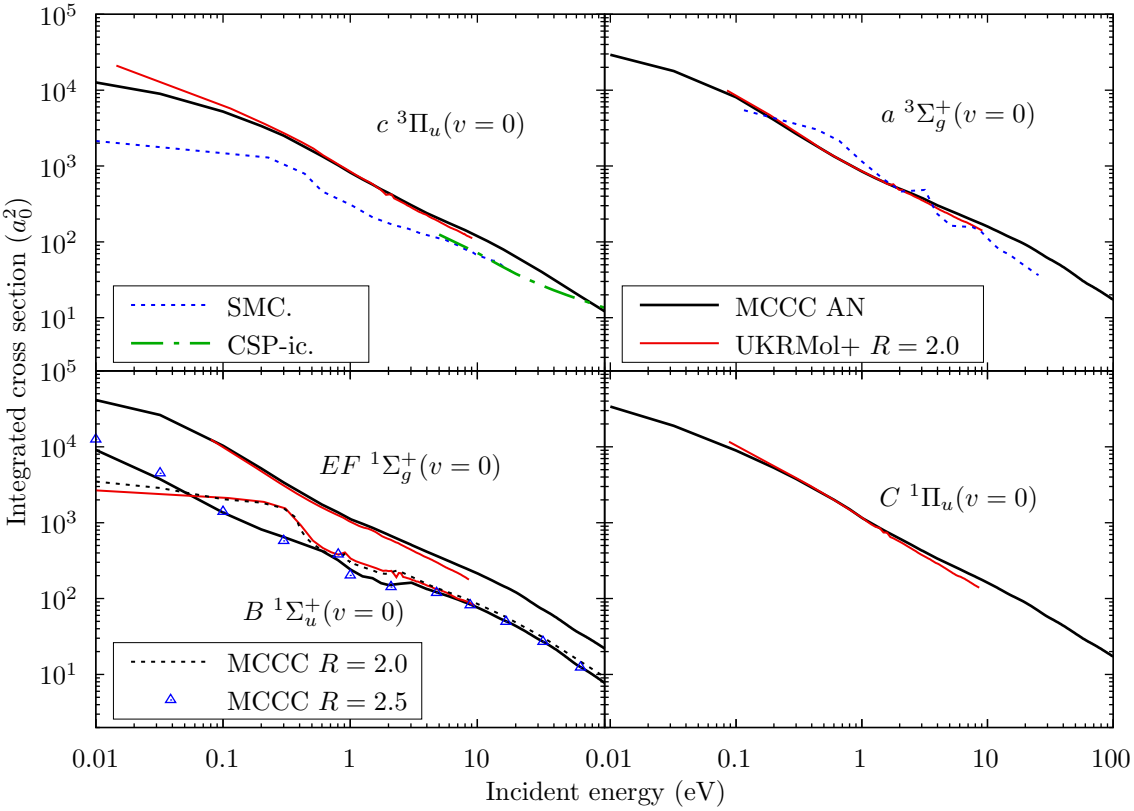

Figure 8.15: Elastic scattering cross sections for electrons scattering on the $B\ ^1\Sigma_u^+$, $c\ ^3\Pi_u$, $a\ ^3\Sigma_g^+$, $C\ ^1\Pi_u$, and $EF\ ^1\Sigma_g^+$ $(v = 0)$ states of H_2. Comparisons are made between the present adiabatic-nuclei (AN) MCCC results and the SMC [94, 95], CSP-ic [97], and UKRMol+ [116] calculations, where available. Fixed-nuclei MCCC cross sections with $R = 2.0$ and 2.5 a_0 are also shown for scattering on the $B\ ^1\Sigma_u^+$ state.

UKRMol+ calculations are in good agreement for elastic scattering on the $c\ ^3\Pi_u$, $a\ ^3\Sigma_g^+$, $C\ ^1\Pi_u$, and $EF\ ^1\Sigma_g^+$ states, and for the $a\ ^3\Sigma_g^+$ state the SMC results are in reasonable agreement with both MCCC and UKRMol+. For the $c\ ^3\Pi_u$ state, both the SMC and CSP-ic calculations are lower than the MCCC and UKRMol+ results, particularly at lower incident energies. The MCCC and UKRMol+ results for elastic scattering on the $B\ ^1\Sigma_u^+$ are in disagreement below around 4 eV, with a pronounced difference in the shape of the cross section below 1 eV. The reason

for this is that the UKRMol+ calculations utilise the FN approximation with $R = 2.0\ a_0$ for all transitions, while the $v = 0$ level of the $B\ ^1\Sigma_u^+$ state has a mean internuclear separation of $R = 2.518\ a_0$ (see Table 7.4). To illustrate the effect of choosing $R = 2.0\ a_0$ for scattering on this state, Fig. 8.15 also includes the $B\ ^1\Sigma_u^+$ elastic-scattering cross sections obtained from FN MCCC calculations with $R = 2.0$ and $2.5\ a_0$. The $R = 2.0\ a_0$ cross section reproduces the UKRMol+ result, while the $R = 2.5\ a_0$ cross section follows the adiabatic-nuclei (AN) MCCC result.

In Fig. 8.16, the CSP-ic cross section for ionisation of the $c\ ^3\Pi_u(v = 0)$ state is in good agreement with the MCCC calculations, which is unexpected given the approximate nature of the CSP-ic calculations. The Gryziński ionisation cross sections are in good agreement with MCCC for the $c\ ^3\Pi_u$, $B\ ^1\Sigma_u^+$, and $C\ ^1\Pi_u$ states, but are somewhat larger than MCCC for the $EF\ ^1\Sigma_g^+$ and $a\ ^3\Sigma_g^+$ states.

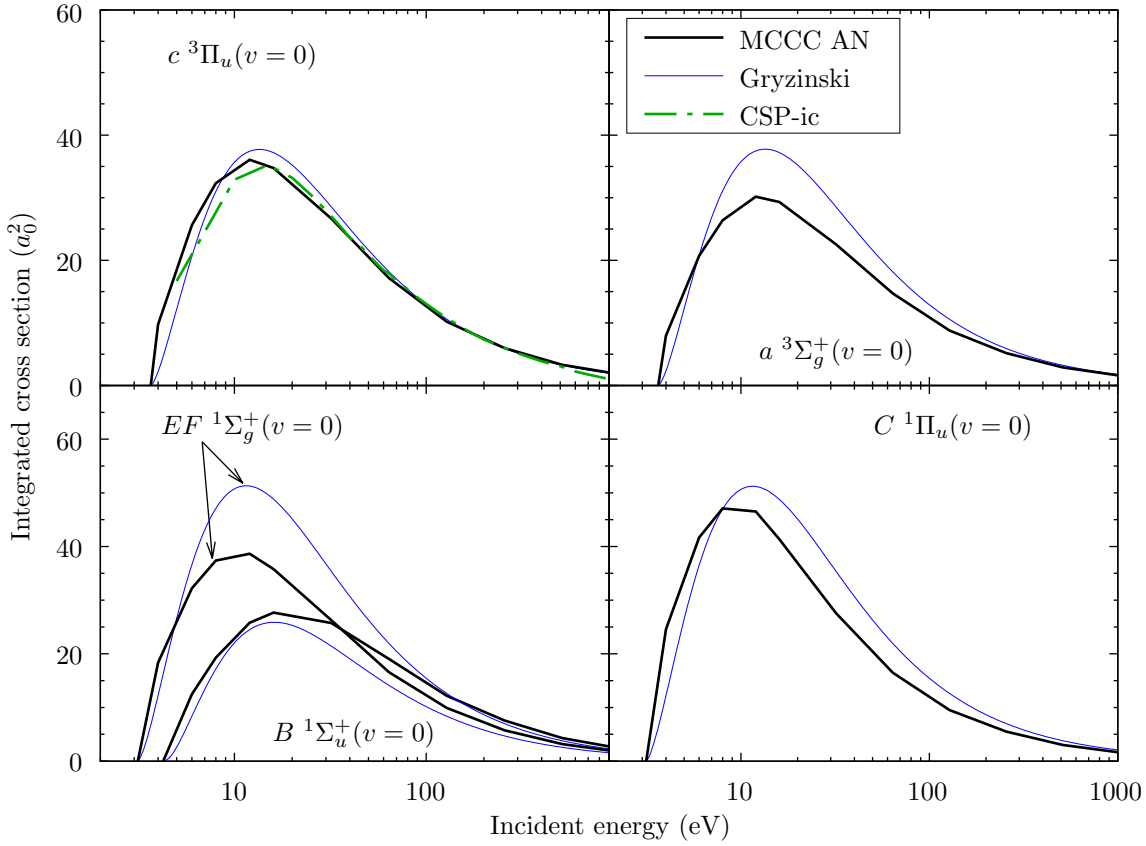

Figure 8.16: Ionisation cross sections for electrons scattering on the $B\ ^1\Sigma_u^+$, $c\ ^3\Pi_u$, $a\ ^3\Sigma_g^+$, $C\ ^1\Pi_u$, and $EF\ ^1\Sigma_g^+$ $(v = 0)$ states of H_2. Comparisons are made between the present MCCC results and the CSP-ic [97] and Gryziński [99] calculations, where available.

In Fig. 8.17, the CSP-ic $c\ ^3\Pi_u$ GTCS is about a factor of two lower than the MCCC cross section. Given the reasonable agreement between the CSP-ic and MCCC elastic and ionisation cross sections, this discrepancy must be due to the cross sections for discrete excitations being underestimated in the CSP-ic calculations. No previous calculations have been attempted of the GTCS for scattering on the other excited electronic states, so in the right panel of Fig. 8.17 the MCCC results are presented alone. The $EF\ ^1\Sigma_g^+$ state has the largest total cross section, being up to an order of magnitude larger than the $B\ ^1\Sigma_u^+$ total cross section. The $c\ ^3\Pi_u$, $a\ ^3\Sigma_g^+$, and $C\ ^1\Pi_u$ total cross sections are all of similar magnitude. In contrast to scattering on the ground electronic state, where ionisation accounts for up to a half of the GTCS at higher energies [93], the GTCS for scattering on the excited states is up to two orders of magnitude larger than the ionisation cross section. The much smaller GTCS for scattering on the $B\ ^1\Sigma_u^+$ state, compared to the other excited states, can be explained by noting that the polarisability of the $B\ ^1\Sigma_u^+$ state is a factor of three smaller than that of the $c\ ^3\Pi_u$ state, and an order of magnitude smaller than the remaining excited-state polarisabilities (see Table 7.8).

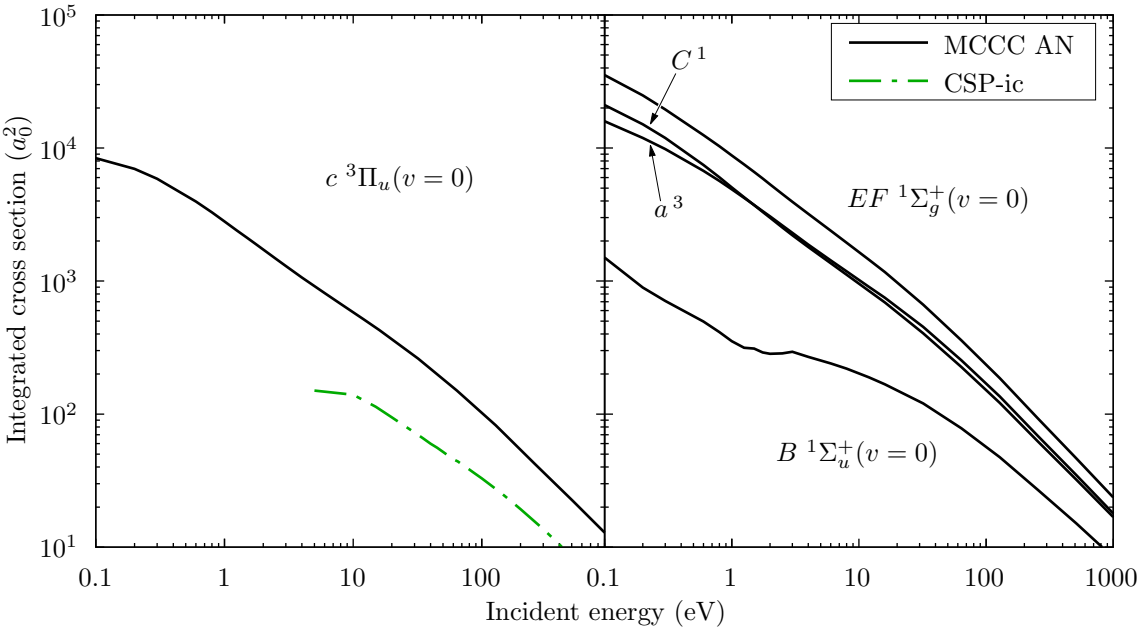

Figure 8.17: Grand-total cross sections for electrons scattering on the $B\ ^1\Sigma_u^+$, $c\ ^3\Pi_u$, $a\ ^3\Sigma_g^+$, $C\ ^1\Pi_u$, and $EF\ ^1\Sigma_g^+$ ($v = 0$) states of H_2. Comparisons are made between the present MCCC results and the CSP-ic [97] calculations, where available.

8.3.3 Superelastic scattering and excitation of $n = 2$ states

Fig. 8.18 presents cross sections for superelastic scattering and excitation of the $n = 2$ states from the $c\ ^3\Pi_u(v = 0)$ state. Since the vibrational levels of different

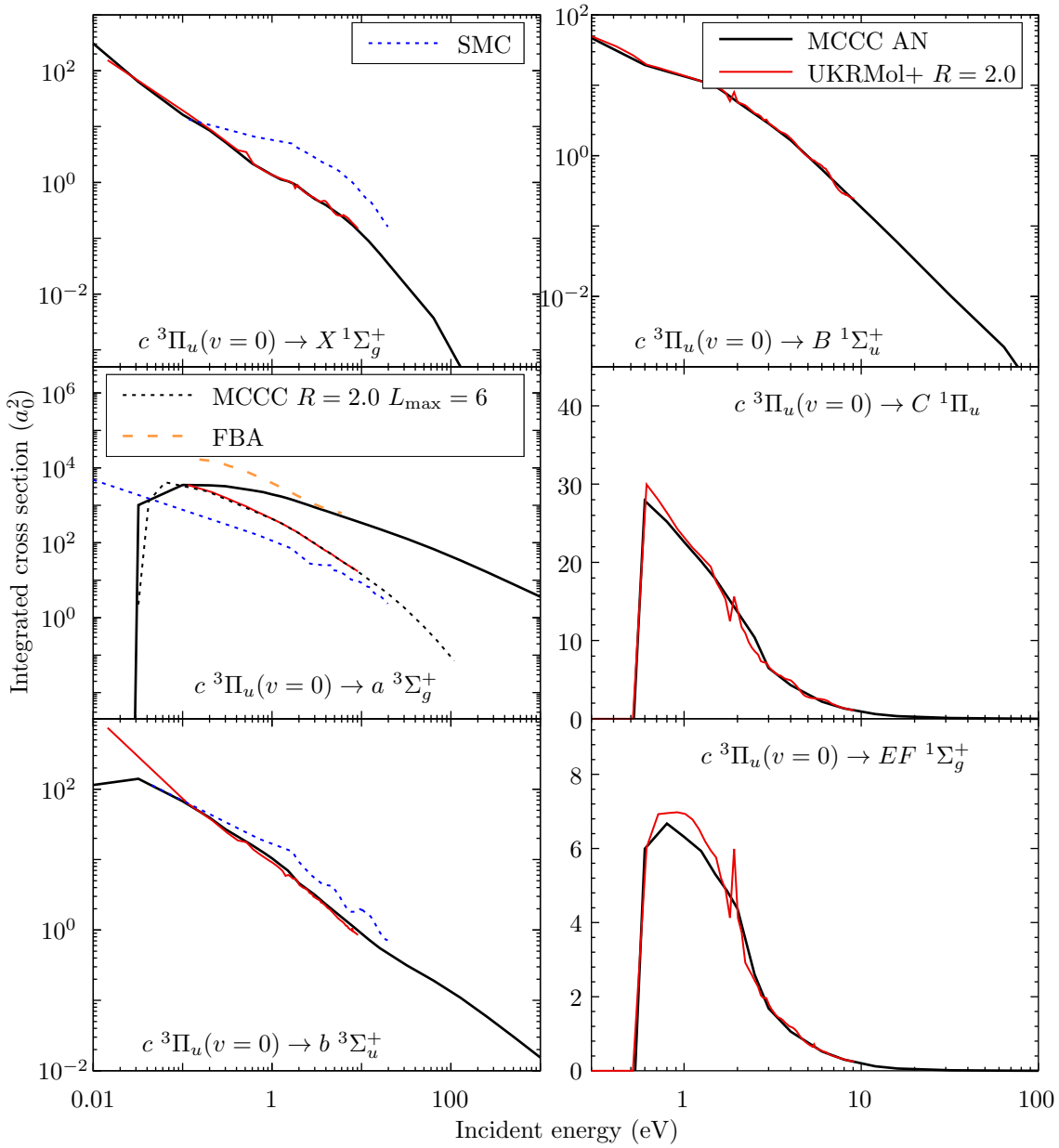

Figure 8.18: Electron-impact cross sections for superelastic scattering and excitation of $n = 2$ states from the $c\ ^3\Pi_u(v{=}0)$ state of H_2. The MCCC results are compared with the UKRMol+ [116], SMC [94, 95], and FBA [241] calculations, where available. The FN ($R = 2.0$) MCCC cross section with $L_{\max}{=}6$ and no Born completion is also shown for the dipole-allowed transitions for proper comparison with the UKRMol+ results.

electronic states overlap, cross sections which are summed over final vibrational levels will contain some contribution from the excitation of levels which are above the initial $c\ ^3\Pi_u(v=0)$ state. The $X\ ^1\Sigma_g^+$ and $b\ ^3\Sigma_u^+$ states are sufficiently lower than the $c\ ^3\Pi_u$ state that this contribution is negligible, however the $B\ ^1\Sigma_u^+$ state has a number of bound vibrational levels which are above the $c\ ^3\Pi_u(v=0)$ state and hence the $c\ ^3\Pi_u(v=0) \rightarrow B\ ^1\Sigma_u^+$ transition can be considered only partially superelastic (in general, many of the electronic transitions between the $n = 2$ states are partially superelastic). For each transition, the present results are compared with results from the UKRMol+ calculations [116], and where available with the SMC [94, 95] and FBA [241] cross sections. For the spin-exchange transitions, there is excellent agreement between the MCCC and UKRMol+ calculations, with small differences at low incident energies arising from the present use of the AN method rather than the FN method utilised in the UKRMol+ calculations.

The dipole-forbidden $c\ ^3\Pi_u(v=0) \rightarrow b\ ^3\Sigma_u^+$ cross section is fast to converge with partial waves, and the ABC procedure is not important. Accordingly, there is good agreement with the UKRMol+ and SMC calculations for this transition, since neither method utilised large partial-wave expansions or the ABC method. The situation is different for the dipole-allowed $c\ ^3\Pi_u(v=0) \rightarrow a\ ^3\Sigma_g^+$ transition. As demonstrated in Fig. 7.7, this transition is fast to converge when the ABC method it utilised, but without it even a large partial-wave expansion with $L_{\max} = 20$ is not sufficient to reach convergence. The UKRMol+ cross section is practically the same as the $L_{\max} = 6$ MCCC cross section without ABC, which has been included in the figure for comparison, and above 1 eV the SMC result is similar. Due to the small difference in energy between these states, the cross section is very large and of similar magnitude to the elastic-scattering cross section. It converges to the Born cross section at relatively low energies, as demonstrated by the agreement between the MCCC and FBA calculations of Rescigno and Orel [241] above 1 eV. The large difference (up to an order of magnitude) between the UKRMol+ and converged MCCC results demonstrates the importance of confirming partial-wave convergence for dipole-allowed transitions.

Fig. 8.19 presents cross sections for superelastic scattering and excitation of the $n = 2$ states from the $a\ ^3\Sigma_g^+(v = 0)$ state. Again, the UKRMol+ and MCCC cross sections are in good agreement for the spin-exchange transitions, while for the dipole-allowed transitions (to the $c\ ^3\Pi_u$ and $b\ ^3\Sigma_u^+$ states) there are substantial

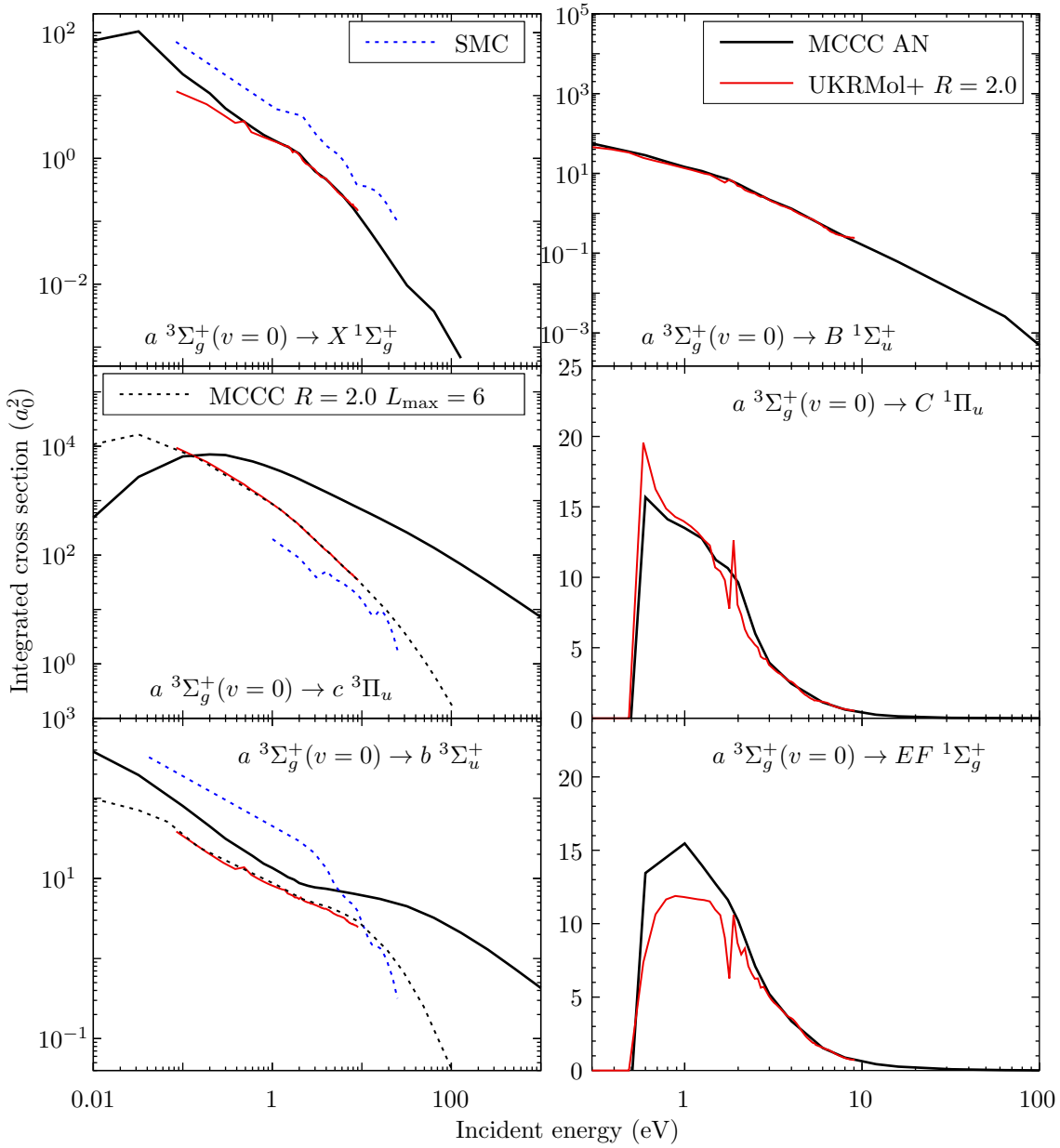

Figure 8.19: Electron-impact cross sections for superelastic scattering and excitation of states up to $n = 2$ from the $a\ ^3\Sigma_g^+(v = 0)$ state of H_2. Comparisons are made between the present MCCC results and the UKRMol+ [116] and SMC [94, 95] calculations, where available. The FN ($R = 2.0\ a_0$) MCCC cross section with $L_{\max} = 6$ and no analytical Born completion is also shown for the dipole-allowed transitions for proper comparison with the UKRMol+ results.

differences due to lack of partial-wave convergence in the UKRMol+ calculations. The $L_{\max} = 6$ MCCC cross section (without ABC) has been included for both of these transitions to demonstrate that the differences between the MCCC and UKRMol+ cross sections arise from partial-wave convergence issues. Where the SMC results are available, they are also significantly different from the MCCC cross sections.

Fig. 8.20 presents cross sections for superelastic scattering and excitation of the $n = 2$ states from the $C\ ^1\Pi_u$ and $EF\ ^1\Sigma_g^+$ states. For these transitions the only available results to compare with are the UKRMol+ calculations. As before, excellent agreement is seen between the MCCC and UKRMol+ calculations for the spin-exchange transitions. There is similarly good agreement for most of the remaining dipole-forbidden transitions, but the UKRMol+ result for the $C\ ^1\Pi_u \rightarrow B\ ^1\Sigma_u^+$ transition is somewhat lower than the MCCC results above 1 eV. Although the $C\ ^1\Pi_u \rightarrow X\ ^1\Sigma_g^+$ transitions are dipole-allowed, the MCCC and UKRMol+ calculations for these transitions are still in good agreement since they are sufficiently converged with $L_{\max} = 6$ at the energies considered in the UKRMol+ calculations. For the remaining dipole-allowed transitions ($C\ ^1\Pi_u \rightarrow EF\ ^1\Sigma_g^+$, $EF\ ^1\Sigma_g^+ \rightarrow C\ ^1\Pi_u$, and $EF\ ^1\Sigma_g^+ \rightarrow B\ ^1\Sigma_u^+$), there are substantial discrepancies between the two calculations due to the lack of partial-wave convergence in the UKRMol+ results.

Fig. 8.21, presents cross sections for superelastic scattering and excitation of the $n = 2$ states from the $B\ ^1\Sigma_u^+$ state. The AN MCCC results are compared with the UKRMol+ results, and the FN MCCC calculations with $R = 2.0\ a_0$, $L_{\max} = 6$, and no use of the ABC procedure are also included for comparison with the UKRMol+ results. Good agreement is seen between the UKRMol+ results and the FN MCCC results with $R = 2.0\ a_0$ and $L_{\max} = 6$, but for many transitions there are considerable discrepancies between these and the actual MCCC results, which use the AN method and $L_{\max} = 20$ along with the ABC method. For comparison with the latter, the $R = 2.5$ FN MCCC results (with ABC) are also shown. For the $B\ ^1\Sigma_u^+ \rightarrow b\ ^3\Sigma_u^+$ transition, the UKRMol+ results are in good agreement with the AN MCCC calculations, since there is little difference between the $R = 2.0\ a_0$ FN MCCC result and the AN MCCC result. For all

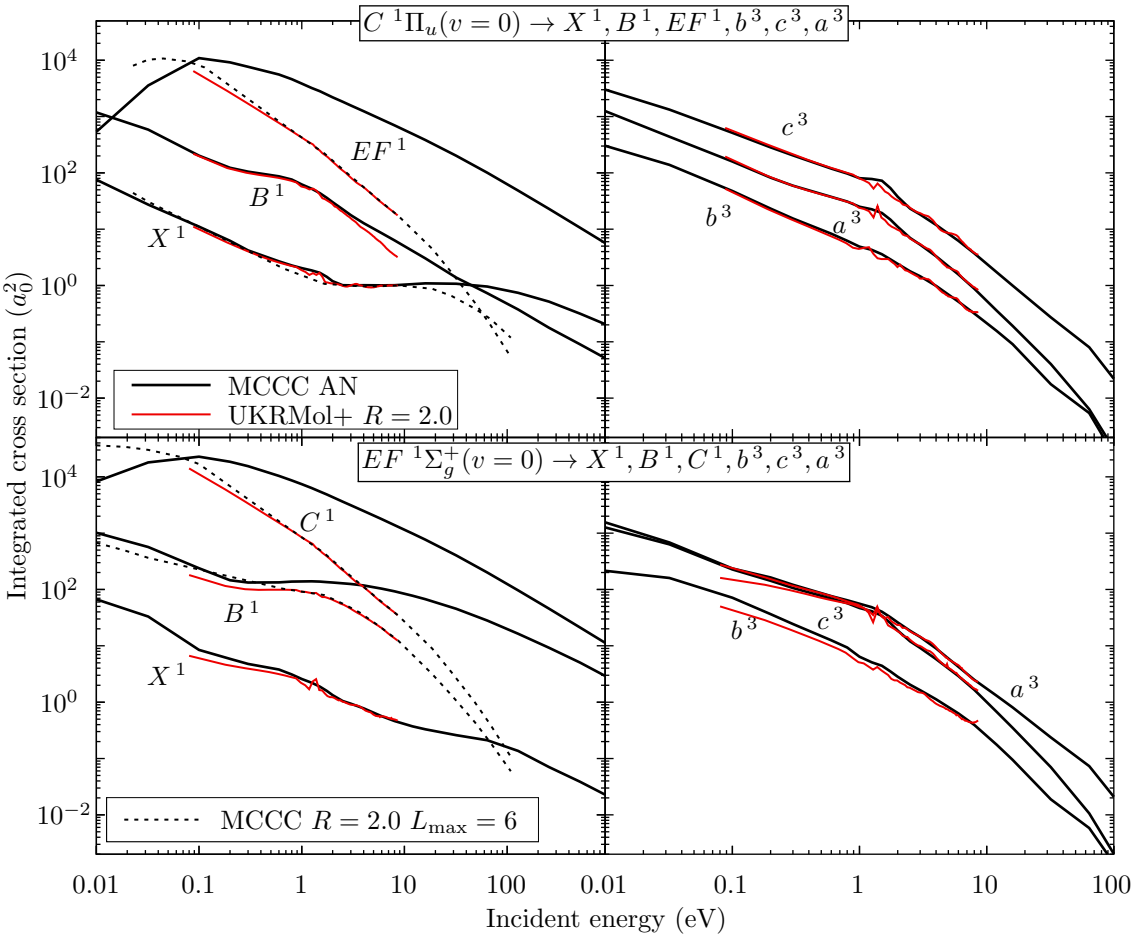

Figure 8.20: Electron-impact cross sections for superelastic scattering and excitation of states up to $n = 2$ from the $C\ ^1\Pi_u$ and $EF\ ^1\Sigma_g^+$ states of H_2 in the $v = 0$ level. Comparisons are made between the present MCCC results and the UKRMol+ [116] calculations. The FN ($R = 2.0\ a_0$) MCCC cross section with $L_{\max} = 6$ and no analytical Born completion is shown for the dipole-allowed transitions for proper comparison with the UKRMol+ results.

other transitions there are substantial differences in both the threshold energy and magnitude of the cross section. For the $B\ ^1\Sigma_u^+ \rightarrow EF\ ^1\Sigma_g^+$ transition, the lack of partial-wave convergence in the UKRMol+ calculations compounds the disagreement with the MCCC result.

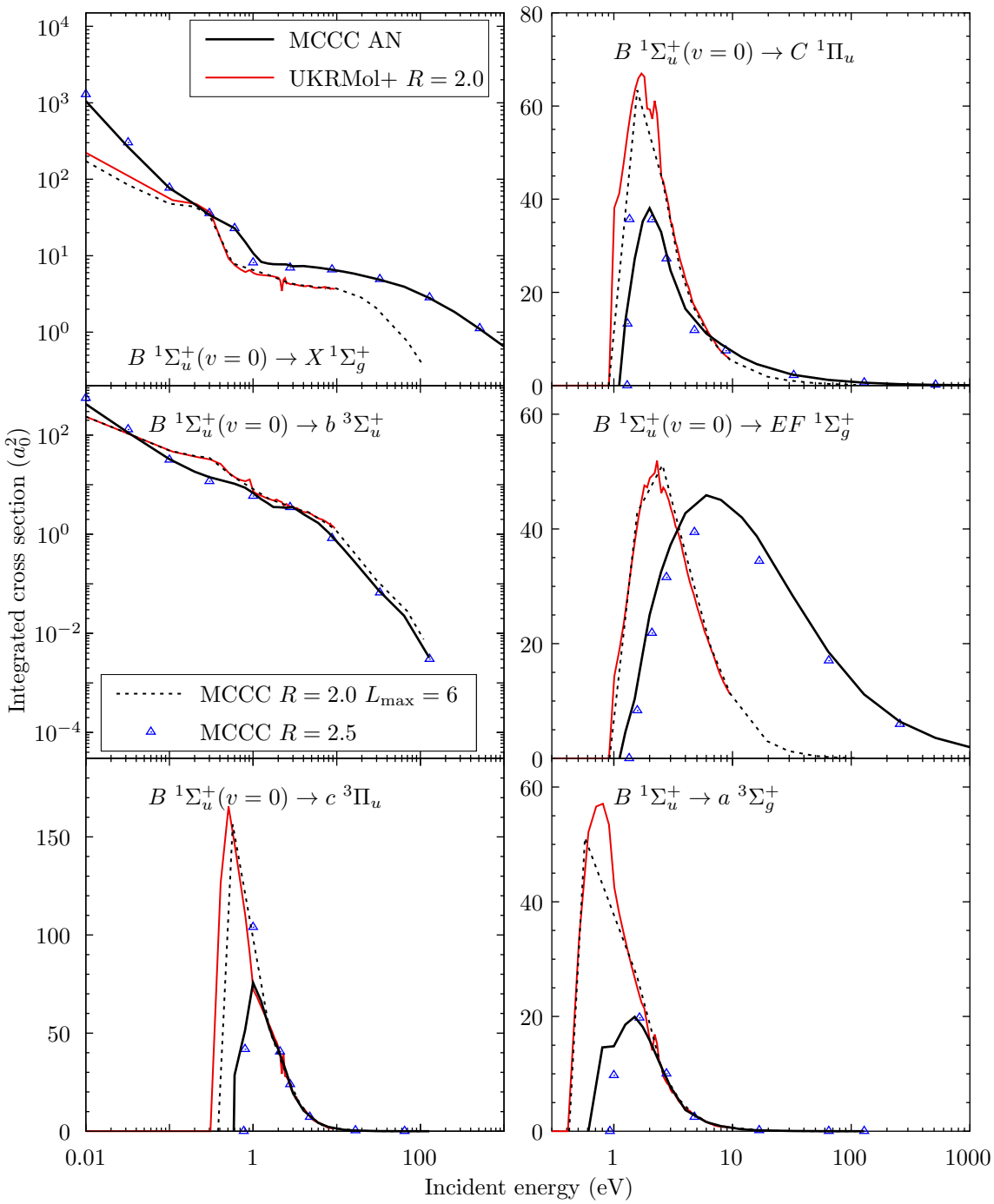

Figure 8.21: Electron-impact cross sections for superelastic scattering and excitation of states up to $n = 2$ from the $B\ ^1\Sigma_u^+(v = 0)$ state of H_2 in the $v = 0$ level. Comparisons are made between the present MCCC results and the UKRMol+ [116] calculations. The FN ($R = 2.0\ a_0$) MCCC cross section with $L_{\max} = 6$ and no analytical Born completion is also shown for the dipole-allowed transitions for proper comparison with the UKRMol+ results. The $R = 2.5\ a_0$ MCCC cross section *with* analytical Born completion and $L_{\max} = 20$ is also shown.

8.3.4 Excitation of $n = 3$ states

Figs. 8.22 and 8.23 present cross sections for excitation of the $n = 3$ triplet states from the $c\ ^3\Pi_u(v = 0)$ and $a\ ^3\Sigma_g^+(v = 0)$ states. Where the UKRMol+ results are available, there is generally poor agreement with the MCCC cross sections. For the dipole-allowed transitions there is the expected lack of partial-wave convergence in the UKRMol+ results, but for excitation of the $n = 3$ states there are a number of dipole-forbidden transitions which are also slow to converge. As before, the $L_{\max} = 6$ MCCC cross sections (without ABC) are included in the figures to demonstrate this. For three of the dipole-allowed transitions there are results from the IP method [96], which show the behaviour expected of semi-classical techniques – agreement with the MCCC calculations in the high-energy limit but substantial disagreement at low to intermediate energies.

Figs. 8.24 and 8.25 present cross sections for excitation of the $n = 3$ singlet states from the $c\ ^3\Pi_u(v = 0)$ and $a\ ^3\Sigma_g^+(v = 0)$ states. As these are spin-exchange transitions, which converge quickly with the number of partial waves, there is good agreement with the UKRMol+ calculations wherever they are available. No other calculations have been previously attempted for these transitions.

Figs. 8.26 and 8.27 present cross sections for excitation of the $n = 3$ singlet and triplet states from the $B\ ^1\Sigma_u^+$, $C\ ^1\Pi_u$, and $EF\ ^1\Sigma_g^+$, states. There is comparison with the UKRMol+ calculations for excitation of the $B'\ ^1\Sigma_u^+$, and $GK\ ^1\Sigma_g^+$ states, and the IP calculations of Celiberto *et al.* [70] for the $B\ ^1\Sigma_u^+ \rightarrow I\ ^1\Pi_g$ transition. There is reasonable agreement between UKRMol+ and MCCC for excitation of the $B'\ ^1\Sigma_u^+$ and $GK\ ^1\Sigma_g^+$ states from the $B\ ^1\Sigma_u^+$ state, but not from the $C\ ^1\Pi_u$ and $EF\ ^1\Sigma_g^+$ states, where the UKRMol+ cross section are substantially lower than the MCCC results at energies more than a few eV above threshold. For the $B\ ^1\Sigma_u^+ \rightarrow I\ ^1\Pi_g$ transition, the MCCC and IP [70] cross sections are in agreement above 100 eV, but the latter are up to a factor of two larger below 100 eV. None of the previous calculations consider the remaining transitions for which the MCCC cross sections are presented in Fig. 8.26.

For excitation of the $n = 3$ triplet states, the UKRMol+ calculations include transitions to the $e\ ^3\Sigma_u^+$, $d\ ^3\Pi_u$, $h\ ^3\Sigma_g^+$, and $g\ ^3\Sigma_g^+$ states (but not $i\ ^3\Pi_g$ or $j\ ^3\Delta_g$). For clarity, the MCCC results in Fig. 8.27 are presented only for the

transitions where the UKRMol+ results are available, but the remaining cross sections for excitation of the $i\ ^3\Pi_g$ and $j\ ^3\Delta_g$ states have been calculated and are available online at mccc-db.org. For scattering on the $B\ ^1\Sigma_u^+$ state, there is poor agreement between the UKRMol+ and MCCC results since these transitions are more affected by the choice of $R = 2.0\ a_0$ in the UKRMol+ calculations rather than the AN approach utilised in the MCCC calculations. For scattering on the $C\ ^1\Pi_u$ and $EF\ ^1\Sigma_g^+$ states there is good agreement for excitation of the $e\ ^3\Sigma_u^+$ state, but for the remaining excitations there are significant discrepancies.

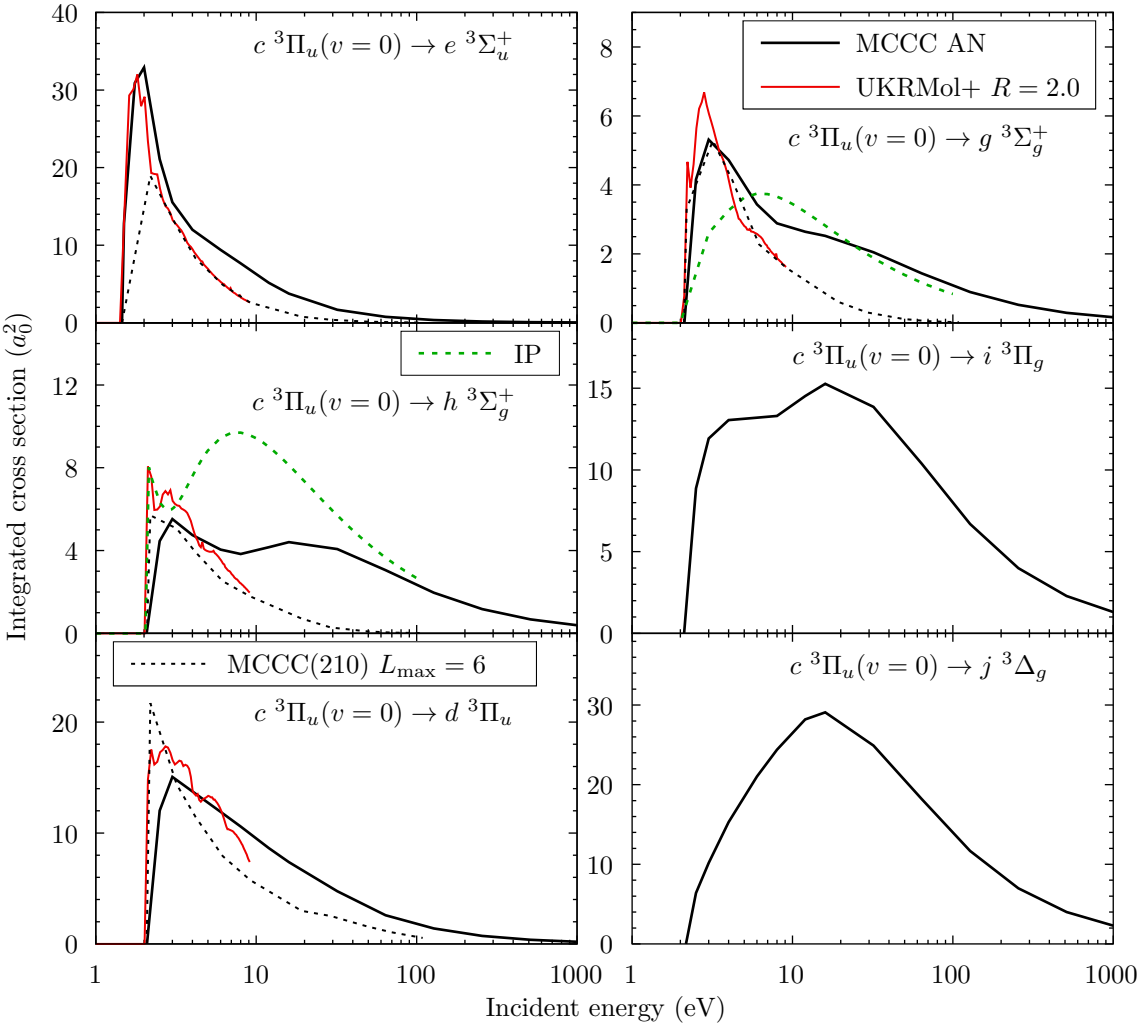

Figure 8.22: Electron-impact cross sections for excitation of the $n = 3$ triplet states from the $c\ ^3\Pi_u(v = 0)$ state of H_2. Comparisons are made between the MCCC results and the UKRMol+ [116] and IP [96] calculations, where available. The FN ($R = 2.0\ a_0$) MCCC cross section with $L_{\max} = 6$ and no analytical Born completion is also shown for the dipole-allowed transitions for proper comparison with the UKRMol+ results.

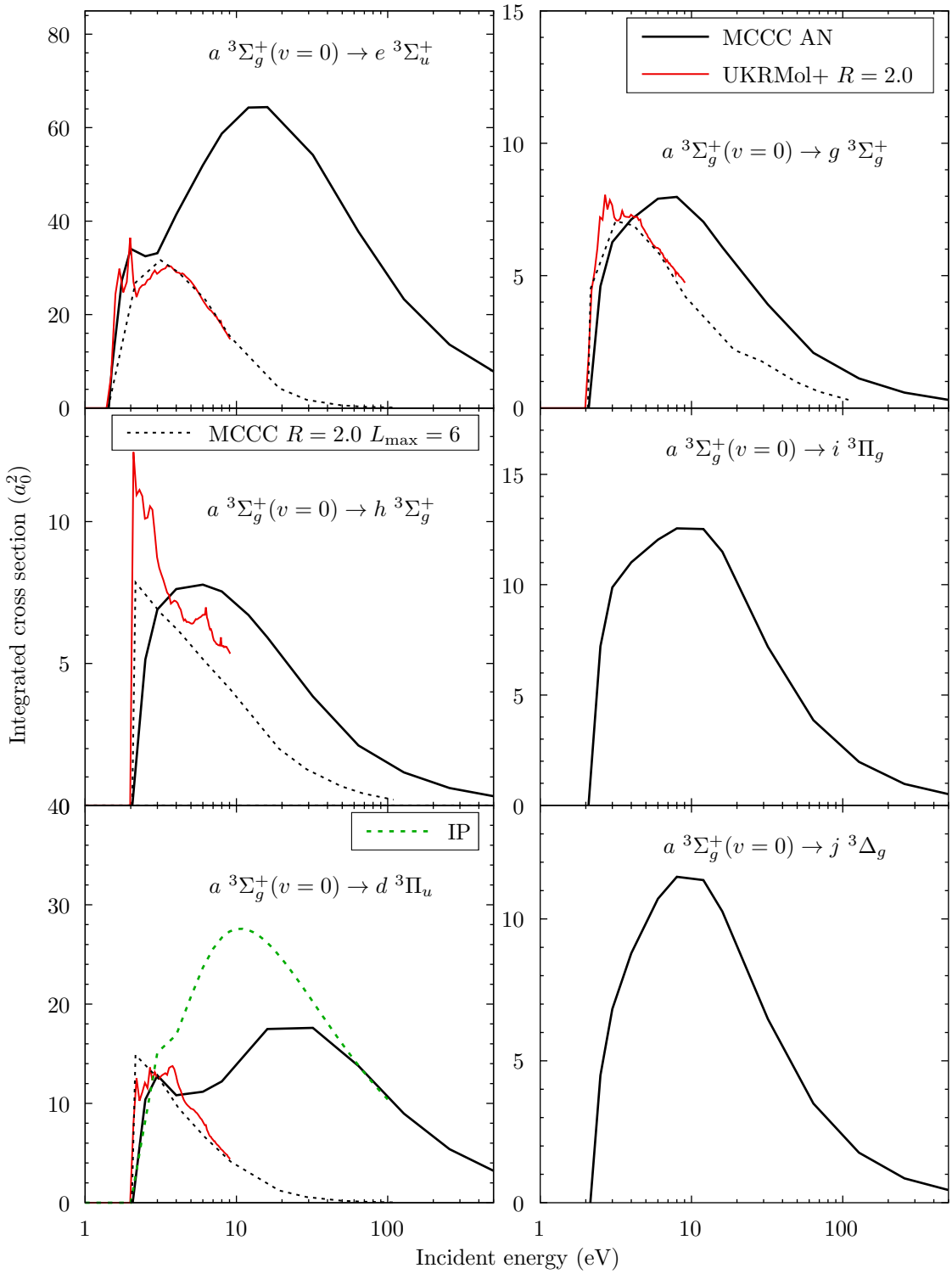

Figure 8.23: Electron-impact cross sections for excitation of the $n = 3$ triplet states from the $a\ ^3\Sigma_g^+(v = 0)$ state of H_2. Comparisons are made between the MCCC results and the UKRMol+ [116] and IP [96] calculations, where available. The FN ($R = 2.0\ a_0$) MCCC cross section with $L_{\max} = 6$ and no analytical Born completion is also shown for the dipole-allowed transitions for proper comparison with the UKRMol+ results.

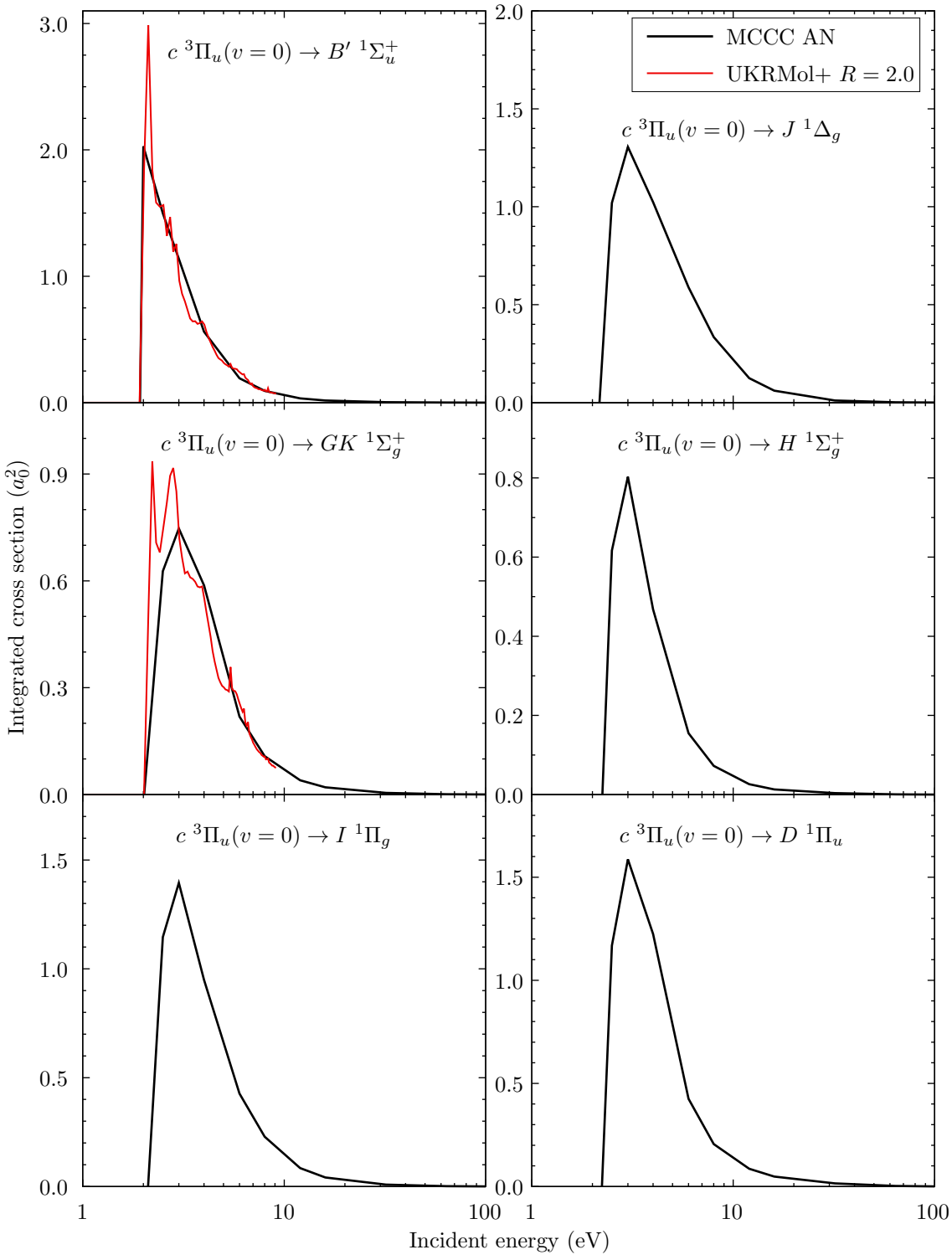

Figure 8.24: Electron-impact cross sections for excitation of the $n = 3$ singlet states from the $c\ ^3\Pi_u(v = 0)$ state of H_2. Comparisons are made between the present MCCC cross sections and the UKRMol+ [116] calculations, where available.

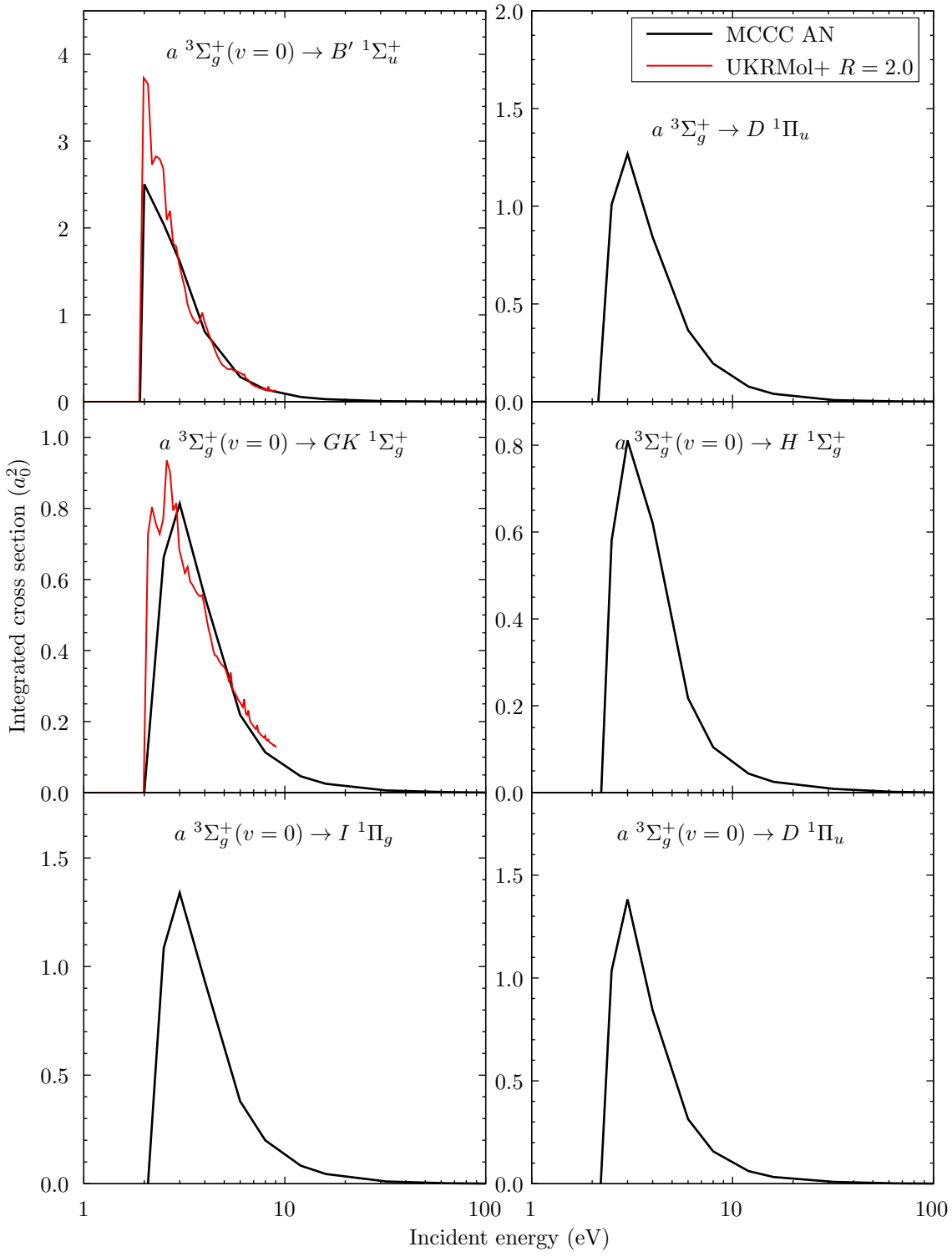

Figure 8.25: Electron-impact cross sections for excitation of the $n = 3$ singlet states from the $a\ ^3\Sigma_g^+(v = 0)$ state of H_2. Comparisons are made between the present MCCC cross sections and the UKRMol+ [116] calculations, where available.

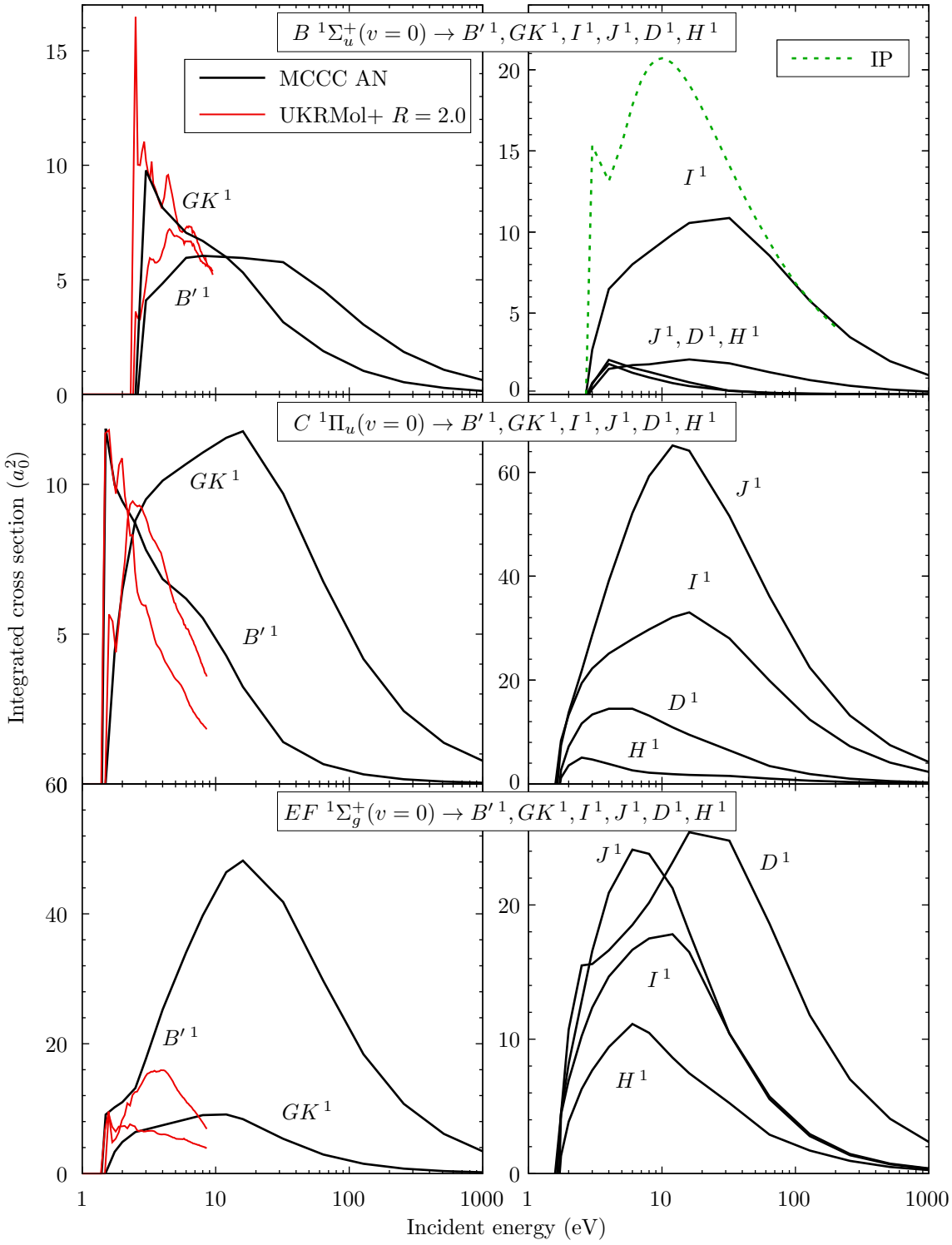

Figure 8.26: Electron-impact cross sections for excitation of the $n = 3$ singlet states from the $B\ ^1\Sigma_u^+$, $C\ ^1\Pi_u$, and $EF\ ^1\Sigma_g^+$ states of H_2 in the $v = 0$ level. Comparisons are made between the present MCCC results and the UKRMol+ [116] and impact-parameter (IP) [70] calculations, where available.

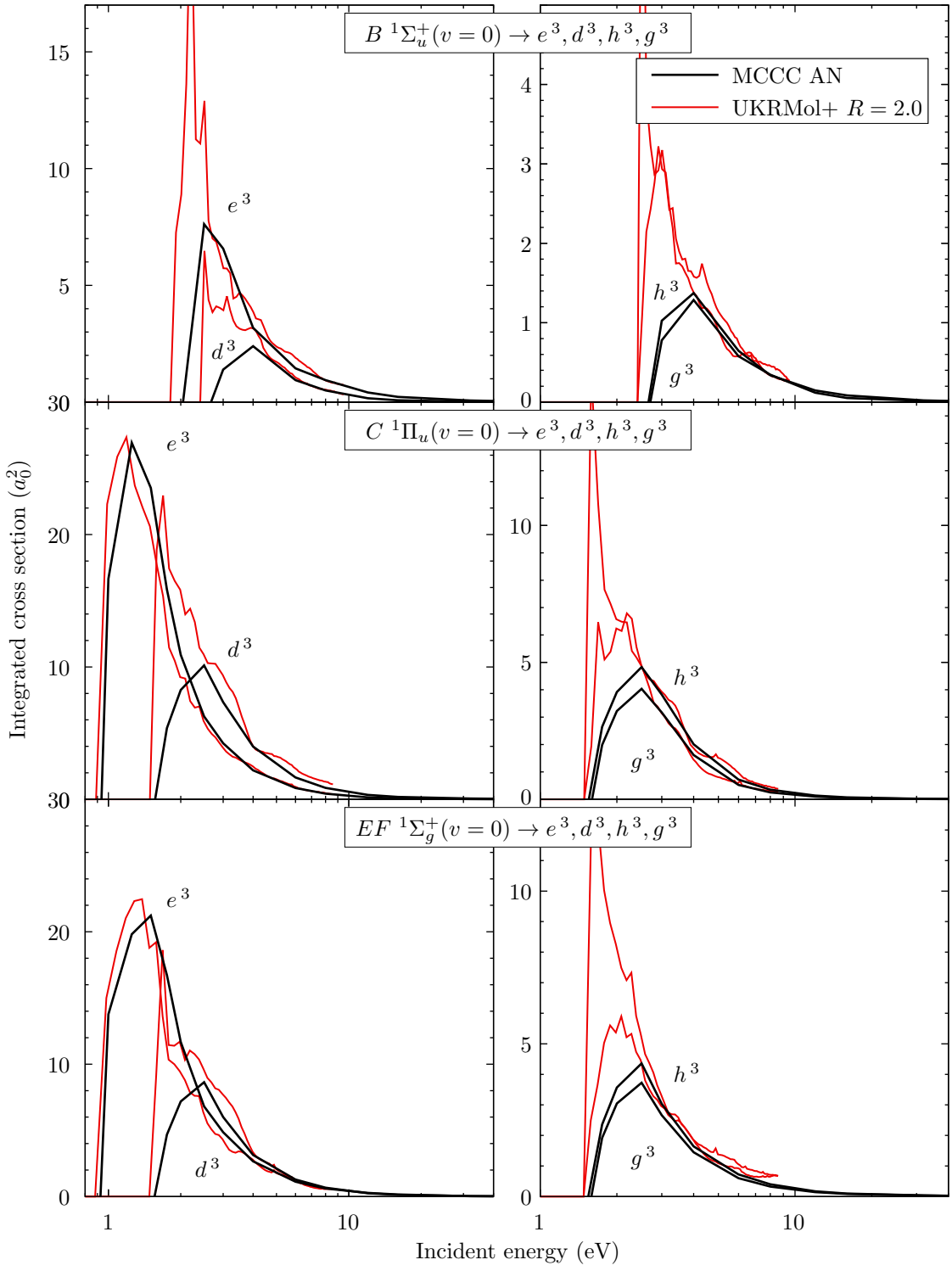

Figure 8.27: Electron-impact cross sections for excitation of the $e\ ^3\Sigma_u^+$, $d\ ^3\Pi_u$, $h\ ^3\Sigma_g^+$, and $g\ ^3\Sigma_g^+$ states from the $B\ ^1\Sigma_u^+$, $C\ ^1\Pi_u$, and $EF\ ^1\Sigma_g^+$ states of H_2 in the $v = 0$ level. Comparisons are made between the present MCCC results and the UKRMol+ [116] calculations.

8.4 Application of MCCC cross sections in a collisional-radiative model

During the course of this PhD project, a collaboration was initiated with the ITER Technology and Diagnostics Division at the Max-Planck Institute for Plasma Physics (IPP) in Garching, Germany. The goal of the collaboration is to implement MCCC cross sections in the Yacora collisional-radiative model developed at IPP [56]. The eventual aim is for a fully vibrationally-resolved collisional-radiative model for H_2 and its isotopologues. At present, a preliminary model which is not vibrationally-resolved and includes only the ground state and excited triplet states has been tested by Wünderlich *et al.* [8]. As an example of the results, Fig. 8.28, presents the population density of the $d\ ^3\Pi_u$ state predicted by the collisional-radiative model using input cross sections from the present MCCC calculations, as well as two previous datasets from Miles *et al.* [140] and Janev *et al.* [139]. Comparison is made with measurements taken at IPP of the $d\ ^3\Pi_u$-state

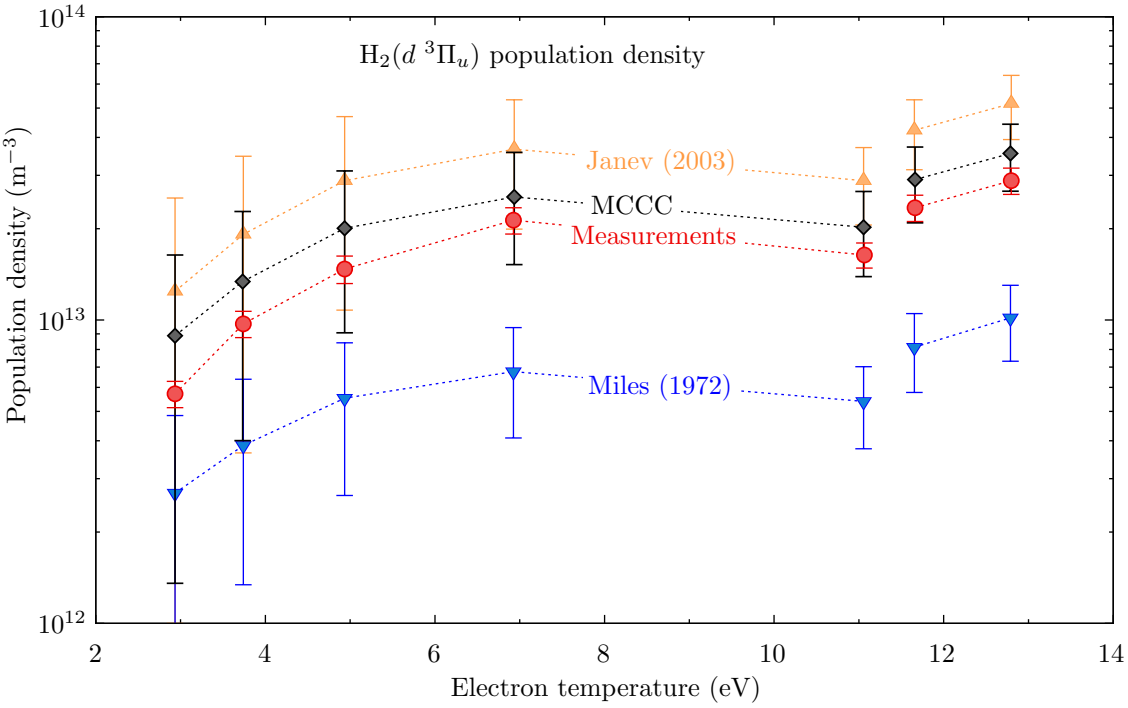

Figure 8.28: Comparison of measured population densities of the $d\ ^3\Pi_u$ to collisional-radiative model results using input cross sections from either Miles *et al.* [140], Janev *et al.* [139], or the MCCC calculations. Figure reproduced with permission from Wünderlich *et al.* [8].

population density using optical-emission spectroscopy on a plasma with parameters determined using a Langmuir probe. Using MCCC cross sections, the model predictions are within the error bars of the measurements, and are substantially better than the results obtained using the older datasets. Since there are very limited experimental data to compare raw cross-section calculations with, this indirect validation of the MCCC cross sections is very useful as a demonstration of their accuracy. As the collisional-radiative model is expanded to include the excited singlet states of H_2, as well as the inclusion of vibrationally-resolved cross sections, the level of agreement with the measurements in Fig. 8.28 may improve even further.

Fig. 8.29 presents three examples of the comparison between the MCCC calculations and the cross sections recommended by Miles *et al.* [140] and Janev *et al.* [139] for total excitation of the $a\ ^3\Sigma_g^+$, $c\ ^3\Pi_u$, and $d\ ^3\Pi_u$ from the $X\ ^1\Sigma_g^+(v_i = 0)$ state. The datasets of Refs. Janev *et al.* [139] and Miles *et al.* [140] both represent

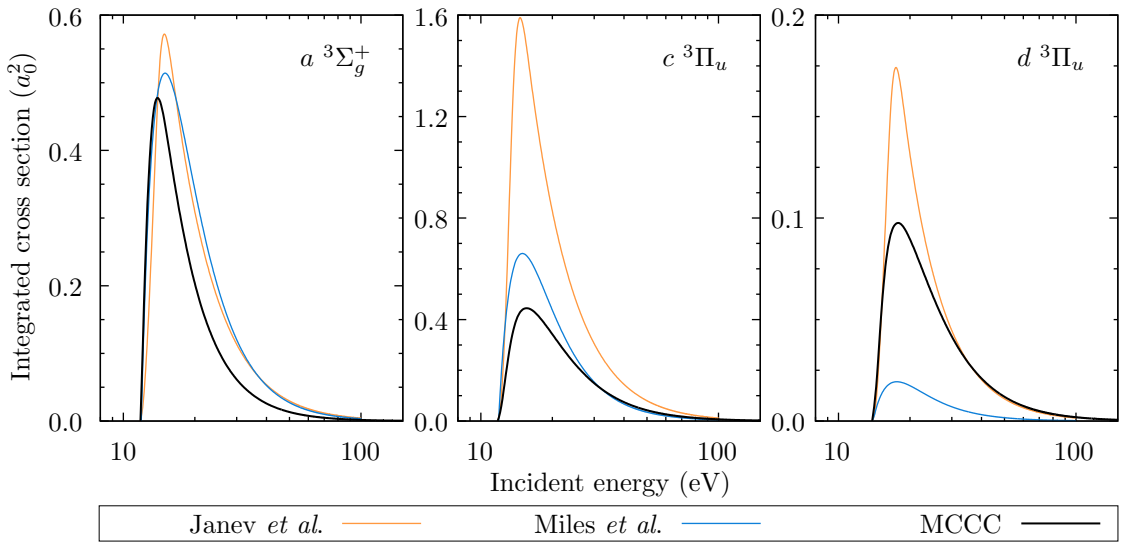

Figure 8.29: Comparison of the $X\ ^1\Sigma_g^+(v_i = 0) \rightarrow \{a\ ^3\Sigma_g^+, c\ ^3\Pi_u, d\ ^3\Pi_u\}$ excitation cross sections from the datasets of Miles *et al.* [140] and Janev *et al.* [139] with the MCCC calculations.

attempts at producing recommended cross sections based on the analysis of the available theoretical and experimental data of the time. These datasets have been used quite extensively in modelling, see for example Refs. [52, 53, 236, 242–249]. In many cases, the two sets of cross sections are in significant disagreement with each other and with the MCCC results. For the $a\ ^3\Sigma_g^+$ excitation, the

discrepancies between the three cross sections are not particularly large, but for the $c\ ^3\Pi_u$ and $d\ ^3\Pi_u$ states the disagreement is severe. Furthermore, the datasets of Refs. [139, 140] are not vibrationally resolved. The MCCC calculations represent a substantial improvement not only in the accuracy of the data, but in the number of transitions considered.

8.5 MCCC database

The MCCC cross sections are hosted on the online databases `lxcat.net` and `db-amdis.org/hcdb`. However, the existing online collision-data repositories are not particularly well-suited for handling datasets with as many target species as considered in this work. In order to easily disseminate the large number of results presented in this chapter to end-users, the candidate designed and coded an online database to host the MCCC cross sections (`mccc-db.org`). The MCCC database is not meant to replace the existing databases, but simply provide a place where the MCCC data can be located and downloaded in the most user-friendly way. Fig. 8.30 shows the main view of the database, where users can select the projectile and target, the type of process (excitation, dissociation, ionisation, etc.), and the initial/final states where applicable. Once the selections are made a graphic of the cross section is produced and presented to the user, and the raw data and fitting parameters for the cross section can be easily viewed by selecting the appropriate tab above the graphic.

The primary issue this website aims to address is the way in which data is downloaded. Many existing databases allow users to either download the data file for a single cross section, or an entire dataset (sometimes in a single text file). The MCCC database is structured so that the user can select a particular initial state and collision process of interest, and a `PHP` script on the server will package together the corresponding data files (one per cross section, as a function of energy) and produce a `.zip` archive for download. It is also possible to select all initial vibrational levels, or all initial electronic states so that large chunks or even the entire dataset can be downloaded at once. This way, a user who requires only a particular subset of the entire collection of MCCC data is not limited to

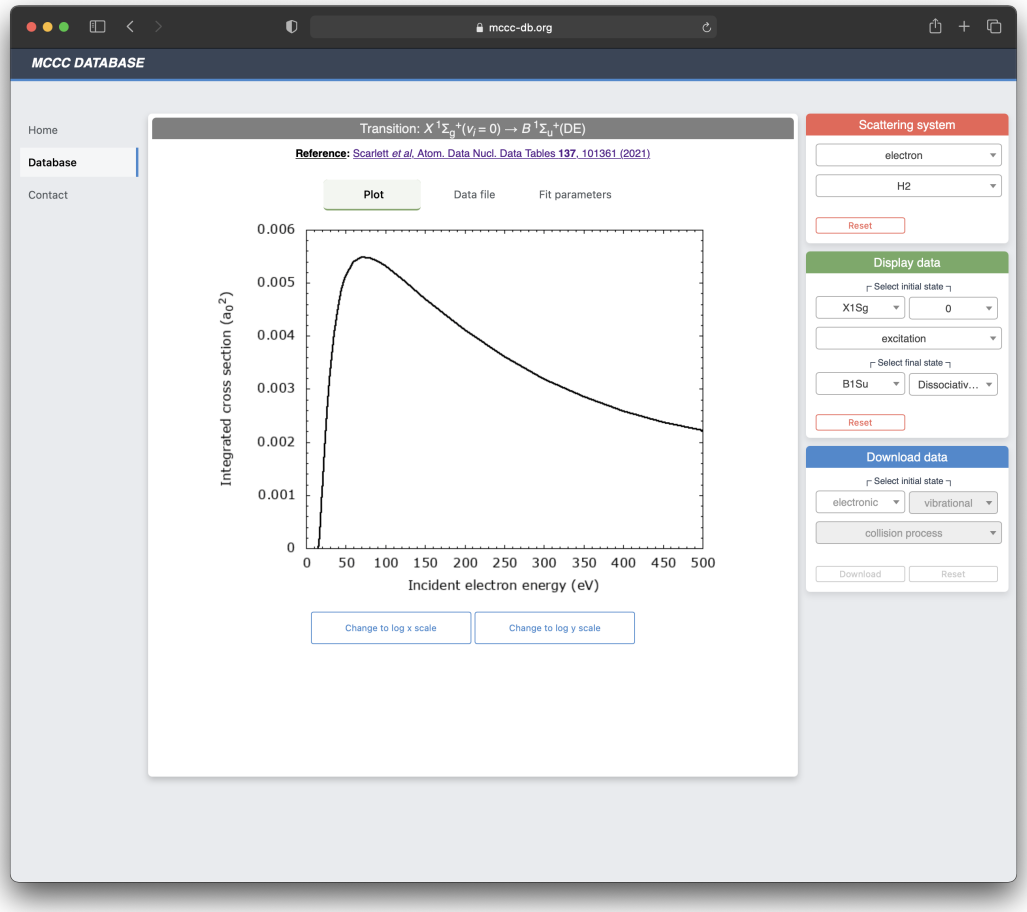

Figure 8.30: Plot view of the MCCC database.

choosing between downloading data one transition at a time or downloading the entire database of over 60,000 transitions. When results are downloaded for multiple initial states or multiple collision processes, the archive is organised into subdirectories to allow for easy navigation.

The cross sections for excitation of bound vibrational levels are provided in text files named in the format

`MCCC-el-H2-[f]_vf=[vf]_X1Sg_vi=[vi].txt`

where `[f]` is the final electronic-state label, `[vf]` is the final vibrational level in the state `[f]`, and `[vi]` is the initial vibrational level in the $X\,^1\Sigma_g^+$ state (`[vi]` $= 0, \ldots, 14$). The symmetry labels are prefaced by Latin letters to uniquely specify the electronic states. The ground electronic state is given the "X" label. States of the same spin as the ground state are assigned upper-case letters while states of different spin are assigned lower-case letters. A number of states which

were initially considered separate based on spectroscopic measurements have been subsequently identified as double-minima states and assigned a conjoined state label (e.g. $E\ ^1\Sigma_g^+ + F\ ^1\Sigma_g^+ \rightarrow EF\ ^1\Sigma_g^+$) [250]. States which were initially identified as double-minima states are assigned a single-character label as usual, but some authors prefer to retain the double-character notation by repeating the letter with a bar, (e.g. $H\bar{H}\ ^1\Sigma_g^+$). For simplicity of converting state labels to alphanumeric strings for file-naming purposes we follow the convention of Sharp [250] which is to specify these states by the single letter only. When converting state labels to alphanumeric form the capital Greek letter is replaced by the corresponding capital Latin letter, and primes on the Latin letters are replaced by a `p`. For example:

$$H\ ^1\Sigma_g^+ \rightarrow \texttt{H1Sg}$$

$$b\ ^3\Sigma_u^+ \rightarrow \texttt{b3Su}$$

$$B'\ ^1\Sigma_u^+ \rightarrow \texttt{Bp1Su}.$$

The file containing the $X\ ^1\Sigma_g^+(v_i = 0) \rightarrow B\ ^1\Sigma_u^+(v_f = 10)$ cross section, for example, is named

`MCCC-el-H2-B1Su_vf=10.X1Sg_vi=0.txt`.

Cross sections for dissociative excitation (DE), cross sections summed over final bound vibrational levels, and cross sections summed over all final levels (including DE) are provided in files named in the format

`MCCC-el-H2-[f]_DE.X1Sg_vi=[vi].txt`
`MCCC-el-H2-[f]_bound.X1Sg_vi=[vi].txt`
`MCCC-el-H2-[f]_total.X1Sg_vi=[vi].txt`.

An example of the data-file format for the $X\ ^1\Sigma_g^+(v_i = 0) \rightarrow B'\ ^1\Sigma_u^+$(DE) cross section is provided in Fig. 8.31. Useful information such as the state energies and excitation threshold can be extracted from the file headers.

```
# MCCC calculations of electron scattering on molecular hydrogen
# Adiabatic nuclei calculations performed with the spheroidal MCCC(210) model
# Reference:  Scarlett et al., Atom.  Data Nucl.  Data Tables (2021)
# MCCC Database:  mccc-db.org
# This file:  e + H2(X1Sg,vi=0) -> e + H2(Bp1Su) (dissociative excitation)
# Initial-state energy:  -1.16453 Hartrees
#
# Threshold:  1.46815E+01 eV
#
# Energy (eV)   CS (a_0^2)
  1.46815E+01   0.00000E+00
  1.50000E+01   1.66274E-04
  1.55000E+01   1.49650E-03
  1.60000E+01   3.46034E-03
  1.65000E+01   5.68862E-03
  1.70000E+01   8.00076E-03
  1.75000E+01   1.03085E-02
  1.80000E+01   1.25784E-02
  1.85000E+01   1.47952E-02
  1.90000E+01   1.69492E-02
  1.95000E+01   1.90362E-02
  2.00000E+01   2.10576E-02
                ⋮
  4.50000E+01   6.86708E-02
  5.00000E+01   7.16277E-02
  6.00000E+01   7.48725E-02
  7.00000E+01   7.58857E-02
  8.00000E+01   7.56072E-02
  9.00000E+01   7.45754E-02
  1.00000E+02   7.31118E-02
  1.25000E+02   6.86458E-02
  1.50000E+02   6.39901E-02
  2.00000E+02   5.56524E-02
  2.50000E+02   4.89227E-02
  3.00000E+02   4.35372E-02
  3.50000E+02   3.91795E-02
  4.00000E+02   3.55968E-02
  4.50000E+02   3.25974E-02
  5.00000E+02   3.00624E-02
```

Figure 8.31: The format of the file `MCCC-el-H2-Bp1Su_DE.X1Sg_vi=0.txt`, containing the numerical MCCC cross-section for dissociative excitation (DE) of the $B'\ ^1\Sigma_u^+$ state from the $X\ ^1\Sigma_g^+(v_i = 0)$ state of H_2. The threshold energy for each transition can be extracted from the file header.

8.6 Chapter 8 summary

The results presented in this chapter represent the most extensive studies ever performed for electron scattering on H_2 and its isotopologues. The spheroidal-coordinate implementation [202] of the fixed-nuclei MCCC method has been utilised to generate accurate cross sections as a function of energy and inter-nuclear separation, for excitation of the $n = 2$–3 electronic states of H_2 from the ground electronic state. The adiabatic-nuclei approximation has been implemented to produce over 60,000 fully vibrationally-resolved cross sections for each of the isotopologues of H_2, and the isotopic dependence of the results has been investigated [6, 7]. The MCCC cross sections have been utilised to study the dissociation of H_2 into neutral fragments [12], and have been implemented in a collisional-radiative model for H_2 plasmas [8]. As discussed in Sec. 7.6 and Ref. [4], the data for low-energy dissociation of H_2 and its isotopologues recommended in the literature have suffered from serious theoretical errors, so the MCCC results for dissociation already have immediate application by replacing the incorrect data in the many plasma models where they were applied [34, 36, 39, 41, 42, 44, 75–86].

Convergence studies have been performed for scattering on the excited $n = 2$ electronic states of H_2 [5]. Here, the faster rate of convergence with respect to the target-state expansion allowed cross sections for elastic scattering and ionisation to be calculated as well as for excitation and superelastic scattering. However, the much smaller energy thresholds for scattering on excited states resulted in substantially slower partial-wave convergence than for scattering on the ground electronic state. Comparison of the MCCC results with the recent state-of-the-art R-matrix calculations [116] revealed that the R-matrix calculations are in substantial error for all dipole-allowed and even some dipole-forbidden transitions, due to a lack of partial-wave convergence.

The results presented in this chapter have been made available online in the MCCC database (`mccc-db-org`), which was designed and coded by the candidate as a part of this PhD project.

Part III

Vibrational-electronic molecular convergent close-coupling

Chapter 9

Vibrational-electronic molecular convergent close-coupling: theory

Over the last few decades it has been the goal of the convergent close-coupling (CCC) method to provide a "complete scattering theory" – one capable of accurately describing all processes of interest over the entire range of collision energies for a given scattering system [251]. The CCC method is particularly well suited for this endeavour, since its expansion of the total scattering wave function over the target states explicitly couples all reaction channels, and the pseudostate representation of the target continuum allows accurate elastic, excitation, and ionisation amplitudes to be extracted from a single calculation [252, 253]. For electron and positron scattering on quasi one- and two-electron targets, the atomic CCC method can be considered a complete scattering theory. The benefits of having a single, unitary theory to describe all reactions are the proper account of inter-channel coupling between the various transitions, and the ability to generate a self-consistent set of calculated cross sections.

The MCCC method has been shown to completely solve the electronic scattering problem for collisions with molecular hydrogen (H_2) within the fixed-nuclei approximation [91]. The extension of the MCCC method to generate vibrationally-resolved cross sections using the adiabatic-nuclei approximation, as discussed in Part II, has been a major step forward in producing a comprehensive set of data for electron scattering on H_2 and its isotopologues. However, it is well-known that the adiabatic-nuclei approximation is unable to describe resonant processes, even approximately. For electron-atom scattering, close-coupling methods are able to properly represent resonances in the calculated cross sec-

tions by virtue of the implicit representation of the compound states in the close-coupling expansion of the scattering wave function. A similar implicit treatment of resonances in molecular scattering requires both electronic and nuclear states of the target to be included in the close-coupling expansion, leading to calculations which have historically been intractable. Current methods for the computation of resonant scattering cross sections typically utilise the projection-operator formalism of Feshbach [254] to project out the non-resonant scattering channels and explicitly couple the target and compound states involved in each transition [104, 105, 112, 114, 115, 255]. These techniques require input from electronic scattering calculations (generally R-matrix) for the resonance energies and widths, before solving the nuclear dynamics problem.

The goal now is to incorporate resonant scattering into the MCCC method, with the motivation of having a single theoretical framework within which all scattering processes of interest can be calculated. As a first step, the rotational motion is continued to be treated adiabatically, but the electronic and vibrational motions are explicitly coupled. We refer to this method as vibrational-electronic MCCC (VE MCCC). The calculations are still performed in the molecule-fixed body frame, and the cross-section expressions given in Section 4.4 still hold, with the adiabatic-nuclei T-matrix elements replaced with the analogous matrix elements obtained from the VE MCCC calculations. In this chapter, the theoretical framework for this process is laid out, with results given in Chapter 10. Some sections contain text or figures from published work by the candidate [1]. The publisher (the American Physical Society) provides the right to use an article or a portion of an article in a thesis or dissertation without requesting permission.

9.1 Vibronic scattering state and scattering-system Hamiltonian

With the electronic and vibrational motions coupled, and rotational motion treated adiabatically, the total scattering state is represented in the following form:

$$|\Psi^{\mathcal{S}}_{n_i v_i N_i m_{N_i}}\rangle \approx |\Psi^{\mathcal{S}}_{n_i v_i}\rangle |N_i m_{N_i}\rangle, \tag{9.1}$$

where n_i, v_i, and $N_i m_{N_i}$ specify the target initial electronic, vibrational, and rotational state, respectively. The vibronic scattering state is the solution to

$$(E - \hat{\mathsf{H}})|\Psi^{\mathcal{S}}_{n_i v_i}\rangle = 0, \tag{9.2}$$

where the vibronic scattering-system Hamiltonian is

$$\hat{\mathsf{H}} = \hat{\mathsf{K}}_0 + \hat{\mathsf{H}}_\mathrm{t} + \hat{\mathsf{V}}_\mathrm{dir}. \tag{9.3}$$

The direct interaction potential $\hat{\mathsf{V}}_\mathrm{dir}$ is defined in the same way as in Section 6.2:

$$\hat{\mathsf{V}}_\mathrm{dir} = \hat{\mathsf{V}}_0 + \hat{\mathsf{V}}_{01} + \hat{\mathsf{V}}_{02}. \tag{9.4}$$

The target Hamiltonian is defined similarly to the fixed-nuclei definition in Chapter 6, but with the addition of the vibrational kinetic-energy operator. For H_2 and its isotopologues it is given by

$$\hat{\mathsf{H}}_\mathrm{t} = \hat{\mathsf{K}}_1 + \hat{\mathsf{K}}_2 + \hat{\mathsf{V}}_1 + \hat{\mathsf{V}}_2 + \hat{\mathsf{V}}_{12} + \hat{\mathsf{K}}_\mathrm{v} + \frac{Z_1 Z_2}{R}. \tag{9.5}$$

In Eqs. (9.3)–(9.5), the index 0 refers to the projectile, while the indices 1 and 2 refer to the target electrons, and the coordinate-space representations of the various operators are:

$$\hat{\mathsf{K}}_i = -\frac{1}{2}\nabla^2_{\boldsymbol{r}_i} \tag{9.6}$$

$$\hat{\mathsf{V}}_i = \left[\frac{z_i Z_1}{\left|\boldsymbol{r}_i - \frac{\boldsymbol{R}}{2}\right|} + \frac{z_i Z_2}{\left|\boldsymbol{r}_i - \frac{\boldsymbol{R}}{2}\right|}\right] \tag{9.7}$$

$$\hat{\mathsf{V}}_{12} = \frac{z_1 z_2}{|\boldsymbol{r}_1 - \boldsymbol{r}_2|} \tag{9.8}$$

$$\hat{\mathsf{K}}_\mathrm{v} = -\frac{1}{2\mu}\frac{\mathrm{d}^2}{\mathrm{d}R^2}. \tag{9.9}$$

9.2 Close-coupling equations for the vibronic T matrix

Following the same approach described in Section 6.2 for the fixed-nuclei MCCC method, the total scattering state is represented in the explicitly antisymmetrised form:

$$|\Psi^{\mathcal{S}}_{n_i v_i}\rangle = \mathcal{A}|\psi^{\mathcal{S}}_{n_i v_i}\rangle, \tag{9.10}$$

where

$$\mathcal{A} = 1 - \sum_{j=1}^{N_\mathrm{e}} \hat{\mathsf{P}}_{0j} \tag{9.11}$$

is the antisymmetrisation operator, and $|\psi^{\mathcal{S}}_{n_i}\rangle$ is the solution to

$$(E - \hat{\mathsf{H}}_0)|\psi^{\mathcal{S}}_{n_i v_i}\rangle = \hat{\mathsf{V}}|\psi^{\mathcal{S}}_{n_i v_i}\rangle. \tag{9.12}$$

As before, $\hat{\mathsf{V}}$ is the sum of the direct and exchange potential operators:

$$\hat{\mathsf{V}} = \hat{\mathsf{V}}_\mathrm{dir} + \hat{\mathsf{V}}_\mathrm{exch}, \tag{9.13}$$

with

$$\hat{\mathsf{V}}_\mathrm{exch} = (E - \hat{\mathsf{H}}) \sum_{j=1}^{2} \hat{\mathsf{P}}_{0j}, \tag{9.14}$$

in terms of the scattering-system Hamiltonian defined in Eq. (9.3).

For simplicity, it is assumed that the Born-Oppenheimer approximation is valid for the target states, allowing the close-coupling expansion for $|\psi^{\mathcal{S}}_{iv_i}\rangle$ to be written as

$$|\psi^{\mathcal{S}}_{iv_i}\rangle = \mathcal{A} \sum_{(n,v)\in\mathcal{N}} |\Phi_n \nu_{nv}\rangle\langle\nu_{nv}\Phi_n|\psi^{\mathcal{S}}_{n_i,v_i}\rangle \tag{9.15}$$

where $|\Phi_n\rangle$ are the electronic target state, $|\nu_{nv}\rangle$ are the target vibrational states in the electronic state n, and $\mathcal{N}$ denotes the set of all vibronic states included in the expansion. The corresponding momentum-space close-coupling equations for the scattering T matrix are derived in exactly the same way as in Sec. 6.2, and

are given by

$$\langle \boldsymbol{q}_f \nu_{fv_f} \Phi_f | \hat{\mathsf{T}}^{\mathcal{N}} | \Phi_i \nu_{iv_i} \boldsymbol{q}_i \rangle = \langle \boldsymbol{q}_f \nu_{fv_f} \Phi_f | \hat{\mathsf{V}} | \Phi_i \nu_{iv_i} \boldsymbol{q}_i \rangle + \sum_{(n,v)\in\mathcal{N}} \iiint_{\mathbb{R}^3} \langle \boldsymbol{q}_f \nu_{fv_f} \Phi_f | \hat{\mathsf{V}} | \Phi_n \nu_{nv} \boldsymbol{q} \rangle G_{nv}^{(+)}(q) \langle \boldsymbol{q} \nu_{nv} \Phi_n | \hat{\mathsf{T}}^{\mathcal{N}} | \Phi_i \nu_{iv_i} \boldsymbol{q}_i \rangle \, \mathrm{d}\boldsymbol{q}, \tag{9.16}$$

where $G_{nv}^{(+)}(q)$ is the asymptotic Green's function with outgoing spherical-wave boundary conditions::

$$G_{nv}^{(+)}(q) = \lim_{\epsilon\to 0^+} \frac{1}{E - \varepsilon_{nv} - \epsilon_q + i\epsilon}. \tag{9.17}$$

Here, E is the total scattering-system energy, ε_{nv} is the energy of the vibronic state $\Phi_n \nu_{nv}$, and $\epsilon_q = q^2/2$. As in Chapter 6, the superscript $\mathcal{N}$ on the transition operator indicates that the solutions to Eq. (9.16) are the $\hat{\mathsf{I}}^{\mathcal{N}}$-projected T-matrix elements

$$\langle \boldsymbol{q}_f \nu_{fv_f} \Phi_f | \hat{\mathsf{T}}^{\mathcal{N}} | \Phi_i \nu_{iv_i} \boldsymbol{q}_i \rangle = \langle \boldsymbol{q}_f \nu_{fv_f} \Phi_f | \hat{\mathsf{I}}^{\mathcal{N}} \hat{\mathsf{V}} \, \hat{\mathsf{I}}^{\mathcal{N}} | \psi_{n_i v_i}^{\mathcal{S}(+)} \rangle, \tag{9.18}$$

where the projection operator $\hat{\mathsf{I}}^{\mathcal{N}}$ is defined by

$$\hat{\mathsf{I}}^{\mathcal{N}} = \sum_{(n,v)\in\mathcal{N}} |\Phi_n \nu_{nv}\rangle \langle \nu_{nv} \Phi_n|. \tag{9.19}$$

The vibrational wave functions ν_{nv} are generated in the same way as outlined in Section 7.1 of Chapter 7, including the use of vibrational pseudostates to discretise the dissociative continuum of each electronic state. Hence, the $\hat{\mathsf{I}}^{\mathcal{N}}$-projected T-matrix elements converge to the true T-matrix elements as the number of vibronic states in the close-coupling expansion (9.15) is increased. From here on, the dependence on $\mathcal{N}$ will be dropped, with the understanding that all calculated cross sections have an inherent dependence on the size of the close-coupling expansion.

The projectile plane waves are expanded in partial waves as per Eq. (4.13), and the resulting equation for the partial-wave T-matrix elements is

$$\langle q_f L_f \Lambda_{L_f} \, \nu_{fv_f} \Phi_f | \hat{\mathsf{T}} | \Phi_i \nu_{iv_i} \, q_i L_i \Lambda_{L_i} \rangle = \langle q_f L_f \Lambda_{L_f} \, \nu_{fv_f} \Phi_f | \hat{\mathsf{V}} | \Phi_i \nu_{iv_i} \, q_i L_i \Lambda_{L_i} \rangle + \sum_{(n,v)\in\mathcal{N}} \sum_{L\Lambda_L} \int_0^\infty \langle q_f L_f \Lambda_{L_f} \nu_{fv_f} \Phi_f | \hat{\mathsf{V}} | \Phi_n \nu_{nv} q L \Lambda_L \rangle G_{nv}^{(+)}(q) \langle q L \Lambda_L \nu_{nv} \Phi_n | \hat{\mathsf{T}} | \Phi_i \nu_{iv_i} q_i L_i \Lambda_{L_i} \rangle \mathrm{d}q. \tag{9.20}$$

Although the total energy E entering Eq. (9.20) via the Green's function (9.17) is determined by the incident projectile energy and the ground-state energy of the target, the solution of Eq. (9.20) can yield results for scattering on excited states as well. Since the total energy is fixed, the T-matrix elements for scattering on an excited state nv must simply be interpreted as corresponding to a modified incident energy given by

$$E_i' = E_i - \varepsilon_{nv,10}, \tag{9.21}$$

where $\varepsilon_{nv,10}$ is the excitation energy of the state nv from the ground state ($n = 1$, $v = 0$).

9.3 Scattering-system symmetries and channels

As discussed in Chapter 6, the body-frame molecular close-coupling equations can be solved independently per total scattering system orbital angular-momentum projection Λ_{tot}, parity Π_{tot}, and electronic spin $\mathcal{S}$. For a given scattering-system symmetry $(\Lambda_{\text{tot}}, \Pi_{\text{tot}}, \mathcal{S})$, only certain combinations of target states and partial-wave projectile states which satisfy the requirements of the symmetry enter the Lippmann-Schwinger equation (9.20). Denoting the orbital angular-momentum projection, parity, and spin of the electronic state n as Λ_n, π_n, and s_n, respectively, these requirements are:

$$\Lambda_n + \Lambda_L = \Lambda_{\text{tot}} \tag{9.22}$$

$$\pi_n \cdot (-1)^L = \Pi_{\text{tot}} \tag{9.23}$$

$$\left| s_n \pm \tfrac{1}{2} \right| = \mathcal{S}. \tag{9.24}$$

Each pair $(nv, L\Lambda_L)$ satisfying Eqs. (9.22)–(9.24) is referred to as a *channel* in the partial-wave close-coupling calculation. For simplicity, the maximum value of Λ_{tot} included in the calculations is always taken to be equal to the projectile L_{max}. Both total parities $\Pi_{\text{tot}} = \pm 1$ are included. The spin channels included depend on the set of initial states for which results are required. For example, if scattering on the ground state of H_2 (singlet, $s = 0$) is all that is considered, then the only total spin possible is $\mathcal{S} = 1/2$. For scattering on triplet ($s = 1$)

states, $\mathcal{S} = 3/2$ is also possible and must be included. To save time, only non-negative $\Lambda_{\rm tot}$ must be considered, as each T-matrix element for negative $\Lambda_{\rm tot}$ has an equivalent matrix element from the positive $\Lambda_{\rm tot}$ calculation:

$$\begin{aligned}\langle \Lambda_{\rm tot} : q'L'\Lambda_{L'}\, \Phi_{n'}^{\Lambda_{n'}} \nu_{n'v'} | \hat{\mathsf{T}} | \Phi_n^{\Lambda_n} \nu_{nv}\, qL\Lambda_L : \Lambda_{\rm tot} \rangle \\ = \langle -\Lambda_{\rm tot} : q'L'(-\Lambda_{L'})\, \Phi_{n'}^{-\Lambda_{n'}} \nu_{n'v'} | \hat{\mathsf{T}} | \Phi_n^{-\Lambda_n} \nu_{nv}\, qL(-\Lambda_L) : -\Lambda_{\rm tot} \rangle.\end{aligned} \tag{9.25}$$

9.4 Solving the Lippmann-Schwinger equation

The solution of the Lippmann-Schwinger equation in the CCC and MCCC methods follows a standard procedure which has been discussed previously [87], but is included here also for completeness. For simplicity, Eq. (9.20) is written in the condensed form

$$T_{f,i}(q_f, q_i) = V_{f,i}(q_f, q_i) + \lim_{\epsilon \to 0^+} \sum_{n=1}^{N} \int_0^\infty \frac{V_{f,n}(q_f, q) T_{n,i}(q, q_i)}{E - \varepsilon_n - \epsilon_q + i\epsilon}\, {\rm d}q, \tag{9.26}$$

where the indices f, i, and n each specify all components of a given channel, and N is the total number of channels included in the calculation. Using standard methods of residue theory, Eq. (9.26) can be transformed into

$$\begin{aligned}T_{f,i}(q_f, q_i) = V_{f,i}(q_f, q_i) + \sum_{n=1}^{N} \mathcal{P} \int_0^\infty \frac{V_{f,n}(q_f, q) T_{n,i}(q, q_i)}{E - \varepsilon_n - \epsilon_q}\, {\rm d}q \\ - i\pi \sum_{n=1}^{N_{\rm open}} \frac{1}{q_n} V_{f,n}(q_f, q_n) T_{n,i}(q_n, q_i),\end{aligned} \tag{9.27}$$

where $N_{\rm open}$ is the number of open channels, and $q_{n'}$ is the on-shell outgoing momentum associated with excitation of channel n'. The symbol $\mathcal{P}$ indicates that the integral is of principle-value type, i.e.:

$$\begin{aligned}\mathcal{P} \int_0^\infty \frac{V_{f,n}(q_f, q) T_{n,i}(q, q_i)}{E - \varepsilon_n - \epsilon_q}\, {\rm d}q \\ = \lim_{\epsilon \to 0^+} \left[\int_0^{E - \varepsilon_n - \epsilon} \frac{V_{f,n}(q_f, q) T_{n,i}(q, q_i)}{E - \varepsilon_n - \epsilon_q}\, {\rm d}q + \int_{E - \varepsilon_n + \epsilon}^\infty \frac{V_{f,n}(q_f, q) T_{n,i}(q, q_i)}{E - \varepsilon_n - \epsilon_q}\, {\rm d}q \right].\end{aligned} \tag{9.28}$$

To avoid using complex arithmetic, the real K matrix is defined by

$$K_{n,i}(q,q_i) = \sum_{n'=1}^{N_{\text{open}}} T_{n,n'}(q,q_{n'}) \left(\delta_{n',i} + \frac{i\pi}{q_{n'}} K_{n',i}(q,q_i) \right). \tag{9.29}$$

Replacing the index i with n' in Eq. (9.27), and then multiplying each term on the right by $\left(\delta_{n',i} + i\pi q_{n'}^{-1} K_{n',i}(q_{n'},q_i)\right)$ and summing over open channels n' gives

$$\begin{aligned}
&\sum_{n'=1}^{N_{\text{open}}} T_{f,n'}(q_f,q_{n'}) \left(\delta_{n',i} + i\pi q_{n'}^{-1} K_{n',i}(q_{n'},q_i)\right) \\
&\quad = \sum_{n'=1}^{N_{\text{open}}} V_{f,n'}(q_f,q_{n'}) \left(\delta_{n',i} + i\pi q_{n'}^{-1} K_{n',i}(q_{n'},q_i)\right) \\
&\qquad + \sum_{n=1}^{N} \mathcal{P} \int_0^{\infty} \frac{V_{f,n}(q_f,q) \sum_{n'=1}^{N_{\text{open}}} T_{n,n'}(q,q_{n'}) \left(\delta_{n',i} + i\pi q_{n'}^{-1} K_{n',i}(q_{n'},q_i)\right)}{E - \varepsilon_n - \epsilon_q} \, \mathrm{d}q \\
&\qquad - i\pi \sum_{n=1}^{N_{\text{open}}} \frac{1}{q_n} V_{f,n}(q_f,q_n) \sum_{n'=1}^{N_{\text{open}}} T_{n,n'}(q_n,q_{n'}) \left[\delta_{n',i} + i\pi q_{n'}^{-1} K_{n',i}(q_{n'},q_i)\right].
\end{aligned} \tag{9.30}$$

Substituting in the definition of the K matrix from Eq. (9.29) simplifies this to

$$\begin{aligned}
K_{f,i}(q_f,q_i) &= V_{f,i}(q_f,q_i) + i\pi \sum_{n'=1}^{N_{\text{open}}} \frac{1}{q_{n'}} V_{f,n'}(q_f,q_{n'}) K_{n',i}(q_{n'},q_i) \\
&\quad + \sum_{n} \mathcal{P} \int_0^{\infty} \frac{V_{f,n}(q_f,q) K_{n,i}(q,q_i)}{E - \varepsilon_n - \epsilon_q} \, \mathrm{d}q - i\pi \sum_{n=1}^{N_{\text{open}}} \frac{1}{q_n} V_{f,n}(q_f,q_n) K_{n,i}(q_n,q_i),
\end{aligned} \tag{9.31}$$

then the summations over the open channels cancel to give the partial-wave Lippmann-Schwinger equation for the K matrix:

$$K_{f,i}(q_f,q_i) = V_{f,i}(q_f,q_i) + \sum_{n=1}^{N} \mathcal{P} \int_0^{\infty} \frac{V_{f,n}(q_f,q) K_{n,i}(q,q_i)}{E - \varepsilon_n - \epsilon_q} \, \mathrm{d}q. \tag{9.32}$$

These coupled integral equations are converted into a system of linear equations by converting the integral into a weighted sum:

$$K_{f,i} = V_{f,i} + \sum_{n=1}^{N} V_{f,n} w_n K_{n,i}, \tag{9.33}$$

where the weights w_n contain both the integration weights, and the value of the Green's function at each point. The indices f, i, and n now specify both a channel and a value of q in the discretised momentum grid. Some rearrangement gives

$$\sum_{n=1}^{N} \left[\delta_{f,n} - w_n V_{f,n}\right] K_{n,i} = V_{f,i}, \tag{9.34}$$

which is solved for the half-on-shell K matrix elements by allowing f to range over the same values as n and then solving the resulting system of linear equations. Since the integral in Eq. (9.32) is of principle-value type, the discretised momentum grid is chosen to have points placed symmetrically around the singularity for each open channel, and does not contain the on-shell points themselves. The on-shell K-matrix elements must then be obtained by substituting the half-off-shell $K_{n,i}$ into Eq. (9.33). Finally, Eq. (9.29) is solved for the on-shell T-matrix elements.

9.5 V-matrix elements

9.5.1 Direct

Since the direct interaction potential $\hat{\mathrm{V}}_{\mathrm{dir}}$ does not contain any operators acting on the internuclear coordinate R, the direct partial-wave V-matrix element can be obtained simply by calculating the electronic matrix element first as a function of the internuclear separation before performing the vibrational integrations:

$$\langle q' L' \Lambda_{L'}\, \nu_{n'v'} \Phi_{n'} | \hat{\mathrm{V}}_{\mathrm{dir}} | \Phi_n \nu_{nv}\, q L \Lambda_L \rangle = \langle \nu_{n'v'} | \, \langle q' L' \Lambda_{L'}\, \Phi_{n'} | \hat{\mathrm{V}}_{\mathrm{dir}} | \Phi_n\, q L \Lambda_L \rangle \, | \nu_{nv} \rangle. \tag{9.35}$$

Although the electronic matrix element is independent of the vibrational levels (v', v), each vibronic state has a unique momentum-space grid (to handle the principle-value integration), and hence the (q', q) mesh on which the electronic matrix element must be evaluated is distinct for each pair of vibrational levels. Rather than recalculating it each time, the electronic matrix element can be evaluated once and then interpolated onto a new (q', q) mesh for each pair of vibrational levels using a bicubic interpolation procedure. To perform the in-

tegration over R, the matrix elements are evaluated over a range of discrete R values before being interpolated onto the finer R grid on which the vibrational wave functions are defined.

9.5.2 Exchange

Since the exchange potential operator in Eq. (9.14) contains the vibrational kinetic-energy operator (in the $\hat{\mathsf{H}}$ operator), the exchange V-matrix element cannot be separated as simply as the direct V-matrix element. However, a similar approach can be taken by treating the electronic and vibrational components of the scattering Hamiltonian separately (writing $\hat{\mathsf{H}} = \hat{\mathsf{H}}_{\rm el} + \hat{\mathsf{K}}_{\rm v}$), giving

$$\begin{aligned}\langle q'L'\Lambda_{L'}\,\nu_{n'v'}\Phi_n|\hat{\mathsf{V}}_{\rm exch}|\Phi_n\nu_{nv}qL\Lambda_L\rangle \\ = \langle\nu_{n'v'}|\,\langle q'L'\Lambda_{L'}\,\Phi_{n'}|(E-\hat{\mathsf{H}}_{\rm el})\sum_{j=1}^{2}\hat{\mathsf{P}}_{0j}|\Phi_n\,qL\Lambda_L\rangle\,|\nu_{nv}\rangle \\ - \langle\nu_{n'v'}|\,\langle q'L'\Lambda_{L'}\,\Phi_{n'}|\sum_{j=1}^{2}\hat{\mathsf{P}}_{0j}|\Phi_n\,qL\Lambda_L\rangle\,\hat{\mathsf{K}}_{\rm v}|\nu_{nv}\rangle. \qquad (9.36)\end{aligned}$$

Here, the electronic matrix elements

$$\langle q'L'\Lambda_{L'}\,\Phi_{n'}|(E-\hat{\mathsf{H}}_{\rm el})\sum_{j=1}^{2}\hat{\mathsf{P}}_{0j}|\Phi_n\,qL\Lambda_L\rangle \qquad (9.37)$$

$$\langle q'L'\Lambda_{L'}\,\Phi_{n'}|\sum_{j=1}^{2}\hat{\mathsf{P}}_{0j}|\Phi_n\,qL\Lambda_L\rangle \qquad (9.38)$$

are evaluated as a function of R before the vibrational integrals are evaluated. The quantity $\hat{\mathsf{K}}_{\rm v}|\nu_{nv}\rangle$ can in principle be evaluated using the analytical properties of the Laguerre basis (7.6), however since the vibrational eigenstates satisfy

$$\hat{\mathsf{K}}_{\rm v}|\nu_{nv}\rangle = [\varepsilon_{nv} - \epsilon_n(R)]\,|\nu_{nv}\rangle, \qquad (9.39)$$

we can immediately write

$$\begin{aligned}\langle\nu_{n'v'}|\,\langle q'L'\Lambda_{L'}\,\Phi_{n'}|\sum_{j=1}^{2}\hat{\mathsf{P}}_{0j}|\Phi_n\,qL\Lambda_L\rangle\,\hat{\mathsf{K}}_{\rm v}|\nu_{nv}\rangle \\ = \langle\nu_{n'v'}|\,\langle q'L'\Lambda_{L'}\,\Phi_{n'}|\sum_{j=1}^{2}\hat{\mathsf{P}}_{0j}|\Phi_n\,qL\Lambda_L\rangle\,[\varepsilon_{nv}-\epsilon_n(R)]\,|\nu_{nv}\rangle. \qquad (9.40)\end{aligned}$$

For the more general case of vibrational pseudostates, which satisfy

$$\langle \nu_{nv'} | \hat{\mathsf{K}}_{\rm v} | \nu_{nv} \rangle = \langle \nu_{nv'} | \left[\varepsilon_{nv} - \epsilon_n(R) \right] | \nu_{nv} \rangle, \tag{9.41}$$

we can insert the identity operator $\sum_{v''} |\nu_{nv''}\rangle\langle\nu_{nv''}|$ before $\hat{\mathsf{K}}_{\rm v}$ to give

$$\begin{aligned}
&\langle \nu_{n'v'} | \langle q' L' \Lambda_{L'} \, \Phi_{n'} | \sum_{j=1}^{2} \hat{\mathsf{P}}_{0j} | \Phi_n \, q L \Lambda_L \rangle \, \hat{\mathsf{K}}_{\rm v} | \nu_{nv} \rangle \\
&\quad = \langle \nu_{n'v'} | \langle q' L' \Lambda_{L'} \, \Phi_{n'} | \sum_{j=1}^{2} \hat{\mathsf{P}}_{0j} | \Phi_n \, q L \Lambda_L \rangle \sum_{v''} | \nu_{nv''} \rangle \langle \nu_{nv''} | \hat{\mathsf{K}}_{\rm v} | \nu_{nv} \rangle \\
&\quad = \langle \nu_{n'v'} | \langle q' L' \Lambda_{L'} \, \Phi_{n'} | \sum_{j=1}^{2} \hat{\mathsf{P}}_{0j} | \Phi_n \, q L \Lambda_L \rangle \sum_{v''} | \nu_{nv''} \rangle \langle \nu_{nv''} | \varepsilon_{nv} - \epsilon_n(R) | \nu_{nv} \rangle \\
&\quad = \langle \nu_{n'v'} | \langle q' L' \Lambda_{L'} \, \Phi_{n'} | \sum_{j=1}^{2} \hat{\mathsf{P}}_{0j} | \Phi_n \, q L \Lambda_L \rangle \left[\varepsilon_{nv} - \epsilon_n(R) \right] | \nu_{nv} \rangle.
\end{aligned} \tag{9.42}$$

It is most convenient to take the electronic matrix elements directly from the existing fixed-nuclei MCCC calculations. However, the fixed-nuclei exchange V-matrix element is evaluated in terms of the R-dependent total scattering energy

$$E_{\rm FN}(R) = E_i + \epsilon_1(R), \tag{9.43}$$

where E_i is the incident projectile energy, and $\epsilon_1(R)$ is the (R-dependent) ground electronic state energy. This must be converted into the vibronic total scattering energy using

$$E = E_{\rm FN}(R) - \epsilon_1(R) + \varepsilon_{10}. \tag{9.44}$$

Denoting the fixed-nuclei exchange V-matrix element by

$$V^{\rm exch}_{n'L'\Lambda_{L'},nL\Lambda_L}(q', q, R) = \langle q' L' \Lambda_{L'} \, \Phi_{n'} | (E_{\rm FN}(R) - \hat{\mathsf{H}}_{\rm el}) \sum_{j=1}^{2} \hat{\mathsf{P}}_{0j} | \Phi_n \, q L \Lambda_L \rangle, \tag{9.45}$$

and defining

$$P_{n'L'\Lambda_{L'},nL\Lambda_L}(q', q, R) = \langle q' L' \Lambda_{L'} \, \Phi_{n'} | \sum_{j=1}^{2} \hat{\mathsf{P}}_{0j} | \Phi_n \, q L \Lambda_L \rangle, \tag{9.46}$$

the vibronic exchange V-matrix element considering both the energy correction from Eq. (9.44) and the contribution of the vibrational kinetic-energy operator

from Eq. (9.42) is

$$\langle q' L' \Lambda_{L'}\, \nu_{n'v'} \Phi_n | \hat{\mathsf{V}}_{\rm exch} | \Phi_n \nu_{nv} q L \Lambda_L \rangle \tag{9.47}$$
$$= \langle \nu_{n'v'} | \left[V_{n'L'\Lambda_{L'},nL\Lambda_L}(q', q, R) + (\epsilon_{n,1}(R) - \varepsilon_{nv,10})\, P_{n'L'\Lambda_{L'},nL\Lambda_L}(q', q, R) \right] | \nu_{nv} \rangle .$$

Note again that $\epsilon_{n,1}(R)$ is the electronic excitation energy of state n from the electronic ground state, and $\varepsilon_{nv,10}$ is the vibronic excitation energy of state nv from the vibronic ground state.

The evaluation of Eq. (9.47) simply requires the electronic matrices in Eqs. (9.45) and (9.46) to be evaluated once at each internuclear separation. Both are interpolated onto a new (q', q) mesh for each pair of vibrational levels. In order to ensure the accuracy of the electronic elements at all relevant internuclear separations, they are each evaluated in spheroidal coordinates and converted into the analogous spherical-coordinate matrix elements using Eq. (6.46). The reason this step is required is that the spheroidal coordinate system is dependent on the internuclear separation, so the integration over R only makes sense in spherical coordinates. Expressions for the spheroidal matrix elements are given in Ref. [202].

9.6 Consequences of the Born-Oppenheimer approximation

In the present formulation the Born-Oppenheimer approximation is applied to the target wave functions (but not to the total scattering wave function). The common assumption that the vibrational kinetic-energy operator does not act on the electronic wave functions is what allows $\hat{\mathsf{K}}_{\rm v}$ to be moved outside the integration over electronic coordinates in Eq. (9.36). An unfortunate consequence of this, however, is that the exchange V-matrix element as defined in Eq. (9.36) is not symmetric. In the numerical implementation of this method, the V matrix is treated as symmetric, with only one triangle of the matrix evaluated and copied into the other. The effect of the lack of symmetry in Eq. (9.36) then is to have two different V matrices depending on whether it is the upper- or lower-triangle

elements which are evaluated. For the case of H_2, it has been determined that the difference between these two choices amounts to an error of less than 1%, with no noticeable effect on the calculated cross sections. It is likely that this will be true for any target where the Born-Oppenheimer approximation is sufficiently accurate to describe the target wave functions, however it will be important to check this explicitly as the method is applied to other target molecules. In the future, it may be necessary to move beyond the Born-Oppenheimer approximation to describe the target wave functions.

9.7 Computer program

A Fortran program was written to perform the calculations as described in this chapter. In order to accommodate the large V matrices, which quickly exceed the memory available on a single supercomputer node before convergence is reached, the code utilises an MPI parallelism scheme. Each node is assigned a block of the V-matrix with approximately equal numbers of matrix elements to evaluate, and once each node has computed its portion of the matrix elements the linear equations are solved using ScaLAPACK routines. Within each node, OpenMP parallelism is used to speed up the calculations and make use of each processor core. Fig. 9.1 shows a simplified flowchart of the program's structure.

9.8 Chapter 9 summary

This chapter has presented the theoretical details of the vibrational-electronic molecular convergent close-coupling (VE MCCC) method, which has been developed during this PhD project. The VE MCCC method does not apply the adiabatic-nuclei approximation to the vibrational motion, instead treating the electronic and vibrational motions on the same footing. This allows for an implicit representation of the vibrational levels in the compound H_2^- states, leading to an accurate treatment of resonant scattering in the calculations while maintaining the proper account of non-resonant scattering. Since the inclusion of both electronic and vibrational levels in the close-coupling expansion leads to large numbers of coupled channels, there has been a strong focus on efficiency in

the code implementation of the VE MCCC method so that physically realistic calculations are tractable.

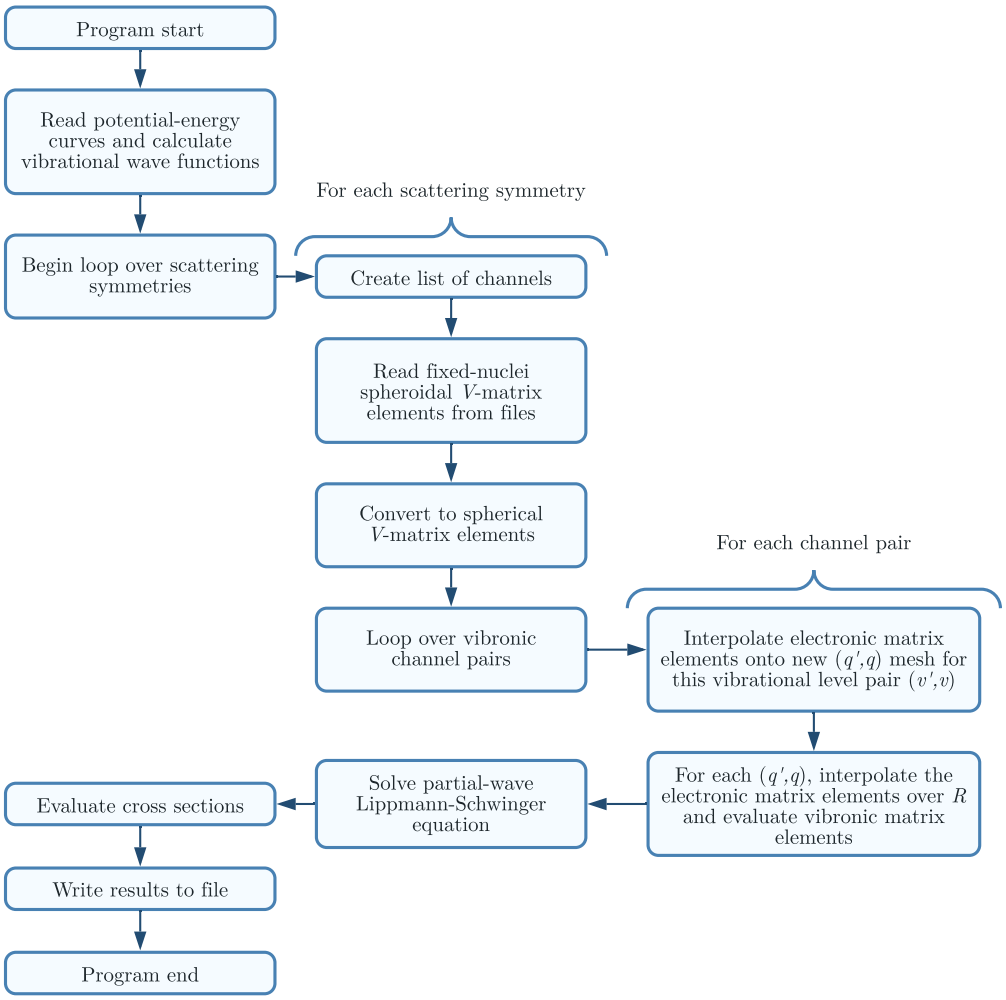

Figure 9.1: Flowchart of the VE MCCC code.

Chapter 10

Vibrational-electronic molecular convergent close-coupling: results

This chapter presents an investigation of resonances in the cross sections for scattering on the ground electronic state of H_2, considering pure vibrational excitation, dissociation via the $b\ ^3\Sigma_u^+$ state, and excitation of the $B\ ^1\Sigma_u^+$ state, in the 10–14 eV energy region. Calculations were performed using the vibrational-electronic molecular convergent close-coupling (VE MCCC) method discussed previously in Chapter 9. The most prominent resonance in the 10–14 eV region is the well-known $C\ ^2\Sigma_g^+$ state of H_2^-, which has been the focus of many previous studies [112, 113, 115]. A number of resonances of other symmetries have also been identified by Stibbe and Tennyson [230]. In the present work the $^2\Sigma_g^+$, $^2\Sigma_u^+$, $^2\Pi_g$, and $^2\Pi_u$ resonances in the 10–14 eV region are studied. In Sec. 10.1, details of the calculations and testing of various input parameters and convergence are discussed. Then in Sec. 10.2 results are presented. Some sections contain text or figures from published work by the candidate [1]. The publisher (the American Physical Society) provides the right to use an article or a portion of an article in a thesis or dissertation without requesting permission.

10.1 Calculation details and testing

The calculated cross sections in the VE MCCC method are affected both by the choice of electronic target states included in the close-coupling expansion, and the number of vibrational levels included per electronic state. With many electronic states supporting a large number of bound vibrational levels, and the

need to include vibrational pseudostates to discretise the dissociative vibrational continua, the size of the calculations can quickly become intractable. Therefore, a number of tests have been performed using model calculations in order to study the effects of including various scattering channels, and determine suitable input parameters. Since this is a newly developed method and computer code, it was important to perform detailed tests, and they will serve as a useful reference for future calculations.

10.1.1 Continuum Franck-Condon factors

In order to determine how densely the dissociative vibrational continua should be discretised, we can study the continuum Franck-Condon (FC) factors, defined by

$$F_{n_f E_\mathrm{k}, n_i v_i} = \left| \langle \nu_{n_f E_\mathrm{k}} | \nu_{n_i v_i} \rangle \right|^2 , \tag{10.1}$$

where $\nu_{n_i v_i}$ is a bound vibrational level in the initial electronic state ($X\,{}^1\Sigma_g^+$ in the present case), and $\nu_{n_f E_\mathrm{k}}$ is a continuum vibrational level of kinetic energy E_k in the electronic state n_f. Fig. 10.1 presents these factors as a function of E_k for continuum vibrational levels in the $b\,{}^3\Sigma_u^+$ state, for each initial vibrational level in the $X\,{}^1\Sigma_g^+$ state. The rich oscillatory structures in the FC factors indicate that a dense discretisation of the $b\,{}^3\Sigma_u^+$ vibrational continuum in the 0 to 15 eV region of E_k will be necessary. In particular, since the positions of the oscillations are different for each initial bound vibrational level, an accurate representation of the vibrational continuum for all initial states will require the discretisation to be sufficiently fine over a relatively large span of energies.

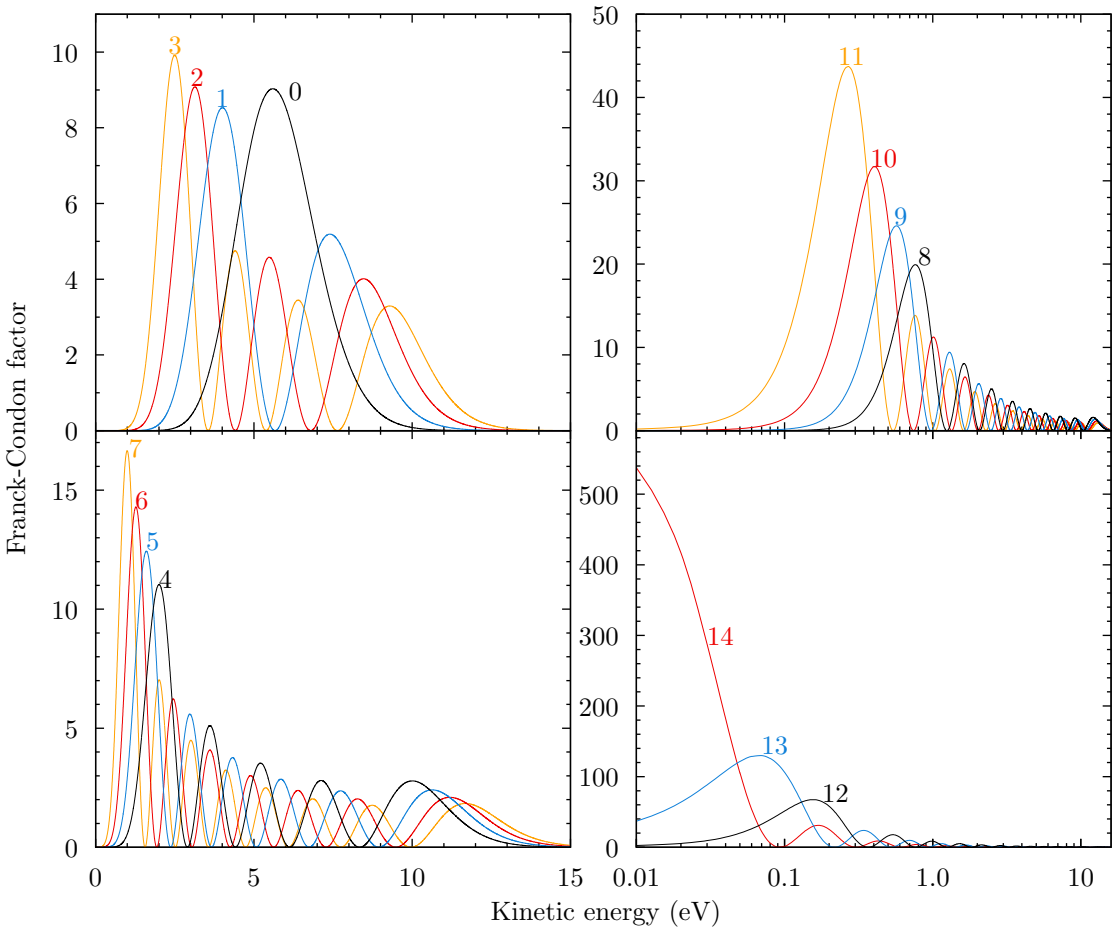

Figure 10.1: Continuum Franck-Condon factors between the bound vibrational levels of the $X\,^1\Sigma_g^+$ state and the dissociative levels of the $b\,^3\Sigma_u^+$ state, as a function of the dissociative-level kinetic energy. Each line corresponds to a different initial vibrational level, as labelled. The results are split over 4 panels for clarity.

In order to determine the accuracy of the vibrational continuum discretisation, the FC factors in Eq. (10.1) can also be calculated using the vibrational pseudostates. Since the pseudostates form a complete set we have that

$$\langle \nu_{n_f E_\mathrm{k}} | \nu_{n_i v_i} \rangle = \sum_{v_f} \langle \nu_{n_f E_\mathrm{k}} | \nu_{n_f v_f} \rangle \langle \nu_{n_f v_f} | \nu_{n_i v_i} \rangle, \tag{10.2}$$

and the overlap $\langle \nu_{n_f E_\mathrm{k}} | \nu_{n_f v_f} \rangle$ is essentially zero except when the true vibrational continuum wave function $\nu_{n_f E_\mathrm{k}}$ and vibrational pseudostate $\nu_{n_f v_f}$ have the same energy. Hence, denoting by $\varepsilon_{n_f v_f}$ the vibrational pseudostate energy (here relative

to the dissociation limit for comparison with $E_{\rm k}$), we have

$$\langle \nu_{n_i v_i} | \nu_{n_f E_{\rm k}} \rangle \approx \langle \nu_{n_f \varepsilon_{n_f v_f}} | \nu_{n_f v_f} \rangle \langle \nu_{n_f v_f} | \nu_{n_i v_i} \rangle, \tag{10.3}$$

and the FC factor for the vibrational pseudostate $\nu_{n_f v_f}$ which can be directly compared with Eq. (10.1) is given by

$$F_{n_f \varepsilon_{n_f v_f}, n_i v_i} = \left| \langle \nu_{n_f \varepsilon_{n_f v_f}} | \nu_{n_f v_f} \rangle \langle \nu_{n_f v_f} | \nu_{n_i v_i} \rangle \right|^2 . \tag{10.4}$$

This simply requires the additional evaluation of the overlap between each vibrational pseudostate and its corresponding true vibrational continuum wave function of the same energy. It is worth noting that this is similar to the method for obtaining single differential ionisation cross sections in the atomic CCC method [256], and can be applied in the future to extract energy-differential (kinetic-energy release) dissociation cross sections in VE MCCC calculations.

Fig. 10.2 presents the $X\ ^1\Sigma_g^+(v_i) \rightarrow b\ ^3\Sigma_u^+$ FC factors for $v_i = 0$, 7, and 14, comparing the calculations using true vibrational continuum wave functions (lines) with those using vibrational pseudostates (points). The distribution of the points along the horizontal axis reflects the distribution of vibrational pseudostate energies obtained from the diagonalisation procedure. Each of the nine panels in Fig. 10.2 represents a calculation with a different Laguerre basis size N (100, 200, 300) and exponential falloff α (5.0, 10.0, 15.0), for the purposes of determining the Laguerre basis parameters offering the best discretisation. For the present work, the Laguerre basis with $N = 300$ and $\alpha = 15.0$ will be used to discretise the $b\ ^3\Sigma_u^+$-state vibrational continuum, since it provides a more-than sufficient number of points per oscillation of the FC factor for every initial vibrational level. This basis generates vibrational pseudostate energies up to 10^5 eV (relative to the dissociative limit), so it will not be necessary to include all 300 vibrational pseudostates. In order to cover the 0–15 eV range of kinetic energies spanned by the $v_i = 0$–14 FC factors (see Fig. 10.1), including the first 204 vibrational pseudostates will suffice. For simplicity, the same Laguerre basis ($N = 300, \alpha = 15.0$) will be used to generate the vibrational levels for all electronic states in this work. This is sufficient to accurately reproduce all bound vibrational levels of the electronic states considered here, and it will be shown

later that coupling to the dissociative vibrational continua of electronic states above the $b\ ^3\Sigma_u^+$ state is not important in the 10–14 eV energy range of interest here so there is no concern about generating too many vibrational pseudostates in the higher electronic states with this large basis. It is worth noting that a

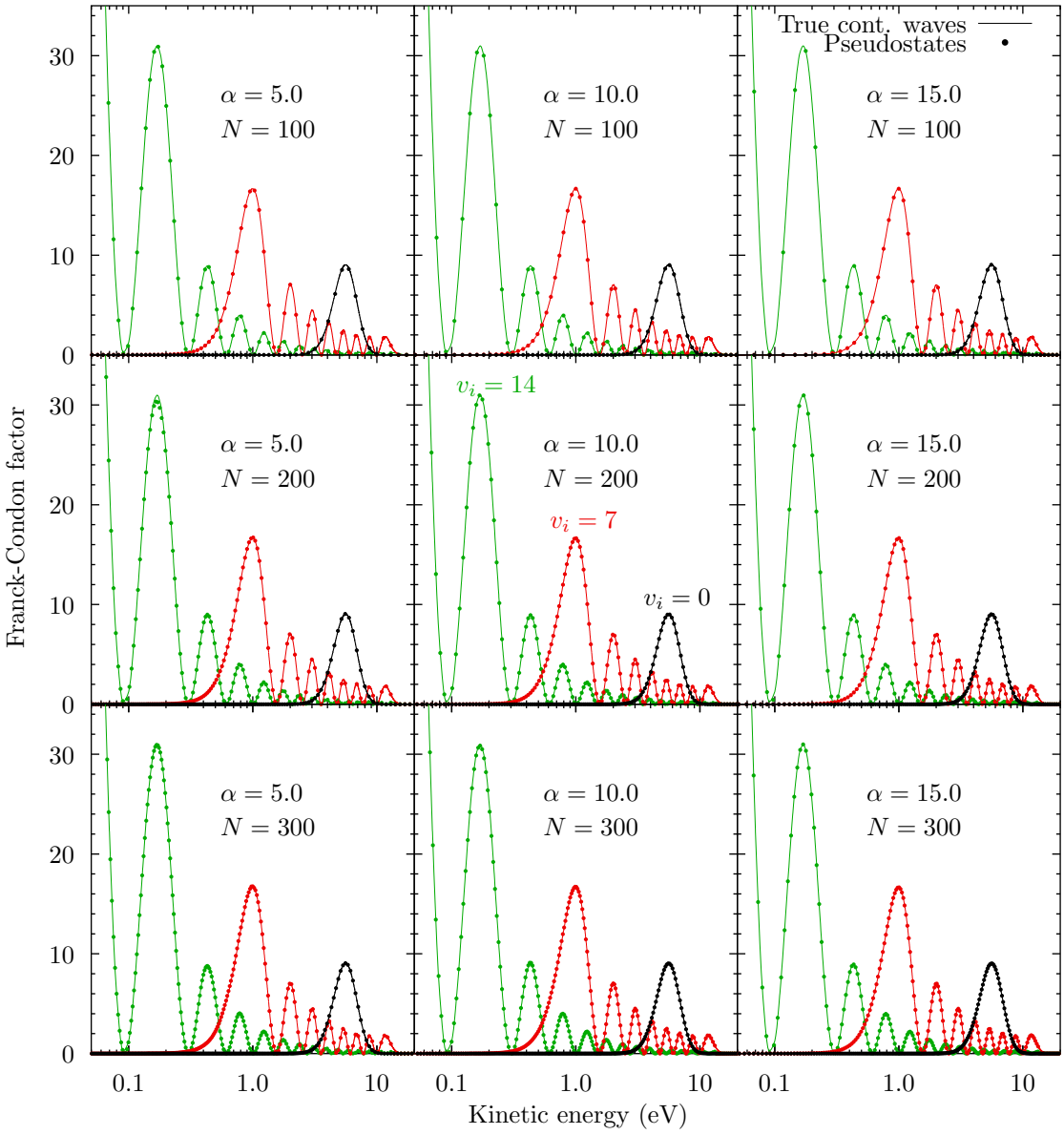

Figure 10.2: Continuum Franck-Condon factors between the bound vibrational levels of the $X\ ^1\Sigma_g^+$ state and the dissociative levels of the $b\ ^3\Sigma_u^+$. Comparison is made between the calculations using true vibrational continuum wave functions, and using the vibrational pseudostates resulting from diagonalising the vibrational Hamiltonian in a Laguerre basis with exponential falloff α and basis size N as specified in each panel. The initial vibrational levels (0, 7, and 14) are as labelled in the centre panel.

large basis can be required to accurately calculate the vibrational wave functions in some of the excited electronic states which support a large number of bound vibrational levels (such as the $B\,{}^1\Sigma_u^+$ state). The vibrational energies generated in the $X\,{}^1\Sigma_g^+$ and $b\,{}^3\Sigma_u^+$ states (up to 20 eV kinetic-energy release) with the $N = 300$ basis are illustrated in Fig. 10.3. The density of the vibrational pseudostates near the dissociative limit is so fine that individual levels cannot be visibly resolved in this region. Recall that this high density of vibrational pseudostates is required to accurately model the integration of the oscillatory energy-differential dissociation cross sections with a summation over the discrete pseudostates.

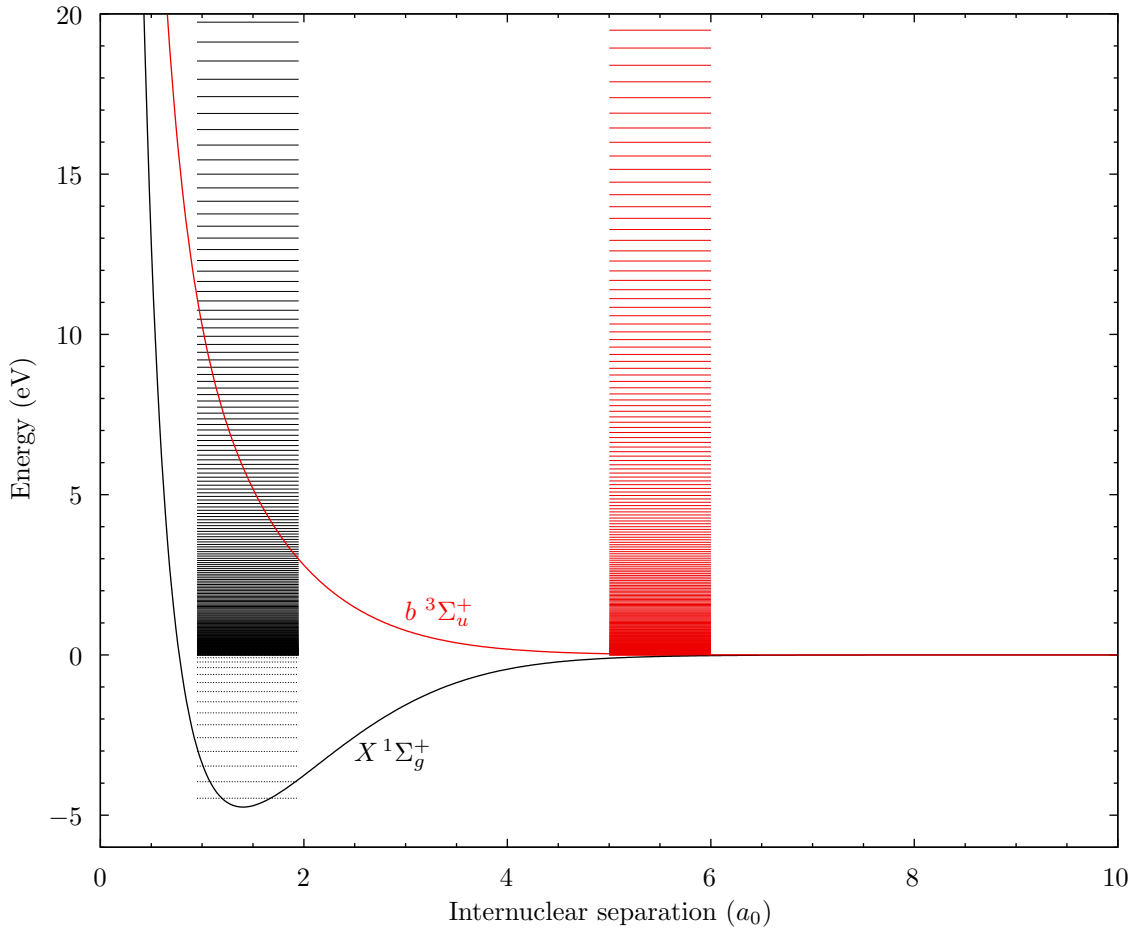

Figure 10.3: Potential-energy curves of the $X\,{}^1\Sigma_g^+$ and $b\,{}^3\Sigma_u^+$ states, and the vibrational energies generated in each using a Laguerre basis with $\alpha = 15.0$ and $N = 300$. Energies are given relative to the dissociative limit (i.e. negative energies correspond to bound levels). Bound levels are indicated by dashed lines.

10.1.2 Two-state convergence studies

Since the $b\ ^3\Sigma_u^+$ state has the largest dissociative excitation cross section, and is the only electronic state without bound vibrational levels, it should be expected that coupling to the $b\ ^3\Sigma_u^+$-state vibrational continuum will be more important than to the vibrational continuum of any other electronic state. Furthermore, the $X\ ^1\Sigma_g^+$ and $b\ ^3\Sigma_u^+$ vibrational continua overlap significantly, so it will be important to verify the importance of coupling to the $X\ ^1\Sigma_g^+$ dissociative levels as well. In this subsection, model VE MCCC calculations are performed involving only the $X\ ^1\Sigma_g^+$ and $b\ ^3\Sigma_u^+$ electronic states to investigate the rate of convergence with respect to the number of vibrational pseudostates included. Since a large Laguerre basis with $N = 300$ and $\alpha = 15.0$ is used for both states, the convergence will be verified with respect to the maximum excitation energy (with respect to the $X\ ^1\Sigma_g^+(v = 0)$ level) of the vibrational pseudostates.

Fig. 10.4 presents cross sections for excitation of the $b\ ^3\Sigma_u^+$ and $X\ ^1\Sigma_g^+$ states (summed over final vibrational levels) from the $v_i = 0$, 3, 6, and 9 levels in the $X\ ^1\Sigma_g^+$. The scattering model includes only bound vibrational levels in the $X\ ^1\Sigma_g^+$ state and has maximum excitation energies of $E_{\max} = 10$, 20, and 30 eV in the $b\ ^3\Sigma_u^+$-state vibrational continuum. A small partial-wave expansion with $L_{\max} = 1$ was used, since there is no reason to expect that the convergence with respect to vibrational levels would be substantially slower for higher partial waves. The cross sections are fully converged with $E_{\max} = 20$ eV, which corresponds to the inclusion of the 204 $b\ ^3\Sigma_u^+$ vibrational pseudostates required to cover the 0–15 range of kinetic-energy release (see Fig. 10.1).

Fig. 10.5 presents a similar convergence analysis, comparing calculations with only bound vibrational levels in the $X\ ^1\Sigma_g^+$ state with those including dissociative vibrational pseudostates in the $X\ ^1\Sigma_g^+$ state up to $E_{\max} = 10.0$ and 20.0 eV excitation energies. Here, the $b\ ^3\Sigma_u^+$ vibrational pseudostates are included up to $E_{\max} = 20$ eV. For scattering on low vibrational levels it is sufficient to include only the bound vibrational levels in the $X\ ^1\Sigma_g^+$ state. However, for scattering on higher levels there is evidently coupling between the $X\ ^1\Sigma_g^+$ and $b\ ^3\Sigma_u^+$ vibrational continua, leading to a reduction of the $b\ ^3\Sigma_u^+$ cross section when vibrational pseudostates are included in the $X\ ^1\Sigma_g^+$ state. Convergence is reached with $E_{\max} =$

10.0 eV in the $X\,^1\Sigma_g^+$ vibrational continuum.

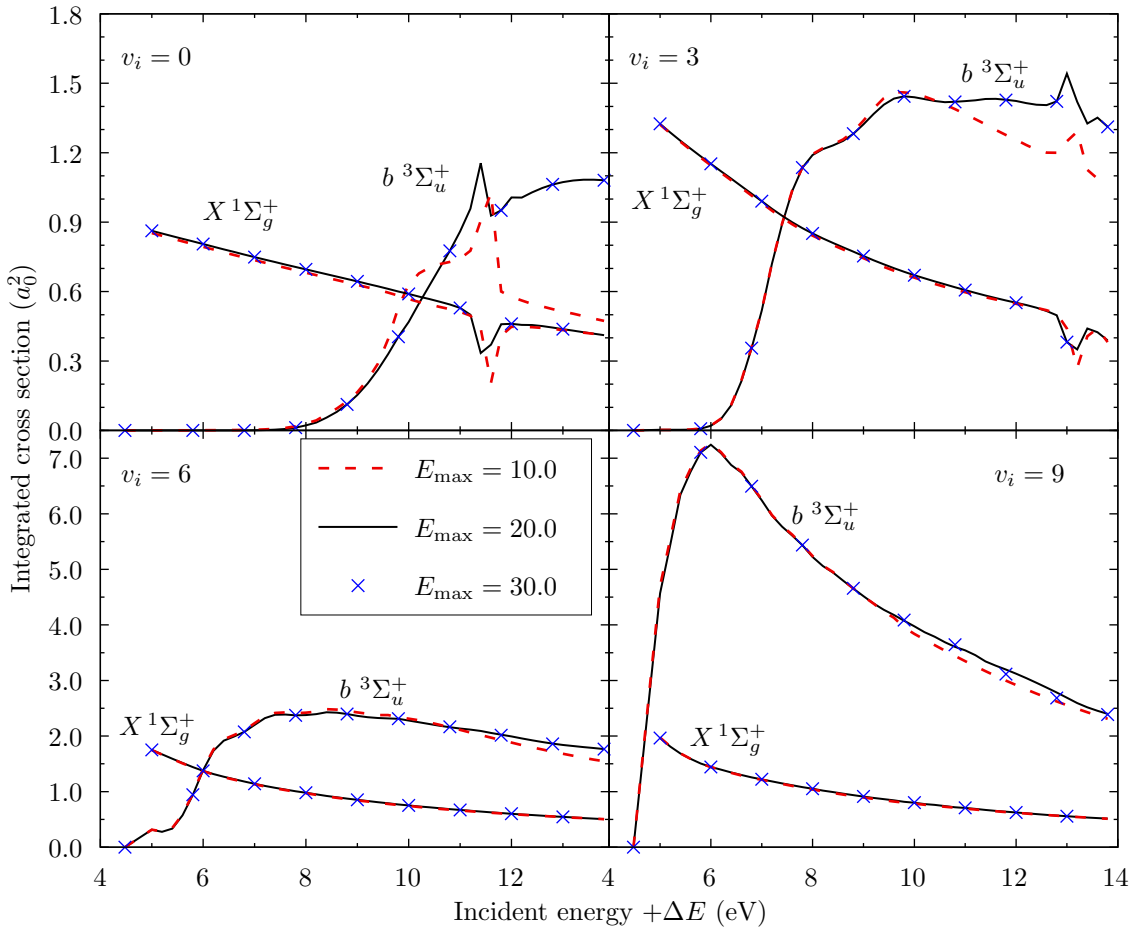

Figure 10.4: Convergence of the $X\,^1\Sigma_g^+$ and $b\,^3\Sigma_u^+$ excitation cross sections with respect to the maximum excitation energy $E_{\max}$ of the $b\,^3\Sigma_u^+$ vibrational pseudostates (from the $X\,^1\Sigma_g^+(v = 0)$ level). The results are from a model calculation with $L_{\max} = 1$ and including only the $X\,^1\Sigma_g^+$ and $b\,^3\Sigma_u^+$ states. Cross sections are displayed as a function of the incident energy plus the excitation energy of the initial state from the $v = 0$ vibrational level.

In Chapter 7, the $b\,^3\Sigma_u^+$ vibrational pseudostates obtained with the $N = 300$ $\alpha = 15$ basis were presented (Fig. 7.11). The pseudostates decay at successively smaller values of R as they increase in energy, but the pseudostates very close to the dissociation threshold can extend to internuclear separations far beyond those where the present electronic structure model is accurate. In order to verify that these larger R values do not substantially contribute to the calculations, a parameter was included in the code which limits the upper bound of the R integration when evaluating V-matrix elements. By varying this parameter during

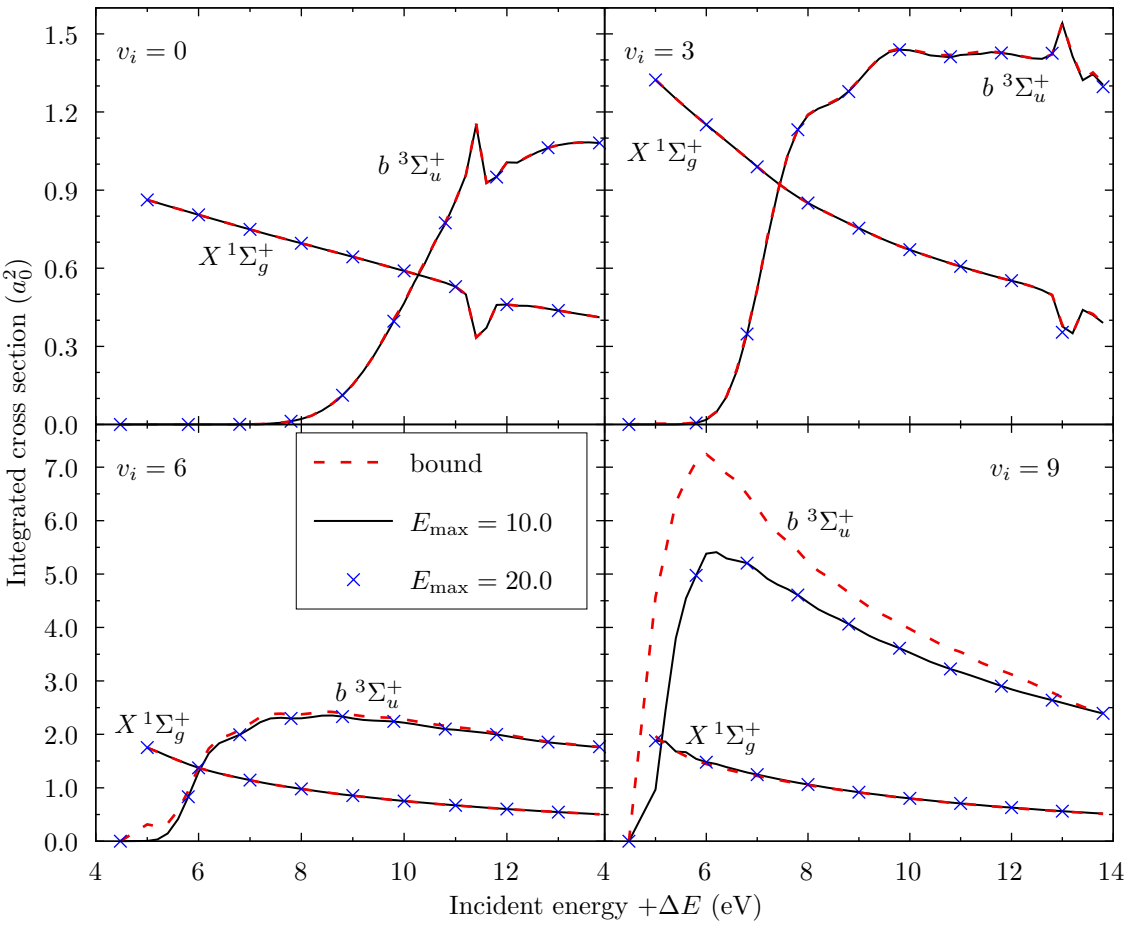

Figure 10.5: Convergence of the $X\ ^1\Sigma_g^+$ and $b\ ^3\Sigma_u^+$ excitation cross sections with respect to the maximum excitation energy $E_{\max}$ of the $X\ ^1\Sigma_g^+$ vibrational pseudostates (from the $X\ ^1\Sigma_g^+(v = 0)$ level). The results are from a model calculation with $L_{\max} = 1$ and including only the $X\ ^1\Sigma_g^+$ and $b\ ^3\Sigma_u^+$ states. Cross sections are displayed as a function of the incident energy plus the excitation energy of the initial state from the $v = 0$ vibrational level.

test calculations is was determined that internuclear separations beyond 10 a_0 do not affect the results for scattering on the $X\ ^1\Sigma_g^+$ vibrational levels, and hence the present electronic structure model is sufficient. If calculations are to be performed for scattering on excited electronic states with much more diffuse vibrational wave functions (such as the higher vibrational levels of the $B\ ^1\Sigma_u^+$ state), then a more accurate electronic structure model would be required.

10.1.3 Dissociative vibrational pseudostates in higher electronic states

In the energy region of interest for the present studies (below 14 eV for scattering on the ground state) the dissociative vibrational continua of the electronic states above the $b\ ^3\Sigma_u^+$ state are all energetically inaccessible. Therefore, it should not be important to include vibrational pseudostates in these electronic states. In this section, this assumption is tested using a model calculation including the $n = 1$–2 electronic states ($X\ ^1\Sigma_g^+$, $b\ ^3\Sigma_u^+$, $B\ ^1\Sigma_u^+$, $a\ ^3\Sigma_g^+$, $c\ ^3\Pi_u$, and $EF\ ^1\Sigma_g^+$) and $L_{\max} = 1$. Dissociative vibrational pseudostates are included in the $X\ ^1\Sigma_g^+$ and $b\ ^3\Sigma_u^+$ according to the converged two-electronic-state model discussed above. For each of the $B\ ^1\Sigma_u^+$, $a\ ^3\Sigma_g^+$, $c\ ^3\Pi_u$, and $EF\ ^1\Sigma_g^+$ states, a calculation is performed with dissociative vibrational pseudostates included in that particular electronic state. For simplicity, all vibrational pseudostates generated from a Laguerre basis with $N = 300$ and $\alpha = 15.0$ are included. By performing the calculations this way, the importance of coupling to each electronic-state vibrational continuum can be tested individually. Fig. 10.6 presents the results of the calculations described above for the single incident energy of 13.0 eV (for scattering on the ground state) in the $^2\Sigma_u$ scattering symmetry. The results are presented as a function of the exit-channel excitation energy from the $X\ ^1\Sigma_g^+(v_i = 0)$ level. For all transitions there is virtually no discernible difference between the calculations including no vibrational pseudostates in the electronic states above the $b\ ^3\Sigma_u^+$ state and those with vibrational pseudostates included in any of the higher electronic states. The interesting oscillations in the $b\ ^3\Sigma_u^+$cross sections are similar to those in the Franck-Condon factors (Fig. 10.1), and reflect the oscillations in the initial vibrational level.

10.1.4 14 electronic-state VE MCCC calculations

The electronic states which will be used in the final VE MCCC scattering equations are the following 11 states: $X\ ^1\Sigma_g^+$, $b\ ^3\Sigma_u^+$, $a\ ^3\Sigma_g^+$, $B\ ^1\Sigma_u^+$, $c\ ^3\Pi_u$, $EF\ ^1\Sigma_g^+$, $C\ ^1\Pi_u$, $e\ ^3\Sigma_u^+$, $h\ ^3\Sigma_g^+$, $B'\ ^1\Sigma_u^+$, and $d\ ^3\Pi_u$. Including the two-fold degeneracy of the $c\ ^3\Pi_u$, $C\ ^1\Pi_u$, and $d\ ^3\Pi_u$ states, this amounts to 14 electronic states en-

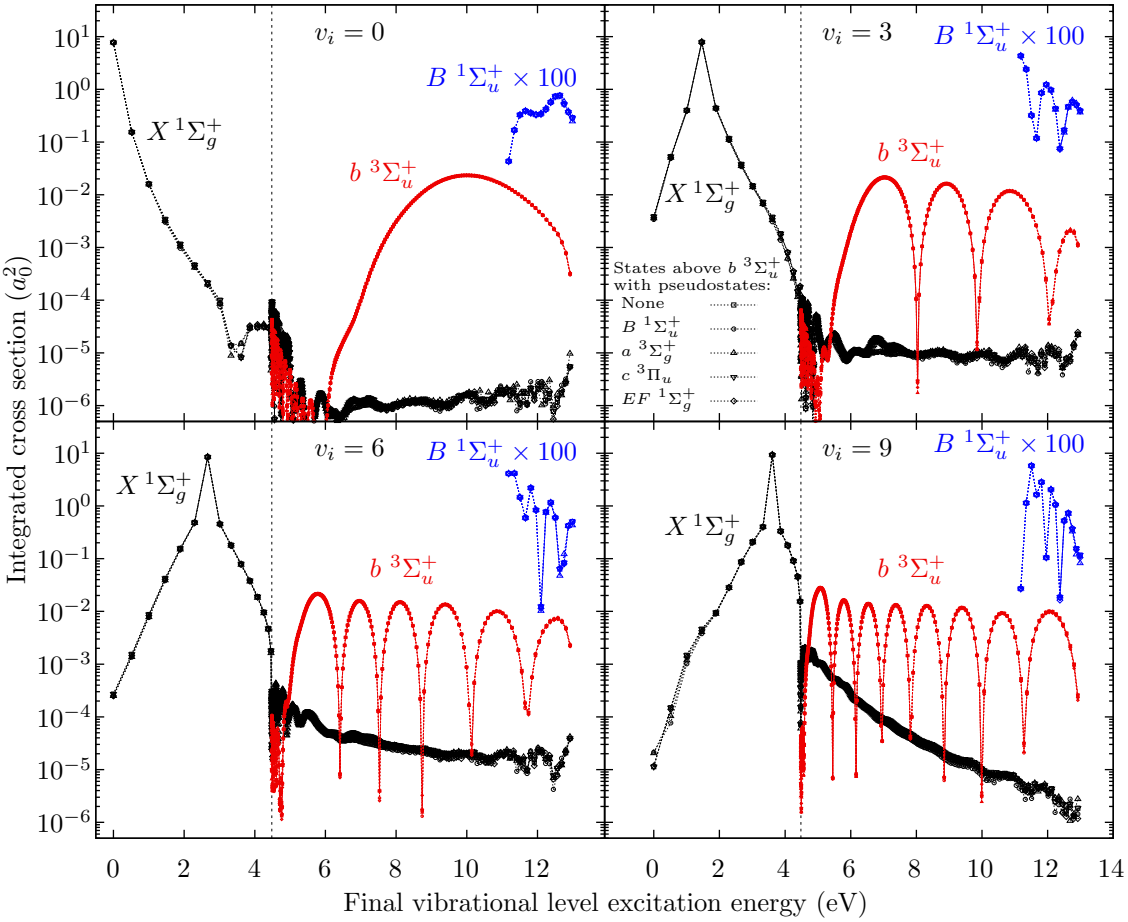

Figure 10.6: Cross sections for transitions from the $X\,^1\Sigma_g^+(v_i = 0, 3, 6, 9)$ levels to the $X\,^1\Sigma_g^+(v_f)$, $b\,^3\Sigma_u^+(v_f)$, and $B\,^1\Sigma_u^+(v_f)$ levels. For the $X\,^1\Sigma_g^+$ and $b\,^3\Sigma_u^+$ states above the H(1s)+H(1s) dissociation limit (indicated by the vertical dashed line), v_f indicates vibrational pseudostates, and the cross sections shown are the vibrational pseudostate excitation cross sections (not true energy-differential cross sections). Results are presented as a function of the exit-channel excitation energy from the $v_i = 0$ level, and have been calculated for 13.0 eV incident energy with respect to scattering on the $v_i = 0$ level (i.e. the $v_i > 0$ results correspond to lower incident energies). Each symbol type indicates a different electronic state above the $b\,^3\Sigma_u^+$ state which has dissociative vibrational pseudostates included. The $B\,^1\Sigma_u^+$ cross sections have been multiplied by 100 for clarity.

tering the close-coupling equations. Previous R-matrix studies have shown that an accurate representation of the H_2^- resonance states can be achieved using an expansion with only the $n = 1$–2 states [230, 257] (up to $C\,^1\Pi_u$ in the list above). The $e\,^3\Sigma_u^+$, $h\,^3\Sigma_g^+$, $B'\,^1\Sigma_u^+$, and $d\,^3\Pi_u$ states are also included since they have the

largest cross sections of the states which become energetically accessible below 14 eV. A partial-wave expansion with $L_{\max} = 6$ is used. This scattering model yields sufficiently converged cross sections for the $b\ ^3\Sigma_u^+$ and $B\ ^1\Sigma_u^+$ states, and electronically-elastic cross sections converged to within 10%. Since the present work is primarily concerned with the demonstration of the new method this model is adequate. Future work in this project will involve implementing GPU acceleration to the VE MCCC code, which will allow much larger calculations to be viable.

Following the model calculations and tests described in previous sections, the vibrational levels for all electronic states are obtained using a Laguerre basis with $N = 300$ and $\alpha = 15.0$, and the $X\ ^1\Sigma_g^+$ and $b\ ^3\Sigma_u^+$ have dissociative vibrational pseudostates included up to 10 and 20 eV excitation energies, respectively. All higher electronic states have all bound vibrational levels included, but no dissociative vibrational pseudostates. The set of final vibronic states included in the scattering calculations is illustrated in Fig. 10.7

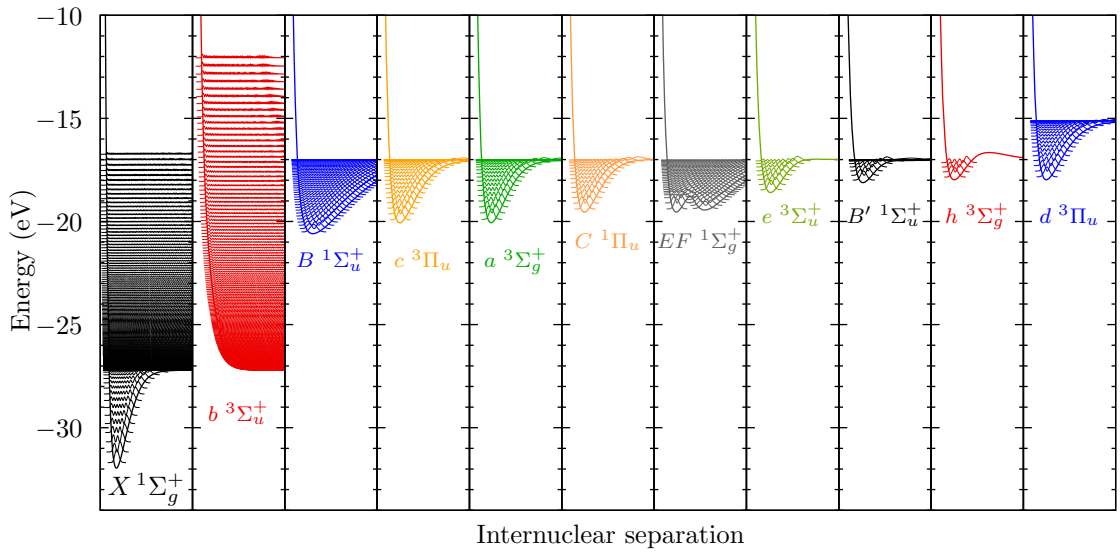

Figure 10.7: Illustration of the vibronic states included in the final VE MCCC scattering model utilised in the present work. Electronic states to the right of the $b\ ^3\Sigma_u^+$ state have only bound vibrational levels included.

10.2 Results

This section presents and discusses results obtained utilising the VE MCCC scattering model described in Sec. 10.1.4. Fig. 10.8, presents the cross sections for excitation of the $b\ ^3\Sigma_u^+$ and $B\ ^1\Sigma_u^+$ states considering only the $^2\Sigma_g$ scattering symmetry. There are prominent resonances in both cross sections, associated

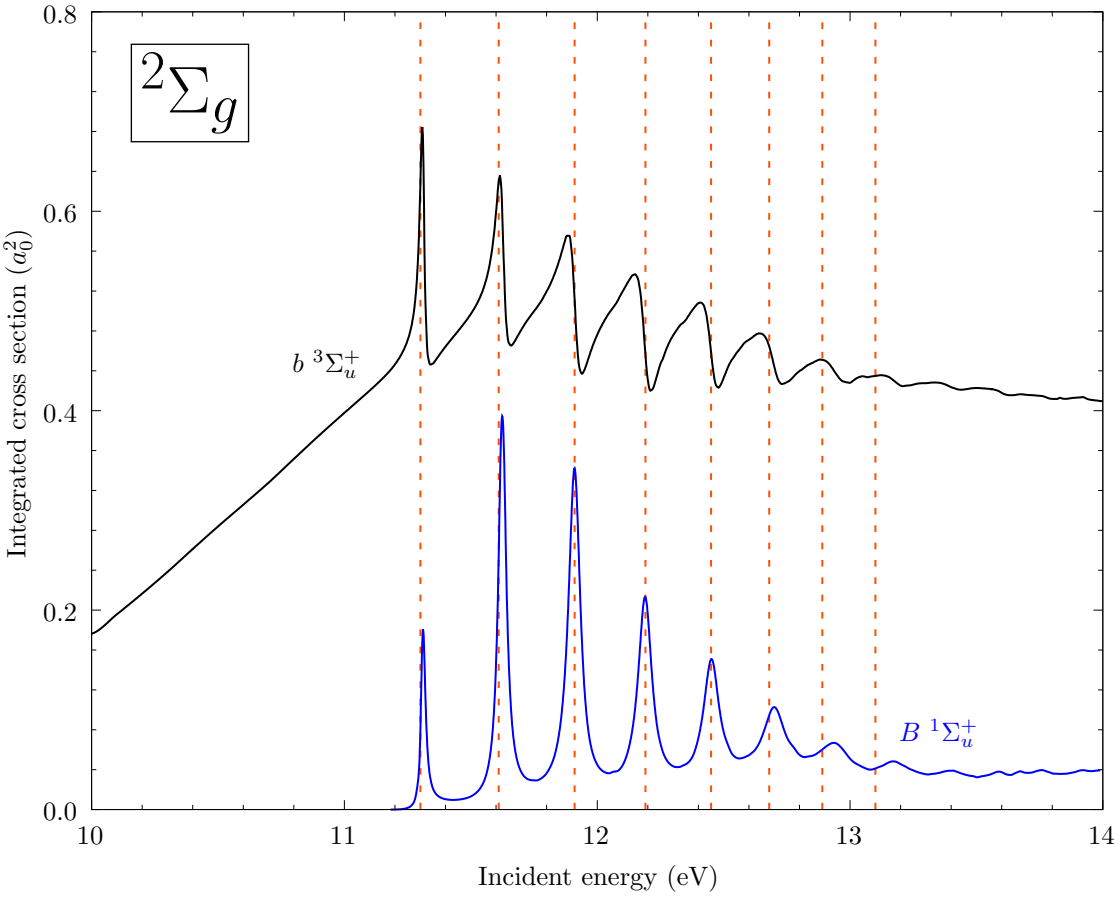

Figure 10.8: Electron-impact cross sections for excitation of the $b\ ^3\Sigma_u^+$ and $B\ ^1\Sigma_u^+$ states of H_2 from the ground state considering only the $^2\Sigma_g$ scattering symmetry. The vertical dashed lines indicate the $C\ ^2\Sigma_g^+$ vibrational energy levels of the H_2^- ion determined experimentally by Comer and Read [258].

with the temporary formation of the excited Rydberg $C\ ^2\Sigma_g^+$ state of the H_2^- ion. The resonance positions are in excellent agreement with the experimentally-determined vibrational energies of Comer and Read [258] for this state, which are indicated by the vertical dashed lines in the figure. Similar resonances were

found in local complex-potential (LCP) calculations [115] of the D_2 $b\ ^3\Sigma_u^+$ excitation, although these calculations do not include the nonresonant contribution. An illustration of the resonant and nonresonant processes contributing to this transition is provided in Fig. 10.9. The nonresonant process corresponds to the

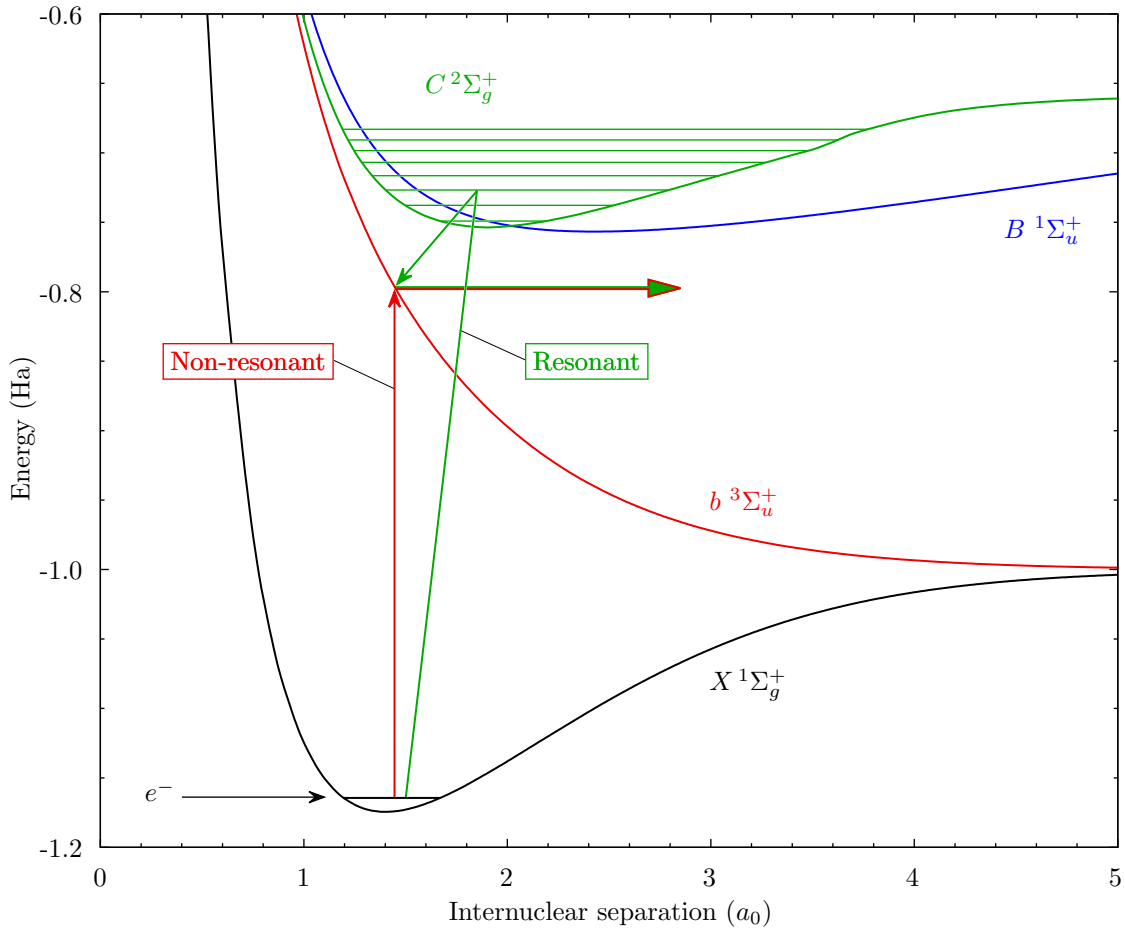

Figure 10.9: Illustration of the resonant and nonresonant processes contributing to the $X\ ^1\Sigma_g^+ \rightarrow b\ ^3\Sigma_u^+$ transition. The H_2 potential-energy curves are taken from Refs. [147, 148, 152], and the H_2^- curve from Ref. [230]. The vibrational energies of the $C\ ^2\Sigma_g^+$ state are taken from Ref. [258].

electronically free scattering channels, while the resonant process corresponds to the electronically bound scattering channels [259, 260]. The resonant process proceeds via capture of the incident electron to form the H_2^- ion in one of a number of possible vibrational levels, before the compound state decays back into one of the H_2 states plus a free electron. For a given final energy in the $b\ ^3\Sigma_u^+$ continuum, the nonresonant process has a lower threshold than the resonant process because it does not require the formation of a higher-energy intermediate state. Each of

the resonance peaks in the calculated cross section corresponds to the formation of a different vibrational level in the compound $C\,^2\Sigma_g^+$ state. The $C\,^2\Sigma_g^+$ state primarily decays into the $X\,^1\Sigma_g^+$, $b\,^3\Sigma_u^+$, and $B\,^1\Sigma_u^+$ states of H_2 [230], leading to resonance structures in the excitation cross sections for each of these states.

Fig. 10.10 presents cross sections for excitation of the $b\,^3\Sigma_u^+$, $B\,^1\Sigma_u^+$, and $X\,^1\Sigma_g^+$ states, showing the contributions from the four dominant scattering symmetries: $^2\Sigma_u$, $^2\Sigma_g$, $^2\Pi_g$, and $^2\Pi_u$. The $B\,^1\Sigma_u^+$ cross section is summed over all

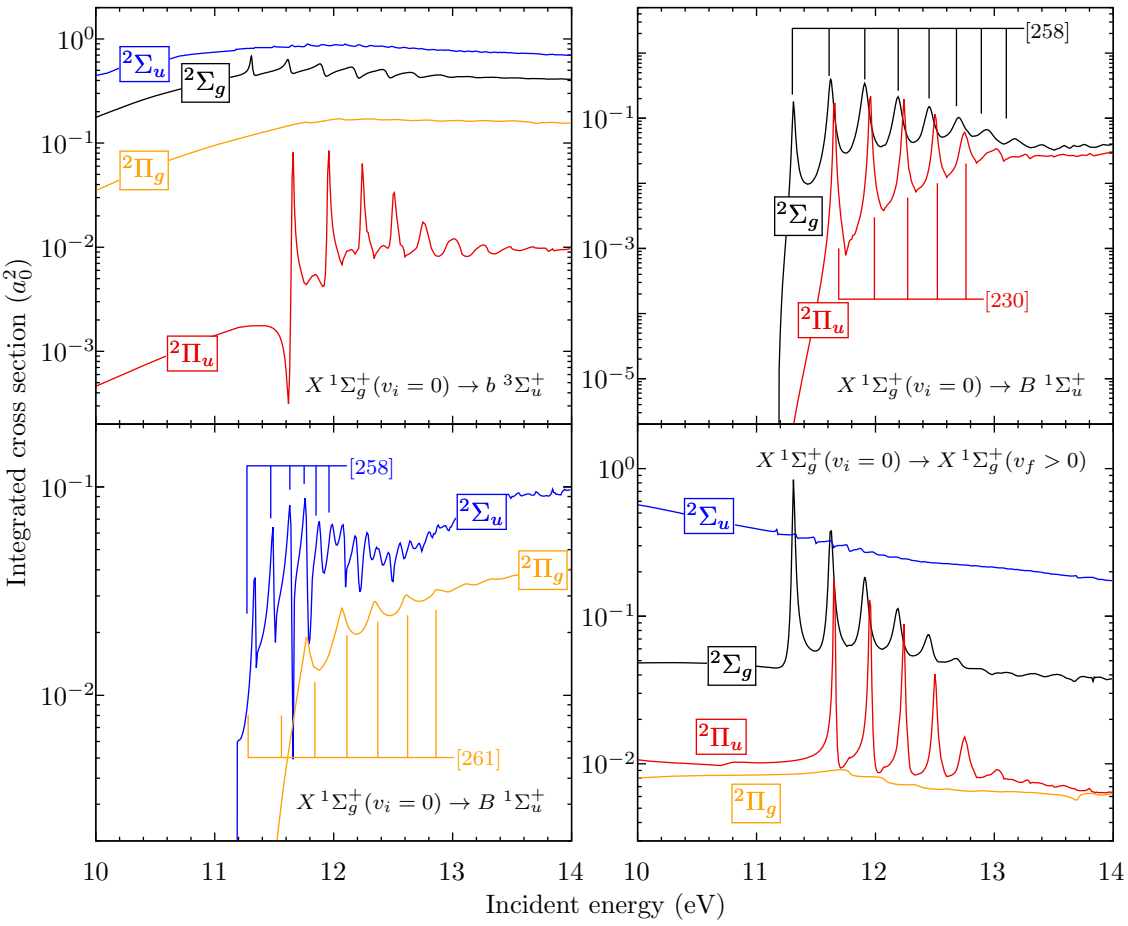

Figure 10.10: Electron-impact cross sections for excitation of the $b\,^3\Sigma_u^+$, $B\,^1\Sigma_u^+$, and $X\,^1\Sigma_g^+$ states of H_2 from the $X\,^1\Sigma_g^+(v_i=0)$ state. The results are displayed separately for each of the four dominant scattering symmetries: $^2\Sigma_u$, $^2\Sigma_g$, $^2\Pi_u$, and $^2\Pi_g$. The $B\,^1\Sigma_u^+$ cross section is summed over final vibrational levels, while the $X\,^1\Sigma_g^+$ cross section is summed over levels $v_f > 0$. Measured/calculated resonance positions from Refs. [230, 258, 261] are also shown.

final vibrational levels, while the $X\,^1\Sigma_g^+$ cross section is summed over levels $v_f > 0$ since the vibrationally-elastic cross section is dominated by nonresonant scatter-

ing and would obscure the resonance structures. For dissociative excitation of the $b\ ^3\Sigma_u^+$ state there are prominent resonances in both the $^2\Sigma_g$ and $^2\Pi_u$ symmetries, and barely visible features in the others. The $B\ ^1\Sigma_u^+$ cross section has resonance structures in all four symmetries, which are compared with measured or calculated resonance positions taken from the literature: $^2\Sigma_g$ and $^2\Sigma_u$ from the measurements of Comer and Read [258], $^2\Pi_u$ from the calculations of Stibbe and Tennyson [230], and $^2\Pi_g$ from the measurements of Kuyatt *et al.* [261]. In the $^2\Sigma_u$ symmetry the present calculations appear to show a number of resonance features above the levels identified in Ref. [258], however inspection of the contributions from each exit vibrational level suggests these are the result of interference between nonresonant channels as higher vibrational levels open with increasing energy. In the $^2\Pi_g$ symmetry the present calculations do not exhibit the first two resonances found by Kuyatt *et al.* [261], either because they were incorrectly identified, or because the calculated cross section is too small near threshold for the resonances to be visible. In the $X\ ^1\Sigma_g^+$ cross sections there are prominent peaks in the $^2\Sigma_g$ and $^2\Pi_u$ symmetries, with only faint features in the other two symmetries.

Fig. 10.11 presents cross sections for pure vibrational excitations (from $v_i = 0$) within the $X\ ^1\Sigma_g^+$ state in the $^2\Sigma_g$ scattering symmetry. The vibrationally-elastic $v = 0 \rightarrow 0$ cross section is dominated by nonresonant scattering. The nonresonant contribution diminishes with increasing exit vibrational level, so that for $v_f > 2$ only the resonance peaks are visible. Celiberto *et al.* [112] have previously calculated cross sections for resonant vibrational excitation of H_2 involving the $^2\Sigma_g$ symmetry in this energy range, using the LCP method. Although the resonance structures seen in the LCP results are similar to those in the present calculations, the two data sets are not directly comparable, since the LCP calculations do not account for nonresonant scattering. In fact, the vibrationally-elastic $v = 0 \rightarrow 0$ cross section presented by Celiberto *et al.* [112] has prominent resonance peaks corresponding to the $C\ ^2\Sigma_g^+$ vibrational-level energies, while in the present calculations there are dips at the resonance energies in this cross section. A novel feature of the VE MCCC method which is not present in alternative approaches is the proper account of coupling between resonant and nonresonant scattering

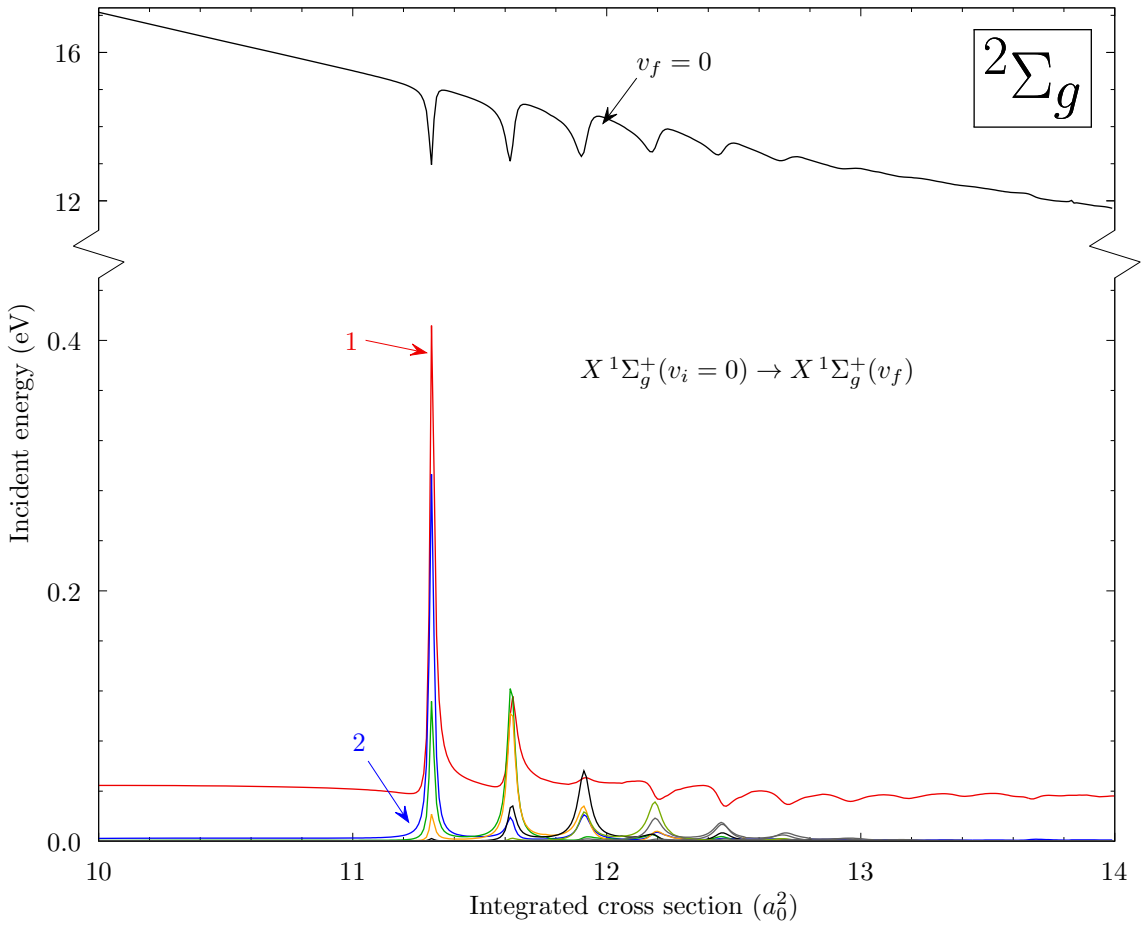

Figure 10.11: Electron-impact cross sections in the $^2\Sigma_g$ scattering symmetry for excitation of the $v_f = 0 \rightarrow 14$ vibrational levels from the $v_i = 0$ level in the $X\,^1\Sigma_g^+$ state of H_2. Note the different vertical scale for the $v = 0 \rightarrow 0$ cross section.

channels, which captures the redistribution of flux from nonresonant elastic scattering into the resonant excitations and leads to the dips in the $v = 0 \rightarrow 0$ cross section.

Resonances also appear in FN calculations of electron-molecule cross sections, associated with the formation of a compound state at the fixed internuclear separation. Fig. 10.12 compares the $^2\Sigma_g$-symmetry $X\,^1\Sigma_g^+(v_i = 0) \rightarrow b\,^3\Sigma_u^+$ cross section obtained using the VE MCCC method with results obtained using the FN approximation. The FN calculation utilises an electronic close-coupling expansion consisting of the same electronic states included in the VE MCCC calculations. Above 13 eV the two methods produce similar results, but in the resonance region the FN approximation clearly breaks down. The FN cross section has a promi-

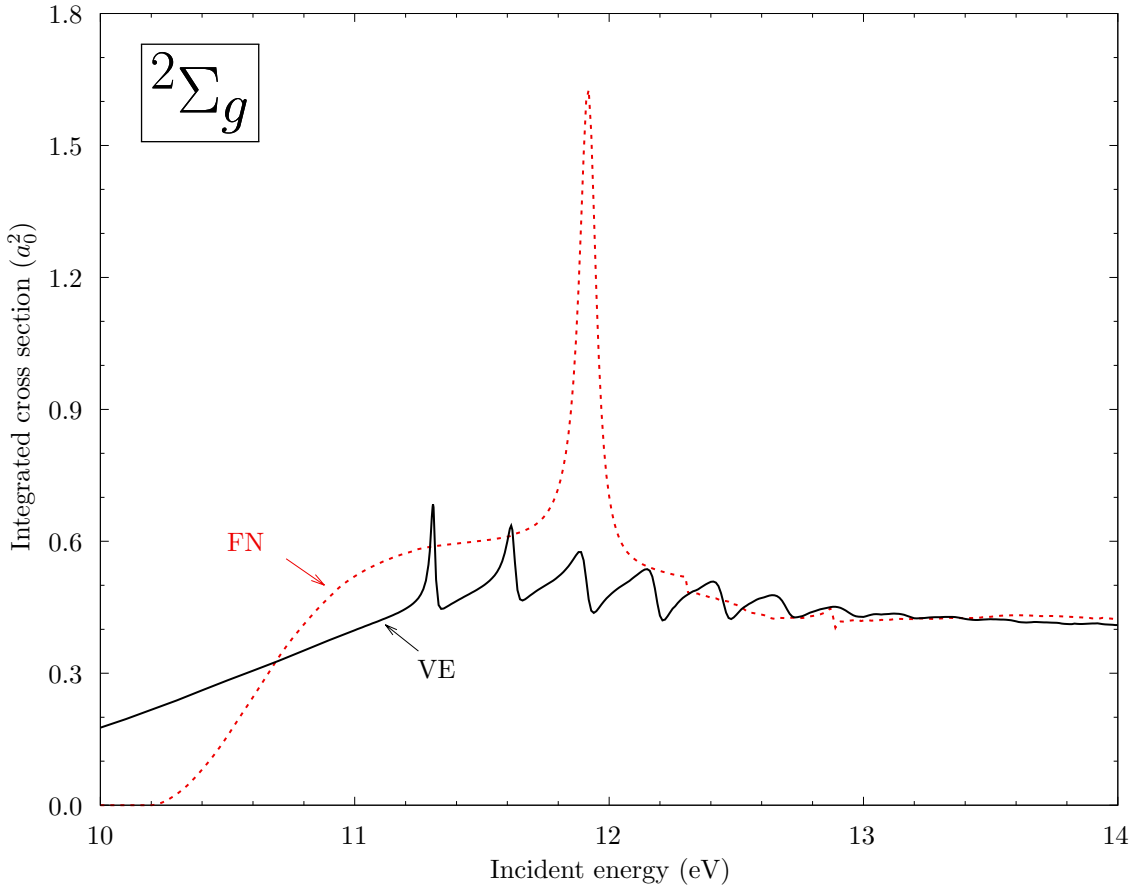

Figure 10.12: Electron-impact cross sections in the $^2\Sigma_g$ scattering symmetry for excitation of the $b\ ^3\Sigma_u^+$ state from the ground state of H_2. Comparison is made between calculations performed with the vibrational-electronic and fixed-nuclei MCCC methods (VE and FN, respectively).

nent resonance just below 12 eV, corresponding to the vertical excitation energy of the H_2^- $C\ ^2\Sigma_g^+$ state at the mean internuclear separation [230]. Evidently, the FN approximation is able to roughly identify the energy region where the resonances should occur, but cannot predict the number of resonances or their positions. The magnitude of the FN resonance peak is also substantially larger than any of the true resonances.

10.2.1 Scattering on excited vibrational levels

Figs. 10.13 and 10.14 provide some example cross sections for scattering on excited vibrational levels in the $^2\Sigma_g$ scattering symmetry. Fig. 10.13 shows results for excitation of the $b\ ^3\Sigma_u^+$ and $B\ ^1\Sigma_u^+$ states, while Fig. 10.14 shows results for vibrationally-elastic and inelastic transitions within the $X\ ^1\Sigma_g^+$ state. The cross sections are presented as a function of the incident energy plus the excitation energy of the initial vibrational level from the $v_i = 0$ level, to allow comparison of the resonance positions. Resonance peaks also appear in the cross sections for scattering on excited vibrational levels, in good agreement with the measured resonance energies of Comer and Read [258]. However, the resonances which show up the strongest (or show at all) in the cross sections are heavily dependent on the initial vibrational level, as a result of the varying overlaps between the $X\ ^1\Sigma_g^+$ and $C\ ^2\Sigma_g^+$ vibrational levels. In all cases there is a trend that cross sections for scattering on higher $X\ ^1\Sigma_g^+$ vibrational levels have stronger resonance peaks at higher energies.

10.3 Chapter 10 summary

This chapter has demonstrated the feasibility of extending the MCCC method to include both electronic and nuclear vibrational states in the close-coupling expansion, allowing the calculation of self-consistent sets of absolute cross sections where the adiabatic-nuclei approximation breaks down. The method treats both resonant and nonresonant scattering on the same footing, and does not require the input of resonance data from external calculations. The appearance of resonance peaks in the calculated cross sections in good agreement with measured or calculated resonance energies from the literature is a satisfying indication that the VE MCCC method treats the coupling of electronic and vibrational motions accurately. As the MCCC method is extended to more complex diatomic molecules in the future, the techniques described here can be immediately applied. This will allow the benefits of large-scale close-coupling calculations, such as rigorous demonstrations of convergence and a proper account of interchannel coupling, to be applied to all molecular scattering processes.

The 14-electronic-state model used in this chapter would not be suitable for studying much lower-energy electronically-elastic scattering, where there are well-known resonances due to the $X\,^2\Sigma_u^+$ ground electronic state of H_2^- [114]. In order to investigate these processes in the future, it will be necessary to include coupling to the electronic (ionisation) continuum in the VE MCCC calculations since this is particularly important for low-energy electronically elastic scattering. This can be done either by explicitly including vibrational levels in the potential-energy curves for the electronic (ionising) pseudostates, or by some approximate method to account for coupling to the closed ionisation channels.

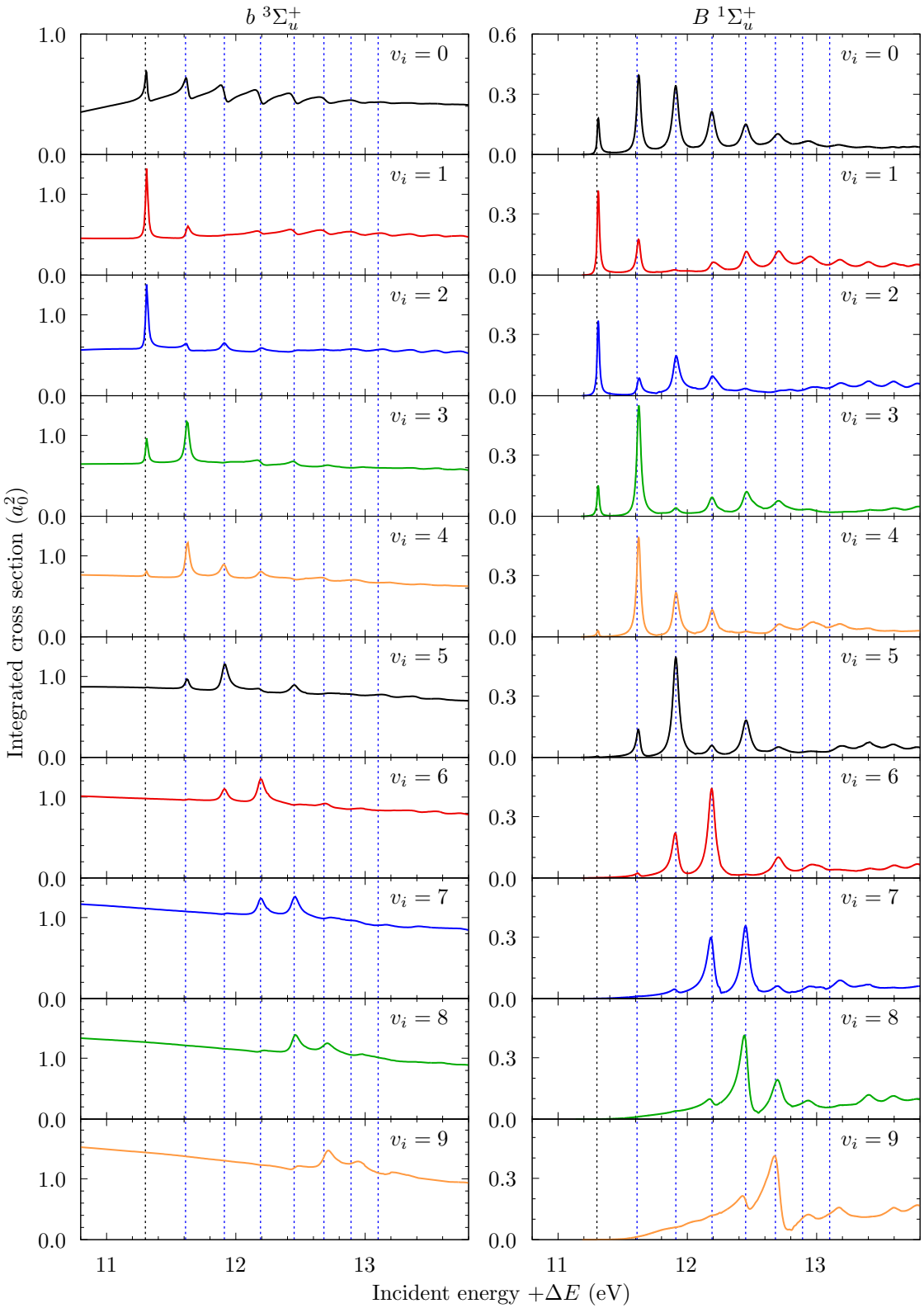

Figure 10.13: Electron-impact cross sections in the $^2\Sigma_g$ scattering symmetry for excitation of the $b\ ^3\Sigma_u^+$ and $B\ ^1\Sigma_u^+$ states from the $v_i = 0$–9 vibrational levels of the $X\ ^1\Sigma_g^+$. Results are presented as a function of the incident energy plus the excitation energy of the initial vibrational level from the $v_i = 0$ level, to allow comparison of the resonance positions with the measured resonance energies of Comer and Read [258] (indicated by vertical dashed lines).

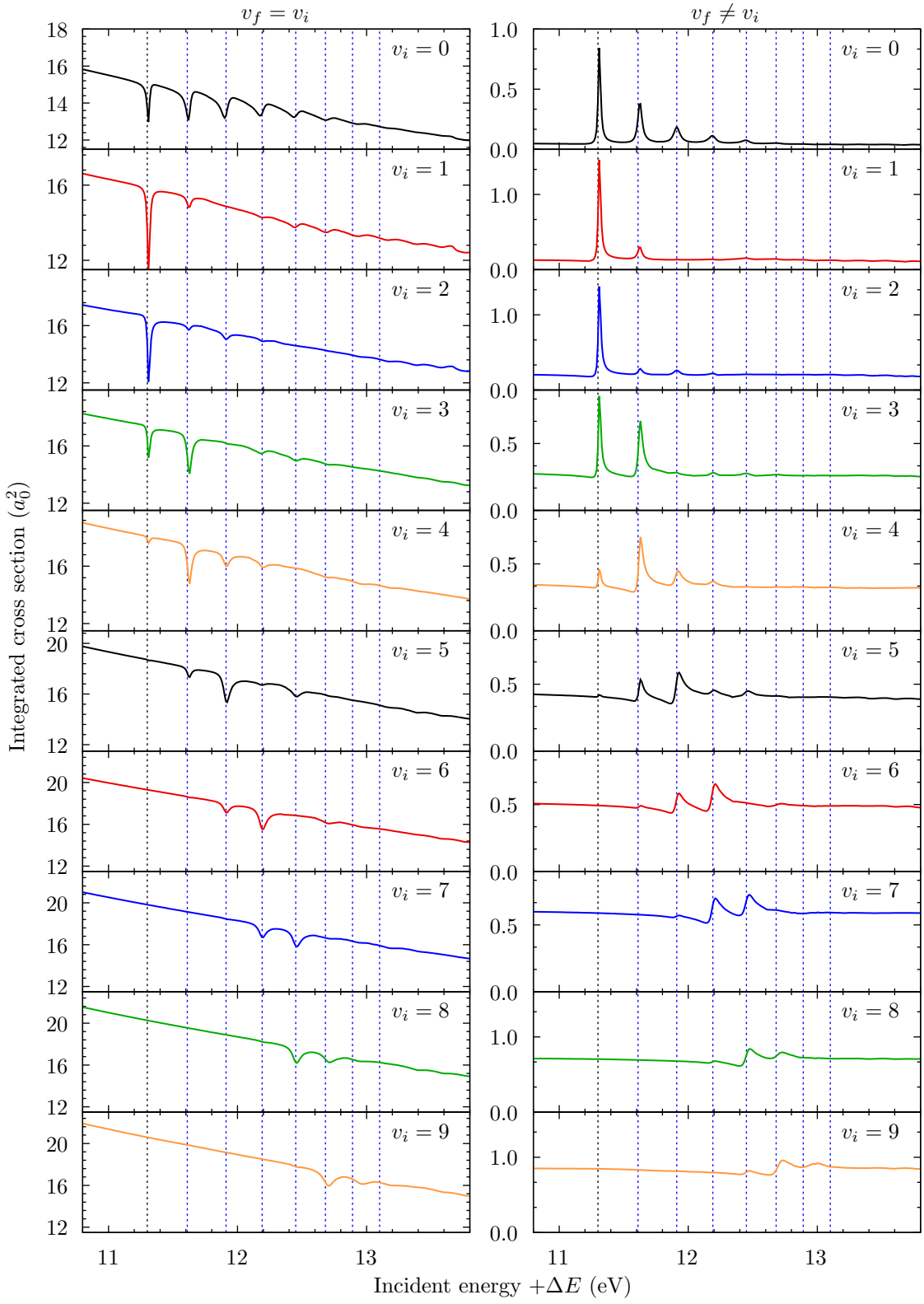

Figure 10.14: Electron-impact cross sections in the $^2\Sigma_g$ scattering symmetry for elastic $v_f = v_i$ and inelastic $v_f \neq n_i$ transitions within the $X\,^1\Sigma_g^+$. Results are presented as a function of the incident energy plus the excitation energy of the initial vibrational level from the $v_i = 0$ level, to allow comparison of the resonance positions with the measured resonance energies of Comer and Read [258] (indicated by vertical dashed lines).

Part IV

Rotational dynamics

Chapter 11

Rotationally-resolved scattering: theory

This chapter presents derivations of rotationally-resolved cross-section formulas for diatomic molecules. Although rotational excitation cross sections have been calculated and various formulas given previously in the literature (for example, Refs. [262–271]), it is difficult to find a single reference in which all quantities are derived in full using the same conventions. Here, the rotationally-resolved cross sections formulas are derived from scratch using the conventions and notation used throughout this thesis, so that they may be applied immediately in molecular convergent close-coupling (MCCC) calculations. The derivations presented here are performed in a more general way than necessary when applying the adiabatic-nuclei approximation, in the hope that future work may investigate the feasibility of full rovibronic close-coupling. In that case, the theory presented here will be of use. Details will also be given for the application of the adiabatic-nuclei approximation.

Limited results for rotationally-resolved scattering are presented in this thesis, as the implementation of the rotationally-resolved cross sections into the MCCC code was performed by Una Rehill as part of her Honours research project. Results for rovibrational excitation of the H_2 $X\,{}^1\Sigma_g^+$ state will be presented in her Honours thesis. The present candidate's contribution to this project was to perform the derivations and supervise the computational implementation. The application of rotational excitations to the study of Fulcher-α fluorescence polarisation, which was performed by the candidate, will be given in the next chapter. Throughout this chapter, any vector quantities are by default assumed to be de-

fined in the lab frame; when they are represented in the body frame they will be given a superscript (b). The theory presented here is specific for homonuclear diatomics, since assumptions have been made about the requirements for (anti)symmetry of the molecular wave function with respect to nuclear permutation. However, it can be fairly easily modified to suit heteronuclear diatomics when necessary.

11.1 Coupled-angular-momentum states and matrix elements

If a rovibronic close-coupling calculation is to be performed, then the close-coupling calculations must be formulated in the laboratory frame, in which the rotational wave functions are defined, rather than the body frame. In this case, the partial-wave expansion of the scattering amplitude can take advantage of the conserved total scattering-system angular momentum. In the non-relativistic approximation, the total electronic spin $\mathcal{S}$, total angular momentum without spin $\mathcal{J}$ (electronic orbital plus nuclear rotational angular momentum), and the total parity Π are conserved.

For convenience, the target electronic states are indexed without accounting for the two-fold degeneracy of the $|\Lambda| > 0$ states (i.e. the label "Φ_n" might refer to the $d\ ^3\Pi_u$ electronic state so $|\Phi_n^{\pm\Lambda_n}\rangle$ refers to the particular case of $d\ ^3\Pi_u$ with $\Lambda = \pm 1$). Unless specified otherwise, when Λ is written without a minus sign it should be assumed to be the positive case. Throughout this chapter, the spin component of the target and projectile wave functions will be written explicitly. The total electronic target state with angular-momentum projection Λ_n, spin s_n and spin projection m_{s_n} then has the following form:

$$|\Phi_n^{\Lambda_n s_n m_{s_n}}\rangle = |\Phi_n^{\Lambda_n}\rangle |s_n m_{s_n}\rangle, \tag{11.1}$$

where $|\Phi_n^{\Lambda_n}\rangle$ is the spatial component. From now on, the subscript n on Λ, s, and m_s will be dropped, with the understanding that the values of $|\Lambda|$ and s are specified by whichever electronic state Φ_n they appear alongside. Following the

definitions given in Sec. 3.6, the total molecular states are written as

$$|\Phi_n\, sm_s\, \nu_{nvN}\, Nm_N\, Im_I\, \pi\rangle \tag{11.2}$$
$$= \frac{1}{\sqrt{2(1+\delta_{\Lambda,0})}}\Big[|\Phi_n^{\Lambda}\, sm_s\, \nu_{nvN}\, Nm_N\Lambda\, Im_I\rangle + \pi(-1)^{N+\sigma}|\Phi_n^{-\Lambda}\, sm_s\, \nu_{nvN}\, Nm_N(-\Lambda)\, Im_I\rangle\Big],$$

where

$$|\Phi_n^{\Lambda}\, sm_s\, \nu_{nvN}\, Nm_N\Lambda\, Im_I\rangle = |\Phi_n^{\Lambda}\rangle|sm_s\rangle|\nu_{nvN}\rangle|Nm_N\Lambda\rangle|Im_I\rangle.$$

Here, $|\nu_{nvN}\rangle$ is the vibrational state (including its dependence on the rotational level), $|Nm_N\Lambda\rangle$ is the rotational state (including its dependence on Λ), and $|Im_I\rangle$ is the nuclear spin state. In Eq. (11.2), π is the total molecular-state parity, and σ is odd for Σ^- states but even otherwise. Note that Λ does not appear on the left-hand side of Eq. (11.2) since the total molecular state is a linear combination of the two $\pm\Lambda$ cases.

The projectile states are written in the form:

$$|\boldsymbol{q}m_{\rm p}\rangle = \frac{1}{q}\sum_{Lm_L} i^L|qLm_L\rangle Y_L^{m_L*}(\hat{\boldsymbol{q}})|\tfrac{1}{2}m_{\rm p}\rangle, \tag{11.3}$$

where $|qLm_L\rangle$ are the same projectile partial-wave states defined in Eq. (4.15), and $m_{\rm p}$ is the projection of the projectile spin on the lab-frame axis (the projectile spin is always 1/2).

An uncoupled projectile-target state is expressed as

$$|\Phi_n\, sm_s\, \nu_{nvN}\, Nm_N\, Im_I\, \pi\, \boldsymbol{q}m_{\rm p}\rangle = |\Phi_n\, sm_s\, \nu_{nvN}\, Nm_N\, Im_I\, \pi\rangle|\boldsymbol{q}m_{\rm p}\rangle, \tag{11.4}$$

and following Fursa and Bray [191] and Bray and Stelbovics [272], this state can be expressed in coupled-angular-momentum (CAM) form with the orbital and spin angular momenta coupled:

$$|\Phi_n\, sm_s\, \nu_{nvN}\, Nm_N\, Im_I\, \pi\, \boldsymbol{q}m_{\rm p}\rangle \tag{11.5}$$
$$= \sum_{\mathcal{J}\Pi}\sum_{\mathcal{S}}\sum_{Lm_L} C^{\mathcal{J}M_{\mathcal{J}}}_{Lm_L,Nm_N} C^{\mathcal{S}M_{\mathcal{S}}}_{\frac{1}{2}m_{\rm p},sm_s}|\Phi_n\, s\, \nu_{nvN}\, N\, Im_I\, \pi\, qL : \mathcal{J}M_{\mathcal{J}}\Pi\mathcal{S}M_{\mathcal{S}}\rangle Y_L^{m_L*}(\hat{\boldsymbol{q}}),$$

where

$$|\Phi_n\, s\, \nu_{nvN}\, N\, I m_I\, \pi\, qL : \mathcal{J} M_{\mathcal{J}} \Pi \mathcal{S} M_{\mathcal{S}}\rangle \tag{11.6}$$
$$= \frac{1}{q} i^L |qLm_L\rangle \sum_{\substack{m_L m_N \\ m_{\rm p} m_s}} C^{\mathcal{J}M_{\mathcal{J}}}_{Lm_L,Nm_N} C^{\mathcal{S}M_{\mathcal{S}}}_{\frac{1}{2}m_{\rm p},sm_s} |\tfrac{1}{2} m_{\rm p}\rangle |\Phi_n\, sm_s\, \nu_{nvN}\, Nm_N\, I m_I\, \pi\rangle,$$

and the (conserved) total scattering system parity is

$$\Pi \equiv \pi \cdot (-1)^L. \tag{11.7}$$

Hence, we can express matrix elements of an operator $\hat{\mathsf{X}}$ between uncoupled states in the following form:

$$\langle \boldsymbol{q}' m'_{\rm p}\, \pi'\, I' m_{I'}\, N' m_{N'}\, \nu_{n'v'N'}\, s' m_{s'}\, \Phi_{n'} |\hat{\mathsf{X}}| \Phi_n\, sm_s\, \nu_{nvN}\, Nm_N\, I m_I\, \pi\, \boldsymbol{q} m_{\rm p}\rangle \tag{11.8}$$
$$= \sum_{\mathcal{J}\Pi} \sum_{\mathcal{S}} \sum_{\substack{L' m_{L'} \\ L m_L}} C^{\mathcal{J}M_{\mathcal{J}}}_{L'm'_L,N'm'_N} C^{\mathcal{J}M_{\mathcal{J}}}_{Lm_L,Nm_N} C^{\mathcal{S}M_{\mathcal{S}}}_{\frac{1}{2}m'_{\rm p},s'm'_s} C^{\mathcal{S}M_{\mathcal{S}}}_{\frac{1}{2}m_{\rm p},sm_s} Y^{m_{L'}}_{L'}(\hat{\boldsymbol{q}}') Y^{m_L *}_{L}(\hat{\boldsymbol{q}})$$
$$\times \langle \mathcal{J} M_{\mathcal{J}} \Pi \mathcal{S} M_{\mathcal{S}} : q' L' \pi I' m_{I'} N' \nu_{n'v'N'} s' m_{s'} \Phi_{n'} |\hat{\mathsf{X}}| \Phi_n sm_s\, \nu_{nvN}\, N\, I m_I\, \pi\, qL : \mathcal{J} M_{\mathcal{J}} \Pi \mathcal{S} M_{\mathcal{S}}\rangle.$$

We can apply the Wigner-Eckhart theorem:

$$\langle j' m' n' |\hat{\mathsf{X}}^{(k)}_q| njm\rangle = C^{jm}_{j'm',kq} \langle j' n' || \hat{\mathsf{X}}^{(k)} || nj\rangle, \tag{11.9}$$

where $\hat{\mathsf{X}}^{(k)}_q$ is the qth component of the rank-k spherical tensor operator $\hat{\mathsf{X}}^{(k)}$. Note that the definition of the Wigner-Eckhart theorem here follows the conventions of Meunier [273]. For a scalar operator (as $\hat{\mathsf{V}}$ and $\hat{\mathsf{T}}$ are), we have

$$\langle j' m' n' |\hat{\mathsf{X}}| njm\rangle = \langle j' n' || \hat{\mathsf{X}} || nj\rangle, \tag{11.10}$$

and hence the expression for the uncoupled matrix element becomes

$$\langle \boldsymbol{q}' m'_{\rm p}\, \pi'\, I' m_{I'}\, N' m_{N'}\, \nu_{n'v'N'}\, s' m_{s'}\, \Phi_{n'} |\hat{\mathsf{X}}| \Phi_n\, sm_s\, \nu_{vnN}\, Nm_N\, I m_I\, \pi\, \boldsymbol{q} m_{\rm p}\rangle \tag{11.11}$$
$$= \sum_{\mathcal{J})\Pi} \sum_{\mathcal{S}} \sum_{\substack{L' m_{L'} \\ L m_L}} C^{\mathcal{J}M_{\mathcal{J}}}_{L'm'_L,N'm'_N} C^{\mathcal{J}M_{\mathcal{J}}}_{Lm_L,Nm_N} C^{\mathcal{S}M_{\mathcal{S}}}_{\frac{1}{2}m'_{\rm p},s'm'_s} C^{\mathcal{S}M_{\mathcal{S}}}_{\frac{1}{2}m_{\rm p},sm_s} Y^{m_{L'}}_{L'}(\hat{\boldsymbol{q}}') Y^{m_L *}_{L}(\hat{\boldsymbol{q}})$$
$$\times \langle \mathcal{J}\Pi\mathcal{S} : q' L' \pi' I' m_{I'} N' \nu_{n'v'N'} s' \Phi_{n'} || \hat{\mathsf{X}} || \Phi_n\, s\, \nu_{nvN}\, N\, I m_I\, \pi\, qL : \mathcal{J}\Pi\mathcal{S}\rangle.$$

The difference between Eqs. (11.8) and (11.11) is that the latter is written in terms of the reduced matrix element of $\hat{\mathsf{X}}$, which is independent of $M_{\mathcal{J}}$ and $M_{\mathcal{S}}$.

To simplify notation, we now remove any dependence on nuclear spins as we assume they are unchanged by the collision, and define

$$\begin{aligned}\langle q' L'\, \pi'\, N'\, \nu_{n'v'N'}\, s'\, \Phi_{n'}||\hat{\mathsf{X}}^{\mathcal{J}\Pi\mathcal{S}}||\Phi_n\, s\, \nu_{nvN}\, N\, \pi\, qL\rangle \\ = \langle \mathcal{J}\Pi\mathcal{S} : q' L'\, \pi'\, N'\, \nu_{n'v'N'}\, s'\, \Phi_{n'}||\hat{\mathsf{X}}||\Phi_n\, s\, \nu_{nvN}\, N\, \pi\, qL : \mathcal{J}\Pi\mathcal{S}\rangle,\end{aligned} \tag{11.12}$$

so we have

$$\begin{aligned}&\langle \boldsymbol{q}' m'_{\rm p}\, \pi'\, N' m_{N'}\, \nu_{n'v'N'}\, s' m_{s'}\, \Phi_{n'}|\hat{\mathsf{X}}|\Phi_n\, s m_s\, \nu_{vnN}\, N m_N\, \pi\, \boldsymbol{q} m_{\rm p}\rangle \\ &\quad = \sum_{\mathcal{J}\Pi}\sum_{\mathcal{S}}\sum_{\substack{L' m_{L'} \\ L m_L}} C^{\mathcal{J}M_{\mathcal{J}}}_{L' m'_L, N' m'_N} C^{\mathcal{J}M_{\mathcal{J}}}_{L m_L, N m_N} C^{\mathcal{S}M_{\mathcal{S}}}_{\frac{1}{2} m'_{\rm p}, s' m'_s} C^{\mathcal{S}M_{\mathcal{S}}}_{\frac{1}{2} m_{\rm p}, s m_s} Y^{m_{L'}}_{L'}(\hat{\boldsymbol{q}}') Y^{m_L *}_{L}(\hat{\boldsymbol{q}}) \\ &\qquad \times \langle q' L'\, \pi'\, N'\, \nu_{n'v'N'}\, s'\, \Phi_{n'}||\hat{\mathsf{X}}^{\mathcal{J}\Pi\mathcal{S}}||\Phi_n\, s\, \nu_{nvN}\, N\, \pi\, qL\rangle.\end{aligned} \tag{11.13}$$

11.2 Scattering amplitudes

The scattering amplitude for a transition fully resolved in angular-momentum and spin sublevels

$$|\Phi_{n_i} s_i m_{s_i}\, \nu_{n_i v_i N_i}\, N_i m_{N_i}\, \pi_i\, \boldsymbol{q}_i m_{{\rm p}_i}\rangle \rightarrow |\Phi_{n_f} s_f m_{s_f}\, \nu_{n_f v_f N_f}\, N_f m_{N_f}\, \pi_f\, \boldsymbol{q}_f m_{{\rm p}_f}\rangle \tag{11.14}$$

is expressed as

$$\begin{aligned}&F_{n_f v_f N_f m_{N_f} \pi_f m_{{\rm p}f}, n_i v_i N_i m_{N_i} \pi_i m_{{\rm p}_i}}(\boldsymbol{q}_f, \boldsymbol{q}_i) \\ &= (-2\pi)^2 \langle \boldsymbol{q}_f m_{{\rm p}f}\, \pi_f\, N_f m_{N_f}\, \nu_{n_f v_f N_f}\, s_f m_{s_f}\, \Phi_{n_f}|\hat{\mathsf{T}}|\Phi_{n_i}\, s_i m_{s_i}\, \nu_{n_i v_i N_i}\, N_i m_{N_i}\, \pi_i\, \boldsymbol{q}_i m_{{\rm p}_i}\rangle,\end{aligned} \tag{11.15}$$

and now substituting in Eq. (11.13) for the case $\hat{\boldsymbol{q}}_i \parallel \hat{\boldsymbol{z}}$ we have

$$\begin{aligned}&F_{n_f v_f N_f m_{N_f} \pi_f m_{{\rm p}f}, n_i v_i N m_{N_i} \pi_i m_{{\rm p}_i}}(\boldsymbol{q}_f, \boldsymbol{q}_i) \\ &\quad = \sum_{\mathcal{J}M_{\mathcal{J}}\Pi}\sum_{\mathcal{S}M_{\mathcal{S}}}\sum_{L_f m_{L_f} L_i} \frac{\hat{L}_i}{\sqrt{4\pi}} C^{\mathcal{J}M_{\mathcal{J}}}_{L_f m_{L_f}, N_f m_{N_f}} C^{\mathcal{J}M_{\mathcal{J}}}_{L_i 0, N_i m_{N_i}} C^{\mathcal{S}M_{\mathcal{S}}}_{\frac{1}{2} m_{{\rm p}f}, s_f m_{s_f}} C^{\mathcal{S}M_{\mathcal{S}}}_{\frac{1}{2} m_{{\rm p}_i}, s_i m_{s_i}} Y^{m_{L_f}}_{L_f}(\hat{\boldsymbol{q}}_f) \\ &\qquad \times F^{\mathcal{J}\Pi\mathcal{S}}_{n_f v_f N_f \pi_f L_f, n_i v_i N_i L_i \pi_i}(q_f, q_i),\end{aligned} \tag{11.16}$$

where $\hat{L} = \sqrt{2L+1}$, and the lab-frame partial-wave scattering amplitudes are defined by

$$F^{\mathcal{J}\Pi\mathcal{S}}_{n_f v_f N_f \pi_f L_f, n_i v_i N_i L_i \pi_i}(q_f, q_i) = (-2\pi)^2 \langle q_f L_f \, \pi_f \, N_f \, \nu_{n_f v_f N_f} \, s_f \, \Phi_{n_f} || \hat{\mathsf{T}}^{\mathcal{J}\Pi\mathcal{S}} || \Phi_{n_i} \, s_i \, \nu_{n_i v_i N_i} \, N_i \, \pi_i \, q_i L_i \rangle, \quad (11.17)$$

11.3 Differential cross section

Following standard definitions, the differential cross section is given by

$$\begin{aligned}
\frac{\mathrm{d}\sigma_{n_f v_f N_f m_{N_f} m_{s_f} m_{\mathrm{p}f}, n_i v_i N_i m_{N_i} m_{s_i} m_{\mathrm{p}i}}}{\mathrm{d}\Omega} &= \frac{q_f}{q_i} \left| F_{n_f v_f N_f m_{N_f} \pi_f m_{\mathrm{p}f}, n_i v_i N m_{N_i} \pi_i m_{\mathrm{p}_i}}(\boldsymbol{q}_f, \boldsymbol{q}_i) \right|^2 \\
= \frac{1}{4\pi} \sum_{\substack{\mathcal{J}\Pi \\ \mathcal{J}'\Pi'}} \sum_{\mathcal{S}\mathcal{S}'} \sum_{\substack{L_f L_i \\ L'_f L'_i}} \sum_{m_{L_f}} & \hat{L}_i \hat{L}'_i F^{\mathcal{J}\Pi\mathcal{S}}_{n_f v_f N_f \pi_f L_f, n_i v_i N_i L_i \pi_i}(q_f, q_i) F^{\mathcal{J}'\Pi'\mathcal{S}'*}_{n_f v_f N_f \pi_f L'_f, n_i v_i N_i L'_i \pi_i}(q_f, q_i) \\
&\times Y^{m_{L_f}}_{L_f}(\hat{\boldsymbol{q}}_f) Y^{m'_{L_f}*}_{L'_f}(\hat{\boldsymbol{q}}_f) C^{\mathcal{J}M_\mathcal{J}}_{L_f m_{L_f}, N_f m_{N_f}} C^{\mathcal{J}M_\mathcal{J}}_{L_i 0, N_i m_{N_i}} C^{\mathcal{S}M_\mathcal{S}}_{\frac{1}{2} m_{\mathrm{p}f}, s_f m_{s_f}} C^{\mathcal{S}M_\mathcal{S}}_{\frac{1}{2} m_{\mathrm{p}i}, s_i m_{s_i}} \\
&\times C^{\mathcal{J}'M'_\mathcal{J}}_{L'_f m'_{L_f}, N_f m_{N_f}} C^{\mathcal{J}'M'_\mathcal{J}}_{L'_i 0, N_i m_{N_i}} C^{\mathcal{S}'M'_\mathcal{S}}_{\frac{1}{2} m_{\mathrm{p}f}, s_f m_{s_f}} C^{\mathcal{S}'M'_\mathcal{S}}_{\frac{1}{2} m_{\mathrm{p}i}, s_i m_{s_i}}. \quad (11.18)
\end{aligned}$$

Now utilising Defs. (A.30) and (A.36), we have:

$$Y^{m_{L_f}}_{L_f}(\hat{\boldsymbol{q}}_f) Y^{m'_{L_f}*}_{L'_f}(\hat{\boldsymbol{q}}_f) = (-1)^{m'_{L_f}} \sum_{LM_L} \frac{\hat{L}_f \hat{L}'_f}{\sqrt{4\pi}\hat{L}} C^{LM_L}_{L_f 0, L'_f 0} C^{LM_L}_{L_f m_{L_f}, L'_f - m'_{L_f}} Y^{M_L}_L(\hat{\boldsymbol{q}}_f). \quad (11.19)$$

Substituting this back into Eq. (11.18), rearranging some of the summations, and noting that having $m_{L_i} = 0$ in the Clebsch-Gordan coefficients forces $m_\mathcal{J} = m'_\mathcal{J} = m_{N_i}$:

$$\begin{aligned}
\frac{\mathrm{d}\sigma_{n_f v_f N_f m_{N_f} m_{s_f} m_{\mathrm{p}f}, n_i v_i N_i m_{N_i} m_{s_i} m_{\mathrm{p}i}}}{\mathrm{d}\Omega} &= \frac{1}{(4\pi)^{3/2}} \sum_{LM_L} \sum_{\substack{\mathcal{J}\Pi\mathcal{S} \\ \mathcal{J}'\Pi'\mathcal{S}'}} \sum_{L_f L'_f} \sum_{L_i L'_i} \frac{1}{\hat{L}} \hat{L}_f \hat{L}'_f \hat{L}_i \hat{L}'_i \\
&\times F^{\mathcal{J}\Pi\mathcal{S}}_{n_f v_f N_f \pi_f L_f, n_i v_i N_i L_i \pi_i}(q_f, q_i) F^{\mathcal{J}'\Pi'\mathcal{S}'*}_{n_f v_f N_f \pi_f L'_f, n_i v_i N_i L'_i \pi_i}(q_f, q_i) \\
&\times C^{\mathcal{J}m_{N_i}}_{L_i 0, N_i m_{N_i}} C^{\mathcal{J}'m_{N_i}}_{L'_i 0, N_i m_{N_i}} C^{LM_L}_{L_f 0, L'_f 0} \sum_{m_{L_f} m'_{L_f}} (-1)^{m_{L'_f}} C^{LM_L}_{L_f m_{L_f}, L'_f - m'_{L_f}} C^{\mathcal{J}m_{N_i}}_{L_f m_{L_f}, N_f m_{N_f}} \\
&\times C^{\mathcal{J}'m_{N_i}}_{L'_f m'_{L_f}, N_f m_{N_f}} \sum_{M_\mathcal{S} M'_\mathcal{S}} C^{\mathcal{S}M_\mathcal{S}}_{\frac{1}{2} m_{\mathrm{p}f}, s_f m_{s_f}} C^{\mathcal{S}'M'_\mathcal{S}}_{\frac{1}{2} m_{\mathrm{p}f}, s_f m_{s_f}} C^{\mathcal{S}M_\mathcal{S}}_{\frac{1}{2} m_{\mathrm{p}i}, s_i m_{s_i}} C^{\mathcal{S}'M'_\mathcal{S}}_{\frac{1}{2} m_{\mathrm{p}i}, s_i m_{s_i}} Y^{M_L}_L(\hat{\boldsymbol{q}}_f). \quad (11.20)
\end{aligned}$$

We want to obtain a DCS summed over the sublevels m_{N_f}, m_{s_f}, and m_{p_f}, and averaged over m_{N_i}, m_{s_i}, and m_{p_i}. First we can perform the summation/averaging over spin projections:

$$\begin{aligned}
&\sum_{M_\mathcal{S}M'_\mathcal{S}} \sum_{m_{\mathrm{p}_f} m_{s_f}} C^{\mathcal{S}M_\mathcal{S}}_{\frac{1}{2}m_{\mathrm{p}_f},s_f m_{s_f}} C^{\mathcal{S}'M'_\mathcal{S}}_{\frac{1}{2}m_{\mathrm{p}_f},s_f m_{s_f}} \frac{1}{2(2s_i+1)} \sum_{m_{\mathrm{p}_i} m_{s_i}} C^{\mathcal{S}M_\mathcal{S}}_{\frac{1}{2}m_{\mathrm{p}_i},s_i m_{s_i}} C^{\mathcal{S}'M'_\mathcal{S}}_{\frac{1}{2}m_{\mathrm{p}_i},s_i m_{s_i}} \\
&\quad = \sum_{M_\mathcal{S}M'_\mathcal{S}} \delta_{\mathcal{S}\mathcal{S}'}\delta_{M_\mathcal{S}M'_\mathcal{S}} \frac{1}{2(2s_i+1)} \delta_{\mathcal{S}\mathcal{S}'}\delta_{M_\mathcal{S}M'_\mathcal{S}} \\
&\quad = \frac{2\mathcal{S}+1}{2(2s_i+1)}\delta_{\mathcal{S}\mathcal{S}'},
\end{aligned} \tag{11.21}$$

which is where the standard spin weights come from. Substituting this back into Eq. (11.20):

$$\begin{aligned}
\frac{\mathrm{d}\sigma_{n_f v_f N_f m_{N_f}, n_i v_i N_i m_{N_i}}}{\mathrm{d}\Omega} &= \sum_\mathcal{S} \frac{2\mathcal{S}+1}{2(2s_i+1)} \frac{1}{(4\pi)^{3/2}} \sum_{LM_L} \sum_{\substack{\mathcal{J}\Pi \\ \mathcal{J}'\Pi'}} \sum_{L_f L'_f} \sum_{L_i L'_i} \frac{1}{\hat{L}} \hat{L}_f \hat{L}'_f \hat{L}_i \hat{L}'_i \\
&\times F^{\mathcal{J}\Pi\mathcal{S}}_{n_f v_f N_f \pi_f L_f, n_i v_i N_i L_i \pi_i}(q_f, q_i) F^{\mathcal{J}'\Pi'\mathcal{S}*}_{n_f v_f N_f \pi_f L'_f, n_i v_i N_i L'_i \pi_i}(q_f, q_i)\, C^{\mathcal{J}m_{N_i}}_{L_i 0, N_i m_{N_i}} C^{\mathcal{J}'m_{N_i}}_{L'_i 0, N_i m_{N_i}} C^{LM_L}_{L_f 0, L'_f 0} \\
&\times \sum_{m_{L_f} m'_{L_f}} (-1)^{m_{L'_f}} C^{LM_L}_{L_f m_{L_f}, L'_f -m'_{L_f}} C^{\mathcal{J}m_{N_i}}_{L_f m_{L_f}, N_f m_{N_f}} C^{\mathcal{J}'m_{N_i}}_{L'_f m'_{L_f}, N_f m_{N_f}} Y^{M_L}_L(\hat{\boldsymbol{q}}_f).
\end{aligned} \tag{11.22}$$

Now we sum over m_{N_f}, and in fact the sums over m_{N_f}, m_{L_f}, and m'_{L_f} can be evaluated together (as shown in Eq. D.26) to give

$$\begin{aligned}
&\sum_{m_{N_f} m_{L_f} m'_{L_f}} (-1)^{m_{L'_f}} C^{LM_L}_{L_f m_{L_f}, L'_f -m'_{L_f}} C^{\mathcal{J}m_{N_i}}_{L_f m_{L_f}, N_f m_{N_f}} C^{\mathcal{J}'m_{N_i}}_{L'_f m'_{L_f}, N_f m_{N_f}} \\
&\qquad = (-1)^{N_f+\mathcal{J}'} \hat{\mathcal{J}}' \hat{L} C^{\mathcal{J}m_{N_i}}_{\mathcal{J}'m_{N_i}, LM_L} \begin{Bmatrix} L'_f & N_f & \mathcal{J}' \\ \mathcal{J} & L & L_f \end{Bmatrix},
\end{aligned} \tag{11.23}$$

and substituting back into Eq. (11.22):

$$\begin{aligned}
\frac{\mathrm{d}\sigma_{n_f v_f N_f, n_i v_i N_i m_{N_i}}}{\mathrm{d}\Omega} &= \sum_\mathcal{S} \frac{2\mathcal{S}+1}{2(2s_i+1)} \frac{(-1)^{N_f}}{(4\pi)^{3/2}} \sum_{LM_L} \sum_{\substack{\mathcal{J}\Pi \\ \mathcal{J}'\Pi'}} \sum_{L_f L'_f} \sum_{L_i L'_i} \hat{\mathcal{J}} \hat{L}_f \hat{L}'_f \hat{L}_i \hat{L}'_i \\
&\times F^{\mathcal{J}\Pi\mathcal{S}}_{n_f v_f N_f \pi_f L_f, n_i v_i N_i L_i \pi_i}(q_f, q_i) F^{\mathcal{J}'\Pi'\mathcal{S}*}_{n_f v_f N_f \pi_f L'_f, n_i v_i N_i L'_i \pi_i}(q_f, q_i) \\
&\times C^{LM_L}_{L_f 0, L'_f 0} \begin{Bmatrix} L'_f & N_f & \mathcal{J}' \\ \mathcal{J} & L & L_f \end{Bmatrix} (-1)^{\mathcal{J}'} C^{\mathcal{J}m_{N_i}}_{L_i 0, N_i m_{N_i}} C^{\mathcal{J}'m_{N_i}}_{L'_i 0, N_i m_{N_i}} C^{\mathcal{J}m_{N_i}}_{\mathcal{J}'m_{N_i}, LM_L} Y^{M_L}_L(\hat{\boldsymbol{q}}_f).
\end{aligned} \tag{11.24}$$

Now averaging over m_{N_i} we use (derived in Eq. D.27):

$$\frac{1}{2N_i+1}\sum_{m_{N_i}}(-1)^{\mathcal{J}'}C^{\mathcal{J}'m_{N_i}}_{L_i'0,N_im_{N_i}}C^{\mathcal{J}m_{N_i}}_{L_i0,N_im_{N_i}}C^{\mathcal{J}m_{N_i}}_{\mathcal{J}'m_{N_i},LM_L} \tag{11.25}$$
$$= \frac{(-1)^{N_i}}{\hat{N}_i^2}\frac{\hat{\mathcal{J}}'\hat{\mathcal{J}}^2}{\hat{L}}C^{L0}_{L_i0,L_i'0}\begin{Bmatrix} L_i' & N_i & \mathcal{J}' \\ \mathcal{J} & L & L_i \end{Bmatrix}\delta_{M_L,0},$$

so the final expression for the DCS summed over m_{N_f} and averaged over m_{N_i} is

$$\begin{aligned}\frac{\mathrm{d}\sigma_{n_fv_fN_f,n_iv_iN_i}}{\mathrm{d}\Omega} &= \sum_{\mathcal{S}}\frac{2\mathcal{S}+1}{2(2s_i+1)}\frac{(-1)^{N_f+N_i}}{\hat{N}_i^2(4\pi)^{3/2}}\sum_L\sum_{\substack{\mathcal{J}\Pi\\ \mathcal{J}'\Pi'}}\sum_{L_fL_f'}\sum_{L_iL_i'}\frac{1}{\hat{L}}\hat{\mathcal{J}}^2\hat{\mathcal{J}}'^2\hat{L}_f\hat{L}_f'\hat{L}_i\hat{L}_i' \\ &\times F^{\mathcal{J}\Pi\mathcal{S}}_{n_fv_fN_f\pi_fL_f,n_iv_iN_iL_i\pi_i}(q_f,q_i)F^{\mathcal{J}'\Pi'\mathcal{S}*}_{n_fv_fN_f\pi_fL_f',n_iv_iN_iL_i'\pi_i}(q_f,q_i) \\ &\times C^{L0}_{L_f0,L_f'0}C^{L0}_{L_i0,L_i'0}\begin{Bmatrix} L_f' & N_f & \mathcal{J}' \\ \mathcal{J} & L & L_f \end{Bmatrix}\begin{Bmatrix} L_i' & N_i & \mathcal{J}' \\ \mathcal{J} & L & L_i \end{Bmatrix}Y^0_L(\hat{\boldsymbol{q}}_f).\end{aligned} \tag{11.26}$$

Now using Def. (A.27) we can write

$$\frac{\mathrm{d}\sigma_{n_fv_fN_f,n_iv_iN_i}}{\mathrm{d}\Omega} = \sum_{\mathcal{S}}\frac{2\mathcal{S}+1}{2(2s_i+1)}\sum_L A^{L\mathcal{S}}_{n_fv_fN_f,n_iv_iN_i}P_L(\cos\theta), \tag{11.27}$$

where

$$\begin{aligned}A^{L\mathcal{S}}_{n_fv_fN_f,n_iv_iN_i} &\equiv \frac{q_f}{q_i}\frac{(-1)^{N_f+N_i}}{\hat{N}_i^2(4\pi)^2}\sum_{\substack{\mathcal{J}\Pi\\ \mathcal{J}'\Pi'}}\sum_{L_fL_f'}\sum_{L_iL_i'}\hat{\mathcal{J}}^2\hat{\mathcal{J}}'^2\hat{L}_f\hat{L}_f'\hat{L}_i\hat{L}_i' \\ &\times F^{\mathcal{J}\Pi\mathcal{S}}_{n_fv_fN_f\pi_fL_f,n_iv_iN_iL_i\pi_i}(q_f,q_i)F^{\mathcal{J}'\Pi'\mathcal{S}*}_{n_fv_fN_f\pi_fL_f',n_iv_iN_iL_i'\pi_i}(q_f,q_i) \\ &\times C^{L0}_{L_f0,L_f'0}C^{L0}_{L_i0,L_i'0}\begin{Bmatrix} L_f' & N_f & \mathcal{J}' \\ \mathcal{J} & L & L_f \end{Bmatrix}\begin{Bmatrix} L_i' & N_i & \mathcal{J}' \\ \mathcal{J} & L & L_i \end{Bmatrix}.\end{aligned} \tag{11.28}$$

11.4 Integrated cross section

To obtain the integrated cross section we evaluate

$$\sigma_{n_f n_v N_f, n_i v_i N_i} = \iint \frac{\mathrm{d}\sigma_{n_f v_f N_f, n_i v_i N_i}}{\mathrm{d}\Omega}\,\mathrm{d}\Omega = 2\pi \int_{-1}^{1} \frac{\mathrm{d}\sigma_{n_f v_f N_f, n_i v_i N_i}}{\mathrm{d}\Omega}\,\mathrm{d}(\cos\theta). \quad (11.29)$$

Since the angular dependence of the DCS is entirely contained in the Legendre polynomial term, we only need to evaluate (using the fact that $P_0 = 1$):

$$2\pi \int_{-1}^{1} P_L(\cos\theta) P_0(\cos\theta)\,\mathrm{d}(\cos\theta) = 4\pi\delta_{L0}. \quad (11.30)$$

Hence, the ICS is

$$\sigma_{n_f n_v N_f, n_i v_i N_i} = 4\pi \sum_{\mathcal{S}} \frac{2\mathcal{S}+1}{2(2s_i+1)} A^{0\mathcal{S}}_{n_f v_f N_f, n_i v_i N_i} \quad (11.31)$$

$$= \sum_{\mathcal{S}} \frac{2\mathcal{S}+1}{2(2s_i+1)} \frac{q_f}{q_i} \frac{(-1)^{N_f+N_i}}{4\pi \hat{N}_i^2} \sum_{\substack{\mathcal{J}\Pi \\ \mathcal{J}'\Pi'}} \sum_{L_f L_f'} \sum_{L_i L_i'} \hat{\mathcal{J}}^2 \hat{\mathcal{J}}'^2 \hat{L}_f \hat{L}_f' \hat{L}_i \hat{L}_i'$$

$$\times F^{\mathcal{J}\Pi\mathcal{S}}_{n_f v_f N_f \pi_f L_f, n_i v_i N_i L_i \pi_i}(q_f, q_i) F^{\mathcal{J}'\Pi'\mathcal{S}*}_{n_f v_f N_f \pi_f L_f', n_i v_i N_i L_i' \pi_i}(q_f, q_i)$$

$$\times C^{00}_{L_f 0, L_f' 0} C^{00}_{L_i 0, L_i' 0} \begin{Bmatrix} L_f' & N_f & \mathcal{J}' \\ \mathcal{J} & 0 & L_f \end{Bmatrix} \begin{Bmatrix} L_i' & N_i & \mathcal{J}' \\ \mathcal{J} & 0 & L_i \end{Bmatrix}. \quad (11.32)$$

Now using Def. (B.10) to simplify the Clebsch-Gordan coefficients we have

$$\sigma_{n_f n_v N_f, n_i v_i N_i} = \sum_{\mathcal{S}} \frac{2\mathcal{S}+1}{2(2s_i+1)} \frac{q_f}{q_i} \frac{(-1)^{N_f+N_i}}{4\pi \hat{N}_i^2} \sum_{\substack{\mathcal{J}\Pi \\ \mathcal{J}'\Pi'}} \sum_{L_f L_i} (-1)^{L_f+L_i} \hat{\mathcal{J}}^2 \hat{\mathcal{J}}'^2 \hat{L}_f \hat{L}_i$$

$$\times F^{\mathcal{J}\Pi\mathcal{S}}_{n_f v_f N_f \pi_f L_f, n_i v_i N_i L_i \pi_i}(q_f, q_i) F^{\mathcal{J}'\Pi'\mathcal{S}*}_{n_f v_f N_f \pi_f L_f, n_i v_i N_i L_i \pi_i}(q_f, q_i)$$

$$\times \begin{Bmatrix} L_f & N_f & \mathcal{J}' \\ \mathcal{J} & 0 & L_f \end{Bmatrix} \begin{Bmatrix} L_i & N_i & \mathcal{J}' \\ \mathcal{J} & 0 & L_i \end{Bmatrix}, \quad (11.33)$$

and using Def. (B.29) to evaluate the 6-j symbols:

$$\sigma_{n_f n_v N_f, n_i v_i N_i} = \sum_{\mathcal{S}} \frac{2\mathcal{S}+1}{2(2s_i+1)} \frac{q_f}{4\pi q_i \hat{N}_i^2} \sum_{\mathcal{J}\Pi} \sum_{L_f L_i} \hat{\mathcal{J}}^2 \left| F^{\mathcal{J}\Pi\mathcal{S}}_{n_f v_f N_f L_f, n_i v_i N_i L_i}(q_f, q_i) \right|. \quad (11.34)$$

11.5 Cross sections resolved in rotational sublevels

In some cases it is desirable to keep the cross sections resolved in the rotational sublevels. For example, studies of Stokes parameters require information of the excited-state sublevel populations. Previously the sums over m_{L_f} and m'_{L_f} were kept in Eq. (11.22) because they made it easier to apply Clebsch-Gordan sum identities when summing over m_{N_f} and m_{N_i}. Now, however, Eq. (11.22) can be simplified by recognising that the Clebsch-Gordan coefficients $C^{\mathcal{J}m_{N_i}}_{L_f m_{L_f},N_f m_{N_f}}$ and $C^{\mathcal{J}'m_{N_i}}_{L'_f m'_{L_f},N_f m_{N_f}}$ force $m_{L_f} = m'_{L_f} = m_{N_i} = m_{N_f}$ (by the selection rule in Eq. (B.3)), and hence also $M_L = 0$, giving

$$\frac{\mathrm{d}\sigma_{n_f v_f N_f m_{N_f},n_i v_i N_i m_{N_i}}}{\mathrm{d}\Omega} = \sum_{\mathcal{S}} \frac{2\mathcal{S}+1}{2(2s_i+1)} \frac{q_f}{q_i} \frac{(-1)^{m_{N_i}-m_{N_f}}}{(4\pi)^{3/2}} \sum_{L} \sum_{\substack{\mathcal{J}\Pi \\ \mathcal{J}'\Pi'}} \sum_{L_f L'_f} \sum_{L_i L'_i} \frac{1}{\hat{L}} \hat{L}_f \hat{L}'_f \hat{L}_i \hat{L}'_i$$

$$\times F^{\mathcal{J}\Pi\mathcal{S}}_{n_f v_f N_f L_f,n_i v_i N_i L_i}(q_f,q_i) F^{\mathcal{J}'\Pi'\mathcal{S}*}_{n_f v_f N_f L'_f,n_i v_i N_i L'_i}(q_f,q_i) C^{\mathcal{J}m_{N_i}}_{L_i 0,N_i m_{N_i}} C^{\mathcal{J}'m_{N_i}}_{L'_i 0,N_i m_{N_i}} C^{L0}_{L_f 0,L'_f 0}$$

$$\times C^{L0}_{L_f m_{N_i}-m_{N_f},L'_f\, m_{N_f}-m_{N_i}} C^{\mathcal{J}m_{N_i}}_{L_f m_{N_i}-m_{N_f},N_f m_{N_f}} C^{\mathcal{J}'m_{N_i}}_{L'_f m_{N_i}-m_{N_f},N_f m_{N_f}} Y^0_L(\hat{\boldsymbol{q}}_f). \quad (11.35)$$

As before, Def. (A.27) is used to write

$$\frac{\mathrm{d}\sigma_{n_f v_f N_f m_{N_f},n_i v_i N_i m_{N_i}}}{\mathrm{d}\Omega} = \sum_{\mathcal{S}} \frac{2\mathcal{S}+1}{2(2s_i+1)} \sum_{L} A^{L\mathcal{S}}_{n_f v_f N_f m_{N_f},n_i v_i N_i m_{N_i}} P_L(\cos\theta) \quad (11.36)$$

with

$$A^{L\mathcal{S}}_{n_f v_f N_f m_{N_f},n_i v_i N_i m_{N_i}} \equiv \frac{q_f}{q_i} \frac{(-1)^{m_{N_i}-m_{N_f}}}{(4\pi)^2} \sum_{\substack{\mathcal{J}\Pi \\ \mathcal{J}'\Pi'}} \sum_{L_f L'_f} \sum_{L_i L'_i} \hat{L}_f \hat{L}'_f \hat{L}_i \hat{L}'_i$$

$$\times F^{\mathcal{J}\Pi\mathcal{S}}_{n_f v_f N_f L_f,n_i v_i N_i L_i}(q_f,q_i) F^{\mathcal{J}'\Pi'\mathcal{S}*}_{n_f v_f N_f L'_f,n_i v_i N_i L'_i}(q_f,q_i)$$

$$\times C^{\mathcal{J}m_{N_i}}_{L_i 0,N_i m_{N_i}} C^{\mathcal{J}'m_{N_i}}_{L'_i 0,N_i m_{N_i}} C^{L0}_{L_f 0,L'_f 0} C^{L0}_{L_f m_{N_i}-m_{N_f},L'_f\, m_{N_f}-m_{N_i}}$$

$$\times C^{\mathcal{J}m_{N_i}}_{L_f m_{N_i}-m_{N_f},N_f m_{N_f}} C^{\mathcal{J}'m_{N_i}}_{L'_f m_{N_i}-m_{N_f},N_f m_{N_f}}. \quad (11.37)$$

The integrated cross section is again obtained using just the $L = 0$ term,

and is given by

$$\sigma_{n_f v_f N_f m_{N_f}, n_i v_i N_i m_{N_i}} = \sum_{\mathcal{S}} \frac{2\mathcal{S}+1}{2(2s_i+1)} \frac{q_f}{q_i} \frac{(-1)^{m_{N_i}-m_{N_f}}}{4\pi} \sum_{\substack{\mathcal{J}\Pi \\ \mathcal{J}'\Pi'}} \sum_{L_f L'_f} \sum_{L_i L'_i} \hat{L}_f \hat{L}'_f \hat{L}_i \hat{L}'_i$$
$$\times F^{\mathcal{J}\Pi\mathcal{S}}_{n_f v_f N_f L_f, n_i v_i N_i L_i}(q_f, q_i) F^{\mathcal{J}'\Pi'\mathcal{S}*}_{n_f v_f N_f L'_f, n_i v_i N_i L'_i}(q_f, q_i)$$
$$\times C^{\mathcal{J} m_{N_i}}_{L_i 0, N_i m_{N_i}} C^{\mathcal{J}' m_{N_i}}_{L'_i 0, N_i m_{N_i}} C^{00}_{L_f 0, L'_f 0} C^{00}_{L_f m_{N_i}-m_{N_f}, L'_f\, m_{N_f}-m_{N_i}}$$
$$\times C^{\mathcal{J} m_{N_i}}_{L_f m_{N_i}-m_{N_f}, N_f m_{N_f}} C^{\mathcal{J}' m_{N_i}}_{L'_f m_{N_i}-m_{N_f}, N_f m_{N_f}}, \qquad (11.38)$$

and applying Def. (B.10) to give

$$C^{00}_{L_f 0, L'_f 0} C^{00}_{L_f m_{N_i}-m_{N_f}, L'_f\, m_{N_f}-m_{N_i}} = \frac{1}{\hat{L}_f^2} (-1)^{m_{N_f}-m_{N_i}} \delta_{L_f L'_f} \qquad (11.39)$$

we have

$$\sigma_{n_f v_f N_f m_{N_f}, n_i v_i N_i m_{N_i}} = \sum_{\mathcal{S}} \frac{2\mathcal{S}+1}{2(2s_i+1)} \frac{q_f}{q_i} \frac{1}{4\pi} \sum_{\substack{\mathcal{J}\Pi \\ \mathcal{J}'\Pi'}} \sum_{L_f} \sum_{L_i L'_i} \hat{L}_i \hat{L}'_i \qquad (11.40)$$
$$\times F^{\mathcal{J}\Pi\mathcal{S}}_{n_f v_f N_f L_f, n_i v_i N_i L_i}(q_f, q_i) F^{\mathcal{J}'\Pi'\mathcal{S}*}_{n_f v_f N_f L_f, n_i v_i N_i L'_i}(q_f, q_i)$$
$$\times C^{\mathcal{J} m_{N_i}}_{L_i 0, N_i m_{N_i}} C^{\mathcal{J}' m_{N_i}}_{L'_i 0, N_i m_{N_i}} C^{\mathcal{J} m_{N_i}}_{L_f m_{N_i}-m_{N_f}, N_f m_{N_f}} C^{\mathcal{J}' m_{N_i}}_{L_f m_{N_i}-m_{N_f}, N_f m_{N_f}}.$$

11.6 Calculating reduced matrix elements

If laboratory-frame rovibronic close-coupling calculations are to be performed, the lab-frame partial-wave V-matrix elements can be expressed in terms of the existing body-frame V-matrix elements. If the rotational motion is to be treated adiabatically, then it is the lab-frame partial-wave scattering amplitudes which can be obtained from the body-frame amplitudes.

The body-frame matrix elements are expanded in terms of partial-wave states $|qL\Lambda_L\rangle$ with definite angular momentum projection Λ_L on the internuclear axis, while the body frame matrix elements are expanded in terms of partial-wave states $|qLm_L\rangle$ with projection m_L on the lab-frame z axis. The lab-frame states

can be expressed in terms of the body-frame states using the Wigner-D functions:

$$\langle \boldsymbol{r}_0 | qLm_L \rangle = \sum_{\Lambda_L} D^{L*}_{m_L\Lambda_L}(\hat{\boldsymbol{R}}) \langle \boldsymbol{r}_0^{(\mathrm{b})} | qL\Lambda_L \rangle, \tag{11.41}$$

where $\boldsymbol{r}_0$ and $\boldsymbol{r}_0^{(\mathrm{b})}$ are the lab-frame and body-frame projectile coordinates, respectively. Similarly, the projectile and target electronic spin states (with the spin quantised with respect to the lab-frame z axis) are expressed in terms of the $\hat{\boldsymbol{R}}$-quantised spin states:

$$|sm_s\rangle = \sum_{\Sigma_s} D^{s*}_{m_s\Sigma_s}(\hat{\boldsymbol{R}}) |s\Sigma_s\rangle \tag{11.42}$$

$$|\tfrac{1}{2}m_\mathrm{p}\rangle = \sum_{\Sigma_\mathrm{p}} D^{\frac{1}{2}*}_{m_\mathrm{p}\Sigma_\mathrm{p}}(\hat{\boldsymbol{R}}) |\tfrac{1}{2}\Sigma_\mathrm{p}\rangle. \tag{11.43}$$

The CAM state in Eq. (11.5) can then be expressed as

$$\begin{aligned} &|\Phi_n\, s\, \nu_{nvN}\, N\, \pi\, qL : \mathcal{J}M_\mathcal{J}\Pi\mathcal{S}M_\mathcal{S}\rangle \\ &\quad = \frac{1}{q} i^L \sum_{\substack{\Lambda_L \\ \Sigma_\mathrm{p}\Sigma_s}} |qL\Lambda_L\rangle |\tfrac{1}{2}\Sigma_\mathrm{p}\rangle \sum_{m_N m_L} C^{\mathcal{J}M_\mathcal{J}}_{Lm_L,Nm_N} |\Phi_n\, s\Sigma_s\, \nu_{nvN}\, Nm_N\, \pi\rangle \\ &\qquad \times \sum_{m_\mathrm{p}m_s} C^{\mathcal{S}M_\mathcal{S}}_{\frac{1}{2}m_\mathrm{p},sm_s} D^{L*}_{m_L\Lambda_L}(\hat{\boldsymbol{R}}) D^{\frac{1}{2}*}_{m_\mathrm{p}\Sigma_\mathrm{p}}(\hat{\boldsymbol{R}}) D^{s*}_{m_s\Sigma_s}(\hat{\boldsymbol{R}}), \end{aligned} \tag{11.44}$$

and substituting in the form of the total molecular state from Eq. (11.2):

$$\begin{aligned} |\Phi_n\, s\, \nu_{nvN}\, N\, \pi\, qL : \mathcal{J}M_\mathcal{J}\Pi\mathcal{S}M_\mathcal{S}\rangle &= \frac{i^L}{q\sqrt{2(1+\delta_{\Lambda,0})}} \sum_{\substack{\Lambda_L \\ \Sigma_\mathrm{p}\Sigma_s}} |qL\Lambda_L\rangle |\tfrac{1}{2}\Sigma_\mathrm{p}\rangle \sum_{m_N m_L} C^{\mathcal{J}M_\mathcal{J}}_{Lm_L,Nm_N} \\ &\quad \times \left[|\Phi_n^{\Lambda}\, s\Sigma_s\, \nu_{nvN}\, Nm_N\Lambda\rangle + \pi(-1)^{N+\sigma} |\Phi_n^{-\Lambda}\, s\Sigma_s\, \nu_{nvN}\, Nm_N(-\Lambda)\rangle \right] \\ &\quad \times \sum_{m_\mathrm{p}m_s} C^{\mathcal{S}M_\mathcal{S}}_{\frac{1}{2}m_\mathrm{p},sm_s} D^{L*}_{m_L\Lambda_L}(\hat{\boldsymbol{R}}) D^{\frac{1}{2}*}_{m_\mathrm{p}\Sigma_\mathrm{p}}(\hat{\boldsymbol{R}}) D^{s*}_{m_s\Sigma_s}(\hat{\boldsymbol{R}}). \end{aligned} \tag{11.45}$$

We can evaluate the sum over the lab-frame spin projections using Eq. (B.49):

$$\sum_{m_\mathrm{p}m_s} C^{\mathcal{S}M_\mathcal{S}}_{\frac{1}{2}m_\mathrm{p},sm_s} D^{\frac{1}{2}*}_{m_\mathrm{p}\Sigma_\mathrm{p}}(\hat{\boldsymbol{R}}) D^{s*}_{m_s\Sigma_s}(\hat{\boldsymbol{R}}) = C^{\mathcal{S}\Sigma_\mathcal{S}}_{\frac{1}{2}\Sigma_\mathrm{p},s\Sigma_s} D^{\mathcal{S}*}_{M_\mathcal{S}\Sigma_\mathcal{S}}(\hat{\boldsymbol{R}}), \tag{11.46}$$

so the CAM state simplifies (somewhat) to

$$|\Phi_n\, s\, \nu_{nvN}\, N\, \pi\, qL : \mathcal{J} M_{\mathcal{J}} \Pi \mathcal{S} M_{\mathcal{S}}\rangle$$
$$= \frac{i^L}{q\sqrt{2(1+\delta_{\Lambda,0})}} \sum_{\substack{\Lambda_L \\ \Sigma_{\rm p}\Sigma_s}} |qL\Lambda_L\rangle |\tfrac{1}{2}\Sigma_{\rm p}\rangle C^{\mathcal{S}\Sigma_{\mathcal{S}}}_{\frac{1}{2}\Sigma_{\rm p}, s\Sigma_s} D^{\mathcal{S}*}_{M_{\mathcal{S}}\Sigma_{\mathcal{S}}}(\hat{\boldsymbol{R}}) \sum_{m_N m_L} C^{\mathcal{J}M_{\mathcal{J}}}_{Lm_L, Nm_N} D^{L*}_{m_L\Lambda_L}(\hat{\boldsymbol{R}})$$
$$\times \left[|\Phi_n^{\Lambda}\, s\Sigma_s\, \nu_{nvN}\, Nm_N\Lambda\rangle + \pi(-1)^{N+\sigma} |\Phi_n^{-\Lambda}\, s\Sigma_s\, \nu_{nvN}\, Nm_N(-\Lambda)\rangle \right], \tag{11.47}$$

and substituting in the form of the rotational wave functions from Eq. (3.42), we have

$$|\Phi_n\, s\, \nu_{nvN}\, N\, \pi\, qL : \mathcal{J} M_{\mathcal{J}} \Pi \mathcal{S} M_{\mathcal{S}}\rangle$$
$$= \frac{i^L \hat{N}}{q\sqrt{8\pi^2}\sqrt{2(1+\delta_{\Lambda,0})}} \sum_{\substack{\Lambda_L \\ \Sigma_{\rm p}\Sigma_s}} |qL\Lambda_L\rangle |\tfrac{1}{2}\Sigma_{\rm p}\rangle C^{\mathcal{S}\Sigma_{\mathcal{S}}}_{\frac{1}{2}\Sigma_{\rm p}, s\Sigma_s} D^{\mathcal{S}*}_{M_{\mathcal{S}}\Sigma_{\mathcal{S}}}(\hat{\boldsymbol{R}})$$
$$\times \Big[|\Phi_n^{\Lambda}\, s\Sigma_s\, \nu_{nvN}\rangle \sum_{m_N m_L} D^{L*}_{m_L\Lambda_L}(\hat{\boldsymbol{R}}) C^{\mathcal{J}M_{\mathcal{J}}}_{Lm_L, Nm_N} D^{N*}_{m_N,\Lambda}(\hat{\boldsymbol{R}}) \tag{11.48}$$
$$+ \pi(-1)^{N+\sigma} |\Phi_n^{-\Lambda}\, s\Sigma_s\, \nu_{nvN}\rangle \sum_{m_N m_L} D^{L*}_{m_L\Lambda_L}(\hat{\boldsymbol{R}}) C^{\mathcal{J}M_{\mathcal{J}}}_{Lm_L, Nm_N} D^{N*}_{m_N,-\Lambda}(\hat{\boldsymbol{R}}) \Big].$$

Now using the same identity we used above to sum over the lab-frame spin projections we can evaluate the sums over m_N and m_L:

$$\sum_{m_N m_L} D^{L*}_{m_L\Lambda_L}(\hat{\boldsymbol{R}}) C^{\mathcal{J}M_{\mathcal{J}}}_{Lm_L, Nm_N} D^{N*}_{m_N,\pm\Lambda}(\hat{\boldsymbol{R}}) = C^{\mathcal{J}(\Lambda_L\pm\Lambda)}_{L\Lambda_L, N\,\pm\Lambda} D^{\mathcal{J}*}_{M_{\mathcal{J}}(\Lambda_L\pm\Lambda)}(\hat{\boldsymbol{R}}), \tag{11.49}$$

giving

$$|\Phi_n\, s\nu_{nvN}\, N\, \pi\, qL : \mathcal{J} M_{\mathcal{J}} \Pi \mathcal{S} M_{\mathcal{S}}\rangle = \frac{i^L \hat{N}}{q\sqrt{8\pi^2}\sqrt{2(1+\delta_{\Lambda,0})}} \tag{11.50}$$
$$\times \Bigg[\sum_{\substack{\Lambda_L \\ \Sigma_{\rm p}\Sigma_s}} |\Phi_n^{\Lambda}\, s\Sigma_s\, \nu_{nvN}\, qL\Lambda_L\Sigma_{\rm p}\rangle C^{\mathcal{J}(\Lambda_L+\Lambda)}_{L\Lambda_L, N\,\Lambda} C^{\mathcal{S}\Sigma_{\mathcal{S}}}_{\frac{1}{2}\Sigma_{\rm p}, s\Sigma_s} D^{\mathcal{J}*}_{M_{\mathcal{J}}(\Lambda_L+\Lambda)}(\hat{\boldsymbol{R}}) D^{\mathcal{S}*}_{M_{\mathcal{S}}\Sigma_{\mathcal{S}}}(\hat{\boldsymbol{R}})$$
$$+ \pi(-1)^{N+\sigma} \sum_{\substack{\Lambda_L \\ \Sigma_{\rm p}\Sigma_s}} |\Phi_n^{-\Lambda} s\Sigma_s \nu_{nvN} qL\Lambda_L\Sigma_{\rm p}\rangle C^{\mathcal{J}(\Lambda_L-\Lambda)}_{L\Lambda_L, N\,-\Lambda} C^{\mathcal{S}\Sigma_{\mathcal{S}}}_{\frac{1}{2}\Sigma_{\rm p}, s\Sigma_s} D^{\mathcal{J}*}_{M_{\mathcal{J}}(\Lambda_L-\Lambda)}(\hat{\boldsymbol{R}}) D^{\mathcal{S}*}_{M_{\mathcal{S}}\Sigma_{\mathcal{S}}}(\hat{\boldsymbol{R}}) \Bigg].$$

By the Wigner-Eckhart theorem the reduced matrix element is independent of $M_{\mathcal{J}}$ and $M_{\mathcal{S}}$, so it can be equated to the non-reduced matrix element with

$M_{\mathcal{J}} = M_{\mathcal{S}} = 0$:

$$\langle q' L' \pi' N' \nu_{n'v'N'} s' \Phi_{n'} || \hat{\mathsf{X}}^{\mathcal{J}\Pi\mathcal{S}} || \Phi_n s \nu_{nvN} N \pi q L \rangle$$
$$= X^{++} + \pi'(-1)^{N'+\sigma'} X^{-+} + \pi(-1)^{N+\sigma} X^{+-} + \pi'\pi(-1)^{N'+N+\sigma'+\sigma} X^{--}, \tag{11.51}$$

where

$$X^{\pm'\pm} \equiv \frac{1}{q'q} \frac{\hat{N}'\hat{N}}{8\pi^2} i^{L-L'} \sum_{\Lambda_\mathrm{e}\Pi_\mathrm{e}\Sigma_\mathcal{S}} \sum_{\substack{\Lambda'_L \Sigma'_\mathrm{p} \Sigma'_s \\ \Lambda_L \Sigma_\mathrm{p} \Sigma_s}} C^{\mathcal{J}\Lambda_\mathrm{e}}_{L'\Lambda'_L, N' \pm'\Lambda'} C^{\mathcal{S}\Sigma_\mathcal{S}}_{\frac{1}{2}\Sigma'_\mathrm{p}, s'\Sigma'_s} C^{\mathcal{J}\Lambda_\mathrm{e}}_{L\Lambda_L, N \pm\Lambda} C^{\mathcal{S}\Sigma_\mathcal{S}}_{\frac{1}{2}\Sigma_\mathrm{p}, s\Sigma_s}$$
$$\times \langle q' L' \Lambda_{L'} \nu_{n'v'N'} s' \Phi^{\pm'\Lambda}_{n'} | \hat{\mathsf{X}}^{\Lambda_\mathrm{e}\Pi_\mathrm{e}\mathcal{S}} | \Phi^{\pm\Lambda}_n s \nu_{nvN} q L \Lambda_L \rangle$$
$$\times \iiint_{\mathbb{R}^3} D^{\mathcal{J}*}_{0(\Lambda'_L \pm' \Lambda')}(\hat{\boldsymbol{R}}) D^{\mathcal{S}*}_{0\Sigma_\mathcal{S}}(\hat{\boldsymbol{R}}) D^{\mathcal{J}}_{0(\Lambda_L \pm \Lambda)}(\hat{\boldsymbol{R}}) D^{\mathcal{S}}_{0\Sigma_\mathcal{S}}(\hat{\boldsymbol{R}}) \, \mathrm{d}\hat{\boldsymbol{R}}. \tag{11.52}$$

The matrix element here is the body-frame partial-wave vibronic matrix element of $\hat{\mathsf{X}}$. We have also introduced sums over the (conserved) total electronic angular-momentum projection on $\hat{\boldsymbol{R}}$, total electronic parity, and total spin projection on $\hat{\boldsymbol{R}}$:

$$\Lambda_\mathrm{e} = \Lambda'_L + \Lambda' = \Lambda_L + \Lambda \tag{11.53}$$

$$\Pi_\mathrm{e} = t' \cdot (-1)^{L'} = t \cdot (-1)^L \tag{11.54}$$

$$\Sigma_\mathcal{S} = \Sigma'_s + \Sigma'_\mathrm{p} = \Sigma_s + \Sigma_\mathrm{p}. \tag{11.55}$$

The partial-wave body-frame matrix element is non-zero only when

$$\Lambda'_L \pm' \Lambda' = \Lambda_L \pm \Lambda = \Lambda_\mathrm{e}, \tag{11.56}$$

so we can simplify $X^{\pm'\pm}$ to

$$X^{\pm'\pm} \equiv \frac{1}{q'q} \frac{\hat{N}'\hat{N}}{8\pi^2} i^{L-L'} \sum_{\Lambda_\mathrm{e}\Pi_\mathrm{e}\Sigma_\mathcal{S}} \sum_{\substack{\Lambda'_L \Sigma'_\mathrm{p} \Sigma'_s \\ \Lambda_L \Sigma_\mathrm{p} \Sigma_s}} C^{\mathcal{J}\Lambda_\mathrm{e}}_{L'\Lambda'_L, N' \pm'\Lambda'} C^{\mathcal{S}\Sigma_\mathcal{S}}_{\frac{1}{2}\Sigma'_\mathrm{p}, s'\Sigma'_s} C^{\mathcal{J}\Lambda_\mathrm{e}}_{L\Lambda_L, N \pm\Lambda} C^{\mathcal{S}\Sigma_\mathcal{S}}_{\frac{1}{2}\Sigma_\mathrm{p}, s\Sigma_s}$$
$$\times \langle q' L' \Lambda_{L'} \nu_{n'v'N'} s' \Phi^{\pm'\Lambda}_{n'} | \hat{\mathsf{X}}^{\Lambda_\mathrm{e}\Pi_\mathrm{e}\mathcal{S}} | \Phi^{\pm\Lambda}_n s \nu_{nvN} q L \Lambda_L \rangle$$
$$\times \iiint_{\mathbb{R}^3} D^{\mathcal{J}*}_{0\Lambda_\mathrm{e}}(\hat{\boldsymbol{R}}) D^{\mathcal{S}*}_{0\Sigma_\mathcal{S}}(\hat{\boldsymbol{R}}) D^{\mathcal{J}}_{0\Lambda_\mathrm{e}}(\hat{\boldsymbol{R}}) D^{\mathcal{S}}_{0\Sigma_\mathcal{S}}(\hat{\boldsymbol{R}}) \, \mathrm{d}\hat{\boldsymbol{R}}. \tag{11.57}$$

Using Eq. (B.50), the integral over $\hat{\boldsymbol{R}}$ can be evaluated to a sum over Clebsch-Gordan coefficients equal to

$$8\pi^2 \sum_j \frac{1}{\hat{j}^2} C^{j0}_{\mathcal{J}0,\mathcal{S}0} C^{j(\Lambda_e+\Sigma_\mathcal{S})}_{\mathcal{J}\Lambda_e,\mathcal{S}\Sigma_\mathcal{S}} C^{j0}_{\mathcal{J}0,\mathcal{S}0} C^{j(\Lambda_e+\Sigma_\mathcal{S})}_{\mathcal{J}\Lambda_e,\mathcal{S}\Sigma_\mathcal{S}}, \tag{11.58}$$

giving:

$$\begin{aligned} X^{\pm'\pm} = \frac{\hat{N}'\hat{N}}{q'q} i^{L-L'} \sum_{\Lambda_e\Pi_e} \sum_{\Lambda'_L\Lambda_L} C^{\mathcal{J}\Lambda_e}_{L'\Lambda'_L,N'\pm'\Lambda'} C^{\mathcal{J}\Lambda_e}_{L\Lambda_L,N\pm\Lambda} \\ \times \langle q'L'\Lambda_{L'}\, \nu_{n'v'N'}\, s'\, \Phi^{\pm'\Lambda}_{n'} | \hat{\mathrm{X}}^{\Lambda_e\Pi_e\mathcal{S}} | \Phi^{\pm\Lambda}_n\, s\, \nu_{nvN}\, qL\Lambda_L\rangle \\ \times \sum_{j\Sigma_\mathcal{S}} \sum_{\substack{\Sigma'_s\Sigma_s \\ \Sigma'_p\Sigma_p}} \frac{1}{\hat{j}^2} C^{j0}_{\mathcal{J}0,\mathcal{S}0} C^{j0}_{\mathcal{J}0,\mathcal{S}0} C^{j(\Lambda_e+\Sigma_\mathcal{S})}_{\mathcal{J}\Lambda_e,\mathcal{S}\Sigma_\mathcal{S}} C^{j(\Lambda_e+\Sigma_\mathcal{S})}_{\mathcal{J}\Lambda,\mathcal{S}\Sigma_\mathcal{S}} C^{\mathcal{S}\Sigma_\mathcal{S}}_{\frac{1}{2}\Sigma'_p,s'\Sigma'_s} C^{\mathcal{S}\Sigma_\mathcal{S}}_{\frac{1}{2}\Sigma_p,s\Sigma_s}. \end{aligned} \tag{11.59}$$

Using Eq. (D.23) the sums over j and spin projections can be evaluated:

$$\sum_{j\Sigma_\mathcal{S}} \sum_{\substack{\Sigma'_s\Sigma_s \\ \Sigma'_p\Sigma_p}} \frac{1}{\hat{j}^2} C^{j0}_{\mathcal{J}0,\mathcal{S}0} C^{j0}_{\mathcal{J}0,\mathcal{S}0} C^{j(\Lambda_e+\Sigma_\mathcal{S})}_{\mathcal{J}\Lambda_e,\mathcal{S}\Sigma_\mathcal{S}} C^{j(\Lambda_e+\Sigma_\mathcal{S})}_{\mathcal{J}\Lambda_e,\mathcal{S}\Sigma_\mathcal{S}} C^{\mathcal{S}\Sigma_\mathcal{S}}_{\frac{1}{2}\Sigma_p,s'\Sigma'_s} C^{\mathcal{S}\Sigma_\mathcal{S}}_{\frac{1}{2}\Sigma_p,s\Sigma_s} = \frac{1}{\hat{\mathcal{J}}^2}. \tag{11.60}$$

Substituting this back into $X^{\pm'\pm}$, the final expression for the reduced matrix element is

$$\begin{aligned} \langle q'L'\,\pi'\,N'\,\nu_{n'v'N'}\,s'\,\Phi_{n'} || \hat{\mathrm{X}}^{\mathcal{J}\Pi\mathcal{S}} || \Phi_n\, s\, \nu_{nvN}\, N\, \pi\, qL\rangle = \frac{\hat{N}'\hat{N} i^{L-L'}}{q'q\sqrt{2(1+\delta_{\Lambda',0})}\sqrt{2(1+\delta_{\Lambda,0})}} \frac{1}{\hat{\mathcal{J}}^2} \\ \times \sum_{\Lambda_e\Pi_e} \sum_{\Lambda'_L\Lambda_L} \Big[C^{\mathcal{J}\Lambda_e}_{L'\Lambda'_L,N'\Lambda'} C^{\mathcal{J}\Lambda_e}_{L\Lambda_L,N\Lambda} \langle q'L'\Lambda_{L'}\, \nu_{n'v'N'}\, s'\, \Phi^{\Lambda'}_{n'} | \hat{\mathrm{X}}^{\Lambda_e\Pi_e\mathcal{S}} | \Phi^{\Lambda}_n\, s\, \nu_{nvN}\, qL\Lambda_L\rangle \\ + \pi'(-1)^{N'+\sigma'} C^{\mathcal{J}\Lambda_e}_{L'\Lambda'_L,N'-\Lambda'} C^{\mathcal{J}\Lambda_e}_{L\Lambda_L,N\Lambda} \langle q'L'\Lambda_{L'}\, \nu_{n'v'N'}\, s'\, \Phi^{-\Lambda'}_{n'} | \hat{\mathrm{X}}^{\Lambda_e\Pi_e\mathcal{S}} | \Phi^{\Lambda}_n\, s\, \nu_{nvN}\, qL\Lambda_L\rangle \\ + \pi(-1)^{N+\sigma} C^{\mathcal{J}\Lambda_e}_{L'\Lambda'_L,N'\Lambda'} C^{\mathcal{J}\Lambda_e}_{L\Lambda_L,N-\Lambda} \langle q'L'\Lambda_{L'}\, \nu_{n'v'N'}\, s'\, \Phi^{\Lambda'}_{n'} | \hat{\mathrm{X}}^{\Lambda_e\Pi_e\mathcal{S}} | \Phi^{-\Lambda}_n\, s\, \nu_{nvN}\, qL\Lambda_L\rangle \\ + \pi'\pi(-1)^{N'+N+\sigma'+\sigma} C^{\mathcal{J}\Lambda_e}_{L'\Lambda'_L,N'-\Lambda'} C^{\mathcal{J}\Lambda_e}_{L\Lambda_L,N-\Lambda} \\ \times \langle q'L'\Lambda_{L'}\, \nu_{n'v'N'}\, s'\, \Phi^{-\Lambda'}_{n'} | \hat{\mathrm{X}}^{\Lambda_e\Pi_e\mathcal{S}} | \Phi^{-\Lambda}_n\, s\, \nu_{nvN}\, qL\Lambda_L\rangle \Big]. \end{aligned} \tag{11.61}$$

For the scattering amplitude in an adiabatic calculation this translates to:

$$F^{\mathcal{J}\mathcal{S}}_{n_f v_f N_f L_f, n_i v_i N_i L_i}(q_f, q_i) = \frac{\hat{N}_f \hat{N}_i i^{L_i - L_f}}{\sqrt{2(1+\delta_{\Lambda_f,0})}\sqrt{2(1+\delta_{\Lambda_i,0})}} \frac{1}{\hat{\mathcal{J}}^2} \sum_{\Lambda_e \Pi_e} \sum_{\Lambda_{L_f} \Lambda_{L_i}} \tag{11.62}$$

$$\times \Big[C^{\mathcal{J}\Lambda_e}_{L_f \Lambda_{L_f}, N_f \Lambda_f} C^{\mathcal{J}\Lambda_e}_{L_i \Lambda_{L_i}, N_i \Lambda_i} F^{\Lambda_e \Pi_e \mathcal{S}}_{n_f(\Lambda_f) v_f L_f \Lambda_{L_f}, n_i(\Lambda_i) v_i L_i \Lambda_{L_i}}$$

$$+ \pi_f (-1)^{N_f + \sigma_f} C^{\mathcal{J}\Lambda_e}_{L_f \Lambda_{L_f}, N_f -\Lambda_f} C^{\mathcal{J}\Lambda_e}_{L_i \Lambda_{L_i}, N_i \Lambda_i} F^{\Lambda_e \Pi_e \mathcal{S}}_{n_f(-\Lambda_f) v_f L_f \Lambda_{L_f}, n_i(\Lambda_i) v_i L_i \Lambda_{L_i}}$$

$$+ \pi_i (-1)^{N_i + \sigma_i} C^{\mathcal{J}\Lambda_e}_{L_f \Lambda_{L_f}, N_f \Lambda_f} C^{\mathcal{J}\Lambda_e}_{L_i \Lambda_{L_i}, N_i -\Lambda_i} F^{\Lambda_e \Pi_e \mathcal{S}}_{n_f(\Lambda_f) v_f L_f \Lambda_{L_f}, n_i(-\Lambda_i) v_i L_i \Lambda_{L_i}}$$

$$+ \pi_f \pi_i (-1)^{N_f + N_i + \sigma_f + \sigma_i} C^{\mathcal{J}\Lambda_e}_{L_f \Lambda_{L_f}, N_f -\Lambda_f} C^{\mathcal{J}\Lambda_e}_{L_i \Lambda_{L_i}, N_i -\Lambda_i} F^{\Lambda_e \Pi_e \mathcal{S}}_{n_f(-\Lambda_f) v_f L_f \Lambda_{L_f}, n_i(-\Lambda_i) v_i L_i \Lambda_{L_i}} \Big].$$

11.7 Procedures for calculating rotationally-resolved cross sections

Rotationally-resolved cross sections can be obtained from three different types of calculations:

Rovibronic close-coupling

If a fully rovibronic close-coupling calculation is performed, then the lab-frame scattering amplitudes will be obtained by solving the Lippmann-Schwinger equation for the reduced T-matrix elements:

$$\langle q_f L_f \, \Phi_{n_f} \, s_f \, \nu_{n_f v_f N_f} \, N_f \, \pi_f || \hat{\mathsf{T}}^{\mathcal{J}\Pi\mathcal{S}} || \Phi_{n_i} \, s_i \, \nu_{n_i v_i N_i} \, N_i \, \pi_i \, q_i L_i \rangle$$

$$= \langle q_f L_f \, \Phi_{n_f} \, s_f \, \nu_{n_f v_f N_f} \, N_f \, \pi_f || \hat{\mathsf{V}}^{\mathcal{J}\Pi\mathcal{S}} || \Phi_{n_i} \, s_i \, \nu_{n_i v_i N_i} \, N_i \, \pi_i \, q_i L_i \rangle$$

$$+ \sum_{nvN} \sum_{L} \int_0^\infty \langle q_f L_f \, \Phi_{n_f} \, s_f \, \nu_{n_f v_f N_f} \, N_f \, \pi_f || \hat{\mathsf{V}}^{\mathcal{J}\Pi\mathcal{S}} || \Phi_n \, s_n \, \nu_{nvN} \, N \, \pi \, qL \rangle G^{(+)}_{nvN}(q)$$

$$\times \langle qL \, \Phi_n \, s_n \, \nu_{nvN} \, N \, \pi || \hat{\mathsf{T}}^{\mathcal{J}\Pi\mathcal{S}} || \Phi_{n_i} \, s_i \, \nu_{n_i v_i N_i} \, N_i \, \pi_i \, q_i L_i \rangle \, \mathrm{d}q, \tag{11.63}$$

where the reduced V-matrix elements are obtained using Eq. (11.61). The reduced T-matrix elements are then substituted into Eq. (11.17) to obtain the lab-frame amplitudes.

Vibrational-electronic molecular convergent close-coupling

Calculations can be performed using vibrational-electronic molecular convergent close-coupling (VE MCCC) with an adiabatic treatment of the rotational motion. In this case, the VE MCCC body-frame partial-wave vibronic scattering amplitudes are used in Eq. (11.62) to obtain the lab-frame amplitudes. Since there is no dependence on rotational levels in the VE MCCC calculations, the vibrational wave functions in this approach cannot depend on N.

Fully adiabatic-nuclei calculation

With both rotational and vibrational motion treated adiabatically, the vibronic body-frame amplitudes in Eq. (11.62) are obtained from adiabatic-nuclei calculations using fixed-nuclei scattering amplitudes calculated over a range of internuclear separations. In this case the vibrational wave functions can be calculated separately for each rotational level N.

Fixed-nuclei calculation

The fixed-nuclei T-matrix element evaluated at the mean internuclear separation $R_{\rm m}$ approximates the adiabatic-nuclei T-matrix element for the $v_i \to v_i$ transition:

$$T(R_{\rm m}) \approx \langle \nu_{n_i v_i} | T(R) | \nu_{n_i v_i} \rangle, \tag{11.64}$$

and hence rotationally-resolved cross sections where the target remains in the ground electronic and vibrational level can be obtained using only fixed-nuclei body-frame T-matrix elements.

Once the lab-frame partial-wave scattering amplitudes are obtained using one of the above four approaches, they can be substituted into any of the cross-section formulas presented throughout the chapter.

11.8 Chapter 11 summary

This chapter has presented derivations of rovibrationally-resolved cross sections suitable for direct application with R-dependent scattering amplitudes obtained from MCCC calculations. A fully-adiabatic implementation of these formulas will be utilised in Chapter 12 in a study of Fulcher-α polarisation. Future work may be directed towards the inclusion of rotational levels in the MCCC close-coupling expansion, in the same way that vibrational levels were included in the VE MCCC method. In this case, the definitions made in this chapter will be of use.

Chapter 12

Linear polarisation fractions of Fulcher-α fluorescence in electron collisions with H_2

Measurements of collisionally-induced fluorescence can reveal features of the collision dynamics not probed in standard scattering experiments, and hence provide some of the most sensitive tests of quantum-mechanical scattering theories. With the considerable progress made in computational methods over the past few decades, it is now commonplace to see outstanding agreement between measured and calculated Stokes parameters for scattering on atomic targets. However, in the case of molecular targets, both measurements and calculations of Stokes parameters are rare, and previous studies have not shown satisfactory agreement between the two.

For low-temperature hydrogen plasmas, the H_2 Fulcher-α ($d\ ^3\Pi_u \rightarrow a\ ^3\Sigma_g^+$) band is of particular interest in optical emission spectroscopy as a diagnostic tool [274], and has therefore attracted much attention from both theorists and experimentalists. The most recent measurements are due to Maseberg *et al.* [275], who measured the linear and circular polarisation fractions of Fulcher-α fluorescence following spin-polarised electron collisions with ortho-H_2. The novel aspect of these results is the behaviour of the linear polarisation fraction, which reaches negative values at near-threshold energies, in contrast to the only previous calculations [270], which predicted the opposite near-threshold behaviour for the $Q(1)$ transition.

In this chapter, the rotationally-resolved MCCC theory outlined in Chap-

ter 11 is applied using the existing body-frame scattering amplitudes from the MCCC(210) model described in Chapter 8 to calculate rovibrationally-resolved cross sections for the electron-impact $X\,^1\Sigma_g^+ \rightarrow d\,^3\Pi_u$ transition, and subsequently calculate the linear polarisation fractions P_1 for the Fulcher-α fluorescence. Some sections contain text or figures from published work by the candidate [3]. The publisher (the American Physical Society) provides the right to use an article or a portion of an article in a thesis or dissertation without requesting permission.

12.1 Definitions of Fulcher-α transitions

The process of collisionally-induced Fulcher-α fluorescence is illustrated in Fig. 12.1. The labelling of rotational levels is according to Hund's case (b) [145]. The H_2 molecule is initially in the ground electronic state with vibrational and rotational levels v_i and N_i, and is excited via electron impact to the $d\,^3\Pi_u$ state with vibrational and rotational levels v_f and N_f. After a short time, a photon is released and the molecule decays into the $a\,^3\Sigma_g^+$ state. We assume the vibrational level is unchanged, to allow comparison with the measurements of [275] where the same assumption was made, and denote by N the rotational level produced in the $a\,^3\Sigma_g^+$ state. The Fulcher-α transitions measured by Maseberg *et al.* [275],

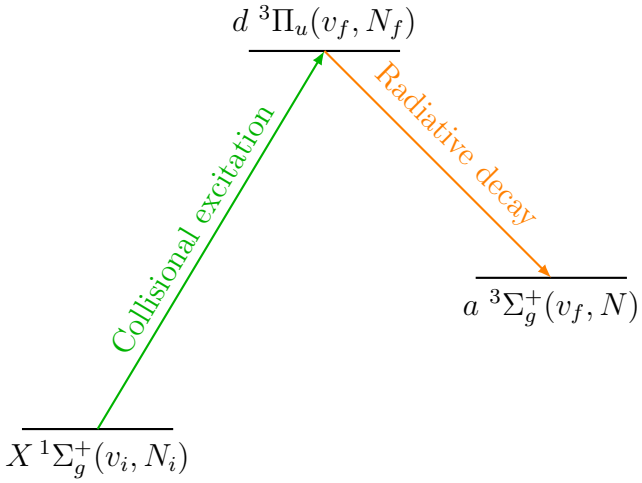

Figure 12.1: Illustration of the excitation and decay processes involved in collisionally-induced Fulcher-α fluorescence.

which are considered here, are $Q(1)$, $R(1)$, and $Q(3)$. These notations are defined in Table 12.1.

Table 12.1: Definitions of the notation for Fulcher-α radiative transitions.

Notation	Transition		
$Q(N)$:	$d\,^3\Pi_u^-(v_f, N)$	$\rightarrow$	$a\,^3\Sigma_g^+(v_f, N)$
$R(N)$:	$d\,^3\Pi_u^+(v_f, N+1)$	$\rightarrow$	$a\,^3\Sigma_g^+(v_f, N)$

12.2 Derivation of polarisation-fraction formulas

This section presents derivations of the formulas required to obtain the linear polarisation fractions for the transitions listed in Table 12.1. The formulas were previously presented by Maseberg *et al.* [275], but during the course of this project it became apparent that there are some errors in the expressions presented there. Hence, they are derived here.

Following Eq. (7.100d) of Blum [276] the linear polarisation fraction P_1 for the transition $N \rightarrow N_1$ is given by

$$P_1 = \frac{(-1)^{N+N_1}\sqrt{2N+1}\begin{Bmatrix} 1 & 1 & 2 \\ N & N & N_1 \end{Bmatrix}\left(\frac{3}{2}\right)^{3/2} A_{20}(N)}{1 + \frac{3(-1)^{N+N_1}}{2\sqrt{6}}\sqrt{2N+1}\begin{Bmatrix} 1 & 1 & 2 \\ N & N & N_1 \end{Bmatrix} A_{20}(N)}, \tag{12.1}$$

where A_{20} is the relative alignment parameter:

$$A_{20}(N) \equiv \frac{\langle T_{20}(N)^\dagger \rangle}{\langle T_{00}(N) \rangle}, \tag{12.2}$$

and $\langle T_{KQ}(N) \rangle$ are the multipole moments. Defining

$$C_1(N, N_1) \equiv (-1)^{N+N_1}\sqrt{2N+1}\begin{Bmatrix} 1 & 1 & 2 \\ N & N & N_1 \end{Bmatrix}\left(\frac{3}{2}\right)^{3/2} \tag{12.3}$$

$$C_2(N, N_1) \equiv \frac{3(-1)^{N+N_1}}{2\sqrt{6}}\sqrt{2N+1}\begin{Bmatrix} 1 & 1 & 2 \\ N & N & N_1 \end{Bmatrix}, \tag{12.4}$$

Eq. (12.1) can be written more succinctly as

$$P_1 = \frac{C_1(N, N_1)A_{20}(N)}{1 + C_2(N, N_1)A_{20}(N)}. \tag{12.5}$$

Regardless of the transition, the ratio between C_1 and C_2 is always

$$\frac{C_1(N, N_1)}{C_2(N, N_1)} = \sqrt{\frac{3}{2}} \cdot \sqrt{6} = 3. \tag{12.6}$$

According to Maseberg *et al.* [275], the multipole moments $\langle T \rangle$ should be replaced by time-averaged multipole moments $\langle \overline{T} \rangle$:

$$\langle \overline{T^\dagger_{KQ}(N)} \rangle = \sum_{K'Q'k'q'} \langle T^\dagger_{K'Q'}(N) \rangle \langle t^\dagger_{k'q'} \rangle G^{Q'q'Q}_{K'k'K}(N), \tag{12.7}$$

where $\langle t^\dagger_{k'q'} \rangle$ are the multipole moments of the electronic spin, and $G^{Q'q'Q}_{K'k'K}(N)$ are the generalised perturbation coefficients which account for the fine- and hyperfine-structure depolarisation effects. In the present case, Eq. (12.7) collapses to:

$$\langle \overline{T^\dagger_{00}(N)} \rangle = \langle T^\dagger_{00}(N) \rangle \langle t^\dagger_{00}(N) \rangle G^{000}_{000} \tag{12.8}$$

$$\langle \overline{T^\dagger_{20}(N)} \rangle = \langle T^\dagger_{20}(N) \rangle \langle t^\dagger_{00}(N) \rangle G^{000}_{202}. \tag{12.9}$$

Therefore the relative alignment parameters should be replaced with

$$\overline{A_{20}(N)} = \frac{\langle \overline{T^\dagger_{20}(N)} \rangle}{\langle \overline{T^\dagger_{00}(N)} \rangle} = \frac{G^{000}_{202}(N)}{G^{000}_{000}(N)} \frac{\langle T(N)^\dagger_{20} \rangle}{\langle T(N)_{00} \rangle} = \frac{G^{000}_{202}(N)}{G^{000}_{000}(N)} A_{20}(N). \tag{12.10}$$

Now defining

$$\overline{C_1(N, N_1)} \equiv \frac{G^{000}_{202}(N)}{G^{000}_{000}(N)} (-1)^{N+N_1} \sqrt{2N+1} \begin{Bmatrix} 1 & 1 & 2 \\ N & N & N_1 \end{Bmatrix} \left(\frac{3}{2}\right)^{3/2} \tag{12.11}$$

$$\overline{C_2(N, N_1)} \equiv \frac{G^{000}_{202}(N)}{G^{000}_{000}(N)} \frac{3(-1)^{N+N_1}}{2\sqrt{6}} \sqrt{2N+1} \begin{Bmatrix} 1 & 1 & 2 \\ N & N & N_1 \end{Bmatrix}, \tag{12.12}$$

the linear polarisation fraction is given by

$$P_1 = \frac{\overline{C_1(N, N_1)}A_{20}(N)}{1 + \overline{C_2(N, N_1)}A_{20}(N)}. \tag{12.13}$$

The generalised perturbation coefficients given by Maseberg *et al.* [275] are:

$$
\begin{aligned}
&G^{Q'q'Q}_{K'k'K}(N) \\
&= \sqrt{\frac{(2K'+1)(2k'+1)(2K+1)}{(2S+1)(2I+1)^2}} \sum_J (-1)^{N-S-J-Q}(2J+1)^2 \begin{pmatrix} K' & k' & K \\ Q' & q' & -Q \end{pmatrix} \\
&\times \begin{Bmatrix} N & J & S \\ J & N & K \end{Bmatrix} \begin{Bmatrix} N & S & K \\ N & S & K \\ K' & k' & K \end{Bmatrix} \sum_F (2F+1)^2 \begin{Bmatrix} F & F & K \\ J & J & I \end{Bmatrix}^2 ,
\end{aligned} \tag{12.14}
$$

where S and I are the target electronic and nuclear spins, respectively. However, there is a typo in the 9-j symbol, and inspection of Eq. (26) from Bartschat *et al.* [277] suggests it should instead be

$$
\begin{aligned}
&G^{Q'q'Q}_{K'k'K}(N) \\
&= \sqrt{\frac{(2K'+1)(2k'+1)(2K+1)}{(2S+1)(2I+1)^2}} \sum_J (-1)^{N-S-J-Q}(2J+1)^2 \begin{pmatrix} K' & k' & K \\ Q' & q' & -Q \end{pmatrix} \\
&\times \begin{Bmatrix} N & J & S \\ J & N & K \end{Bmatrix} \begin{Bmatrix} N & S & J \\ N & S & J \\ K' & k' & K \end{Bmatrix} \sum_F (2F+1)^2 \begin{Bmatrix} F & F & K \\ J & J & I \end{Bmatrix}^2 .
\end{aligned} \tag{12.15}
$$

Simplifying Eq. (12.15) for the case where $Q' = q' = Q = k' = 0$ and $K' = K$, and applying Eqs. (B.26) and (B.31), the perturbation coefficients can be expressed as

$$
\begin{aligned}
G^{000}_{K0K}(N) = \frac{1}{(2S+1)(2I+1)} &\sum_{J=|N-S|}^{N+S} (2J+1)^2 \begin{Bmatrix} N & N & K \\ J & J & S \end{Bmatrix}^2 \\
&\times \sum_{F=|J-I|}^{J+I} (2F+1)^2 \begin{Bmatrix} F & F & K \\ J & J & I \end{Bmatrix}^2 .
\end{aligned} \tag{12.16}
$$

This is equivalent to Eq. (4.135) in Blum [276] (once Blum's Eq. (4.135) is time-averaged). The sum over J and first 6-j symbol are responsible for the fine-

structure contribution to the depolarisation, while the sum over F and second 6-j symbol are responsible for the hyperfine-structure contribution. The effects of including both, just fine-structure, or neither can be compared by setting $I = 0$ (to remove hyperfine-structure effects) or $S = 0$ (to remove fine-structure effects).

Now we evaluate Eq. (12.16) for $K = 0$. Applying Eq. (B.30) to evaluate the 6-j symbols with $K = 0$, we have

$$\begin{aligned} G^{000}_{000} &= \frac{1}{(2S+1)(2I+1)(2N+1)} \sum_{J=|N-S|}^{N+S} \sum_{F=|J-I|}^{J+I} (2F+1) \\ &= \frac{1}{(2S+1)(2I+1)(2N+1)} \sum_{J=|N-S|}^{N+S} (2J+1)(2I+1) \\ &= \frac{1}{(2S+1)(2N+1)} (2N+1)(2S+1) \\ &= 1. \end{aligned} \tag{12.17}$$

The linear polarisation fraction formulas obtained using Eqs. (12.11)–(12.13), (12.16), and (12.17) are presented in Table 12.2.

Table 12.2: Formulas for the linear polarisation fractions of the $Q(1)$, $R(1)$, and $Q(3)$ transitions, without depolarisation, with fine-structure (FS) depolarisation, and with fine- and hyperfine-structure (HFS) depolarisation.

	No depolarisation	FS depolarisation	FS + HFS depolarisation
$Q(1)$:	$\frac{0.530A_{20}(1)}{1+0.177A_{20}(1)}$	$\frac{0.147A_{20}(1)}{1+0.049A_{20}(1)}$	$\frac{0.061A_{20}(1)}{1+0.020A_{20}(1)}$
$R(1)$:	$\frac{-0.627A_{20}(2)}{1-0.209A_{20}(2)}$	$\frac{-0.297A_{20}(2)}{1-0.099A_{20}(2)}$	$\frac{-0.178A_{20}(2)}{1-0.059A_{20}(2)}$
$Q(3)$:	$\frac{0.650A_{20}(3)}{1+0.217A_{20}(3)}$	$\frac{0.456A_{20}(3)}{1+0.152A_{20}(3)}$	$\frac{0.321A_{20}(3)}{1+0.107A_{20}(3)}$

12.3 Calculation details

Following definitions in Blum [276] and Maseberg *et al.* [275], the relative alignment parameters are given by

$$A_{20}(1) = \sqrt{2}(\sigma_1 - \sigma_0)/\sigma(N = 1) \tag{12.18}$$

$$A_{20}(2) = \sqrt{10/7}(2\sigma_2 - \sigma_1 - \sigma_0)/\sigma(N = 2) \tag{12.19}$$

$$A_{20}(3) = \sqrt{1/3}(5\sigma_3 - 3\sigma_1 - 2\sigma_0)/\sigma(N = 3), \tag{12.20}$$

where $\sigma_{m_{N_f}}$ are the cross sections for excitation of the rotational sublevel m_{N_f} in the rotational level N_f, and $\sigma(N_f)$ is the total cross section for final rotational level N_f. In this work, all cross sections are summed over initial rotational levels N_i and sublevels m_{N_i} in the $X\,^1\Sigma_g^+$ state assuming a Boltzmann distribution at 300 K to allow comparison with the experimental data of Maseberg *et al.* [275]:

$$\sigma_{m_{N_f}}[n_f v_f N_f \leftarrow n_i v_i] = \sum_{N_i m_{N_i}} p_{N_i}\, \sigma_{n_f v_f N_f m_{N_f}, n_i v_i N_i m_{N_i}} \tag{12.21}$$

$$\sigma(N_f)[n_f v_f \leftarrow n_i v_i] = \sum_{m_{N_f}} \sigma_{m_{N_f}}[n_f v_f N_f \leftarrow n_i v_i], \tag{12.22}$$

where p_{N_i} are the Boltzmann weights, v_f is the vibrational level in the electronic state n_f ($d\,^3\Pi_u$), and v_i is the vibrational level in the electronic state n_i ($X\,^1\Sigma_g^+$). At 300K the excited initial vibrational levels $v_i > 0$ are essentially unpopulated. In this work we consider scattering on ortho-H_2 (nuclear spin $I = 1$), which has only odd N in the $X\,^1\Sigma_g^+$ state. Assuming the nuclear spin is unchanged during the collision, the restriction of $I = 1$ allows us to associate odd N_f in the $d\,^3\Pi_u$ state with the $d\,^3\Pi_u^-$ branch and even N_f with the $d\,^3\Pi_u^+$ branch.

The vibrational wave functions used here were obtained in the same way as described in Sec. 7.1, but with the inclusion of the centrifugal term in the vibrational kinetic-energy operator to allow the wave functions to depend properly on the rotational level. The Laguerre basis and matrix elements for this case are given in Appendix C.

12.4 Results

Fig. 12.2 presents the MCCC P_1 fractions for the $Q(1)$, $R(1)$, and $Q(3)$ branches. Calculations have been performed for excitation of the $v_f = 0$ and $v_f = 2$ vibra-

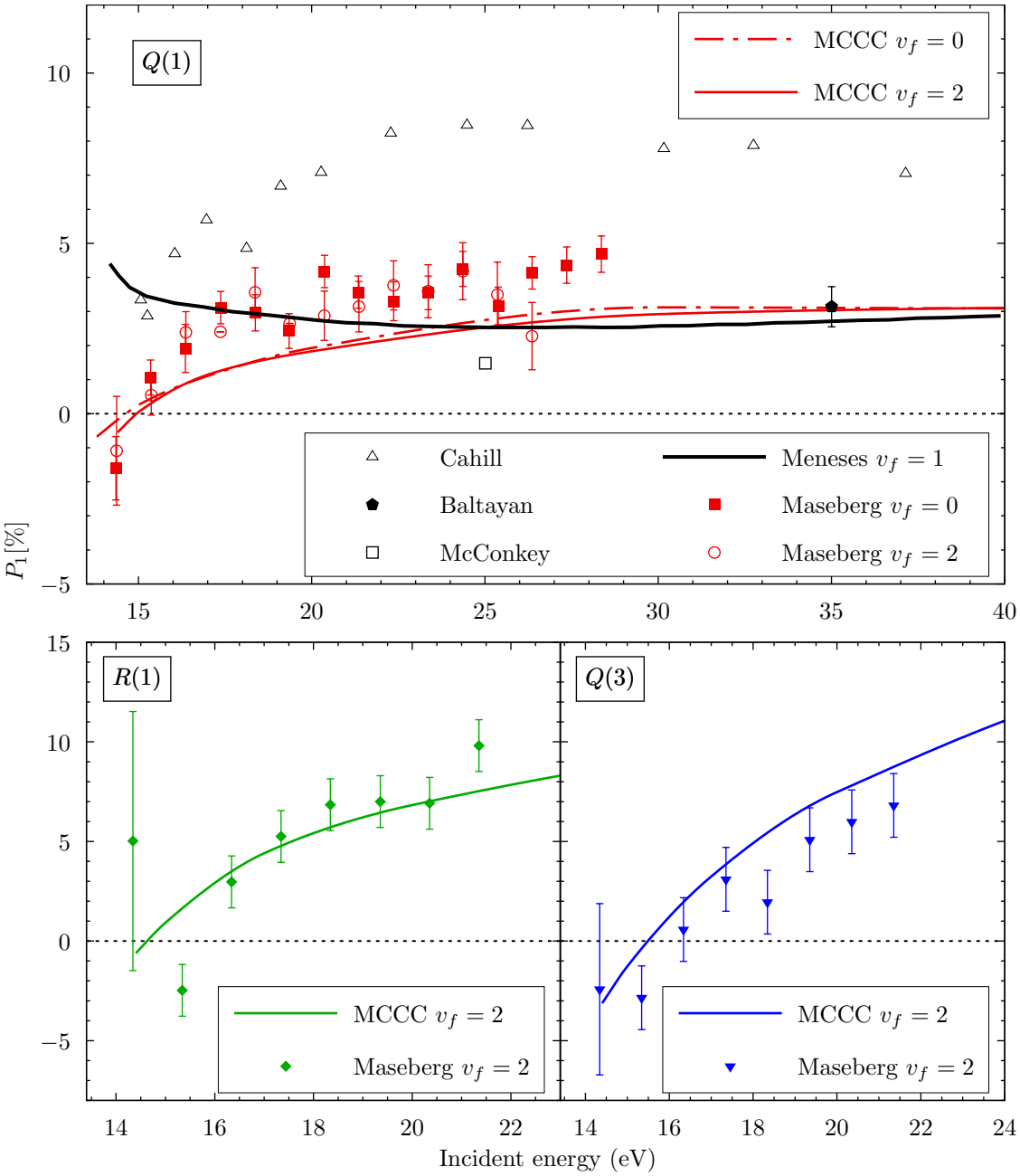

Figure 12.2: Linear polarisation fraction for the $Q(1)$, $R(1)$, and $Q(3)$ branches in the Fulcher-α band, following electron collisions with ortho-$H_2(X\ ^1\Sigma_g^+)$. Comparisons are made with the measurements of Maseberg *et al.* [275], McConkey *et al.* [278], Baltayan and Nedelec [279], and Cahill *et al.* [280], and the calculations of Meneses *et al.* [270].

tional levels in the $d\ ^3\Pi_u$ state, with essentially no difference between the two for the $Q(1)$ and $R(1)$ transitions, and only a small difference at low energies for the $Q(3)$ transition. Since the measurements of Maseberg *et al.* [275] include only $v_f = 2$ for $R(1)$ and $Q(3)$, the $v_f = 0$ results for these transitions are not presented for clarity. It is worth noting that the $d\ ^3\Pi_u$ vibrational levels considered here are not affected by predissociation into the $a\ ^3\Sigma_g^+$ continuum [281]. The MCCC results reproduce the near-threshold behaviour seen in the $Q(1)$ measurements of Maseberg *et al.* [275], in contrast to the calculations of Meneses *et al.* [270] that predicted the opposite threshold behaviour. Quantitatively, the MCCC results are somewhat lower than the measurements of Maseberg *et al.* [275] above 16 eV, with the exception of one point at 26.5 eV, where the measured P_1 fraction for $v_f = 2$ drops slightly below the MCCC line. At higher energies, the present results appear to converge to the distorted-wave results of Meneses *et al.* [270], and are in agreement with the single data point of Baltayan and Nedelec [279] at 35 eV. The incorrect near-threshold energy dependence predicted by Meneses *et al.* [270] is likely due to the application of a high-energy approximation (distorted wave) at low incident energies, where it is not accurate. Although the distorted-wave calculations were performed with $v_f = 1$ only, we have confirmed that the MCCC results for the $Q(1)$ transition with $v_f = 1$ are similar to those for $v_f = 0$ and 2, ensuring that the comparison between the two theoretical methods is valid. For the $R(1)$ and $Q(3)$ branches, no previous calculations have been attempted, and measurements have only been reported by Maseberg *et al.* [275]. The agreement between the present results and the measurements for $R(1)$ is better than for the $Q(1)$ branch, with the MCCC lines passing through the majority of the experimental data points. There is also satisfactory agreement for the $Q(3)$ branch, although there appears to be a systematic shift in the calculated values towards the upper limit of the error bars for most experimental points. The reason for this, and for the opposite trend in the $Q(1)$ results, is not clear at this point.

12.5 Chapter 12 summary

The good agreement between the MCCC calculations and the most recent measurements [275] of the Fulcher-α P_1 fractions is satisfying for three reasons. Firstly, it is a verification of the novel threshold behaviour observed in the experiment, which is unique to molecular targets due to the more complex threshold dynamics than that seen in atomic targets. Secondly, it is a demonstration that the MCCC method is capable of satisfying one of the most sensitive tests of a quantum-mechanical scattering theory. Cross-section measurements for this scattering system are rare, and for many transitions the only argument for the accuracy of the MCCC calculations has been the demonstration of convergence [93]. For the $X\ ^1\Sigma_g^+ \rightarrow d\ ^3\Pi_u$ transition, the MCCC results have now also been validated by experiment. Finally, information of the Stokes parameters is vital in plasma polarisation spectroscopy [282], and the present work demonstrates that the MCCC method is capable of providing the necessary data for this diagnostic tool.

Chapter 13

Conclusions and future work

13.1 Summary

This thesis has presented extensive studies of electron collisions with the H_2 molecule and its isotopologues using the molecular convergent close-coupling (MCCC) method. The particular focus has been on the incorporation of nuclear motion in the calculations, with the application of the well-known adiabatic-nuclei approximation to generate large sets of collision data, and the development of a new MCCC implementation in which the vibrational motion is treated without invoking the adiabatic-nuclei approximation.

The work presented in this thesis has been reported at numerous international conferences, including ICPEAC (2019), POSMOL (2019) GEC (2018, 2020, 2021), ICAMDATA (2018), GEM (2018), and the 2021 International Atomic Energy Agency (IAEA) Technical Meeting on CR properties of W and Hydrogen in Edge Plasmas. The data are hosted on the IAEA HCDB database for fusion energy research (db-amdis.org/hcdb), the LXCat database (lxcat.net/CCC), and on a dedicated MCCC database designed by the candidate during this project (mccc-db.org).

13.1.1 Adiabatic-nuclei calculations for scattering on the $X\,^1\Sigma_g^+$ state

The spheroidal-coordinate implementation [202] of the MCCC method has been utilised to produce accurate fixed-nuclei cross sections for excitation of the $n = 2$–3 electronic states of H_2 over the range of internuclear separations spanned by

the $X\ ^1\Sigma_g^+$ vibrational levels. The convergence of the cross sections was verified by comparison [10] with the rigorous convergence studies for this system performed previously with the spherical-coordinate MCCC implementation [87, 91, 93, 201]. A post-processing code was written in Fortran 90 to calculate diatomic vibrational wave functions, read R-dependent electronic collision data, and perform the adiabatic-nuclei calculations. The "energy-balancing" modification to the adiabatic-nuclei approximation developed by Stibbe and Tennyson [71] was found to be a reliable method to correct unphysical behaviour in the vibrationally-resolved cross sections due to the violation of energy conservation at near-threshold energies, and was applied in all adiabatic-nuclei calculations.

In total, cross sections for more than 60,000 collisionally-induced transitions in H_2 and its five isotopologues (HD, D_2, HT, DT, and T_2) were produced [6, 7]. These data were applied in studies of vibrational excitation via electronic excitation and radiative decay [13], and dissociation of vibrationally-excited H_2 into all neutral fragments [12]. The important cross sections for dissociative excitation of vibrationally-excited and isotopically-substituted H_2 through the repulsive $b\ ^3\Sigma_u^+$ state were compared with the previous R-matrix calculations recommended in the literature [72–74], with substantial discrepancies found. The theory of dissociation derived in Refs. [72–74] was found to suffer from a number of errors, which resulted in an incorrect dependence on the initial vibrational level, and erroneously predicted a scaling of the cross sections with isotopic mass. The derivation was corrected [4] and found to produce the standard equations for dissociative excitation, which were applied in the MCCC calculations.

Through a collaboration with the Max-Planck Institute for Plasma Physics in Garching, Germany, the H_2 data produced during this project was applied in a collisional-radiative model for the triplet system of H_2, with comparisons made of the predicted state-population densities obtained using MCCC data or previously recommended data from the literature [139, 140]. The collisional-radiative model with MCCC data as input was found to produce results in much better agreement with measured population densities.

13.1.2 Scattering on excited electronic states of H_2

Convergence studies were performed for electron scattering on the non-dissociative $n = 2$ excited states of H_2 ($B\ ^1\Sigma_u^+$, $a\ ^3\Sigma_g^+$, $c\ ^3\Pi_u$, $C\ ^1\Pi_u$, and $EF\ ^1\Sigma_g^+$). Convergence was established with respect to both the projectile and target expansions. The importance of coupling to the ionisation continuum was found to be much smaller in this case than it is for scattering on the $X\ ^1\Sigma_g^+$ state, but the projectile partial-wave convergence was substantially slower. Even utilising the analytic Born completion method, partial waves up to $L = 20$ had to be included in the close-coupling calculations in order to achieve convergence in all transitions. Adiabatic-nuclei cross sections for scattering on the $v_i = 0$ vibrational level of each electronic state were obtained, for excitation of all $n = 1$–3 states, elastic scattering, and ionisation. Comparison with state-of-the-art R-matrix calculations [116], which included partial waves up to $L = 6$ and did not utilise analytic Born completion, showed excellent agreement between the two methods for the spin-exchange transitions and most spin-allowed dipole-forbidden transitions. However, a lack of partial-wave convergence in the R-matrix calculations for the dipole-allowed transitions resulted in substantial errors compared to the converged MCCC cross sections.

The MCCC calculations for scattering on excited electronic states proved vital for the collaborative collisional-radiative project mentioned above. For most of the transitions there were no previous attempts at even approximate calculations, so the modelling community had no option but to crudely infer the cross sections from atomic data. As shown in Ref. [8], there are deviations up to an order of magnitude between rate coefficients obtained using cross sections inferred from atomic data compared to those obtained using the accurate MCCC cross sections.

13.1.3 Vibrational-electronic molecular convergent close-coupling method

The adiabatic-nuclei approximation is well-known to break down at near-threshold energies and at resonances. For some resonant transitions, such as the important

dissociative attachment processes, it is impossible to obtain even an approximate cross section using the adiabatic-nuclei approximation. A grand goal of the MCCC project, which extends well beyond the scope of this PhD, is to have an MCCC implementation in which all molecular scattering processes are treated on the same footing, and without the use of the adiabatic-nuclei approximation. As a first step in this direction, a new code has been developed in Fortran 90 which includes both electronic and vibrational levels in the close-coupling expansion. To demonstrate the abilities of the new vibrational-electronic molecular convergent close-coupling (VE MCCC) method, e^--H_2 cross sections have been calculated in the 10–14 eV incident energy region, where there are a number of well-known resonances (states of the negative H_2^- ion). The VE MCCC calculations produce detailed resonance structures in the calculated cross sections for excitation of the $X\ ^1\Sigma_g^+$, $b\ ^3\Sigma_u^+$, and $B\ ^1\Sigma_u^+$ states from the $X\ ^1\Sigma_g^+$, which are in good agreement with measured or calculated resonance positions available in the literature. A hybrid OpenMP-MPI parallelism scheme has been implemented to distribute the VE MCCC calculations over many supercomputer nodes, with the calculations performed here consisting of ≈ 2200 scattering channels and requiring ≈ 420 GB of memory per energy. Substantial attention has been paid to optimising the computational efficiency, and the MAP profiler from the ARM debug and profile suite was utilised to identify and resolve bottlenecks. As a result, the calculations are not prohibitively expensive to run, allowing the detailed studies of resonances to be performed.

13.1.4 Rotationally-resolved scattering

Expressions for rotationally-resolved cross sections within the MCCC conventions were performed by the candidate, and implemented in the adiabatic-nuclei code by Una Rehill as part of her Honours research project under the candidate's supervision. Results for rovibrational excitation of the H_2 $X\ ^1\Sigma_g^+$ state have been produced by Rehill, and will be presented in a paper currently in preparation [283]. These results have already been adopted in a study of the cosmic-ray ionisation rate in molecular clouds [284].

The candidate has performed studies of the Fulcher-α fluorescence linear

polarisation fractions, utilising MCCC calculations of rotationally-resolved cross sections for the $X\ ^1\Sigma_g^+ \rightarrow d\ ^3\Pi_u$ transition. Measurements of the $Q(1)$, $R(1)$, and $Q(3)$ linear polarisation fractions were performed within the past decade by Maseberg *et al.* [275], however only one previous calculation has been attempted. The measurements demonstrated novel threshold behaviour of the linear polarisation fractions which were in stark contrast to the previous theoretical predictions. However, the MCCC calculations were found to reproduce the threshold behaviour seen in experiment, and are in overall good agreement with the measured values.

13.2 Conclusions

The data produced during this project represent the most comprehensive and accurate cross sections for the e^--H_2 scattering system ever produced, and they will have immediate use in a variety of applications. The methods and codes developed during this project will all be applicable to whichever diatomic molecules the MCCC method is applied to in the future, allowing similarly large datasets to be produced. Although alternative methods exist for studying electron collisions with molecules much more complex than H_2, none have proven capable of producing data as comprehensive or as accurate as the MCCC method, even for a target as simple as H_2. The aim of the MCCC project is to focus on molecules which can be treated as quasi one- and two-electron targets, and to apply the highest standards of rigour in verifying the accuracy of the calculated collision data to serve as benchmarks for other methods and various approximations. This approach has proven successful in the atomic CCC project, and in the MCCC project for the H_2 and H_2^+ molecules, demonstrating a need in the community for *accurate* data. We have still only seen the beginning of what the MCCC method is capable of, and in the coming years and decades, as supercomputing resources continue to improve and evolve, there will be no shortage of interesting work to do.

13.3 Future work

The next steps in the MCCC project will be focused towards application of the electronic scattering codes to more complex diatomic molecules, and the extension of the VE MCCC code to treat dissociative attachment and efficiently include the effects of coupling to ionisation channels. Both will require modification of the codes to support GPU acceleration in order to allow much larger calculations to be performed efficiently. GPU acceleration has already been implemented in the electron-atom and heavy-particle scattering CCC codes [285, 286], resulting in 1–2 orders of magnitude speed-up in the calculations. The similar structure of all CCC codes suggests that a similar improvement could be achieved in the MCCC method.

The HeH^+ molecule is the natural next target to apply the MCCC method to, as it is a two-electron target. Beyond this, the MCCC method will be applied to scattering systems dominated by one- and two-electron excitations, for which the target can be modelled by two electrons above a frozen Hartree-Fock core. This approach has been adopted with success in the atomic CCC method to allow studies of electron and positron collisions with quasi one- and two-electron atoms [190].

The extension of the VE MCCC method to study dissociative attachment will require the explicit inclusion of dissociative-attachment channels in the close-coupling expansion. This is conceptually similar to the two-centre close coupling method for positron scattering on atoms [194, 203], which includes a second expansion in terms of positronium states in order to account for the positronium-formation rearrangement process. This extension of the VE MCCC method would allow for explicit coupling between nonresonant excitation, resonant excitation, and dissociative attachment in a single calculation, with self-consistent cross sections produced for all processes.

APPENDICES

Appendix A

Special functions and expansions

A.1 Kronecker delta function

The Kronecker delta function is a piecewise function of two integer arguments, defined by

$$\delta_{ij} = \begin{cases} 0, & i \neq j \\ 1, & i = j \end{cases} . \tag{A.1}$$

A.2 Dirac delta function

The Dirac delta function is a generalised function which, loosely speaking, is equal to zero every where but the origin, and has an integral over the real line equal to unity. It can be defined as the limit of a normalised Gaussian distribution as the standard deviation tends to zero:

$$\delta(x) = \lim_{\sigma \to 0} \frac{1}{\sigma\sqrt{2\pi}} e^{-\frac{1}{2}\left(\frac{x}{\sigma}\right)^2}. \tag{A.2}$$

The Dirac delta function satisfies

$$\int_{-\infty}^{\infty} f(x)\delta(x - x_0)\,\mathrm{d}x = f(x_0). \tag{A.3}$$

The generalisation to higher dimensions is trivial, e.g. in three dimensions:

$$\delta(\boldsymbol{r} - \boldsymbol{r}_0) = \delta(x - x_0)\delta(y - y_0)\delta(z - z_0) \tag{A.4}$$

$$\iiint_{\mathbb{R}^3} f(\boldsymbol{r})\delta(\boldsymbol{r} - \boldsymbol{r}_0)\,\mathrm{d}\boldsymbol{r} = f(\boldsymbol{r}_0). \tag{A.5}$$

A.3 Laguerre polynomials

The Laguerre polynomials $L_n(x)$ are the solutions on the interval $[0, \infty)$ to Laguerre's differential equation:

$$\left[x\frac{\mathrm{d}^2}{\mathrm{d}x^2} + (1-x)\frac{\mathrm{d}}{\mathrm{d}x} + n\right] L_n(x) = 0. \tag{A.6}$$

The solutions $L_n^\alpha(x)$ to the associated equation (for $\alpha \in \mathbb{R}$)

$$\left[x\frac{\mathrm{d}^2}{\mathrm{d}x^2} + (1+\alpha-x)\frac{\mathrm{d}}{\mathrm{d}x} + n\right] L_n^\alpha(x) = 0 \tag{A.7}$$

are known as the associated Laguerre polynomials. The standard Laguerre polynomials are the special case of the associated Laguerre polynomials with $\alpha = 0$.

Being the solution of a Sturm-Liouville problem, the Laguerre polynomials are orthogonal, with a weight function of $x^\alpha e^{-x}$:

$$\int_0^\infty L_n^\alpha(x) L_m^\alpha(x) x^\alpha e^{-x}\,\mathrm{d}x = \frac{\Gamma(n+\alpha+1)}{n!}\delta_{nm}. \tag{A.8}$$

The first two associated Laguerre polynomials are

$$L_0^\alpha(x) = 1 \tag{A.9}$$

$$L_1^\alpha(x) = -x + (\alpha+1), \tag{A.10}$$

after which the remaining polynomials can be generated using the following second-order recurrence relation:

$$L_n^\alpha(x) = \frac{(2n+\alpha-1-x)L_{n-1}^\alpha(x) - (n+\alpha-1)L_{n-2}^\alpha(x)}{n}. \tag{A.11}$$

The Laguerre polynomials also satisfy the following useful identity:

$$L_n^\alpha(x) = L_n^{\alpha+1}(x) - L_{n-1}^{\alpha+1}(x). \tag{A.12}$$

A.4 Legendre polynomials

The Legendre polynomials are the solutions on the interval $[-1, 1]$ of Legendre's differential equation:

$$\left[(1-x^2)\frac{\mathrm{d}^2}{\mathrm{d}x^2} - 2x\frac{\mathrm{d}}{\mathrm{d}x} + n(n+1)\right] P_n(x) = 0. \tag{A.13}$$

This is also a Sturm-Liouville problem, with a weight function of 1. The Legendre polynomials then satisfy

$$\int_{-1}^{1} P_n(x)P_m(x)\,\mathrm{d}x = \frac{2}{2n+1}\delta_{nm}. \tag{A.14}$$

The Legendre polynomials have definite parity given by $(-1)^n$:

$$P_n(-x) = (-1)^n P_n(x). \tag{A.15}$$

The first polynomial $P_0(x)$ is simply equal to unity, which along with the orthogonality property gives the following useful identity:

$$\int_{-\infty}^{\infty} P_n(x) = \delta_{n,0}. \tag{A.16}$$

The following identity will also be useful later in Sec. A.7:

$$\int_{-1}^{1} x^n P_n(x)\,\mathrm{d}x = \frac{2^{n+1}n!n!}{(2n+1)!}. \tag{A.17}$$

A.5 Bessel functions

The Bessel functions of the first kind, $J_\alpha(x)$, are the regular solutions on the interval $[0, \infty)$ of Bessel's differential equation (for $\alpha \in \mathbb{C}$):

$$\left[x^2\frac{\mathrm{d}^2}{\mathrm{d}x^2} + x\frac{\mathrm{d}}{\mathrm{d}x} + (x^2-\alpha^2)\right] J_\alpha(x) = 0. \tag{A.18}$$

The *spherical* Bessel functions are the solutions to the similar equation (for $n \in \mathbb{Z}_{\geq 0}$):

$$\left[x^2 \frac{\mathrm{d}^2}{\mathrm{d}x^2} + 2x \frac{\mathrm{d}}{\mathrm{d}x} + (x^2 - n(n+1))\right] j_n(x) = 0, \tag{A.19}$$

and are so-called because they arise when solving the Helmholtz equation in spherical coordinates. They are related to the standard Bessel functions by

$$j_n(x) = \sqrt{\frac{\pi}{2x}} J_{n+\frac{1}{2}}(x). \tag{A.20}$$

The Ricatti-Bessel functions

$$S_n(x) = x j_n(x) \tag{A.21}$$

are the solutions to

$$\left[\frac{\mathrm{d}^2}{\mathrm{d}x^2} - \frac{n(n+1)}{x^2} + 1\right] j_n(x) = 0. \tag{A.22}$$

The Schrödinger equation for a free electron with momentum k is

$$\left[\frac{\mathrm{d}^2}{\mathrm{d}r^2} - \frac{\ell(\ell+1)}{r^2} + k^2\right] u_\ell(r; l) = 0, \tag{A.23}$$

which can be put in the form of Eq. (A.22) by dividing through by k^2 and defining $x = kr$. Hence the free-electron continuum waves are given by the Ricatti-Bessel functions:

$$u_\ell(r; k) = S_\ell(kr). \tag{A.24}$$

A.6 Spherical harmonics

The spherical harmonics $Y_\ell^m(\theta, \phi)$ are the solutions to the angular part of Laplace's equation in spherical coordinates:

$$\frac{1}{\sin\theta} \frac{\partial}{\partial\theta} \left(\sin\theta \frac{\partial Y_\ell^m}{\partial\theta}\right) + \frac{1}{\sin^2\theta} \frac{\partial^2 Y_\ell^m}{\partial\phi^2} = -\ell(\ell+1) Y_\ell^m. \tag{A.25}$$

They can be expressed in terms of the Legendre polynomials:

$$Y_\ell^m(\theta,\phi) = \sqrt{\frac{\hat{\ell}^2}{4\pi}\frac{(\ell-m)!}{(\ell+m)!}} P_\ell^m(\cos\theta) e^{im\phi} \tag{A.26}$$

$$Y_\ell^0(\theta,\phi) = \frac{\hat{\ell}}{\sqrt{4\pi}} P_\ell(\cos\theta),, \tag{A.27}$$

where $\hat{\ell} = \sqrt{2\ell+1}$, and hence they too have definite parity:

$$Y_\ell^m(-\theta,\phi) = (-1)^m Y_\ell^m(\theta,\phi). \tag{A.28}$$

In this thesis, the following notation is commonly used:

$$Y_\ell^m(\hat{\mathbf{\Omega}}) = Y_\ell^m(\theta_{\hat{\mathbf{\Omega}}}, \phi_{\hat{\mathbf{\Omega}}}), \tag{A.29}$$

where $\theta_{\hat{\mathbf{\Omega}}}$ and $\phi_{\hat{\mathbf{\Omega}}}$ are the angles associated with the unit vector $\hat{\mathbf{\Omega}}$.

The spherical harmonics satisfy the following identities:

- Symmetry properties

$$Y_\ell^{m*}(\hat{\mathbf{\Omega}}) = (-1)^m Y_\ell^{-m}(\hat{\mathbf{\Omega}}) \qquad \text{(complex conjugation)} \tag{A.30}$$

$$Y_\ell^{-m}(\hat{\mathbf{\Omega}}) = (-1)^{-m} Y_\ell^{m*}(\hat{\mathbf{\Omega}}) \qquad \text{(sign reversal of } m\text{)} \tag{A.31}$$

- Completeness

$$\sum_{\ell m} Y_\ell^{m*}(\hat{\mathbf{\Omega}}_1) Y_\ell^m(\hat{\mathbf{\Omega}}_2) = \sum_{\ell m} \langle \hat{\mathbf{\Omega}}_1 | \ell m \rangle \langle \ell m | \hat{\mathbf{\Omega}}_2 \rangle = \langle \hat{\mathbf{\Omega}}_1 | \hat{\mathbf{\Omega}}_2 \rangle = \delta(\hat{\mathbf{\Omega}}_1 - \hat{\mathbf{\Omega}}_2) \tag{A.32}$$

- Orthogonality

$$\iint_{\mathbb{R}^2} Y_\ell^{m*}(\hat{\mathbf{\Omega}}) Y_{\ell'}^{m'}(\hat{\mathbf{\Omega}}) \, \mathrm{d}\hat{\mathbf{\Omega}} = \iint_{\mathbb{R}^2} \langle \ell m | \hat{\mathbf{\Omega}} \rangle \langle \hat{\mathbf{\Omega}} | \ell' m' \rangle \, \mathrm{d}\hat{\mathbf{\Omega}} = \langle \ell m | \ell' m' \rangle = \delta_{\ell\ell'} \delta_{mm'} \tag{A.33}$$

- Addition

$$\sum_{m=-\ell}^{\ell} Y_\ell^{m*}(\hat{\mathbf{\Omega}}_1) Y_\ell^m(\hat{\mathbf{\Omega}}_2) = \frac{\hat{\ell}^2}{4\pi} P_\ell(\hat{\mathbf{\Omega}}_1 \cdot \hat{\mathbf{\Omega}}_2) \tag{A.34}$$

$$\sum_{m=-\ell}^{\ell} Y_\ell^{m*}(\hat{\mathbf{\Omega}}) Y_\ell^m(\hat{\mathbf{\Omega}}) = \frac{\hat{\ell}^2}{4\pi} \tag{A.35}$$

- Contraction

$$Y_{\ell_1}^{m_1}(\hat{\mathbf{\Omega}}) Y_{\ell_2}^{m_2}(\hat{\mathbf{\Omega}}) = \sum_{LM} \frac{\hat{\ell}_1 \hat{\ell}_2}{\sqrt{4\pi}\hat{L}} C^{L0}_{l_1 0, l_2 0} C^{LM}_{l_1 m_1, l_2 m_2} Y_L^M(\hat{\mathbf{\Omega}}), \tag{A.36}$$

  where $C^{LM}_{\ell_1 m_1, \ell_2 m_2}$ are the Clebsch-Gordan coefficients.

A.7 Plane-wave expansion in spherical harmonics

The plane wave $|\boldsymbol{k}\rangle$ with momentum $\boldsymbol{k}$ is the solution to the Schrödinger equation with zero potential

$$\nabla^2 |\boldsymbol{k}\rangle + k^2 |\boldsymbol{k}\rangle = 0. \tag{A.37}$$

The coordinate-space representation of the three-dimensional plane wave $|\boldsymbol{k}\rangle$ with momentum $\boldsymbol{k}$ is

$$\langle \boldsymbol{r} | \boldsymbol{k} \rangle = \frac{1}{(2\pi)^{3/2}} e^{i\boldsymbol{k}\cdot\boldsymbol{r}}, \tag{A.38}$$

where the $(2\pi)^{-3/2}$ factor is included to give the following normalisation:

$$\langle \boldsymbol{k}' | \boldsymbol{k} \rangle = \delta(\boldsymbol{k}' - \boldsymbol{k}). \tag{A.39}$$

The plane wave can be expanded in the spherical harmonics by inserting the identity operator $\hat{\mathsf{I}} = \sum_{\ell m} |\ell m\rangle\langle \ell m|$ to give

$$\langle \boldsymbol{r} | \boldsymbol{k} \rangle = \sum_{\ell m} \langle \boldsymbol{r} | \ell m \rangle \langle \ell m | \boldsymbol{k} \rangle \tag{A.40}$$

$$= \sum_{\ell m} \langle \hat{\boldsymbol{r}} | \ell m \rangle \langle r \ell m | k \ell m \rangle \langle \ell m | \hat{\boldsymbol{k}} \rangle \tag{A.41}$$

$$= \sum_{\ell m} \langle r \ell m | k \ell m \rangle Y_\ell^m(\hat{\boldsymbol{r}}) Y_\ell^{m*}(\hat{\boldsymbol{k}}), \tag{A.42}$$

where $\langle r\ell m|k\ell m\rangle$ is some ℓ- and m-dependent function of r and k to be determined. From experience seeking separable solutions to the Schrödinger equation, we know it is most convenient to solve for the radial function multiplied by the radial coordinate. Since the plane waves have symmetric dependence on $\boldsymbol{r}$ and $\boldsymbol{k}$ it is then reasonable to define

$$f_{\ell m}(r,k) = kr\langle r\ell m|k\ell m\rangle, \tag{A.43}$$

so that

$$\langle \boldsymbol{r}|\boldsymbol{k}\rangle = \frac{1}{kr}\sum_{\ell m} f_{\ell m}(k,r)Y_\ell^m(\hat{\boldsymbol{r}})Y_\ell^{m*}(\hat{\boldsymbol{k}}). \tag{A.44}$$

Now expressing the Laplacian operator in terms of the orbital angular momentum operator $\hat{\mathsf{L}}^2$:

$$\nabla^2 = \frac{1}{r}\frac{\partial^2}{\partial r^2}(r\cdot\quad) - \frac{\hat{\mathsf{L}}^2}{r^2}, \tag{A.45}$$

and noting that $Y_\ell^m(\hat{\boldsymbol{r}})$ is eigenfunction of $\hat{\mathsf{L}}^2$ with eigenvalue $\ell(\ell+1)$ we have for each ℓm:

$$\left[\frac{1}{r}\frac{\partial^2}{\partial r^2}(r\cdot\quad) - \frac{\ell(\ell+1)}{r^2} + k^2\right]\frac{1}{kr}f_{\ell m}(r,k)Y_\ell^m(\hat{\boldsymbol{r}})Y_\ell^{m*}(\hat{\boldsymbol{k}}) = 0 \tag{A.46}$$

$$\left[\frac{1}{kr}\frac{\partial^2}{\partial r^2} - \frac{\ell(\ell+1)}{kr^3} + \frac{k}{r}\right]f_{\ell m}(r,k) = 0 \tag{A.47}$$

$$\left[\frac{\partial^2}{\partial r^2} - \frac{\ell(\ell+1)}{r^2} + k^2\right]f_{\ell m}(r,k) = 0. \tag{A.48}$$

Hence, following Sec. A.5, the solutions $f_{\ell m}(r,k)$ are the Ricatti-Bessel functions (and are therefore independent of m). Including an as-yet unknown normalisation constant c_ℓ, the plane-wave expansion is then given by

$$\langle \boldsymbol{r}|\boldsymbol{k}\rangle = \frac{1}{kr}\sum_{\ell m} c_\ell S_\ell(kr)Y_\ell^m(\hat{\boldsymbol{r}})Y_\ell^{m*}(\hat{\boldsymbol{k}}). \tag{A.49}$$

To determine c_ℓ, we multiply both sides by $Y_\alpha^{0*}(\hat{\boldsymbol{r}})$, for some arbitrary $\alpha \in \mathbb{Z}_{\geq 0}$,

and integrate over solid angle:

$$\frac{1}{(2\pi)^{3/2}}\int Y^*_{\alpha 0}(\hat{\boldsymbol{r}})e^{i\boldsymbol{k}\cdot\boldsymbol{r}}\,\mathrm{d}\Omega$$
$$= \frac{1}{kr}\sum_{\ell=0}^{\infty}\sum_{m=-\ell}^{\ell} c_\ell S_\ell(kr)\int Y^*_{\alpha 0}(\hat{\boldsymbol{r}})Y_{\ell m}(\hat{\boldsymbol{r}})\,\mathrm{d}\Omega\; Y^*_{\ell m}(\hat{\boldsymbol{k}}), \tag{A.50}$$

and now using the orthogonality of the spherical harmonics to simplify the right-hand side:

$$\frac{1}{(2\pi)^{3/2}}\int Y^*_{\alpha 0}(\hat{\boldsymbol{r}})e^{i\boldsymbol{k}\cdot\boldsymbol{r}}\,\mathrm{d}\Omega$$
$$= \frac{1}{kr}\sum_{\ell=0}^{\infty}\sum_{m=-\ell}^{\ell} c_\ell S_\ell(kr)\delta_{\alpha\ell}\delta_{0m}Y^*_{\ell m}(\hat{\boldsymbol{k}}) \tag{A.51}$$
$$= \frac{1}{kr}c_\alpha S_\alpha(kr)Y^*_{\alpha 0}(\hat{\boldsymbol{k}}). \tag{A.52}$$

The constants c_α are independent of $\boldsymbol{r}$ and $\boldsymbol{k}$, so the above equation can be evaluated for $kr \to 0$ to allow simplification. The Ricatti-Bessel functions satisfy

$$S_\alpha(kr) \xrightarrow[kr\to 0]{} \frac{2^\alpha \alpha!}{(2\alpha+1)!}(kr)^{\alpha+1}, \tag{A.53}$$

and since the operations $\lim\limits_{kr\to\infty}$ and $\dfrac{\partial^\alpha}{\partial(kr)^\alpha}$ can be interchanged, we can obtain the following:

$$\lim_{kr\to 0}\frac{\partial^\alpha}{\partial(kr)^\alpha}\frac{1}{(2\pi)^{3/2}}\int Y^*_{\alpha 0}(\hat{\boldsymbol{r}})e^{i\boldsymbol{k}\cdot\boldsymbol{r}}\,\mathrm{d}\Omega = \frac{\partial^\alpha}{\partial(kr)^\alpha}\lim_{kr\to 0}\frac{1}{kr}c_\alpha S_\alpha(kr)Y^*_{\alpha 0}(\hat{\boldsymbol{k}}) \tag{A.54}$$

$$\lim_{kr\to 0}\frac{1}{(2\pi)^{3/2}}\int Y^*_{\alpha 0}(\hat{\boldsymbol{r}})(i\hat{\boldsymbol{k}}\cdot\hat{\boldsymbol{r}})^\alpha e^{i\boldsymbol{k}\cdot\boldsymbol{r}}\,\mathrm{d}\Omega = \frac{\partial^\alpha}{\partial(kr)^\alpha}c_\alpha\frac{2^\alpha\alpha!(kr)^\alpha}{(2\alpha+1)!}Y^*_{\alpha 0}(\hat{\boldsymbol{k}}) \tag{A.55}$$

$$\frac{1}{(2\pi)^{3/2}}\int (i\hat{\boldsymbol{k}}\cdot\hat{\boldsymbol{r}})^\alpha Y^*_{\alpha 0}(\hat{\boldsymbol{r}})\,\mathrm{d}\Omega = c_\alpha\frac{2^\alpha\alpha!\alpha!}{(2\alpha+1)!}Y^*_{\alpha 0}(\hat{\boldsymbol{k}}). \tag{A.56}$$

Since the constants c_ℓ are independent of $\boldsymbol{k}$, we can temporarily set $\boldsymbol{k} = k\hat{\boldsymbol{z}}$ (i.e. align the incident momentum with the z axis), to give

$$\frac{1}{(2\pi)^{3/2}}\int (i\hat{\boldsymbol{z}}\cdot\hat{\boldsymbol{r}})^\alpha Y^*_{\alpha 0}(\hat{\boldsymbol{r}})\,\mathrm{d}\Omega = c_\alpha\frac{2^\alpha\alpha!\alpha!}{(2\alpha+1)!}Y^*_{\alpha 0}(\hat{\boldsymbol{z}}) \tag{A.57}$$

$$\frac{i^\alpha}{(2\pi)^{3/2}}\int (\cos\theta)^\alpha Y^*_{\alpha 0}(\hat{\boldsymbol{r}})\,\mathrm{d}\Omega = c_\alpha\frac{2^\alpha\alpha!\alpha!}{(2\alpha+1)!}\frac{\hat{\alpha}}{\sqrt{4\pi}}, \tag{A.58}$$

where we have used Eq. (A.27) to give $Y_{\alpha 0}(\hat{\boldsymbol{z}}) = \hat{\alpha}/\sqrt{4\pi} P_\ell(\cos 0)$.

Now we attend to the integral on the left-hand side:

$$\frac{i^\alpha}{(2\pi)^{3/2}} \int (\cos\theta)^\alpha Y^*_{\alpha 0}(\hat{\boldsymbol{r}})\, \mathrm{d}\Omega = \frac{i^\alpha}{(2\pi)^{3/2}} \int_0^\pi \int_0^{2\pi} (\cos\theta)^\alpha \frac{\hat{\alpha}}{\sqrt{4\pi}} P_\alpha(\cos\theta) \sin\theta \,\mathrm{d}\theta \,\mathrm{d}\phi$$

$$= \frac{2\pi i^\alpha}{(2\pi)^{3/2}} \frac{\hat{\alpha}}{\sqrt{4\pi}} \int_{-1}^{1} (\cos\theta)^\alpha P_\alpha(\cos\theta)\, \mathrm{d}(\cos\theta), \quad \text{(A.59)}$$

where $P_\alpha(\cos\theta)$ is a Legendre polynomial. Now using Eq. (A.17) we have

$$\frac{i^\alpha}{\sqrt{2\pi}} \frac{\hat{\alpha}}{\sqrt{4\pi}} \frac{2^{\alpha+1}\alpha!\alpha!}{(2\alpha+1)!} = c_\alpha \frac{2^\alpha \alpha!\alpha!}{(2\alpha+1)!} \frac{\hat{\alpha}}{\sqrt{4\pi}}, \quad \text{(A.60)}$$

finally giving

$$c_\alpha = \frac{2i^\alpha}{\sqrt{2\pi}}, \quad \text{(A.61)}$$

and the final form of the plane-wave expansion:

$$\langle \boldsymbol{r}|\boldsymbol{k}\rangle = \frac{1}{(2\pi)^{3/2}} e^{i\boldsymbol{k}\cdot\boldsymbol{r}} = \sqrt{\frac{2}{\pi}} \frac{1}{kr} \sum_{\ell=0}^{\infty} \sum_{m=-\ell}^{+\ell} i^\ell S_\ell(kr) Y_{\ell m}(\hat{\boldsymbol{r}}) Y^*_{\ell m}(\hat{\boldsymbol{k}}). \quad \text{(A.62)}$$

Using the addition theorem for the spherical harmonics (A.34), this can be simplified to

$$\langle \boldsymbol{r}|\boldsymbol{k}\rangle = \frac{1}{(2\pi)^{3/2}} \sum_{\ell=0}^{\infty} (2\ell+1) i^\ell j_\ell(kr) P_\ell(\hat{\boldsymbol{k}}\cdot\hat{\boldsymbol{r}}). \quad \text{(A.63)}$$

In the case where $\boldsymbol{k}$ is aligned with the z axis, this becomes

$$\langle \boldsymbol{r}|\boldsymbol{k}\rangle = \frac{1}{(2\pi)^{3/2}} \sum_{\ell=0}^{\infty} (2\ell+1) i^\ell j_\ell(kr) P_\ell(\cos\theta), \quad \text{(A.64)}$$

where θ is the azimuthal angle associated with the $\boldsymbol{r}$ vector.

Appendix B

Angular-momentum algebra and rotations

This chapter lists a number of useful identities which have been utilised in derivations presented in this thesis, and additional information about rotations of quantum states. Unless specified otherwise, all identities have been taken from Varshalovich *et al.* [287].

B.1 Angular-momentum identities

B.1.1 Clebsch-Gordan coefficients

- Notation

$$C^{JM}_{j_1 m_1, j_2 m_2} \equiv \langle j_1 m_1 \, j_2 m_2 | JM \rangle \tag{B.1}$$

- Selection rules

$$|j_1 - j_2| \leq J \leq j_1 + j_2 \qquad \text{(triangular conditions)} \tag{B.2}$$

$$m_1 + m_2 = M \tag{B.3}$$

$$j_1, j_2, J \ \in \ \tfrac{1}{2}\mathbb{Z}_{\geq 0} \tag{B.4}$$

$$m_1, m_2, M \ \in \ \tfrac{1}{2}\mathbb{Z} \tag{B.5}$$

$$|m_1| \leq j_1, \ |m_2| \leq j_2, \ |M| \leq J \tag{B.6}$$

$$j_1 + m_1, j_2 + m_2, J + M \ \in \ \mathbb{Z}_{\geq 0} \tag{B.7}$$

- Unitarity

$$\sum_{m_1 m_2} C^{JM}_{j_1 m_1, j_2 m_2} C^{J'M'}_{j_1 m_1, j_2 m_2} = \delta_{JJ'} \delta_{MM'} \tag{B.8}$$

$$\sum_{J(M)} C^{JM}_{j_1 m_1, j_2 m_2} C^{JM}_{j_1' m_1', j_2' m_2'} = \delta_{j_1 j_1'} \delta_{j_2 j_2'} \delta_{m_1 m_1'} \delta_{m_2 m_2'} \tag{B.9}$$

- Special cases

$$C^{00}_{j_1 m_1, j_2 m_2} = \frac{1}{\hat{j}_1} (-1)^{j_1 - m_1} \delta_{j_1 j_2} \delta_{m_1, -m_2} \tag{B.10}$$

$$C^{JM}_{j_1 m_1, 00} = \delta_{j_1 J} \delta_{m_1 M} \tag{B.11}$$

- Symmetry properties

$$C^{JM}_{j_1 m_1, j_2 m_2}$$

$$= (-1)^{j_1 + j_2 - J} C^{JM}_{j_2 m_2, j_1 m_1} \qquad \text{(interchange of } j_1 m_1 \text{ and } j_2 m_2\text{)} \tag{B.12}$$

$$= (-1)^{j_2 + m_2} \frac{\hat{J}}{\hat{j}_1} C^{j_1 - m_1}_{J-M, j_2 m_2} \qquad \text{(interchange of } j_1 m_1 \text{ and } JM\text{)} \tag{B.13}$$

$$= (-1)^{j_1 - m_1} \frac{\hat{J}}{\hat{j}_2} C^{j_2 - m_2}_{j_1 m_1, J-M} \qquad \text{(interchange of } j_2 m_2 \text{ and } JM\text{)} \tag{B.14}$$

$$= (-1)^{j_1 - m_1} \frac{\hat{J}}{\hat{j}_2} C^{j_2 m_2}_{JM, j_1 - m_1} \qquad \text{(anti-clockwise rotation of indices)} \tag{B.15}$$

$$= (-1)^{j_2 + m_2} \frac{\hat{J}}{\hat{j}_1} C^{j_1 m_1}_{j_2 - m_2, JM} \qquad \text{(clockwise rotation of indices)} \tag{B.16}$$

$$= (-1)^{j_1 + j_2 - J} C^{J-M}_{j_1 - m_1, j_2 - m_2} \qquad \text{(make all projections negative)} \tag{B.17}$$

- Relationship to 3-j symbols

$$C^{JM}_{j_1 m_2, j_2 m_2} = (-1)^{j_1 - j_2 + M} \hat{J} \begin{pmatrix} j_1 & j_2 & J \\ m_1 & m_2 & -M \end{pmatrix} \tag{B.18}$$

- Sums involving products of Clebsch-Gordan coefficients

$$\sum_{j_1 j_2} C^{JM}_{j_1 m_1, j_2 m_2} C^{J'M'}_{j_1 m_1, j_2 m_2} = \delta_{JJ'}\delta_{MM'} \tag{B.19}$$

$$\sum_{m_1 m_2 m_6} C^{j_1 m_1}_{j_2 m_2, j_3 m_3} C^{j_6 m_6}_{j_2 m_2, j_4 m_4} C^{j_6 m_6}_{j_1 m_1, j_5 m_5} = (-1)^{j_2+j_3+j_5+j_6} \frac{\hat{j}_1 \hat{j}_6^2}{\hat{j}_4} C^{j_4 m_4}_{j_3 m_3, j_5 m_5} \begin{Bmatrix} j_1 & j_2 & j_3 \\ j_4 & j_5 & j_6 \end{Bmatrix} \tag{B.20}$$

$$\sum_{m_1 m_2 m_6} (-1)^{j_1 - m_1} C^{j_3 m_3}_{j_1 m_1, j_2 m_2} C^{j_4 m_4}_{j_6 m_6, j_2 m_2} C^{j_5 m_5}_{j_6 m_6, j_1 - m_1} = (-1)^{j_2+j_3+j_5+j_6} \hat{j}_3 \hat{j}_5 C^{j_4 m_4}_{j_3 m_3, j_5 m_5} \begin{Bmatrix} j_1 & j_2 & j_3 \\ j_4 & j_5 & j_6 \end{Bmatrix} \tag{B.21}$$

$$\tag{B.22}$$

B.1.2 3-j symbols

- Relationship to Clebsch-Gordan coefficients

$$\begin{pmatrix} j_1 & j_2 & J \\ m_1 & m_2 & M \end{pmatrix} = (-1)^{-j_1+j_2+M} \frac{1}{\hat{J}} C^{J-M}_{j_1 m_2, j_2 m_2} \tag{B.23}$$

- Symmetry properties - even permutation of columns

$$\begin{pmatrix} j_1 & j_2 & J \\ m_1 & m_2 & M \end{pmatrix} = \begin{pmatrix} j_2 & J & j_1 \\ m_2 & M & m_1 \end{pmatrix} = \begin{pmatrix} J & j_1 & j_2 \\ M & m_1 & m_2 \end{pmatrix} \tag{B.24}$$

- Symmetry properties - odd permutation of columns

$$\begin{pmatrix} j_1 & j_2 & J \\ m_1 & m_2 & M \end{pmatrix} = (-1)^{j_1+j_2+J} \begin{pmatrix} j_1 & J & j_2 \\ m_1 & M & m_2 \end{pmatrix} = (-1)^{j_1+j_2+J} \begin{pmatrix} j_2 & j_1 & J \\ m_2 & m_1 & M \end{pmatrix} = (-1)^{j_1+j_2+J} \begin{pmatrix} J & j_2 & j_1 \\ M & m_2 & m_1 \end{pmatrix} \tag{B.25}$$

- Special cases

$$\begin{pmatrix} j & 0 & j \\ 0 & 0 & 0 \end{pmatrix} = \frac{(-1)^j}{\hat{j}} \tag{B.26}$$

B.1.3 6-j symbols

- Classical symmetries

$$\left\{ \begin{array}{ccc} j_1 & j_2 & j_3 \\ j_4 & j_5 & j_6 \end{array} \right\} = \left\{ \begin{array}{ccc} j_2 & j_1 & j_3 \\ j_5 & j_4 & j_6 \end{array} \right\} = \left\{ \begin{array}{ccc} j_3 & j_2 & j_1 \\ j_6 & j_5 & j_4 \end{array} \right\} = \quad \ldots \tag{B.27}$$

(any even or odd permutation of columns)

$$\left\{ \begin{array}{ccc} j_1 & j_2 & j_3 \\ j_4 & j_5 & j_6 \end{array} \right\} = \left\{ \begin{array}{ccc} j_4 & j_5 & j_3 \\ j_1 & j_2 & j_6 \end{array} \right\} = \left\{ \begin{array}{ccc} j_1 & j_5 & j_6 \\ j_4 & j_2 & j_3 \end{array} \right\} = \quad \ldots \tag{B.28}$$

(interchange of upper and lower indices in any two columns)

- Special cases

$$\left\{ \begin{array}{ccc} j_1 & j_2 & j_3 \\ j_4 & 0 & j_6 \end{array} \right\} = (-1)^{j_1+j_2+j_4} \frac{\delta_{j_1 j_6} \delta_{j_3 j_4}}{\hat{j}_1 \hat{j}_3} \tag{B.29}$$

$$\left\{ \begin{array}{ccc} j_1 & j_1 & 0 \\ j_2 & j_2 & j_3 \end{array} \right\}^2 = \frac{1}{\hat{j}_1^2 \hat{h}_2^2} \tag{B.30}$$

B.1.4 9-j symbols

- Special cases

$$\left\{ \begin{array}{ccc} j_1 & j_2 & j_3 \\ j_1 & j_2 & j_3 \\ j_4 & 0 & j_4 \end{array} \right\} = \frac{(-1)^{j_1+j_2+j_4+j_3}}{\hat{j}_2 \hat{j}_4} \left\{ \begin{array}{ccc} j_1 & j_1 & j_4 \\ j_3 & j_3 & j_2 \end{array} \right\} \tag{B.31}$$

B.2 Rotation operators and Wigner-D matrices

B.2.1 Euler angles

The rotation of a coordinate system xyz into a new frame XYZ can be described using the three Euler angles α, β, γ in the following steps:

1. The space-fixed frame xyz is rotated about the z axis by an angle α to give the first intermediate rotated frame $x'y'z'$ ($z' = z$).

2. The frame $x'y'z'$ is rotated about the resultant y' axis by an angle β to give the second intermediate rotated frame $x''y''z''$ ($x'' = x'$).

3. The frame $x''y''z''$ is rotated about the resultant z'' axis by an angle γ to give the final rotated frame $x'''y'''z'''$ ($z''' = z''$) we may also refer to the final frame as XYZ.

B.2.2 Rotation operators

Suppose a vector $\boldsymbol{r}$ is represented in the xyz coordinate frame, i.e. $r = (r_x, r_y, r_z)$. To find the representation (r_X, r_Y, r_Z) of $\boldsymbol{r}$ in the frame XYZ which is related to xyz by a rotation δ about some vector $\hat{\boldsymbol{u}}$, we define a rotation operator $\hat{\mathsf{R}}_{\hat{\boldsymbol{u}}}(\delta)$. It can be shown that the form of this operator is

$$\hat{\mathsf{R}}_{\hat{\boldsymbol{u}}}(\delta) = e^{i\delta \hat{J}_{\hat{\boldsymbol{u}}}}, \tag{B.32}$$

where $\hat{J}_{\hat{\boldsymbol{u}}}$ is the projection of the total angular-momentum operator on the rotation axis $\hat{\boldsymbol{u}}$. Note here that the exponential of an operator A is defined by

$$e^A \equiv \sum_{n=0}^{\infty} \frac{A^n}{n!}. \tag{B.33}$$

If the frame rotation is described by the Euler angles, the rotation operator is[1]

$$\hat{\mathsf{R}}(\alpha, \beta, \gamma) = e^{i\alpha \hat{J}_z} e^{i\beta \hat{J}_y} e^{i\gamma \hat{J}_z}. \tag{B.34}$$

[1] This is specific to the *passive* convention where it is the coordinate axes being rotated.

The effect of $\hat{\mathsf{R}}$ on a position ket $|\boldsymbol{r}\rangle$ is to transform it into its representation $|\boldsymbol{r}'\rangle$ in the rotated frame:

$$|\boldsymbol{r}'\rangle = \hat{\mathsf{R}}(\alpha,\beta,\gamma)|\boldsymbol{r}\rangle, \tag{B.35}$$

and it follows that

$$\langle\boldsymbol{r}'| = \langle\boldsymbol{r}|\hat{\mathsf{R}}^{\dagger}(\alpha,\beta,\gamma). \tag{B.36}$$

It is important to keep in mind that the Euler angles are defined here as those which rotate the unprimed frame into the primed framed.

B.2.3 Rotations in an angular-momentum basis

The operations required to represent a general state $|\psi\rangle$ in a rotated reference frame can be simplified by expanding it in a basis $\{|j,m\rangle\}$ of angular-momentum eigenkets, which satisfy

$$\hat{J}^2|j,m\rangle = j(j+1)|j,m\rangle \tag{B.37}$$

$$\hat{J}_z|j,m\rangle = m|j,m\rangle, \tag{B.38}$$

with $j = 0, \frac{1}{2}, 1, \frac{3}{2}, \ldots$ and $m = -j, -j+1, \ldots, j-1, j$ as usual. The expansion of $|\psi\rangle$ is then given by

$$|\psi\rangle = \sum_j \sum_m |j,m\rangle\langle j,m|\psi\rangle, \tag{B.39}$$

and its representation in the rotated reference frame is

$$\langle\boldsymbol{r}'|\psi\rangle = \langle\boldsymbol{r}|\hat{\mathsf{R}}^{\dagger}(\alpha,\beta,\gamma)|\psi\rangle \tag{B.40}$$

$$= \sum_j \sum_m \langle\boldsymbol{r}|\hat{\mathsf{R}}(\alpha,\beta,\gamma)|j,m\rangle\langle j,m|\psi\rangle. \tag{B.41}$$

We can use the closure of the eigensubspace defined by j to write

$$\begin{aligned}\langle\boldsymbol{r}|\hat{\mathsf{R}}^{\dagger}(\alpha,\beta,\gamma)|j,m\rangle &= \sum_{\mu=-j}^{+j} \langle\boldsymbol{r}|j,\mu\rangle\langle j,\mu|\hat{\mathsf{R}}^{\dagger}(\alpha,\beta,\gamma)|j,m\rangle \\ &= \sum_{\mu=-j}^{+j} \langle\boldsymbol{r}|j,\mu\rangle D^{j}_{\mu,m}(\alpha,\beta,\gamma),\end{aligned} \tag{B.42}$$

where we have defined the Wigner D-matrix

$$D^{j}_{\mu,m}(\alpha,\beta,\gamma) \equiv \langle j,\mu|\hat{\mathsf{R}}^{\dagger}(\alpha,\beta,\gamma)|j,m\rangle, \tag{B.43}$$

and hence

$$\langle \boldsymbol{r}'|\psi\rangle = \sum_{j}\sum_{m=-j}^{+j}\sum_{\mu=-j}^{+j}\langle \boldsymbol{r}|j,\mu\rangle D^{j}_{\mu,m}(\alpha,\beta,\gamma)\langle j,m|\psi\rangle. \tag{B.44}$$

B.2.4 Rotation of the spherical harmonics

Rotation of the spherical harmonics is a simpler case of the above, with $|\psi\rangle = |\ell m\rangle$:

$$\begin{aligned}\langle \boldsymbol{r}'|\ell,m\rangle &= \sum_{\mu=-\ell}^{+\ell}\langle \boldsymbol{r}|\ell,\mu\rangle D^{\ell}_{\mu,m}(\alpha,\beta,\gamma)\\ Y^{m}_{\ell}(\theta',\phi') &= \sum_{\mu=-\ell}^{+\ell} Y^{\mu}_{\ell}(\theta,\phi) D^{\ell}_{\mu,m}(\alpha,\beta,\gamma).\end{aligned} \tag{B.45}$$

B.2.5 Lab- to body-frame transformations

In Sec. 11.6, it was necessary to express the lab-frame projectile partial-wave states $|qLm_L\rangle$ in terms of body-frame states $|qL\Lambda_L\rangle$, where m_L and Λ_L are the projections of $\boldsymbol{L}$ on the lab-frame z axis and internuclear axis, respectively. Since the angular component of the partial-wave states is a spherical harmonic, the rotation of a body-frame state $|qL\Lambda_L\rangle$ into the lab frame is given simply by

$$\langle \boldsymbol{r}_0|qLm_L\rangle = \sum_{\Lambda_L} D^{L}_{\Lambda_L m_L}(\alpha,\beta,\gamma)\langle \boldsymbol{r}_0^{(\mathrm{b})}|qL\Lambda_L\rangle, \tag{B.46}$$

where $\boldsymbol{r}_0$ and $\boldsymbol{r}_0^{(\mathrm{b})}$ are the lab- and body-frame projectile coordinates, respectively, and (α,β,γ) are the Euler angles associated with the rotation from the body frame to the lab frame.

The rotational wave functions defined in Chapter 3 and utilised in Sec. 11.6 are expressed as

$$\langle \hat{\boldsymbol{R}}|Nm_N\Lambda\rangle = \sqrt{\frac{2N+1}{8\pi^2}} D^{N*}_{m_N,\Lambda}(\hat{\boldsymbol{R}}), \tag{B.47}$$

where $D^{N*}_{m_N,\Lambda}(\hat{\boldsymbol{R}})$ is shorthand for $D^{N*}_{m_N,\Lambda}(\alpha_{\hat{\boldsymbol{R}}},\beta_{\hat{\boldsymbol{R}}},\gamma_{\hat{\boldsymbol{R}}})$, with $(\alpha_{\hat{\boldsymbol{R}}},\beta_{\hat{\boldsymbol{R}}},\gamma_{\hat{\boldsymbol{R}}})$ being the Euler angles associated with the rotation from the lab frame to the body frame

(whose z axis is represented in the lab frame by $\hat{\boldsymbol{R}}$). For the convenience of having the same arguments to all Wigner-D functions, Eq. (B.46) can be expressed in terms of the lab-body rotation rather than the body-lab rotation:

$$\langle \boldsymbol{r}_0 | qLm_L \rangle = \sum_{\Lambda_L} D^{L*}_{m_L\Lambda_L}(\hat{\boldsymbol{R}}) \langle \boldsymbol{r}_0^{(\mathrm{b})} | qL\Lambda_L \rangle, \tag{B.48}$$

where we have used the fact that conjugating the Wigner-D function and swapping the angular-momentum projections is equivalent to reversing the direction of the rotation.

B.2.6 Identities involving the Wigner-D functions

$$\sum_{m'm} D^{j_1}_{m_1m'}(\hat{\boldsymbol{R}}) C^{JM}_{j_1m',j_2m} D^{j_2}_{m_2m}(\hat{\boldsymbol{R}}) = C^{J(m_1+m_2)}_{j_1m_1,j_2m_2} D^{J}_{(m_1+m_2)M}(\hat{\boldsymbol{R}}) \tag{B.49}$$

$$\begin{aligned} &\iiint_{\mathbb{R}^3} D^{j_1*}_{m_1m'_1}(\hat{\boldsymbol{R}}) D^{j_2*}_{m_2m'_2}(\hat{\boldsymbol{R}}) D^{j_1}_{m_3m'_3}(\hat{\boldsymbol{R}}) D^{j_2}_{m_4m'_4}(\hat{\boldsymbol{R}}) \,\mathrm{d}\hat{\boldsymbol{R}} \\ &\qquad = 8\pi^2 \sum_j \frac{1}{\hat{j}^2} C^{j(m_1+m'_1)}_{j_1m_1,j_2m'_1} C^{j(m_2+m'_2)}_{j_1m_2,j_2m'_2} C^{j(m_3+m'_3)}_{j_1m_3,j_2m'_3} C^{j(m'_4+m'_4)}_{j_1m_4,j_2m'_4} \end{aligned} \tag{B.50}$$

- Unitarity:

$$\sum_{m=-j}^{J} D^{j*}_{mm'}(\hat{\boldsymbol{R}}) D^{j}_{mm''}(\hat{\boldsymbol{R}}) = \sum_{m=-j}^{J} D^{j*}_{m'm}(\hat{\boldsymbol{R}}) D^{j}_{m''m}(\hat{\boldsymbol{R}}) = \delta_{m',m''}. \tag{B.51}$$

Appendix C

Laguerre basis and matrix elements

The one-dimensional basis utilised in the vibrational structure calculations is

$$\varphi_n(R) = A_{nN}(2\alpha r)^{N+1} e^{-\alpha R} L_n^{2N+1}(2\alpha R), \qquad n = 0, \ldots \tag{C.1}$$

where α the exponential fall-off parameter, N is the Hund's case (b) rotational quantum number, and A_{nN} is a normalisation constant to be determined. Note that when non-rotationally-resolved calculations are performed, N is set to zero.

C.1 Overlap matrix elements

The overlap matrix elements are

$$\begin{aligned} B_{nm} &= \int_0^\infty \varphi_n(R)\varphi_m(R)\,\mathrm{d}R \\ &= A_{kN}A_{mN} \int_0^\infty (2\alpha R)^{2N+2} e^{-2\alpha R} L_n^{2N+1}(2\alpha R) L_m^{2N+1}(2\alpha R)\,\mathrm{d}R. \end{aligned} \tag{C.2}$$

To simplify things, let $x \equiv 2\alpha R$, so that

$$\begin{aligned} \varphi_n(x) &= A_{nN} x^{N+1} e^{-x/2} L_n^{2N+1}(x) \\ B_{nm} &= \frac{1}{2\alpha} A_{nN}A_{mN} \int_0^\infty x^{2N+2} e^{-x} L_n^{2N+1}(x) L_m^{2N+1}(x)\,\mathrm{d}x. \end{aligned} \tag{C.3}$$

Now applying Eq. (A.12), we have

$$
\begin{aligned}
B_{nm} &= \frac{1}{2\alpha} A_{nN} A_{mN} \int_0^\infty x^{2N+2} e^{-x} \left[L_n^{2N+2}(x) - L_{n-1}^{2N+2}(x)\right] \left[L_m^{2N+2}(x) - L_{m-1}^{2N+2}(x)\right] \mathrm{d}x \\
&= \frac{1}{2\alpha} A_{nN} A_{mN} \int_0^\infty x^{2N+2} e^{-x} L_n^{2N+2}(x) L_m^{2N+2}(x) \, \mathrm{d}x \\
&\qquad - \frac{1}{2\alpha} A_{nN} A_{mN} \int_0^\infty x^{2N+2} e^{-x} L_n^{2N+2}(x) L_{m-1}^{2N+2}(x) \, \mathrm{d}x \\
&\qquad - \frac{1}{2\alpha} A_{nN} A_{mN} \int_0^\infty x^{2N+2} e^{-x} L_{n-1}^{2N+2}(x) L_m^{2N+2}(x) \, \mathrm{d}x \\
&\qquad + \frac{1}{2\alpha} A_{nN} A_{mN} \int_0^\infty x^{2N+2} e^{-x} L_{n-1}^{2N+2}(x) L_{m-1}^{2N+2}(x) \, \mathrm{d}x, \qquad \text{(C.4)}
\end{aligned}
$$

and applying the Laguerre orthogonality property (A.8):

$$
\begin{aligned}
B_{nm} &= \frac{1}{2\alpha} A_{nN}^2 \frac{(n+2N+2)!}{n!} \delta_{nm} - \frac{1}{2\alpha} A_{nN} A_{(n+1)N} \frac{(n+2N+2)!}{n!} \delta_{n,m-1} \\
&\quad - \frac{1}{2\alpha} A_{nN} A_{(n-1)N} \frac{(n+2N+1)!}{(n-1)!} \delta_{n-1,m} + \frac{1}{2\alpha} A_{nN}^2 \frac{(n+2N+1)!}{(n-1)!} \delta_{nm} \\
&= \frac{1}{2\alpha} A_{nN}^2 \frac{2(n+N+1)(n+2N+1)!}{n!} \delta_{nm} - \frac{1}{2\alpha} A_{nN} A_{(n+1)N} \frac{(n+2N+2)!}{n!} \delta_{n,m-1} \\
&\quad - \frac{1}{2\alpha} A_{nN} A_{(n-1)N} \frac{(n+2N+1)!}{(n-1)!} \delta_{n-1,m}. \qquad \text{(C.5)}
\end{aligned}
$$

We now choose the normalisation constant A_{nN} in such a way as to yield unity along the main diagonal of the overlap matrix:

$$
A_{nN} \equiv \sqrt{\frac{\alpha n!}{(n+N+1)(n+2N+1)!}}, \qquad \text{(C.6)}
$$

giving

$$
\begin{aligned}
B_{nm} &= \delta_{nm} - \frac{1}{2} \sqrt{1 - \frac{N(N+1)}{(n+N+1)(n+N+2)}} \delta_{n,m-1} \\
&\quad - \frac{1}{2} \sqrt{1 - \frac{N(N+1)}{(n+N)(n+N+1)}} \delta_{n-1,m}. \qquad \text{(C.7)}
\end{aligned}
$$

Since the overlap matrix is symmetric, the third term here is superfluous. The matrix can be constructed by setting the diagonal elements equal to 1, setting the superdiagonal elements equal to

$$-\frac{1}{2}\sqrt{1-\frac{N(N+1)}{(n+N+1)(n+N+2)}}, \tag{C.8}$$

and then reflecting the superdiagonal about the diagonal onto the subdiagonal.

C.2 Kinetic-energy matrix elements

The kinetic-energy operator for the vibrational motion is

$$\hat{\mathsf{K}} = -\frac{1}{2\mu}\frac{\mathrm{d}^2}{\mathrm{d}R^2} + \frac{N(N+1)-\Lambda^2}{2\mu R^2}, \tag{C.9}$$

where Λ is the orbital-angular-momentum projection of the electronic state. When non-rotationally-resolved calculations are performed, the centrifugal term is neglected altogether by setting $N = \Lambda = 0$. In terms of the variable x defined above:

$$\hat{\mathsf{K}} = -\frac{2\alpha^2}{\mu}\left[\frac{\mathrm{d}^2}{\mathrm{d}x^2} - \frac{N(N+1)}{x^2} + \frac{\Lambda^2}{x^2}\right]. \tag{C.10}$$

By expanding out the second derivative of φ_n with respect to x, and applying the defining equation of the Laguerre polynomials (A.6), it is straightforward to show that

$$\frac{\mathrm{d}^2\varphi_n}{\mathrm{d}x^2} = \frac{N(N+1)}{x^2}\varphi_n + \frac{1}{4}\varphi_n - \frac{n+N+1}{x}\varphi_n \tag{C.11}$$

The effect of the kinetic-energy operator on φ_n is then

$$\begin{aligned}\hat{\mathsf{K}}\varphi_n = &-\frac{2\alpha^2}{\mu}\left[\frac{\mathrm{d}^2}{\mathrm{d}x^2} - \frac{N(N+1)}{x^2} + \frac{\Lambda^2}{x^2}\right]\varphi_n \\ &-\frac{2\alpha^2}{\mu}\left[\frac{1}{4} - \frac{n+N+1+\Lambda^2}{x}\right]\varphi_n,\end{aligned} \tag{C.12}$$

and the matrix elements of $\hat{\mathsf{K}}$ are

$$
\begin{aligned}
K_{nm} &= \int_0^\infty \phi_n(R)\hat{\mathsf{K}}\phi_m(R)\,\mathrm{d}R \\
&= -\frac{2\alpha^2}{\mu}\int_0^\infty \phi_n(R)\left[\frac{1}{4} - \frac{m+N+1+\Lambda^2}{x}\right]\phi_n\,\mathrm{d}R \\
&= -\frac{\alpha^2}{2\mu}\int_0^\infty \phi_n(R)\phi_m(R)\,\mathrm{d}R + \frac{2\alpha^2}{\mu}(m+N+1+\Lambda^2)\int_0^\infty \phi_n(x)\frac{1}{x}\phi_m(x)\frac{\mathrm{d}x}{2\alpha} \\
&= -\frac{\alpha^2}{2\mu}B_{nm} + \frac{\alpha}{\mu}A_{nN}A_{mN}(m+N+1+\Lambda^2)\int_0^\infty x^{2N+1}e^{-x}L_n^{2N+1}(x)L_m^{2N+1}(x)\,\mathrm{d}x \\
&= -\frac{\alpha^2}{2\mu}B_{nm} + \frac{\alpha}{\mu}A_{nN}^2(n+N+1+\Lambda^2)\frac{(n+2N+1)!}{n!}\delta_{nm} \\
&= -\frac{\alpha^2}{2\mu}B_{nm} + \frac{\alpha}{\mu}\frac{(n+N+1+\Lambda^2)}{(n+N+1)}\delta_{nm}. \qquad \text{(C.13)}
\end{aligned}
$$

Appendix D

Miscellaneous derivations

D.1 More detailed derivations of commutators in Sec. 3.4.1

- Orbital angular-momentum (squared) operator $\hat{\mathsf{L}}^2$

  The $\hat{\mathsf{L}}^2$ operator can be written as

$$\hat{\mathsf{L}}^2 = \sum_{i=1}^{N_e} \left[\frac{1}{\sin^2\theta_i} \frac{\partial^2}{\partial \phi_i^2} + \frac{1}{\sin\theta_i} \frac{\partial}{\partial \theta_i} \sin\theta_i \frac{\partial}{\partial \theta_i} \right]. \tag{D.1}$$

  To evaluate the commutator $[\hat{\mathsf{L}}^2, \hat{\mathsf{V}}]$, we require

$$\begin{aligned} \frac{\partial}{\partial \theta_i} \left[\sin\theta_i \frac{\partial}{\partial \theta_i} \right] \hat{\mathsf{V}} &= \sin\theta_i \left[V \frac{\partial^2}{\partial \theta_i^2} + 2 \frac{\partial V}{\partial \theta_i} \frac{\partial}{\partial \theta_i} + \frac{\partial^2 V}{\partial \theta_i^2} \right] + \cos\theta_i \left[V \frac{\partial}{\partial \theta_i} + \frac{\partial V}{\partial \theta_i} \right] \\ &= \hat{\mathsf{V}} \frac{\partial}{\partial \theta_i} \left[\sin\theta_i \frac{\partial}{\partial \theta_i} \right] + \sin\theta_i \left[2 \frac{\partial V}{\partial \theta_i} \frac{\partial}{\partial \theta_i} + \frac{\partial^2 V}{\partial \theta_i^2} \right] + \cos\theta_i \frac{\partial V}{\partial \theta_i} \end{aligned} \tag{D.2}$$

$$\begin{aligned} \frac{1}{\sin^2\theta_i} \frac{\partial^2}{\partial \phi^2}_i \hat{\mathsf{V}} &= \frac{1}{\sin^2\theta_i} \left[V \frac{\partial^2}{\partial \phi_i^2} + 2 \frac{\partial V}{\partial \phi_i} \frac{\partial}{\partial \phi_i} + \frac{\partial^2 V}{\partial \phi_i^2} \right] \\ &= \hat{\mathsf{V}} \frac{1}{\sin^2\theta_i} \frac{\partial^2}{\partial \phi_i^2} + \frac{1}{\sin^2\theta_i} \left[2 \frac{\partial V}{\partial \phi_i} \frac{\partial}{\partial \phi_i} + \frac{\partial^2 V}{\partial \phi_i^2} \right], \end{aligned} \tag{D.3}$$

  and hence the commutator is

$$\begin{aligned} [\hat{\mathsf{L}}^2, \hat{\mathsf{V}}] = \sum_{i=1}^{N_e} \Big[& \sin\theta_i \left(2 \frac{\partial V}{\partial \theta_i} \frac{\partial}{\partial \theta_i} + \frac{\partial^2 V}{\partial \theta_i^2} \right) + \cos\theta_i \frac{\partial V}{\partial \theta_i} \\ & + \frac{1}{\sin^2\theta_i} \left(2 \frac{\partial V}{\partial \phi_i} \frac{\partial}{\partial \phi_i} + \frac{\partial^2 V}{\partial \phi_i^2} \right) \Big]. \end{aligned} \tag{D.4}$$

  As a result, the orbital angular momentum is not a good quantum number for diatomic molecules since the θ dependence of the nuclear potential leads

to

$$\frac{\partial V}{\partial \theta_i} \neq 0. \tag{D.5}$$

- Orbital angular-momentum projection operator $\hat{\Lambda}$

  The orbital angular-momentum projection operator can be written as

$$\hat{\Lambda} = -i \sum_{i=1}^{N_e} \frac{\partial}{\partial \phi_i}. \tag{D.6}$$

  To evaluate the commutator $[\hat{\Lambda}, \hat{\mathsf{V}}]$ we require

$$\frac{\partial}{\partial \phi_i} \hat{\mathsf{V}} = V \frac{\partial}{\partial \phi} + \frac{\partial V}{\partial \phi_i}, \tag{D.7}$$

  and hence the commutator is

$$[\hat{\Lambda}, \hat{\mathsf{V}}] = -i \sum_{i=1}^{N_e} \frac{\partial V}{\partial \phi_i}. \tag{D.8}$$

  As a result, the orbital angular-momentum projection *is* a good quantum number for diatomic molecules (when $\hat{\boldsymbol{z}}$ and $\hat{\boldsymbol{R}}$ are aligned). To verify this, note that the diatomic electron-nuclear and electron-electron potentials satisfy

$$\frac{\partial V_i}{\partial \phi_i} = 0 \tag{D.9}$$

$$\frac{\partial V_{ij}}{\partial \phi_i} = -\frac{\partial V_{ij}}{\partial \phi_j} \tag{D.10}$$

  and hence

$$[\hat{\Lambda}, \hat{\mathsf{V}}] = -i \sum_k \frac{\partial}{\partial \phi_k} \left[-\sum_{i=1}^{N_e} V_i + \sum_{i=1}^{N_e} \sum_{j>1}^{N_e} V_{ij} \right] \tag{D.11}$$

$$= i \sum_{i=1}^{N_e} \frac{\partial V_i}{\partial \phi_i} - i \sum_{i=1}^{N_e} \sum_{j>1}^{N_e} \left[\frac{\partial V_{ij}}{\partial \phi_i} + \frac{\partial V_{ij}}{\partial \phi_j} \right] \tag{D.12}$$

$$= 0. \tag{D.13}$$

- Body-frame space inversion operator $\hat{\mathsf{t}}$

  The effect of the body-frame space inversion operator on the electron-

electron and electron-nuclear potentials is

$$\hat{\mathsf{t}}V_{ij} = \frac{1}{|-\boldsymbol{r}_i + \boldsymbol{r}_j|} = V_{ij} \tag{D.14}$$

$$\hat{\mathsf{t}}V_i = \frac{Z_2}{\left|\frac{\boldsymbol{R}}{2} - \boldsymbol{r}_i\right|} + \frac{Z_1}{\left|\frac{\boldsymbol{R}}{2} + \boldsymbol{r}_i\right|}, \tag{D.15}$$

and hence the commutator is

$$[\hat{\mathsf{t}}, \hat{\mathsf{V}}] = \sum_{i=1}^{N_\mathrm{e}} \left[\frac{Z_2 - Z_1}{\left|\frac{\boldsymbol{R}}{2} - \boldsymbol{r}_i\right|} + \frac{Z_1 - Z_2}{\left|\frac{\boldsymbol{R}}{2} + \boldsymbol{r}_i\right|} \right] \hat{\mathsf{t}}. \tag{D.16}$$

As a result, the electronic parity is a good quantum number for homonuclear diatomics ($Z_1 = Z_2$).

D.2 Derivation of Eq. (3.50)

The space-fixed inversion operator E^* operates in coordinate space, not spin space, and hence has no effect on the $|sm_s\rangle$ and $|Im_I\rangle$ spin states. In a Hund's case (a) scheme where the electronic spin is coupled to the internuclear axis, E^* would have an effect on the $|s\Sigma_s\rangle$ spin state due to its dependence on the molecular Euler angles when represented in the lab frame, however since we are working in Hund's case (b) we can ignore the two spin states for now. Hence we are looking to form parity-adapted states with well defined parity $\pi = \pm 1$:

$$|nvNm_N\pi\rangle = \text{linear combination of } |n\,\pm\Lambda\rangle|vN\rangle|Nm_N\,\pm\Lambda\rangle \text{ states.} \tag{D.17}$$

Note that on the left-hand side we no longer specify Λ since, as we will show now, the total molecular states take into account both signs of Λ. The index n still specifies $|\Lambda|$. Brown and Carrington [145] give us the effect of $\hat{\mathsf{E}}^*$ on the electronic, vibrational, and rotational basis states:

$$\hat{\mathsf{E}}^*|\Phi_n^{\pm\Lambda}\rangle = (-1)^{\Lambda+\sigma}|\Phi_n^{\mp\Lambda}\rangle \tag{D.18}$$

$$\hat{\mathsf{E}}^*|\nu_{nvN}\rangle = |\nu_{nvN}\rangle \tag{D.19}$$

$$\hat{\mathsf{E}}^*|Nm_N\,\pm\Lambda\rangle = (-1)^{N\mp\Lambda}|Nm_N\,\mp\Lambda\rangle, \tag{D.20}$$

for an overall effect of

$$\hat{\mathsf{E}}^*|\Phi_n^{\pm\Lambda}\rangle|\nu_{nvN}\rangle|Nm_N\ \pm\Lambda\rangle = (-1)^{N+\sigma}|\Phi_n^{\mp\Lambda}\rangle|\nu_{nvN}\rangle|Nm_N\ \mp\Lambda\rangle. \tag{D.21}$$

Here, σ is defined to be odd for Σ^- states, and even otherwise. Hence the states of well-defined parity π are

$$|\Phi_n\,\nu_{nvN}\,Nm_N:\pi\rangle = \frac{1}{\sqrt{2(1+\delta_{\Lambda,0})}}\Big[|\Phi_n^{+\Lambda}\rangle|\nu_{nvN}\rangle|Nm_N\ +\Lambda\rangle + \pi(-1)^{N+\sigma}|\Phi_n^{-\Lambda}\rangle|\nu_{nvN}\rangle|Nm_N\ -\Lambda\rangle\Big], \tag{D.22}$$

where the $\delta_{\Lambda,0}$ in the normalisation constant ensures that the state is still properly normalised in the $\Lambda = 0$ case.

D.3 Derivation of Eq. (11.60)

$$\begin{aligned}
&\sum_{j\Sigma_\mathcal{S}}\sum_{\substack{\Sigma'_s\Sigma_s\\ \Sigma'_\mathrm{p}\Sigma_\mathrm{p}}}\frac{1}{\hat{j}^2}C^{j0}_{\mathcal{J}0,\mathcal{S}0}C^{j0}_{\mathcal{J}0,\mathcal{S}0}C^{j(\Lambda_\mathrm{e}+\Sigma_\mathcal{S})}_{\mathcal{J}\Lambda_\mathrm{e},\mathcal{S}\Sigma_\mathcal{S}}C^{j(\Lambda_\mathrm{e}+\Sigma_\mathcal{S})}_{\mathcal{J}\Lambda_\mathrm{e},\mathcal{S}\Sigma_\mathcal{S}}C^{\mathcal{S}\Sigma_\mathcal{S}}_{\frac{1}{2}\Sigma_\mathrm{p},s'\Sigma'_s}C^{\mathcal{S}\Sigma_\mathcal{S}}_{\frac{1}{2}\Sigma_\mathrm{p},s\Sigma_s}\\
&\quad=\sum_j\frac{1}{\hat{j}^2}C^{j0}_{\mathcal{J}0,\mathcal{S}0}C^{j0}_{\mathcal{J}0,\mathcal{S}0}\sum_{\Sigma_\mathcal{S}}C^{j(\Lambda_\mathrm{e}+\Sigma_\mathcal{S})}_{\mathcal{J}\Lambda_\mathrm{e},\mathcal{S}\Sigma_\mathcal{S}}C^{j(\Lambda_\mathrm{e}+\Sigma_\mathcal{S})}_{\mathcal{J}\Lambda_\mathrm{e},\mathcal{S}\Sigma_\mathcal{S}}\sum_{\substack{\Sigma'_s\Sigma_s\\ \Sigma'_\mathrm{p}\Sigma_\mathrm{p}}}C^{\mathcal{S}\Sigma_\mathcal{S}}_{\frac{1}{2}\Sigma'_\mathrm{p},s'\Sigma'_s}C^{\mathcal{S}\Sigma_\mathcal{S}}_{\frac{1}{2}\Sigma_\mathrm{p},s\Sigma_s}\to 1\\
&\quad=\sum_j\frac{1}{\hat{j}^2}C^{j0}_{\mathcal{J}0,\mathcal{S}0}C^{j0}_{\mathcal{J}0,\mathcal{S}0}\sum_{\Sigma_\mathcal{S}}C^{j(\Lambda_\mathrm{e}+\Sigma_\mathcal{S})}_{\mathcal{J}\Lambda_\mathrm{e},\mathcal{S}\Sigma_\mathcal{S}}C^{j(\Lambda_\mathrm{e}+\Sigma_\mathcal{S})}_{\mathcal{J}\Lambda_\mathrm{e},\mathcal{S}\Sigma_\mathcal{S}}\to\frac{\hat{j}^2}{\hat{\mathcal{J}}^2}\\
&\quad=\frac{1}{\hat{\mathcal{J}}^2}\sum_j C^{j0}_{\mathcal{J}0,\mathcal{S}0}C^{j0}_{\mathcal{J}0,\mathcal{S}0}\to 1\\
&\quad=\frac{1}{\hat{\mathcal{J}}^2}.
\end{aligned} \tag{D.23}$$

D.4 Derivation of Eq. (11.23)

$$\sum_{m_{N_f} m_{L_f} m'_{L_f}} (-1)^{m_{L'_f}} C^{LM_L}_{L_f m_{L_f}, L'_f - m'_{L_f}} C^{\mathcal{J} m_{N_i}}_{L_f m_{L_f}, N_f m_{N_f}} C^{\mathcal{J}' m_{N_i}}_{L'_f m'_{L_f}, N_f m_{N_f}} \tag{D.24}$$

$$= (-1)^{-L'_f} \sum_{m_{N_f} m_{L_f} m'_{L_f}} (-1)^{L'_f - m_{L'_f}} C^{\mathcal{J}' m_{N_i}}_{L'_f m'_{L_f}, N_f m_{N_f}} C^{\mathcal{J} m_{N_i}}_{L_f m_{L_f}, N_f m_{N_f}} C^{LM_L}_{L_f m_{L_f}, L'_f - m'_{L_f}},$$

and now applying Def. (B.21):

$$(-1)^{-L'_f} \sum_{m_{N_f} m_{L_f} m'_{L_f}} (-1)^{L'_f - m_{L'_f}} C^{\mathcal{J}' m_{N_i}}_{L'_f m'_{L_f}, N_f m_{N_f}} C^{\mathcal{J} m_{N_i}}_{L_f m_{L_f}, N_f m_{N_f}} C^{LM_L}_{L_f m_{L_f}, L'_f - m'_{L_f}}$$

$$= (-1)^{-L'_f} (-1)^{N_f + \mathcal{J}' + L_f + L} \hat{\mathcal{J}}' \hat{L} C^{\mathcal{J} m_{N_i}}_{\mathcal{J}' m_{N_i}, LM_L} \begin{Bmatrix} L'_f & N_f & \mathcal{J}' \\ \mathcal{J} & L & L_f \end{Bmatrix}$$

$$= (-1)^{N_f + \mathcal{J}' + L_f - L'_f + L} C^{\mathcal{J} m_{N_i}}_{\mathcal{J}' m_{N_i}, LM_L} \hat{\mathcal{J}}' \hat{L} \begin{Bmatrix} L'_f & N_f & \mathcal{J}' \\ \mathcal{J} & L & L_f \end{Bmatrix}. \tag{D.25}$$

The selection rules for the Clebsch-Gordan coefficient $C^{LM_L}_{L_f 0, L'_f 0}$ in Eq. (11.22) forces $L_f + L'_f + L$ to be even, and hence $(-1)^{L_f - L'_f + L} = 1$, so we can write

$$\sum_{m_{N_f} m_{L_f} m'_{L_f}} (-1)^{m_{L'_f}} C^{LM_L}_{L_f m_{L_f}, L'_f - m'_{L_f}} C^{\mathcal{J} m_{N_i}}_{L_f m_{L_f}, N_f m_{N_f}} C^{\mathcal{J}' m_{N_i}}_{L'_f m'_{L_f}, N_f m_{N_f}} \tag{D.26}$$

$$= (-1)^{N_f + \mathcal{J}'} \hat{\mathcal{J}}' \hat{L} C^{\mathcal{J} m_{N_i}}_{\mathcal{J}' m_{N_i}, LM_L} \begin{Bmatrix} L'_f & N_f & \mathcal{J}' \\ \mathcal{J} & L & L_f \end{Bmatrix}.$$

D.5 Derivation of Eq. (11.25)

$$\sum_{m_{N_i}}(-1)^{\mathcal{J}'}\underbrace{C^{\mathcal{J}'m_{N_i}}_{L_i'0,N_im_{N_i}}C^{\mathcal{J}m_{N_i}}_{L_i0,N_im_{N_i}}}_{\text{(B.12)}}\underbrace{C^{\mathcal{J}m_{N_i}}_{\mathcal{J}'m_{N_i},LM_L}}_{\text{(B.12)}}$$

$$=\sum_{m_{N_i}}(-1)^{\mathcal{J}'}\overbrace{(-1)^{L_i'+N_i'-\mathcal{J}'}C^{\mathcal{J}'m_{N_i}}_{N_im_{N_i},L_i'0}}\overbrace{(-1)^{L_i+N_i-\mathcal{J}}C^{\mathcal{J}m_{N_i}}_{N_im_{N_i},L_i0}}C^{\mathcal{J}m_{N_i}}_{\mathcal{J}'m_{N_i},LM_L}$$

$$=(-1)^{L_i+L_i'-\mathcal{J}}\sum_{m_{N_i}}C^{\mathcal{J}'m_{N_i}}_{N_im_{N_i},L_i'0}C^{\mathcal{J}m_{N_i}}_{N_im_{N_i},L_i0}C^{\mathcal{J}m_{N_i}}_{\mathcal{J}'m_{N_i},LM_L}$$

$$=(-1)^{L_i+L_i'-\mathcal{J}}\underbrace{\sum_{m_{N_i}\beta\delta}}_{\substack{\text{sum over } \beta \,\&\, \delta \text{ allowed since}\\ \text{selection rules force } \beta=\delta=m_{N_i}}}C^{\mathcal{J}'m_{N_i}}_{N_i\beta,L_i'0}C^{\mathcal{J}\delta}_{N_i\beta,L_i0}C^{\mathcal{J}\delta}_{\mathcal{J}'m_{N_i},L0}\delta_{M_L,0}$$

$m_{N_i}+M_L=m_{N_i}$
$\Rightarrow M_L=0$

$$=(-1)^{L_i+L_i'-\mathcal{J}}\overbrace{(-1)^{N_i+L_i'+L+\mathcal{J}}\frac{\hat{\mathcal{J}}'\hat{\mathcal{J}}^2}{\hat{L}_i}C^{L_i0}_{L_i'0,L0}\begin{Bmatrix}\mathcal{J}' & N_i & L_i'\\ L_i & L & \mathcal{J}\end{Bmatrix}}^{\text{(B.20)}}\delta_{M_L,0}$$

$$=(-1)^{N_i+L_i+L}\frac{\hat{\mathcal{J}}'\hat{\mathcal{J}}^2}{\hat{L}_i}\underbrace{C^{L_i0}_{L_i'0,L0}}_{\text{(B.15)}}\begin{Bmatrix}\mathcal{J}' & N_i & L_i'\\ L_i & L & \mathcal{J}\end{Bmatrix}\delta_{M_L,0}$$

$$=(-1)^{N_i+L_i+L}\frac{\hat{\mathcal{J}}'\hat{\mathcal{J}}^2}{\hat{L}_i}\overbrace{(-1)^{L_i'}\frac{\hat{L}_i}{\hat{L}}C^{L0}_{L_i0,L_i'0}}\begin{Bmatrix}\mathcal{J}' & N_i & L_i'\\ L_i & L & \mathcal{J}\end{Bmatrix}\delta_{M_L,0}$$

$$=(-1)^{N_i+L_i+L_i'+L}\frac{\hat{\mathcal{J}}'\hat{\mathcal{J}}^2}{\hat{L}}C^{L0}_{L_i0,L_i'0}\underbrace{\begin{Bmatrix}\mathcal{J}' & N_i & L_i'\\ L_i & L & \mathcal{J}\end{Bmatrix}}_{\text{(B.27)}}\delta_{M_L,0}$$

$$=\underbrace{(-1)^{N_i+L_i+L_i'+L}}_{L_i+L_i'+L=\text{even}}\frac{\hat{\mathcal{J}}'\hat{\mathcal{J}}^2}{\hat{L}}C^{L0}_{L_i0,L_i'0}\overbrace{\begin{Bmatrix}L_i' & N_i & \mathcal{J}'\\ \mathcal{J} & L & L_i\end{Bmatrix}}\delta_{M_L,0}$$

$$=\overbrace{(-1)^{N_i}}\frac{\hat{\mathcal{J}}'\hat{\mathcal{J}}^2}{\hat{L}}C^{L0}_{L_i0,L_i'0}\begin{Bmatrix}L_i' & N_i & \mathcal{J}'\\ \mathcal{J} & L & L_i\end{Bmatrix}\delta_{M_L,0}\qquad\text{(D.27)}$$

Appendix E

Publication co-authorship statements

To whom it may concern

I, Liam Scarlett, performed the code development and calculations, and prepared the figures and manuscript for the following publication:

L. H. Scarlett, I. Bray, and D. V. Fursa, "Electronic and vibrational close-coupling method for resonant electron-molecule scattering", Phys. Rev. Lett. **127**, 223401 (2021)

I, as a Co-Author, endorse that this level of contribution by the candidate indicated above is appropriate.

Igor Bray 

Dmitry Fursa 

To whom it may concern

I, Liam Scarlett, provided cross-section data, technical assistance, and comments on the manuscript for the following publication:

R. K. Horton, **L. H. Scarlett**, M. C. Zammit, I. Bray, and D. V. Fursa, "Electron energy deposition in molecular hydrogen gas: a Monte-Carlo simulation using convergent close-coupling cross sections", Plasma Sources Sci. Technol. **30**, 115004 (2021)

I, as a Co-Author, endorse that this level of contribution by the candidate indicated above is appropriate.

Reese Horton 

Mark Zammit 

Igor Bray 

Dmitry Fursa 

To whom it may concern

I, Liam Scarlett, contributed to the code development, performed the calculations, and prepared the figures and manuscript for the following publication:

L. H. Scarlett, U. S. Rehill, M. C. Zammit, K. Bartschat, I. Bray, and D. V. Fursa, "Linear polarization fractions of Fulcher-α fluorescence in electron collisions with H_2", Phys. Rev. A **104**, L040801 (2021)

I, as a Co-Author, endorse that this level of contribution by the candidate indicated above is appropriate.

Una Rehill 

Mark Zammit 

Klaus Bartschat 

Igor Bray 

Dmitry Fursa 

To whom it may concern

I, Liam Scarlett, performed the derivations and calculations (not including rate coefficients), and prepared the figures and manuscript for the following publication:

L. H. Scarlett, D. V. Fursa, J. Knol, M. C. Zammit, and I. Bray, "Isotopic and vibrational-level dependence of H_2 dissociation by electron impact", Phys. Rev. A **103**, L020801 (2021)

I, as a Co-Author, endorse that this level of contribution by the candidate indicated above is appropriate.

Dmitry Fursa 

Jack Knol 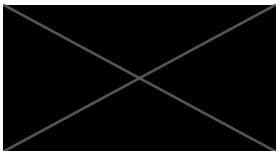

Mark Zammit 

Igor Bray 

To whom it may concern

I, Liam Scarlett, contributed to the code development, performed the calculations, and prepared the figures and manuscript for the following publication:

L. H. Scarlett, J. S. Savage, D. V. Fursa, I. Bray, M. C. Zammit, and B. I. Schneider, "Convergent close-coupling calculations of electrons scattering on electronically-excited molecular hydrogen", Phys. Rev. A **103**, 032802 (2021)

I, as a Co-Author, endorse that this level of contribution by the candidate indicated above is appropriate.

Jeremy Savage 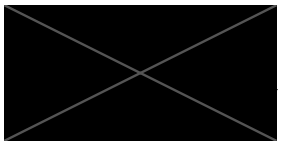

Dmitry Fursa 

Igor Bray 

Mark Zammit 

Barry Schneider 

To whom it may concern

I, Liam Scarlett, contributed to the code development, performed the calculations (not including analytic fits), and prepared the figures and manuscript for the following publication:

L. H. Scarlett, D. V. Fursa, M. C. Zammit, I. Bray, and Yu. Ralchenko, "Complete collision data set for electrons scattering on molecular hydrogen and its isotopologues: II. Fully vibrationally-resolved electronic excitation of the isotopologues of $H_2(X\,^1\Sigma_g^+)$", At. Data Nucl. Data Tables **139**, 101403 (2021)

I, as a Co-Author, endorse that this level of contribution by the candidate indicated above is appropriate.

Dmitry Fursa 

Mark Zammit 

Igor Bray 

Yuri Ralchenko 

To whom it may concern

I, Liam Scarlett, contributed to the code development, performed the calculations (not including analytic fits), and prepared the figures and manuscript for the following publication:

L. H. Scarlett, D. V. Fursa, M. C. Zammit, I. Bray, Yu. Ralchenko, and K. D. Davie, "Complete collision data set for electrons scattering on molecular hydrogen and its isotopologues: I. Fully vibrationally-resolved electronic excitation of $H_2(X\,^1\Sigma_g^+)$", At. Data Nucl. Data Tables **137**, 101361 (2021)

I, as a Co-Author, endorse that this level of contribution by the candidate indicated above is appropriate.

Dmitry Fursa 

Mark Zammit 

Igor Bray 

Yuri Ralchenko 

Kayla Davie 

To whom it may concern

I, Liam Scarlett, supplied the MCCC data and wrote section 3 of the manuscript for the following publication:

D. Wünderlich, **L. H. Scarlett**, S. Briefi, U. Fantz, M. C. Zammit, D. V. Fursa, and I. Bray, "Application of molecular convergent close-coupling cross sections in a collisional radiative model for the triplet system of molecular hydrogen", J. Phys. D. Appl. Phys. **54**, 115201 (2021)

I, as a Co-Author, endorse that this level of contribution by the candidate indicated above is appropriate.

Dirk Wünderlich 

Stefan Briefi 

Ursel Fantz 

Mark Zammit 

Dmitry Fursa 

Igor Bray 

To whom it may concern

I, Liam Scarlett, performed the AN MCCC calculations, and wrote section 2.2 of the manuscript for the following publication:

T. Meltzer, J. Tennyson, Z. Masin, M. C. Zammit, **L. H. Scarlett**, D. V. Fursa, and I. Bray, "Benchmark calculations of electron impact electronic excitation of the hydrogen molecule", J. Phys. B **53**, 145204 (2020)

I, as a Co-Author, endorse that this level of contribution by the candidate indicated above is appropriate.

Thomas Meltzer 

Jonathan Tennyson 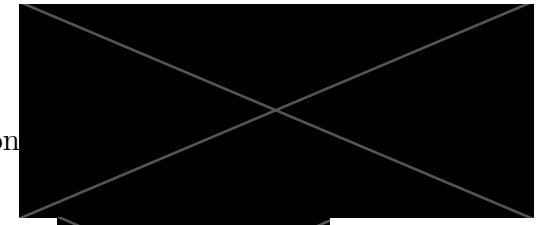

Zdenek Mašín 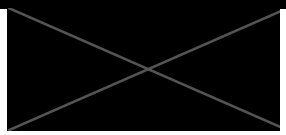

Mark Zammit 

Dmitry Fursa 

Igor Bray 

To whom it may concern

I, Liam Scarlett, contributed to the code development and calculations, and prepared the figures and manuscript for the following publication:

L. H. Scarlett, J. S. Savage, D. V. Fursa, I. Bray, and M. C. Zammit, "Electron-scattering on molecular hydrogen: convergent close-coupling approach", Eur. Phys. J. D **74**, 36 (2020)

I, as a Co-Author, endorse that this level of contribution by the candidate indicated above is appropriate.

Jeremy Savage 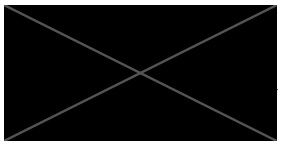

Dmitry Fursa 

Igor Bray 

Mark Zammit 

To whom it may concern

I, Liam Scarlett, provided technical assistance and comments on the manuscript for the following publication:

N. Mori, R. Utamuratov, **L. H. Scarlett**, D. V. Fursa, A. S. Kadyrov, I. Bray, and M. C. Zammit, "Calculations of positron scattering on the hydrogen molecular ion", J. Phys. B **53**, 015203 (2020)

I, as a Co-Author, endorse that this level of contribution by the candidate indicated above is appropriate.

Nicolas Mori 

Ravshanbek Utamuratov 

Dmitry Fursa 

Alisher Kadyrov 

Igor Bray 

Mark Zammit 

To whom it may concern

I, Liam Scarlett, contributed to the code development, performed the calculations, and prepared the figures and manuscript for the following publication:

L. H. Scarlett, J. S. Savage, D. V. Fursa, M. C. Zammit, and I. Bray, "Electron-impact dissociation of vibrationally-excited molecular hydrogen into neutral fragments", Atoms **7**, 75 (2019)

I, as a Co-Author, endorse that this level of contribution by the candidate indicated above is appropriate.

Jeremy Savage 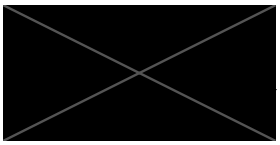

Dmitry Fursa 

Mark Zammit 

Igor Bray 

To whom it may concern

I, Liam Scarlett, contributed to the code development, performed the calculations, and prepared the figures and manuscript in collaboration with Jonathan Tapley for the following publication:

L. H. Scarlett, J. K. Tapley, J. S. Savage, D. V. Fursa, M. C. Zammit, and I. Bray, "Vibrational excitation of the H_2 $X\,^1\Sigma_g^+$ state via electron-impact excitation and radiative cascade", Plasma Sources Sci. Technol. **28**, 025004 (2019)

I, as a Co-Author, endorse that this level of contribution by the candidate indicated above is appropriate.

Jonathan Tapley 

Jeremy Savage 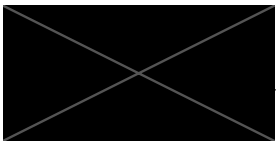

Dmitry Fursa 

Mark Zammit 

Igor Bray 

To whom it may concern

I, Liam Scarlett, performed the AN MCCC calculations, and wrote section 3 of the manuscript for the following publication:

M. Zawadzki, R. Wright, G. Dolmat, M. F. Martin, B. Diaz, L. Hargreaves, D. Coleman, D. V. Fursa, M. C. Zammit, **L. H. Scarlett**, J. K. Tapley, J. S. Savage, I. Bray, and M. A. Khakoo, "Low-energy scattering from molecular hydrogen: excitation of the $X\,^1\Sigma_g^+ \rightarrow b\,^3\Sigma_u^+$ transition", Phys. Rev. A **98**, 062704 (2018)

I, as a Co-Author, endorse that this level of contribution by the candidate indicated above is appropriate.

Mateusz Zawadzki 

Robert Wright p.p 

Grant Dolmat p.p 

Merl Martin p.p 

Bianca Diaz p.p 

Leigh Hargreaves 

Daniel Coleman p.p 

Dmitry Fursa 

Mark Zammit 

Jonathan Tapley 

Jeremy Savage 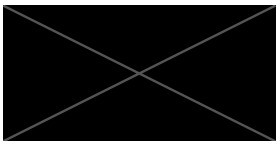

Igor Bray 

Murtadha Khakoo 

To whom it may concern

I, Liam Scarlett, contributed to the code development, performed the calculations, and prepared the figures and manuscript in collaboration with Jonathan Tapley for the following publication:

J. K. Tapley, **L. H. Scarlett**, J. S. Savage, D. V. Fursa, M. C. Zammit, and I. Bray, "Electron-impact dissociative excitation of singlet states of molecular hydrogen", Phys. Rev. A **98**, 032701 (2018)

I, as a Co-Author, endorse that this level of contribution by the candidate indicated above is appropriate.

Jonathan Tapley 

Jeremy Savage 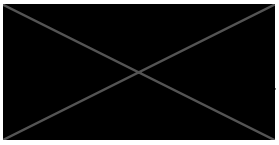

Mark Zammit 

Dmitry Fursa 

Igor Bray 

To whom it may concern

I, Liam Scarlett, contributed to the code development, performed the calculations, and prepared the figures and manuscript in collaboration with Jonathan Tapley for the following publication:

J. K. Tapley, **L. H. Scarlett**, J. S. Savage, M. C. Zammit, D. V. Fursa, and I. Bray, "Vibrationally resolved electron-impact excitation cross sections for singlet states of molecular hydrogen", J. Phys. B **51**, 144007 (2018)

I, as a Co-Author, endorse that this level of contribution by the candidate indicated above is appropriate.

Jonathan Tapley 

Jeremy Savage 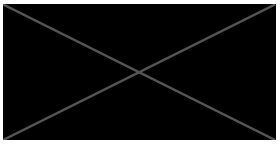

Mark Zammit 

Dmitry Fursa 

Igor Bray 

To whom it may concern

I, Liam Scarlett, performed the AN MCCC calculations, and wrote the text pertaining to the MCCC method in the manuscript for the following publication:

M. Zawadzki, R. Wright, G. Dolmat, M. F. Martin, L. Hargreaves, D. V. Fursa, M. C. Zammit, **L. H. Scarlett**, J. K. Tapley, J. S. Savage, I. Bray, and M. A. Khakoo, "Time-of-flight electron scattering from molecular hydrogen: Benchmark cross sections for excitation of the $X\,^1\Sigma_g^+ \rightarrow b\,^3\Sigma_u^+$ transition", Phys. Rev. A **97**, 050702(R) (2018)

I, as a Co-Author, endorse that this level of contribution by the candidate indicated above is appropriate.

Mateusz Zawadzki 

Robert Wright p.p 

Grant Dolmat p.p 

Merl Martin p.p 

Leigh Hargreaves 

Dmitry Fursa 

Mark Zammit 

Jonathan Tapley 

Jeremy Savage 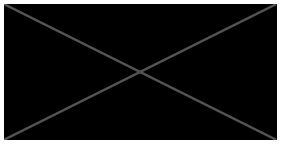

Igor Bray 

Murtadha Khakoo 

Bibliography

[1] **L. H. Scarlett**, I. Bray, and D. V. Fursa, "Electronic and vibrational close-coupling method for resonant electron-molecule scattering", Phys. Rev. Lett. **127**, 223401 (2021) (cit. on pp. 11, 216, 229, 314).

[2] R. K. Horton, **L. H. Scarlett**, M. C. Zammit, I. Bray, and D. V. Fursa, "Electron energy deposition in molecular hydrogen gas: a Monte-Carlo simulation using convergent close-coupling cross sections", Plasma Sources Sci. Technol. **30**, 115004 (2021) (cit. on pp. 11, 315).

[3] **L. H. Scarlett**, U. S. Rehill, M. C. Zammit, K. Bartschat, I. Bray, and D. V. Fursa, "Linear polarization fractions of Fulcher-α fluorescence in electron collisions with H_2", Phys. Rev. A **104**, L040801 (2021) (cit. on pp. 11, 271, 316).

[4] **L. H. Scarlett**, D. V. Fursa, J. Knol, M. C. Zammit, and I. Bray, "Isotopic and vibrational-level dependence of H_2 dissociation by electron impact", Phys. Rev. A **103**, L020801 (2021) (cit. on pp. 11, 129, 159, 171, 213, 281, 317).

[5] **L. H. Scarlett**, J. S. Savage, D. V. Fursa, I. Bray, M. C. Zammit, and B. I. Schneider, "Convergent close-coupling calculations of electrons scattering on electronically-excited molecular hydrogen", Phys. Rev. A **103**, 032802 (2021) (cit. on pp. 11, 129, 172, 173, 189, 190, 213, 318).

[6] **L. H. Scarlett**, D. V. Fursa, M. C. Zammit, I. Bray, and Yu. Ralchenko, "Complete collision data set for electrons scattering on molecular hydrogen and its isotopologues: II. Fully vibrationally-resolved electronic excitation of the isotopologues of $H_2(X\,^1\Sigma_g^+)$", At. Data Nucl. Data Tables **139**, 101403 (2021) (cit. on pp. 11, 129, 172, 173, 174, 186, 213, 281, 319).

[7] **L. H. Scarlett**, D. V. Fursa, M. C. Zammit, I. Bray, Yu. Ralchenko, and K. D. Davie, "Complete collision data set for electrons scattering on molecular hydrogen and its isotopologues: I. Fully vibrationally-resolved electronic excitation of $H_2(X\,^1\Sigma_g^+)$", At. Data Nucl. Data Tables **137**, 101361 (2021) (cit. on pp. 12, 129, 172, 173, 174, 178, 180, 213, 281, 320).

[8]D. Wünderlich, **L. H. Scarlett**, S. Briefi, U. Fantz, M. C. Zammit, D. V. Fursa, and I. Bray, "Application of molecular convergent close-coupling cross sections in a collisional radiative model for the triplet system of molecular hydrogen", J. Phys. D. Appl. Phys. **54**, 115201 (2021) (cit. on pp. 12, 173, 207, 213, 282, 321).

[9]T. Meltzer, J. Tennyson, Z. Masin, M. C. Zammit, **L. H. Scarlett**, D. V. Fursa, and I. Bray, "Benchmark calculations of electron impact electronic excitation of the hydrogen molecule", J. Phys. B **53**, 145204 (2020) (cit. on pp. 12, 47, 107, 322).

[10]**L. H. Scarlett**, J. S. Savage, D. V. Fursa, I. Bray, and M. C. Zammit, "Electron-scattering on molecular hydrogen: convergent close-coupling approach", Eur. Phys. J. D **74**, 36 (2020) (cit. on pp. 12, 144, 146, 281, 323).

[11]N. Mori, R. Utamuratov, **L. H. Scarlett**, D. V. Fursa, A. S. Kadyrov, I. Bray, and M. C. Zammit, "Calculations of positron scattering on the hydrogen molecular ion", J. Phys. B **53**, 015203 (2020) (cit. on pp. 12, 324).

[12]**L. H. Scarlett**, J. S. Savage, D. V. Fursa, M. C. Zammit, and I. Bray, "Electron-impact dissociation of vibrationally-excited molecular hydrogen into neutral fragments", Atoms **7**, 75 (2019) (cit. on pp. 12, 172, 173, 178, 213, 281, 325).

[13]**L. H. Scarlett**, J. K. Tapley, J. S. Savage, D. V. Fursa, M. C. Zammit, and I. Bray, "Vibrational excitation of the H_2 $X\ ^1\Sigma_g^+$ state via electron-impact excitation and radiative cascade", Plasma Sources Sci. Technol. **28**, 025004 (2019) (cit. on pp. 12, 281, 326).

[14]M. Zawadzki, R. Wright, G. Dolmat, M. F. Martin, B. Diaz, L. Hargreaves, D. Coleman, D. V. Fursa, M. C. Zammit, **L. H. Scarlett**, J. K. Tapley, J. S. Savage, I. Bray, and M. A. Khakoo, "Low-energy scattering from molecular hydrogen: excitation of the $X\ ^1\Sigma_g^+ \rightarrow b\ ^3\Sigma_u^+$ transition", Phys. Rev. A **98**, 062704 (2018) (cit. on pp. 12, 47, 109, 327).

[15]J. K. Tapley, **L. H. Scarlett**, J. S. Savage, D. V. Fursa, M. C. Zammit, and I. Bray, "Electron-impact dissociative excitation of singlet states of molecular hydrogen", Phys. Rev. A **98**, 032701 (2018) (cit. on pp. 13, 160, 161, 328).

[16]J. K. Tapley, **L. H. Scarlett**, J. S. Savage, M. C. Zammit, D. V. Fursa, and I. Bray, "Vibrationally resolved electron-impact excitation cross sections for singlet states of molecular hydrogen", J. Phys. B **51**, 144007 (2018) (cit. on pp. 13, 146, 329).

[17]M. Zawadzki, R. Wright, G. Dolmat, M. F. Martin, L. Hargreaves, D. V. Fursa, M. C. Zammit, **L. H. Scarlett**, J. K. Tapley, J. S. Savage, I. Bray, and M. A. Khakoo, "Time-of-flight electron scattering from molecular hydrogen: Benchmark cross sections for excitation of the $X\ ^1\Sigma_g^+ \rightarrow b\ ^3\Sigma_u^+$ transition", Phys. Rev. A **97**, 050702(R) (2018) (cit. on pp. 13, 47, 109, 330).

[18]**L. H. Scarlett**, J. K. Tapley, D. V. Fursa, M. C. Zammit, J. S. Savage, and I. Bray, "Electron-impact dissociation of molecular hydrogen into neutral fragments", Eur. Phys. J. D **72**, 34 (2018) (cit. on pp. 13, 188).

[19]**L. H. Scarlett**, J. K. Tapley, D. V. Fursa, M. C. Zammit, J. S. Savage, and I. Bray, "Low-energy electron-impact dissociative excitation of molecular hydrogen and its isotopologues", Phys. Rev. A **96**, 062708 (2017) (cit. on pp. 13, 160, 161).

[20]**L. H. Scarlett**, M. C. Zammit, D. V. Fursa, and I. Bray, "Kinetic-energy release of fragments from electron-impact dissociation of the molecular hydrogen ion and its isotopologues", Phys. Rev. A **96**, 022706 (2017) (cit. on pp. 13, 160, 161).

[21]K. Bartschat and M. J. Kushner, "Electron collisions with atoms, ions, molecules, and surfaces: Fundamental science empowering advances in technology", Proc. Natl. Acad. Sci. U. S. A. **113**, 7026 (2016) (cit. on p. 39).

[22]D. E. Shemansky, X. Liu, and H. Melin, "The Saturn hydrogen plume", Planet. Sp. Sci. **57**, 1659 (2009) (cit. on pp. 39, 40, 172).

[23]H. Melin, D. E. Shemansky, and X. Liu, "The distribution of atomic hydrogen and oxygen in the magnetosphere of Saturn", Planet. Sp. Sci. **57**, 1743 (2009) (cit. on pp. 39, 172).

[24]H. Abgrall, E. Roueff, X. Liu, and D. E. Shemansky, "The emission continuum of electron-excited molecular hydrogen", Astrophys. J. **481**, 557 (1997) (cit. on pp. 39, 40, 172).

[25]T. L. Stephens and A. Dalgarno, "Spontaneous radiative dissociation in molecular hydrogen", J. Quant. Spectrosc. Radiat. Transf. **12**, 569 (1972) (cit. on pp. 39, 40, 172).

[26]C. Jonin, X. Liu, J. M. Ajello, G. K. James, and H. Abgrall, "High resolution electron-impact emission spectrum of H_2. I. Cross sections and emission yields 900-1200 Å", Astrophys. J. Suppl. Ser. **129**, 247 (2000) (cit. on p. 39).

[27]X. Liu, S. M. Ahmed, R. A. Multari, G. K. James, and J. M. Ajello, "High-resolution electron-impact study of the far-ultraviolet emission spectrum of molecular hydrogen", Astrophys. J. Suppl. Ser. **101**, 375 (1995) (cit. on p. 39).

[28]D.-H. Ki and Y.-D. Jung, "Electron impact dissociation $X\,{}^1\Sigma_g^+ \to b\,{}^3\Sigma_u^+$ and excitations $X\,{}^1\Sigma_g^+ \to a\,{}^3\Sigma_g^+$ and $X\,{}^1\Sigma_g^+ \to B\,{}^1\Sigma_u^+$ of molecular hydrogen in nonthermal astrophysical plasmas", Astrophys. J. Suppl. Ser. **204**, 18 (2013) (cit. on p. 40).

[29]C. Tao, S. V. Badman, and M. Fujimoto, "UV and IR auroral emission model for the outer planets: Jupiter and Saturn comparison", Icarus **213**, 581 (2011) (cit. on p. 40).

[30]A. Bhardwaj and G. R. Gladstone, "Auroral emissions of the giant planets", Rev. Geophys. **38**, 295 (2000) (cit. on p. 40).

[31]A. Laricchiuta, R. Celiberto, F. Esposito, and M. Capitelli, "State-to-state cross sections for H_2 and its isotopic variants", Plasma Sources Sci. Technol. **15**, S62 (2006) (cit. on pp. 40, 172).

[32]G. Colonna, L. D. Pietanza, G. D'Ammando, R. Celiberto, M. Capitelli, and A. Laricchiuta, "Vibrational kinetics of electronically excited states in H_2 discharges", Eur. Phys. J. D **71**, 279 (2017) (cit. on pp. 40, 172).

[33]V. Bromm, N. Yoshida, L. Hernquist, and C. F. McKee, "The formation of the first stars and galaxies", Nature **459**, 49 (2009) (cit. on p. 40).

[34]S. C. O. Glover and T. Abel, "Uncertainties in H_2 and HD chemistry and cooling and their role in early structure formation", Mon. Not. R. Astron. Soc. **388**, 1627 (2008) (cit. on pp. 40, 45, 163, 213).

[35]J. Wolcott-Green and Z. Haiman, "Suppression of HD cooling in protogalactic gas clouds by Lyman-Werner radiation", Mon. Not. R. Astron. Soc. **412**, 2603 (2011) (cit. on p. 40).

[36]S. C. O. Glover and D. W. Savin, "Is H_3^+ cooling ever important in primordial gas?", Mon. Not. R. Astron. Soc. **393**, 911 (2009) (cit. on pp. 40, 45, 163, 213).

[37]C. Safranek-Shrader, M. Agarwal, C. Federrath, A. Dubey, M. Milosavljević, and V. Bromm, "Star formation in the first galaxies - I. Collapse delayed by Lyman-Werner radiation", Mon. Not. R. Astron. Soc. **426**, 1159 (2012) (cit. on p. 40).

[38]H. Susa and M. Umemura, "Secondary star formation in a population III object", Astrophys. J. **645**, L93 (2006) (cit. on p. 40).

[39]A. J. Richings, J. Schaye, and B. D. Oppenheimer, "Non-equilibrium chemistry and cooling in the diffuse interstellar medium - I. Optically thin regime", Mon. Not. R. Astron. Soc. **440**, 3349 (2014) (cit. on pp. 40, 45, 163, 213).

[40]J. M. Ajello, I. Kanik, S. M. Ahmed, and J. T. Clarke, "Line profile of H Lyman α from dissociative excitation of H_2 with application to Jupiter", J. Geophys. Res. **100**, 26411 (1995) (cit. on p. 40).

[41]P. C. Clark, S. C. O. Glover, R. S. Klessen, and V. Bromm, "Gravitational fragmentation in turbulent primordial gas and the initial mass function of population III stars", Astrophys. J. **727**, 110 (2011) (cit. on pp. 40, 45, 163, 213).

[42]C. Shin, J. Park, J. Jung, S. Bong, S. Kim, Y. J. Lee, and J. Yi, "Control of micro void fraction and optical band gap in intrinsic amorphous silicon thin films (VHF-PECVD) for thin film solar cell application", Mater. Res. Bull. **60**, 895 (2014) (cit. on pp. 40, 45, 163, 213).

[43]C. W. Chen, T. C. Chang, P. T. Liu, H. Y. Lu, K. C. Wang, C. S. Huang, C. C. Ling, and T. Y. Tseng, "High-performance hydrogenated amorphous-Si TFT for AMLCD and AMOLED applications", IEEE Electron Device Lett. **26**, 731 (2005) (cit. on p. 40).

[44]M. Moravej, S. E. Babayan, G. R. Nowling, X. Yang, and R. F. Hicks, "Plasma enhanced chemical vapour deposition of hydrogenated amorphous silicon at atmospheric pressure", Plasma Sources Sci. Technol. **13**, 8 (2004) (cit. on pp. 40, 45, 163, 213).

[45]F. Romanelli, *Fusion electricity: A roadmap to the realisation of fusion energy*, Garching, 2012 (cit. on p. 41).

[46]K. Sawada and T. Fujimoto, "Effective ionization and dissociation hydrogen in plasma", J. Appl. Phys. **78**, 2913 (1995) (cit. on p. 41).

[47]S. I. Krasheninnikov, A. Y. Pigarov, and D. J. Sigmar, "Plasma recombination and divertor detachment", Contrib. to Plasma Phys. **214**, 285 (1996) (cit. on p. 42).

[48]S. I. Krasheninnikov, A. S. Kukushkin, and A. A. Pshenov, "Divertor plasma detachment", Phys. Plasmas **23**, 055602 (2016) (cit. on p. 42).

[49]S. I. Krasheninnikov and A. S. Kukushkin, "Physics of ultimate detachment of a tokamak divertor plasma", J. Plasma Phys. **83**, 155830501 (2017) (cit. on p. 42).

[50]R. S. Hemsworth, D. Boilson, P. Blatchford, M. D. Palma, G. Chitarin, H. P. De Esch, F. Geli, M. Dremel, J. Graceffa, D. Marcuzzi, G. Serianni, D. Shah, M. Singh, M. Urbani, and P. Zaccaria, "Overview of the design of the ITER heating neutral beam injectors", New J. Phys. **19**, 025005 (2017) (cit. on p. 42).

[51]U. Fantz, P. Franzen, W. Kraus, M. Berger, S. Christ-Koch, H. Falter, M. Fröschle, R. Gutser, B. Heinemann, C. Martens, P. McNeely, R. Riedl, E. Speth, A. Stäbler, and D. Wünderlich, "Physical performance analysis and progress of the development of the negative ion RF source for the ITER NBI system", Nucl. Fusion **49**, 125007 (2009) (cit. on p. 43).

[52]D. Wünderlich, M. Giacomin, R. Ritz, and U. Fantz, "Yacora on the Web: Online collisional radiative models for plasmas containing H, H_2 or He", J. Quant. Spectrosc. Radiat. Transf. **240**, 106695 (2020) (cit. on pp. 43, 44, 208).

[53]D. Wünderlich and U. Fantz, "Evaluation of state-resolved reaction probabilities and their application in population models for He, H, and H_2", Atoms **4**, 26 (2016) (cit. on pp. 43, 208).

[54]F. F. Chen, "Langmuir probe measurements in the intense RF field of a helicon discharge", Plasma Sources Sci. Technol. **21**, 055013 (2012) (cit. on p. 43).

[55]U. Fantz, "Emission spectroscopy of molecular low pressure plasmas", Contrib. to Plasma Phys. **44**, 508 (2004) (cit. on p. 43).

[56]D. Wünderlich, S. Dietrich, and U. Fantz, "Application of a collisional radiative model to atomic hydrogen for diagnostic purposes", J. Quant. Spectrosc. Radiat. Transf. **110**, 62 (2009) (cit. on pp. 43, 207).

[57]U. Fantz, "Basics of plasma spectroscopy", Plasma Sources Sci. Technol. **15**, S137 (2006) (cit. on p. 44).

[58]T. N. Rescigno and B. I. Schneider, "Electronic excitation of the $b\ ^3\Sigma_u^+$ state of H_2 using the complex Kohn method: R dependence of the cross section", J. Phys. B At. Mol. Phys. **21**, L691 (1988) (cit. on pp. 45, 160, 161).

[59]S. D. Parker, C. W. McCurdy, T. N. Rescigno, and B. H. Lengsfield, "Electronic excitation of H_2 by electron impact: Close-coupling calculations using the complex Kohn variational method", Phys. Rev. A **43**, 3514 (1991) (cit. on p. 45).

[60]M. A. Lima, T. L. Gibson, V. McKoy, and W. M. Huo, "Cross sections for excitation of the $b\ ^3\Sigma_u^+$, $a\ ^3\Sigma_g^+$, and $c\ ^3\Pi_u$ states of H_2 by low-energy electrons", Phys. Rev. A **38**, 4527 (1988) (cit. on p. 45).

[61]M. A. P. Lima, T. L. Gibson, W. M. Huo, and V. McKoy, "Cross sections for electron impact excitation of the $b\ ^3\Sigma_u^+$ state of H_2: an application of the Schwinger multichannel variational method", J. Phys. B At. Mol. Phys. **18**, L865 (1985) (cit. on pp. 45, 160, 161).

[62]T. L. Gibson, M. A. P. Lima, V. McKoy, and W. M. Huo, "Application of the Schwinger multichannel formulation to electron-impact excitation of the $B\ ^1\Sigma_u^+$ state of H_2", Phys. Rev. A **35**, 2473 (1987) (cit. on p. 45).

[63]M. A. P. Lima, T. L. Gibson, K. Takatsuka, and V. McKoy, "Multichannel Schwinger variational cross sections for electron-impact excitation of the $b\ ^3\Sigma_u^+$ state in H_2", Phys. Rev. A **30**, 1741 (1984) (cit. on pp. 45, 160, 161).

[64]S. E. Branchett, J. Tennyson, and L. A. Morgan, "Electronic excitation of molecular hydrogen using the R-matrix method", J. Phys. B **23**, 4625 (1990) (cit. on pp. 45, 160, 161).

[65]S. E. Branchett and J. Tennyson, "Resonances in the electronic excitation of molecular hydrogen", Phys. Rev. Lett. **64**, 2889 (1990) (cit. on pp. 45, 107).

[66]S. E. Branchett, J. Tennyson, L. A. Morgan, J. Tennyson, and L. A. Morgan, "Differential cross sections for electronic excitation of molecular hydrogen using the R-matrix method", J. Phys. B **24**, 3479 (1991) (cit. on p. 45).

[67]T. N. Rescigno, J. C. W. McCurdy, V. McKoy, and C. F. Bender, "Low-energy electron-impact excitation of the hydrogen molecule", Phys. Rev. A **13**, 216 (1976) (cit. on pp. 45, 106).

[68]A. W. Fliflet and V. McKoy, "Distorted-wave-approximation cross sections for excitation of the $b\,^3\Sigma_u^+$ and $B\,^1\Sigma_u^+$ states of H_2 by low-energy-electron impact", Phys. Rev. A **21**, 1863 (1980) (cit. on pp. 45, 106, 160, 161).

[69]L. Mu-Tao, R. R. Lucchese, and V. McKoy, "Electron-impact excitation and dissociation processes in H_2", Phys. Rev. A **26**, 3240 (1982) (cit. on pp. 45, 106).

[70]R. Celiberto, R. Jenev, A. Laricchiuta, M. Capitelli, J. Wadehra, and D. Atems, "Cross section data for electron-impact inelastic processes of vibrationally excited molecules of hydrogen and its isotopes", At. Data Nucl. Data Tables **77**, 161 (2001) (cit. on pp. 45, 46, 105, 160, 161, 172, 174, 175, 176, 178, 189, 190, 200, 205).

[71]D. T. Stibbe and J. Tennyson, "Near-threshold electron impact dissociation of H_2 within the adiabatic nuclei approximation", New J. Phys. **1**, 2 (1998) (cit. on pp. 45, 100, 101, 107, 155, 160, 161, 164, 281).

[72]C. S. Trevisan and J. Tennyson, "Differential cross sections for near-threshold electron impact dissociation of molecular hydrogen", J. Phys. B **34**, 2935 (2001) (cit. on pp. 45, 96, 159, 160, 161, 164, 167, 171, 176, 281).

[73]C. Trevisan and J. Tennyson, "Calculated rates for the electron impact dissociation of molecular hydrogen, deuterium and tritium", Plasma Phys. Contr. F. **44**, 1263 (2002) (cit. on pp. 45, 159, 162, 164, 166, 167, 171, 176, 281).

[74]C. S. Trevisan and J. Tennyson, "Calculated rates for the electron impact dissociation of molecular hydrogen: Mixed isotopomers and scaling laws", Plasma Phys. Control. Fusion **44**, 2217 (2002) (cit. on pp. 45, 159, 167, 171, 176, 281).

[75]U. Ziegler, "A chemistry and cooling module for the NIRVANA code", Astron. Astrophys. **620**, A81 (2018) (cit. on pp. 45, 163, 213).

[76]E. I. Vorobyov, R. Matsukoba, K. Omukai, and M. Guedel, "Thermal evolution of protoplanetary disks: From β-cooling to decoupled gas and dust temperatures", Astron. Astrophys. **638**, A102 (2020) (cit. on pp. 45, 163, 213).

[77]M. C. Sormani, R. G. Treß, M. Ridley, S. C. O. Glover, R. S. Klessen, J. Binney, J. Magorrian, and R. Smith, "A theoretical explanation for the central molecular zone asymmetry", Mon. Not. R. Astron. Soc. **475**, 2383 (2018) (cit. on pp. 45, 163, 213).

[78]B. D. Smith, G. L. Bryan, S. C. O. Glover, N. J. Goldbaum, M. J. Turk, J. Regan, J. H. Wise, H. Y. Schive, T. Abel, A. Emerick, B. W. O'Shea, P. Anninos, C. B. Hummels, and S. Khochfar, "Grackle: A chemistry and cooling library for astrophysics", Mon. Not. R. Astron. Soc. **466**, 2217 (2017) (cit. on pp. 45, 163, 213).

[79]D. R. Schleicher, D. Galli, F. Palla, M. Camenzind, R. S. Klessen, M. Bartelmann, and S. C. O. Glover, "Effects of primordial chemistry on the cosmic microwave background", Astron. Astrophys. **490**, 521 (2008) (cit. on pp. 45, 163, 213).

[80]M. Micic, S. C. O. Glover, C. Federrath, and R. S. Klessen, "Modelling H_2 formation in the turbulent interstellar medium: Solenoidal versus compressive turbulent forcing", Mon. Not. R. Astron. Soc. **421**, 2531 (2012) (cit. on pp. 45, 163, 213).

[81]M. Micic, S. C. O. Glover, R. Banerjee, and R. S. Klessen, "Cloud formation in colliding flows: Influence of the choice of cooling function", Mon. Not. R. Astron. Soc. **432**, 626 (2013) (cit. on pp. 45, 163, 213).

[82]R. Matsukoba, S. Z. Takahashi, K. Sugimura, and K. Omukai, "Gravitational stability and fragmentation condition for discs around accreting supermassive stars", Mon. Not. R. Astron. Soc. **484**, 2605 (2019) (cit. on pp. 45, 163, 213).

[83]J. MacKey, S. Walch, D. Seifried, S. C. O. Glover, R. Wünsch, and F. Aharonian, "Non-equilibrium chemistry and destruction of CO by X-ray flares", Mon. Not. R. Astron. Soc. **486**, 1094 (2019) (cit. on pp. 45, 163, 213).

[84]C. M. Coppola, D. Galli, F. Palla, S. Longo, and J. Chluba, "Non-thermal photons and H_2 formation in the early universe", Mon. Not. R. Astron. Soc. **434**, 114 (2013) (cit. on pp. 45, 163, 213).

[85]P. C. Clark, S. C. O. Glover, S. E. Ragan, and A. Duarte-Cabral, "Tracing the formation of molecular clouds via [C II], [C I], and CO emission", Mon. Not. R. Astron. Soc. **486**, 4622 (2019) (cit. on pp. 45, 163, 213).

[86]B. H. P. Broks, K. Garloff, and J. J. A. M. Van Der Mullen, "Nonlocal-thermal-equilibrium model of a pulsed capillary discharge waveguide", Phys. Rev. E **71**, 016401 (2005) (cit. on pp. 45, 163, 213).

[87]M. C. Zammit, D. V. Fursa, J. S. Savage, and I. Bray, "Electron– and positron-molecule scattering: development of the molecular convergent close-coupling method", J. Phys. B **50**, 123001 (2017) (cit. on pp. 46, 89, 93, 111, 119, 120, 124, 167, 221, 281).

[88]M. C. Zammit, D. V. Fursa, and I. Bray, "Calculations of electron scattering from H_2^+", Phys. Rev. A **88**, 062709 (2013) (cit. on pp. 46, 109).

[89]M. C. Zammit, D. V. Fursa, and I. Bray, "Convergent-close-coupling formalism for positron scattering from molecules", Phys. Rev. A **87**, 020701(R) (2013) (cit. on pp. 46, 109).

[90]M. C. Zammit, D. V. Fursa, and I. Bray, "Electron scattering from the molecular hydrogen ion and its isotopologues", Phys. Rev. A **90**, 022711 (2014) (cit. on pp. 46, 109, 160, 161).

[91]M. C. Zammit, J. S. Savage, D. V. Fursa, and I. Bray, "Complete solution of electronic excitation and ionization in electron-hydrogen molecule scattering", Phys. Rev. Lett. **116**, 233201 (2016) (cit. on pp. 46, 109, 215, 281).

[92]M. C. Zammit, D. V. Fursa, J. S. Savage, L. Chiari, A. Zecca, and M. J. Brunger, "Adiabatic-nuclei calculations of positron scattering from molecular hydrogen", Phys. Rev. **95**, 022707 (2017) (cit. on pp. 46, 109).

[93]M. C. Zammit, J. S. Savage, D. V. Fursa, and I. Bray, "Electron-impact excitation of molecular hydrogen", Phys. Rev. A **95**, 022708 (2017) (cit. on pp. 46, 47, 109, 142, 144, 145, 149, 158, 193, 279, 281).

[94]C. S. Sartori, F. J. da Paixão, and M. A. P. Lima, "Superelastic cross sections in e^--H_2 scattering", Phys. Rev. A **55**, 3243 (1997) (cit. on pp. 46, 105, 189, 190, 191, 194, 195, 196).

[95]C. S. Sartori, F. J. da Paixão, and M. A. P. Lima, "Transitions between excited electronic states of H_2 molecules by electron impact", Phys. Rev. A **58**, 2857 (1998) (cit. on pp. 46, 105, 189, 190, 191, 194, 195, 196).

[96]A. Laricchiuta, R. Celiberto, and R. K. Janev, "Electron-impact-induced allowed transitions between triplet states of H_2", Phys. Rev. A **69**, 022706 (2004) (cit. on pp. 46, 160, 161, 172, 189, 190, 200, 201, 202).

[97]K. N. Joshipura, H. N. Kothari, F. A. Shelat, P. Bhowmik, and N. J. Mason, "Electron scattering with metastable $H_2^*(c\,^3\Pi_u)$ molecules: ionization and other total cross sections", J. Phys. B **43**, 135207 (2010) (cit. on pp. 46, 107, 189, 190, 191, 192, 193).

[98]D. Wünderlich, "Vibrationally resolved ionization cross sections for the ground state and electronically excited states of the hydrogen molecule", Chem. Phys. **390**, 75 (2011) (cit. on pp. 46, 104).

[99]D. Wünderlich, "Vibrationally resolved ionization cross sections for the ground state and electronically excited states of the hydrogen molecule and its isotopomeres", At. Data Nucl. Data Tables **140**, 101424 (2021) (cit. on pp. 46, 104, 189, 190, 191, 192).

[100]A. P. Hickman, "Dissociative attachment of electrons to vibrationally excited H_2", Phys. Rev. A **43**, 3495 (1991) (cit. on p. 47).

[101]G. A. Gallup, Y. Xu, and I. I. Fabrikant, "Nonlocal theory of dissociative electron attachment to H_2 and HF molecules", Phys. Rev. A **57**, 2596 (1998) (cit. on p. 47).

[102]D. E. Atems and J. M. Wadehra, "Nonlocal effects in dissociative electron attachment to H_2", Phys. Rev. A **42**, 5201 (1990) (cit. on p. 47).

[103]J. M. Wadehra and J. N. Bardsley, "Vibrational- and rotational-state dependence of dissociative attachment in e^--H_2 collisions", Phys. Rev. Lett. **41**, 1795 (1978) (cit. on p. 47).

[104]C. Mundel and W. Domcke, "Nuclear dynamics in resonant electron-molecule scattering beyond the local approximation: Model calculations on dissociative attachment and vibrational excitation", J. Phys. B At. Mol. Phys. **17**, 3593 (1984) (cit. on pp. 47, 216).

[105]J. Horáček, M. Cízek, K. Houfek, P. Kolorenč, W. Domcke, M. Čížek, K. Houfek, P. Kolorenč, and W. Domcke, "Dissociative electron attachment and vibrational excitation of H_2 by low-energy electrons: Calculations based on an improved nonlocal resonance model", Phys. Rev. A **70**, 052712 (2004) (cit. on pp. 47, 216).

[106]M. Čížek, J. Horáček, and W. Domcke, "Nuclear dynamics of the H_2^- collision complex beyond the local approximation: Associative detachment and dissociative attachment to rotationally and vibrationally excited molecules", J. Phys. B **31**, 2571 (1998) (cit. on p. 47).

[107]Y. Xu, G. A. Gallup, and I. I. Fabrikant, "Dissociative electron attachment to vibrationally and rotationally excited H_2 and HF molecules", Phys. Rev. A **61**, 052705 (2000) (cit. on p. 47).

[108]H. P. Gauyacq, "Dissociative attachment in e^--H_2 collisions", J. Phys. B At. Mol. Phys. **18**, 1859 (1985) (cit. on p. 47).

[109]W. Domcke, "Theory of resonance and threshold effects in electron-molecule collisions: The projection-operator approach", Phys. Rep. **208**, 97 (1991) (cit. on p. 47).

[110]C. Bottcher and B. D. Buckley, "Dissociative electron attachment to the metastable $c\,^3\Pi_u$ state of molecular hydrogen", J. Phys. B At. Mol. Phys. **12**, L497 (1979) (cit. on p. 47).

[111]D. Rabli and M. A. Morrison, "Importance of nonresonant scattering in low-energy dissociative electron attachment to molecular hydrogen", Phys. Rev. Lett. **97**, 013201 (2006) (cit. on p. 47).

[112]R. Celiberto, R. K. Janev, V. Laporta, J. Tennyson, and J. M. Wadehra, "Electron-impact vibrational excitation of vibrationally excited H_2 molecules involving the resonant $^2\Sigma_g^+$ Rydberg-excited electronic state", Phys. Rev. A **88**, 062701 (2013) (cit. on pp. 47, 216, 229, 244).

[113]R. Celiberto, R. K. Janev, J. M. Wadehra, and A. Laricchiuta, "Cross sections for 11–14-eV e^--H_2 resonant collisions: Vibrational excitation", Phys. Rev. A **77**, 012714 (2008) (cit. on pp. 47, 229).

[114]J. Horáček, M. Cízek, K. Houfek, P. Kolorenč, and W. Domcke, "Dissociative electron attachment and vibrational excitation of H_2 by low-energy electrons: Calculations based on an improved nonlocal resonance model. II. Vibrational excitation", Phys. Rev. A **73**, 022701 (2006) (cit. on pp. 47, 216, 248).

[115]V. Laporta, R. Agnello, G. Fubiani, I. Furno, C. Hill, D. Reiter, and F. Taccogna, "Vibrational excitation and dissociation of deuterium molecule by electron impact", Plasma Phys. Control. Fusion **63**, 085006 (2021) (cit. on pp. 47, 216, 229, 242).

[116]T. Meltzer and J. Tennyson, "Electron collisions with molecular hydrogen from electronically excited states using the R-matrix method", J. Phys. B **53**, 245203 (2020) (cit. on pp. 47, 107, 173, 189, 190, 191, 194, 195, 196, 198, 199, 201, 202, 203, 204, 205, 206, 213, 282).

[117]M. J. Brunger, S. J. Buckman, D. S. Newman, and D. T. Alle, "Elastic scattering and rovibrational excitation of H_2 by low-energy electrons", J. Phys. B **24**, 1435 (1991) (cit. on p. 47).

[118]H. Ehrhardt, L. Langhans, F. Linder, and H. S. Taylor, "Resonance scattering of slow electrons from H_2 and CO angular distributions", Phys. Rev. **173**, 222 (1968) (cit. on p. 47).

[119]F. Linder and H. Schmidt, "Rotational and vibrational excitation of H_2 by slow electron impact", Zeitschrift fur Naturforsch.ung - Sect. A J. Phys. Sci. **26**, 1603 (1971) (cit. on p. 47).

[120]J. Furst, M. Mahgerefteh, and D. E. Golden, "Absolute total electronically elastic differential e^--H_2 scattering cross-section measurements from 1 to 19 eV", Phys. Rev. A **30**, 2256 (1984) (cit. on p. 47).

[121]T. W. Shyn and W. E. Sharp, "Angular distributions of electrons elastically scattered from H_2", Phys. Rev. A **24**, 1734 (1981) (cit. on p. 47).

[122]D. E. Golden, H. W. Bandel, and J. A. Salerno, "Absolute total electron scattering cross sections in H_2 and D_2 for low electron energies", Phys. Rev. **146**, 40 (1966) (cit. on p. 47).

[123]G. Joyez, J. Comer, and F. H. Read, "Resonant rotational excitation of H_2 by electron impact", J. Phys. B At. Mol. Phys. **6**, 2427 (1973) (cit. on p. 47).

[124]W. R. Crompton, D. K. Gibson, and A. I. McIntosh, "The cross section for the $J = 0 \rightarrow 2$ rotational excitation of hydrogen by slow electrons", Aust. J. Phys. **22**, 715 (1969) (cit. on p. 47).

[125]D. Gibson, "The cross sections for rotational excitation of H_2 and D_2 by low energy electrons", Aust. J. Phys. **23**, 683 (1970) (cit. on p. 47).

[126]H. Ehrhardt and F. Linder, "Rotational excitation of H_2 by slow electrons in a beam experiment", Phys. Rev. Lett. **21**, 419 (1968) (cit. on p. 47).

[127]S. F. Wong and G. J. Schultz, "Rotational and vibrational excitation of H_2 by electron impact at 4.5 eV: angular distributions", Phys. Rev. Lett. **20**, 1089 (1974) (cit. on p. 47).

[128]K. Jung, K. M. Scheuerlein, W. Sohn, K. H. Kochem, and H. Ehrhardt, "Breakdown of the adiabatic-nuclei approximation in the rotational excitation of H_2 by very slow electrons", J. Phys. B At. Mol. Phys. **20**, L327 (1987) (cit. on p. 47).

[129]S. K. Srivastava and S. Jensen, "Experimental differential and integral electron impact cross sections for the $B\ ^1\Sigma_u^+$ state of H_2 in the intermediate-energy region", J. Phys. B At. Mol. Phys. **10**, 3341 (1977) (cit. on p. 47).

[130]M. A. Khakoo and J. Segura, "Differential cross sections for the electron impact excitation of the $b\ ^3\Sigma_u^+$ continuum of molecular hydrogen", J. Phys. B **27**, 2355 (1994) (cit. on p. 47).

[131]H. Nishimura and A. Danjo, "Differential cross section of electron scattering from molecular hydrogen. II. $b\ ^3\Sigma_u^+$ excitation", J. Phys. Soc. Japan **55**, 3031 (1986) (cit. on p. 47).

[132]R. I. Hall and L. Andric, "Electron impact excitation of $H_2(D_2)$. Resonance phenomena associated with the $X\,^2\Sigma_u^+$ and $B\,^2\Sigma_g^+$ states of H_2^- in the 10 eV region", J. Phys. B At. Mol. Phys. **17**, 3815 (1984) (cit. on p. 47).

[133]M. Khakoo and S. Trajmar, "Electron-impact excitation of the $a\,^3\Sigma_g^+$, $B\,^1\Sigma_u^+$, $c\,^3\Pi_u$, and $C\,^1\Pi_u$ states of H_2", Phys. Rev. A **34**, 146 (1986) (cit. on p. 47).

[134]J. Wrkich, D. Matthews, I. Knaik, S. Trajmar, and M. A. Khakoo, "Differential cross-sections for the electron impact excitation of the $B\,^1\Sigma_u^+$, $c\,^3\Pi_u$, $a\,^3\Sigma_g^+$, $C\,^1\Pi_u$, $EF\,^1\Sigma_g^+$, and $e\,^3\Sigma_u^+$ states of molecular hydrogen", J. Phys. B **35**, 4695 (2002) (cit. on p. 47).

[135]H. Kato, H. Kawahara, M. Hoshino, H. Tanaka, L. Campbell, and M. J. Brunger, "Electron-impact excitation of the $B\,^1\Sigma_u^+$ and $C\,^1\Pi_u$ electronic states of H_2", Phys. Rev. A **77**, 062708 (2008) (cit. on p. 47).

[136]S. Trajmar, D. F. Register, and A. Chutjian, "Electron scattering by molecules II. Experimental methods and data", Phys. Rep. **97**, 219 (1983) (cit. on p. 47).

[137]N. J. Mason and W. R. Newell, "Electron resonance structure observed in the $c\,^3\Pi_u$ and $B\,^1\Sigma_u^+$ cross sections of H_2", J. Phys. B **19**, L203 (1986) (cit. on p. 47).

[138]J.-S. Yoon, Y.-W. Kim, D.-C. Kwon, M.-Y. Song, W.-S. Chang, C.-G. Kim, V. Kumar, and B. Lee, "Electron-impact cross sections for deuterated hydrogen and deuterium molecules", Reports Prog. Phys. **73**, 116401 (2010) (cit. on pp. 48, 159, 163).

[139]R. K. Janev, D. Reiter, and U. Samm, *Collision processes in low-temperature hydrogen plasmas* (Forschungszentrum, Zentralbibliothek, Jülich, 2003) (cit. on pp. 48, 207, 208, 209, 281).

[140]W. T. Miles, R. Thompson, and A. E. S. Green, "Electron-impact cross sections and energy deposition in molecular hydrogen", J. Appl. Phys. **43**, 678 (1972) (cit. on pp. 48, 207, 208, 209, 281).

[141]B. H. Bransden, *Atomic collision theory* (Benjamin-Cummings, Reading, Massachusetts, 1983) (cit. on p. 50).

[142]J. R. Taylor, *Scattering theory: The quantum theory of nonrelativistic collisions* (John Wiley & Sons, New York, NY, 1972) (cit. on p. 50).

[143]J. J. Sakurai and J. Napolitano, *Modern quantum mechanics*, 3rd (Cambridge University Press, Cambridge, 2020) (cit. on pp. 50, 167, 168, 170).

[144]C. Cohen-Tannoudji, B. Diu, and F. Laloe, *Quantum mechanics. Volume II* (Wiley-VCH, Weinheim, 2020) (cit. on pp. 50, 160, 169).

[145]J. Brown and A. Carrington, *Rotational spectroscopy of diatomic molecules* (Cambridge University Press, Cambridge, 2003) (cit. on pp. 66, 77, 82, 271, 310).

[146]H. Lefebvre-Brion and R. W. Field, *The spectra and dynamics of diatomic molecules* (Academic Press Inc., Amsterdam, 2004) (cit. on p. 66).

[147]W. Kolos, K. Szalewicz, and H. J. Monkhorst, "New Born-Oppenheimer potential energy curve and vibrational energies for the electronic ground state of the hydrogen molecule", J. Chem. Phys. **84**, 3278 (1986) (cit. on pp. 73, 74, 131, 138, 140, 158, 242).

[148]G. Staszewska and L. Wolniewicz, "Adiabatic energies of excited $^1\Sigma_u$ states of the hydrogen molecule", J. Mol. Spectrosc. **212**, 208 (2002) (cit. on pp. 73, 74, 131, 138, 140, 158, 242).

[149]L. Wolniewicz and K. Dressler, "Adiabatic potential curves and nonadiabatic coupling functions for the first five excited $^1\Sigma_g^+$ states of the hydrogen molecule", J. Chem. Phys. **100**, 444 (1994) (cit. on pp. 73, 74, 131, 138, 140, 158).

[150]L. Wolniewicz and G. Staszewska, "Excited $^1\Pi_u$ states and the $^1\Pi_u \to X^1\Sigma_g^+$ transition moments of the hydrogen molecule", J. Mol. Spectrosc. **220**, 45 (2003) (cit. on pp. 73, 74, 131, 138, 140, 158).

[151]L. Wolniewicz, "Adiabatic potentials of the lowest $^1\Pi_g$ and $^{1,3}\Delta_g$ states of the hydrogen molecule", J. Mol. Spectrosc. **169**, 329 (1995) (cit. on pp. 73, 74, 131, 138, 140, 158).

[152]G. Staszewska and L. Wolniewicz, "Transition moments among $^2\Sigma$ and $^3\Pi$ states of the H_2 molecule", J. Mol. Spectrosc. **198**, 416 (1999) (cit. on pp. 73, 74, 131, 138, 140, 158, 242).

[153]M. Born and V. Fock, "Beweis des adiabatensatzes", Zeitschrift für Phys. **51**, 165 (1928) (cit. on p. 88).

[154]M. Shugard and A. U. Hazi, "Theory of electron-molecule scattering: Comments on the adiabatic-nuclei approximation", Phys. Rev. A **12**, 1895 (1975) (cit. on p. 100).

[155]M. Gryziński, "Classical theory of atomic collisions. I. Theory of inelastic collisions", Phys. Rev. **138**, A336 (1965) (cit. on p. 103).

[156]E. Bauer and C. D. Bartky, "Calculation of inelastic electron-molecule collision cross sections by classical methods", J. Chem. Phys. **43**, 2466 (1965) (cit. on p. 103).

[157]R. Celiberto, M. Capitelli, and M. Cacciatore, "Electron impact direct dissociative-ionization cross sections from vibrationally excited H_2 molecules and translational energy distribution functions of protons", Chem. Phys. **140**, 209 (1990) (cit. on p. 104).

[158]R. Celiberto, M. Cacciatore, M. Capitelli, and C. Gorse, "Electron impact direct dissociation processes of vibrationally excited H_2 molecules to excited atomic hydrogen $H^*(n = 1\text{–}5)$. I. Cross sections", Chem. Phys. **133**, 355 (1989) (cit. on pp. 104, 161).

[159]A. U. Hazi, "Impact-parameter method for electronic excitation of molecules by electron impact", Phys. Rev. A **23**, 2232 (1981) (cit. on pp. 104, 172).

[160]R. Celiberto and T. N. Rescigno, "Dependence of electron-impact excitation cross sections on the initial vibrational quantum number in H_2 and D_2 molecules: $X\,{}^1\Sigma_g^+ \rightarrow B\,{}^1\Sigma_u^+$ and $X\,{}^1\Sigma_g^+ \rightarrow C\,{}^1\Pi_u$ transitions", Phys. Rev. A **47**, 1939 (1993) (cit. on pp. 104, 105, 172, 173).

[161]R. Celiberto, M. Capitelli, and U. T. Lamanna, "Vibrational excitation of $H_2(X\,{}^1\Sigma_g^+, v)/D_2(X\,{}^1\Sigma_g^+, v)$ through excitation of electronically excited singlet states and radiative cascade", Chem. Phys. **183**, 101 (1994) (cit. on p. 105).

[162]R. Celiberto, U. T. Lamanna, and M. Capitelli, "Dependence of electron-impact dissociative excitation cross sections on the initial vibrational quantum number in H_2 and D_2 molecules: $X\,{}^1\Sigma_g^+ \rightarrow B\,{}^1\Sigma_u^+$ and $X\,{}^1\Sigma_g^+ \rightarrow C\,{}^1\Pi_u$ transitions", Phys. Rev. A **50**, 4778 (1994) (cit. on pp. 105, 161, 172).

[163]R. Celiberto, M. Capitelli, N. Durante, and U. T. Lamanna, "Electron-impact cross sections involving electronically excited states in H_2 molecules: $B^1\Sigma_u^+ \rightarrow I^1\Pi_u$ transition", Phys. Rev. A **54**, 432 (1996) (cit. on p. 105).

[164]R. Celiberto, A. Laricchiuta, U. T. Lamanna, R. K. Janev, and M. Capitelli, "Electron-impact excitation cross sections of vibrationally excited $X^1\Sigma_g^+$ H_2 and D_2 molecules to Rydberg states", Phys. Rev. A **60**, 2091 (1999) (cit. on p. 105).

[165]B. A. Lippmann and J. Schwinger, "Variational principles for scattering processes. I", Phys. Rev. **79**, 469 (1950) (cit. on p. 105).

[166]D. K. Watson, R. R. Lucchese, V. McKoy, and T. N. Rescigno, "Schwinger variational principle for electron-molecule scattering: Application to electron-hydrogen scattering", Phys. Rev. A **21**, 738 (1980) (cit. on p. 105).

[167]R. R. Lucchese, D. K. Watson, and V. McKoy, "Iterative approach to the Schwinger variational principle for electron-molecule collisions", Phys. Rev. A **22**, 421 (1980) (cit. on p. 105).

[168]K. Takatsuka and V. McKoy, "Variational scattering theory using a functional of fractional form. I. General theory", Phys. Rev. A **23**, 2352 (1981) (cit. on p. 105).

[169]K. Takatsuka and V. McKoy, "Variational scattering theory using a functional of fractional form. II. An L^2 approach", Phys. Rev. A **23**, 2359 (1981) (cit. on p. 105).

[170]Lee Mu-Tao, K. Takatsuka, and V. McKoy, "Application of a new variational functional for electron-molecule collisions: An extension of the Schwinger variational principle", J. Phys. B At. Mol. Phys. **14**, 4115 (1981) (cit. on p. 105).

[171]D. K. Watson, T. N. Rescigno, and B. V. McKoy, "Schwinger variational calculations for electron scattering by polar molecules", J. Phys. B At. Mol. Phys. **14**, 1875 (1981) (cit. on p. 105).

[172]K. Takatsuka and V. McKoy, "Theory of electronically inelastic scattering of electrons by molecules", Phys. Rev. A **30**, 1734 (1984) (cit. on p. 105).

[173]R. F. Da Costa, M. T. N. Varella, M. H. Bettega, and M. A. Lima, "Recent advances in the application of the Schwinger multichannel method with pseudopotentials to electron-molecule collisions", Eur. Phys. J. D **69**, 159 (2015) (cit. on p. 105).

[174]M. A. Lima, L. M. Brescansin, A. J. Da Silva, C. Winstead, and V. McKoy, "Applications of the Schwinger multichannel method to electron-molecule collisions", Phys. Rev. A **41**, 327 (1990) (cit. on p. 105).

[175]J. S. Germano and M. A. Lima, "Schwinger multichannel method for positron-molecule scattering", Phys. Rev. A **47**, 3976 (1993) (cit. on p. 105).

[176]M. H. Bettega, L. G. Ferreira, and M. A. Lima, "Transferability of local-density norm-conserving pseudopotentials to electron-molecule-collision calculations", Phys. Rev. A **47**, 1111 (1993) (cit. on p. 105).

[177]R. F. Da Costa, F. J. Da Paixão, and M. A. Lima, "Cross sections for electron-impact excitation of the H_2 molecule using the MOB-SCI strategy", J. Phys. B **38**, 4363 (2005) (cit. on pp. 105, 160, 161).

[178]D. H. Madison and W. N. Shelton, "Distorted-wave approximation and its application to the differential and integrated cross sections for electron-impact excitation of the 2P1 state of helium", Phys. Rev. A **7**, 499 (1973) (cit. on p. 105).

[179]A. M. Lane and R. G. Thomas, "R-Matrix theory of nuclear reactions", Rev. Mod. Phys. **30**, 257 (1958) (cit. on p. 106).

[180]P. G. Burke, A. Hibbert, and W. D. Robb, "Electron scattering by complex atoms", J. Phys. B At. Mol. Phys. **4**, 153 (1971) (cit. on p. 106).

[181]P. G. Burke, C. J. Noble, and P. Scott, "R-matrix theory of electron scattering at intermediate energies", Proc. R. Soc. Lond. A **410**, 289 (1987) (cit. on p. 106).

[182]K. L. Baluja, C. J. Noble, and J. Tennyson, "Electronic excitation of the $b^3\Sigma_u^+$ state of H_2 using the R-matrix method", J. Phys. B At. Mol. Phys. **18**, L851 (1985) (cit. on p. 107).

[183]K. N. Joshipura, M. Vinodkumar, and U. M. Patel, "Electron impact total cross sections of CHx, NHx and OH radicals vis-à-vis their parent molecules", J. Phys. B **34**, 509 (2001) (cit. on p. 107).

[184]K. N. Joshipura, M. Vinodkumar, C. G. Limbachiya, and B. K. Antony, "Calculated total cross sections of electron-impact ionization and excitations in tetrahedral (XY_4) and SF_6 molecules", Phys. Rev. A **69**, 022705 (2004) (cit. on p. 107).

[185]M. Vinodkumar, K. N. Joshipura, C. Limbachiya, and N. Mason, "Theoretical calculations of the total and ionization cross sections for electron impact on some simple biomolecules", Phys. Rev. A **74**, 022721 (2006) (cit. on p. 107).

[186]K. N. Joshipura, B. G. Vaishnav, and S. Gangopadhyay, "Electron impact ionization cross-sections of plasma relevant and astrophysical silicon compounds: SiH_4, Si2H_6, $Si(CH_3)_4$, SiO, SiO_2, SiN and SiS", Int. J. Mass Spectrom. **261**, 146 (2007) (cit. on p. 107).

[187]K. N. Joshipura and S. Gangopadhyay, "Electron collisions with sulfur compounds SO, SO2 and SO 2AB (A, B = Cl, F): Various total cross sections", J. Phys. B **41**, 215205 (2008) (cit. on p. 107).

[188]I. Bray, D. H. Madison, and I. E. McCarthy, "Coupled-channel optical calculation of electron-hydrogen scattering: The distorted-wave optical potential", Phys. Rev. A **41**, 5916 (1990) (cit. on p. 108).

[189]I. Bray and A. T. Stelbovics, "Convergent close-coupling calculations of electron-hydrogen scattering", Phys. Rev. A **46**, 6995 (1992) (cit. on p. 108).

[190]I. Bray, "Convergent close-coupling method for the calculation of electron scattering on hydrogenlike targets", Phys. Rev. A **49**, 1066 (1994) (cit. on pp. 108, 142, 285).

[191]D. V. Fursa and I. Bray, "Calculation of electron-helium scattering", Phys. Rev. A **52**, 1279 (1995) (cit. on pp. 108, 254).

[192]D. V. Fursa and I. Bray, "Convergent close-coupling calculations of electron - helium scattering scattering", J. Phys. B At. Mol. Phys. **30**, 757 (1997) (cit. on p. 108).

[193]A. S. Kadyrov and I. Bray, "Convergence of two-centre expansions in positron-hydrogen collisions", J. Phys. B **33**, L635 (2000) (cit. on p. 108).

[194]A. S. Kadyrov and I. Bray, "Two-center convergent close-coupling approach to positron-hydrogen collisions", Phys. Rev. A **66**, 012710 (2002) (cit. on pp. 108, 285).

[195]I. B. Abdurakhmanov, A. S. Kadyrov, I. Bray, and A. T. Stelbovics, "Coupled-channel integral-equation approach to antiproton-hydrogen collisions", J. Phys. B **44**, 075204 (2011) (cit. on p. 108).

[196]I. B. Abdurakhmanov, A. S. Kadyrov, and I. Bray, "Wave-packet continuum-discretization approach to ion-atom collisions: Nonrearrangement scattering", Phys. Rev. A **94**, 022703 (2016) (cit. on p. 108).

[197]A. S. Kadyrov, I. B. Abdurakhmanov, I. Bray, and A. T. Stelbovics, "Three-dimensional integral-equation approach to proton- and antiproton-hydrogen collisions", Phys. Rev. A **80**, 022704 (2009) (cit. on p. 108).

[198]A. S. Kadyrov, I. B. Abdurakhmanov, S. U. Alladustov, J. J. Bailey, and I. Bray, "Development of convergent close-coupling approach to hadron interactions with matter", J. Phys. Conf. Ser. **1154**, 012013 (2019) (cit. on p. 108).

[199]S. U. Alladustov, I. B. Abdurakhmanov, A. S. Kadyrov, I. Bray, and K. Bartschat, "Wave-packet continuum-discretization approach to proton collisions with helium", Phys. Rev. A **99**, 052706 (2019) (cit. on p. 108).

[200]I. Bray, I. B. Abdurakhmanov, J. J. Bailey, A. W. Bray, D. V. Fursa, A. S. Kadyrov, C. M. Rawlins, J. S. Savage, A. T. Stelbovics, and M. C. Zammit, "Convergent close-coupling approach to light and heavy projectile scattering on atomic and molecular hydrogen", J. Phys. B **50**, 202001 (2017) (cit. on p. 108).

[201]M. C. Zammit, "Electron and positron scattering from diatomic molecules", PhD thesis (Curtin University, 2015) (cit. on pp. 108, 127, 281).

[202]J. S. Savage, "Scattering from diatomic molecules in the spheroidal convergent close-coupling formalism", PhD thesis (Curtin University, 2018) (cit. on pp. 108, 111, 120, 123, 124, 127, 138, 213, 226, 280).

[203]R. Utamuratov, A. S. Kadyrov, D. V. Fursa, M. C. Zammit, and I. Bray, "Two-center close-coupling calculations of positron-molecular-hydrogen scattering", Phys. Rev. A **92**, 32707 (2015) (cit. on pp. 109, 285).

[204]H. A. Yamani and W. P. Reinhardt, "L^2 discretizations of the continuum: Radial kinetic energy and Coulomb Hamiltonian", Phys. Rev. A **11**, 1144 (1975) (cit. on p. 114).

[205]E. Bank and M. E. Ismail, "The attractive Coulomb potential polynomials", Constr. Approx. **1**, 103 (1985) (cit. on p. 114).

[206]A. T. Stelbovics, "L^2 discretisation of the Coulomb problem in an orthonormal Laguerre function basis", J. Phys. B **22**, L159 (1989) (cit. on p. 114).

[207]W. P. Reinhardt, "L^2 discretization of atomic and molecular electronic continua: Moment, quadrature and J-matrix techniques", Comput. Phys. Commun. **17**, 1 (1979) (cit. on p. 114).

[208]S. Singh, W. F. Richards, J. R. Zinecker, and D. R. Wilton, "Accelerating the convergence of series representing the free space periodic Green's function", IEEE Trans. Antennas Propag. **38**, 1958 (1990) (cit. on p. 123).

[209]U. Fantz and D. Wünderlich, "Franck-Condon factors, transition probabilities, and radiative lifetimes for hydrogen molecules and their isotopomeres", At. Data Nucl. Data Tables **92**, 853 (2006) (cit. on pp. 133, 135).

[210]S. C. Ross, T. Yoshinari, Y. Ogi, and K. Tsukiyama, "Decay dynamics of the long-range $\bar{H}\,^1\Sigma_g^+$ state of D_2 and H_2: Experiment and theory", J. Chem. Phys. **125**, 133205 (2006) (cit. on p. 133).

[211]W. Kołos and L. Wolniewicz, "Polarizability of the hydrogen molecule", J. Chem. Phys. **46**, 1426 (1967) (cit. on p. 144).

[212]J.-S. Yoon, M.-Y. Song, D.-C. Kwon, H. Choi, C.-G. Kim, and V. Kumar, "Electron impact cross sections of vibrationally and electronically excited molecules", Phys. Rep. **543**, 199 (2014) (cit. on p. 159).

[213]N. F. Lane, "The theory of electron-molecule collisions", Rev. Mod. Phys. **52**, 29 (1980) (cit. on pp. 160, 161).

[214]B. I. Schneider and L. A. Collins, "Electronic excitation of the $b\ ^3\Sigma_u^+$ state of H_2 by electron impact in the linear algebraic approach", J. Phys. B **18**, L857 (1985) (cit. on pp. 160, 161).

[215]K. L. Baluja, C. J. Noble, and J. Tennyson, "Electronic excitation of the $b\ ^3\Sigma_u^+$ state of H_2 using the R-matrix method", J. Phys. B At. Mol. Phys. **18**, L851 (1985) (cit. on pp. 160, 161).

[216]J. D. Gorfinkiel and J. Tennyson, "Electron impact ionization of small molecules at intermediate energies: the molecular R-matrix with pseudostates method", J. Phys. B **38**, 1607 (2005) (cit. on pp. 160, 161).

[217]M. C. Zammit, J. S. Savage, J. Colgan, D. V. Fursa, D. P. Kilcrease, I. Bray, C. J. Fontes, P. Hakel, and E. Timmermans, "State-resolved photodissociation and radiative association data for the molecular hydrogen ion", Astrophys. J. **851**, 64 (2017) (cit. on p. 161).

[218]A. Dalgarno and T. L. Stephens, "Discrete absorbtion and photodissociation of molecular hydrogen", Astrophys. J. **160**, L107 (1970) (cit. on p. 162).

[219]U. Fantz, B. Schalk, and K. Behringer, "Calculation and interpretation of the continuum radiation of hydrogen molecules", New J. Phys. **2**, 7 (2000) (cit. on p. 162).

[220]M. A. Morrison and W. Sun, "How to calculate rotational and vibrational cross sections for low-energy electron scattering from diatomic molecules using close-coupling techniques", in *Computational methods for electron-molecule collisions*, edited by W. Huo and F. A. Gianturco (Springer, Boston, MA, 1994) (cit. on pp. 163, 170).

[221]J.-S. Yoon, M.-Y. Song, J.-M. Han, S. H. Hwang, W.-S. Chang, B. Lee, and Y. Itikawa, "Cross sections for electron collisions with hydrogen molecules", J. Phys. Chem. Ref. Data **37**, 913 (2008) (cit. on pp. 163, 172, 179, 180).

[222]J. Tennyson, S. Rahimi, C. Hill, L. Tse, A. Vibhakar, D. Akello-Egwel, D. B. Brown, A. Dzarasova, J. R. Hamilton, D. Jaksch, S. Mohr, K. Wren-Little, J. Bruckmeier, A. Agarwal, K. Bartschat, A. Bogaerts, J. P. Booth, M. J. Goeckner, K. Hassouni, Y. Itikawa, B. J. Braams, E. Krishnakumar, A. Laricchiuta, N. J. Mason, S. Pandey, Z. L. Petrovic, Y. K. Pu, A. Ranjan, S. Rauf, J.

Schulze, M. M. Turner, P. Ventzek, J. C. Whitehead, and J. S. Yoon, "QDB: A new database of plasma chemistries and reactions", Plasma Sources Sci. Technol. **26**, 055014 (2017) (cit. on p. 163).

[223]J. D. Gorfinkiel, L. A. Morgan, and J. Tennyson, "Electron impact dissociative excitation of water within the adiabatic nuclei approximation", J. Phys. B **35**, 543 (2002) (cit. on p. 163).

[224]J. Tennyson and C. S. Trevisan, "Low energy electron collisions with molecular hydrogen", Contrib. to Plasma Phys. **42**, 573 (2002) (cit. on p. 163).

[225]P. G. Burke and J. Tennyson, "*R*-matrix theory of electron molecule scattering", Mol. Phys. **103**, 2537 (2005) (cit. on p. 163).

[226]K. Chakrabarti and J. Tennyson, "*R*-matrix calculation of the continuum states of carbon monoxide", J. Phys. B **40**, 2135 (2007) (cit. on p. 163).

[227]W. J. Brigg, J. Tennyson, and M. Plummer, "*R*-matrix calculations of low-energy electron collisions with methane", J. Phys. B **47**, 185203 (2014) (cit. on p. 163).

[228]K. Chakrabarti and J. Tennyson, "*R*-matrix calculation of electron collisions with the BF^+ molecular ion", J. Phys. B **42**, 105204 (2009) (cit. on p. 163).

[229]K. Chakrabarti, A. Dora, R. Ghosh, B. S. Choudhury, and J. Tennyson, "*R*-matrix study of electron impact excitation and dissociation of CH^+ ions", J. Phys. B **50**, 175202 (2017) (cit. on p. 163).

[230]D. T. Stibbe and J. Tennyson, "Electron-H_2 scattering resonances as a function of bond length", J. Phys. B **31**, 815 (1998) (cit. on pp. 165, 229, 239, 242, 243, 244, 246).

[231]G. G. Ohlsen, "Kinematic relations in reactions of the form A+B→C+D+E", Nucl. Instruments Methods **37**, 240 (1965) (cit. on p. 168).

[232]H. Fuchs, "On cross section transformations in reactions with three outgoing fragments", Nucl. Instruments Methods Phys. Res. **200**, 361 (1982) (cit. on p. 168).

[233]J. A. Tostevin, S. Rugmai, and R. C. Johnson, "Coulomb dissociation of light nuclei", Phys. Rev. C **57**, 3225 (1998) (cit. on p. 168).

[234]L. Malegat, "DCS - a program for calculating differential cross sections for the electronic excitation of diatomic molecules at fixed nuclei", Comput. Phys. Commun. **60**, 391 (1990) (cit. on p. 171).

[235]C. M. Samuell and C. S. Corr, "Low-pressure hydrogen plasmas explored using a global model", Plasma Sources Sci. Technol. **25**, 015014 (2016) (cit. on p. 172).

[236]K. Sawada and M. Goto, "Rovibrationally resolved time-dependent collisional-radiative model of molecular hydrogen and its application to a fusion detached plasma", Atoms **4**, 29 (2016) (cit. on pp. 172, 208).

[237]R. Celiberto, M. Capitelli, A. Laricchiuta, M. Capitelli, and A. Laricchiuta, "Towards a cross section database of excited atomic and molecular hydrogen", Phys. Scr. **T96**, 32 (2002) (cit. on p. 172).

[238]M. J. Redmon, B. C. Garrett, L. T. Redmon, and C. W. McCurdy, "Improved impact-parameter method for electronic excitation and dissociation of diatomic molecules by electron impact", Phys. Rev. A **32**, 3354 (1985) (cit. on p. 172).

[239]X. Liu, D. E. Shemansky, P. V. Johnson, C. P. Malone, M. A. Khakoo, and I. Kanik, "Electron and photon dissociation cross sections of the H_2 singlet ungerade continua", J. Phys. B **45**, 105203 (2012) (cit. on pp. 175, 176).

[240]S. J. B. Corrigan, "Dissociation of molecular hydrogen by electron impact", J. Chem. Phys. **43**, 4381 (1965) (cit. on p. 179).

[241]D. A. Erwin and J. A. Kunc, "Rate coefficients for some collisional processes in high-current hydrogen discharges", IEEE Transactions on Plasma Science **PS-11**, 266 (1983) (cit. on pp. 189, 190, 194, 195).

[242]J. Komppula and O. Tarvainen, "VUV diagnostics of electron impact processes in low temperature molecular hydrogen plasma", Plasma Sources Sci. Technol. **24**, 045008 (2015) (cit. on p. 208).

[243]F. Gaboriau and J. P. Boeuf, "Chemical kinetics of low pressure high density hydrogen plasmas: Application to negative ion sources for ITER", Plasma Sources Sci. Technol. **23**, 065032 (2014) (cit. on p. 208).

[244]D. Reiter, M. Baelmans, and P. Börner, "The eirene and B2-eirene codes", Fusion Sci. Technol. **47**, 172 (2005) (cit. on p. 208).

[245]S. J. Houston, N. Ozak, J. Young, T. E. Cravens, and D. R. Schultz, "Jovian auroral ion precipitation: Field-aligned currents and ultraviolet emissions", J. Geophys. Res. Sp. Phys. **123**, 2257 (2018) (cit. on p. 208).

[246]V. A. Shakhatov and Y. A. Lebedev, "Collisional-radiative model of hydrogen low-temperature plasma: Processes and cross sections of electron-molecule collisions", High Temp. **49**, 257 (2011) (cit. on p. 208).

[247]A. Eviatar, M. Podolak, and J. D. Richardson, "Atomic and molecular hydrogen from Titan in the Kronian magnetosphere", J. Geophys. Res. **95**, 21007 (1990) (cit. on p. 208).

[248]J.-C. Gerard and V. Singh, "A model of energy deposition of energetic electrons and EUV emission in the Jovian and Saturnian atmospheres and implications", J. Geophys. Res. **87**, 4525 (1982) (cit. on p. 208).

[249]A. Dalgarno, M. B. McElroy, and R. J. Moffett, "Electron temperatures in the ionosphere", Planet. Space Sci. **11**, 463 (1963) (cit. on p. 208).

[250]T. E. Sharp, "Potential-energy curves for molecular hydrogen and its ions", At. Data Nucl. Data Tables **2**, 119 (1971) (cit. on p. 211).

[251]I. Bray and D. V. Fursa, "Convergent close-coupling method: A "complete scattering theory"?", Phys. Rev. Lett. **76**, 2674 (1996) (cit. on p. 215).

[252]X. Ren, I. Bray, D. V. Fursa, J. Colgan, M. S. Pindzola, T. Pflüger, A. Senftleben, S. Xu, A. Dorn, and J. Ullrich, "Electron-impact ionization of helium: A comprehensive experiment benchmarks theory", Phys. Rev. A **83**, 052711 (2011) (cit. on p. 215).

[253]I. Bray, D. V. Fursa, A. S. Kadyrov, A. T. Stelbovics, A. S. Kheifets, and A. M. Mukhamedzhanov, "Electron- and photon-impact atomic ionisation", Phys. Rep. **520**, 135 (2012) (cit. on p. 215).

[254]H. Feshbach, "Unified theory of nuclear reactions", Ann. Phys. (N. Y). **5**, 357 (1958) (cit. on p. 216).

[255]R. Celiberto, R. K. Janev, J. M. Wadehra, and J. Tennyson, "Dissociative electron attachment to vibrationally excited H_2 molecules involving the $^2\Sigma_g^+$ resonant Rydberg electronic state", Chem. Phys. **398**, 206 (2012) (cit. on p. 216).

[256]I. Bray and D. V. Fursa, "Calculation of ionization within the close-coupling formalism", Phys. Rev. A **54**, 2991 (1996) (cit. on p. 232).

[257]D. T. Stibbe and J. Tennyson, "Ab initio calculations of vibrationally resolved resonances in electron collisions with H_2, HD, and D_2", Phys. Rev. Lett. **79**, 4116 (1997) (cit. on p. 239).

[258]J. Comer and F. H. Read, "Potential curves and symmetries of some resonant states of H_2^-", J. Phys. B At. Mol. Phys. **4**, 368 (1971) (cit. on pp. 241, 242, 243, 244, 247, 249, 250).

[259]U. Fano, "Effects of configuration interaction on intensities and phase shifts", Phys. Rev. **124**, 1866 (1961) (cit. on p. 242).

[260]Y. K. Yang, Y. Cheng, Y. Wu, Y. Z. Qu, J. G. Wang, and S. B. Zhang, "Particle scattering and resonances involving avoided crossing", New J. Phys. **22**, 123022 (2020) (cit. on p. 242).

[261]C. E. Kuyatt, J. A. Simpson, and S. R. Mielczarek, "Resonances in electron scattering from H_2, HD, and D_2", J. Chem. Phys. **44**, 437 (1966) (cit. on pp. 243, 244).

[262]N. F. Lane and S. Geltman, "Differential elastic and rotational excitation cross sections for electron-H_2 scattering", Phys. Rev. **184**, 46 (1969) (cit. on p. 252).

[263]M. A. Morrison, A. N. Feldt, and D. Austin, "Adiabatic approximations for the nuclear excitation of molecules by low-energy electron impact: Rotational excitation of H_2", Phys. Rev. A **29**, 2518 (1984) (cit. on p. 252).

[264]E. S. Chang and A. Temkin, "Rotational excitation of diatomic molecular systems. II. H_2^+", J. Phys. Soc. Japan **29**, 172 (1970) (cit. on p. 252).

[265]N. Chandra, "Rotational excitation in e-N_2 scattering", J. Phys. B At. Mol. Phys. **8**, 1338 (1975) (cit. on p. 252).

[266]A. M. Arthurs and A. Dalgarno, "The theory of scattering by a rigid rotator", Proc. Natl. Acad. Sci. U. S. A. **256**, 540 (1960) (cit. on p. 252).

[267]T. Mukherjee and A. S. Ghosh, "Rotational excitation in e^+-H_2^+ scattering", Phys. Rev. A **52**, 1772 (1995) (cit. on p. 252).

[268]S. Ray and A. K. Barua, "Rotational excitation of HD+ by electron and positron impact", J. Phys. B At. Mol. Phys. **8**, 2283 (1975) (cit. on p. 252).

[269]P. Baille, J. W. Darewych, and J. G. Lodge, "Elastic scattering and rotational excitation of molecular hydrogen by low energy positrons", Can. J. Phys. **52**, 667 (1974) (cit. on p. 252).

[270]G. D. Meneses, L. M. Brescansin, M. T. Lee, S. E. Michelin, L. E. Machado, and G. Csanak, "Electron-impact excitation of the $d\ ^3\Pi_u(v = 0, 1, 2, 3; N = 1)$ states of H_2: Cross sections and anisotropy parameters", Phys. Rev. A **52**, 404 (1995) (cit. on pp. 252, 270, 277, 278).

[271]M. T. Lee, S. E. Michelin, G. D. Meneses, L. M. Brescansin, and L. E. Machado, "State-to-state cross sections and anisotropy parameters for the excitation of the $c\ ^3\Pi_u(v = 0, 1, 2, 3; N = 2)$ states of H_2 by electron impact", J. Phys. B **29**, 2337 (1996) (cit. on p. 252).

[272]I. Bray and A. T. Stelbovics, "Calculation of electron scattering on hydrogenic targets", Adv. At. Mol. Opt. Phys. **35**, 209 (1995) (cit. on p. 254).

[273]J. L. Meunier, "A simple demonstration of the Wigner-Eckart theorem", Eur. J. Phys. **8**, 114 (1987) (cit. on p. 255).

[274]S. Briefi and U. Fantz, "A revised comprehensive approach for determining the H_2 and D_2 rovibrational population from the Fulcher-α emission in low temperature plasmas", Plasma Sources Sci. Technol. **29**, 125019 (2020) (cit. on p. 270).

[275]J. W. Maseberg, K. Bartschat, and T. J. Gay, "Threshold alignment reversal and circularly polarized fluorescence in rotationally resolved H_2", Phys. Rev. Lett. **111**, 253201 (2013) (cit. on pp. 270, 271, 272, 273, 274, 276, 277, 278, 279, 284).

[276]K. Blum, *Density matrix theory and applications*, 3rd (Springer, Berlin, 2012) (cit. on pp. 272, 274, 276).

[277]K. Bartschat, H. J. Andrä, and K. Blum, "Selective valence electron transfer in alkali atom-alkali ion collisions", Zeitschrift für Phys. A Atoms Nucl. **314**, 257 (1983) (cit. on p. 274).

[278]J. W. McConkey, S. Trajmar, J. C. Nickel, and G. Csanak, "A polarisation correlation study of the excitation of the H_2 $d\ ^3\Pi_u(v_1 = 0, N_1 = 1)$ level by electron impact", J. Phys. B At. Mol. Phys. **19**, 2377 (1986) (cit. on p. 277).

[279]P. Baltayan and O. Nedelec, "Relative intensities and polarizations in H_2 rotational lines excited by electron impact", J. Phys. Fr. **36**, 125 (1975) (cit. on pp. 277, 278).

[280]P. Cahill, R. Schwartz, and A. N. Jette, "Polarization of light emitted from the excitation of H_2 by electron impact", Phys. Rev. Lett. **19**, 283 (1967) (cit. on p. 277).

[281]D. Yamasaki, S. Kado, B. Xiao, Y. Iida, S. Kajita, and S. Tanaka, "Experimental evaluation of predissociation rate in $v = 4$ state usable for analysis of H_2 Fulcher-α band emission", J. Phys. Soc. Japan **75**, 044501 (2006) (cit. on p. 278).

[282]T. Fujimoto, "Introduction", in *Plasma polarization spectroscopy*, edited by T. Fujimoti and A. Iwamae, 1st ed. (Springer-Verlag, Berlin, Germany, 2008) Chap. 1, pp. 1–12 (cit. on p. 279).

[283]U. S. Rehill, **L. H. Scarlett**, N. Mori, I. Bray, and D. Fursa, "Rovibrational excitation of $H_2(X\,^1\Sigma_g^+)$ by electron impact with the molecular convergent close coupling method", **In Preparation** (2022) (cit. on p. 283).

[284]M. Padovani, S. Bialy, D. Galli, A. V. Ivlev, S. Belli, T. Grassi, **L. H. Scarlett**, U. S. Rehill, M. C. Zammit, D. V. Fursa, and I. Bray, "Cosmic rays in molecular clouds probed by H_2 rovibrational lines – Perspectives for the James Webb Space Telescope", Astron. Astrophys. **In Press** (2022) (cit. on p. 283).

[285]I. Bray, H. Hayat, D. V. Fursa, A. S. Kadyrov, A. W. Bray, and M. Cytowski, "Calculations of electron scattering on H-like ions", Phys. Rev. A **101**, 022703 (2020) (cit. on p. 285).

[286]I. B. Abdurakhmanov, K. Massen-Hane, S. U. Alladustov, J. J. Bailey, A. S. Kadyrov, and I. Bray, "Ionization and electron capture in collisions of bare carbon ions with hydrogen", Phys. Rev. A **98**, 062710 (2018) (cit. on p. 285).

[287]D. A. Varshalovich, A. N. Moskalev, and V. K. Khersonkii, *Quantum theory of angular momentum* (World Scientific, Singapore, 1988) (cit. on p. 296).